University of Southampton
Faculty of Engineering
Department of Electronics and Computer Science
Southampton S017 1BJ

Reduced-Complexity Near-Optimal Ant-Colony-Aided Multi-User Detection For CDMA Systems

by

Chong Xu
M. Sc.

A doctoral thesis submitted in partial fulfilment of the
requirements for the award of Doctor of Philosophy
at the University of Southampton

June 2009

SUPERVISOR: *Professor Lajos Hanzo*
Dipl Ing, MSc, PhD, FIEEE
Chair of Telecommunications
Professor Lie-Liang Yang
MSc, PhD, SMIEEE
Department of Electronics and Computer Science
University of Southampton
Southampton SO17 1BJ
United Kingdom

This thesis is dedicated to:
My husband and family.

UNIVERSITY OF SOUTHAMPTON

ABSTRACT

FACULTY OF ENGINEERING AND APPLIED SCIENCE
DEPARTMENT OF ELECTRONICS AND COMPUTER SCIENCE

Doctor of Philosophy

Reduced-Complexity Near-Optimal Ant-Colony-Aided Multi-User Detection for CDMA Systems

by Chong Xu

Reduced-complexity near-maximum-likelihood Ant-Colony Optimization (ACO) assisted Multi-User Detectors (MUDs) are proposed and investigated. The exhaustive search complexity of the optimal detection algorithm may be deemed excessive for practical applications. For example, a Space-Time Block Coded (STBC) two transmit assisted $K = 32$-user system has to search through the candidate-space for finding the final detection output during 2^{64} times per symbol duration by invoking the Euclidean-distance-calculation of a 64-element complex-valued vector. Hence, a near-optimal or near-ML MUDs are required in order to provide a near-optimal BER performance at a significantly reduced complexity.

Specifically, the ACO assisted MUD algorithms proposed are investigated in the context of a Multi-Carrier DS-CDMA (MC DS-CDMA) system, in a Multi-Functional Antenna Array (MFAA) assisted MC DS-CDMA system and in a STBC aided DS-CDMA system. The ACO assisted MUD algorithm is shown to allow a fully loaded MU system to achieve a near-single user performance, which is similar to that of the classic Minimum Mean Square Error (MMSE) detection algorithm. More quantitatively, when the STBC assisted system support $K = 32$ users, the complexity imposed by the ACO based MUD algorithm is a fraction of 1×10^{-18} of that of the full search-based optimum MUD.

In addition to the hard decision based ACO aided MUD a soft-output MUD was also developed, which was investigated in the context of an STBC assisted DS-CDMA system using a three-stage concatenated, iterative detection aided system. It was demonstrated that the soft-output system is capable of achieving the optimal performance of the Bayesian detection algorithm.

Acknowledgements

I would like to express my heartfelt gratitude to Professor Lajos Hanzo for his interest in my work, consistent encouragement and outstanding guidance. My research during the PhD years was an unforgettable and fruitful one because of him. I have gained a lot while working with him, not only expertise knowledge, research methodologies, but also a role model and invaluable friendship.

I would also like to express my gratitute to Professor Lie-Liang Yang, for his most important guidance at the initial stage which helps me to open the door of research as well as for his continous support throughout my PhD study. Without the first several key steps guided by him, the following exploration could never be as smooth as it was.

I would also like to thank for Mrs. Ritta Hanzo and Mrs. Denise Harvey for their enormous support and help during the correction of the thesis.

I would also like to thank Dr. Rob G. Maunder for his insightful suggestion and unselfish share of his knowledge, Dr. Augustine Koh for his proof reading and consistent encouragement, Dr. Mohammed El-Hajjar, Dr. Li Wang for their practical help and Professor Sheng Chen who has given me the first encouragement in my research life.

Special thanks goes to Dr. Tao Sun, who has offered me his invaluable trust and tremendous support during my difficult times.

Last but not the least, I would like to thank for my parents, without their enormous support, I could achieve nothing.

List of Publications

1. **C. Xu, B. Hu, L.-L. Yang and L. Hanzo**, "Multi-functional antenna array assisted MC DS-CDMA using downlink preprocessing based on singular value decomposition", Proceedings of the IEEE Vehicular Technology conference, Spring, Dublin, Ireland, April 2007, pp. 1936-1940.

2. **C. Xu, L.-L. Yang and L. Hanzo**, "Ant-colony-based multiuser detection for MC DS-CDMA systems", Proceedings of the IEEE Vehicular Technology conference, Fall, Baltimore, U.S.A., October 2007, pp. 960–964.

3. **C. Xu, B. Hu, L.-L. Yang and L. Hanzo**, "Ant-colony-based multiuser detection for multi-functional antenna array assisted MC DS-CDMA system", IEEE Transactions on Vehicular Technology, vol. 57, Janurary 2008, pp. 658-663.

4. **C. Xu, R. G. Maunder, L.-L. Yang and L. Hanzo**, "Near-optimum soft-output ant-colony-optimization based multiuser detection for the DS-CDMA", Proceedings of the IEEE International Conference on Communications, Beijing, China, May 2008, pp. 795-799.

5. **C. Xu, R. G. Maunder, L.-L. Yang and L. Hanzo**, "Near-optimum multiuser detectors using soft-output ant-colony-optimization for the DS-CDMA uplink", IEEE Signal Processing Letters, vol. 16, no. 2, January 2009, pp. 137-140.

6. **C. Xu, L.-L. Yang and L. Hanzo**, "Ant-Colony Based Near-ML Space-Time Multiuser Detection for the STBC Assisted DS-CDMA Uplink", In Vehicular Technology Conference, Taipei, May 2010, pp. 1-5.

7. **C. Xu, M. El-Hajjar, R. G. Maunder, L.-L. Yang and Hanzo, L.**, "Performance of the Space-Time Block Coded DS-CDMA Uplink Employing Soft-Output ACO-Aided Multiuser Space-Time Detection and Iterative Decoding", In Vehicular Technology Conference, Taipei, May 2010, pp. 1-5.

Contents

Chapter 1

Introduction

1.1 Trends in Wireless Communications

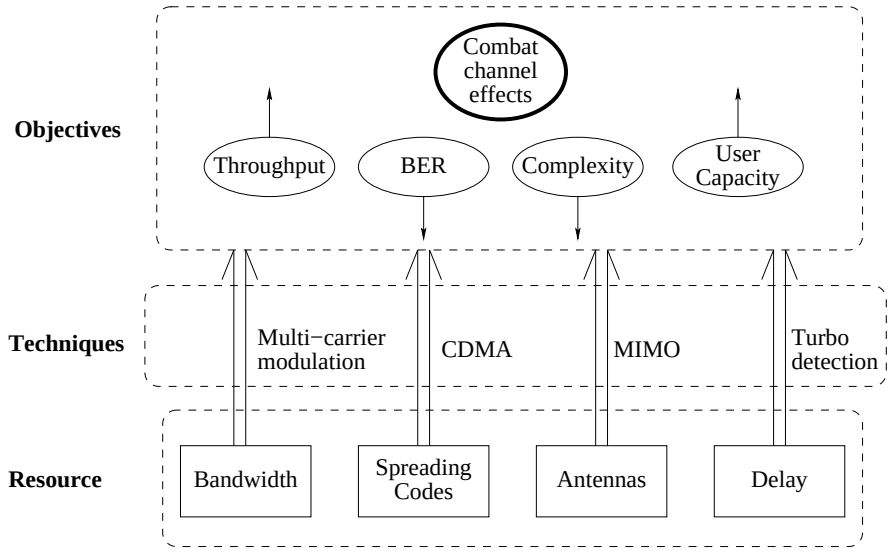

Figure 1.1: Stylized inter-relationship of the objectives, techniques and resources in wireless communication systems.

The trends in the development of wireless communcations are motivated by making efficient use of the limited resources, in order to achieve either an increased throughput, a reduced Bit Error Ratio (BER), or to reduce the system's complexity and hence cost as well as power consumption per user, as shown in the stylized illustration of Fig. 1.3. Below we will provide a brief literature review of the related techniques.

1.1.1 MC DS-CDMA

As a state-of-the-art technique that may potentially be employed by the Long-Term Evolution (LTE) [1, 2] initiative in order to resolve the problems imposed by the high data rates required by future generations of wireless communication systems, the research of Multi-Carrier (MC) Direct Sequence Code-Division Multiple Access (DS-CDMA) [3] endeavours to support reliable communications over hostile

wireless radio links.

The main limitation imposed by high-data-rate wireless communications is constituted by the Inter-Symbol-Interference (ISI), which severely degrades the attainable system performance, when the symbol duration T_s is lower than the delay spread of the wireless channel. If the transmission rate is high, the multipath components induced by a symbol may overlap with those of other symbols, resulting in ISI.

MC DS-CDMA aims for supporting a high data rate by extending the symbol-duration with the aid of a serial-parallel (SP) converter and then mapping these reduced-rate streams to a number of narrowband subcarriers.

It is also possible to map the same bits to several parallel subcarriers, which may fade independently, provided that their frequency-seperation is higher than the channel's coherence bandwidth. This can also be achieved by spreading each subcarrier's data across the entire bandwidth using a spreading code and overlaying K spreading codes on top of each other. This results in valuable frequency-diversity gains. More explicitly, if N_s-chip Walsh Hadamard (WH) spreading sequences are applied in the Frequency-Domain (FD) for spreading the signal accross the different subcarriers, the number of users supported by the system is N_s. However, the Bit-Error-Ratio (BER) of FD-spreading may be significantly worse than that of FD-repetition, which on the other hand has a lower effective throughput.

Below, we will briefly outline the evolution of MC CDMA techniques in Table 1.1.

Table 1.1: Main contributions on MC DS-CDMA systems.

Year	Author(s)	Contribution
1993	Yee, Linnartz and Fettweis [3]	A novel digital modulation/multiple access technique referred to as MC-CDMA is presented, where the data symbols are mapped to multiple reduced-rate substreams. This scheme is evaluated in an indoor wireless multipath radio channel.
1993	Fazel and Papke [4]	The concept of combining OFDM with the CDMA technique is proposed.
1993	Chouly, Brajal and Jourdan [5]	A novel design technique is introduced that combines an orthogonal multicarrier transmission scheme with DS-CDMA systems.
1993	Vandendorpe [6]	The so-called multitone CDMA scheme is proposed, which relies on overlapping subcarries and hence supports an increased number of users with in a given bandwidth.

Continued on next page

Table 1.1 Main contributions on MC DS-CDMA systems.
continued from previous page

Year	Author(s)	Contribution
1994	Dasilva and Sousa [7]	Multicarrier DS-CDMA is proposed as a means of reducing the amount of interference inflicted. Furthermore, a range of spreading codes and chip pulse shapes are proposed for minimizing the multiple-access interference in case of quasi-synchronous operation.
1995	Vandendorpe [8]	The performance of multitone CDMA systems is analyzed in an indoor wireless channel. It is demonstrated that the extended symbol duration advocated is favourable in terms of multipath interference reduction.
1996	Sourour and Nakagawa [9]	The multicarrier DS-CDMA system presented spreads each of the S/P-converted data branches and transmits them using orthogonal subcarriers, while efficiently exploiting the available transmission band-width, reducing the effects of multipath interference as well as achieving a beneficial frequency/time diversity.
1997	Prasad and Hara [10]	An overview of multiple access schemes based on a combination of CDMA and multicarrier techniques, such as MC- CDMA, MC DS-CDMA and MT-CDMA, is presented.
2002	Yang and Hanzo [11]	A class of generalized MC DS-CDMA schemes is proposed and its performance is characterized for transmission over multipath Nakagami-fading channels. This scheme subsumes the subclasses of multitone DS-CDMA and orthogonal MC DS-CDMA as special cases.
2003	Yang and Hanzo [12]	The investigation of generalized MC DS-CDMA is extended by considering two practical chip-waveforms, namely, the time-domain half-sine and raised-cosine chip waveforms, in addition to the rectangular chip-waveform.
2003	Hanzo, Yang, Kuan and Yen [13]	A detailed discussion of multicarrier CDMA schemes is provided, including the family of non-frequency-hopping MC CDMA and the class of frequency-hopping assisted MC CDMA schemes. The performance of different MC CDMA systems is investigated for transmission over frequency-selective Rayleigh fading channels.

1.1.2 Multi-Input Multi-Output Systems

Multi-Input Multi-Output (MIMO) systems employ several transmit and/or receive antennas to achieve an increased throughput, and/or to support more users and/or to reduce the BER by achieving a Signal-to-Noise-Ratio (SNR) gain, as alluded to in the context of Fig. 1.1.

Naturally, this is achieved at an increased cost, but without increasing the transmit power or the bandwidth required.

Hence, MIMO techniques constitute attractive potential solutions for next generation communication systems, which were combined with OFDM techniques for employment in the IEEE 802.16e WIMAX broadband mobile standard [14] as well as in the Third-Generation Partnership Project Long-Term Evolution (3GPP-LTE) [15] initiative.

The initial concept of MIMOs originates from the 1970s and was proposed by Kaye and George [16]. Bell Labs provided the first laboratory prototype to demonstrate a practical spatial multiplexing gain in 1998. The family of MIMO techniques may be classified into four basic types: beamforming, Space-Time Coding (STC), Spatial Division Multiplexing (SDM) as in the Bell Laboratories-Layered-Space-Time (BLAST) technique and Spatial Division Multiple Access (SDMA) [17].

In this treatise, we will consider both antenna diversity and beamforming, which are amalgamated into Multi-Functional Antenna Arrays (MFAA), as detailed in later Chapter 4, while the emphasis of Chapters 5 and 7 is on STBCs. In Table 1.2, we will briefly outline the main contributions to the broad field of MIMO techniques.

Table 1.2: Main contributions on MIMO techniques.

Year	Author(s)	Contribution
1990	Swales, Beach, Edwards and McGeehan [18]	A multiple-beam adaptive base-station antenna is proposed, which is capable of resolving the angular distribution of mobile users and of directing the transmitter/receiver antenna beams toward the desired mobile users.
1991	Anderson, Millnert, Viberg and Wahlberg [19]	An application of adaptive angularly selective antenna techniques is presented for the sake of increasing the channel capacity.
1996	Foschini [20]	The concept of the BLAST SDM architecture is introduced.
1997	Paulraj and Papadias [21]	An overview of space-time signal processing techniques is provided, emphasizing the capacity versus diversity trade-offs in MIMO systems.

Continued on next page

Table 1.2 Main contributions on MIMO techniques.

continued from previous page

Year	Author(s)	Contribution
1997	Godara [22, 23]	In Part I a comprehensive treatment of antenna arrays is provided with the aim of improving the efficiency of mobile communications systems. The focus of Part II is on different beamforming schemes, adaptive array-weight adjustment algorithms and direction-of-arrival estimation methods.
1998	Affes and Mermelstein [24]	A spatio-temporal array-receiver (STAR) using a new space/time structure is proposed for asynchronous CDMA, offering a high capacity enhancement potential at a relatively low computational complexity.
1998	Wong, Lok, Lehnert and Zoltowski [25]	A linear receiver is designed for antenna array aided CDMA systems.
1998	Wolniansky, Foschini, Golden and Valenzuela [26]	A wireless communication architecture known as Vertical BLAST (V-BLAST) is proposed and its throughput potential is quantified.
1999	Li and Sollenberger [27]	Adaptive antenna arrays are designed for OFDM systems subjected to cochannel interference.
1999	Dell'Anna and Aghvami [28]	The performance of an array of antennas combined with a Rake receiver at the base station of a wideband CDMA system is investigated in a single-user scenario.
2000	Onggosanusi, Sayeed Veen [29]	A canonical space-time characterization of wireless channels is provided.
2001	Herscovici and Christodoulou [30]	Diverse applications of smart antennas in DS- CDMA systems are presented.
2002	Zekavat, Nassar and Shattil [31]	A novel smart antenna aided multi-tone-CDMA system is proposed.
2002	Trees [32]	An in-depth overview of optimum beamforming schemes is provided.

Continued on next page

Table 1.2 Main contributions on MIMO techniques.
continued from previous page

Year	Author(s)	Contribution
2002	Blogh and Hanzo [33]	A detailed portrayal of beamforming techniques is provided, which are then combined with High-Speed Packet Access (HSPA)-style adaptive modulation and the resultant tele-traffic improvements are quantified for both Frequency Division Duplex (FDD) and for Time Division Duplex (TDD) HSPA-style systems.
2002	Hanzo, Wong and Yee [34]	An overview of adaptive modulation aided Space-Time Coded TDMA, CDMA, MC-CDMA and OFDM Systems is provided.
2003	Hanzo, Munster, Choi and T.Keller [17]	A detailed overview of MIMO-aided OFDM systems is provided, with special emphasis on OFDM and MC-CDMA systems.

1.1.3 Iterative Detection

The concept of concatenated codes was originally proposed in [35]. However, due to its complexity which was deemed to be excessive in the 1960s, it failed to stimulate significant research interests. Following the discovery of turbo codes [36], it was demonstrated that efficient iterative decoding of concatenated codes can be carried out at a low complexity by employing simple constituent codes. Since then, the iterative decoding of concatenated codes has inspired numerous authors to extend the technique to other transmission schemes consisting of a concatenation of two or more constituent decoding stages [37–51]. For example, the turbo principle was extended to multiple parallel concatenated codes in 1995 [37], to serially concatenated block- and convolutional codes in 1996 [38], and to multiple serially concatenated codes in 1998 [39].

A few further applications of the turbo concept are listed below. For example, in [48], iterative decoding was invoked for exchanging extrinsic information between a soft-output symb ol detector and an outer channel decoder in order to combat the detrimental effects of inter-symbol interference (ISI). In [44] iterative decoding was carried out by exchanging extrinsic information between an outer convolutional decoder and an inner Trellis Coded Modulation (TCM) decoder. The authors of [45, 46] proposed Bit-Interleaved Coded Modulation (BICM), while in [45] the employment of the turbo principle was considered for iterative soft-demapping in the context of BICM, where the soft demapper was used between the multilevel demodulator and the channel decoder. In addition, iterative multiuser detection and channel decoding was proposed in [51] for Code-Division Multiple-Access (CDMA) schemes. Finally, in [52], a turbo coding scheme was proposed for an orthogonal STBC scheme which was the inner code combined with an additional block code as the outer channel code of the concatenated scheme considered.

It was shown in [53] that a recursive inner code is required in order to maximise the achievable interleaver gain and to avoid having a BER floor, when employing iterative decoding. This principle

has been adopted by several authors for designing powerful serially concatenated schemes, where unity-rate inner codes were employed for designing high-performance, yet low-complexity turbo codes suitable for bandwidth and power limited systems having stringent BER requirements [54–58].

1.1.4 Multi-User Detection

All the above-mentioned state-of-the-art arrangements, namely MC DS-CDMA, MIMO techniques and iterative detection are readily applicable to single-user systems in order to improve their throughput and/or their BER performance. However, to be more realistic, all these techniques should be investigated in the context of multi-user wireless systems, where the Multi-User Interference (MUI) is also taken into account. Hence the concept of MU-MIMOs was proposed in [59] and attracted further in-depth investigations in [60]- [61].

Hence, below we will provide a rudimentary review of a range of related topics. It is plausible that the binary vector encompassing all the MK BPSK-modulated bits transmitted by the K users over M antennas may be optimally detected by the Maximum Likelihood (ML) algorithm upon exhaustively calculating the likelihood of each of the 2^{MK} vectors being transmitted. However, the complexity imposed by the ML algorithm may become excessive. Therefore, the quest for algorithms capable of approaching the BER performance of the ML algorithm at a fraction of its complexity has attracted substantial research interests, leading to the range of schemes shown in Fig. 1.2.

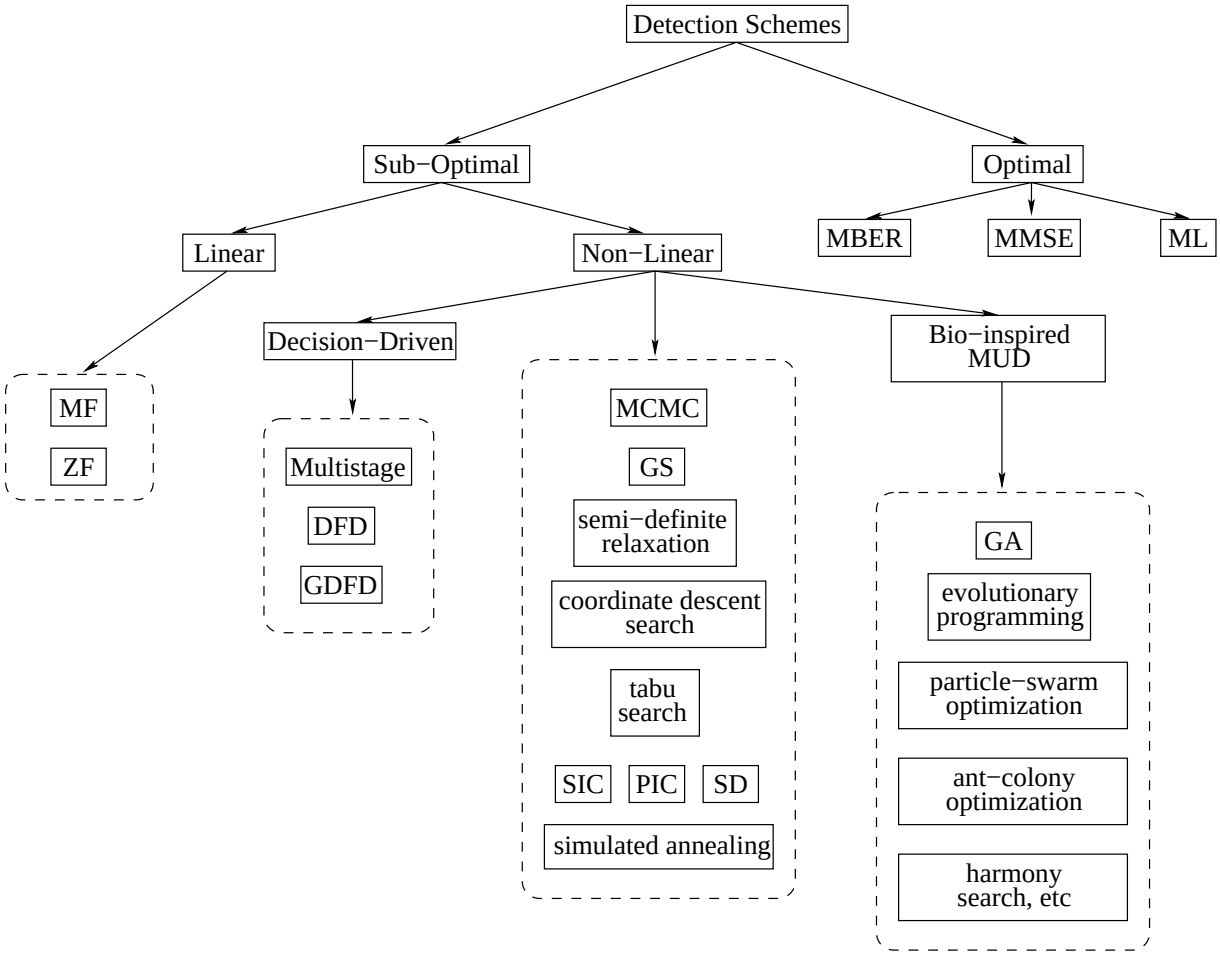

Figure 1.2: Stylized family-tree of detection techniques designed for wireless communication systems.

Generally speaking, signal detection and estimation is the area of study that deals with the processing of information-bearing signals for the purpose of extracting high-reliability information from them. In practice, we have to infer from the imperfect i.e. faded and noise-contaminated observation of the receiver antenna output what the transmitted signal is. Detection theory provides numerous meritorious techniques of achieving this goal [62]. In general, detection and estimation techniques involve making inferences from observations that are distorted or corrupted in some unknown manner [62]. Naturally, the information that one wishes to extract from such observations is unknown to the observer. Thus it is useful to cast practical detection and estimation problems in a probabilistic framework, where the unknown behaviour is assumed to be random. In this light, detection and estimation theory fits the context of statistical inference, and hence this is the interpretation to be used throughout this treatise [62].

The simplest single-user receiver, namely the Matched Filter (MF) was found by North [63] as the maximal signal-to-noise ratio solution in the context of a radar detection problem. A detection algorithm is referred to as a single-user detector, if it assumes that the received signal was engendered entirely by the desired user.

The derivation and analysis of the optimum multiuser receiver dates back to the early 1980s [64–66], which finds the most likely K-symbol vector of K users, rather than minimizing the BER of any of the K users in isolation. Hence it may be viewed as an optimum K-bit sequence estimator. The direct BER optimization of a CDMA MUD was proposed by Samingan, Chen and Hanzo [67].

When the users' signals assume only binary values, solving the MUD problem corresponds to a Binary Quadratic Programming (BQP) problem [68]. Generally, the BQP problem has an exponentially increasing complexity as a function of the search space size [69] (the number of users in the context of MUD). Therefore, only sub-optimal algorithms exhibiting polynomially increasing complexities are considered in practice [68].

Eliminating multiuser interference with the aid of a linear receiver was proposed as early as 1967 by Shnidman [70]. The derivation of the asymptotic efficiency of the decorrelating detector for synchronous channels and the proof of its optimum near-far resistance was provided by Verdú [71] in the case of non-singular received signal correlation matrices.

Nonadaptive MMSE multiuser detection was proposed by Xie *et al.* [72] as well as by Madhow and Honig [73]. Further insights on MMSE MUD were also provided by Rupf *et al.* [74]. An early attempt to derive an adaptive linear MUD was made by Kashihara [75].

The family of decision-driven multiuser detectors, including the multistage detector [76], the Decision Feedback Detector (DFD) [76] [77], and Varariasi's so-called group detector [78] [79], were proposed during the 1990s. The performance of the class of the decision-driven multiuser detectors is significantly better than that of linear detectors. However, it is widely recognized that the performance of decision-driven detectors substantially affected by the detection order of the users [80]. This problem was tackled by the optimal user ordering techniques of [77, 79] designed for the DFD and the Group Decision Feedback Detector (GDFD).

In addition to linear and decision-driven multiuser detectors, numerous other MUDs have been developed during the past two decades. A potent group of suboptimal detectors is based on iterative Monte Carlo techniques that are capable of finding the optimum Bayesian solution of challenging

high-dimensional estimation problems. Most of these methods belong to the class of Markov Chain Monte Carlo (MCMC) techniques [81], which aim for estimating the entire *a posteriori* density, rather than finding only the maximum *a posteriori* (MAP) estimates of the parameters [82]. One of the most popular methods is constituted by the Gibbs Sampler (GS), which was proposed by Chen and Li in [83] for the recovery of symbols in a Bayesian MUD . Other powerful algorithms are constituted by sphere decoding [84,85], semi-definite relaxation [86], coordinate descent search [87], the tabu search [88], the simulated annealing method [89], the Lagrangian relaxation method [89], the roll-out method [90] and the Boltzmann machine [91].

Another important group of suboptimal detectors relies on a bio-inspired MUD philosophy. Representatives of this class include the multistage detector using a Genetic Agorithm (GA) [92–95], evolutionary programming [96], particle swarm optimization [97] and ant-colony optimization (ACO) [98–100].

In Table 1.3 we provide a succinct literature review of some of these MUD algorithms in the context of MIMO systems.

Table 1.3: Main contributions on narrowband MIMO detection.

Year	Author(s)	Contribution
1996	Thoen *et. al.* [101]	A Least Square (LS) MIMO detector is introduced and its performance is investigated in the context of an SDMA OFDM system.
	Foschini [102]	The V-BLAST receiver designed for MIMO systems is proposed.
1999	Wang and Poor [103]	The conventional MMSE detector is extended to soft-output MMSE detection, which may be employed in iterative receivers.
	Viterbo and Boutros [60]	First application of the Shpere Decoder proposed by Fink and Pohst in [104] to the detection of received signals. This contribution inspired a whole new research area.
2000	Damen *et. al.* [105]	In this paper the original SD is extended to a Generalized SD (GSD), which is capable of operating in rank-deficient systems.
2003	Gesbert [106]	Gesbert presented a robust MBER MIMO detector, which can be constructed using a closed-form expression, provided that certain channel conditions are fulfilled.
	Hochwald and ten Brink [107]	The authors propose a List Sphere Decoder (LSD), which is capable of processing soft information. They also compare the attainable performance of their LSD to the channel capacity bound, which is also derived in the paper.
2004	Vikalo *et. al.* [108]	A SISO SD is proposed, which is employed in an iterative system using different convolutional codes as well as Low-Density Parity-Check (LDPC) [109] codes.

Continued on next page

Table 1.3 Main contributions on narrowband MIMO detection.
s continued from previous page

Year	Author(s)	Contribution
2005	Chen *et. al.* [110]	Presents a MBER beamformer designed for BPSK and 4QAM signals operating under static channel conditions.
	Yang *et. al.* [111]	An improved generalized hard-output SD is introduced, which is designed for rank-deficient MIMO systems. The high-complexity detection process is divided into two detection stages, which significantly reduced the complexity imposed.
	Zhu *et. al.* [112]	In this paper MCMC aided MIMO detection is proposed and the attainable performance is compared to that of SD algorithms. The results suggest that MCMC aided detection is capable of outperforming SD at a similar computational cost.
2006	Lee *et. al.* [113]	The original V-BLAST technique is extended to a SISO algorithm and is employed in an OFDM system. For the scenarios considered the proposed V-BLAST detector approaches the ML performance.
	Guo and Nilsson [114]	A SD algorithm based on K-best Schnorr-Euchner (KSE) decoding is proposed, which is capable of providing both hard as well as soft outputs. Furthermore, hardware based performance results are presented.
	Wang and Giannakis [115]	The original SD algorithm is extended to an exact Max-Log detector, which is employed in an iterative system.
	Santiago Mozos and Fernandez-Getino Garcia [116]	Extends the SD using real-valued signals to a SD considering complex-valued modulated signals, which is capable of detecting arbitrary modulation constellations. The performance of the proposed SD is investigated in the context of MC-CDMA.
	Boroujeny *et. al.* [117]	MCMC based MIMO detection is discussed and the benefits of different methods used for generating soft-information are presented. These methods include taking the empirical average as well as using importance sampling.
2007	Aggarwal and Wang [61]	Presents a MCMC based detector optimized for MIMO systems employing higher-order QAM signals. In order to reduce the computational complexity of the proposed system, the received signal space is partitioned into subspaces, each of which is optimized independently.

1.1.5 Ant-Colony Optimization

Ant-Colony Optimization (ACO) was inspired by the foraging behavior of the ant-colony in nature. The ACO algorithm was proposed by Colorni in 1991 and became popular for solving so-called Non-deterministic Polynomial (NP)-hard combinatorial optimization problems that have been applied in diverse research areas. A specific example of NP-hard problems is constituted by the Traveling Salesman Problem (TSP) [118–121], which has been encountered in diverse areas, such as planning, logistics, micro-chip manufacturing and DNA sequencing. The Quadratic Assignment Problem (QAP) [119, 120, 122] is also NP-hard, which is encountered for example during the placement of interconnected electronic components onto a printed circuit board or on a microchip die during their computer aided design. Similarly, the Job-Shop Scheduling Problem (JSP) [120, 123] is an NP-hard problem in computer science, where jobs are assigned to resources at particular times as well as in the packet routing algorithms of telecommunication networks [124–126].

The ACO framework defined by Marco [127] comprises a number of algorithms, including the 'ant system' [118, 120], the 'ant colony system' [121] and the 'MAX-MIN ant system' [119, 128]. The authors of [129–131] employed the 'ant colony system' [121, 132] to simplify the exhaustive search imposed by the optimum ML detector, while approaching the Bit-Error-Ratio (BER) performance of the latter. On the other hand, the authors of [133–136] developed a slightly different near-ML MUD. The ACO based MUDs of both [129–131] and of [133–136] are capable of achieving a lower BER as well as a lower complexity than the Genetic Algorithm (GA)-based MUDs of [94, 95]. The authors of [130, 131] achieved a near-ML BER performance in the context of various Multi-Carrier (MC) DS-CDMA systems employing 31-chip Gold codes as the TD spreading sequence, while supporting $K = 32$ users. The required number of FLoating point Operations Per Second (FLOPS) was a factor of 10^8 lower than that of the ML MUD.

Below we will provide a brief historic perspective of ACO in Table 1.4 and on its applications in MUD algorithms in Table 1.5.

Table 1.4: Main contributions on ant-colony optimization.

Year	Author(s)	Contribution
1959	Pierre-Paul Grass [137]	The nest-building behaviour of termites has been explained using 'stigmergy', which is a mechanism of indirect coordination between agents or actions. The principle is that the trace left in the environment by the agents stimulates the next action, either by the same or a different agent.
1983	Deneubourg *et. al* [138]	The randomness of the foraging behaviour of ants has been demonstrated with the aid of a simple mathematical model, where the degree of randomness has been optimally tuned to the particular ecological conditions encountedred, such as the food quantity and distribution of food.

Continued on next page

Table 1.4 Main contributions on ant-colony optimization.
continued from previous page

Year	Author(s)	Contribution
1988	Moyson Manderick [139]	Investigated the self-organizing behaviour of ants
1989	Goss, Aron, Deneubourg and Pasteels [140]	The foraging behaviour of Argentine ants has been studied and its model has been constructed, which illustrates how the complex collective structures in insect colonies may be modeled by the individual workers' simple trail-laying and pursuing behaviour.
1989	Ebling *et. al* [141]	An accurate model of the ants' foraging was implemented on the Time Warp Operating System (TWOS) designed to run large-scale, irregular, distributed, discrete event simulations in parallel.
1991	M. Dorigo *et. al* [142]	A mathematical Ant-Colony Optimization (ACO) model has been proposed to implement problem solving and optimization procedures based on studying the foraging behaviour of ants, which was applied to the solution of the Travelling Salesman Problem (TSP).
1996	M. Dorigo, V. Maniezzo and A. Colorni [143]	A new computational paradigm termed as the 'Ant System' (AS) was proposed, which exhibited the main characteristics of positive feedback, distributed computation and the employment constructive greedy solutions. The AS was also compared to the so-called reactive tabu search and to simulated annealing to solve the TSP.
1996	Hoos and Sttzle [144]	A novel ACO algorithm referred to as the 'MAX-MIN Ant System' (MMAS) was proposed, which constituted an evolution from the AS algorithm [143]. The MMAS uses a greedier search than the AS of [143] to achieve a better performance. The computational results generated for the TSP and the Quadratic Assignment Problem (QAP) show that the MMAS is currently among the best-performing algorithms for solving these problems.
1997	Dorigo and Gambardella [145]	The Ant Colony System (ACS) algorithm was introduced to solve the TSP. The results provided show that ACS is capable of outperforming other nature-inspired algorithms, such as simulated annealing and evolutionary computation.

Continued on next page

Table 1.4 Main contributions on ant-colony optimization.
continued from previous page

Year	Author(s)	Contribution
1997	Schoonderwoerd *et. al.* [146]	A telecommunication network supporting a population of simple mobile agents exhibiting behaviours modelled on the trail-laying abilities of ants was considered. The multi-angent mechanism referred to as 'Ant-Based Control' (ABC), which is similar to the ACO algorithm, was applied in order to balance the traffic-load among routes of different length. The ABC-aided system was shown to outperform the system using the fixed shortest-path routes and a range of other algorithms.
1998	Sttzle [147]	The MAX-MIN Ant System has been implemented based on efficient parallelization strategies.
1999	Bonabeau, Dorigo and Theraulaz [148]	The different behaviours, namely foraging, division of labour, clustering and sorting, building and cooperative transport observed in social insect swarm were described and modelled by ethologists.
2000	Dorigo, Garo and Sttzle [149]	Different models derived from the observation of real ants in nature were reviewed and the role of stigmergy as a distributed communication paradigm was analyzed. These models were shown to have inspired a number of novel algorithms for the solution of distributed optimization and control problems.
2000	Merkle *et. al.* [150]	An ACO approach designed for the Resource-Constrained Project Scheduling Problem (RCPSP) was presented. The employment of a combination of two pheromone evaluation methods by the ants to find new solutions were studied. Furthermore, the influence of heuristics on the decisions of ants were also investigated.
2000	Gutjahr [151]	The solutions generated in each iteration of the graph-based Ant System can be shown to converge to the optimal solution of the given problem, with a probability that may arbitrarily approach one.
2001	Eurobios and AntOptima	These are the first two companies using Canonical Ant Colonies (COA) to develop optimization and prediction software products.
2001	Iredi *et. al.* [152]	A novel ant-colony based algorithm was proposed to solve bicriterion optimization problems, where several colonies of ants cooperated in finding good solutions.

Continued on next page

Table 1.4 Main contributions on ant-colony optimization.
continued from previous page

Year	Author(s)	Contribution
2002	Campos *et. al.* [153]	ACO's first application for the design of Bayesian learning networks.
2002	Bianchi *et. al.* [154]	Two ACO algorithms, namely the Ant Colony System (ACS) introduced by Dorigo for the TSP and a variant of it (pACS) were studided in order to answer the question of whether and in which context an *a priori* tour found by a TSP heuristic can also be a good solution for the PTSP.
2004	Zlochin and Dorigo *et. al.* [155]	Some metaheuristics were introduced for combinatorial optimization problems found in ACO, stochastic gradient ascent and in the estimation of distributions, which were unified in a model-based search mechanism.
2002	Shmygelska, Hernandez and Hoos [156]	The prediction of a protein's structure from its amino-acid sequence is one of the most important problems in computational biology. The 2-Dimensional Hydrophobic-Polar (2D HP) protein folding problem is a widely studied abstraction of this problem. A novel ACO algorithm invoked for 2D HP protein folding was introduced as a state-of-the-art method for employment in bioinformatics.

Table 1.5: Main contributions on ACO-based MUD algorithm

Year	Author(s)	Contribution
2004	Hijazi and Natarajan [134]	proposed an ACO-based MUD algorithm for a DS CDMA system.
2005	Hijazi, Best, Natarajan and Das [133]	ACO-based MUD algorithm for employment in an synchronous MC DS-CDMA system.
	Lai and Lain [129]	investigated an antenna-diversity-aided ACO-based MUD algorithm in the context of a DS CDMA system.

Continued on next page

Table 1.5 Main contributions on ACO-based MUD algorithms.
continued from previous page

Year	Author(s)	Contribution
2009	Hijazi and Natarajan [136]	applied in ACO-based MUD algorithm in the context of an asynchronous MC DS-CDMA system.

1.2 Outline and Novel Contributions

- **Chapter 2:** A rudimentary introduction to CDMA systems is provided, highlighting the objective functions that may be used in single- and multi-user CDMA systems.
- **Chapter 3:** The foraging behaviour of ants is discussed in nature, and applied to design ACO-based MUD algorithms. Each component constituting the ACO-based MUD algorithm is analyzed. A simple $K = 5$-user example is employed for highlighting the role of each ACO parameter affecting the performance of the ACO-based MUD algorithm. Finally the ACO-based MUD is compared to the GA-based MUD algorithm.
- **Chapter 4:** Then we design a MFAA aided MC DS-CDMA system using a powerful ACO-based MUD algorithm and characterize its achievable performance.
- **Chapter 5:** Space-Time Block Coded (STBC) DS-CDMA is proposed in order to provide diversity gain for the uplink, while using an advanced ACO-based hard-decision-aided space-time MUD algorithm. It is demonstrated that the system is capable of approaching the corresponding single-user performance at a fraction of the ML MUD's complexity.
- **Chapter 6:** The first ACO-based soft-output MUD algorithm is proposed based on the previously discussed HO MUD in the context of the convolutional coded DS-CDMA UL. Two novel algorithms, namely the MAximum Approximation (MAA) and the MUlti-input Approximation (MUA) technique are proposed to generate the LLRs depending on the affordable complexity and performance requirements. The critical parts of the MUA algorithm are exemplified with the aid of the same $K = 5$-user example as in Chapter 3.
- **Chapter 7:** Concatenated Unit-Rate-Coding (URC) and half-rate Recursive Systematic Coding (RSC) schemes are emloyed for each UL user in order to further enhance the achievable BER performance of the MU STBC assisted DS-CDMA system. An advanced ACO-based SO ST/MUD algorithm is proposed for the system considered. Furthermore a novel EXtrinsic Information Transfer (EXIT) band-chart is used for characterizing the achievable performance. We will demonstrate that the multiuser system's performance approaches the single-user performance, while imposing a modest complexity, which is only linearly increased upon increasing the number of users supported.

- **Chapter 8:** We conclude this study with a detailed comparative study of the MC DS-CDMA system, the MFAA assisted MC DS-CDMA system, the STBC assisted DS-CDMA system and of the iteratively detected URC-RSC aided STBC assisted DS-CDMA system. The differences and similarities of the main components constituting the ACO-based HO/SO MUD algorithms employed in each of the systems are also summarized. The complexity imposed by the above-mentioned four systems operating at a target BER of 10^{-4} and their required E_b/N_0 values are plotted. Hence the merits of the different systems at different E_b/N_0 values become explicit.

The structure of the thesis is outlined in Fig. 1.3

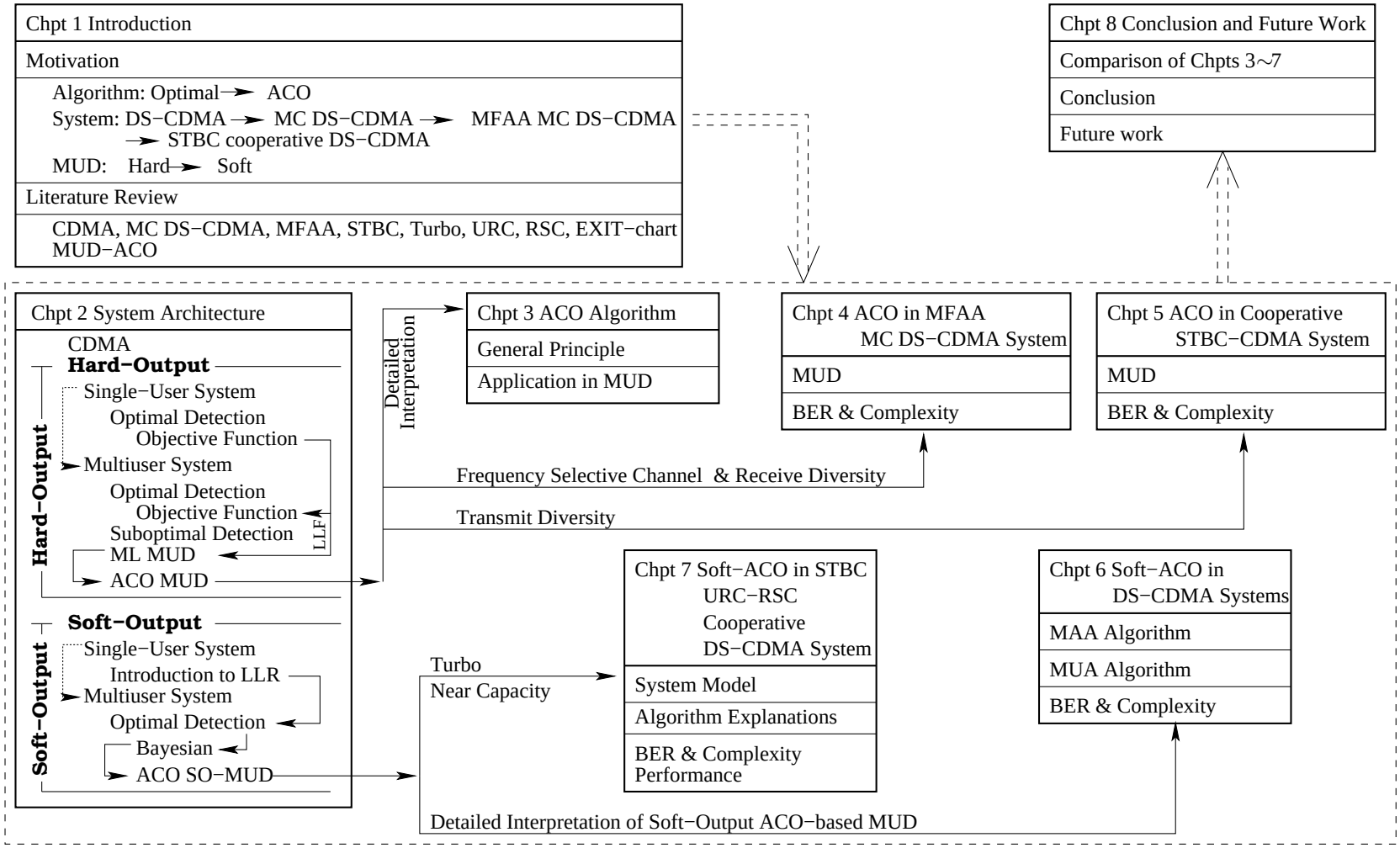

Figure 1.3: Structure of the thesis.

The fundamental motivation and the rationale of the thesis is to design powerful ACO-based HO or SO MUD algorithms for different multi-user systems incorporating state-of-the-art technologies, so that a single-user BER performance can be achieved at a moderate implementational complexity.

The research was concluded by comparing the benefits versus the resources required by the state-of-the-art systems investigated in this thesis.

The novel contributions of the thesis are as follows:

- An ACO-based MUD designed for synchronous MC DS-CDMA systems is proposed. The ACO-based MUD aims for approaching the BER-performance of the optimum ML-MUD at a fraction of its complexity. As an example, it will be demonstrated that the number of FLoating Point Operations Per Second (FLOPS) is a factor of 10^8 lower for the proposed ACO-based MUD than that of the ML MUD, when supporting $K = 32$ users in an MC DS-CDMA system employing 31-chip Gold codes as the TD spreading sequences [130].

- The ACO-based MUD is then further developed for employment in the MFAA assisted MC DS-CDMA UL, which supports both receiver diversity and receiver beamforming. Again, we will demonstrate that similarly to the single-carrier CDMA system of Chapter 3 and regardless of the number of the subcarriers or of the MFAA configuration, the MD DS-CDMA system employing the proposed ACO-based MUD is capable of supporting 32 users with the aid of 31-chip Gold codes used as the TD spreading sequence without any significant performance degradation compared to the corresponding single-user benchmark system. As a further benefit, similarly to the single-carrier CDMA system in Chapter 3, the number of FLOPS imposed by the proposed ACO-based MUD is a factor of 10^8 lower than that of the ML MUD. We also demonstrate that at a given increase of the complexity, the MFAA will allow the ACO-based MUD to achieve a higher SNR gain than the corresponding Single-Input Single-Output (SISO) MC DS-CDMA system [131].

- The above-mentioned HO ACO-MUD is then further developed to create a novel soft-output ACO-MUD capable of delivering soft-LLRs, which allows a CDMA system to achieve a near-single-user performance, even when the number of users supported is as high as the number of chips in the spreading sequence. Our numerical results show that at a BER of 10^{-3}, the performance of the currently known ACO-assisted state-of-the-art systems may be improved by about 17dB with the aid of the proposed soft-output ACO-MUD. More explicitly, the soft-output ACO-MUD is capable of approaching the optimum performance of the Bayesian detector, when $K = 32$ UL users are supported with the aid of 31-chip Gold codes, while the complexity of the former is only a fraction of 10^{-8} of the latter [157].

- Apart from the MAximum-Approximation (MAA) assisted SO-ACO algorithm, a novel MUA assisted SO-ACO algorithm is proposed, which subsumes the MAA algorithm as a particular case and outperforms the MAA algorithm. More explicitly, at an SNR of 13dB, the BER performance of the Convolutional Coding (CC) aided CDMA UL employing the MAA SO-ACO is improved from $5.2 \cdot 10^{-6}$ to $2.7 \cdot 10^{-6}$ by employing the MUA SO-ACO. Our numerical results also demonstrate that the MUA assisted SO ACO-MUD is capable of approaching the optimum performance of the Bayesian detector, when $K = 32$ UL users are supported with the aid of

31-chip Gold codes, while the complexity of the former is a fraction of 10^{-8} lower than that of the latter [158].

- As a further development, an ACO-based Space-Time (ST) MUD is proposed in order to improve the BER versus SNR performance achieved by the Space-Time Block Code (STBC) assisted two transmit antenna aided fully loaded DS-CDMA system. Our simulation results demonstrate that the corresponding ACO-based MUD algorithm enables the fully loaded system to approach the single-user performance associated with a second-order diversity gain. Furthermore, the complexity of the improved ACO based MUD algorithm is a factor of 10^{18} lower than that of the ML MUD, when $K = 32$ users are supported by the STBC $\mathcal{G}_2$ assisted DS-CDMA systems employing Gold codes having a length of 31 chips.

- Finally, a three-stage twin-transmit-antenna assisted MU DS-CDMA system employing both a URC and an RSC is invoked in order to exchange their extrinsic information with the aid of iterative turbo detection. An STBC scheme is used to provide second-order diversity gain in conjunction with a novel SO ACO-based ST/MUD algorithm, which is capable of carrying out STBC decoding, while mitigating the MultiUser Interference (MUI). The proposed system becomes capable of approaching the performance of the corresponding single-user system within about 0.5dB, when $K = 32$ users are supported with the aid of 31-chip Gold-codes. EXtrinsic Information Transfer (EXIT) band-charts are used for characterizing the achievable performance. When the transmission frames contain $10,000$ bits, the corresponding EXIT-band-charts are capable of adequately predicting the achievable performance. Finally, the complexity imposed by the SO/ACO-based ST/MUD algorithm allowing the $K = 32$-user system to approach the single-user performance is a factor of 10^{17} lower compared to that of the ML MUD.

Having presented an overview of the thesis, let us now commence our detailed discourse in the following chapter.

Chapter 2

System Architecture

In this chapter, we highlight the basic blocks, considered throughout this treatise. In Section 2.2 the basic principles of code-division multiple access (CDMA) techniques are detailed, while the objective function of single-user hard-output detection are detailed in Section 2.3.

By contrast, in Section 2.4 the objective function of the corresponding multiuser system is considered. Simple logic dictates that for K users 2^K evaluations of the objective function are needed.

The Objective Function (OF) typically employed by the ML MUD algorithm is the so-called Logarithmic Likelihood Function (LLF) of a certain legitimate K-element signal vector $\dot{\mathbf{v}}$, which is derived from the Euclidean distance of the vector $\dot{\mathbf{v}}$, orginating from the *a posteriori* probability of $\dot{\mathbf{v}}$ being transmitted based on the received signal.

The complexity of evaluating the OF 2^K times may become excessive in practical real-time communication systems supporting a high number of users. Hence numerous suboptimum MUDs have been designed, which are capable of 'capturing' the optimum 'ML' solution to a high probability at a fraction of the ML-complexity [93]. For example, the ant-colony-optimization (ACO) based hard-output MUD algorithm has been designed to find the optimal ML vector by evaluating the objective function a substantially reduced number of times.

The Log-Likelihood Ratio (LLR) [159] will be introduced in Section 2.5 in a general context.

In Section 2.6, the LLRs associated with a single bit will be quantified in the context of a single-user system. Furthermore, the derivation of the LLRs will be exemplified by a series of figures.

2.1 Basic Structure of Wireless Transceivers

A communication system of Fig. 2.1 is constituted by the transmitter, the channel and the receiver. The transmitted electromagnetic waves will be gradually attenuated as the distance they travel over becomes larger. Additionally, they will be reflected and scattered by the ground and the surrounding buildings. When they finally impinge at the receiver antenna, they will be contaminated by the noise of the receiver device. The channel-induced errors may be corrected by a channel codec [159], as seen in the more detailed schematic of Fig. 2.2.

Since the frequency band that can be used to transmit and receive messages is limited, not each

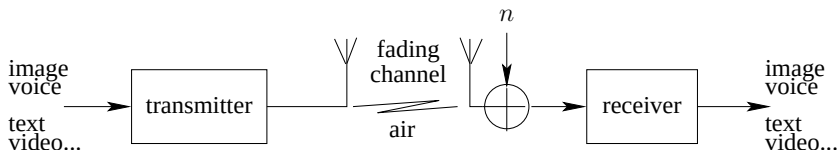

Figure 2.1: The most basic block diagrams comprising the simplest wireless communciation system.

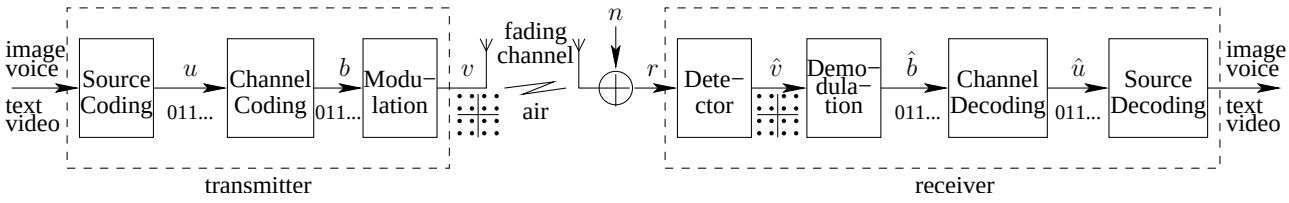

Figure 2.2: More detailed system block diagram evolving from Fig. 2.1.

pair of transceivers is allowed to employ a unique user-specific frequency band. Hence in wireless systems the effects of multiuser interference are often more severe, than the contamination by noise and the effects of the channel-induced fading.

In order to allow multiple users to utilize the same channel for transmitting their signals within the same frequency band without mutually interfering with each other, we assign each pair of users roaming within the same geographic area a unique N_s-chip code. Ideally, these codes are designed to be orthogonal with each other. Suppose the code assigned to user k is $\mathbf{c}_k = [c_{k1}, c_{k2}, \ldots, c_{kN_s}]$. Provided that $\mathbf{c}_k$ is orthogonal to the code $\mathbf{c}_j = [c_{j1}, c_{j2}, \ldots, c_{jN_s}]$ assigned to user j, then we have $\mathbf{c}_k^T \mathbf{c}_j = 0$. Ideally, a set of K orthogonal codes should satisfy $\mathbf{c}_k^T \mathbf{c}_j = 0$ and $\mathbf{c}_k^T \mathbf{c}_k = 1$ at the same time, for any $1 \leqslant k \leqslant K$, $1 \leqslant j \leqslant K$ and $k \neq j$.

2.2 CDMA Introduction

$\mathbf{c}_1$	$\delta \cdot [1$	1	1	$1]^T$
$\mathbf{c}_2$	$\delta \cdot [1$	-1	1	$-1]^T$
$\mathbf{c}_3$	$\delta \cdot [1$	1	-1	$-1]^T$
$\mathbf{c}_4$	$\delta \cdot [1$	-1	-1	$1]^T$

Table 2.1: The set of 4-chip orthogonal Walsh Hadamard codes associated with the normalized factor of $\delta = \frac{1}{\sqrt{4}}$.

The orthogonal codes listed in Tab. 2.1 are the Walsh-Hadamard codes having a length of $N_s = 4$ chips. The length of Walsh-Hadamard codes can only be an integer power of 2, i.e. 4, 8, 16, ..., etc. Additionally, the quasi-orthogonal codes listed in Tab. 2.2, Tab. 2.3 and Tab. 2.5 are the $N_s = 7$ or 15 chip m-sequences and the $N_s = 63$-chip Gold code. The length of m-sequences can only be $2^m - 1$, i.e. 3, 7, 15, ..., etc. The m-sequences having a length of 7 are listed in Tab. 2.3, while the Gold codes

$\mathbf{c}_1$	$\delta \cdot [\ 1 \quad -1 \quad -1]^T$
$\mathbf{c}_2$	$\delta \cdot [-1 \quad 1 \quad -1]^T$
$\mathbf{c}_3$	$\delta \cdot [-1 \quad -1 \quad 1]^T$

Table 2.2: The set of 3-chip quasi-orthogonal m-sequences associated with the normalized factor of $\delta = \frac{1}{\sqrt{3}}$.

having a length of 31 are listed in Tab. 2.5, which will be employed as the spreading codes throughout our simulations. Since both of them are non-orthogonal codes, we have $\mathbf{c}_i^T \mathbf{c}_j \neq 0$ for all the $i \neq j$.

$\mathbf{c}_1$	$\delta \cdot [-1 \quad -1 \quad 1 \quad 1 \quad -1 \quad 1 \quad -1]^T$
$\mathbf{c}_2$	$\delta \cdot [-1 \quad -1 \quad -1 \quad 1 \quad 1 \quad -1 \quad 1]^T$
$\mathbf{c}_3$	$\delta \cdot [\ 1 \quad -1 \quad -1 \quad -1 \quad 1 \quad 1 \quad -1]^T$
$\mathbf{c}_4$	$\delta \cdot [-1 \quad 1 \quad -1 \quad -1 \quad -1 \quad 1 \quad 1]^T$
$\mathbf{c}_5$	$\delta \cdot [\ 1 \quad -1 \quad 1 \quad -1 \quad -1 \quad -1 \quad 1]^T$
$\mathbf{c}_6$	$\delta \cdot [\ 1 \quad 1 \quad -1 \quad 1 \quad -1 \quad -1 \quad -1]^T$
$\mathbf{c}_7$	$\delta \cdot [-1 \quad 1 \quad 1 \quad -1 \quad 1 \quad -1 \quad -1]^T$

Table 2.3: The seven 7-chip m-sequences associated with the normalized factor of $\delta = \frac{1}{\sqrt{7}}$, which will be used as the spreading codes of the system investigated in Chapter 5.

	1	2	3	4	5	6	7
1	1	-0.14	-0.14	-0.14	-0.14	-0.14	-0.14
2	-0.14	1	-0.14	-0.14	-0.14	-0.14	-0.14
3	-0.14	-0.14	1	-0.14	-0.14	-0.14	-0.14
4	-0.14	-0.14	-0.14	1	-0.14	-0.14	-0.14
5	-0.14	-0.14	-0.14	-0.14	1	-0.14	-0.14
6	-0.14	-0.14	-0.14	-0.14	-0.14	1	-0.14
7	-0.14	-0.14	-0.14	-0.14	-0.14	-0.14	1

Table 2.4: The scalar listed in the ith row and the jth column is the correlation factor between $\mathbf{c}_i$ and $\mathbf{c}_j$, as quantified by $\rho_{ij}^c = \mathbf{c}_i^T \mathbf{c}_j$. The value of $\mathbf{c}_i$ for $i = 1, 2, \ldots, 33$ is illustrated in the ith row of Table 2.3.

The correlation factor $\rho_{ij}^c = \mathbf{c}_i^T \mathbf{c}_j$ quantifies the similarity between the ith code and the jth code. The correlation factors between each pair of spreading sequences of the seven 7-chip m-sequences and that of the thirty-three 31-chip Gold codes are exemplified in Tables 2.4 and 2.6, respectively.

$\mathbf{c}_1$	$\delta \cdot [-1\ \ 1-1\ \ 1-1-1-1\ \ 1-1-1\ \ 1\ \ 1\ \ 1-1-1-1-1-1\ \ 1\ \ 1-1-1\ \ 1-1\ \ 1\ \ 1-1\ \ 1\ \ 1\ \ 1\ \ 1]^T$
$\mathbf{c}_2$	$\delta \cdot [-1\ \ 1-1-1\ \ 1-1\ \ 1-1\ \ 1\ \ 1\ \ 1-1-1-1\ \ 1-1-1-1-1-1\ \ 1\ \ 1-1\ \ 1\ \ 1-1-1\ \ 1\ \ 1\ \ 1\ \ 1]^T$
$\mathbf{c}_3$	$\delta \cdot [\ 1\ \ 1\ \ 1-1-1\ \ 1-1-1-1-1\ \ 1-1-1\ \ 1-1\ \ 1\ \ 1\ \ 1-1-1-1-1-1-1\ \ 1-1\ \ 1\ \ 1\ \ 1\ \ 1]^T$
$\mathbf{c}_4$	$\delta \cdot [-1-1-1-1\ \ 1-1\ \ 1\ \ 1\ \ 1-1\ \ 1\ \ 1-1\ \ 1\ \ 1-1\ \ 1\ \ 1-1-1\ \ 1-1\ \ 1\ \ 1\ \ 1\ \ 1\ \ 1-1\ \ 1\ \ 1\ \ 1]^T$
$\mathbf{c}_5$	$\delta \cdot [-1\ \ 1\ \ 1\ \ 1\ \ 1\ \ 1-1-1-1\ \ 1\ \ 1\ \ 1\ \ 1\ \ 1\ \ 1\ \ 1-1\ \ 1-1-1\ \ 1\ \ 1\ \ 1-1-1\ \ 1-1-1-1\ \ 1\ \ 1]^T$
$\mathbf{c}_6$	$\delta \cdot [-1\ \ 1-1-1-1\ \ 1\ \ 1\ \ 1\ \ 1-1-1\ \ 1\ \ 1-1\ \ 1\ \ 1\ \ 1-1-1-1\ \ 1\ \ 1-1-1\ \ 1-1-1\ \ 1-1-1\ \ 1]^T$
$\mathbf{c}_7$	$\delta \cdot [-1\ \ 1-1\ \ 1\ \ 1-1\ \ 1-1-1\ \ 1\ \ 1-1\ \ 1-1-1\ \ 1\ \ 1\ \ 1\ \ 1-1\ \ 1\ \ 1-1\ \ 1\ \ 1\ \ 1\ \ 1\ \ 1\ \ 1-1-1]^T$
$\mathbf{c}_8$	$\delta \cdot [\ 1\ \ 1-1\ \ 1-1\ \ 1-1-1\ \ 1-1-1\ \ 1-1-1-1-1\ \ 1\ \ 1-1\ \ 1\ \ 1\ \ 1-1\ \ 1-1\ \ 1-1-1\ \ 1\ \ 1-1]^T$
$\mathbf{c}_9$	$\delta \cdot [\ 1-1-1\ \ 1-1-1\ \ 1\ \ 1\ \ 1\ \ 1\ \ 1-1\ \ 1\ \ 1-1-1-1\ \ 1-1-1-1\ \ 1-1\ \ 1-1-1-1\ \ 1-1\ \ 1\ \ 1]^T$
$\mathbf{c}_{10}$	$\delta \cdot [-1-1\ \ 1\ \ 1-1-1-1-1-1-1\ \ 1-1\ \ 1-1-1\ \ 1-1-1-1-1-1-1\ \ 1-1-1\ \ 1-1-1\ \ 1\ \ 1\ \ 1-1\ \ 1]^T$
$\mathbf{c}_{11}$	$\delta \cdot [-1\ \ 1\ \ 1-1-1-1-1-1\ \ 1\ \ 1-1-1-1\ \ 1\ \ 1-1\ \ 1-1-1\ \ 1-1\ \ 1\ \ 1\ \ 1\ \ 1-1-1\ \ 1-1\ \ 1\ \ 1-1]^T$
$\mathbf{c}_{12}$	$\delta \cdot [\ 1\ \ 1-1-1\ \ 1-1-1\ \ 1-1\ \ 1\ \ 1-1-1-1-1\ \ 1-1\ \ 1-1\ \ 1\ \ 1\ \ 1\ \ 1-1-1-1-1-1\ \ 1-1-1\ \ 1\ \ 1]^T$
$\mathbf{c}_{13}$	$\delta \cdot [-1-1-1\ \ 1\ \ 1\ \ 1-1\ \ 1-1-1-1-1\ \ 1-1\ \ 1-1\ \ 1-1\ \ 1\ \ 1\ \ 1-1\ \ 1-1\ \ 1\ \ 1-1\ \ 1-1-1-1-1\ \ 1]^T$
$\mathbf{c}_{14}$	$\delta \cdot [-1\ \ 1\ \ 1\ \ 1-1\ \ 1\ \ 1\ \ 1-1-1\ \ 1-1\ \ 1\ \ 1\ \ 1-1\ \ 1-1-1\ \ 1-1-1-1-1\ \ 1-1\ \ 1\ \ 1-1-1-1-1-1]^T$
$\mathbf{c}_{15}$	$\delta \cdot [\ 1\ \ 1-1-1-1-1-1\ \ 1-1-1-1-1\ \ 1\ \ 1-1-1-1\ \ 1\ \ 1-1\ \ 1\ \ 1-1-1-1-1\ \ 1\ \ 1-1-1-1-1-1-1-1-1]^T$
$\mathbf{c}_{16}$	$\delta \cdot [\ 1-1-1-1\ \ 1\ \ 1-1-1-1-1\ \ 1-1\ \ 1\ \ 1\ \ 1\ \ 1-1\ \ 1\ \ 1-1-1-1\ \ 1\ \ 1-1\ \ 1-1-1-1-1\ \ 1\ \ 1-1-1-1-1]^T$
$\mathbf{c}_{17}$	$\delta \cdot [\ 1-1\ \ 1\ \ 1-1\ \ 1-1\ \ 1\ \ 1\ \ 1\ \ 1\ \ 1\ \ 1-1\ \ 1-1\ \ 1\ \ 1\ \ 1-1-1-1\ \ 1\ \ 1-1\ \ 1-1\ \ 1-1\ \ 1-1-1-1]^T$
$\mathbf{c}_{18}$	$\delta \cdot [\ 1-1\ \ 1-1-1-1-1\ \ 1\ \ 1-1\ \ 1-1\ \ 1\ \ 1-1-1-1\ \ 1-1\ \ 1-1\ \ 1\ \ 1-1-1-1-1\ \ 1\ \ 1\ \ 1-1-1-1\ \ 1-1-1]^T$
$\mathbf{c}_{19}$	$\delta \cdot [\ 1-1\ \ 1-1\ \ 1-1-1-1-1-1-1-1-1-1\ \ 1-1-1-1-1\ \ 1-1-1-1-1-1\ \ 1\ \ 1\ \ 1\ \ 1\ \ 1-1-1-1-1-1\ \ 1]^T$
$\mathbf{c}_{20}$	$\delta \cdot [-1-1\ \ 1-1\ \ 1\ \ 1-1\ \ 1\ \ 1-1\ \ 1-1-1-1-1-1-1-1\ \ 1\ \ 1-1\ \ 1-1-1-1-1-1\ \ 1-1\ \ 1-1-1-1-1]^T$
$\mathbf{c}_{21}$	$\delta \cdot [\ 1\ \ 1\ \ 1-1\ \ 1\ \ 1\ \ 1\ \ 1-1\ \ 1\ \ 1\ \ 1-1\ \ 1-1-1-1-1-1-1\ \ 1\ \ 1\ \ 1\ \ 1\ \ 1\ \ 1-1-1\ \ 1\ \ 1-1-1]^T$
$\mathbf{c}_{22}$	$\delta \cdot [\ 1-1-1-1-1\ \ 1\ \ 1\ \ 1-1-1-1-1-1\ \ 1\ \ 1\ \ 1\ \ 1-1-1-1-1\ \ 1-1-1\ \ 1-1-1-1-1\ \ 1\ \ 1\ \ 1\ \ 1\ \ 1-1]^T$
$\mathbf{c}_{23}$	$\delta \cdot [\ 1-1\ \ 1\ \ 1\ \ 1\ \ 1\ \ 1-1\ \ 1-1\ \ 1-1\ \ 1-1\ \ 1\ \ 1-1-1-1\ \ 1\ \ 1\ \ 1-1-1\ \ 1\ \ 1-1-1-1-1\ \ 1\ \ 1\ \ 1]^T$
$\mathbf{c}_{24}$	$\delta \cdot [-1-1\ \ 1-1-1-1\ \ 1\ \ 1-1\ \ 1\ \ 1\ \ 1\ \ 1-1-1-1-1\ \ 1\ \ 1-1\ \ 1\ \ 1-1\ \ 1\ \ 1\ \ 1-1\ \ 1\ \ 1\ \ 1-1\ \ 1\ \ 1]^T$
$\mathbf{c}_{25}$	$\delta \cdot [-1\ \ 1\ \ 1-1\ \ 1-1\ \ 1-1\ \ 1\ \ 1-1\ \ 1\ \ 1\ \ 1-1-1-1\ \ 1\ \ 1\ \ 1\ \ 1-1-1-1-1-1-1-1-1-1\ \ 1-1\ \ 1]^T$
$\mathbf{c}_{26}$	$\delta \cdot [-1\ \ 1-1-1\ \ 1\ \ 1-1-1-1\ \ 1\ \ 1-1-1\ \ 1-1\ \ 1-1-1-1\ \ 1-1\ \ 1-1-1-1\ \ 1\ \ 1\ \ 1-1\ \ 1\ \ 1-1\ \ 1-1]^T$
$\mathbf{c}_{27}$	$\delta \cdot [\ 1\ \ 1-1\ \ 1\ \ 1\ \ 1\ \ 1\ \ 1\ \ 1\ \ 1-1-1-1-1-1-1\ \ 1-1-1-1-1-1-1-1-1\ \ 1-1-1\ \ 1\ \ 1-1\ \ 1-1\ \ 1]^T$
$\mathbf{c}_{28}$	$\delta \cdot [-1-1-1\ \ 1-1\ \ 1\ \ 1-1-1\ \ 1-1-1-1-1\ \ 1-1-1-1\ \ 1-1\ \ 1-1\ \ 1-1\ \ 1-1\ \ 1-1-1-1-1-1\ \ 1\ \ 1-1]^T$
$\mathbf{c}_{29}$	$\delta \cdot [\ 1\ \ 1\ \ 1\ \ 1-1-1\ \ 1-1\ \ 1-1-1-1-1-1\ \ 1\ \ 1-1-1\ \ 1\ \ 1\ \ 1\ \ 1\ \ 1\ \ 1-1\ \ 1\ \ 1\ \ 1\ \ 1-1-1\ \ 1]^T$
$\mathbf{c}_{30}$	$\delta \cdot [-1-1-1-1-1-1-1-1-1\ \ 1\ \ 1\ \ 1-1-1\ \ 1\ \ 1\ \ 1-1-1-1-1\ \ 1-1\ \ 1-1-1-1\ \ 1\ \ 1-1-1\ \ 1-1-1]^T$
$\mathbf{c}_{31}$	$\delta \cdot [\ 1\ \ 1\ \ 1\ \ 1\ \ 1-1-1\ \ 1\ \ 1\ \ 1-1\ \ 1-1\ \ 1\ \ 1\ \ 1\ \ 1-1\ \ 1-1-1-1-1-1\ \ 1\ \ 1\ \ 1-1\ \ 1-1\ \ 1-1]^T$

$\mathbf{c}_{32}$	$\delta \cdot [\ 1 -1 -1 -1 -1 -1\ \ 1 -1\ \ 1 -1\ \ 1 -1 -1 -1\ \ 1\ \ 1\ \ 1\ \ 1\ \ 1\ \ 1\ \ 1\ \ 1 -1\ \ 1\ \ 1 -1\ \ 1 -1 -1\ \ 1\ \ 1 -1\ \ 1]^T$
$\mathbf{c}_{33}$	$\delta \cdot [-1 -1\ \ 1\ \ 1\ \ 1 -1\ \ 1\ \ 1 -1 -1 -1 -1 -1 -1 -1\ \ 1\ \ 1\ \ 1\ \ 1 -1\ \ 1 -1\ \ 1\ \ 1 -1 -1 -1 -1 -1\ \ 1\ \ 1\ \ 1 -1]^T$

Table 2.5: The thirty-three 31-chip Gold spreading codes having the normalized factor of $\delta = \frac{1}{\sqrt{31}}$, which will be used in each of the following chapters.

	1	2	3	4	5	6	7	8	9	10	11	12	13	14	15	16	17	18	19	20	21	22	23	24	25	26	27	28	29	30	31	32	33
1	1	-0.03	-0.03	-0.03	-0.03	-0.03	-0.03	-0.03	-0.03	-0.03	-0.03	-0.03	-0.03	-0.03	-0.03	-0.03	-0.03	-0.03	-0.03	-0.03	-0.03	-0.03	-0.03	-0.03	-0.03	-0.03	-0.03	-0.03	-0.03	-0.03	-0.03	-0.03	-0.03
2	-0.03	1	-0.03	0.23	-0.03	0.23	0.23	-0.03	0.23	0.23	-0.03	0.23	-0.29	-0.29	-0.03	-0.29	-0.29	-0.29	-0.03	-0.03	0.23	-0.03	0.23	-0.03	-0.03	0.23	-0.03	-0.03	-0.03	0.23	-0.03	-0.29	-0.03
3	-0.03	-0.03	1	-0.03	-0.03	-0.03	-0.03	-0.03	-0.03	-0.03	-0.03	-0.03	-0.03	-0.03	-0.03	-0.03	-0.03	-0.03	-0.03	-0.03	-0.03	-0.03	-0.03	-0.03	-0.03	-0.03	-0.03	-0.03	-0.03	-0.03	-0.03	-0.03	-0.03
4	-0.03	0.23	-0.03	1	-0.03	-0.03	-0.03	-0.03	-0.03	-0.03	-0.03	-0.03	-0.03	-0.03	-0.03	-0.03	-0.03	-0.03	-0.03	-0.03	-0.03	-0.03	-0.03	-0.03	-0.03	-0.03	-0.03	-0.03	-0.03	-0.03	-0.03	-0.03	-0.03
5	-0.03	-0.03	-0.03	-0.03	1	-0.03	-0.03	-0.03	-0.03	-0.03	-0.03	-0.03	-0.03	-0.03	-0.03	-0.03	-0.03	-0.03	-0.03	-0.03	-0.03	-0.03	-0.03	-0.03	-0.03	-0.03	-0.03	-0.03	-0.03	-0.03	-0.03	-0.03	-0.03
6	-0.03	0.23	-0.03	-0.03	-0.03	1	-0.03	-0.03	-0.03	-0.03	-0.03	-0.03	-0.03	-0.03	-0.03	-0.03	-0.03	-0.03	-0.03	-0.03	-0.03	-0.03	-0.03	-0.03	-0.03	-0.03	-0.03	-0.03	-0.03	-0.03	-0.03	-0.03	-0.03
7	-0.03	0.23	-0.03	-0.03	-0.03	-0.03	1	-0.03	-0.03	-0.03	-0.03	-0.03	-0.03	-0.03	-0.03	-0.03	-0.03	-0.03	-0.03	-0.03	-0.03	-0.03	-0.03	-0.03	-0.03	-0.03	-0.03	-0.03	-0.03	-0.03	-0.03	-0.03	-0.03
8	-0.03	-0.03	-0.03	-0.03	-0.03	-0.03	-0.03	1	-0.03	-0.03	-0.03	-0.03	-0.03	-0.03	-0.03	-0.03	-0.03	-0.03	-0.03	-0.03	-0.03	-0.03	-0.03	-0.03	-0.03	-0.03	-0.03	-0.03	-0.03	-0.03	-0.03	-0.03	-0.03
9	-0.03	0.23	-0.03	-0.03	-0.03	-0.03	-0.03	-0.03	1	-0.03	-0.03	-0.03	-0.03	-0.03	-0.03	-0.03	-0.03	-0.03	-0.03	-0.03	-0.03	-0.03	-0.03	-0.03	-0.03	-0.03	-0.03	-0.03	-0.03	-0.03	-0.03	-0.03	-0.03
10	-0.03	0.23	-0.03	-0.03	-0.03	-0.03	-0.03	-0.03	-0.03	1	-0.03	-0.03	-0.03	-0.03	-0.03	-0.03	-0.03	-0.03	-0.03	-0.03	-0.03	-0.03	-0.03	-0.03	-0.03	-0.03	-0.03	-0.03	-0.03	-0.03	-0.03	-0.03	-0.03
11	-0.03	-0.03	-0.03	-0.03	-0.03	-0.03	-0.03	-0.03	-0.03	-0.03	1	-0.03	-0.03	-0.03	-0.03	-0.03	-0.03	-0.03	-0.03	-0.03	-0.03	-0.03	-0.03	-0.03	-0.03	-0.03	-0.03	-0.03	-0.03	-0.03	-0.03	-0.03	-0.03
12	-0.03	0.23	-0.03	-0.03	-0.03	-0.03	-0.03	-0.03	-0.03	-0.03	-0.03	1	-0.03	-0.03	-0.03	-0.03	-0.03	-0.03	-0.03	-0.03	-0.03	-0.03	-0.03	-0.03	-0.03	-0.03	-0.03	-0.03	-0.03	-0.03	-0.03	-0.03	-0.03
13	-0.03	-0.29	-0.03	-0.03	-0.03	-0.03	-0.03	-0.03	-0.03	-0.03	-0.03	-0.03	1	-0.03	-0.03	-0.03	-0.03	-0.03	-0.03	-0.03	-0.03	-0.03	-0.03	-0.03	-0.03	-0.03	-0.03	-0.03	-0.03	-0.03	-0.03	-0.03	-0.03
14	-0.03	-0.29	-0.03	-0.03	-0.03	-0.03	-0.03	-0.03	-0.03	-0.03	-0.03	-0.03	-0.03	1	-0.03	-0.03	-0.03	-0.03	-0.03	-0.03	-0.03	-0.03	-0.03	-0.03	-0.03	-0.03	-0.03	-0.03	-0.03	-0.03	-0.03	-0.03	-0.03
15	-0.03	-0.03	-0.03	-0.03	-0.03	-0.03	-0.03	-0.03	-0.03	-0.03	-0.03	-0.03	-0.03	-0.03	1	-0.03	-0.03	-0.03	-0.03	-0.03	-0.03	-0.03	-0.03	-0.03	-0.03	-0.03	-0.03	-0.03	-0.03	-0.03	-0.03	-0.03	-0.03
16	-0.03	-0.29	-0.03	-0.03	-0.03	-0.03	-0.03	-0.03	-0.03	-0.03	-0.03	-0.03	-0.03	-0.03	-0.03	1	-0.03	-0.03	-0.03	-0.03	-0.03	-0.03	-0.03	-0.03	-0.03	-0.03	-0.03	-0.03	-0.03	-0.03	-0.03	-0.03	-0.03
17	-0.03	-0.29	-0.03	-0.03	-0.03	-0.03	-0.03	-0.03	-0.03	-0.03	-0.03	-0.03	-0.03	-0.03	-0.03	-0.03	1	-0.03	-0.03	-0.03	-0.03	-0.03	-0.03	-0.03	-0.03	-0.03	-0.03	-0.03	-0.03	-0.03	-0.03	-0.03	-0.03
18	-0.03	-0.29	-0.03	-0.03	-0.03	-0.03	-0.03	-0.03	-0.03	-0.03	-0.03	-0.03	-0.03	-0.03	-0.03	-0.03	-0.03	1	-0.03	-0.03	-0.03	-0.03	-0.03	-0.03	-0.03	-0.03	-0.03	-0.03	-0.03	-0.03	-0.03	-0.03	-0.03
19	-0.03	-0.03	-0.03	-0.03	-0.03	-0.03	-0.03	-0.03	-0.03	-0.03	-0.03	-0.03	-0.03	-0.03	-0.03	-0.03	-0.03	-0.03	1	-0.03	-0.03	-0.03	-0.03	-0.03	-0.03	-0.03	-0.03	-0.03	-0.03	-0.03	-0.03	-0.03	-0.03
20	-0.03	-0.03	-0.03	-0.03	-0.03	-0.03	-0.03	-0.03	-0.03	-0.03	-0.03	-0.03	-0.03	-0.03	-0.03	-0.03	-0.03	-0.03	-0.03	1	-0.03	-0.03	-0.03	-0.03	-0.03	-0.03	-0.03	-0.03	-0.03	-0.03	-0.03	-0.03	-0.03
21	-0.03	0.23	-0.03	-0.03	-0.03	-0.03	-0.03	-0.03	-0.03	-0.03	-0.03	-0.03	-0.03	-0.03	-0.03	-0.03	-0.03	-0.03	-0.03	-0.03	1	-0.03	-0.03	-0.03	-0.03	-0.03	-0.03	-0.03	-0.03	-0.03	-0.03	-0.03	-0.03
22	-0.03	-0.03	-0.03	-0.03	-0.03	-0.03	-0.03	-0.03	-0.03	-0.03	-0.03	-0.03	-0.03	-0.03	-0.03	-0.03	-0.03	-0.03	-0.03	-0.03	-0.03	1	-0.03	-0.03	-0.03	-0.03	-0.03	-0.03	-0.03	-0.03	-0.03	-0.03	-0.03
23	-0.03	0.23	-0.03	-0.03	-0.03	-0.03	-0.03	-0.03	-0.03	-0.03	-0.03	-0.03	-0.03	-0.03	-0.03	-0.03	-0.03	-0.03	-0.03	-0.03	-0.03	-0.03	1	-0.03	-0.03	-0.03	-0.03	-0.03	-0.03	-0.03	-0.03	-0.03	-0.03
24	-0.03	-0.03	-0.03	-0.03	-0.03	-0.03	-0.03	-0.03	-0.03	-0.03	-0.03	-0.03	-0.03	-0.03	-0.03	-0.03	-0.03	-0.03	-0.03	-0.03	-0.03	-0.03	-0.03	1	-0.03	-0.03	-0.03	-0.03	-0.03	-0.03	-0.03	-0.03	-0.03
25	-0.03	-0.03	-0.03	-0.03	-0.03	-0.03	-0.03	-0.03	-0.03	-0.03	-0.03	-0.03	-0.03	-0.03	-0.03	-0.03	-0.03	-0.03	-0.03	-0.03	-0.03	-0.03	-0.03	-0.03	1	-0.03	-0.03	-0.03	-0.03	-0.03	-0.03	-0.03	-0.03
26	-0.03	0.23	-0.03	-0.03	-0.03	-0.03	-0.03	-0.03	-0.03	-0.03	-0.03	-0.03	-0.03	-0.03	-0.03	-0.03	-0.03	-0.03	-0.03	-0.03	-0.03	-0.03	-0.03	-0.03	-0.03	1	-0.03	-0.03	-0.03	-0.03	-0.03	-0.03	-0.03
27	-0.03	-0.03	-0.03	-0.03	-0.03	-0.03	-0.03	-0.03	-0.03	-0.03	-0.03	-0.03	-0.03	-0.03	-0.03	-0.03	-0.03	-0.03	-0.03	-0.03	-0.03	-0.03	-0.03	-0.03	-0.03	-0.03	1	-0.03	-0.03	-0.03	-0.03	-0.03	-0.03
28	-0.03	-0.03	-0.03	-0.03	-0.03	-0.03	-0.03	-0.03	-0.03	-0.03	-0.03	-0.03	-0.03	-0.03	-0.03	-0.03	-0.03	-0.03	-0.03	-0.03	-0.03	-0.03	-0.03	-0.03	-0.03	-0.03	-0.03	1	-0.03	-0.03	-0.03	-0.03	-0.03
29	-0.03	-0.03	-0.03	-0.03	-0.03	-0.03	-0.03	-0.03	-0.03	-0.03	-0.03	-0.03	-0.03	-0.03	-0.03	-0.03	-0.03	-0.03	-0.03	-0.03	-0.03	-0.03	-0.03	-0.03	-0.03	-0.03	-0.03	-0.03	1	-0.03	-0.03	-0.03	-0.03
30	-0.03	0.23	-0.03	-0.03	-0.03	-0.03	-0.03	-0.03	-0.03	-0.03	-0.03	-0.03	-0.03	-0.03	-0.03	-0.03	-0.03	-0.03	-0.03	-0.03	-0.03	-0.03	-0.03	-0.03	-0.03	-0.03	-0.03	-0.03	-0.03	1	-0.03	-0.03	-0.03
31	-0.03	-0.03	-0.03	-0.03	-0.03	-0.03	-0.03	-0.03	-0.03	-0.03	-0.03	-0.03	-0.03	-0.03	-0.03	-0.03	-0.03	-0.03	-0.03	-0.03	-0.03	-0.03	-0.03	-0.03	-0.03	-0.03	-0.03	-0.03	-0.03	-0.03	1	-0.03	-0.03
32	-0.03	-0.29	-0.03	-0.03	-0.03	-0.03	-0.03	-0.03	-0.03	-0.03	-0.03	-0.03	-0.03	-0.03	-0.03	-0.03	-0.03	-0.03	-0.03	-0.03	-0.03	-0.03	-0.03	-0.03	-0.03	-0.03	-0.03	-0.03	-0.03	-0.03	-0.03	1	-0.03
33	-0.03	-0.03	-0.03	-0.03	-0.03	-0.03	-0.03	-0.03	-0.03	-0.03	-0.03	-0.03	-0.03	-0.03	-0.03	-0.03	-0.03	-0.03	-0.03	-0.03	-0.03	-0.03	-0.03	-0.03	-0.03	-0.03	-0.03	-0.03	-0.03	-0.03	-0.03	-0.03	1

Table 2.6: The scalar listed in the ith row and the jth column is the correlation factor between $\mathbf{c}_i$ and $\mathbf{c}_j$, quantified by $\rho^c_{ij} = \mathbf{c}_i^T \mathbf{c}_j$. The value of $\mathbf{c}_i$ for $i = 1, 2, \ldots, 33$ is illustrated in the ith row of Tab. 2.5.

Given that a symbol is transmitted every $1/f$ seconds, the bandwidth occupied by the signal's main spectral lobe is the $(\sin x/x)$- shaped spectrum is f Hz. Since now the original symbol duration is further divided into N_s chip durations to transmit the N_s chip-values representing the original symbol, the original bandwidth f will be spread by a factor of N_s, which justifies the terminology of *spreading* codes associated with a spreading factor of N_s.

In general, the receiver has access to and exploits some auxiliary information. In a multiuser system employing the CDMA technique, where the channel impulse response (CIR) of each channel is assumed to be non-dispersive, yielding $h = 1$, the auxiliary information user k has access to is the knowledge of his/her spreading code, namely $\mathbf{A}_k = \mathbf{c}_k$. In a single-user system, where the envelope $|h|$ of the CIR h is assumed to be Rayleigh faded, the auxiliary information that may be exploited by the receiver is the knowledge of the CIR of $A = h$. Furthermore, in a Rayleigh-faded multiuser system employing CDMA techniques, where the CIR is assumed to be constant within a symbol corresponding to N_s chip durations, the auxiliary infromation of user k will be the Rayleigh faded sequence $\mathbf{A}_k = h_k\mathbf{c}_k$. Moreover, in a Rayleigh faded multiuser system employing Spatial Division Multiple Access (SDMA) techniques [**?**] in conjunction with N_r receive antennas, the auxiliary information of user k will be the CIR vector related to that particular user, which is formulated as $\mathbf{A}_k = \mathbf{h}_k = [h_{k1}, \ldots, h_{kN_r}]$.

As shown in the above example, as long as the auxiliary information $\mathbf{A}_k$ and $\mathbf{A}_j$ of the kth and the jth user is not orthogonal to each other, i.e. we have $\mathbf{A}_k^T\mathbf{A}_j \neq 0$ when $k \neq j$, Multi-User Interference (MUI) is imposed. However, in realistic dispersive communication systems the channel-impairments destroy the orthogonality, even if orthogonal codes were transmitted. Therefore, when $K > 1$ users are supported by the system, diverse MUD algorithms may be invoked [93], which are capable of operating without the auxiliary information of the desired user. According to the amount of knowledge they utilize, the MUI can be mitigated to a different extent, which results in different BER performances. In section 2.3, we commence our discourse from the concept of the most intuitive optimal detection algorithm in the context of a single-user system and then in Secion 2.4 we briefly introduce some well-known MUD algorithms.

2.3 Hard-Output SUD

We will commence our discourse from the simplest scenario, when only a single user is transmitting his/her signal in the uplink of a cell, which can be modeled as in Fig. 2.3.

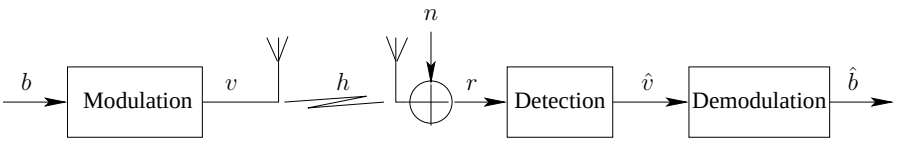

Figure 2.3: Block diagram of the system considered in Section 2.3.

2.3.1 Definitions

The variable b represents the bit 0 or 1, the complex variable v represents the modulated symbol, the complex variable h quantifies the point-to-point single link's CIR, the complex-valued variable n

denotes the noise imposed by the receiver, the complex variable r is the received signal, $\hat{v}$ denotes the legitimate modulated symbol recovered from r before being demodulated, namely the hard-decision based result for v, and finally, $\hat{b}$ is the bit recovered from r, i.e. the hard-decision based result for b.

Then at any bit interval, b is an instanciation of the uniformly distributed random variable $\mathfrak{b}$, which has the legitimate values of 0 and 1 that are equi-probable. If BPSK mudulation is used, the modulated symbol will be $v = +1 + j \cdot 0$ given $b = 0$ and $v = -1 + j \cdot 0$ given $b = 1$.

Similarly, h is an instanciation of the random variable $\mathfrak{h} = \Re\{\mathfrak{h}\} + j \cdot \Im\{\mathfrak{h}\} = |\mathfrak{h}|e^{j\theta}$, where $\Re\{\mathfrak{h}\}$ and $\Im\{\mathfrak{h}\}$ are uncorrelated and real-valued Gaussian distributed variables having a mean of 0 and a variance of $\frac{1}{2}$, hence the envelope $|\mathfrak{h}|$ is a Rayleigh distributed random variable and the phase θ is uniformly distributed in $[0, 2\pi]$. Unless otherwise stated, the channel considered is an uncorrelated flat Rayleigh-faded medium. The following further assumptions are stipulated:

1. The CIR h obeys a flat-fading Rayleigh envelope which remains constant during any symbol interval.

2. When considering any two symbol intervals, namely t_i, t_j ($t_i \neq t_j$), h_{t_i} and h_{t_j} are uncorrelated, hence we have $E\{h_{t_i}h_{t_j}\} = E\{h_{t_i}\}E\{h_{t_j}\}$.

3. Provided that two receive or transmit antennas are at least 10λ[1] apart from each other, their CIRs of h_m and h_n may also be deemed uncorrelated, i.e. we have $E\{h_m h_n\} = E\{h_m\}E\{h_n\}$.

The noise n is a sample of the complex-valued Gaussian distributed random variable $\mathfrak{n} = \Re\{\mathfrak{n}\}+j\cdot\Im\{\mathfrak{n}\}$. Both $\Re\{\mathfrak{n}\}$ and $\Im\{\mathfrak{n}\}$ are real-valued Gaussian distributed variables with a mean of $\mu_{\Re\{\mathfrak{n}\}} = \mu_{\Im\{\mathfrak{n}\}} = 0$ and a variace of $\sigma^2_{\Re\{\mathfrak{n}\}} = \sigma^2_{\Im\{\mathfrak{n}\}} = \frac{1}{2}\sigma^2_{\mathfrak{n}}$.

The PDF of any complex-valued Gaussian distributed random variable $\mathfrak{x} = \Re\{\mathfrak{x}\} + j \cdot \Im\{\mathfrak{x}\}$, where both the real and imaginary components have the same variance of $\sigma^2_{\Re\{\mathfrak{x}\}}$, is given by [160]

$$p(x) = \frac{1}{2\pi\sigma^2_{\Re\{\mathfrak{x}\}}} \exp\left(-\frac{\left(\Re\{x\} - \mu_{\Re\{\mathfrak{x}\}}\right)^2 + \left(\Im\{x\} - \mu_{\Im\{\mathfrak{x}\}}\right)^2}{2\sigma^2_{\Re\{\mathfrak{x}\}}}\right). \tag{2.1}$$

Upon substituting x with n, $\mu_{\Re\{\mathfrak{x}\}}$ and $\mu_{\Im\{\mathfrak{x}\}}$ with 0, and $\sigma^2_{\Re\{\mathfrak{x}\}}$ with $\frac{1}{2}\sigma^2_{\mathfrak{n}}$, we arrive at the PDF of $\mathfrak{n} = (n = \Re\{n\} + j \cdot \Im\{n\})$ in the following form:

$$p(\mathfrak{n} = n) = \frac{1}{\pi\sigma^2_{\mathfrak{n}}} \exp\left(-\frac{|n|^2}{\sigma^2_{\mathfrak{n}}}\right), \tag{2.2}$$

where $|n| = \sqrt{\Re\{n\}^2 + \Im\{n\}^2}$ is the modulus or absolute value of n. Unlike the CIR h that is constant across all the chips within a single symbol duration, the noise samples n_i, n_j encountered at two different chip intervals are two different instantaneous samples of $\mathfrak{n}$, where n_i, n_j are independent of each other.

Therefore, the received signal can be formulated as

$$r = hv + n. \tag{2.3}$$

Throughout our discussions, we stipulate the simplifying assumption that the CIR h is perfectly known at the receiver.

[1] A practical requirement for the two channels to be uncorrelated.

2.3.2 Optimal Detection and Matched-Filter Solution

The goal of a single user system's detector is to determine $\hat{v}$ based on r and the CIR h, which is assumed to be known. Due to the employment of a BPSK modulation scheme, v can either be $+1$ or -1. Therefore, the goal of the optimal hard-output detector[2] is to quantify the probability of $v = +1$ and $v = -1$ based on the received signal r and to make a final verdict based on these two probabilities. More quantatively, $P(v = +1|r)$ can be represent the probabiltiy that $v = +1$ was transmitted based on the observation of r, while $P(v = +1|r)$ can be used to quantify the probability that $v = -1$ was transmitted, given that r was observed. Then the final verdict of the optimal Hard-Output (HO) detector would be $\hat{v} = +1$ if $P(v = +1|r) > P(v = -1|r)$ and $\hat{v} = -1$ otherwise. However, the PDF describing the *a posteriori* conditional probabilites of $P(v = +1|r)$ and $P(v = -1|r)$ is unknown.

According to Bayes' rule [160], the above-mentioned unknown *a posteriori* probabilities can be represented with the aid of the *a priori* conditional probability, which can be derived from the PDF of the Gaussian distribution. More quantatively, according to Bayes' rule [160], we have

$$P(v = \pm 1|r) = \frac{P(v = \pm 1)p(r|v = \pm 1)}{p(r)}. \tag{2.4}$$

For BPSK modulation, $+1$ and -1 will be transmitted with equal probability, yielding

$$P(v = +1) = P(v = -1) = 0.5. \tag{2.5}$$

When the CIR h is known at the receiver for the symbol duration considered, the probability of receiving r is given by

$$p(r) = P(v = +1)p(r|v = +1) + P(v = -1)p(r|v = -1). \tag{2.6}$$

Since we have $P(v = +1) = P(v = -1) = 0.5$, the final verdict concerning whether $v = +1$ or $v = -1$ was transmitted is determined by the *a priori* probability of

$$p(r|v = \pm 1). \tag{2.7}$$

We will hence focus our attention on the derivation of the *a priori* probability $p(r|v = \pm 1)$.

For BPSK modulation we have $v = \pm 1$, hence according to Eq. (2.3), we have $r = \pm h + n$, where the CIR h is a known complex number and n is a sample of the complex-valued Gaussian distributed random variable $\mathfrak{n} = \Re\{\mathfrak{n}\} + j \cdot \Im\{\mathfrak{n}\}$, with a mean of $\mu_{\Re\{\mathfrak{n}\}} = \mu_{\Im\{\mathfrak{n}\}} = 0$ and a variace of $\sigma^2_{\Re\{\mathfrak{n}\}} = \sigma^2_{\Im\{\mathfrak{n}\}} = \frac{1}{2}\sigma^2_{\mathfrak{n}}$ in each of the complex dimensions.

The family of complex-valued Gaussian distributions is closed under linear transformations [161], implying that if n is complex-valued Gaussian distributed with a mean of $\mu_{\mathfrak{n}}$ and a variance of $\sigma^2_{\mathfrak{n}}$, then the linear transform of $\pm h + n$ is also complex-valued Gaussian distributed:

$$\begin{aligned}
\mathfrak{n} \pm h &\sim \mathcal{N}^{\mathrm{c}}\left(\mu_{\mathfrak{n}} \pm h, \quad \sigma^2_{\mathfrak{n}}\right) \\
(\Re\{\mathfrak{n} \pm h\}|) &\sim \mathcal{N}^{\mathrm{r}}\left(\mu_{\Re\{\mathfrak{n}\}} \pm \Re\{h\}, \quad \frac{1}{2}\sigma^2_{\mathfrak{n}}\right) \\
(\Im\{\mathfrak{n} \pm h\}|) &\sim \mathcal{N}^{\mathrm{r}}\left(\mu_{\Im\{\mathfrak{n}\}} \pm \Im\{h\}, \quad \frac{1}{2}\sigma^2_{\mathfrak{n}}\right).
\end{aligned} \tag{2.8}$$

[2] A hard-output detector only provides the estimated value for v, instead of the reliability of its estimate, which is furnished by a soft-output detector, as it will be detailed in Sections 2.6

Hence, for $v = +1$, $(r|v = +1)$ is a sample of the complex-valued Gaussian distributed variable, obeying

$$\begin{aligned}(\mathfrak{r}|v=+1) &\sim \mathcal{N}^{\mathrm{c}}\big(\mu_{\mathfrak{n}} - h, \quad \sigma_{\mathfrak{n}}^2\big)\\ (\Re\{\mathfrak{r}\}|v=+1) &\sim \mathcal{N}^{\mathrm{r}}\Big(\mu_{\Re\{\mathfrak{n}\}} + \Re\{h\}, \quad \frac{1}{2}\sigma_{\mathfrak{n}}^2\Big)\\ (\Im\{\mathfrak{r}\}|v=+1) &\sim \mathcal{N}^{\mathrm{r}}\Big(\mu_{\Im\{\mathfrak{n}\}} + \Im\{h\}, \quad \frac{1}{2}\sigma_{\mathfrak{n}}^2\Big)\end{aligned} \tag{2.9}$$

and for $v = -1$, $(r|v = -1)$ is a sample of the complex-valued Gaussian distributed variable, obeying

$$\begin{aligned}(\mathfrak{r}|v=-1) &\sim \mathcal{N}^{\mathrm{c}}\big(\mu_{\mathfrak{n}} + h, \quad \sigma_{\mathfrak{n}}^2\big)\\ (\Re\{\mathfrak{r}\}|v=-1) &\sim \mathcal{N}^{\mathrm{r}}\Big(\mu_{\Re\{\mathfrak{n}\}} - \Re\{h\}, \quad \frac{1}{2}\sigma_{\mathfrak{n}}^2\Big)\\ (\Im\{\mathfrak{r}\}|v=-1) &\sim \mathcal{N}^{\mathrm{r}}\Big(\mu_{\Im\{\mathfrak{n}\}} - \Im\{h\}, \quad \frac{1}{2}\sigma_{\mathfrak{n}}^2\Big).\end{aligned} \tag{2.10}$$

According to Eq. (2.1), we have

$$p(x) = \frac{1}{2\pi\sigma_{\Re\{\mathfrak{r}\}}^2} \exp\left(-\frac{\big(\Re\{x\} - \mu_{\Re\{\mathfrak{r}\}}\big)^2 + \big(\Im\{x\} - \mu_{\Im\{\mathfrak{r}\}}\big)^2}{2\sigma_{\Re\{\mathfrak{r}\}}^2}\right), \tag{2.11}$$

with $x = (r|v = +1)$, $\mu_{\Re\{\mathfrak{r}\}} = \mu_{\Re\{\mathfrak{n}\}} + \Re\{h\} = \Re\{h\}$, $\mu_{\Im\{\mathfrak{r}\}} = \mu_{\Im\{\mathfrak{n}\}} + \Im\{h\} = \Im\{h\}$ and $\sigma_{\Re\{\mathfrak{r}\}}^2 = \frac{1}{2}\sigma_{\mathfrak{n}}^2$, which determines the PDF of $(r|v = +1)$ $p(r|v = +1)$, yielding

$$\begin{aligned}p(r|v=+1) &= \frac{1}{\pi\sigma_{\mathfrak{n}}^2} \exp\left(-\frac{\big(\Re\{r\} - \Re\{h\}\big)^2 + \big(\Im\{r\} - \Im\{h\}\big)^2}{\sigma_{\mathfrak{n}}^2}\right)\\ &= \frac{1}{\pi\sigma_{\mathfrak{n}}^2} \exp\left(-\frac{\big(\Re\{r-h\}\big)^2 + \big(\Im\{r-h\}\big)^2}{\sigma_{\mathfrak{n}}^2}\right)\\ &= \frac{1}{\pi\sigma_{\mathfrak{n}}^2} \exp\left(-\frac{(|r-h|)^2}{\sigma_{\mathfrak{n}}^2}\right).\end{aligned} \tag{2.12}$$

Similarly, with $x = (r|v = -1)$, $\mu_{\Re\{\mathfrak{r}\}} = \mu_{\Re\{\mathfrak{n}\}} - \Re\{h\} = -\Re\{h\}$, $\mu_{\Im\{\mathfrak{r}\}} = \mu_{\Im\{\mathfrak{n}\}} - \Im\{h\} = -\Im\{h\}$ and $\sigma_{\Re\{\mathfrak{r}\}}^2 = \frac{1}{2}\sigma_{\mathfrak{n}}^2$, the PDF of $(r|v = -1)$, i.e. $p(r|v = -1)$ can be formulated as

$$\begin{aligned}p(r|v=-1) &= \frac{1}{\pi\sigma_{\mathfrak{n}}^2} \exp\left(-\frac{\big(\Re\{r\} + \Re\{h\}\big)^2 + \big(\Im\{r\} + \Im\{h\}\big)^2}{\sigma_{\mathfrak{n}}^2}\right)\\ &= \frac{1}{\pi\sigma_{\mathfrak{n}}^2} \exp\left(-\frac{\big(\Re\{r+h\}\big)^2 + \big(\Im\{r+h\}\big)^2}{\sigma_{\mathfrak{n}}^2}\right)\\ &= \frac{1}{\pi\sigma_{\mathfrak{n}}^2} \exp\left(-\frac{(|r+h|)^2}{\sigma_{\mathfrak{n}}^2}\right).\end{aligned} \tag{2.13}$$

Hence, the final verdict, whether $v = +1$ or $v = -1$ was transmitted, based on the two *a priori* conditional probabilities given in Eq. (2.12) and Eq. (2.13), can be formulated as

$$\begin{aligned}\hat{v} &= +1 \qquad \text{if } p(r|v=+1) > p(r|v=-1)\\ \hat{v} &= -1 \qquad \text{otherwise.}\end{aligned} \tag{2.14}$$

We use a new symbol $\dot{v}$ to resemble a trial BPSK modulated symbol with its two legitimate values in the set $\mathbb{V}^{(1)} = \{+1, -1\}$, hence Eq. (2.14) can be alternatively represented as

$$\hat{v} = \arg \max_{\dot{v} \in \{+1,-1\}} \big\{p(r|\dot{v})\big\}. \tag{2.15}$$

Furthermore Eq. (2.12) and Eq. (2.13) can also be unified with the aid of $\dot{v}$ as

$$p(r|\dot{v}) = \frac{1}{\pi\sigma_{\mathfrak{n}}^2} \exp\left(-\frac{(|r - h\dot{v}|)^2}{\sigma_{\mathfrak{n}}^2}\right). \tag{2.16}$$

During any symbol duration considered, the component $1/(\pi\sigma_{\mathfrak{n}}^2)$ in Eq. (2.16) is a constant positive scalar, hence the *a priori* probability quantified by Eq. (2.16) is monotonically increasing according to the exponential component in Eq. (2.16), since the function $\exp(x)$ of a real-valued scalar x is a monotonically increasing function of x. Additionally, the exponential component in Eq. (2.16) may alternatively be represented as

$$\begin{aligned} \exp(x_1) &= \exp\left(-\frac{x_2}{\sigma_{\mathfrak{n}}^2}\right), \qquad \text{with } x_1 = -\frac{x_2}{\sigma_{\mathfrak{n}}^2} \\ &= \exp\left(-\frac{(|r - h\dot{v}|)^2}{\sigma_{\mathfrak{n}}^2}\right), \quad \text{with } x_2 = (|r - h\dot{v}|)^2. \end{aligned} \tag{2.17}$$

Since the constant $(-1/\sigma_{\mathfrak{n}}^2)$ in Eq. (2.17) is a negative scalar, Eq. (2.17) is a monotonically decreasing function of x_2. Thanks to the monotonically decreasing relationship between $p(r|\dot{v})$ and $x_2 = (|r - h\dot{v}|)^2$, because upon decreasing x_2 the value of x_1 increases, hence $\exp(x_1)$ also increase, which results in an increased value for $p(r|\dot{v}) \uparrow$. Therefore, the decision that maximizes $p(r|\dot{v})$ is identical to that which minimizes $x_2 = (|r - h\dot{v}|)^2$. Hence the objective function of the optimal detection algorithm of a single-user system as initially quantified in Eq. (2.15) can be more concisely represented by $x_2 = (|r - h\dot{v}|)^2$. More explicitly, we have

$$\hat{v} = \arg \min_{\dot{v}\in\{+1,-1\}} \left\{|r - h\dot{v}|^2\right\}. \tag{2.18}$$

To elaborate a little further, the calculation of $|r - h\dot{v}|^2$ may be simplifed by expanding it as

$$\begin{aligned} |r - h\dot{v}|^2 &= (r - h\dot{v})^*(r - h\dot{v}) = (r^* - \dot{v}^*h^*)(r - h\dot{v}) \\ &= r^*r - \dot{v}^*h^*r - r^*h\dot{v} + \dot{v}^*|h|^2\dot{v}. \end{aligned} \tag{2.19}$$

Since we have $\dot{v}^*|h|^2\dot{v} = |\dot{v}|^2|h|^2 = 1 \cdot |h|^2$, and because r^*r is independent of whether we have $\dot{v} = +1$ or $\dot{v} = -1$, hence only the 2nd and 3rd terms of Eq. (2.19), namely only the value of $(-\dot{v}^*h^*r - r^*h\dot{v})$ has to be calculated for $\dot{v} = +1$ and $\dot{v} = -1$. Since $x = \dot{v}^*h^*r$ is a complex-valued scalar and since we have $x^* = r^*h\dot{v}$, and $x + x^* = 2\Re\{x\}$; hence the only computation we need is $-\dot{v}^*h^*r - r^*h\dot{v} = -2\Re\{\dot{v}^*h^*r\} = -2\Re\{r^*h\dot{v}\}$.

Because $|r - h\dot{v}|^2$ is a monotonelly decreasing function of $\Re\{\dot{v}^*h^*r\}$, and our goal is to make a final decision between $v = +1$ and $v = -1$, the optimal detector of a single-user system can be further expressed with the aid of Eq. (2.18) as

$$\hat{v} = \arg \max_{\dot{v}\in\{+1,-1\}} \left[\Re\{\dot{v}^*h^*r\}\right]. \tag{2.20}$$

Since a BPSK modulation scheme is employed, v is a real number, thus we have $\dot{v}^* = \dot{v} = \Re\{\dot{v}\}$. Hence $\Re\{\dot{v}^*h^*r\} = \Re\{\dot{v}\}\Re\{h^*r\}$. Therefore, the detection quantified in Eq. (2.20) can be further expressed as:

$$\hat{v} = \arg \max_{\dot{v}\in\{+1,-1\}} \left[\Re\{\dot{v}\}\Re\{h^*r\}\right]. \tag{2.21}$$

For $\Re\{h^*r\} > 0$, $\max\big[\Re\{\dot{v}\}\Re\{h^*r\}\big]$ corresponds to the decision of $\dot{v} = +1$. By contrast, for $\Re\{h^*r\} < 0$, $\max\big[\Re\{\dot{v}\}\Re\{h^*r\}\big]$ will always be obtained for $\dot{v} = -1$. Therefore, instead of Eq. (2.21), the optimal hard-output detector of a single user system can be formulated as

$$\hat{v} = \begin{cases} +1 & , \quad \text{if } \Re\{h^*r\} \geqslant 0 \\ -1 & , \quad \text{if } \Re\{h^*r\} < 0 \end{cases} . \tag{2.22}$$

Upon assigning the product of h^*r to y defined in Eq. (2.22) as

$$y = h^*r, \tag{2.23}$$

we arrive at the Matched Filter (MF) algorithm of the single-user system:

$$\hat{v} = \text{sgn}\big\{\Re\{h^*r\}\big\}. \tag{2.24}$$

Based on the above arguments, when a single-user system is BPSK modulated, the optimal hard-output detection algorithm is identical to the MF algorithm.

2.4 Hard-Output MUD

2.4.1 System Model

CDMA techniques are capable of supporting K users by assigning unique user-specific spreading sequences, which are transmitted within the same frequency band and same time slot. The most basic block diagram of a CDMA system supporting K users is depicted in Fig. 2.4. The system structure to be used in Chapters 3 and 4 will be developed from this schematic. According to Fig. 2.4, the

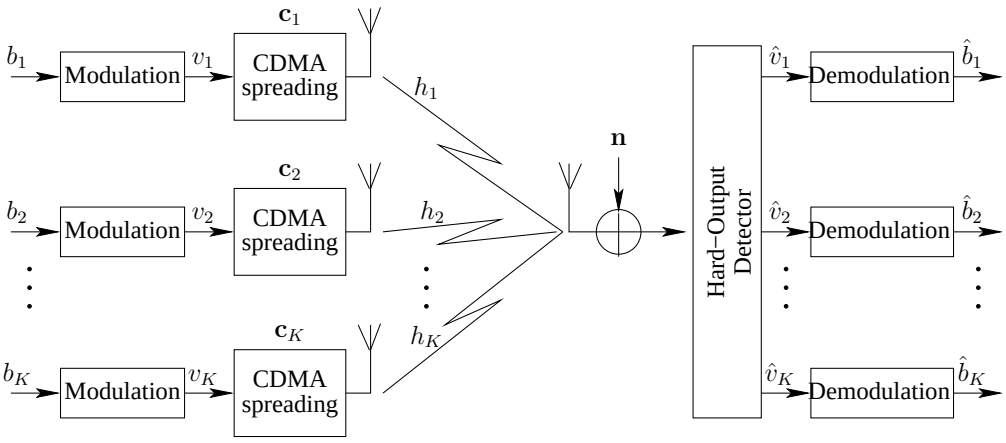

Figure 2.4: Block diagram of the multiuser system described in Section 2.4 and Chapter 3. More sophisticated block diagrams will be developed in Chapters 3 and 4 and Chapter 5.

signal received during the chip-interval n_s, for $n_s = 1, 2, \ldots, N_s$, can be represented by the following equations:

$$\begin{array}{rcccccccccc} r_1 & = & c_{11}\,h_1v_1 & + & c_{21}\,h_2v_2 & + & \cdots & + & c_{K1}\,h_Kv_K & + & n_1 \\ r_2 & = & c_{12}\,h_1v_1 & + & c_{22}\,h_2v_2 & + & \cdots & + & c_{K2}\,h_Kv_K & + & n_2 \\ \vdots & & \vdots & & \vdots & & & & \vdots & & \vdots \\ r_{N_s} & = & c_{1N_s}h_1v_1 & + & c_{2N_s}h_2v_2 & + & \cdots & + & c_{KN_s}h_Kv_K & + & n_{N_s} \end{array} , \tag{2.25}$$

where the index of r represents the chip-interval during which the signal is received. The first subscript of c ranges from 1 to K and indicates the user index to whom the code is assigned, while the second integer ranging from 1 to N_s specifies the chip-interval during which the signal is transmitted. Hence c_{kn_s} specifies the value of the n_sth chip of the kth N_s-chip CDMA spreading sequence.

Observe in Eq. (2.25) that apart from the AWGN, the received signal r_{n_s} contains K superimposed chip-components contributed by the K users. Each of the K superimposed branches represents the n_sth chip $c_{kn_s}v_k$ of the symbol v_k after travelling through its fading channel h_k, finally yeilding $c_{kn_s}h_kv_k$. When considering all the K users, we have

$$r_{n_s} = \sum_{k=1}^{K} c_{kn_s}h_kv_k + n_{n_s}. \tag{2.26}$$

Alternatively, Eq. (2.25) can be expressed in a compact matrix formulated as:

$$\mathbf{r} = \mathbf{CHv} + \mathbf{n} \tag{2.27}$$

or expanded as:

$$\begin{bmatrix} r_1 \\ r_2 \\ \vdots \\ r_{N_s} \end{bmatrix} = \begin{bmatrix} c_{11} & c_{21} & \cdots & c_{K1} \\ c_{12} & c_{22} & \cdots & c_{K2} \\ \vdots & \vdots & \cdots & \vdots \\ c_{1N_s} & c_{2N_s} & \cdots & c_{KN_s} \end{bmatrix} \begin{bmatrix} h_1 & 0 & \cdots & 0 \\ 0 & h_2 & \cdots & 0 \\ \vdots & \vdots & \ddots & \vdots \\ 0 & 0 & \cdots & h_K \end{bmatrix} \begin{bmatrix} v_1 \\ v_2 \\ \vdots \\ v_K \end{bmatrix} + \begin{bmatrix} n_1 \\ n_2 \\ \vdots \\ n_{N_s} \end{bmatrix}, \tag{2.28}$$

where the $(N_s \times 1)$-element complex-valued vector $\mathbf{r} = [r_1, r_2, \cdots, r_{N_s}]^T$ quantifies the received signal vector over a symbol interval constituted by N_s chip durations; the $(N_s \times 1)$-element complex-valued vector $\mathbf{n} = [n_1, n_2, \cdots, n_{N_s}]^T$ quantifes the N_s unknown mutually indepedent AWGN samples encountered over the N_s chip durations, where each of the elements n_{n_s} in $\mathbf{n}$ is a sample of the random variable $\mathfrak{n}$, which has a complex-valued Gaussian distribution with a mean of $\mu_{\mathfrak{n}} = 0$ and a variance of $\sigma_{\mathfrak{n}}^2$ $\mathfrak{n} \sim \mathcal{N}^c(0, \sigma_{\mathfrak{n}}^2)$; the $(K \times 1)$-element signal vector $\mathbf{v} = [v_1, v_2, \cdots, v_K]^T$ represents the $\mathcal{M}$-ary modulated symbol of each user; the $(K \times K)$-element CIR diagonal matrix

$$\mathbf{H} = \text{diag}\{h_1, h_2, \ldots, h_K\} \tag{2.29}$$

defines the complex-valued CIR h_k of each user, where both the real part $\Re\{h_k\}$ and the imaginary part $\Im\{h_k\}$ of $h_k = \Re\{h_k\} + j \cdot \Im\{h_k\}$ is real Gaussian distributed with a mean of 0 and a variance of $\frac{1}{2}$, hence having a Rayleigh distributed envelope of $|h_k|$.

We will refer to the product of the spreading code $\mathbf{c}_k$ and the CIR h_k of the kth user as his/her auxiliary information, which will be denoted by $\mathbf{A}_k = h_k\mathbf{c}_k$. In Eq. 2.27, the spreading code matrix $\mathbf{C}$ was represented as the matrix constituted by the row-vectors comprising the kth user's spreading code $\mathbf{c}_k$, $k = 1, \ldots, K$, yielding

$$\mathbf{C} = [\mathbf{c}_1 \quad \mathbf{c}_2 \quad \cdots \quad \mathbf{c}_K]. \tag{2.30}$$

Hence the matrix product of the matrix $\mathbf{C}$ and $\mathbf{H}$ in Eq. (2.27) may be expressed in a compact form as:

$$\mathbf{A} = \mathbf{CH} \tag{2.31}$$

or in an expanded form as

$$\begin{aligned}
\mathbf{A} &= \begin{bmatrix} c_{11} & c_{21} & \cdots & c_{K1} \\ c_{12} & c_{22} & \cdots & c_{K2} \\ \vdots & \vdots & \cdots & \vdots \\ c_{1N_\mathrm{s}} & c_{2N_\mathrm{s}} & \cdots & c_{KN_\mathrm{s}} \end{bmatrix} \begin{bmatrix} h_1 & 0 & \cdots & 0 \\ 0 & h_2 & \cdots & 0 \\ \vdots & \vdots & \ddots & \vdots \\ 0 & 0 & \cdots & h_K \end{bmatrix} \\
&= \begin{bmatrix} h_1 c_{11} & h_2\, c_{21} & \cdots & h_K c_{K1} \\ h_1 c_{12} & h_2\, c_{22} & \cdots & h_K c_{K2} \\ \vdots & \vdots & \cdots & \vdots \\ h_1 c_{1N_\mathrm{s}} & h_2\, c_{2N_\mathrm{s}} & \cdots & h_K c_{KN_\mathrm{s}} \end{bmatrix} \\
&= \begin{bmatrix} h_1\mathbf{c}_1 & h_2\mathbf{c}_2 & \cdots & h_K\mathbf{c}_K \end{bmatrix} \\
&= \begin{bmatrix} \mathbf{A}_1 & \mathbf{A}_2 & \cdots & \mathbf{A}_K \end{bmatrix}.
\end{aligned} \tag{2.32}$$

Hence the correlation matrix of the auxiliary matrix $\mathbf{A}$ quantified in Eq. (2.31) can be defined as

$$\begin{aligned}
\mathbf{R} &= \mathbf{A}^H\mathbf{A} \\
&= [\mathbf{A}_1^H \;\; \mathbf{A}_2^H \;\; \cdots \;\; \mathbf{A}_K^H]^T [\mathbf{A}_1 \;\; \mathbf{A}_2 \;\; \cdots \;\; \mathbf{A}_K] \\
&= \begin{bmatrix} \mathbf{A}_1^H\mathbf{A}_1 & \mathbf{A}_1^H\mathbf{A}_2 & \cdots & \mathbf{A}_1^H\mathbf{A}_K \\ \mathbf{A}_2^H\mathbf{A}_1 & \mathbf{A}_2^H\mathbf{A}_2 & \cdots & \mathbf{A}_2^H\mathbf{A}_K \\ \vdots & \vdots & \ddots & \vdots \\ \mathbf{A}_K^H\mathbf{A}_1 & \mathbf{A}_K^H\mathbf{A}_2 & \cdots & \mathbf{A}_K^H\mathbf{A}_K \end{bmatrix} \\
&= \begin{bmatrix} h_1\, \mathbf{c}_1^H\mathbf{c}_1 h_1 & h_1\, \mathbf{c}_1^H\mathbf{c}_2 h_2 & \cdots & h_1\, \mathbf{c}_1^H\mathbf{c}_K h_K \\ h_2\, \mathbf{c}_2^H\mathbf{c}_1 h_1 & h_2\, \mathbf{c}_2^H\mathbf{c}_2 h_2 & \cdots & h_2\, \mathbf{c}_2^H\mathbf{c}_K h_K \\ \vdots & \vdots & \ddots & \vdots \\ h_K \mathbf{c}_K^H\mathbf{c}_1 h_1 & h_K \mathbf{c}_K^H\mathbf{c}_2 h_2 & \cdots & h_K \mathbf{c}_K^H\mathbf{c}_K h_K \end{bmatrix} \\
&= \begin{bmatrix} h_1 \;\; 1 \;\; h_1 & h_1\, \rho_{12}^{\mathrm{c}}\, h_2 & \cdots & h_1\, \rho_{1K}^{\mathrm{c}} h_K \\ h_2\, \rho_{21}^{\mathrm{c}}\, h_1 & h_2 \;\; 1 \;\; h_2 & \cdots & h_2\, \rho_{2K}^{\mathrm{c}} h_K \\ \vdots & \vdots & \ddots & \vdots \\ h_K \rho_{K1}^{\mathrm{c}} h_1 & h_K \rho_{K2}^{\mathrm{c}} h_2 & \cdots & h_K \;\; 1 \;\; h_K \end{bmatrix} \\
&= \begin{bmatrix} |h_1|^2 & \rho_{12}^{\mathrm{c}}\, \rho_{12}^{\mathrm{h}} & \cdots & \rho_{1K}^{\mathrm{c}} \rho_{1K}^{\mathrm{h}} \\ \rho_{21}^{\mathrm{c}}\, \rho_{21}^{\mathrm{h}} & |h_2|^2 & \cdots & \rho_{2K}^{\mathrm{c}} \rho_{2K}^{\mathrm{h}} \\ \vdots & \vdots & \ddots & \vdots \\ \rho_{K1}^{\mathrm{c}} \rho_{K1}^{\mathrm{h}} & \rho_{K2}^{\mathrm{c}} \rho_{K2}^{\mathrm{h}} & \cdots & |h_K|^2 \end{bmatrix},
\end{aligned} \tag{2.33}$$

where $\rho_{ij}^{\mathrm{c}} = \mathbf{c}_i^T\mathbf{c}_j$ is the correlation factor between the ith and the jth spreading code, as exemplified by the correlation matrix $\mathbf{C}^T\mathbf{C}$ of the seven m-sequences having 7 chips in Table 2.4 and by the correlation matrix of the thirty-three Gold codes having a length of 31 chips in Table 2.6. In Eq. (2.33), ρ_{ij}^{h} represents the correlation factor between the CIRs h_i and h_j, given by $\rho_{ij}^{\mathrm{h}} = h_i^* h_j$. For $i = j$, we have $\rho_{ii}^{\mathrm{c}} = 1$ and $\rho_{ii}^{\mathrm{h}} = |h_i|^2$.

Eq. (2.27) formulates the most basic system model, which will used to develop more sophisticated systems that will be investigated throughout this treatise. Each of the matrices in Eq. (2.27) can be extended to encompass the time, spatial-, and frequency-domain, i.e. a number of subcarries.

In the multi-carrier DS-CDMA system to be investigated in Chapter 4, where the number of subcarriers increases from 1 to uv, the vector $\mathbf{r}$ of the received signal, the channel matrix $\mathbf{H}$ and the AWGN vector $\mathbf{n}$ will be expanded to incorporate a subcarrier index. More specifically, for a total of UV subcarriers, there will be UV counterparts of $\mathbf{r}$, $\mathbf{H}$ and $\mathbf{n}$, yielding $\mathbf{r}_{uv}$, $\mathbf{H}_{uv}$ and $\mathbf{n}_{uv}$ for $u = 1, \ldots, U$ and $v = 1, \ldots, V$. Hence, for each subcarrier v, the received signal $\mathbf{r}_v$ asosciated with the particular subcarrier f_v can be expressed as

$$\mathbf{r}_v = \mathbf{C}\mathbf{H}_v\mathbf{v} + \mathbf{n}_v. \tag{2.34}$$

In the mMlti-Functional Antenna Array (MFAA) assisted MC DS-CDMA system to be proposed in Chapter 4, where N_r number of receive antennas are employed at the BS, each of which is comprised of L elements, there will be $(N_\mathrm{r}LUV)$ number of counterparts of Eq. (2.27). Therefore, the received signal $\mathbf{r}_v^{(n_\mathrm{r}l)}$ asosciated with a particular antenna element l comprising the n_rth receive antenna associated with a particular subcarrier f_v can be formulated as

$$\mathbf{r}_v^{(n_\mathrm{r}l)} = \mathbf{C}\mathbf{H}_v^{(n_\mathrm{r}l)}\mathbf{v} + \mathbf{n}_v^{(n_\mathrm{r}l)}. \tag{2.35}$$

Furthermore, in the Space-Time Block Coded (STBC) DS-CDMA system to be investigated in Chapters 5 and 7, the vector $\mathbf{v}$ of transmitted signal is expanded to include two symbols that are transmitted within two consecutive symbol durations, the vector $\mathbf{v}$ will be expanded to a $(2K \times 1)$-element vector, and the channel matrix $\mathbf{H}$ will be accordingly expanded to a $(2K \times 2K)$-element matrix. Similarly, the spreading code matrix has twice the number of rows, since $2N_\mathrm{s}$ chips have to be used in order to transmit the signal vector $\mathbf{v}$. Similarly, we also have to double the number of columns to $2K$, because two symbols are transmitted during $2N_\mathrm{s}$ chip intervals. Accordingly, the size of $\mathbf{r}$ and $\mathbf{n}$ is also doubled due to having $2N_\mathrm{s}$ observations of the received signal, which are contaminated by $2N_\mathrm{s}$ AWGN samples.

2.4.2 Objective of Optimal Detection

The reference user's transmitted signal is v_1, while the Hard-Output (HO) detected result is $\hat{v}_1$, which is based on the observation r and on the OF of the optimal detector, which is formulated as:

$$\hat{v}_1 = \arg \max_{\dot{v} \in \{+1,-1\}} P(\dot{v}|r). \tag{2.36}$$

However, when employing Bayes' rule given by

$$P(v = \dot{v}|r) = \frac{P(v = \dot{v})p(r|v = \dot{v})}{p(r)}, \tag{2.37}$$

the probability $p(r|v = \dot{v})$ is unknown to the detector. As suggested by Eq. (2.25), provided that the vector $\mathbf{v} = [v_1, v_2, \ldots, v_K]$ of the signals transmitted by the K users is known to the detector, the signal received during any chip interval n_s, where $n_\mathrm{s} \in [1, N_\mathrm{s}]$ can be expressed as

$$r_{n_\mathrm{s}} = \dot{r}_{n_\mathrm{s}} + n_{n_\mathrm{s}}, \tag{2.38}$$

where

$$\dot{r}_{n_s} = \sum_{k=1}^{K} c_{kn_s} h_k v_k \tag{2.39}$$

quantifies the legitimate received signal during the chip interval n_s, when $\mathbf{v}$ is transmitted. The corresponding N_s-chip received signal vector $\mathbf{r}$ can also be expressed as

$$\mathbf{r} = \dot{\mathbf{r}} + \mathbf{n}, \tag{2.40}$$

where

$$\dot{\mathbf{r}} = \mathbf{CHv} \tag{2.41}$$

represents the legitimate received signal vector within the N_s chip durations, when $\mathbf{v}$ is transmitted. Since n_{n_s} is a sample of the complex-valued Gaussian distributed random variable and $\mathbf{n}$ is a sample of the N_s dimensional complex-valued Gaussian distributed random vector, the PDFs $p(n_{n_s})$ and $p(\mathbf{n})$ are known. Additionally, $\dot{r}_{n_s}$ is a known scalar whose value can be calculated according to Eq. (2.39) and $\dot{\mathbf{r}}$ is a known N_s-element vector whose value can be calculated from Eq. (2.41). Since the Gaussian distribution is closed under linear transformation, both $p(r_{n_s}|\mathbf{v})$ and $p(\mathbf{r}|\mathbf{v})$ can be precisely quantified.

It is worth noting that there are 2^{K-1} optional $(K-1)$-element vectors $[v_2, v_3, \ldots, v_K]$, when for example v_1 is fixed to $+1$. Therefore, when observing $\mathbf{r}$ the probability of $v_k = +1$ is given by the sum of the probability of all the above-mentioned 2^{K-1} vectors, which is expressed as

$$P(v_1 = +1|r) = \sum_{i=1}^{2^{K-1}} P(\mathbf{v}_{1+,i}^{(K)}|\mathbf{r}), \tag{2.42}$$

where $\mathbf{v}_{1+,i}^{(K)}$ denotes the specific K-element vector with the first symbol being positive and with the remaining $(K-1)$ elements assuming all the 2^{K-1} legitimate candidates. An example interpreting this scenario is illustrated in Tab. 2.7, when we have $K = 5$ and the 3rd user is the reference user. In order to determine $P(v_1 = +1|r)$, the PDF has to be calculated 2^{K-1} times for the 2^{K-1} different K-bit vectors. Additionally, the *a posteriori* probability associated with $v_1 = +1$ quantified in Eq. (2.42) can be generalized as

$$P(v_1 = \pm 1|r) = \sum_{i=1}^{2^{K-1}} P(\mathbf{v}_{1\pm,i}^{(K)}|\mathbf{r}) \tag{2.43}$$

in order to represent the *a posteriori* probabilities associated with the legitimate transmitted values of $+1$ and -1 for v_1. In order to compare the values of $P(v_1 = -1|r)$ and $P(v_1 = +1|r)$, the PDF of $P(\mathbf{v}_{1\pm,i}^{(K)}|\mathbf{r})$ included in Eq. (2.43) has to be calculated 2^K times to evaluate both $P(v_1 = +1|r)$ and $P(v_1 = -1|r)$. The final decision concerning the transmission of $+1$ or -1 for user k in the K-user system can be formulated as

$$\hat{v}_k = \arg \max_{\dot{v} \in \{+1,-1\}} \sum_{i=1}^{2^{K-1}} P(\mathbf{v}_{k\dot{v},i}^{(K)}|\mathbf{r}). \tag{2.44}$$

The complexity of the detector is exponentially proportional to the number of users K. However, at the Base Station (BS), all the signals transmitted by the K UpLink (UL) users during a symbol

$v_3 = +1$							$v_3 = -1$				
		$\mathbb{V}_{3+}^{(5)}$							$\mathbb{V}_{3-}^{(5)}$		
0	0	0	0	0	$\mathbf{v}_{3+,1}^{(5)}$	$\mathbf{v}_{3-,1}^{(5)}$	0	0	1	0	0
0	0	0	0	1	$\mathbf{v}_{3+,2}^{(5)}$	$\mathbf{v}_{3-,2}^{(5)}$	0	0	1	0	1
0	0	0	1	0	$\mathbf{v}_{3+,3}^{(5)}$	$\mathbf{v}_{3-,3}^{(5)}$	0	0	1	1	0
0	0	0	1	1	$\mathbf{v}_{3+,4}^{(5)}$	$\mathbf{v}_{3-,4}^{(5)}$	0	0	1	1	1
0	1	0	0	0	$\mathbf{v}_{3+,5}^{(5)}$	$\mathbf{v}_{3-,5}^{(5)}$	0	1	1	0	0
0	1	0	0	1	$\mathbf{v}_{3+,6}^{(5)}$	$\mathbf{v}_{3-,6}^{(5)}$	0	1	1	0	1
0	1	0	1	0	$\mathbf{v}_{3+,7}^{(5)}$	$\mathbf{v}_{3-,7}^{(5)}$	0	1	1	1	0
0	1	0	1	1	$\mathbf{v}_{3+,8}^{(5)}$	$\mathbf{v}_{3-,8}^{(5)}$	0	1	1	1	1
1	0	0	0	0	$\mathbf{v}_{3+,9}^{(5)}$	$\mathbf{v}_{3-,9}^{(5)}$	1	0	1	0	0
1	0	0	0	1	$\mathbf{v}_{3+,10}^{(5)}$	$\mathbf{v}_{3-,10}^{(5)}$	1	0	1	0	1
1	0	0	1	0	$\mathbf{v}_{3+,11}^{(5)}$	$\mathbf{v}_{3-,11}^{(5)}$	1	0	1	1	0
1	0	0	1	1	$\mathbf{v}_{3+,12}^{(5)}$	$\mathbf{v}_{3-,12}^{(5)}$	1	0	1	1	1
1	1	0	0	0	$\mathbf{v}_{3+,13}^{(5)}$	$\mathbf{v}_{3-,13}^{(5)}$	1	1	1	0	0
1	1	0	0	1	$\mathbf{v}_{3+,14}^{(5)}$	$\mathbf{v}_{3-,14}^{(5)}$	0	1	1	0	1
1	1	0	1	0	$\mathbf{v}_{3+,15}^{(5)}$	$\mathbf{v}_{3-,15}^{(5)}$	1	1	1	1	0
1	1	0	1	1	$\mathbf{v}_{3+,16}^{(5)}$	$\mathbf{v}_{3-,16}^{(5)}$	1	1	1	1	1

Table 2.7: An example when $K = 5$ users are supported and each user transmits a BPSK symbol within a symbol interval. The full set $\mathbb{V}^{(5)}$ containing all the 32 legitimate transmitted vectors is divided into two subsets, namely $\mathbb{V}_{3+}^{(5)}$, $\mathbb{V}_{3-}^{(5)}$ according to the polarity of the symbol transmitted by the 3rd user.

interval have to be detected. If we invoke the optimal detector of Eq. (2.44) on a user-by-user basis to in order to furnish $\hat{v}_k$ individually for all $k = 1, 2, \ldots, K$ in order to obtain the detected signal vector $\hat{\mathbf{v}}$, the 2^K-order detection complexity imposed by Eq. (2.44) is increased by a factor of K.

Let us now assume that $\hat{\mathbf{v}}$ is the detection result of the optimal MUD algorithm, where each symbol $\hat{v}_k$ of $\hat{\mathbf{v}}$ should maximize the corresponding individual single-bit objective function quantified by Eq. (2.44), which requires that

$$P(v_k = \hat{v}_k|\mathbf{r}) > P(v_k = -\hat{v}_k|\mathbf{r}) \quad , \quad \forall k = 1, \ldots, K \tag{2.45}$$

should always be satisfied. Hence

$$P(\hat{\mathbf{v}}|\mathbf{r}) = \prod_{k=1}^{K} P(v_k = \hat{v}_k|\mathbf{r}) \tag{2.46}$$

should be the highest of the 2^K probabilities recorded for all the legitimate vectors in $\mathbb{V}^{(K)}$. Therefore, instead of evaluating the OF given in Eq. (2.44) K times for all the K users supported by the system,

$\hat{\mathbf{v}} = [\hat{v}_1, \hat{v}_2, \ldots, \hat{v}_K]$ can be found with the aid of the single OF of

$$\hat{\mathbf{v}} = \arg \max_{\dot{\mathbf{v}} \in \mathbb{V}^{(K)}} \big\{ P(\hat{\mathbf{v}}|\mathbf{r}) \big\}. \tag{2.47}$$

According to the Bayes' rule [160], the *a posteriori* conditional probability can be expressed with the aid of the *a priori* conditional probability according to

$$P(\dot{\mathbf{v}}|\mathbf{r}) = \frac{p(\mathbf{r}|\dot{\mathbf{v}})P(\dot{\mathbf{v}})}{p(\mathbf{r}}. \tag{2.48}$$

For the equi-probable BPSK modulated K-bit vectors of the full set $\mathbb{V}^{(K)}$ we have

$$P(\dot{\mathbf{v}}) = \frac{1}{2^K}, \forall \dot{\mathbf{v}} \in \mathbb{V}^{(K)}. \tag{2.49}$$

Given a specific CIR and set of spreading codes contained in $\mathbf{A}$, while having no *a priori* knowledge as to which vector has been transmitted, the probability of receiving $\mathbf{r}$ is the sum of the probabilities of each legitimate vector being transmitted, which is multiplied with the probability of receiving $\mathbf{r}$, given that the legitimate vector $\dot{\mathbf{v}}$ was transmitted, yielding

$$p(\mathbf{r}) = \sum_{\dot{\mathbf{v}} \in \mathbb{V}^{(K)}} p(\mathbf{r}|\dot{\mathbf{v}})P(\dot{\mathbf{v}}). \tag{2.50}$$

Both the probabilities given by Eq. (2.49) and Eq. (2.50) are constant, regardless of the value assumed by the transmitted signal vector $\dot{\mathbf{v}}$. Therefore, as suggested by Eq. (2.48) in conjunction with Eq. (2.49) and Eq. (2.50), the vector having the highest *a posteriori* probability to have been transmitted, given that the vector $\mathbf{r}$ has been received, is the same as that predicted at the transmitter to have the maximum *a priori* probability to result in the received signal vector $\mathbf{r}$. In mathematical terms, the vector $\dot{\mathbf{v}}$ maximizing the OF of Eq. (2.47) is identical to the one that maximizes the following OF:

$$\hat{\mathbf{v}} = \arg \max_{\dot{\mathbf{v}} \in \mathbb{V}^{(K)}} p(\mathbf{r}|\dot{\mathbf{v}}). \tag{2.51}$$

Eq. (2.51) formulates a so-called NP-hard problem [162], where the optimal solution can only be formed by exhaustively searching through all the legitimate solutions. However, the complexity of the optimal search procedure increases exponentionaly with K. For example, for $K = 32$, the above OF has to be evaluated 4.2950×10^9 times.

To avoid the exponentially increasing complexity imposed by the optimal algorithm, numerous reduced-complexity sub-optimum algorithms have been proposed [?,93], some of which are highlighted in the next section.

2.4.3 Sub-Optimal Detection Algorithms

According to Fig. 2.4, the signal received at any chip-interval n_s, $n_s = 1, 2, \ldots, N_s$, can be represented by the following equations:

$$\begin{array}{lcccccccccc} r_1 & = & c_{11}\, h_1 v_1 & + & c_{21}\, h_2 v_2 & + & \cdots & + & c_{K1}\, h_K v_K & + & n_1 \\ r_2 & = & c_{12}\, h_1 v_1 & + & c_{22}\, h_2 v_2 & + & \cdots & + & c_{K2}\, h_K v_K & + & n_2 \\ \vdots & & \vdots & & \vdots & & & & \vdots & & \vdots \\ r_{N_s} & = & c_{1N_s} h_1 v_1 & + & c_{2N_s} h_2 v_2 & + & \cdots & + & c_{KN_s} h_K v_K & + & n_{N_s} \end{array}, \tag{2.52}$$

where the signal received during the N_s-chip symbol interval is hosted by a vector $\mathbf{r} = [r_1, r_2, \ldots, r_{N_s}]$. The MUD's hard output recorded for the K users is given by the solution of the set of N_s equations in Eq. (2.25). Depending on the amount of knowledge related to the coefficients c, h, n in Eq. (2.25), different algorithms emerge, such as the MF [80] based Single-User Detector (SUD), the Zero Forcing (ZF) [69] MUD and the MMSE [73] MUD, which are characterized in Table 2.8.

	$\mathbf{A}_k$	$\mathbf{R}$	σ_n^2	BER	per-user complexity
MF	$\surd$			worst	constant
ZF	$\surd$	$\surd$		medium	$\mathcal{O}(K^3)$
MMSE	$\surd$	$\surd$	$\surd$	medium$^+$	$\mathcal{O}(K^3)$

$\mathbf{A}_k = \mathbf{c}_k \times h_k$: the code and channel information associated with each individual user
$\mathbf{R} = \mathbf{A}^H\mathbf{A}$: the correaltion of code and channel information between each two users

Table 2.8: Comparison of different hard-output detection algorithms in terms of the information required, the achievable performance and the complexity imposed.

2.4.3.1 Matched Filter Algorithm

Let us commence our more detailed discussions with the simplest scenario, when the sole information available for the MF SUD is that related to a particular single user. More specifically, if only the knowledge of $\mathbf{A}_k$ containing the spreading code $\mathbf{c}_k = [c_{k1}, c_{k2} \ldots, c_{kN_s}]$ and the CIR h_k of the kth user is available to the SUD, the MF is the only technique of detecting v_k. Provided that $\mathbf{c}_k = [c_{k1}, c_{k2} \ldots, c_{kN_s}]$ is orthogonal to all the other codes $\mathbf{c}_j$, $j \neq k$ and $1 \leqslant j \leqslant K$ or $\mathbf{c}_k^T\mathbf{c}_j = 0$, the products $c_{jn_s}h_jv_j$, $j = 1, \ldots, K$ and $j \neq k$ when $n_s = 1, \ldots, N_s$ are automatically eliminated by the simple MF operation upon multiplying $\mathbf{r}$ with $\mathbf{c}_k^T$ in Eq. (2.25), where $c_{jn_s}h_jv_j$ contains the signals transmitted by all the other users. If the orthogonality of each two codes is retained, the MF output $\mathbf{z}_{\text{MF}} = \mathbf{c}_k^T$ will contain information contributed only by the wanted user, namely the kth user. Hence the estimated MF output $\hat{b}_k$ is generated by the simple decision of

$$\begin{cases} \hat{b}_k = 0, \hat{v}_k = +1, & \text{if } z_k \geqslant 0 \\ \hat{b}_k = 1, \hat{v}_k = -1, & \text{if } z_k < 0 \end{cases} \tag{2.53}$$

based on the polarity of the MF's output z_k.

With the aid of Eq. (2.52), z_k can be expressed as

$$\begin{aligned} z_k =& \mathbf{A}_k^H\mathbf{r} = h_k^*\mathbf{c}_k^T\mathbf{r} \\ =& \begin{bmatrix} h_k^*c_{k1} & h_k^*c_{k2} & \cdots & h_k^*c_{kN_s} \end{bmatrix} \begin{bmatrix} r_1 \\ r_2 \\ \vdots \\ r_{N_s} \end{bmatrix} \\ =& h_k^*c_{k1}r_1 + h_k^*c_{k2}r_2 + \cdots + h_k^*c_{kN_s}r_{N_s} \end{aligned}$$

$$
\begin{aligned}
=&h_k^*(c_{k1}c_{k1}+c_{k2}c_{k2}+\cdots+c_{kN_\mathrm{s}}c_{kN_\mathrm{s}})h_kv_k\\
&+\sum_{j=1,j\neq k}^{K}h_k^*(c_{k1}c_{j1}+c_{k2}c_{j2}+\cdots+c_{kN_\mathrm{s}}c_{jN_\mathrm{s}})h_jv_j\\
&+\sum_{n_\mathrm{s}=1}^{N_\mathrm{s}}h_k^*c_{kn_\mathrm{s}}n_{n_\mathrm{s}}\\
=&h_k^*\mathbf{c}_k^T\mathbf{c}_kh_kv_k+\sum_{j=1,j\neq k}^{K}h_k^*\mathbf{c}_k^T\mathbf{c}_jh_jv_j+\sum_{n_\mathrm{s}=1}^{N_\mathrm{s}}h_k^*c_{kn_\mathrm{s}}n_{n_\mathrm{s}}\\
=&|h_k|^2v_k+\sum_{j=1,j\neq k}^{K}\rho_{kj}^{\mathrm{c}}\rho_{kj}^{\mathrm{h}}v_j+\tilde{n}_k. \qquad (2.54)
\end{aligned}
$$

If $\rho_{kj}^{\mathrm{c}}=0$ or $\mathbf{c}_k^T\mathbf{c}_j=0$ as long as $k\neq j$, which suggests that any pair of spreading codes assigned to two different users are mutually orthogonal to each other, the second term of Eq. (2.54) namely $\sum_{j=1,j\neq k}^{K}\rho_{kj}^{\mathrm{c}}\rho_{kj}^{\mathrm{h}}v_j$ becomes zero, which facilitates interference-free detection. However, below we will demonstrate that the interference may or may not be cancelled in this way. For example, the 3G systems indeed employ the family of Orthogonal Variable Spreading Factor (OVSF) codes [163], but their orthogonality is destroyed by the dispersive CIRs routinely encountered in hight-rate systems having short symbol and chip-durations. Secondly, the number of users supported is limited by the number of chips in the WH codes, while in the non-orthogonal code families many more codes may be created than the number of chips, provided that the MUD is capable of mitigating the MAI imposed by the non-orthogonal codes.

To elaborate a little further, provided that $\mathbf{c}_k$ and h_k are known to the MF detector for $k=1,2,\ldots,K$, the K MF outputs $\hat{\mathbf{z}}_{\mathrm{MF}}=[\hat{v}_1,\ldots,\hat{v}_K]$, which are also often denoted as $\mathbf{y}$ may alternatively be obtained by implementing

$$
\begin{aligned}
\mathbf{y}=\hat{\mathbf{z}}_{\mathrm{MF}}&=\mathbf{A}^H\mathbf{r}=\mathbf{A}^H\mathbf{A}\mathbf{v}+\mathbf{A}^H\mathbf{n}\\
&=\mathbf{R}\mathbf{v}+\tilde{\mathbf{n}}, \qquad (2.55)
\end{aligned}
$$

where $\mathbf{R}=\mathbf{A}^H\mathbf{A}=\mathbf{H}^H\mathbf{C}^H\mathbf{C}\mathbf{H}$ is the *correlation matrix*, defining the correlation of $\mathbf{A}$ constructed from $\mathbf{A}_k=\mathbf{c}_kh_k$ according to $\mathbf{A}=[\mathbf{A}_1,\mathbf{A}_2,\ldots,\mathbf{A}_K]$.

More specifically, the (i,j)th element $R_{ij}=\mathbf{A}_i^H\mathbf{A}_j$ located in the ith row and the jth column of $\mathbf{R}$ represents the correlation between $\mathbf{A}_i=h_i\mathbf{c}_i$ associated with the ith user and $\mathbf{A}_j=h_j\mathbf{c}_j$ of the jth user, for $i=1,\ldots,K$ and $j=1,\ldots,K$. In other words, R_{ij} is quantified as

$$
R_{ij}=\mathbf{A}_i^H\mathbf{A}_j=(\mathbf{c}_ih_i)^H(\mathbf{c}_jh_j)=h_i^*\mathbf{c}_i^T\mathbf{c}_jh_j,\quad \forall i=1,\ldots,K;j=1,\ldots,K. \qquad (2.56)
$$

Hence the kth diagonal element of $\mathbf{R}=\mathbf{A}_k^H\mathbf{A}_k$ is the auto-correlation of $\mathbf{A}_k=h_k\mathbf{c}_k$ associated with the kth user, which is formulated as

$$
R_{kk}=\mathbf{A}_k^H\mathbf{A}_k=(\mathbf{c}_kh_k)^H(\mathbf{c}_kh_k)=h_k^*\mathbf{c}_k^T\mathbf{c}_kh_k=h_k^*\cdot 1\cdot h_k=|h_k|^2,\quad \forall k=1,\ldots,K. \qquad (2.57)
$$

Again, the orthogonality of the spreading codes guarantees that we have $\mathbf{c}_i^T\mathbf{c}_j=0$ when $i\neq j$, hence the correlation coefficients obey $R_{ij}=\mathbf{A}_i^H\mathbf{A}_j=0$, when $\mathbf{R}$ becomes a $(K\times K)$-element diagonal matrix with all the off-diagonal elements being $R_{ij}=0$ when $i\neq j$, which correponds to the MUI-free detection output.

By contrast, as shown in Eq. (2.54), in case of non-orthogonal spreading codes, apart from the AWGN quantified as $\tilde{n}_k = \mathbf{A}_k^H \mathbf{n}$, the MF's detection output z_k dedicated to the kth user is additionally contaminated by the interference imposed by all the other $(K-1)$ users, where the interference contribution is quantified as $\sum_{j=1,j\neq k}^{K} \mathbf{A}_k^H \mathbf{A}_j v_j$. By defining the correlation factor of spreading code $\mathbf{c}_k$ and $\mathbf{c}_j$ as $\rho_{kj}^{\mathrm{c}} = \mathbf{c}_k^T \mathbf{c}_j$ and the correlation factor between the CIRs h_k and h_j as $\rho_{kj}^{\mathrm{h}} = h_k^* h_j$, the above-mentioned interference term may be represented by $\sum_{j=1,j\neq k}^{K} \rho_{kj}^{\mathrm{c}} \rho_{kj}^{\mathrm{h}} v_j$.

2.4.3.2 Zero-Forcing Algorithm

As seen from Eq. (2.54), the MUI imposed by all the $(K-1)$ interfering users contaminates the MF detector's output. Hence, further processing is required to mitigate the MUI component and to reduce the effects of the noise. The $(K \times 1)$-element solution vector $\mathbf{z}$ of a linear MUD characterized by the $(K \times N_{\mathrm{s}})$-element MUD weight-matrix $\mathbf{W}$ may be expressed as

$$\mathbf{z} = \mathbf{W}\mathbf{y}. \tag{2.58}$$

Then, according to Eq. (2.55) we expand $\mathbf{y}$, yielding

$$\begin{aligned} \mathbf{z} &= \mathbf{W}\mathbf{y} \\ &= \mathbf{W}\mathbf{R}\mathbf{v} + \mathbf{W}\tilde{\mathbf{n}}. \end{aligned} \tag{2.59}$$

Therefore, if we could arrange for the coefficient matrix $\mathbf{WR}$ multiplying the transmitted signal vector $\mathbf{v}$ to become a diagonal matrix in Eq. (2.59), then no undesired interference would be imposed on $z_k^{(\mathrm{ZF})}$ in the kth row of the detection output $\mathbf{z}^{\mathrm{ZF}}$ by any other user. Therefore, as long as the number of users K does not exceed the number of chips N_{s}, $\mathbf{R}$ is an invertable $(K \times K)$-element square matrix, and $\mathbf{W}^{(\mathrm{ZF})}$ may be obtained by

$$\mathbf{W}^{(\mathrm{ZF})} = \mathbf{R}^{-1}, \tag{2.60}$$

which yields $\mathbf{W}^{(\mathrm{ZF})}\mathbf{R} = \mathbf{I}^{(K)}$, where $\mathbf{I}^{(K)}$ represents the $(K \times K)$-element square identity matrix. Furthermore the solution vector of the ZF algorithm may be formulated as

$$\begin{aligned} \mathbf{z}^{(\mathrm{ZF})} &= \mathbf{W}^{(\mathrm{ZF})}\mathbf{y} = \mathbf{R}^{-1}\mathbf{y} \\ &= \mathbf{R}^{-1}\mathbf{R}\mathbf{v} + \mathbf{R}^{-1}\tilde{\mathbf{n}} \\ &= \mathbf{v} + \mathbf{R}^{-1}\tilde{\mathbf{n}}. \end{aligned} \tag{2.61}$$

As implied in Eq. (2.61), to obtain the detection output $z_k^{(\mathrm{ZF})}$ for the kth user, the composite information vectors $\mathbf{A}_j$ of all the $j = 1, \ldots, K$ users are required by the ZF detector in order to evaluate the correlation factor between $\mathbf{A}_k$ and each of the auxiliary vectors $\mathbf{A}_j$ of other users. However, during the entire detection process carried out by the ZF based MUD, the presence of the AWGN is ignored. More quantatively, although the instantenous value of the noise is unknown at the receiver, the mean $\mu_{\mathfrak{n}}$, the deviation $\sigma_{\mathfrak{n}}^2$ and the PDF of the AWGN variable $\mathfrak{n}$ can be estimated at the receiver. However, none of these two auxiliary information sources are exploited by the ZF detector.

2.4.3.3 Minimum-Mean-Square-Error Algorithm

By extending the definition of the vector solution to a linear MUD algorithm given by

$$\begin{aligned}\mathbf{z} &= \mathbf{W}\mathbf{y} \\ &= \mathbf{W}\mathbf{R}\mathbf{v} + \mathbf{W}\tilde{\mathbf{n}},\end{aligned} \tag{2.62}$$

we will attempt to minimize the MSE between the estimated result $\hat{\mathbf{v}}$ and the actually transmitted signal vector $\mathbf{v}$. When BPSK modulation is employed, the detected K-user vector can be further simplified from Eq. (2.62) as

$$\hat{\mathbf{v}} = \Re\{\mathbf{z}\}. \tag{2.63}$$

Hence, the MUD's weight-matrix $\mathbf{W}$ is the one that minimizes the MSE $E\{\|\mathbf{v} - \hat{\mathbf{v}}\|^2\}$, which is formulated as

$$\mathbf{W} = \arg\min_{\dot{\mathbf{W}}} E\{\|\mathbf{v} - \hat{\mathbf{v}}\|^2\}, \tag{2.64}$$

where $\mathbf{W}$ may be expressed as

$$\begin{aligned}\mathbf{W}^{(\mathrm{MMSE})} &= \left(E\{\mathbf{y}\mathbf{y}^H\}\right)^{-1} E\{\mathbf{y}\mathbf{v}^H\} \\ &= (\mathbf{R}^2 + 2\sigma_{\mathfrak{n}}^2\mathbf{R})^{-1}\mathbf{R} \\ &= (\mathbf{R} + 2\sigma_{\mathfrak{n}}^2)^{-1}.\end{aligned} \tag{2.65}$$

Hence, the K-element vector solution provided by the MMSE algorithm can be formulated as

$$\mathbf{z}^{(\mathrm{MMSE})} = \mathbf{W}^{(\mathrm{MMSE})}\mathbf{y} = (\mathbf{R} + 2\sigma_{\mathfrak{n}}^2)^{-1}\mathbf{y}. \tag{2.66}$$

2.4.4 Maximum Likelihood Detection Algorithm

Below, we will further simplify Eq. (2.51), which will lead to the formation of the Likelihood Function (LLF). Below, we will derive the *a priori* conditional probability given by Eq. (2.51) from the most basic D-dimensional complex-valued Gaussian PDF.

In Eq. (2.27) the N_{s}-element AWGN vector was denoted by $\mathbf{n}$, where each element $n_{n_{\mathrm{s}}}$ for $n_{\mathrm{s}} = 1, 2, \ldots, N_{\mathrm{s}}$ is an instantaneous sample of the complex-valued Gaussian random variable $\mathfrak{n}$ having a mean of $\mu_{\mathfrak{n}} = 0$ and a variance of $\sigma_{\mathfrak{n}}^2$, which is formulated as $n_{n_{\mathrm{s}}} \sim \mathcal{N}^{\mathrm{c}}(\mu_{\mathfrak{n}}, \sigma_{\mathfrak{n}}^2)$, where the PDF of the complex-valued Gaussian distributed scalar random variable was defined in Eq. (2.2).

In addition, the $(N_{\mathrm{s}} \times 1)$-element vector $\mathbf{n}$ is a sample of the $(N_{\mathrm{s}} \times 1)$-element complex-valued Gaussian vector-variable $\mathfrak{n}$. According to [160], the PDF of the D-dimensional complex Gaussian variable $\mathfrak{n} \sim \mathcal{N}_D^{\mathrm{c}}(\mathbf{M}_{\mathfrak{n}}, \mathbf{\Sigma}_{\mathfrak{n}})$ is given by

$$p(\mathbf{n}) = \frac{1}{\pi^D} \frac{\exp\left[-\frac{1}{2}(\mathbf{n} - \mathbf{M}_{\mathfrak{n}})^H 2\mathbf{\Sigma}_{\mathfrak{n}}^{-1}(\mathbf{n} - \mathbf{M}_{\mathfrak{n}})\right]}{\det(\mathbf{\Sigma}_{\mathfrak{n}})}. \tag{2.67}$$

In Eq.(2.67), the number of elements in the random vector $\mathbf{n}$ is N_{s} and $\mathbf{M}_{\mathfrak{n}}$ as well as $\mathbf{\Sigma}_{\mathfrak{n}}$ denote the vector of means and the vector of variances containing the mean and variance of each random element

of $\mathbf{n}$, which can be expressed as

$$\begin{aligned}\mathbf{M}_{\mathfrak{n}} &= \mathbf{0}^{(N_\mathrm{s})}; \quad D = N_\mathrm{s} \\ \mathbf{\Sigma}_{\mathfrak{n}} &= E\left((\mathbf{n}-\mathbf{M}_{\mathfrak{n}})(\mathbf{n}-\mathbf{M}_{\mathfrak{n}})^H\right) \\ &= E(\mathbf{n}\mathbf{n}^H) = \sigma_{\mathfrak{n}}^2\mathbf{I}^{(N_\mathrm{s})},\end{aligned} \tag{2.68}$$

where $\mathbf{0}^{(N_\mathrm{s})}$ and $\mathbf{I}^{(N_\mathrm{s})}$ are the $(N_\mathrm{s}\times 1)$-element null-vector and the $(N_\mathrm{s}\times N_\mathrm{s})$-element identity matrix respectively.

In Eq. (2.27), the composite matrix $\mathbf{A}$ is known to the receiver. Hence, assigning to the variable $\mathbf{v}$ in Eq. (2.27) a particular vector $\dot{\mathbf{v}}\in\mathbb{V}^{(K)}$, $\mathbf{r}$ in Eq. (2.27) equals to a constant $\mathbf{CH}\dot{\mathbf{v}}$ plus a random sample $\mathbf{n}$. Hence, according to the properties of the complex-valued Gaussian random vector, given that $\dot{\mathbf{v}}$ was transmitted, the vector $\mathbf{r}$ constitutes an instantiation of the N_s-dimensional complex-valued Gassisan random variable $\mathfrak{r}$ having a mean of $\mathbf{M}_{\mathfrak{r}}=\mathbf{M}_{\mathfrak{n}}+\mathbf{CH}\mathbf{v}_i^{(K)}$ and a variance of $\mathbf{\Sigma}_{\mathfrak{r}}=\mathbf{\Sigma}_{\mathfrak{n}}$. Based on the above discussions associated with Eq. (2.68), the *a priori* conditional PDF of receiving $\mathbf{r}$ given $\dot{\mathbf{v}}$ was transmitted under $\mathbf{A}$ can be defined as

$$\begin{aligned}p(\mathbf{r}|\dot{\mathbf{v}}) &= \frac{1}{\pi^D}\frac{\exp\left[-\frac{1}{2}(\mathbf{r}-\mathbf{M}_{\mathfrak{r}})^H 2\mathbf{\Sigma}_{\mathfrak{r}}^{-1}(\mathbf{r}-\mathbf{M}_{\mathfrak{r}})\right]}{\det(\mathbf{\Sigma}_{\mathfrak{r}})} \\ &= \frac{1}{(\pi\sigma_{\mathfrak{n}}^2)^{N_\mathrm{s}}}\exp\left(-\frac{1}{\sigma_{\mathfrak{n}}^2}\|\mathbf{r}-\mathbf{CH}\dot{\mathbf{v}}\|^2\right),\end{aligned} \tag{2.69}$$

in the system context described by Eq. (2.25).

As observed from Eq. (2.69), the value of π, $\sigma_{\mathfrak{n}}^2$ and N_s are constants and hence will not influence the value of $p(\mathbf{r}|\dot{\mathbf{v}})$, when the trial vectors $\dot{\mathbf{v}}$ associated with different values are considered. Therefore, the detection output expressed in terms of the objective function of Eq. (2.51) can be further simplified to

$$\hat{\mathbf{v}} = \arg\min_{\dot{\mathbf{v}}\in\mathbb{V}^{(K)}}\|\mathbf{r}-\mathbf{CH}\dot{\mathbf{v}}\|^2, \tag{2.70}$$

where $\|\mathbf{r}-\mathbf{CH}\dot{\mathbf{v}}\|^2$ defines the norm of the $(N_\mathrm{s}\times 1)$-element vector of

$$\begin{aligned}\mathbf{d} &= \mathbf{r}-\mathbf{CH}\dot{\mathbf{v}} \\ &= \mathbf{r}-\dot{\mathbf{r}}.\end{aligned} \tag{2.71}$$

Hereby, the $(N_\mathrm{s}\times 1)$-element vector $\dot{\mathbf{r}}$ denotes the legitimate received signal given $\dot{\mathbf{v}}$ is transmitted in the absence of the noise.

As it may be readily observed from Eq. (2.25) and its matrix counterpart seen in Eq. (2.27), the n_sth element $d_{n_\mathrm{s}}=r_{n_\mathrm{s}}-\dot{r}_{n_\mathrm{s}}$ of the $(N_\mathrm{s}\times 1)$-element vector $\mathbf{d}=\mathbf{r}-\dot{\mathbf{r}}=\mathbf{r}-\mathbf{CH}\dot{\mathbf{v}}$ can be derived from the n_sth equation in the system of N_s equations given by Eq. (2.25), which can be quantified as

$$d_{n_\mathrm{s}} = r_{n_\mathrm{s}} - \sum_{k=1}^{K} c_{kn_\mathrm{s}}h_k\dot{v}_k. \tag{2.72}$$

The absolute value of the complex-valued scalar d_{n_s} quantified in Eq. (2.72) is expressed as

$$\sqrt{\mathfrak{D}_{n_\mathrm{s}}(\dot{\mathbf{v}})} = |d_{n_\mathrm{s}}| = \left|r_{n_\mathrm{s}} - \sum_{k=1}^{K} c_{kn_\mathrm{s}}h_k\dot{v}_k\right|, \tag{2.73}$$

where

$$\mathfrak{D}_{n_s}(\dot{\mathbf{v}}) \triangleq \left| r_{n_s} - \sum_{k=1}^{K} c_{kn_s} h_k \dot{v}_k \right|^2 \tag{2.74}$$

quantifies the **Euclidean distance** between the potentially faded and

$$noisecontaminated \tag{2.75}$$

received signal r_{n_s} and the legitimate, i.e. noise-free, received signal $\dot{r} = \sum_{k=1}^{K} c_{kn_s} h_k \dot{v}_k$, given that $\dot{\mathbf{v}}$ was transmitted during the n_sth chip-duration. Therefore, when n_s ranges from $n_s = 1$ to $n_s = N_s$, $\mathfrak{D}_1(\dot{\mathbf{v}})$, $\mathfrak{D}_2(\dot{\mathbf{v}})$,...,$\mathfrak{D}_2(\dot{\mathbf{v}})$ denotes the N_s squared Euclidean distances between the received signal and the legitimate (noise-free) received signal during each of the N_s chip intervals. Furthermore, $\|\mathbf{r} - \mathbf{CH}\dot{\mathbf{v}}\|^2$ in Eq. (2.70) is the sum of above-mentioned N_s squared Euclidean distances. More quantatively, when $\mathbf{r}$ is received, the Euclidean distance norm associated with a particluar K-symbol vector $\dot{\mathbf{v}}$ during a particular symbol duration may be expressed as

$$\begin{aligned}
\mathfrak{D}(\dot{\mathbf{v}}) &\triangleq \|\mathbf{r} - \mathbf{CH}\dot{\mathbf{v}}\|^2 \\
&= \sum_{n_s=1}^{N_s} \mathfrak{D}_{n_s}(\dot{\mathbf{v}}) \\
&= \sum_{n_s=1}^{N_s} \left| r_{n_s} - \sum_{k=1}^{K} c_{kn_s} h_k \dot{v}_k \right|^2 .
\end{aligned} \tag{2.76}$$

Hence, the OF quantifying the detection result of an optimal hard-output algorithm in the context of the K-user DS-CDMA UL characterized in Eq. (2.70) may be readily represented by the vector that minimizes the Euclidean distance norm of

$$\hat{\mathbf{v}} = \arg \min_{\dot{\mathbf{v}} \in \mathbb{V}^{(K)}} \{\mathfrak{D}(\dot{\mathbf{v}})\}. \tag{2.77}$$

Futhermore, the OF given in Eq. (2.70) in the form of the Euclidean distances can be further simplified after eliminating the common part in $\|\mathbf{r} - \mathbf{CH}\dot{\mathbf{v}}\|^2$, which does not depend on the specific value assumed by $\dot{\mathbf{v}}$. Therefore, we will further expand the Euclidean distance of $\|\mathbf{r} - \mathbf{CH}\dot{\mathbf{v}}\|^2$ as follows:

$$\begin{aligned}
\mathfrak{D}(\dot{\mathbf{v}}) =& \|\mathbf{r} - \mathbf{CH}\dot{\mathbf{v}}\|^2 \\
=& \left(\mathbf{r} - \mathbf{CH}\dot{\mathbf{v}}\right)^H \left(\mathbf{r} - \mathbf{CH}\dot{\mathbf{v}}\right) \\
=& \left(\mathbf{r}^H - \left(\mathbf{CH}\dot{\mathbf{v}}\right)^H\right) \left(\mathbf{r} - \mathbf{CH}\dot{\mathbf{v}}\right) \\
=& \left(\mathbf{r} - \dot{\mathbf{v}}^H \mathbf{H}^H \mathbf{C}^H\right) \left(\mathbf{r} - \mathbf{CH}\dot{\mathbf{v}}\right) \\
=& \mathbf{r}^H\mathbf{r} - \dot{\mathbf{v}}^H \underbrace{\mathbf{H}^H\mathbf{C}^H\mathbf{r}}_{\mathbf{y}} - \underbrace{\mathbf{r}^H\mathbf{CH}}_{\mathbf{y}^H} \dot{\mathbf{v}} + \dot{\mathbf{v}}^H \underbrace{\mathbf{H}^H\mathbf{C}^H\mathbf{CH}}_{\mathbf{R}} \dot{\mathbf{v}} \\
=& \mathbf{r}^H\mathbf{r} - \left(\ddot{\mathbf{v}}^H\mathbf{y} + \mathbf{y}^H\dot{\mathbf{v}} - \dot{\mathbf{v}}^H\mathbf{R}\dot{\mathbf{v}}\right).
\end{aligned}$$

Since we have $\mathbf{y}^H\dot{\mathbf{v}} = \left(\dot{\mathbf{v}}^H\mathbf{y}\right)^H = \left(\dot{\mathbf{v}}^H\mathbf{y}\right)^*$, we arrive at

$$\mathfrak{D}(\dot{\mathbf{v}}) = \mathbf{r}^H\mathbf{r} - \left(\dot{\mathbf{v}}^H\mathbf{y} + \left(\dot{\mathbf{v}}^H\mathbf{y}\right)^* - \dot{\mathbf{v}}^H\mathbf{R}\dot{\mathbf{v}}\right)$$

Given the complex-valued variable $x = \Re\{x\} + \Im\{x\}j$ and that $x + x^* = 2\Re\{x\}$, we get

$$\mathfrak{D}(\dot{\mathbf{v}}) = \mathbf{r}^H\mathbf{r} - \left(2\Re\{\dot{\mathbf{v}}^H\mathbf{y}\} - \dot{\mathbf{v}}^H\mathbf{R}\dot{\mathbf{v}}\right). \tag{2.78}$$

Since $\mathbf{r}^H\mathbf{r}$ is a constant, which is independent of the specific value assumed by $\dot{\mathbf{v}}$, it can be excluded from the calculation of the OF. More explicitly, only a comparison of the $\mathfrak{D}(\dot{\mathbf{v}})$ values corresponding to $\dot{\mathbf{v}}$ assuming all the legitimate vector is necessary for the optimal HO detector in order to make its final decision after considering all the 2^K possible legitimate vectors. Therefore, the detector output associated with the OF of Eq. (2.70) can be further simplified to

$$\hat{\mathbf{v}} = \arg \max_{\mathbf{v}_i^{(K)} \in \mathbb{V}^{(K)}} \left\{2\Re\{\dot{\mathbf{v}}^H\mathbf{y}\} - \dot{\mathbf{v}}^H\mathbf{R}\dot{\mathbf{v}}\right\}. \tag{2.79}$$

It may be worth mentioning that the OF $2\Re\{\dot{\mathbf{v}}^H\mathbf{y}\} - \dot{\mathbf{v}}^H\mathbf{R}\dot{\mathbf{v}}$ derived from Eq. (2.70) defining the *a priori* conditional PDF $p(\mathbf{r}|\dot{\mathbf{v}})$ is also often referred to as the **Log-Likelihood Function (LLF)** associated with vector $\dot{\mathbf{v}}^H$. The LLF associated with a specific vector $\dot{\mathbf{v}}$ in conjunction with a particular received signal vector $\mathbf{r}$ quantifies the *a priori* 'likelihood' of receiving $\mathbf{r}$ provided that $\dot{\mathbf{v}}$ was transmitted. More explicitly, when $\mathbf{r}$ is received within a certain symbol duration, the LLF associated with a particular K-symbol vector $\dot{\mathbf{v}}$ is defined as

$$\mathfrak{L}(\dot{\mathbf{v}}) \triangleq 2\Re\{\dot{\mathbf{v}}^H\mathbf{y}\} - \dot{\mathbf{v}}^H\mathbf{R}\dot{\mathbf{v}}. \tag{2.80}$$

As observed from Eq. (2.77) and Eq. (2.79), the vector that minimizes the Euclidean distance norm $\mathfrak{D}(\dot{\mathbf{v}})$ defined in Eq. (2.76) maximizes the LLF $\mathfrak{L}(\dot{\mathbf{v}})$ defined in Eq. (2.80) over the entire set of all the 2^K vectors. Hence for a particular symbol duration associated with the received signal vector $\mathbf{r}$, we have

$$\hat{\mathbf{v}} = \arg \min_{\dot{\mathbf{v}} \in \mathbb{V}^{(K)}} \mathfrak{D}(\dot{\mathbf{v}}) \equiv \arg \max_{\dot{\mathbf{v}} \in \mathbb{V}^{(K)}} \mathfrak{L}(\dot{\mathbf{v}}). \tag{2.81}$$

The Maximum-Likelihood (ML) detector, evaluates the above OF for the entire set comprising 2^K legitimate vectors, in order to find the K-symbol vector maximizing the LLF of Eq. (2.80). More quantatively, the ML detection result of the K-user DS-CDMA UL may be expressed as

$$\hat{\mathbf{v}}_{\mathrm{ML}} = \arg \max_{\dot{\mathbf{v}} \in \mathbb{V}^{(K)}} \mathfrak{L}(\dot{\mathbf{v}}). \tag{2.82}$$

As alluded to before, the optimization problem of Eq. (2.82) is an NP-hard problem, where the optimal solution can only be found by an exhaustive search [160]. However, the complexity quantified as the number of times the OF has to be evaluated increases exponentionally with the population size containing all the candidates, as defined by the number of users K in this DS-CDMA scenario. For example, when the number of users is $K = 32$, the ML MUD's complexity becomes excessive.

Against this background, near-optimal algorithms have been conceived in order to circumvent the above-mentioned complexity problem. As an example, the ant-colony optimization (ACO) algorithm generates a reduced number of K-symbol candidate vectors with the aim of ensuring that the optimal one is among them with a high probability. The comprehensive interpretation of the ACO algorithm will be provided in the context of the DS CDMA system of Chapter 3. Following the introduction of the ACO-based MUD algorithm, the family of suboptimal MUD algorithms listed in Table 2.8 will be further expanded in Table 2.9.

	$\mathbf{A}_k$	$\mathbf{R}$	$\mathbf{n}$		BER	complexity	
			$\sigma_{\mathbf{n}}^2$	LLF			
MF	$\surd$				$\bigstar$	constant	$\times$
ZF		$\surd$			$\bigstar\bigstar$	$\mathcal{O}(K^2)$	$\times\times$
MMSE	$\surd$	$\surd$	$\surd$		$\bigstar\bigstar\bigstar$	$\mathcal{O}(K^3)$	$\times\times\times$
ML	$\surd$	$\surd$		$\surd$	$\bigstar\bigstar\bigstar\bigstar$	$\mathcal{O}(2^K)$	$\times\times\times\cdots\times$
ACO	$\surd$	$\surd$		$\surd$	$\bigstar\bigstar\bigstar\bigstar$	$\mathcal{O}(K^2)$	$\times\times$

$\mathbf{A}_k = \mathbf{c}_k \times h_k$: the code and channel information associated with each individual user
$\mathbf{R} = \mathbf{A}^H\mathbf{A}$: the correaltion of code and channel information between each two users

Table 2.9: Comparison of different hard-output detective algorithms in terms of the employed resource, the achieved performance and the cost complexity.

2.5 Logorithmic Likelihood Ratios

In turbo transcivers we typically concatenate several encoders/decoders, so that the *extrinsic* information generated by one of the decoders can be forwarded as *a priori* information for the other decoder, as shown in Fig. 2.5. In a multiuser system with each user employing the turbo transceivers, as shown

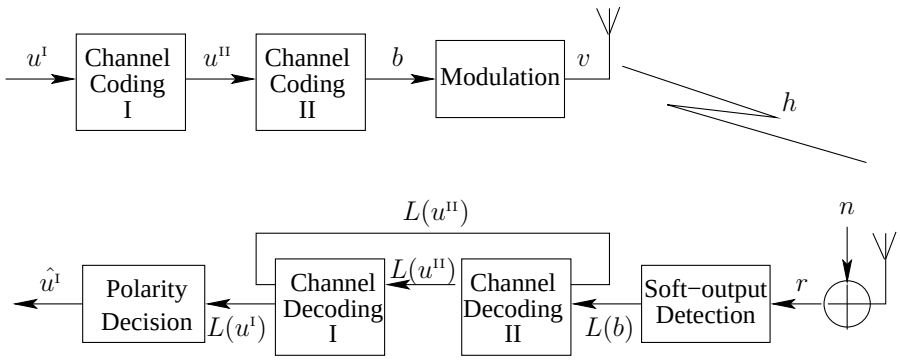

Figure 2.5: Block diagram of a channel coded single-user system, when iterative soft-output detection is employed.

in Fig. 2.6, the Soft-Output (SO) MUD is the first component employed by the BS at the output of the receive antenna. The main function of the SO MUD is to 'process' the superimposed received signal-vector $\mathbf{r}$ throughout the N_{s} chip intervals constituting a symbol duration, so that the effects of MUI are mitigated. Having eliminated the effects of the co-channel users, the soft information associated with each user can be generated by the SO MUD, which is then forwarded to the per-user iterative decoding components. As shown in Fig. 2.6, $L(b_k)$, $k = 1, \ldots, K$ denotes the soft information provided by the SO MUD for each of the K users.

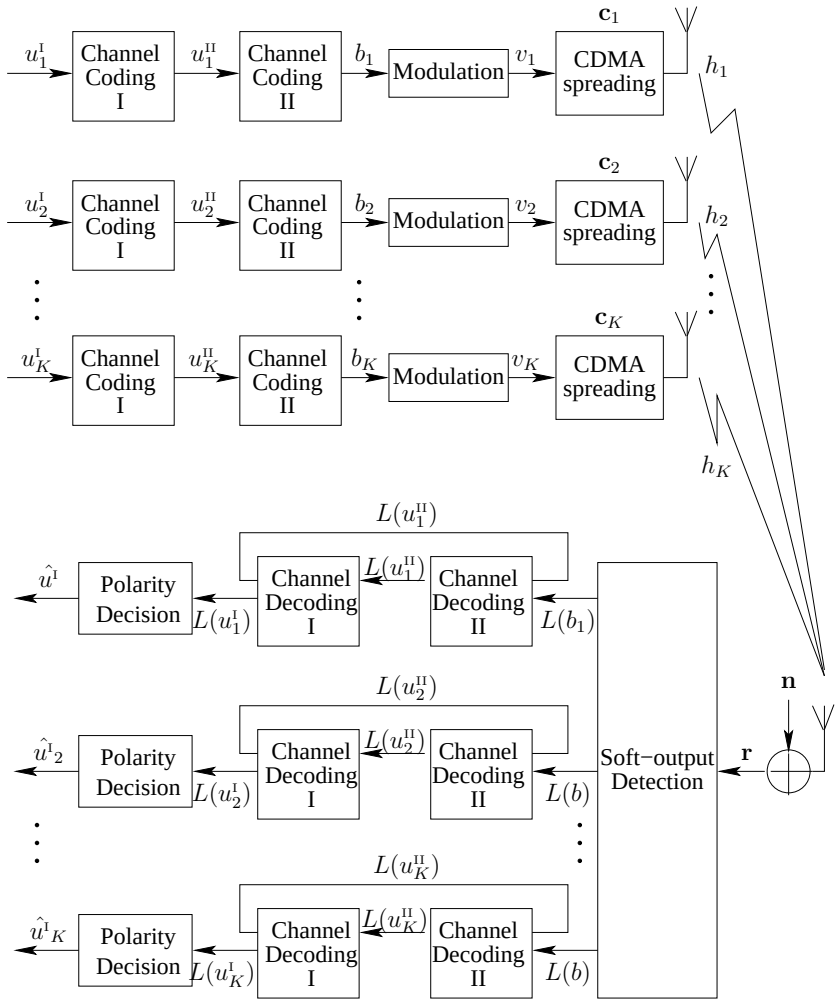

Figure 2.6: Block diagram of a channel-coded multi-user system, when iterative soft-output detection is employed, which is the foundation of the more sophisticated block diagram of the system to be investigated later in Chapter 7.

2.5.1 Relationship between the LLRs and the *A Posteriori* Conditional Probabilities

The LLR $L(b)$ of Fig. 2.6, associated with a coded bit is a function of its *a posteriori* conditional probability based on the observation of r, i.e. on $P(b = 0|r)$ (or $P(b = 1|r)$). More quantatively, the LLR $L(b)$ of Fig. 2.6 is defined as

$$L(b) = \ln \frac{P(b = 0|r)}{P(b = 1|r)}. \tag{2.83}$$

Since each coded bit is BPSK modulated at the transmitter, the LLR of each bit can also be alternatively represented as a function of its modulated symbol $v \in \{+1, -1\}$, yielding:

$$L(v) = \ln \frac{P(v = +1|r)}{P(v = -1|r)}. \tag{2.84}$$

As suggested by the fact that

$$P(v = +1|r) + P(v = -1|r) = 1, \tag{2.85}$$

Eq. (2.84) can be alternatively represented as a single-variable function of $P(b = +1|r)$ or $P(b = -1|r)$ in the form of

$$L(v) = \ln \frac{P(v = +1|r)}{1 - P(v = +1|r)}. \tag{2.86}$$

Fig. 2.7 quantifies the relationship between the LLR $L(b)$ and the *a posteriori* conditional probability

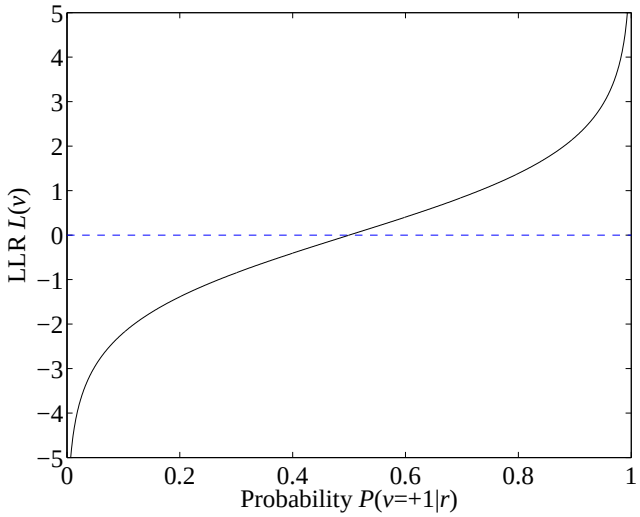

Figure 2.7: Value of LLR $L(v)$ as a function of the *a posteriori* probability $P(v = +1|r)$ ranging from 0 to 1.

$P(b = \pm 1|r)$. As seen from Fig. 2.7, the definition of the LLR given by Eq. (2.83) or Eq. (2.84) translates the probabilities of two binary options into a single real-valued scalar, the polarity of which represents the binary decision, while the absolute value of the LLR represents our confidence in that decision, because the absolute value is propotional to the value of the *a posteriori* conditional probability of $P(v = \pm 1|r)$.

We will exploit in our iterative turbo MUD, that the *extrinsic* LLR of one of the component decoders will provide *a priori* information for the other decoder component by generating the *a priori* probability $P(v = +1)$ with the aid of

$$\begin{aligned} L(v) &= \ln \frac{P(v = +1|r)}{1 - P(v = +1|r)} \Rightarrow \\ P(v = +1|r) &= [1 - P(v = +1|r)]L(v) \Rightarrow \\ P(v = +1|r) &= \frac{L(v)}{1 + L(v)}. \end{aligned} \tag{2.87}$$

Similarly, the *a priori* probability $P(v = -1)$ can also be quantified by $L(v)$ as

$$P(v = -1|r) = \frac{1}{1 + L(v)}. \tag{2.88}$$

Below we will focus our attention on the properties of the LLR related to a single coded bit for transmission over a Rayleigh-faded channel contaminated by complex-valued Gaussian distributed noise under the assumption that the perfect knowledge of the CIR is available at the receiver. More detailed discussions related to the LLR of a single coded bit transmitted by a particular user will be provided for two scenarios, namely for a single-user system and for a multiple user system. More

specifically, the simplified formula quantifying the LLR associated with a single bit in a single-user system is derived both mathematically and graphically. The derivation of the simplified form of the LLR associated with a certain bit in a CDMA aided multi-user system will be detailed in Chapter 6, followed by the Soft-Output (SO) ACO-based MUD algorithm invoked for finding solutions representing the LLRs as accurately as possible, but at a reduced complexity.

2.6 Soft-Output Detection in a Single-User System

The received signal r can be formulated as

$$r = hv + n, \tag{2.89}$$

and when $v = +1$ is transmitted, we have $r = h + n$, where n is a sample of the complex-valued Gaussian distributed random variable $\mathfrak{n} = \Re\mathfrak{n} + j \cdot \Im\mathfrak{n}$ with a mean of $\mu_{\Re\mathfrak{n}} = \mu_{\Im\mathfrak{n}} = 0$ and a variance of $\sigma^2_{\Re\mathfrak{n}} = \sigma^2_{\Im\mathfrak{n}} = \frac{1}{2}\sigma^2_{\mathfrak{n}}$ in each domain, which can be denoted as $\mathfrak{n} \sim \mathcal{N}^{\mathrm{c}}(\mu_{\mathfrak{n}}, \sigma^2_{\mathfrak{n}})$. Hence, given the knowledge of h, samples of $\mathfrak{r}|(v = +1)$ are complex-valued Gaussian distributed with a mean of h and a variance of $\sigma^2_{\mathfrak{n}}$. In other words, $(\mathfrak{r}|v = +1) \sim \mathcal{N}^{\mathrm{c}}(h, \sigma^2_{\mathfrak{n}})$. The complex-valued Gaussian distribution function of $\mathfrak{x} \sim \mathcal{N}^{\mathrm{c}}(\mu_{\mathfrak{x}}, \sigma^2_{\mathfrak{x}})$ is given by

$$p(x) = \frac{1}{\pi\sigma^2_{\mathfrak{x}}} \exp\left(-\frac{|x - \mu_{\mathfrak{x}}|^2}{\sigma^2_{\mathfrak{x}}}\right), \tag{2.90}$$

where the PDF of the random variable $(\mathfrak{r}|v = +1)$ is given by

$$p(r|v = +1) = \frac{1}{\pi\sigma^2_{\mathfrak{n}}} \exp\left(-\frac{|r - h|^2}{\sigma^2_{\mathfrak{n}}}\right). \tag{2.91}$$

Similarly, when we have $v = -1$, $r = -h + n$, then r becomes a sample of the random variable $(\mathfrak{r}|v = -1) \sim \mathcal{N}^{\mathrm{c}}(-h, \sigma^2_{\mathfrak{n}})$, and the PDF of $(\mathfrak{r}|v = -1)$ is formulated as

$$p(r|v = -1) = \frac{1}{\pi\sigma^2_{\mathfrak{n}}} \exp\left(-\frac{|r + h|^2}{\sigma^2_{\mathfrak{n}}}\right). \tag{2.92}$$

2.6.1 Geometric Representation

Below, we will assume that $v = +1$ and $v = -1$ was transmitted with equal probability, which results in an *a priori* information of zero. This can be expressed as $p(v = +1) = 0.5$ and $p(v = -1) = 0.5$. Under this assumption, the derivation of the LLRs corresponding to a given r can be provided by substituting $p(r|v = +1)$ and $p(r|v = -1)$ in Eq. (**??**) in conjunction with Eq. (2.91) and Eq. (2.92). However, in order to provide an intuitive relationship between the real-valued LLR and the complex-valued received signal r, let us consider Fig. 2.8 to 2.11.

Figs. 2.8 to 2.13 rely on the parameters of Tab. 2.10.

Let us now portray the LLR-surface denoted by S_3 in Fig. 2.9, which is the logarithm of the ratio of surfaces S_1 and S_2. The *a priori* LLR value of each point on the LLR-surface is given by

$$L(r) = \ln \frac{p(r|v = +1)}{p(r|v = -1)}. \tag{2.93}$$

channel h	$h = 0.5 + 0.5j$
noise n	$n \in \mathfrak{n} \sim \mathcal{N}^{\mathrm{c}}(\mu_{\mathfrak{n}}, \sigma_{\mathfrak{n}}^2)$ $\mu_{\mathfrak{n}} = 0,\ \sigma_{\mathfrak{n}}^2 = 2$
transmit signal v	$v \in \{+1, -1\}$ $P(v = +1) = P(v = -1) = 0.5$

Table 2.10: Parameters used in Figs. 2.8 to 2.13

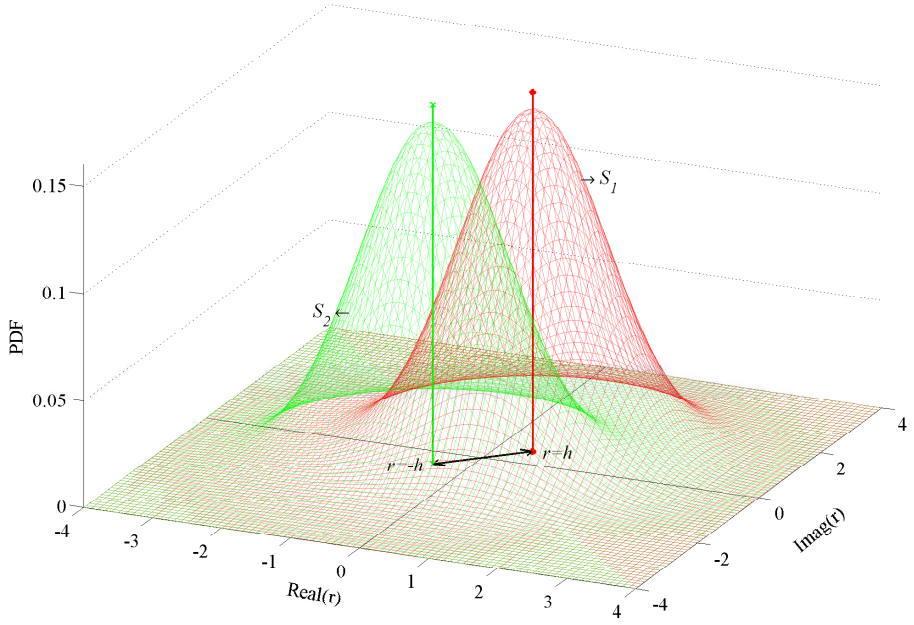

Figure 2.8: Surface S_1 of Eq. (2.91) represents the conditional PDF of r, given that $v = +1$ is transmitted, while S_2 graphically portrays Eq. (2.92), when using the system parameters of Tab. 2.10.

Given the (x, y) coordinate of a point on the horizontal x-y plane, let us assume that the LLR value corresponding to this point's projection onto S_1 is z_1, which that onto S_2 is z_2. Then the resultant LLR surface may be directly obtained as the logarithm of the ratio of z_1 by z_2.

Although S_1 and S_2 are cylindrically symmetric surfaces, the logarithm of the ratio between them is a flat plane.

Observe furthermore in Fig. 2.9, that albeit S_3 is a 3-D surface of two variables, it is actually a flat 3-D surface, which is determined by a single independent value denoted as d. Hence we have $z = f_1(d)$. If we can find the relationship between r and d on the x-y plane in the form of $d = f_2(r)$, we arrive at $z = L(r) = f_1(d) = f_1[f_2(r)]$.

In order to find the analytical representation of the function $z = f_1(d)$, we show the view of intersection between S_3 and the x-y plane, as denoted by m in Fig. 2.9. Then, based on the simple geometry of Fig. 2.9, the z coordinate of any point on S_3 is a linear function of the perpendicular

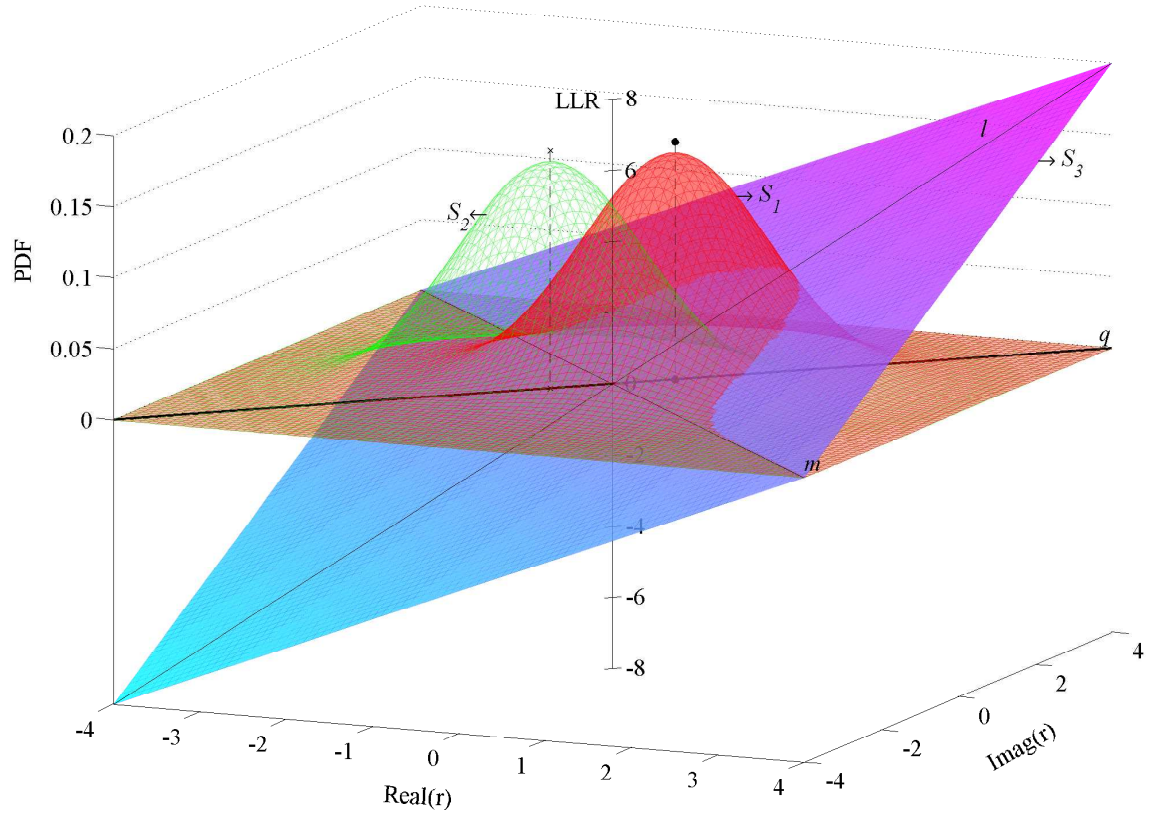

Figure 2.9: Surface S_3 graphically quantifies the rudical LLR l as a function $L(r)$ of r when each value on the xy-plane is taken by r and the system parameters take their value from Tab. 2.10. S_3 representing $l = L(r)$ is plotted by taking the logarithm value of S_1 and S_2 according to Eq. (2.93).

distance d of its projection onto the x-y plane from the line m.

To elaborate on Fig. 2.9 a little further, the real-valued projection d of r onto the axis q can be alternatively represented as the real component of a complex number, which is the received signal vector r rotated anti-clockwise according to the phase-angle of the CIR, namely by $\angle h$. More quantatively

$$d = \Re\left\{re^{j\cdot\angle h}\right\} = \Re\left\{r\frac{h^*}{|h|}\right\} = \frac{1}{|h|}\Re\{h^* r\}, \tag{2.94}$$

where h^* is the conjugate of the CIR h, $|h|$ is the absolute value of h and hence we have $h^*/|h| = -\angle h$.

Therefore the evaluation of the LLR in the context of Fig. 2.9 can be carried on within a vertical plane having an angle of $\angle h$, with respect to the real axis as denoted by S_4 in Fig. 2.10. To expound further in the context of Fig. 2.10 and Fig. 2.11, l is the line of intersection between S_3 of Fig. 2.9 and the vertical plane S_4 of Fig. 2.10, while p_p is the curve of intersection between the surface S_1 and the vertical plane S_4. Finally p_m of Fig. 2.10 is the curve of intersection between the surface S_2 and the vertical plane S_4. In order to provide an alternative view of Figures 2.8∼2.10, S_1, S_2, S_3 and S_4 were made transparent in Fig. 2.11, which will assist us further during the derivation of $l = L(r)$ below.

As observed from Fig. 2.9, the LLR $L(d)$ is propotional to d with a slope of a, yieldig

$$L(d) = ad. \tag{2.95}$$

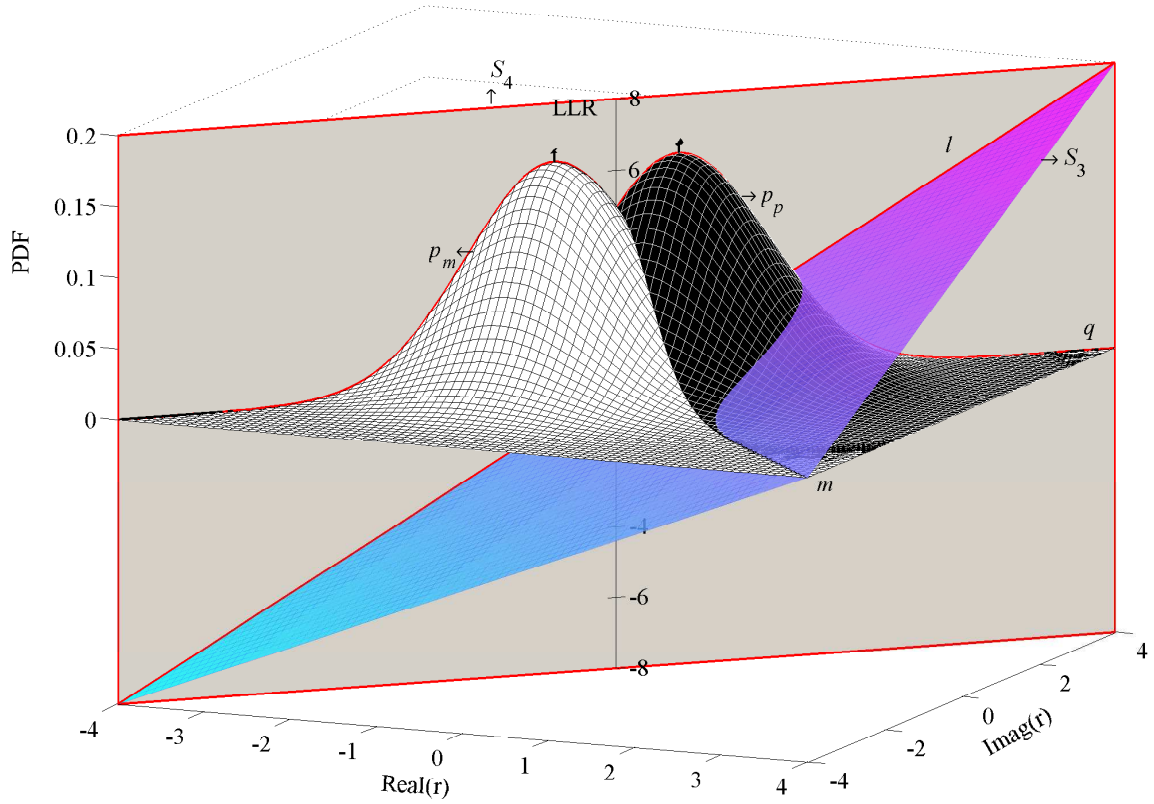

Figure 2.10: Vertical plane S_4 that is perpendicular to the xy-plane with an intersection line overlapping $r = h$, when the system parameters take their value from Tab. 2.10.

As seen from Fig. 2.11, the line l, and the curves p_p and p_m on the plane S_4 are at the same time on LLR flat plane S_3, PDF curved palne S_1 and S_2 respectively. Hence the equation

$$L(r) = \ln \frac{p(r|v=+1)}{p(r|v=-1)} \tag{2.96}$$

quantifying the relationship of the z-coordinates of the points on S_1, S_2, S_3 associated with the same r value on the x-y plane remains also valid for the points on the line l as well as for the curves p_p and p_m. More quantatively, we have

$$L(d) = \ln \frac{p(d|v=+1)}{p(d|v=-1)}. \tag{2.97}$$

As seen from Fig. 2.9, when the received signal r assumes values along the axis q, it obeys a real-valued Gaussian distribution having a mean of $|h|$, and a one-dimensional variance of $\sigma^2_{\Re\mathfrak{n}} = \frac{1}{2}\sigma^2_{\mathfrak{n}}$. Hence the real coordinate d on the axis q may be regarded as a sample of the real-valued Gaussian distributed variable $\mathfrak{d}$, with a mean of $\mu_{\mathfrak{d}} = |h|$ and a variance of $\sigma^2_{\mathfrak{d}} = \sigma^2_{\Re\mathfrak{n}} = \frac{1}{2}\sigma^2_{\mathfrak{n}}$. The corresponding conditional probability distribution function (CPDF) under the assumption that $v = +1$ was transmitted maybe expressed as

$$\begin{aligned} p(d|v=+1) &= \frac{1}{\sigma_{\mathfrak{d}}\sqrt{2\pi}} \exp\left(-\frac{(d-\mu_{\mathfrak{d}})^2}{2\sigma^2_{\mathfrak{d}}}\right) \\ &= \frac{1}{\frac{1}{\sqrt{2}}\sigma_{\mathfrak{n}}\sqrt{2\pi}} \exp\left(-\frac{(d-|h|)^2}{\sigma^2_{\mathfrak{n}}}\right) \end{aligned} \tag{2.98}$$

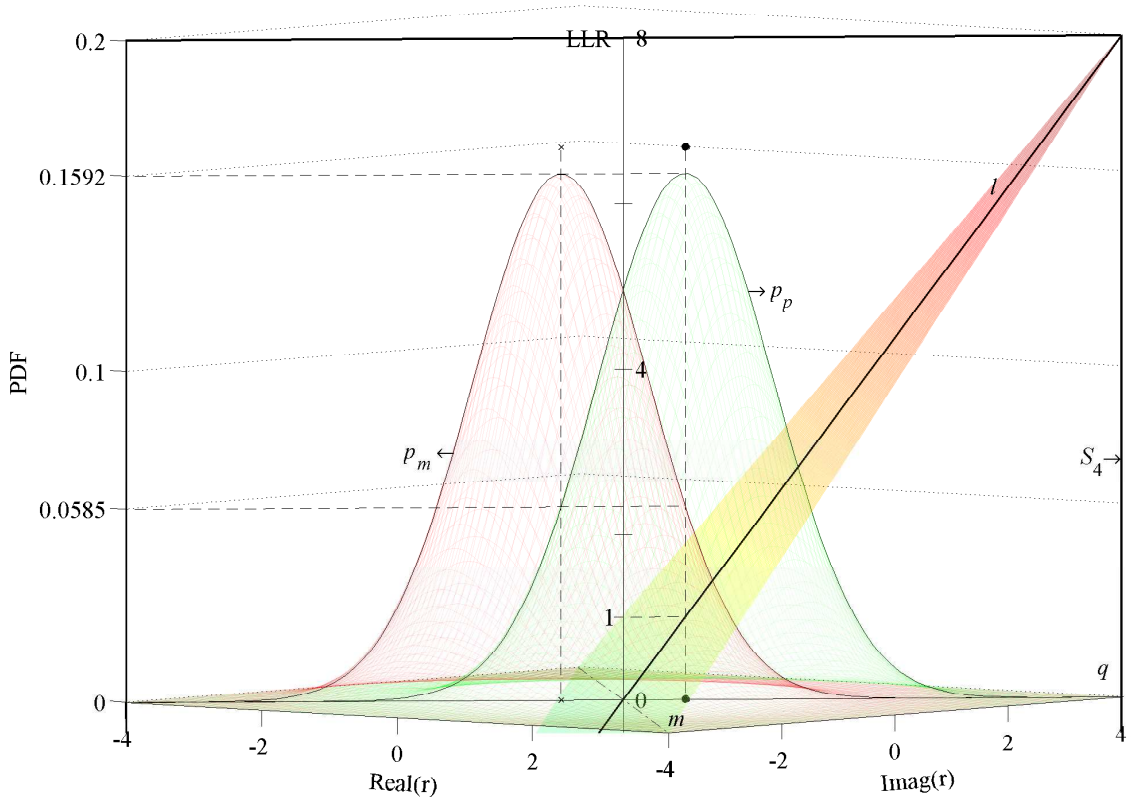

Figure 2.11: Z-axis values of the points on plane S_4 demonstrating the realtionship between $l(r)$ and $p(r|v=+1)$, $p(r|v=-1)$ associated with an identical r as defined by Eq. (2.93), when the system parameters take their value from Tab. 2.10.

Similarly, the CPDF of d under the assumption of $v=-1$, is expressed as:

$$\begin{aligned} p(d|v=-1) &= \frac{1}{\sigma_{\mathfrak{d}}\sqrt{2\pi}} \exp\left(-\frac{(d-\mu_{\mathfrak{d}})^2}{2\sigma_{\mathfrak{d}}^2}\right) \\ &= \frac{1}{\frac{1}{\sqrt{2}}\sigma_{\mathfrak{n}}\sqrt{2\pi}} \exp\left(-\frac{(d+|h|)^2}{\sigma_{\mathfrak{n}}^2}\right). \end{aligned} \tag{2.99}$$

Upon substituting $p(d|v=+1)$ and $p(d|v=-1)$ into Eq.(2.97) along with Eq.(2.98) and Eq.(2.99), the LLR as a function of d is derived from the traditional definition as

$$\begin{aligned} L(d) &= \ln \frac{p(d|v=+1)}{p(d|v=-1)} \\ &= \ln \frac{\frac{1}{\frac{1}{\sqrt{2}}\sigma_{\mathfrak{n}}\sqrt{2\pi}} \exp\left(-\frac{(d-|h|)^2}{\sigma_{\mathfrak{n}}^2}\right)}{\frac{1}{\frac{1}{\sqrt{2}}\sigma_{\mathfrak{n}}\sqrt{2\pi}} \exp\left(-\frac{(d+|h|)^2}{\sigma_{\mathfrak{n}}^2}\right)} \\ &= -\frac{(d-|h|)^2}{\sigma_{\mathfrak{n}}^2} - \left(-\frac{(d+|h|)^2}{\sigma_{\mathfrak{n}}^2}\right) \\ &= -\frac{1}{\sigma_{\mathfrak{n}}^2}\left[(d-|h|)^2 - (d+|h|)^2\right] \\ &= \frac{1}{\sigma_{\mathfrak{n}}^2} 4d|h|. \end{aligned} \tag{2.100}$$

When comparing Eq. (2.95) and Eq. (2.100), the factor a can be interpretated as

$$a = \frac{4|h|}{\sigma_{\mathfrak{n}}^2}. \tag{2.101}$$

Therefore, the LLR maybe expressed as a function of d as

$$\begin{aligned} L(r) &= f_1(d) = ad \\ &= \frac{4|h|}{\sigma_{\mathfrak{n}}^2} d. \end{aligned} \tag{2.102}$$

As defined in Eq. (2.94), the real number d is another function of the complex number r defined by $d = f_2(r) : r \to d$, which can be quantified as

$$d = f_2(r) = \frac{1}{|h|} \Re(h^* r), \tag{2.103}$$

Therefore, since d is a function of r and the LLR is a function of d,the LLR is also a function of r, which can be represented by the function composition of $(f_1 \circ f_2)(r)$ as

$$\begin{aligned} L(r) &= f_1[f_2(r)] = ad \\ &= \frac{4|h|}{\sigma_{\mathfrak{n}}^2} f_2(r) \\ &= \frac{4|h|}{\sigma_{\mathfrak{n}}^2} \frac{1}{|h|} \Re(h^* r) \\ &= \frac{4}{\sigma_{\mathfrak{n}}^2} \Re(h^* r). \end{aligned} \tag{2.104}$$

Sicne the MF output is defined by the function

$$y = f_4(r) = h^* r, \tag{2.105}$$

the LLR can be alternatively represented as a function of the MF output y as

$$L(r) = f_3(y) = \frac{4}{\sigma_{\mathfrak{n}}^2} \Re(y), \tag{2.106}$$

which is demonstrated in Fig. 2.11 correspondingly.

Again, the curves in Fig. 2.11 illustrate the unique one-to-one relationship between l and r for the scenario using the parameters of Table. (2.10). More specifically, the LLR value l of $r = h$ will be evaluated for the scenario of Table. (2.10).

Firstly, when $r = h$, we have $d = |h|$ on the q axis. In conjunction with $\sigma_{\mathfrak{n}}^2 = 2$ and $h = 0.5 + 0.5j$ of Table. 2.10, the LLR when $r = h$ is received can be calculated using Eq. (2.102), yielding:

$$\begin{aligned} L(r) = f_1(d) &= \frac{4|h|}{\sigma_{\mathfrak{n}}^2} d \\ &= \frac{4|h|}{2} |h| \\ &= 2|h|^2 = 2 \times \frac{1}{2} = 1. \end{aligned} \tag{2.107}$$

Additionally, when $r = h$, the MF output is given by

$$\begin{aligned} y = h^* r = (0.5 - 0.5j)(0.5 + 0.5j) \Rightarrow \\ \Re\{y\} = 0.25 + 0.25 = 0.5. \end{aligned} \tag{2.108}$$

By substituting $\Re\{y\} = 0.5$ in Eq. (2.106), the LLR becomes

$$\begin{aligned} L(r) = f_3(y) &= \frac{4}{\sigma_{\mathfrak{n}}^2}\Re(y) \\ &= \frac{4}{2} \times 0.5 = 1. \end{aligned} \tag{2.109}$$

Alternatively, when $r = h$, the conditional PDF values $p(r|v = +1)$ and $p(r|v = -1)$ can be read from the z-coordinate of the curve p_p and p_m in Fig 2.11 as $p(r|v = +1) = 0.1592$ and $p(r|v = -1) = 0.0585$. Furthermore when $r = h$ is received, the LLR may be calculated from Eq. (2.102) as

$$\begin{aligned} L(r) &= \ln \frac{p(r|v = +1)}{p(r|v = -1)} \\ &= \ln \frac{0.1592}{0.0585} = \ln 2.7214 = 1. \end{aligned} \tag{2.110}$$

By comparing Eq. (2.107) and Eq. (2.110), we can see that the LLR of a specific received signal value r can be written as a function of $l = f_1(d)$ of the independent variable d, or as a function of $l = f_3(y)$ of the MF output, as defined by Eq. (2.106).

Alternatively, the final form of the LLRs expressed as a function of r can be directly obtained from Eq. (2.84), when $p(v = +1) = p(v = -1) = 0.5$. When using the PDF $p(r|v = +1)$ from Eq. (2.91) and the PDF $p(r|v = -1)$ from Eq. (2.92) provided that r was received, the LLR of a coded bit may be represented by

$$\begin{aligned} L(r) &= \ln \frac{p(r|v = +1)}{p(r|v = -1)} \\ &= \ln \frac{\frac{1}{\pi\sigma_{\mathfrak{n}}^2} \exp\left(-\frac{|r-h|^2}{\sigma_{\mathfrak{n}}^2}\right)}{\frac{1}{\pi\sigma_{\mathfrak{n}}^2} \exp\left(-\frac{|r+h|^2}{\sigma_{\mathfrak{n}}^2}\right)} \\ &= -\frac{1}{\sigma_{\mathfrak{n}}^2}\left[|r-h|^2 - |r+h|^2\right] \\ &= -\frac{1}{\sigma_{\mathfrak{n}}^2}\left[(r^* - h^*)(r-h) - (r^* + h^*)(r+h)\right] \\ &= -\frac{1}{\sigma_{\mathfrak{n}}^2}\left[|r|^2 - h^* r - r * h + |h|^2 - |r|^2 - h^* r - r * h - |h|^2\right] \\ &= \frac{1}{\sigma_{\mathfrak{n}}^2} 4\Re\{h^* r\} \\ &= \frac{4}{\sigma_{\mathfrak{n}}^2}\Re\{y\}, \end{aligned} \tag{2.111}$$

which matches the final expression given in Eq. (2.102) and derived with the aid of Fig. 2.8 to Fig. 2.11 according to plausible geometric rules.

2.6.2 Summary of LLR Characteristics in a Single-User System

When r is received in a single-user system defined by $r = hv + n$, different techniques of generating the LLRs $l = L(r)$ may be used:

1. First we obtain the projection d of the received signal r assording to $d = f_2(r)$, as given in Eq. (2.103). Then we calculate $l = f_1(d)$ using Eq. (2.102); Alternatively,
2. First generate the MF output $y = f_4(r)$ with the aid of Eq. (2.105), then calculate the LLR as $l = f_3(y)$ using Eq. (2.106); or
3. Calculate $p(r|v = +1)$ and $p(r|v = -1)$ for the received signal r accoding to the PDF quantified in Eq. (**??**) and Eq. (**??**) respectively, then calculate $l = L(r)$ using Eq. (2.93).

In summary, the LLR depends on the single variable onstituted by the MF's output $Re\{y\}$ rather than on the received signal r.

2.6.3 Symmetric Properties of the LLRs

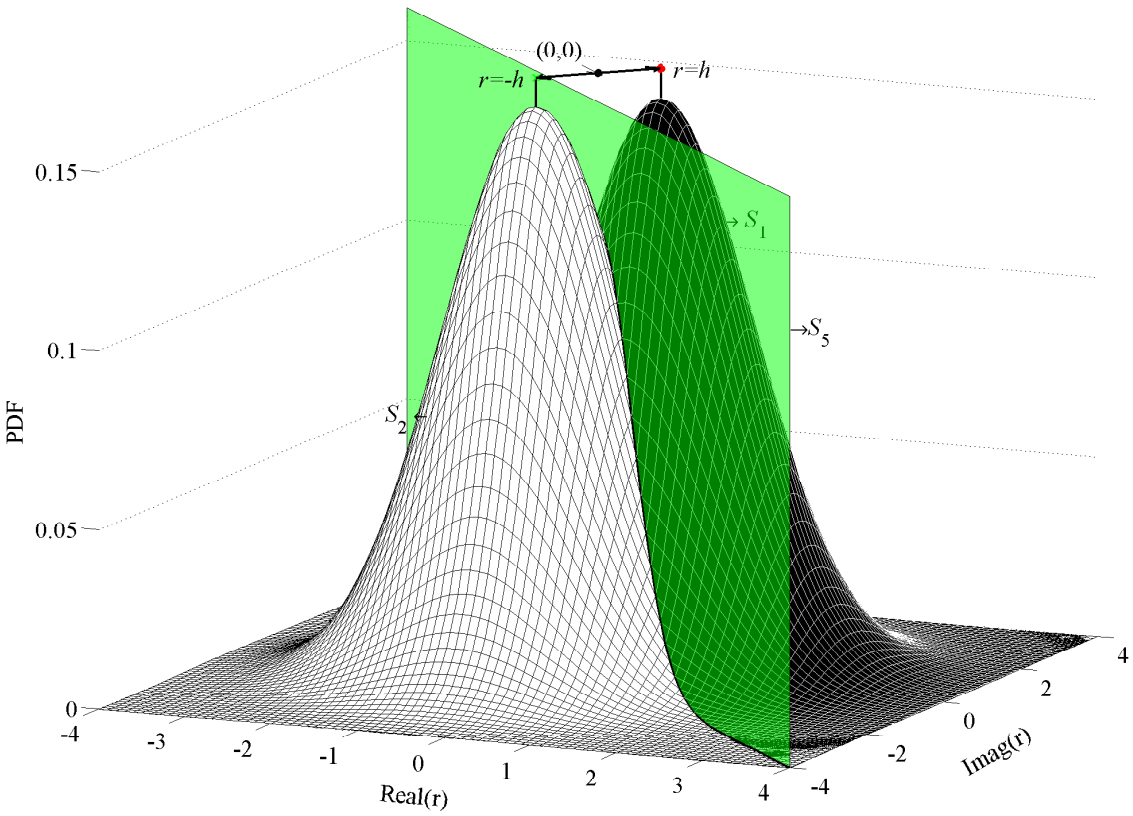

Figure 2.12: Symmetric property achieved by S_1 and S_2 depicting the conditional PDF $p(r|v = +1)$ and $p(r|v = -1)$ respectively, when the system parameter is set according to the value given in Tab. 2.10. r is the indepedent variable of the two 3D surafaces that changes over the whole complex plane namely the xy-plane.

As seen from Fig. 2.12 the PDF surfaces of $p(r|v=+1)$ and $p(r|v=-1)$ are cylindrically symmetric with respect to the vertical plane S_5 of Fig. 2.12 that is perpendicular to the x-y plane and to the vector h. Hence we have

$$\begin{aligned} p(h*r|v=+1) = p(-(h*r)|v=-1) \quad &\Rightarrow \\ p(y|v=+1) = p(-y|v=-1) \end{aligned} \tag{2.112}$$

Additionally, as seen from Fig. 2.9, the LLR plane is also symmetric with respect to the line m, which can be alternatively written as More quantatively,

$$\begin{aligned} L(h\cdot r) = -L[-(h\cdot r)] \quad &\Rightarrow \\ L(y) = -L(-y). \end{aligned} \tag{2.113}$$

Furthermore, as the LLR plane denoted by S_3 in Fig. 2.9 is a flat plane in the 3D space, the LLR value is a function of $\Re\{y\}$, where we have

$$L(\Re\{y\}) = -L(-\Re\{y\}) = -L(\Re\{-y\}). \tag{2.114}$$

This observation extracted from Fig. 2.9 may alternatively be encorporated in the following equations

$$L(\Re\{y\}) = \frac{4}{\sigma_{\mathfrak{n}}^2}\Re\{y\} = -\frac{4}{\sigma_{\mathfrak{n}}^2}\Re\{-y\} = -\frac{4}{\sigma_{\mathfrak{n}}^2}(-\Re\{y\}). \tag{2.115}$$

2.6.4 Consistency Condition for the LLRs

The LLR $l = L(y; x=\pm 1)$ of making a decision between ± 1 for x based on y is defined as

$$l = L(y; x=\pm 1) = \ln \frac{p(y|x=+1)}{p(y|x=-1)}. \tag{2.116}$$

Thus, we can make a decision based on the polarity of l, while $|l|$ indicates the reliability of the decision.

However, if we want to quantify the reliability of making the final verdict based on the LLR l rather than on y, we can evaluate the probability of $x=+1$ resulting in l and $x=-1$ resulting in l, respectively, and then evaluating the logarithm of the ratio of these two probabilities, yielding

$$l' = L(l; x=\pm 1) = \ln \frac{p(l|x=+1)}{p(l|x=-1)}. \tag{2.117}$$

Inuitively, the reliability of making a binary decision based on the polarity of l should be the same as that based on y, which is indicated by the absolute value of l. For a correctly calculated LLR l, the decision should be a stable and **consistent** one, regardless of how many times we take the logarithm. More quantatively, for a correctly calculated l, we should always have

$$l' = L(l) = \ln \frac{p(l|v=+1)}{p(l|v=-1)} \equiv l. \tag{2.118}$$

Below, we will show that the consistency condition quantified by Eq. (2.118) will be satisfied if the LLR $l_1 = L(r)$ of a single-user wireless communication system is correctly calculated based on $r = hv + n$. Based on Fig. 2.13 we will demonstrate that the consistency condition will not be fulfilled, if the LLR

is inaccurately calculated. We will also show that evaluating the logarithmic likelihood ratio of the inaccurately calculated l_2, given by

$$L(l_2) = \ln \frac{p(l_2|v=+1)}{p(l_2|v=-1)} \tag{2.119}$$

assists the detector in finding the correct LLR $l_1 = L(r)$ based on the incorrect l_2.

We can plot the conditional PDF of the LLR $p(l|v=+1)$ and $p(l|v=-1)$ versus the value of l under the condition of $v=+1$ and $v=-1$, respectively. As seen in Fig. 2.13, the two curves associated with $p(l|v=+1)$ and $p(l|v=-1)$ obey the real-valued Gaussian distribution, which also describe the final form of the LLRs in a single-user system, as given by $l = \frac{4}{\sigma_{\mathfrak{n}}^2}\Re\{y\}$. Assuming that we have $h = \Re\{h\} + j\Im\{h\}$ and that $n = \Re\{n\} + j\Im\{n\}$ is a sample of $\mathfrak{n} \sim \mathcal{N}^{\mathrm{c}}(0, \sigma_{\mathfrak{n}}^2)$ as

$$\begin{aligned} \because y &= h^* r = |h|^2 v + h^* n, \\ \therefore \Re\{y\} &= |h|^2 v + \Re\{h^* n\} \\ &= |h|^2 v + \Re\{h\}\Re\{n\} - \Im\{h\}\Im\{n\}, \quad v \in \{+1, -1\}, \end{aligned} \tag{2.120}$$

where both the real and the imaginary component of h are real-valued Gaussian distributed random variables, where mean is given by $\mu_{\Re\{\mathfrak{n}\}} = \mu_{\Im\{\mathfrak{n}\}} = 0$ and variance is given by $\sigma^2_{\Re\{\mathfrak{n}\}} = \sigma^2_{\Im\{\mathfrak{n}\}} = \frac{1}{2}\sigma^2_{\mathfrak{n}}$.

Furthermore, if $\mathfrak{X}_1$, $\mathfrak{X}_2$ are two independent normally distributed random variables, with means of μ_1, μ_2 and standard deviations of σ_1, σ_2, then their linear combination will also be normally distributed:

$$a\mathfrak{X}_1 + b\mathfrak{X}_2 \sim \mathcal{N}^{\mathrm{r}}(a\mu_1 + b\mu_2,\, a^2\sigma_1^2 + b^2\sigma_2^2). \tag{2.121}$$

Hence, regardless of the value of v, $\Re\{y\}$ is a sample of a real-valued Gaussian distributed random process $\mathfrak{y}^{\mathrm{r}}$ obeying

$$\begin{aligned} \mathfrak{y}^{\mathrm{r}} &\sim \mathcal{N}^{\mathrm{r}}\left(|h|^2 v, (\Re\{h\}^2 + \Im\{h\}^2) \cdot \frac{1}{2}\sigma_{\mathfrak{n}}^2\right) \\ \Rightarrow \mathfrak{y}^{\mathrm{r}} &\sim \mathcal{N}^{\mathrm{r}}\left(|h|^2 v, \frac{1}{2}|h|^2\sigma_{\mathfrak{n}}^2\right). \end{aligned} \tag{2.122}$$

Sicne we have $l = L(\Re\{y\}) = \frac{4}{\sigma_{\mathfrak{n}}^2}\Re\{y\}$, therefore l is a sample of the real-valued Gaussian distributed random process

$$\mathfrak{l} \sim \mathcal{N}^{\mathrm{r}}\left(\frac{4|h|^2 v}{\sigma_{\mathfrak{n}}^2}, \frac{8|h|^2}{\sigma_{\mathfrak{n}}^2}\right). \tag{2.123}$$

If the variance of $\mathfrak{l}$ is defined as

$$\sigma_{\mathfrak{l}}^2 = \frac{8|h|^2}{\sigma_{\mathfrak{n}}^2}, \tag{2.124}$$

when $v=+1$ is transmitted, the mean of $\mathfrak{l}$ is

$$\mu_{\mathfrak{l}}|v=+1 = \frac{1}{2}\sigma_{\mathfrak{l}}^2, \tag{2.125}$$

while provided that $v=-1$ is transmitted, the mean of $\mathfrak{l}$ is

$$\mu_{\mathfrak{l}}|v=-1 = -\frac{1}{2}\sigma_{\mathfrak{l}}^2. \tag{2.126}$$

With the mean and variance represented in Eq. (2.124), Eq. (2.125) and Eq. (2.126), Eq. (2.123) can be rewriten as:

$$\mathfrak{l}|v = \pm 1 \sim \mathcal{N}^{\mathrm{r}}(\pm\frac{1}{2}\sigma_{\mathfrak{l}}^2, \sigma_{\mathfrak{l}}^2). \tag{2.127}$$

Given the normal PDF of a random vairable $\mathfrak{x} \sim \mathcal{N}^{\mathrm{r}}(\mu, \sigma^2)$

$$p(x) = \frac{1}{\sqrt{2\pi\sigma^2}} \exp\left(-\frac{(x-\mu)^2}{2\sigma^2}\right), \tag{2.128}$$

in single-user system, the conditional PDF of $\mathfrak{l}$ under the condition of$v = \pm 1$ can be quantified as:

$$p(l|v = \pm 1) = \frac{1}{\sqrt{2\pi\sigma_{\mathfrak{l}}^2}} \exp\left(-\frac{\left(l \mp \frac{1}{2}\sigma_{\mathfrak{l}}^2\right)^2}{2\sigma_{\mathfrak{l}}^2}\right), \tag{2.129}$$

with

$$\sigma_{\mathfrak{l}}^2 = \frac{8|h|^2}{\sigma_{\mathfrak{n}}^2}. \tag{2.130}$$

Hence, if we calculate the LLR of l over all the real numbers of set $\mathbb{R}$, the result $L(l)$ may be expressed as

$$\begin{aligned}
L(l) &= \ln \frac{p(l|v=+1)}{p(l|v=-1)} \\
&= \ln \frac{\frac{1}{\sqrt{2\pi\sigma_{\mathfrak{l}}^2}} \exp\left(-\frac{\left(l - \frac{1}{2}\sigma_{\mathfrak{l}}^2\right)^2}{2\sigma_{\mathfrak{l}}^2}\right)}{\frac{1}{\sqrt{2\pi\sigma_{\mathfrak{l}}^2}} \exp\left(-\frac{\left(l + \frac{1}{2}\sigma_{\mathfrak{l}}^2\right)^2}{2\sigma_{\mathfrak{l}}^2}\right)} \\
&= \frac{1}{2\sigma_{\mathfrak{l}}^2}\left[\left(l - \frac{1}{2}\sigma_{\mathfrak{l}}^2\right)^2 - \left(l + \frac{1}{2}\sigma_{\mathfrak{l}}^2\right)^2\right] \\
&= \frac{1}{2\sigma_{\mathfrak{l}}^2} \cdot 4l\frac{1}{2}\sigma_{\mathfrak{l}}^2 \\
&= l.
\end{aligned} \tag{2.131}$$

The derivations spanning from Eq. (2.120) to Eq. (2.131) priovide the proof of the **consistency condition** cite of LLRs in the context of single-user system described by

$$r = hv + n, \tag{2.132}$$

with $n \in \mathfrak{n} \sim \mathcal{N}^{\mathrm{c}}(0, \sigma_{\mathfrak{n}}^2)$. More precisely the **consistency condition** can be formulated for a single user system defined by Eq. (2.132) as

$$l = \ln \frac{p(l|v=+1)}{p(l|v=-1)}, \tag{2.133}$$

where

$$l = \ln \frac{p(r|v=+1)}{p(r|v=-1)}, \tag{2.134}$$

can be fulfilled, when the LLR $l = L(r)$ calculated from the received signal is correctly evaluated and under a given h, l is a sample of the real-valued Gaussian distributed random variable

$$\mathfrak{l} \sim \mathcal{N}^{\mathrm{r}}(\frac{1}{2}\sigma_{\mathfrak{l}}^2, \sigma_{\mathfrak{l}}^2), \tag{2.135}$$

with

$$\sigma_{\mathfrak{l}}^2 = \frac{8|h|^2}{\sigma_{\mathfrak{n}}^2}. \tag{2.136}$$

Thus the consistency condition can be used to examine the correctness of the LLR calculated by a

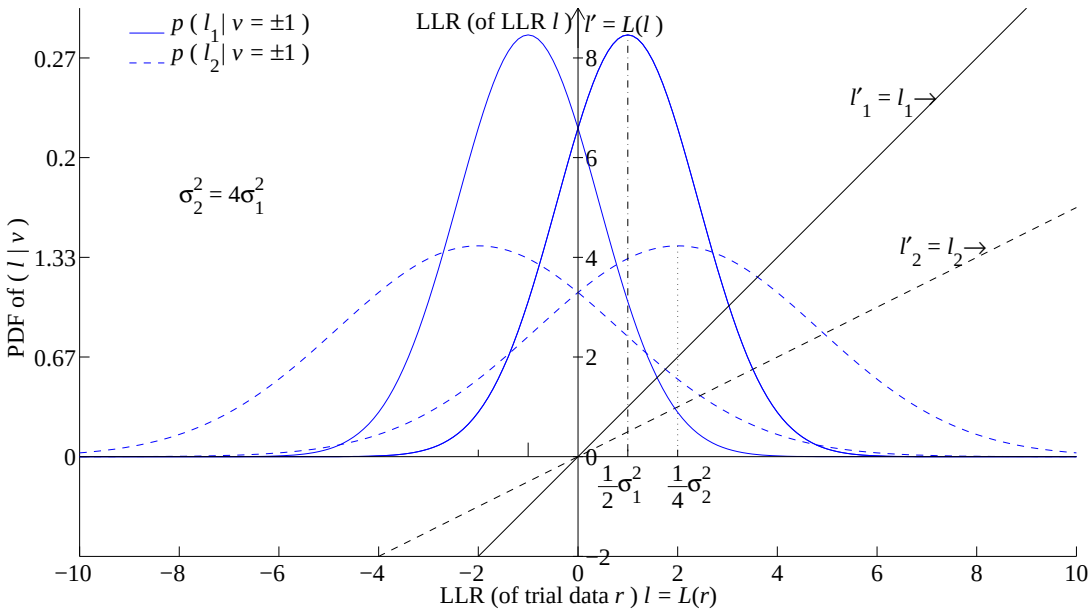

Figure 2.13: The two solid bell-shaped curves represents the PDF $p(l_1|v=+1)$ and $p(l_1|v=-1)$ quantifying the probability of the LLR l_1 when it is correctly calculated accoding to Eq. (2.93) and when the system parameter is set according to the value given in Tab. 2.10. The y-coordinate of the solid straight line l' related to each x-coordinate l_1 is calculated by evaluating the logarithm of the ratio of l_1's two conditional probability $p(l_1|v=+1)$, $p(l_1|v=-1)$. The equation of calcualting l_1' versus l_1 is detailed in Eq. (2.117). While the two dashed bell-shaped curves quantifies the PDF $p(l_2|v=+1)$ and $p(l_2|v=-1)$ of a incorrectly calculated LLR value $l_2 = 2l_1$ when $v=+1$ and $v=-1$ is transmitted, when all the system parameters take their value from Tab. 2.10. And the y-coordinate y_2' associated with the dashed straight line is achieved based on Eq. (2.117) by substituting $l = l_2$ in right hand side of the equation and we will obtain l_2' at the left hand side of the equation.

certain algorithm. When the LLR is for example inaccurately calculated, the consistency condition

of Eq. (2.133) will no longer be satisfied. An example based on 'over-confident' LLRs is illustrated in Fig. 2.13. The 'over-confident' LLR $l_2 = 2l_1$, which was wrongly calculated by a certain algorithm, for example owing to a low-resolution fixed-point multiplied the LLRs by a factor of two. The PDFs $p(l|v = +1)$ and $p(l|v = -1)$ are now plotted in Fig. 2.13 in dashed lines. As seen in Eq. (2.135), l_1 is an instantaneous value of the random variable $\mathfrak{l}_1 \sim \mathcal{N}^{\mathrm{r}}(\mu_1, \sigma_1^2)$, which has a mean, which is half of the variance, yilding $\mu_1 = \frac{1}{2}\sigma_1^2$. Since $l_2 = 2l_1$, l_2 will be an instantenous value of the random variable $\mathfrak{l}_2 \sim \mathcal{N}^{\mathrm{r}}(\mu_2, \sigma_2^2)$ with a mean of $\mu_2 = 2\mu_1 = \sigma_1^2$, and a variance of $\sigma_2^2 = 4\sigma_1^2$. Hence we arrive at $\mu_2 = \frac{1}{4}\sigma_2^2$, for the PDFs shown in Fig. 2.13 in dashed lines, which obey the PDF of $\mathfrak{l}_2 \sim \mathcal{N}^{\mathrm{r}}(\sigma_1^2, 4\sigma_1^2)$. However, when the value of the LLR has been changed to l_2, the consistency condition quantified by Eq. (2.133) is not satisfied.

The line defining LLR of l_2, $l_2' = L(l_2)$ is given by

$$l_2' = \ln \frac{p(l_2|v = +1)}{p(l_2|v = -1)} = \frac{1}{2} l_2 \tag{2.137}$$

with a slope of $\frac{1}{2}$, instead of the diagonal line having a slope of 1, which yields

$$l_1' = l_1, \tag{2.138}$$

which is as asociated with a slope of 1 given by the LLR l_1' of the LLR l_1 calcualted accurately from the received data r as $l_1' = L(l_1)$. However, after calculating the PDFs of l_2 for both $v = +1$ and $v = -1$, the resultant LLR of l_2, namely l_2' becomes the correct value, which is specific value that the over-confident l_2 should have assumed, when the same r is received as the one from which l_2 was calculated. In other words, the consistency condition can be used as a tool to examine the reliability of the algorithm of calculating the LLR from the received signal r.

The application of the LLR's consistency condition is summarized below as follows:

- Provided that the LLR $l_1 = L(r)$ is correctly calculated, the LLR $l' = L(l)$ of the LLR l will give the same value, namely l. In this case the consistency condition of the LLR was satisfied.
- By contrast, if the LLR $l_2 = L(r)$ was incorrectly calculated, but this incorrect value l_2 is a monotonically increasing function f of the correct LLR l_1 i.e. we have $l_2 = f(l_1)$, and provided that the inverse function f^{-1} of l_2 can be found, then the correct LLR value l_1 can be still determined by evaluating l_1 related to each value of l_2 accoding to $l_1 = f^{-1}(l_2)$. The calculation of the LLR of the incorrect LLR l_2 resulting in $l_2' = L(l_2)$ is identical to the value calculated according to the inverse function f^{-1} of l_2. Until the incorrect LLR is recovered according to $l_2' = f(l_2)$, the consistency condition can not be satisfied, suggesting $l_2' = l_1 = L(r)$ is the correct value of the LLR of r.

2.7 Summary

The CDMA techniques designed for supporting multiple users have been considered. We discussed MUD families of quasi-orthogonal codes, namely m-sequences having a length of 7 chips and Gold codes associated with a length of 31 chips. In Section 2.3, we demonstrated that the optimal detection algorithm in a single-user system is the MF algorithm.

The most well-known linear MUD algorithms, such as the ZF and MMSE algorithms were discussed in Section 2.4. Equation was used for quantifying the likelihood of each legitimate K-element vector, which we referred to as the ML algorithm's objective function in order to locate the most likely K-element vector, with the aid of exhaustive search. The objective function employed by the ML algorithm, which is also known as the Log-Likelihood Function (LLF) of a certain legitimate K-element vector $\dot{\mathbf{v}}$ was derived in Section 2.4.4 from the Euclidean distance between the legitimate noise-free received signal vector and the vector actually received during the symbol duration, given $\dot{\mathbf{v}}$ is transmitted.

The LLF of a certain legitimate K-element vector $\dot{\mathbf{v}}$ is employed as the OF by the ACO-based MUD algorithm. The ACO-based MUD algorithm will be introduced in Chapter 3 is capable of converging to the same K-element vector solution as the one located by the ML algorithm with the aid of exhaustive search, but ML-solution is found with a high probability at a significantly reduced complexity. The artificial ants will commence their journey from the MF solution, gradually maneuvering their way through visiting a limited number of vectors, and with the aid of the ACO principle finally converge to the ML solution. Therefore only a limited number of vectors' LLF has to be evaluated, as compared to the ML algorithm, which evaluated the LLF of all the 2^K legitimate K-element vectors. Hence the complexity imposed by the exhaustive search employed by the ML algorithm is significantly decreased.

In Sections 2.6.3 and 2.6.4, we demonstrated that the consistency condition may be employed to assess the accuracy of the LLRs and to recover the accurate LLR from the inaccurate LLRs, provided it was generated by linear distrotion.

The optimal Bayesian SO-MUD algorithm evaluates the exponential of the Euclidean distances associated with all the 2^K legitimate K-element vector-values to generate the LLR associated with a single bit. By contrast, the ACO-based soft-output MUD algorithm will find a limited number of dominant vectors, which constitute the primary contributors of the final LLR values.

As seen from Table 2.11, except for the ACO-based HO- or SO-MUD algorithms, all the other HO-SUD or HO/SO-MUD algorithms listed in Table 2.11 have been sufficiently reviewed in this chapter.

1. MF SUD algorithm

As seen from Table 2.11, since the MF constitutes a single-user receiver, the MU system employing the MF algorithm has an inferior BER performance compared with the ones employing the other MUD algorithms listed in the table. Naturally, the single-user MF has however the lowest complexity, which is independent of the number of users K.

2. ZF and MMSE MUD algorithms

As seen from Table. 2.11, since the size of the $(K \times K)$-element matrix $\mathbf{R}$ increases linearly with K, the complexity of the ZF and the MMSE algorithm may be deemed proportional to the cube of K owing to the evaluation of the matrix inverse of $\mathbf{R}$. As a benefit of this cubically increasing complexity, the BER performance in comparison to the MF SUD.

3. ML algorithm

In contrast to the suboptimal ZF and the MMSE MUD algorithms, the complexity imposed by the ML algorithm is generated in terms of how many times the Objective Function (OF) has to be evaluated. The specific complexity of evaluating the OF once is different for the different system

	$\mathbf{A}_k$	$\mathbf{R}$	$\mathbf{n}$			Turbo	BER	per-user complexity	Chapter
			σ_n^2	LLF	EUC				
MF	√						worst	constant	
ZF	√	√					medium	$\mathcal{O}(K^3)$	
MMSE	√	√	√				medium$^+$	$\mathcal{O}(K^3)$	
ML	√	√		√			optimal	$\mathcal{O}(2^K)$	
HO ACO	√	√		√			optimal	$\mathcal{O}(K^2)$	3, 4, 5
Bayesian	√	√	√		√		optimal	$\mathcal{O}(2^K)$	
SO ACO	√	√	√	√	√		optimal	$\mathcal{O}(K^2)$	6
Bayesian	√	√	√		√	√	optimal	$\mathcal{O}(2^K)$	
SO ACO	√	√	√	√	√	√	optimal	$\mathcal{O}(K^2)$	7

$\mathbf{A}_k = \mathbf{c}_k \times h_k$: the code and channel information associated with each individual user
$\mathbf{R} = \mathbf{A}^H\mathbf{A}$: the correlation of code and channel information between each two users

Table 2.11: Comparison of different Hard-Output (HO) and Soft-Output (SO) MUD algorithms in terms of the resources employed, the performance achieved and the complexity imposed, along with the number of the chapters, where the algorithm will be investigated. K denotes the total number of users supported by the MU system.

architectures considered. Naturally, the specific complexity of evaluating the OF once is determined by the size of $\mathbf{R}$. However, again the number of users is high, the complexity is dominated by the number of OF evaluations. More specifically, regardless of the specific complexity of evaluating the OF once, the complexity increases exponentially with the total number of users K. This complexity may be deemed excessive but it guarantees attaining the optimal BER performance.

4. ACO-based HO MUD algorithm

In contrast to the ML algorithm, the ACO-based HO MUD algorithm constitutes a sub-optimal solution to the MUD problem, but its complexity increases with the square rather than cube of the total number of users K. Hence the ACO-based HO MUD algorithm will be employed in the systems designed in Chapters 3, 4 and 5.

5. Bayesian SO MUD algorithm

In contrast to the exhaustive search based ML algorithm, which employs the LLF associated with a K-bit vector as the OF, the SO exhaustive search based Bayesian algorithm employs the Euclidian distance values associated all the 2^K legitimate K-bit vectors constituting the full set of K-symbol vectors. Although the Bayesian SO-MUD imposes a higher complexity than the ML HO-MUD algorithm, it enables the channel-coded MU system to achieve a further imposed BER performance at the cost of a complexity, which increases exponentially with the number of users K.

6. ACO-based SO-MUD algorithm

The ACO-based MUD algorithm is also employed as an efficient solution to the MUD problem which exploits both the knowledge of the other users' CIRs as well as their spreading codes and relies on the HO MUD's OF to select the decision candidates. It relies on an exponential function

of the Euclidean distance values invoked for evaluating the LLRs associated with all the K users. However,in contrast to the Bayesian algorithm, the ACO-based SO-MUD algorithm calculates the above-mentioned exponential function of the Euclidean distance values only for the most dominant decision candidates, hence reducing the per-user complexity imposed by the Bayesian algorithm from 2^K to the order of K^2, while achieving a similar BER performance. The detailed algorithm and the associated performance results will be presented in Chapters 6 and 7.

7. Turbo-Bayesian and ACO-based Turbo SO-MUD Algorithm

Given our iterative detection aided three-stage concatenated URC and RSC assisted system, the above-mentioned SO MUD is capable of achieving a near-capacity performance. Despite achieving a near-capacity performance, the per-user complexity imposed by the ACO-based MUD algorithm remains quadratically proportional to K, while that imposed by the Bayesian algorithm increases exponentially with the total number of users K.

Chapter 3

ACO-based MUD Algorithm

Each simple, local-decision oriented ant enables the entire ant-colony to collectively present an intelligent solution to sophisticated problems. The useful meta-heuristic behaviour of the ant-colony inspired the invention of the ant-colony optimization (ACO) algorithm [129]. In this chapter, we will outline its benefits, when applied to solving the hard-output MUD problem at a low complexity, as proposed in Section 2.4.4.

The properties of the ant-colony in the real world and their foraging behaviour is introduced in Section 3.1. The similarities between MUD as an optimization problem and the foraging behaviour of ants in nature are detailed in Section 3.2, leading to the conception of the ACO-based MUD algorithm. Following the simple five-user MUD example to be introduced in Section 3.2.2, the flow-chart of the ACO-based MUD algorithm is detailed in Section 3.3.

Each variable and their properties exploited by the ACO-based MUD algorithm are further analyzed in Section 3.4 for our five-user example. Then, following a comprehensive analysis of the ACO-based MUD algorithm, the effects of each parameter of the ACO-based MUD algorithm are discussed in Section 3.5. Finally, the ACO-based MUD algorithm is compared to another population-based, biologically-insprired optimization algorithm, i.e. the GA-based MUD algorithm.

3.1 Ant Colony and Multi-Agents

Individual ants are simple insects with limited cognition and ability to act. However, an ant colony is capable of expressing a sophisticated collective behaviour, hence providing intelligent solutions to problems, such as carrying large items, forming bridges and finding the shortest routes from the anthill to the source of food. Below we will introduce the properties of ants in the real world and study the ant-colony's foraging behaviour.

3.1.1 Properties of the ant-colony

A single ant has no global knowledge about the task it is performing. The ant's actions are based on local decisions and are usually unpredictable. The above-mentioned intelligent joint action emerges as a consequence of the self-organization and indirect communication between the ants.

More specificially, the following properties of the ant-colony enable them to carry out complicated tasks:

- Most ants have poor-to-mediocre eyesight and some species are completely blind. Moreover, they are endowed with two sensors on their heads to detect chemicals;
- Ants communicate with each other using 'pheromones', which is a hormone produced by them. The paired sensors provide information about the direction and intensity of scents;
- An isolated ant moves randomly, but when it finds a pheromone trail, there is a high probability that this ant will follow the pheromone trail and this probability is propotional to the associated pheromone density;
- However, there is also a probability that the ant will receive a 'perturbation' from the environment, diverting them from the direction of pheromone;
- Over time, however, the pheromone starts to evaporate, thus reducing its ability to attract or constrain the ants.

The above-mentioned biological instincts of the individual ants enables the entire ant-colony to find the shortest route connecting the anthill to the source of food.

3.1.2 Foraging behaviour of the ant-colony

Below, we will frequently utilize the 'shortest' route terminology in the context of both the 'globally shortest' route and the 'locally shortest' route. These terms will then evolve to those of the 'globally optimal' or 'locally optimal' K-bit vector in terms of the MUD solution.

Nevertheless, in both cases, 'globally shortest' route means the shortest route among all the possible candidate routes connecting the anthill and the source of food. This route may or may not appear in the initial search-pool of the first round of search for routes carried out by the ant-colony. However, as illustrated in Section 3.1.2.2, the 'globally shortest' route will eventually be found.

By contrast, the 'locally shortest' route refers to the best solution among all the routes that have been found so far or among all the routes have been found recently, which have a certain amount of pheromone, despite its tendency to evaporate. Before the 'globally shortest' route has been found, the 'locally shortest' route may be viewed as an intermediate solution, which will gradually evolve towards the globally shortest route throughout a successful search.

For example, the 'globally shortest' route refers to the central route in Fig. 3.2(e)∼(g), and equivalently, to the right-most route in Fig. 3.2(d). By contrast, the 'locally shortest' route, say during the first search round illustrated in Fig. 3.2(a), refers to the right-most route, which is not necessarily the 'globally shortest' route illustratred in Fig. 3.2(d)∼(g). We commence by interpreting the rationale behind the ant-colony's foraging behaviour from a real-life experiment, representing the simplest scenario of the environment encompassing an anthill and the source of food.

3.1.2.1 Double-bridge experiment

Fig. 3.1 portrays the stylized process of the ant-colony's tendency to converge to the shorter route betweeen the anthill and the source of food in our experiment. As seen from Fig. 3.1(a), there are only two allowed routes from the anthill to the source of food.

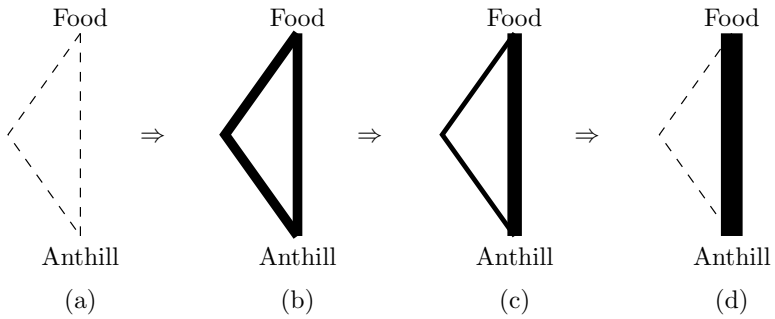

Figure 3.1: Sketch illustrating the 'double-bridge experiment', carried out by biologists to study the foraging behaviour of the ant-colony.

Initially, no pheromone is deposited in the environment, hence each ant will randomly choose either of the two bridges of Fig. 3.1 as its path. Thus, among the first group of ants setting out from the anthill, potentially half of the group may be found on both of the two bridges, as shown in Fig. 3.1(b).

Additionally, each ant will return to the anthill after it reaches the source of food by its original route. Naturally, less time will be required by the ant for a round-trip between the anthill and the source of food if it takes the shorter route. Thus the ants taking the shorter bridge will return earlier than the others. Hence the shorter bridge will have a higher pheromone density than the longer bridge, especially near the anthill. During the specific interval when half of the ants arrived back to the anthill from the shorter route, while none from the longer one, an ant just emerging from the anthill is more likely to choose the shorter bridge, since this has a higher pheromone density near the anthill. Hence, from now on, a higher portion of ants will choose the shorter bridge. As a result, a higher amount of pheromone is deposited on the shorter bridge, as shown in Fig. 3.1(c).

Clearly, a gradually increasing portion of ants will choose the shorter bridge. As a result, increasingly more pheromone is deposited on the shorter bridge, attracting increasingly more ants. By contrast, since the pheromone evaporates as time passes, with less and less ants depositing pheromone on the longer bridge, the pheromone density on the longer bridge becomes increasingly weaker. As a result, increasingly less ants take the longer route. Finally, all the ants converge to the shorter bridge, as shown in Fig. 3.1(d).

3.1.2.2 Convergence to the shortest route

In this section, we will further elaborate on the foraging behaviour of ants highlighted in the above-mentioned double-bridge experiment by focusing our attention on a more realistic and more sophisticated scenario, as illustrated in Fig. 3.2, where the number of routes is no longer limited to two.

Let us assume that no restrictions are imposed on the routes that may be followed by the ants.

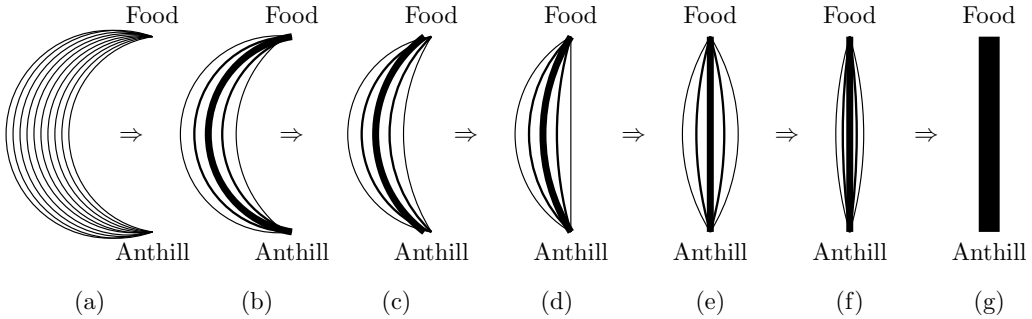

Figure 3.2: Sketch illustrating the ant-colony's convergence to the globally shortest route as part of their foraging behaviour.

Then the first group of ants setting out from the anthill may follow diverse routes, as shown in Fig. 3.2(a). As seen in the double-bridge experiment, the ants taking the shortest route will return to the anthill first. Thus the shortest route seen in Fig. 3.2 will have a higher concentration of pheromone. As a result, the next group of ants setting out from the anthill will favour the locally shortest route from the set of all routes, as observed in Fig. 3.2(a).

Therefore, more and more ants will converge to the locally shortest route appearing in Fig. 3.2(a). However, since there are no restrictions concerning the routes and any small perturbation may distract the ants, they may deviate to places which have no deposited pheromone. Thus, new routes may be created by the perturbed ants around the existing shortest route. Some of these routes are longer, but some may even be shorter than the existing shortest route, as shown in Fig. 3.2(b).

Then the pheromone trail constituting the new shortest route will attract more ants. Furthermore, as a benefit of its shortest length, more ants will come back via this shortest route within the same period of time, while depositing more pheromone than that along any other existing routes. As shown in Fig. 3.2(c) to Fig. 3.2(d), while the ants converge to the existing shortest route, new routes are also being created, until the globally shortest route is found.

While the ant-colony converges to the globally shortest route, further perturbations may still motivate the ants to follow different routes, rather than the globally shortest route. Naturally, once the globally shortest route has been found, further perturbations may only lead to longer routes, as shown in Fig. 3.2(e). Hence, convergence to the globally shortest route has been achieved. Since pheromone is a volatile steroid, the pheromone concentration around the shortest route will become weaker over time and finally all the ants will converge on the globally shortest route, as shown in Fig. 3.2(f) and Fig. 3.2(g).

3.1.2.3 Modeling the ant colony as a multi-agent system

Upon considering the family of agent-based search techniques and the foraging behaviour of ants, we readily identify the similarity between these two problems. While ants try to find the best route between two places within an environment, an agent-based graph search algorithm attempts to find the best path connecting two nodes within a graph.

The MUD problem of Chapter 2 is illustrated in Fig. 3.3, which may also be interpreted with the

aid of the ant-colony's foraging behaviour of converging to the shortest route, which may be contrasted to Fig. 3.2.

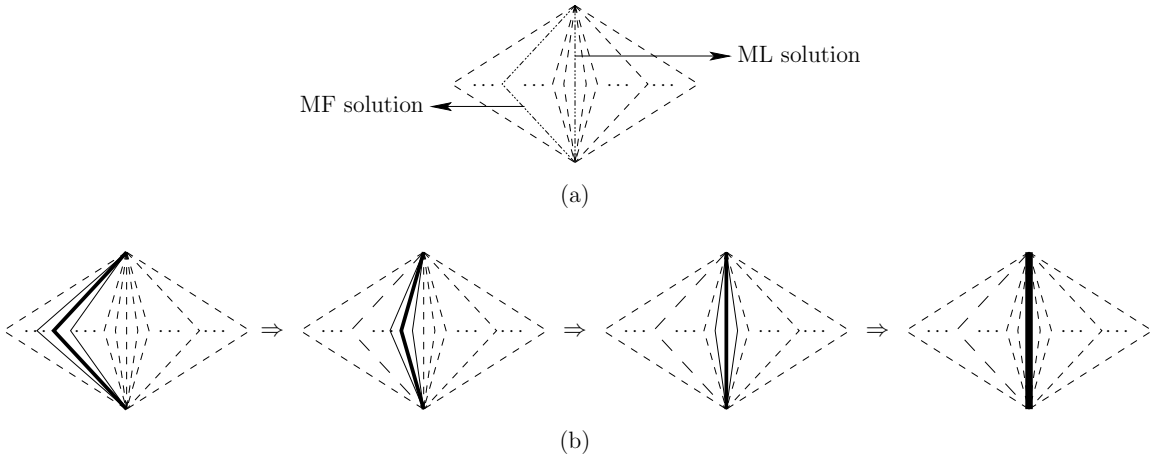

Figure 3.3: Stylized analogy between the foraging behaviour of the ant-colony and the MUD problem of Chapter 2.
(a) Relationship of the MF and ML solutions in a graph-based context;
(b) Relationship of the MUD and the 'shortest route' problems

3.2 Overview of the ACO-based MUD Algorithm

3.2.1 MUD optimization problem

The system model employed in this chapter is plotted in Fig. 3.4 for a K-user DS-CDMA UL model, which was discussed in Fig. 2.4 of Section 2.4. Recall from Section 2.4 that N_s-chip CDMA spreading

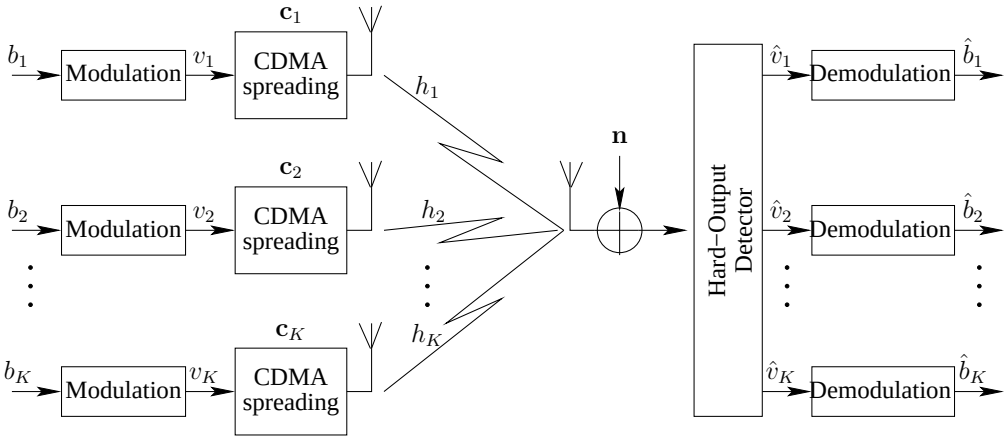

Figure 3.4: Block diagram of the multiuser system described in Section 2.4. Further refined schematics will be developed in Chapters 4 - 5.

codes are employed to support K users and the received signal vector $\mathbf{r}$ may be expressed as

$$\mathbf{r} = \mathbf{CHv} + \mathbf{n}, \tag{3.1}$$

where $\mathbf{r} = [r_1, r_2, \ldots, r_{N_s}]$ contains the complex-valued received signal during each chip-interval; $\mathbf{C} = [\mathbf{c}_1, \mathbf{c}_1, \ldots, \mathbf{c}_K]$ is the $(N_s \times K)$-element spreading code matrix, encompassing the spreading code $\mathbf{c}_k$ for each of the K users; $\mathbf{H} = \text{diag}\{[h_1, h_2, \ldots, h_K]\}$ is the diagonal CIR matrix having the CIR h_k of the kth UL user and $\mathbf{v} = [v_1, v_2, \ldots, v_K]^T$ is the transmit signal vector comprising the BPSK modulated transmit signal v_k of each user; finally $\mathbf{n}$ is the $(N_s \times 1)$-element AWGN vector corresponding to the N_s chip-intervals constituting a symbol duration. For more details regarding the interpretation of each symbol, the interested readers are referred to Section 2.4.1.

Hence the MF-output vector $\mathbf{y} = [y_1, y_2, \ldots, y_K]^T$ associated with all the K users may be formulated as

$$\begin{aligned} \mathbf{y} &= \mathbf{H}^H \mathbf{C}^T \mathbf{C} \mathbf{H} \mathbf{v} + \tilde{\mathbf{n}} \\ &= \mathbf{R}\mathbf{v} + \tilde{\mathbf{n}}, \qquad (3.2) \\ \text{with } \mathbf{R} &= \mathbf{H}^H \mathbf{C}^T \mathbf{C} \mathbf{H}, \qquad (3.3) \end{aligned}$$

where $\mathbf{R} = \mathbf{H}^H \mathbf{C}^T \mathbf{C} \mathbf{H}$ is the $(K \times K)$-element correlation matrix, with the kth diagonal element being $|h_k|^2$. Then, the K-symbol BPSK modulated MF solution $\hat{\mathbf{v}}^{\text{MF}}$ may be readily derived by evaluating the polarity of the real parts of all the element in $\mathbf{y}$, yielding

$$\hat{\mathbf{v}}^{\text{MF}} = \text{sgn}\big(\Re\{\mathbf{y}\}\big). \qquad (3.4)$$

For more details regarding the system model and the MF algorithm in the multiuser DS-CDMA UL, please refer to Section 2.4.3.1.

As detailed in Section 2.4.2, the various MUD algorithms applied in a K-user system may be formulated as an optimization problem, namely that of finding the globally optimal K-symbol vector having the highest probability to have been transmitted. Hence the 'Objective Function' (OF) of this optimization problem is related to the *a posteriori* probability of a certain K-symbol vector being transmitted. Naturally, the OF may be different in different system contexts. It is important to note that the OF of our MUD problem may be considered to be the LLF defined in Section 2.4.2, which is repeated here for convenience:

$$\mathfrak{L}(\dot{\mathbf{v}}) \triangleq 2\Re\{\dot{\mathbf{v}}^H \mathbf{y}\} - \dot{\mathbf{v}}^H \mathbf{R} \dot{\mathbf{v}}, \qquad (3.5)$$

where the $(K \times K)$-element square Hemitian matrix $\mathbf{R}$ was quantified in Eq. (3.3). Different objective functions defined for more sophisticated systems will be detailed in Chapters 4 and 5, respectively.

Hence, given the OF of Eq. (3.5), the MUD problem of the K-user DS-CDMA UL may be expressed as the maximization of the LLF of Eq. (3.5) over the full decision space $\mathbb{V}^{(K)}$ containing all the legitimate vectors $\hat{\mathbf{v}}$, which is formulated as:

$$\begin{aligned} \hat{\mathbf{v}} &= \arg \max_{\dot{\mathbf{v}} \in \mathbb{V}^{(K)}} \mathfrak{L}(\dot{\mathbf{v}}) \\ &= \arg \max_{\dot{\mathbf{v}} \in \mathbb{V}^{(K)}} \big[2\Re\{\dot{\mathbf{v}}^H \mathbf{y}\} - \dot{\mathbf{v}}^H \mathbf{R} \dot{\mathbf{v}}\big], \qquad (3.6) \end{aligned}$$

where the $(K \times K)$-element square Hermitian matrix $\mathbf{R}$ is quantified by Eq. (3.3). The ML MUD solves the optimization problem defined in Eq. (3.6) by exhaustively evaluating the OF of Eq. (3.5) over all the legitimate $K = 5$-bit vectors of the solution-space $\mathbb{V}^{(K)}$. If the signal transmitted by each

	h_k	spreading code $\mathbf{c}_k^T$	v_k	$\Re\{y_k\}$	$\hat{v}_k^{\mathrm{MF}}$	$\hat{v}_k^{\mathrm{ML}}$
$k=1$	$-1.38+1.30i$	$\delta[-1-1+1+1-1+1-1]$	-1	-3.291	-1	-1
$k=2$	$0.34-0.27i$	$\delta[-1-1-1+1+1-1+1]$	$+1$	0.030	$+1$	$+1$
$k=3$	$-0.08+0.25i$	$\delta[+1-1-1-1+1+1-1]$	-1	0.027	$+1$	-1
$k=4$	$0.08-0.21i$	$\delta[-1+1-1-1-1+1+1]$	$+1$	-0.035	-1	$+1$
$k=5$	$0.10-0.31i$	$\delta[+1-1+1-1-1-1+1]$	$+1$	-0.010	-1	$+1$
		index i in full set $\mathbb{V}^{(5)}$:	21		20	21

Table 3.1: The CIR h_k, the spreading code $\mathbf{c}_k$ and the real part $\Re\{y_k\}$ of the MF's output as well as the transmit signal v_k, the MF's detection output $\hat{v}_k^{\mathrm{MF}}$ and the ML detection output $\hat{v}_k^{\mathrm{ML}}$ for each user $k = 1, 2, \ldots, 5$ in the five-user example, which were used to generate Fig. 3.8 to Fig. 3.10. The spreading codes were m-sequences having a length of $N_{\mathrm{s}} = 7$ chips, which were weighted by the normalization factor $\delta = 1/\sqrt{7}$. It is important to mention that there are many more 7-chip m-sequences than 2^7. In our example $K = 5$ sequences were used, which were randomly selected. If those having the lowest cross-correlation are used, the achievable performance is improved.

user is BPSK modulated, the size of the search space is 2^K, which is unaffordable for large values of K.

The ACO-based MUD algorithm is dedicated to solve the optimization problem of Eq. (3.6) by gradually evolving its search-pool from the vicinity of the MF solution to the globally optimal solution, so that the ML solution can be found with a high probability, while searching through a fraction of the entire search space.

3.2.2 A $K = 5$-user example

We will now illustrate the ACO-based MUD algorithm's operation and its convergence to the $K = 5$-bit ML solution within a particular symbol duration. The associated CIRs, transmit signals and the real parts of the MF output are listed in Table 3.1 for the five-user DS-CDMA UL obeying the system model of Fig. 3.4. The complex-valued scalar $r_{n_{\mathrm{s}}}$ is the received N_{s}-chip signal during the chip-interval n_{s}.

The LLF values associated with all the $2^K = 32$ $K = 5$-bit vectors constituting the full set $\mathbb{V}^{(5)}$ for the specific CIR matrix $\mathbf{H}$, spreading-code matrix $\mathbf{C}$ and MF output real parts $\Re\{\mathbf{y}\}$ within a particular symbol duration given in Table 3.1 is provided in Table 3.2. More specifically, the LLF value of each legitimate $K = 5$-bit vector $\mathbf{v}_i^{(5)}$ listed in Table 3.2 is obtained by substituting the values of $\mathbf{C}$, $\mathbf{H}$ and $\Re\{y\}$ into Eq. (3.5) for generating Table 3.1. Observe that the $K = 5$-bit vectors listed in Table 3.2 are ranked in descending order according to their LLF values for the specific symbol duration considered. Furthermore, the MF solution and the ML solution having the highest LLF in the full set are marked in the right-most column of Table 3.2. The $K = 5$-bit vectors, generated by the ACO-based MUD algorithm during the first eight iterations are illustrated in Fig. 3.5(a). As seen from Fig. 3.5(a), the entire search-pool may be viewed as evolving from the vicinity of the $K = 5$-bit MF solution $\mathbf{v}_{20}^{(5)}$ of Table 3.2 during the 1st iteration, until incorporating the ML solution $\mathbf{v}_{21}^{(5)}$ of Table 3.2

rank	i	$\mathbf{v}_i^{(5)}$					num of errors	LLF	note
1	21	-1	$+1$	-1	$+1$	$+1$	0	3.25	$\hat{\mathbf{v}}^{\mathrm{ML}}$
2	23	-1	$+1$	-1	-1	$+1$	1	3.05	
3	17	-1	$+1$	$+1$	$+1$	$+1$	1	2.97	
4	19	-1	$+1$	$+1$	-1	$+1$	2	2.85	
5	22	-1	$+1$	-1	$+1$	-1	1	2.83	
6	24	-1	$+1$	-1	-1	-1	2	2.71	
7	18	-1	$+1$	$+1$	$+1$	-1	2	2.65	
8	20	-1	$+1$	$+1$	-1	-1	3	2.60	$\hat{\mathbf{v}}^{\mathrm{MF}}$
9	29	-1	-1	-1	$+1$	$+1$	1	2.49	
10	31	-1	-1	-1	-1	$+1$	2	2.39	
11	25	-1	-1	$+1$	$+1$	$+1$	2	2.32	
12	27	-1	-1	$+1$	-1	$+1$	3	2.29	
13	30	-1	-1	-1	$+1$	-1	2	2.20	
14	32	-1	-1	-1	-1	-1	3	2.18	
15	28	-1	-1	$+1$	-1	-1	4	2.18	
16	26	-1	-1	$+1$	$+1$	-1	3	2.13	
17	12	$+1$	-1	$+1$	-1	-1	5	-9.74	
18	10	$+1$	-1	$+1$	$+1$	-1	4	-10.22	
19	16	$+1$	-1	-1	-1	-1	4	-10.24	
20	11	$+1$	-1	$+1$	-1	$+1$	4	-10.25	
21	4	$+1$	$+1$	$+1$	-1	-1	4	-10.26	
22	3	$+1$	$+1$	$+1$	-1	$+1$	4	-10.63	
23	9	$+1$	-1	$+1$	$+1$	$+1$	3	-10.65	
24	2	$+1$	$+1$	$+1$	$+1$	-1	3	-10.65	
25	15	$+1$	-1	-1	-1	$+1$	3	-10.65	
26	8	$+1$	$+1$	-1	-1	-1	3	-10.65	
27	14	$+1$	-1	-1	$+1$	-1	3	-10.66	
28	7	$+1$	$+1$	-1	-1	$+1$	2	-10.92	
29	1	$+1$	$+1$	$+1$	$+1$	$+1$	2	-10.94	
30	6	$+1$	$+1$	-1	$+1$	-1	2	-10.97	
31	13	$+1$	-1	-1	$+1$	$+1$	2	-10.98	
32	5	$+1$	$+1$	-1	$+1$	$+1$	1	-11.16	

Table 3.2: All the 32 legitimate vectors in the full set $\mathbb{V}^{(5)}$ ranked by the LLF value under the system parameters given in Table 3.1.

for the first time during the 4th iteration and then gradually converging to the $K = 5$-bit ML solution. The entire search-pool shifts its centre of gravity from the $K = 5$-bit MF solution of $\mathbf{v}_{20}^{(5)}$ surrounded

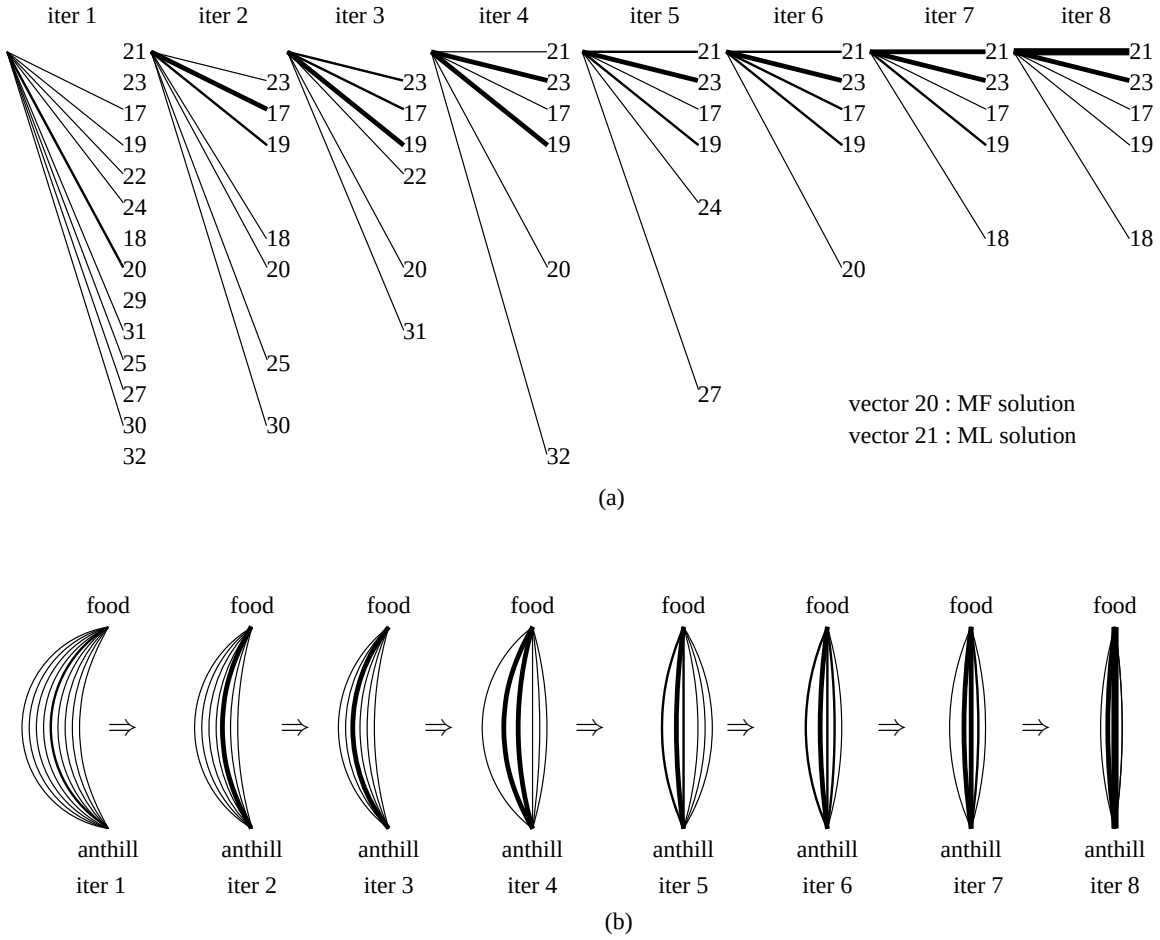

Figure 3.5: (a) The vector-values of all the 10 vectors constituting the search-pool during the 1st to the 8th iteration of the five-user example. The system parameters for the five-user example are listed in Table 3.1. The width of the line quantifies the number of vectors taking the corresponding vector-value, whose index in the full set is listed at the right side of the line's ending point, during the specific iteration. The vector-values, whose indeces are listed at the right side of the subplot during each iteration, are ranked in descending order of their LLF values from top to bottom. The ACO-based MUD search process of the first nine iterations are plotted in Fig. 3.10.
(b) The corresponding 10 vectors having different LLFs plotted in (a) are represented as the 10 routes having different lengths and connecting the anthill to the source of food during the eight iterations.

by a group of inferior vectors having low LLF vlaues, in the direction of superior $K = 5$-bit vectors associated with higher LLF values. Once the globally optimal $K = 5$-bit vector having the highest LLF value was found, the iterations begin to converge to it. The ant-colony's behaviour in nature is depicted in Fig. 3.5(b) for comparison with the MUD's search-pool depicted in Fig. 3.5(a).

3.2.3 ACO model emulating the action of the MUD

As mentioned in Section 3.1, as long as the optimization problem considered may be formulated as that of finding the optimal path in a graph, the ACO algorithm can be invoked to provide a solution.

1. Similarities between the action of the MUD and the ants' foraging behaviour

As mentioned in Section 3.2.1, the ACO-based MUD algorithm endeavours to solve the optimization problem defined by Eq. (3.6) without exhaustively searching through the entire 2^K-element solution-space constituted by the independent variable of the objective function. Hence the key point in solving an optimization problem with the aid of an ACO-based algorithm is to find a way of representing both the global optimum of the optimization problem as well as all the legitimate candidates for the globally optimal solutions in a graph.

In the context of the BPSK modulation scheme employed by each of the K users, there are two legitimate binary symbol-values for each user, as indicated by the $(2\times K)$-element table-like illustration at the top of Fig. 3.6, namely in Fig. 3.6(a) for the specific example of $K = 5$. Then each of the 2^K candidates for the global K-bit optimum may be uniquely represented by one of the 2^K routes passing through the route-table of Fig. 3.6(a), proceeding from left to right, which includes a single cell of each column, comprising a binary 0 or 1.

As indicated by Eq. (3.6), the goal of the optimum MUD is to find the K-bit ML solution having the highest LLF value. In order to minimize the search complexity imposed, the initial routes of the optimization procedure are determined by the K outputs of the simplest SUD, namely by the K normalized MF outputs, rather than by random binary vector-elements. For example, in the absence of any channel impairments the maximum output of the 7-chip hard-decision-based correlator is 7, which is then normalized to unity.

The similarities between the MUD problem and the process of finding the shortest route to the source of food relying on the ants' foraging behaviour allow us to employ the ACO search algorithm in order to find the K-bit ML solution. The corresponding analogies are summarized in Table 3.3. The

OPTIMIZATION	NATURE	MUD
SEARCH-POOL	routes	vector-elements
CRITERION	short length	high LLF
INITIAL SEARCH-POOL	random routes	MF-based vector-elements
GLOBAL OPTIMUM SOLUTION	shortest route	ML solution
SEARCH DRIVERS	pheromone and perturbation	pheromone and intrinsic affinity

Table 3.3: Comparison between characters of ant-colony algorithm used to saerch for the optimal route between anthill and source of food and to search for the optimal K-user MUD solution during any symbol duration under a certain system scenario.

terminology 'intrinsic affinity' with respect to a specific logical value of 0 or 1, which was introduced in Table 3.3 is a 'static' quantity characterizing each cell of the route table in Fig. 3.6(a), which is derived from the 7-chip MF outputs' real parts according to the BPSK demodulator considered and hence remains unchanged throughout the search. The static intrinsic affinity may be contrasted to the dynamically updated pheromone, which is adjusted proportionally to the LLF values of the K-bit solution candidates in the search-pool during the latest iteration.

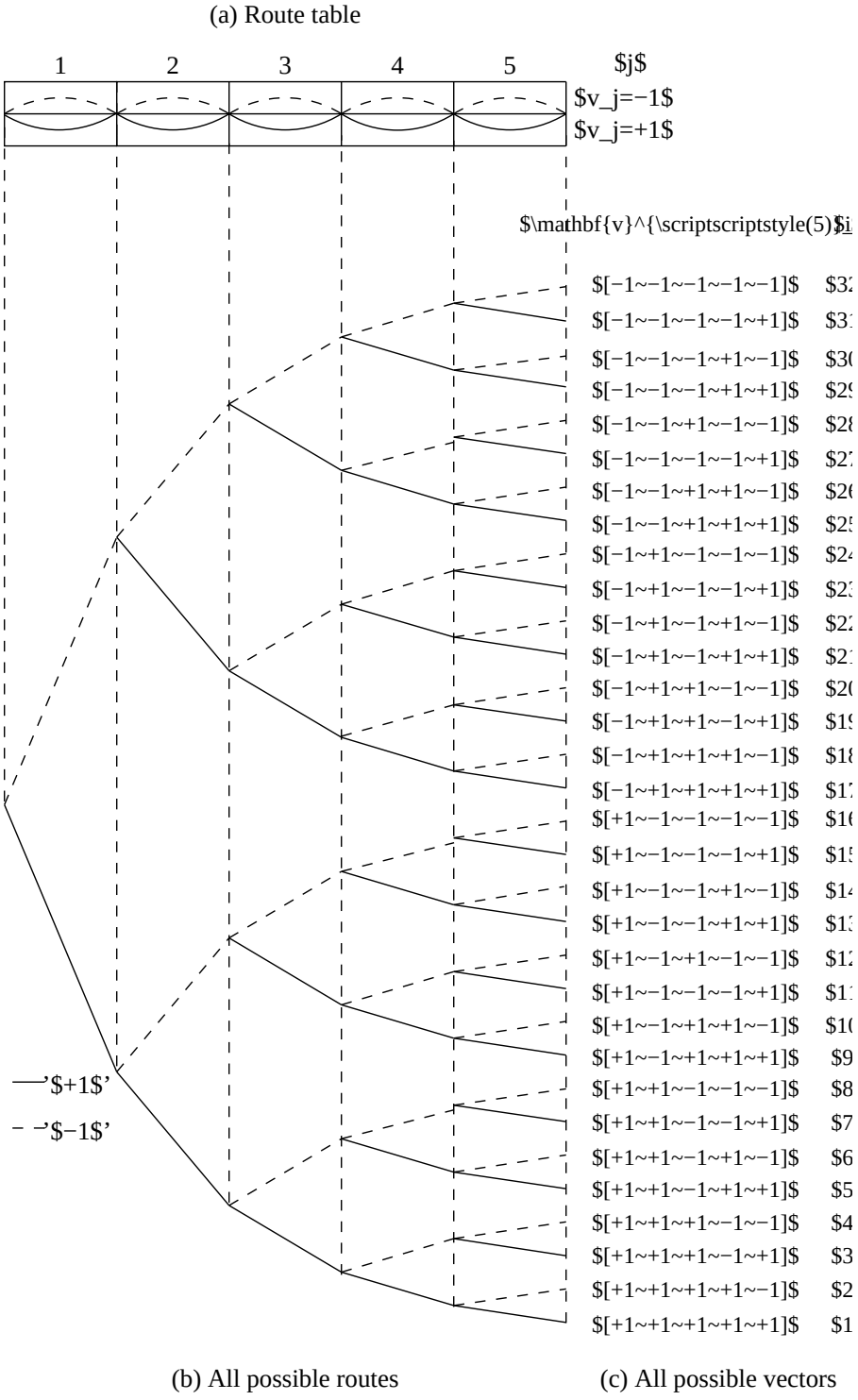

Figure 3.6: Unique mapping between all the possible routes and all the legitimate $K = 5$-bit BPSK vectors constituting the full set $\mathbb{V}^{(5)}$.

2. Overview of the optimization procedure

Below, we will briefly describe the entire search process carried out by the ACO-based MUD algorithm with the aim of finding the K-bit ML solution. Again, each of the $2K$ cells of Fig. 3.6(a) constituting the route-table uniquely corresponds to one of the $2K$ legitimate BPSK symbol-values. The symbol-value probability associated with each cell of Fig. 3.6(a) will uniquely correspond to the

probability of that particular binary symbol-value being chosen by the artificial ants. During any search iteration, there will be a K-bit vector, which is given by connecting the specific K cells of Fig. 3.6(a) that have the higher probability of the two within each of the K columns. Naturally, the resultant K-bit vector is not necessarily the most likely K-bit sequence, it rather contains the more likely bit value in each of the K-bit positions. It may be expected that the K-bit vectors constituting the search-pool will be scattered or centered around this vector. The specific K-bit vector having the highest LLF at any stage i.e. iteration of the search process is often referred to as the 'elite' vector.

Then, as we discussed in the context of Fig. 3.5(a), the K-bit symbol probabilities are updated upon progressing from iteration $I = 1$ to $I = 2$, and so on. Again, at iteration $I = 4$ the 'would-be' K-bit ML vector $\mathbf{v}_{21}^{(5)}$ appears in the pool. Observe in Fig. 3.5(a) that from this iteration onwards the vectors found in the search-pool continue to converge towards the K-bit ML solution $\mathbf{v}_{21}^{(5)}$. Convergence to the ML solution is deemed to have been approached, once all the binary symbol-values constituting the ML solution have reached a probability close to unity, as observed in Fig. 3.5(a).

The flow chart of the ACO-based MUD algorithm will be detailed at a later stage in Fig. 3.9, which is then further augmented with the aid of Fig. 3.10. Let us, however, continue by first providing a more specific interpretation of the route-table and of the modulation constellation diagram.

3. Terminology interpretation

1. Route-table

The $(2 \times K)$-element route-table of Fig. 3.6(a) comprises all the $2K$ possible BPSK symbol-values for the K-symbol solution. More specifically, the (i, k)th cell in the route-table of Fig. 3.6(a) in the ith row and kth column represents the ith legitimate symbol-value for v_k. For our BPSK scenario we may set $v_k = -1$ for $i = 1$ and $v_k = +1$ for $i = 2$. Hence, the two cells constituting the kth column of the route-table of Fig. 3.6(a) can be alternatively represented as the $(\pm, k)$th cell.

We define any legitimate K-bit vector, such as for example '$[-1, +1, -1, +1, -1]$', as a route passing through the route-table of Fig. 3.6(a) from left to right. Given $\dot{\mathbf{v}}^{(5)} = [-1, +1, -1, +1, -1]$, the corresponding route may be uniquely identified by concatenating the elements having the indexes of $(1, 1)$, $(2, 1)$, $(1, 3)$, $(2, 4)$ and $(1, 5)$ in the route-table of Fig. 3.6(a). Then, each of the 2^K legitimate K-symbol vectors constituting the full vector-set $\mathbf{V}^{(5)}$ may be uniquely mapped to one of the 2^K possible ways of passing through the route-table from left to right. All the $2^K = 2^5$ possible routes passing through the $K = 5$-symbol route-table are illustrated in Fig. 3.6(b), with the vector and its index in the full set $\mathbb{V}^{(5)}$ listed at the right.

The route-table of Fig. 3.6(a) has allows us to simplify the MUD algorithm, because we will demonstrate that it is sufficient to evaluate $2K$ rather than 2^K candidates. More explicitly, the ML MUD algorithm's complexity increases exponentially with K, while that of the ACO-based MUD increases only linearly with the dimension of the problem, i.e. with the number of users K.

2. Received signal constellation diagram

For every legitimate K-symbol vector $\dot{\mathbf{v}} = [\ \dot{v}_1,\ \dot{v}_2,\ \ldots,\ \dot{v}_K]$ transmitted during the n_sth chip-interval associated with $n_s = 1, 2, \ldots, N_s$, there will be a unique complex-valued scalar $\dot{r}_{n_s}$ representing the received signal, given $\mathbf{C}$, $\mathbf{H}$ defined for the specific symbol-duration considered, which can be formulated in the absence of noise as the superposition of the channel-faded and spread transmitted

symbols:

$$\dot{r}_{n_s} = \sum_{k=1}^{K} c_{kn_s} h_k \dot{v}_k, \tag{3.7}$$

where $\dot{r}_{n_s}$ may be referred to as the legitimate signal received during the n_sth chip, $n_s = 1, \ldots, N_s$ corresponding to the legitimate signal vector $\dot{\mathbf{v}}$ transmitted during the chip interval n_s. More specifically, for each legitimate K-bit transmitted signal vector $\mathbf{v}_i^{(K)} \in \mathbb{V}^{(K)}$, there will be a unique complex value corresponding to the legitimate received chip-signal $\dot{r}_{i,n_s}$, $n_s = 1, \ldots, N_s$, given that $\mathbf{v}_i^{(K)}$ was transmitted during the chip-interval n_s. Each of the 2^K complex-valued legitimate chip-related signals received during any chip-interval $n_s = 1, \ldots, N_s$, can be assigned to a specific point on the complex plane. The complex plane containing all the 2^K noise-free received signal-points during the chip interval n_s, $n_s = 1, \ldots, N_s$ is also often referred to as the received signal constellation diagram.

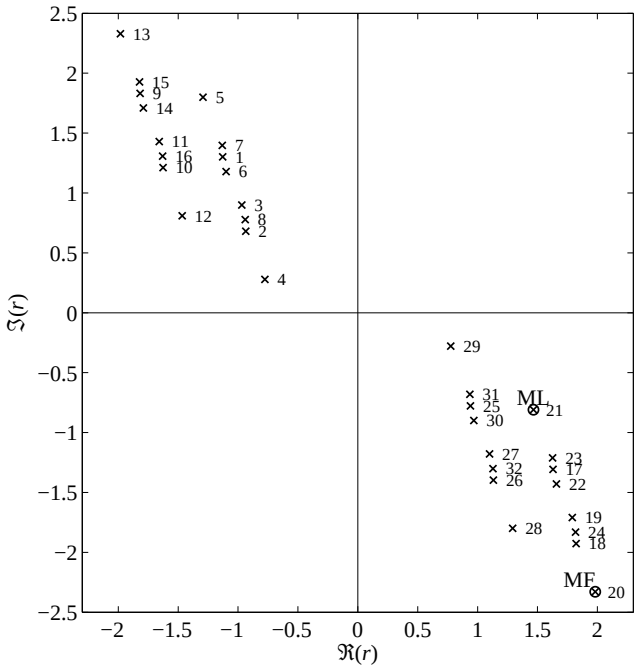

Figure 3.7: The constellation diagram constituted by all the thirty-two legitimate noise-free signals received in the $K = 5$-user DS-CDMA UL during the 4th chip-interval of the 7-chip spreading sequence plotted on the complex plane. The CIR coefficients and the spreading codes used to generate this constellation diagram are given in Table 3.1.

Therefore, given the system parameters of Table 3.1 and a certain chip-interval index n_s, each of the thirty-two legitimate transmit vector-values in $\mathbb{V}^{(5)}$ may be uniquely represented by a point plotted on the complex plane, as shown in Fig. 3.7 for the $n_s = 4$th chip of the spreading codes of Table 3.1.

It may be worth emphasizing that for all the N_s chip-intervals constituting a BPSK symbol-duration the K-bit transmitted signal-vector $\dot{\mathbf{v}}$ (or $\dot{\mathbf{v}}_i$) is fixed and the elements of the CIR matrix $\mathbf{H}$ are also assumed to have constant values. The sole variable in Eq. (3.7) as a function of the chip-interval index is the chip-value of the spreading code assigned to the different chips, i.e. $c_{k,n_s} \in \delta \cdot \{+1, -1\}$. The absolute value of $|c_{k,n_s}|$ is identical for all possible values of k and n_s. It is only the polarity of $\text{sgn}(c_{k,n_s})$ that differs, when the value of k or n_s changes.

The n_sth chip of the K different spreading codes assigned to each of the K users can be hosted by the K-element row vector $\mathbf{c}^{(n_s)} = [c_{1,n_s}, c_{2,n_s}, \ldots, c_{K,n_s}]$. Hence, during the n_{s1}st and the n_{s2}nd chip-interval, both $\mathbf{v}_{i_1}$ and $\mathbf{v}_{i_2}$ will result in the same legitimate received signal, as long as the 'element-product' of $\mathbf{v}_{i_1} \odot \mathbf{c}^{(n_{s1})}$ and $\mathbf{v}_{i_2} \odot \mathbf{c}^{(n_{s2})}$ will result in the equivalent vector-values of $[v_{i_1,1}c_{1,n_{s1}}, v_{i_1,2}c_{2,n_{s1}}, \ldots, v_{i_1,K}c_{K,n_{s1}}]$ and $[v_{i_2,1}c_{1,n_{s2}}, v_{i_2,2}c_{2,n_{s2}}, \ldots, v_{i_2,K}c_{K,n_{s2}}]$. The above-mentioned 'element-product' operation of $\mathbf{a} \odot \mathbf{b}$ is defined as the product of the vectors $\mathbf{a}$ and $\mathbf{b}$ having the same length on an element-by-element basis. More specifically, given $\mathbf{a} = [a_1, a_2, \ldots, a_N]$ and $\mathbf{b} = [b_1, b_2, \ldots, b_N]$, we have

$$\mathbf{a} \odot \mathbf{b} = [a_1 b_1 \quad a_2 b_2 \quad \ldots \quad a_N b_N]. \tag{3.8}$$

ACO Parameter	Value
Initial pheromone	$\tau = 0.01$
Evaporation rate	$\rho = 0.5$
Number of ants	$\zeta = 10$
Number of iterations	$\Xi = 10$
Weight of pheromone	$\alpha = 0.9$
Weight of intrinsic affinity	$\beta = 6$
Weight for the elite ant	$\sigma = 8$

Table 3.4: Parameters of the ACO-based MUD algorithm applied in our $K = 5$-user example.

The additional parameters used by the ACO-based MUD algorithm to generate Fig. 3.5, Fig. 3.8, Fig. 3.13(b) and Fig. 3.10 are listed in Table 3.4.

3.3 Flow chart of the ACO-based MUD Algorithm

During each search iteration constituting the search process carried out within any symbol-duration, the probability of each of the 2^K legitimate K-bit vectors included in the search-pool can be predicted before the search is initiated, which will be consistently referred to as the K-bit vector probability'. To clarify our terminology further, there are $2K$ symbol-value probabilities corresponding to the $2K$ legitimate symbol-values of the K users and 2^K K-bit vector probabilities corresponding to the 2^K legitimate vectors during each search iteration. As shown in Fig. 3.8 in the specific example considered, there are sixteen K-bit vectors having non-zero predicted probabilities, which hence appear in the search-pool during all the search iterations, where the probabilities are indicated by the bars. Fig. 3.8 may also be extended to include all the thirty-two legitimate vectors, however, since the predicted probability of the other sixteen $K = 5$-bit vectors to have been transmitted is zero, there is no need to include them in this simplified example. The sixteen $K = 5$-bit vectors included in Fig. 3.8 all have positive LLF values, while the other sixteen vector-values have negative LLF values, as shown in Table 3.1.

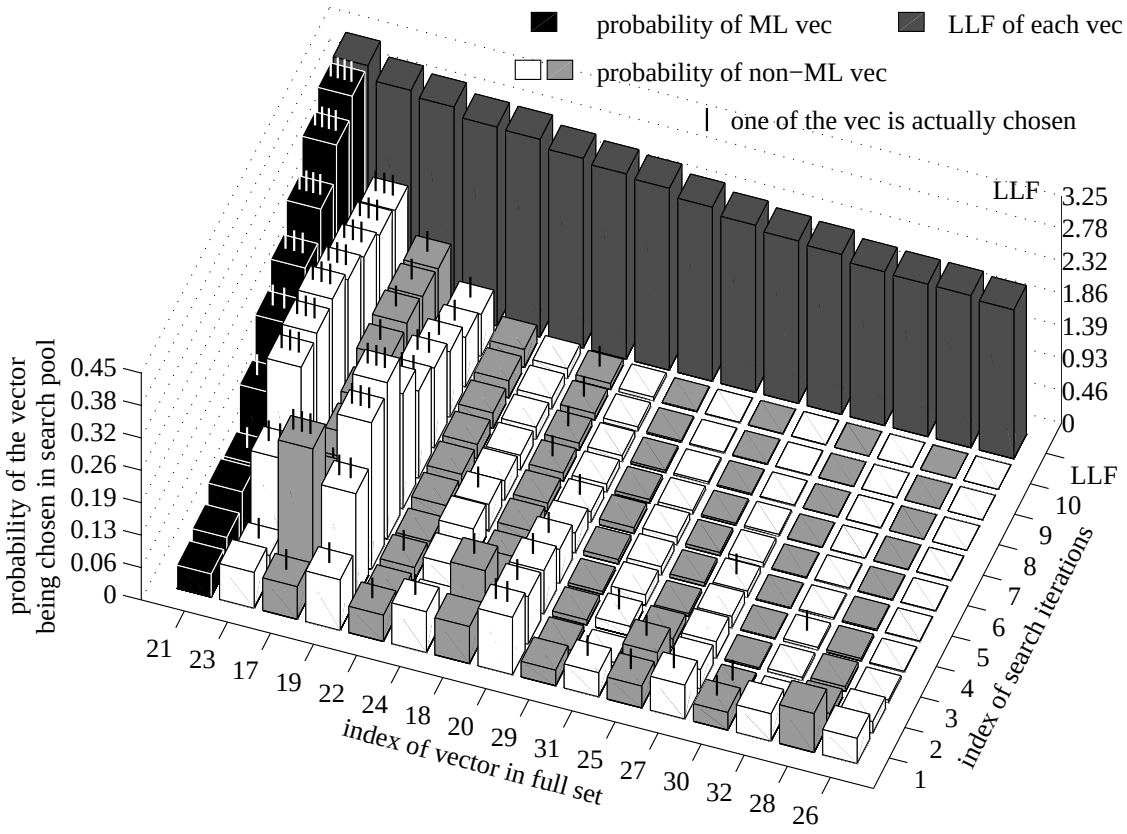

Figure 3.8: LLFs and probabilities of the 16 vectors in the full set $\mathbb{V}^{(5)}$ having higher-than-zero probabilities of being included in the search-pool of the ACO-aided MUD from the first to the tenth search iteration. The vectors during each iteration are ranked in a descending order according to their LLF value. All the ACO parameters are defined in Table 3.1. The specific vectors actually chosen for inclusion in the search-pool on the basis of the route-table of Fig. 3.6(a) followed by the artificial ants during each search iteration are indicated by the thin black or white bars on top of the hollow or shaded thick bars representing the probability of each vector being chosen during each specific iteration. The black bars at the left of Fig. 3.8 represent the probabilities of the ML vector having the highest LLF of '3.25', which was hence included in the search-pool during each iteration. By contrast, the white and light-grey bars represent the probabilities of the other vectors being chosen in the search-pool during each iteration. The simple reason for alternatively using two different colors is merely to more visibly separate the bars associated with different vectors.

The $K = 5$-bit vectors included in the search-pool during the $I = 10$ iterations portrayed are also indicated with the aid of black or white bars in Fig. 3.8. The K-bit vectors included in the initial search-pool are constructed from the specific binary symbols gleaned from the MF's outputs at the commencement of iterations and are then later updated by the ACO algorithm. We note again at this stage that the actual probability of each K-bit vector in the search-pool will deviate from the probability calculated as the product of the K bit probabilities, as we will demonstrate in Secion 3.4.6.2.

As seen from Fig. 3.8, both the predicted as well as the actual probability of the optimal K-bit vector-value $\mathbf{v}_{21}^{(5)}$, which is the ML solution having the highest LLF value, is consistently increased as the search process progresses. The flow-chart of the ACO-based MUD algorithm employed for

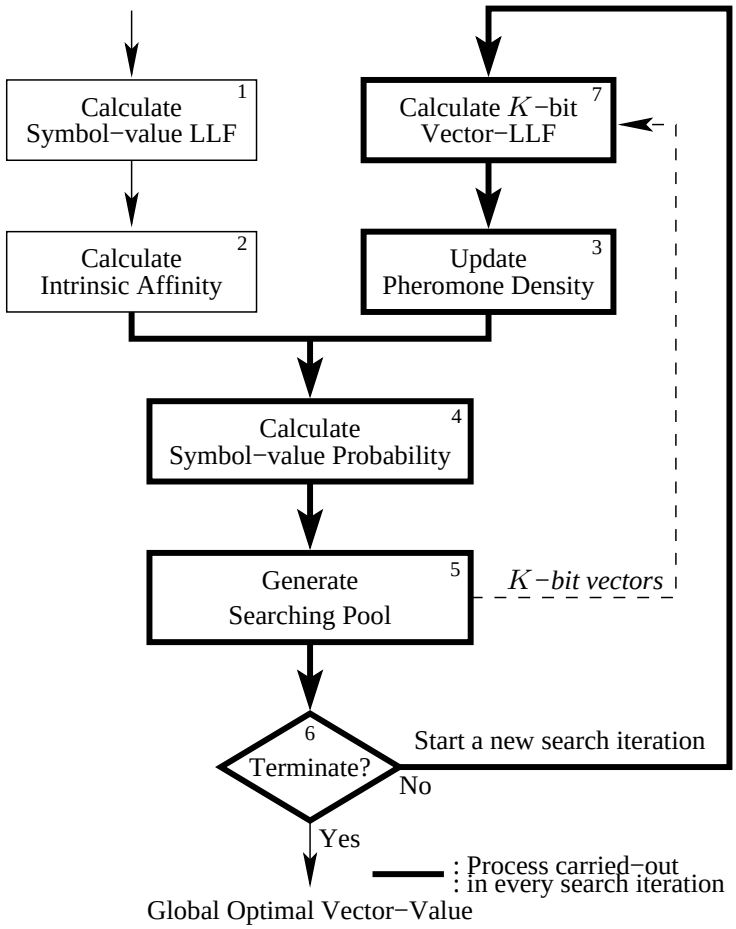

Figure 3.9: Flow-chart of the ACO-based MUD algorithm, which is carried out to detect the K-bit vector transmitted by the K users during every bit-interval.

generating Fig. 3.8 is depicted in Fig. 3.9.

The intrinsic affinity calculation of Step 2 displayed in Fig. 3.9 for our $K = 5$-user example is illustrated in Fig. 3.13(a). The steps drawn in bold lines in Fig. 3.9 are carried out during each search iteration, as detailed in depth in Fig. 3.10. Before we delve into discussing the intricate details of Fig. 3.10, let us briefly explore it structure. Firstly, subfigures a, b, c,..., i, represent the first nine iterations also featured in Fig. 3.8. Secondly, each of the nine subfigures a, b, c,..., i is constituted by three parts, namely Parts I, II and III at the upper-left, lower-left and right of the subfigures. Parts I and II characterize the evaluation of the route-table contents, while Part III that of the K-bit vector probabilities. More specifically, the pheromone density update of Step 3 is explicitly indicated by the height of the grey bars, which is carried out during each ACO iteration and it is depicted in Fig. 3.10(a)∼(i)(I). This illustration may be viewed as a further evolved 3D version of the route-table in Fig. 3.6. Furthermore, the numbers represented with an accuracy of two decimal points on top of each bar represents the symbol probability calculated in Step 4 of Fig. 3.9. The search-pool generated in Step 5 is illustrated by the different routes seen in Fig. 3.10(a)∼(i) Part (II), where the thickest line indicates the most likely route. In order to illustrate the search-pool's convergence to the ML solution from different perspectives, Fig. 3.10(a)∼(i) Part (III) portrays the K-bit vector probabilities calculated from the numbers quantifying the symbol probabilities and seen on top of each bar in Fig. 3.10(a)∼(i) Part (I) as well as from the search-pool characterized in Fig. 3.10(a)∼(i) Part (II).

As seen from Fig. 3.10(a) Part (III), the K-bit vector probability peaks of the surface plotted on the complex plane are rather similar and they are scattered across the multi-user constellation space at the beginning of the iterations, and no local peak dramatically exceeds the others. The centroids of the peaks are the same K-user constellation points as those seen in Fig. 3.7 during the 4th chip interval. However, as the search process continues, more dominant global peaks have emerged from the second ACO iteration onwards. More specifically, observe in the Fig. 3.10(a)∼(i) Part (III) that for example $\mathbf{v}_{17}^{(5)}$ during the 2nd iteration, $\mathbf{v}_{19}^{(5)}$ during the 3rd iteration, $\mathbf{v}_{19}^{(5)}$ and $\mathbf{v}_{23}^{(5)}$ during the 4th iteration, $\mathbf{v}_{23}^{(5)}$ during the 5th iteration, $\mathbf{v}_{23}^{(5)}$ in the 6th iteration, $\mathbf{v}_{23}^{(5)}$ and $\mathbf{v}_{21}^{(5)}$ during the 7th iteration, $\mathbf{v}_{21}^{(5)}$ and $\mathbf{v}_{23}^{(5)}$ during the 8th iteration and $\mathbf{v}_{21}^{(5)}$ during the 9th iteration tend to have prominent peaks.

Since the symbol probability of $v_1 = +1$ is 0.00, as shown in Fig. 3.10(a) Part (I), all the sixteen $K = 5$-bit vectors associated with $v_1 = +1$ have zero probability of being included in the search-pool. Therefore, only the remaining sixteen specific $K = 5$-bit vectors beginning with $v_1 = -1$ are depicted in Fig. 3.10(a)∼(i)(III).

We will continue exemplifying the search process of the ACO-based MUD algorithm for our $K = 5$-user scenario, highlighting the properties associated with each of the $(2 \times K)$ cells constituting the $(2 \times K)$-element route-table seen in Fig. 3.6..

1. Calculate the symbol-value LLF - Step 1

Before the ACO-based search for the optimal K-bit ML vector commences, some preliminary calculations have to be carried out in order to initialize the intrinsic affinity associated with each of the $2K$ cells constituting the route-table. The intrinsic affinity is a 'single-user quantity', which is extracted without considering the existence of co-channel users. Firstly, the symbol-LLF $\mathfrak{l}(v_k = +1)$ associated with the $(2, k)$th cell of Fig. 3.6 and $\mathfrak{l}(v_k = -1)$ of the $(1, k)$th cell of Fig. 3.6 is derived for our BPSK modulation as the real part of the MF output $\Re\{y_k\}$ for the legitimate inputs $v_1^{(1)} = +1$ and $v_2^{(1)} = -1$, respectively. More explicitly, the likelihood of the two legitimate symbol values of $+1$ and -1 being transmitted by the kth user is quantified by the symbol-LLF value associated with $v_k = +1$ and $v_k = -1$, which is denoted as $\mathfrak{l}(v_k = +1)$ and $\mathfrak{l}(v_k = +1)$ or simply as $\mathfrak{l}_{2k}$ and $\mathfrak{l}_{1k}$. Alternatively, $\mathfrak{l}(v_k = \pm 1) = f(\pm 1, \Re\{y_k\})$ may be written as a function of two independent variables, which are $\Re\{y_k\}$ and $\dot{v}$, respectively. For a given user k, the real part of the MF output $\Re\{y_k\}$ is independent of the value $\dot{v}$ taken by the symbol $\hat{v}_k$. Hence for a given user k, the symbol-LLF $\mathfrak{l}_{k,\pm 1}$ solely depends on the trial value $\dot{v}$ being $+1$ or -1. The calculation of the symbol LLF $\mathfrak{l}_{ik}$, for $i = 1, 2$, $k = 1, \ldots, K$ is represented by Step 1 in the flow chart of Fig. 3.9.

2. Calculate the intrinsic affinity - Step 2

Secondly, based on the symbol LLF associated with each cell (i, k) for $i = 1, 2$, $k = 1, 2, \ldots, K$ of the route-table, the intrinsic affinity η_{ik} may be readily obtained, which reflects the difference between the two symbol LLF values of the two cells in the same column. In other words, during the difference between the two intrinsic affinities η_{1k} and η_{2k} of cells $(1, j)$ and $(2, j)$ constituting the same column k is a monotonically increasing function of the MF output's real part for user k, denoted as $\Re\{y_k\}$. This process is represented by Step 2 of Fig. 3.9. Additionally, the intrinsic affinity η_{ik} associated with the (i, k)th cell for $i = 1, 2$, $k = 1, 2, \ldots, 5$ of our $K = 5$-user example is also illustrated by the height of the bars seen in Fig. 3.13(a).

3. Set the initial pheromone - Step 3

Thirdly, the pheromone deposit τ_{ik} associated with the (i,k)th cell may be initialized as $\tau_{ik} = 0.01$ for $i = 1, 2$ and $k = 1, 2, \ldots, K$, which is then updated during Step 3 of Fig. 3.9. In other words, the initial pheromone densities associated with all the $(2 \times K)$ cells during the 1st iteration are set to 0.01, again as illustrated by the height of the corresponding bars in Fig. 3.10(a) Part (I).

4. Calculate the symbol-value LLF - Step 4

Each ACO-based iterative search process commences with calculating the symbol-probability P_{ik} of each legitimate value $\dot{v}$ of either $+1$ or -1 being transmitted by user k, for $k = 1, 2, \ldots, K$, as indicated by Step 4 of Fig. 3.9. More explicitly, P_{ik} is calculated as a ratio of the product of the pheromone density and the intrinsic affinity of the cell $(1,k)$ and $(2,k)$ cell within the kth column. The value of P_{ik} is exemplified by the decimal numbers seen on top of the bars in Part (I) throughout Figs. 3.10 (a)$\sim$(i).

5. Generate the search-pool - Step 5

The search-pool is populated on the basis of the symbol-probabilities P_{ik}. More explicitly, the formation of each of the K columns in the search-pool $\mathbf{X}$ obeys the probability P_{1k} and P_{2k}, which takes place during Step 5 of Fig. 3.9. As exemplified for our $K = 5$-user scenario in Part (II) during the 1st iteration of Fig. 3.10(a), given $P_{13} = 0.41$, $P_{23} = 0.59$, 41% of the vectors in the search-pool will have their 3rd symbol set to -1, and the remaining 59% of the vectors will have $+1$. Since the total number of vectors in the search-pool is determined by the number of ants given by $\Xi = 10$, the rounded probabilities suggest that four routes should include the cell $(1,3)$, and six routes should include the cell $(2,3)$. This is reflected in Fig. 3.10(a) Part (II).

6. Termination condition - Step 6

The optimization procedure of the ACO-based MUD designed for finding the globally optimal K-symbol vector will terminate at the n_eth iteration, if either all the ants produce the same K-symbol vector during their passage through the route-table of Fig. 3.6, or all the Ξ number of affordable ACO-based search iterations have been carried out, i.e. all ants traversed through the route-table and hence we have $n_e = \Xi$. Then the MUD's output $\hat{\mathbf{v}}$ is given by the globally optimal $K = 5$-bit vector.

7. Calculate the vector-value LLF - Step 7

If the termination condition has not been fulfilled, the search procedure will continue to Step 7 of Fig. 3.9. In order for the search-pool to incorporate K-bit vectors associated with higher LLFs in the next iteration, the pheromone density has to be updated according to the LLF values of all the K-bit vectors in the current search-pool. The reason for the LLF being chosen as the metric to evaluate the merit of each K-bit vector included in the search-pool is, because the LLF is the objective function employed by the ML MUD.

8. Update the pheromone - Step 3

The pheromone level will be updated according to the LLFs of all the K-bit vectors generated during the current search iteration in conjunction with the current level of pheromone as well as the LLF of the most 'meritorious' K-bit vector generated so far, as indicated by Step 3 of Fig. 3.9. The LLF of each of the ζ K-bit vectors constituting the search-pool will be used to update the pheromone level associated with all the K cells representing the K symbol-values constituting the vector. As shown in Fig. 3.10(b)$\sim$(i) Part (I), the pheromone level quantified by the bars seen at the top left

corner of the illustration representing each iteration is updated based on the specific fraction of the pheromone quantified by bars in the previous subfigure, also taking into account the LLFs of the previous iteration's search-pool as visualized by the line-width seen in the different routes of the previous iteration's corresponding Part (II) illustration. This is achieved with the aid of the extra amount of pheromone proportional to the LLF of the 'elite' vector as highlighted by the light-grey of the previous iteration's corresponding Part (II) subfigure.

From the above process of flow-chart of Fig. 3.9, we may draw the following conclusions.

1. Firstly, the calculation of both the intrinsic affinity and of the symbol probability as well as the construction of the search-pool may be deemed to be independent operations. In MUD parlance, the three may be deemed to be carried in a single-user mode.
2. Secondly, the pheromone level associated with each bit constituting a specific K-symbol vector in the search-pool is determined by the likelihood of this specific vector being transmitted.
3. Based on the observations 1 and 2 above, the ACO-aided MUD algorithm invokes the MF algorithm to initialize all the parameter values of the ACO-based search process and then gradually updates them with the aid of the additional information provided by all the remaining $(K-1)$ users.

3.4 Detailed Description of the ACO-based MUD Algorithm

In this section, all the key variables characterizing the ACO-based MUD algorithm listed in Table 3.5 will be defined and further detailed.

3.4.1 Logarithmic Likelihood Function of the Symbols

For A BPSK system, the LLF $\mathfrak{l}_{ik}$ of the symbol-value associated with cell (i,k) is simply determined by the real part of the MF output $\Re\{y_k\}$ of the kth user and the trial symbol-value ± 1. Given the uplink model of the multi-user system seen in Fig. 3.4 and that the DS CDMA spreading sequences have a length of N_s, the signal vector $\mathbf{r}$ received during the N_s chip intervals of the spreading sequence is quantified by Eq. (3.1). The LLF $\mathfrak{l}_k(\hat{v}_k = \pm 1) \equiv \mathfrak{l}_k(\pm 1)$ of a symbol-value of either $+1$ or -1 being transmitted by the kth user under the simplest K-user DS-CDMA UL model may be expressed as

$$\begin{aligned} \mathfrak{l}_k(\pm 1) &= \pm 2\Re\{y_k\} - R_{kk} \\ &= \pm 2\Re\{y_k\} - h_k^T \mathbf{c}_k^T \mathbf{c}_k h_k \\ &= \pm 2\Re\{y_k\} - |h_k|^2, \qquad k = 1, \ldots, K. \end{aligned} \tag{3.9}$$

Since a unique mapping was specified in Fig. 3.6 between the pair of cells constituting the kth column of the route-table and the pair of legitimate BPSK symbol-values that may be transmitted by the kth user, we have

$$\begin{aligned} i = 1 &\Leftrightarrow \ \mathfrak{l}_{1k} = \mathfrak{l}_k(-1) \\ i = 2 &\Leftrightarrow \ \mathfrak{l}_{2k} = \mathfrak{l}_k(+1), \end{aligned} \tag{3.10}$$

noting that under certain circumstances the symbol LLF may become negative.

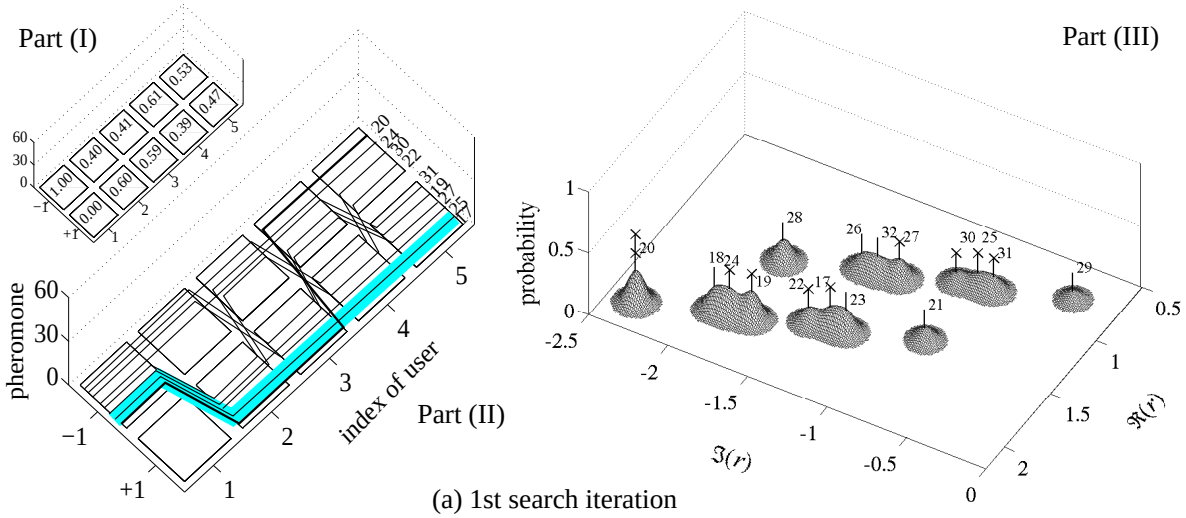

(a) 1st search iteration

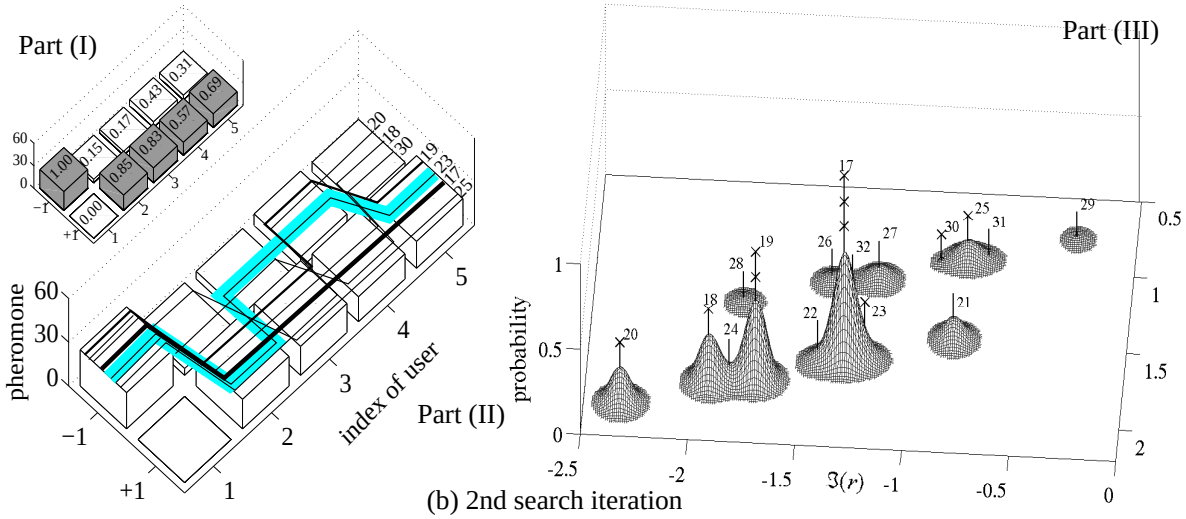

(b) 2nd search iteration

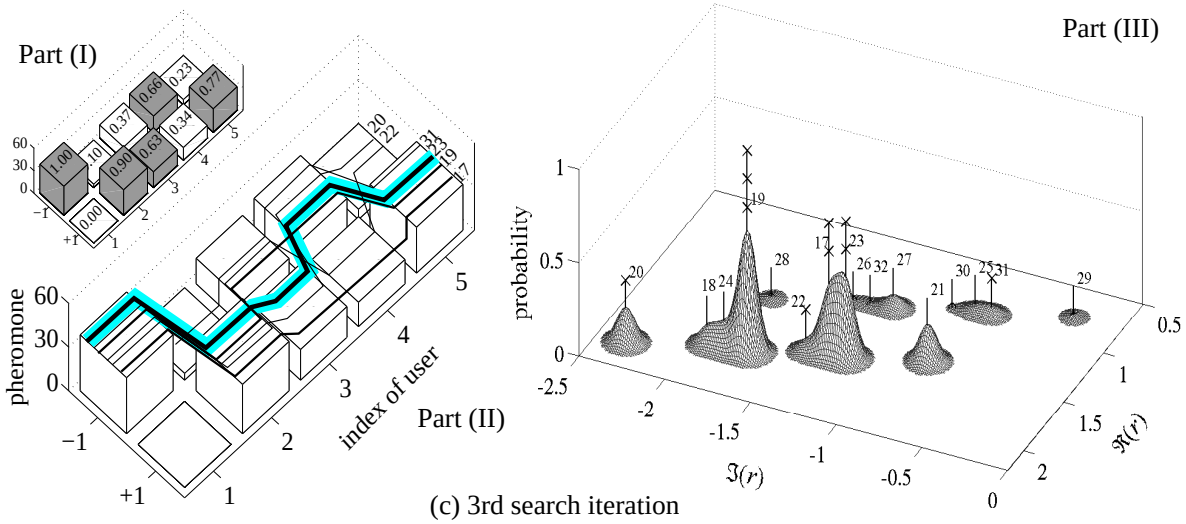

(c) 3rd search iteration

Figure 3.10: Part (I) The grey and white bars quantify the pheromone deposit, while the three-digit numbers quantify the symbol-probability associated with each cell. More specifically, the grey bars highlight the 'most-favourable' routes encompassing the specific cells having the higher pheromone deposit between each pair of constituent columns;

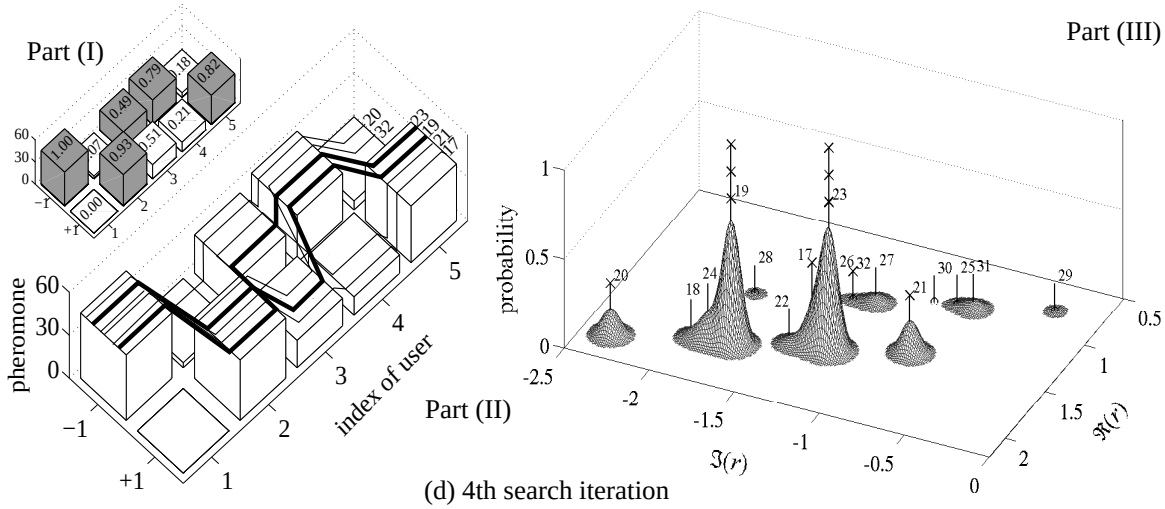

(d) 4th search iteration

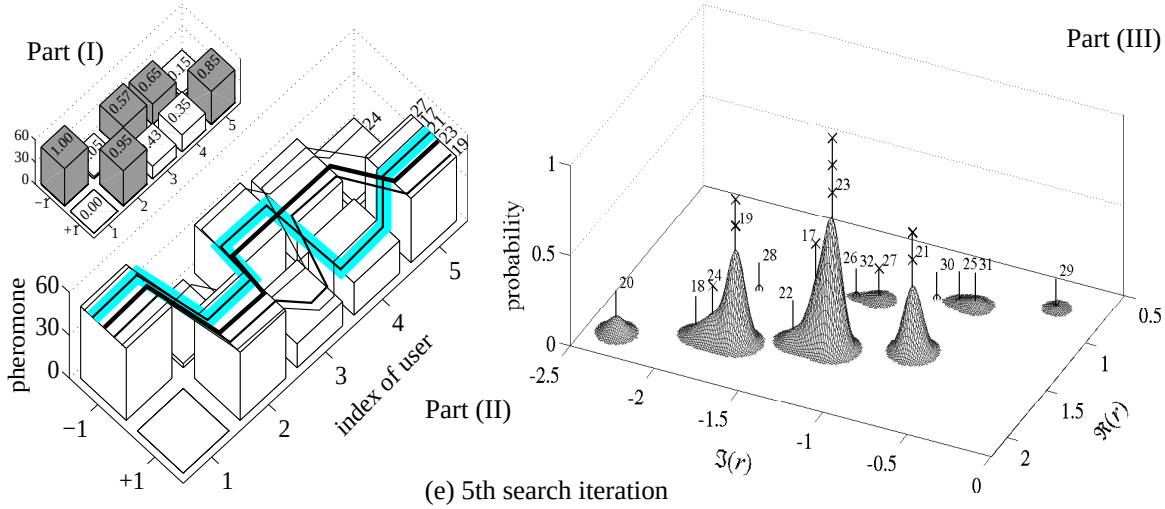

(e) 5th search iteration

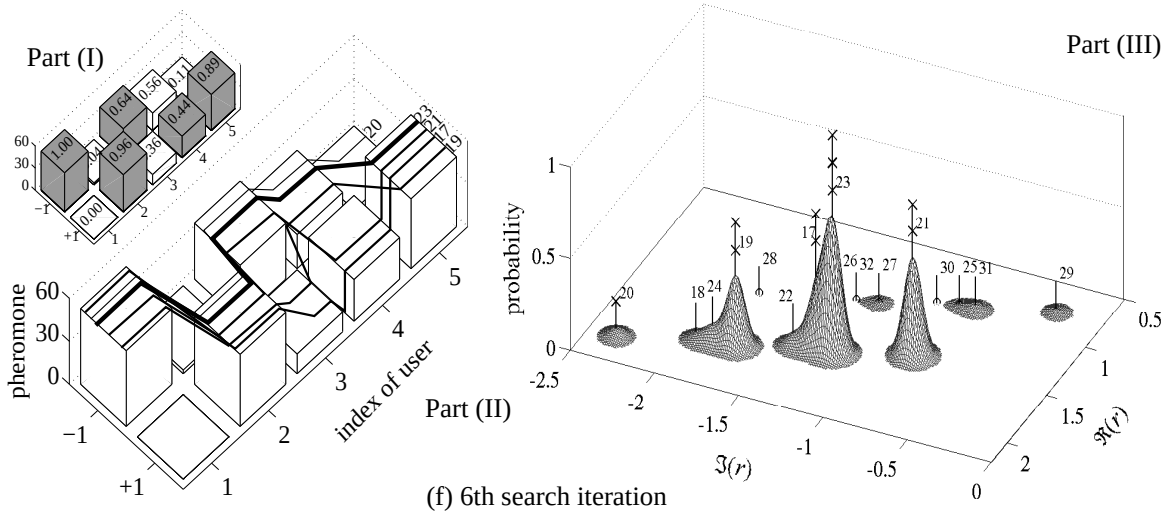

(f) 6th search iteration

Part (II) The lines mark the routes representative of all K-bit vector constituting the search-pool, which is visualized by appropriately connecting the top of the pheromone-concentration-related bars of the route-table. The elite-route is highlighted by the grey stripe having a width of $\sigma = 8$;

3.4.2 Intrinsic Affinity

3.4.2.1 Intrinsic Affinity Definition

The intrinsic affinity η_{ik} associated with the (i,k)th cell is determined by the two symbol LLF values $\mathfrak{l}_{1k}$ and $\mathfrak{l}_{2k}$ associated with the pair of cells constituting the kth column of the route-table, as shown

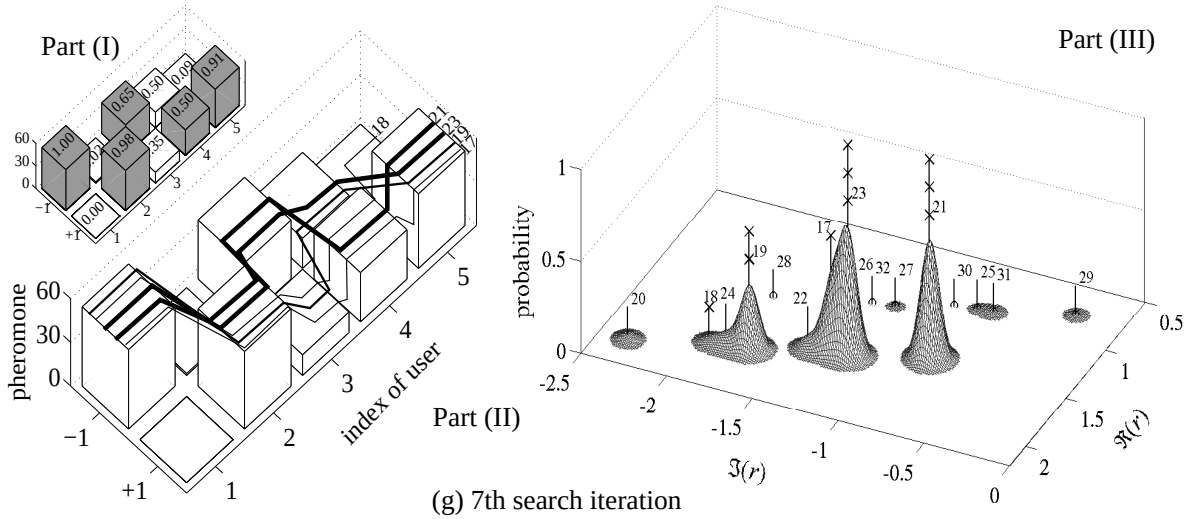

(g) 7th search iteration

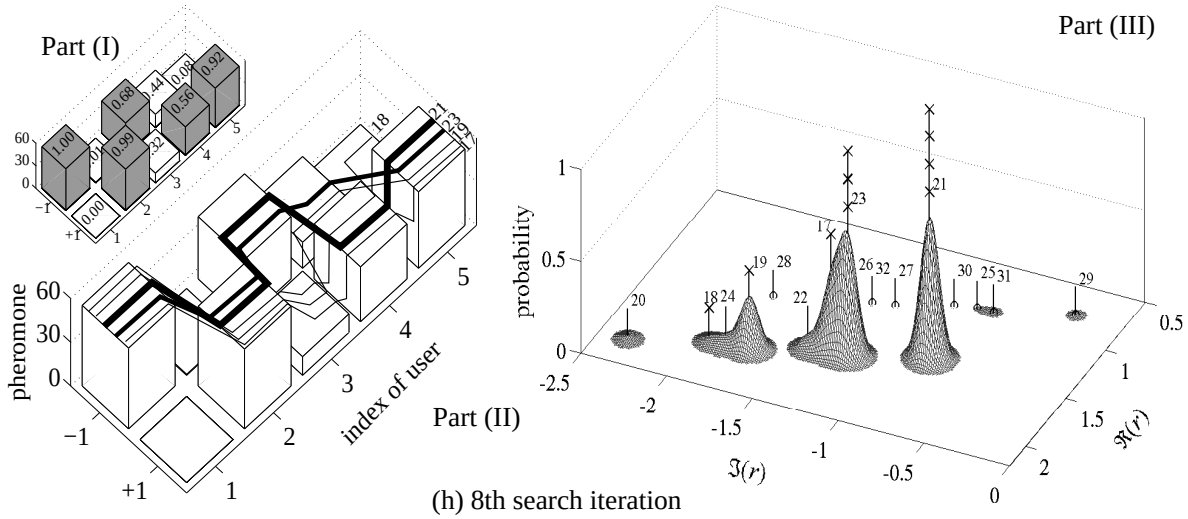

(h) 8th search iteration

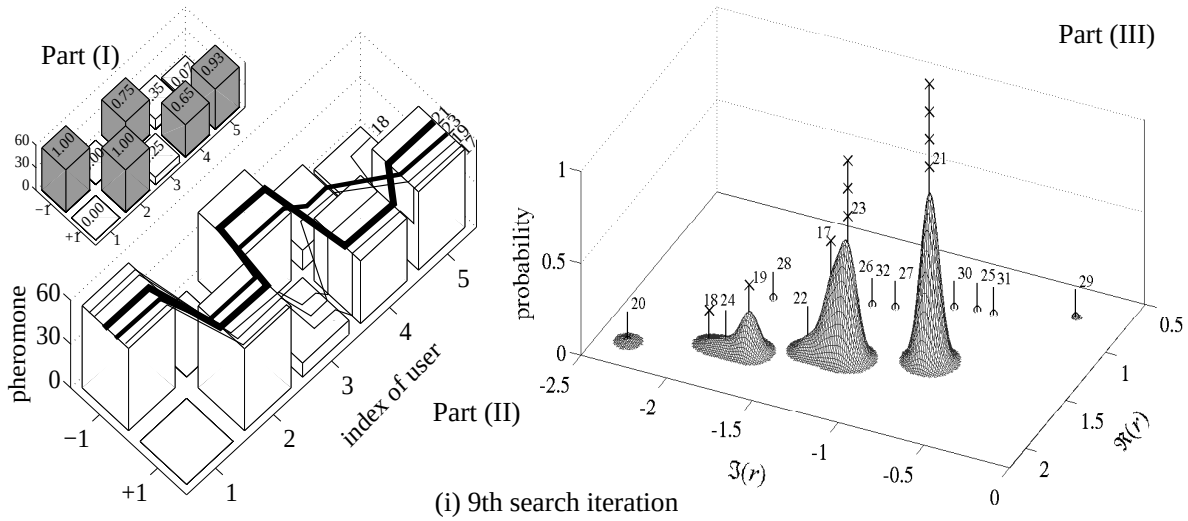

(i) 9th search iteration

Part (III) The crosses indicate the K-bit vectors in the search-pool, while the 3D surfaces represent the probability of each K-bit vector. The peaks of the 3D surfaces tend to be centered around the received signal constellation points of Fig. 3.7, which was recorded during the 4th chip interval. There are nine Part III illustrations corresponding to the 1st, 2nd, ..., 9th ACO-search iterations. The system conditions as well as the ACO-based MUD algorithm's parameters are listed in Table 3.1 and Table 3.4, respectively.

Variable	Notation	Property of	Size	Determined by	Determining
Intrinsic affinity	$\boldsymbol{\eta}$, η_{ik} $\eta_j(\pm 1)$, $\eta_{\pm k}$	each cell of route-table	$\boldsymbol{\eta}$ $2 \times K$	$\eta_{ik} \leftarrow \mathfrak{l}_{ik}$	$\eta_{\pm k} \rightarrow P_{\pm k}^{(\dot{n})}$ $\dot{n} = 1, 2, \ldots, \Xi$
				Eqs. (3.11) (3.12) Step 2	Eq. (3.26) Step 4
Pheromone	$\boldsymbol{\tau}^{(n)}$, $\boldsymbol{\tau}_m^{(n)}$, $\boldsymbol{\tau}_*^{(n)}$ $\tau_{ik}^{(n)}$ $\tau_{\pm k}^{(n)}$	Each cell of route-table	$\boldsymbol{\tau}^{(n)}$ $\boldsymbol{\tau}_m^{(n)}$ $\boldsymbol{\tau}_*^{(n)}$ $2 \times K$	$\boldsymbol{\tau}^{(n+1)} \leftarrow$ $\boldsymbol{\tau}^{(n)}$,$\boldsymbol{\tau}_m^{(n)}$,$\boldsymbol{\tau}_*^{(n)}$	$\tau_{\pm k}^{(n)} \rightarrow P_{\pm k}^{(n)}$
				Eqs. (3.20)$\sim$(3.23) Step 6	Eq. (3.26) Step 4
Symbol probability	$\mathbf{P}^{(n)}$, $P_{ik}^{(n)}$, $P^{(n)}(v_k = \pm 1)$ $P_{\pm k}^{(n)}$	Each cell ofroute-table	$\mathbf{P}^{(n)}$ $2 \times K$	$P_{\pm k}^{(n)} \leftarrow \eta_{\pm k}$,$\tau_{\pm k}^{(n)}$	$\mathbf{P}^{(n)} \rightarrow \mathbf{x}^{(n)}$
				Eq. (3.26) Step 4	Fig. 3.15 Step 5
search-pool	$\mathbf{x}^{(n)}$, $\mathbf{x}_m^{(n)}$, $\mathbb{X}$, $\mathbb{X}^{(n)}$		$\mathbf{x}^{(n)}$ $\zeta \times K$	$\mathbf{x}^{(n)} \leftarrow \mathbf{P}^{(n)}$	$\mathbf{x}_m^{(n)} \rightarrow \mathfrak{L}(\mathbf{x}_m^{(n)})$
				Fig. 3.15 Step 5	Eq.(3.18) Step 6
Symbol LLF	$\mathfrak{l}$, $\mathfrak{l}_{ik}$, $\mathfrak{l}_{\pm k}$, $\mathfrak{l}_k(\pm 1)$	Each cell of route-table	$\mathbf{x}^{(n)}$ $K \times \zeta$	$\mathfrak{l}_{ik} \leftarrow \Re\{y_k\}$,$i$,$h_k$	$\mathfrak{l}_{\pm k} \rightarrow \eta_{\pm k}$
				Eq. (3.9) Step 1	Eq.(3.11)(3.12) Step 2
K-bit Vector LLF	$\mathfrak{L}(\mathbf{x}^{(n)})$, $\mathfrak{L}(\mathbf{x}_m^{(n)})$	each vector of search pool	$\mathfrak{L}(\mathbf{x}^{(n)})$ $1 \times \zeta$ $\mathfrak{L}(\mathbf{x}_m^{(n)})$ 1×1	$\mathfrak{L}(\mathbf{x}_m^{(n)}) \leftarrow$ $\Re\{\mathbf{y}\}$,$\mathbf{x}_m^{(n)}$,$\mathbf{H}$,$\mathbf{C}$	$\mathfrak{L}(\mathbf{x}_m^{(n)}) \rightarrow \boldsymbol{\tau}_m^{(n)}$ $\mathfrak{L}(\mathbf{x}_*^{(n)}) \rightarrow \boldsymbol{\tau}_*^{(n)}$
				Eq. (3.18) Step 6	Eq.(3.11)(3.12) Step 3

Table 3.5: Properties of the ACO-based MUD algorithm.

in Table 3.5. An intermediate variable d_{ik} associated with each cell is introduced, when determining the intrinsic affinity from the symbol LLF as follows:

$$d_{ik} = 1 + \exp(-\mathfrak{l}_{ik}), \tag{3.11}$$

which simply maps the symbol LLF domain of $-\infty$ to $+\infty$ to the positive domain spanning the interval $[1, +\infty)$. However, the intermediate variable d_{ik} monotonically decreases with the value of $\mathfrak{l}_{ik}$. By contrast, as suggested by the terminology, the intrinsic affinity η_{ik} associated with the (i,k)th cell monotonically increases with the LLF of the symbol transmitted. The intrinsic affinity η_{ik} associated with the (i,k)th cell may be defined as the sum of the LLF-dependent intermediate variables d_{1k} and d_{2k} normalized by d_{ik}, yielding:

$$\eta_{ik} = \frac{d_{1k} + d_{2k}}{d_{ik}}. \tag{3.12}$$

Just like the symbol LLF defined in Eq. (3.9) and the mapping between the row index i and the symbol-value $+1$ or -1 associated with a certain cell, as formulated in Eq. (3.10) in terms of the symbol LLF, the subscript i associated with the intrinsic affinity η_{ik} or the corresponding intermediate variable d may also be alternatively represented with the aid of the symbol-value of the (i,k)th cell, as follows:

$$\begin{aligned} i = 1 \Leftrightarrow\ & d_{1k} \equiv d_k(-1) \equiv d_{-k},\ \eta_{1k} \equiv \eta_k(-1) \equiv \eta_{-k} \\ i = 2 \Leftrightarrow\ & d_{2k} \equiv d_k(+1) \equiv d_{+k},\ \eta_{2k} \equiv \eta_k(+1) \equiv \eta_{+k}. \end{aligned} \tag{3.13}$$

Eq.(3.12) may alternatively be expressed with the aid of Eq. (3.13) as

$$\begin{aligned} \eta_{\pm k} &= \frac{d_{+k} + d_{-k}}{d_{\pm k}} \\ &= 1 + \frac{d_{\mp k}}{d_{\pm k}}. \end{aligned} \tag{3.14}$$

Therefore, the intrinsic affinity η_{ik} associated with the (i,k)th cell increases monotonically with the LLF value $\mathfrak{l}_{ik}$ of the corresponding transmitted symbol-value.

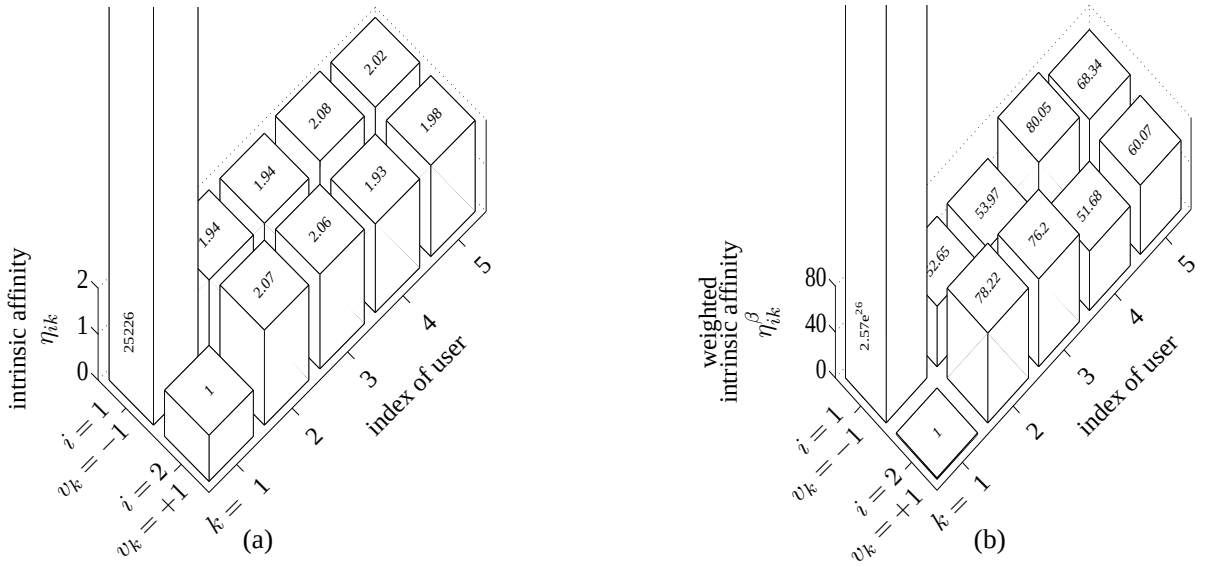

Figure 3.13: (a) Intrinsic affinity η_{ik} of the (i,k)th cell constituting the route-table for $i = 1, 2$, $k = 1, 2, \ldots, 5$. (b) Weighted intrinsic affinity η_{ik}^{β} of the (i,k)th cell constituting the route-table for $i = 1, 2$, $k = 1, 2, \ldots, 5$. The weighting factor β is a parameter of the ACO-based MUD algorithm and the value of β in this example is $\beta = 6$, as is listed in conjunction with the values of other ACO-based MUD algorithm parameters in Table. 3.4.

3.4.2.2 Intrinsic Affinity Properties

Based on Eq. (3.11) and Eq. (3.12), the following conclusions may be drawn regarding the intrinsic affinity values of the route-table.

1. Thresholding the MF's Output

Let us now define the threshold T_i used as the intrinsic-affinity threshold to decide, which of the two legitimate BPSK symbol candidates is more likely to have been transmitted by the kth user, based

on the real part of the MF solution $\Re\{y_k\}$.

$$
\begin{aligned}
&\because d_{-k}, d_{+k} \in [1, +\infty) \\
&\therefore \eta_{\pm k} = \frac{d_{+k} + d_{-k}}{d_{\pm k}} \in (1, +\infty) \\
&\therefore \text{if } \mathfrak{l}_{-k} \geqslant \mathfrak{l}_{+k} \Rightarrow d_{+k} \geqslant d_{-k} \Rightarrow \eta_{-k} \geqslant 2 \\
&\quad \text{if } \mathfrak{l}_{-k} < \mathfrak{l}_{+k} \Rightarrow d_{+k} < d_{-k} \Rightarrow \eta_{-k} < 2. \\
\text{And } &\because \mathfrak{l}_k(\pm 1) = \pm 2\Re\{y_k\} - |h_k|^2 \\
&\therefore \mathfrak{l}_{-k} \geqslant \mathfrak{l}_{+k}, \text{ given } \Re\{y_k\} \leqslant 0 \\
&\quad \mathfrak{l}_{-k} < \mathfrak{l}_{+k}, \text{ given } \Re\{y_k\} > 0. \\
\text{And } &\therefore d_{-k} \leqslant d_{+k}, \text{given } \Re\{y_k\} \leqslant 0 \\
&\quad d_{-k} > d_{+k}, \text{ given } \Re\{y_k\} > 0. \\
\text{And } &\therefore \eta_{-k} \geqslant 2 > \eta_{+k} > 1, \text{ given } \Re\{y_k\} \leqslant 0 \\
&\quad 1 < \eta_{-k} < 2 \leqslant \eta_{+k}, \text{ given } \Re\{y_k\} > 0.
\end{aligned} \tag{3.15}
$$

Therefore, the value of the intrinsic affinity associated with the 1st cell belonging to a specific column of the route-table may immediately reflect the polarity of the MF output of the corresponding user. More explicitly, if the intrinsic affinity associated with a certain cell is higher than $T_i = 2$, then the MF solution of the user considered will become the corresponding symbol-value represented by the cell.

This can also be demonstrated by the intrinsic affinity table of the $K = 5$-user example shown in Fig. 3.13(a). As suggested by Table 3.1, the MF solutions for the $K = 5$ users are -1, $+1$, $+1$, -1, -1, respectively. As a result, in Fig. 3.13(a), we portrayed the intrinsic affinity associated with the cells $(1, 1)$, $(2, 2)$, $(2, 3)$, $(1, 4)$ and $(1, 5)$ of the route-table of Fig. 3.6(a), which is higher than 2, while the intrinsic affinity associated with the remaining $K = 5$ cells is smaller than 2.

2. Dynamic Range of the Intrinsic Affinity

In this section we will demonstrate that the dynamic range of the intrinsic affinity seen on top of each cell in Fig. 3.13 is $[2, +\infty)$, when we consider a specific BPSK symbol corresponding to the MF solution. This is a monotonically increasing quantity with an absolute value given by the MF output's real part. We will also show that by contrast, the dynamic range of the intrinsic affinity associated with the specific cell, which is the opposite of the MF solution is restricted to $(1, 2)$, and its value is monotonically decreasing from 2 to 1 upon increasing the absolute value of the real part of the MF's output.

To elaborate a little further, below we will demonstrate the above-mentioned trends by expanding the expression of $\eta_{\pm k}$ as a function of the independent variable $\Re\{y_k\}$ given by:

$$
\because \ \eta_{\pm k} = 1 + \frac{1 + c \cdot e^{\pm 2\Re\{y_k\}}}{1 + c \cdot e^{\mp 2\Re\{y_k\}}}.
$$

$$
\begin{aligned}
\therefore \text{ When } \Re\{y_k\} \geqslant 0,\ & \frac{1+c\cdot e^{+2\Re\{y_k\}}}{1+c\cdot e^{-2\Re\{y_k\}}} \in [1,+\infty) \ \Rightarrow\ \eta_{+k} \in [2,+\infty) \\
& \because\ |\Re\{y_k\}| \uparrow \ \Rightarrow\ \eta_{+k} \uparrow \\
& \therefore \lim_{|\Re\{y_k\}|\to\infty} \eta_{+k} = +\infty, \quad \lim_{|\Re\{y_k\}|\to 0} \eta_{+k} = 2; \\
\text{and } & \frac{1+c\cdot e^{-2\Re\{y_k\}}}{1+c\cdot e^{+2\Re\{y_k\}}} \in (0,1) \ \Rightarrow\ \eta_{-k} \in (1,2) \\
& \because\ |\Re\{y_k\}| \uparrow \ \Rightarrow\ \eta_{-k} \downarrow \\
& \therefore \lim_{|\Re\{y_k\}|\to\infty} \eta_{-k} = 1, \quad \lim_{|\Re\{y_k\}|\to 0} \eta_{-k} = 2; \\
\text{When } \Re\{y_k\} < 0,\ & \frac{1+c\cdot e^{+2\Re\{y_k\}}}{1+c\cdot e^{-2\Re\{y_k\}}} \in (0,1) \ \Rightarrow\ \eta_{+k} \in (1,2) \\
& \because\ |\Re\{y_k\}| \uparrow \ \Rightarrow\ \eta_{+k} \downarrow \\
& \therefore \lim_{|\Re\{y_k\}|\to\infty} \eta_{+k} = 1, \quad \lim_{|\Re\{y_k\}|\to 0} \eta_{+k} = 2; \\
\text{and } & \frac{1+c\cdot e^{-2\Re\{y_k\}}}{1+c\cdot e^{+2\Re\{y_k\}}} \in (1,+\infty) \ \Rightarrow\ \eta_{-k} \in (2,+\infty) \\
& \because\ |\Re\{y_k\}| \uparrow \ \Rightarrow\ \eta_{-k} \uparrow \\
& \therefore \lim_{|\Re\{y_k\}|\to\infty} \eta_{-k} = +\infty, \quad \lim_{|\Re\{y_k\}|\to 0} \eta_{-k} = 2;
\end{aligned} \tag{3.16}
$$

Alternatively, Eq. (3.16) can be consolidated in conjunction with $\dot{v} \in \{\pm 1\}$ as follows:

$$
\left.\begin{array}{ll} \lim\limits_{|\Re\{y_k\}|\to\infty} & \eta_j(\dot{v}) = +\infty \\ \lim\limits_{|\Re\{y_k\}|\to 0} & \eta_j(\dot{v}) = 2 \end{array}\right\} \text{given } \dot{v} = \operatorname{sgn}\big\{\Re\{y_k\}\big\}
$$

$$
\left.\begin{array}{ll} \lim\limits_{|\Re\{y_k\}|\to\infty} & \eta_j(\dot{v}) = 1 \\ \lim\limits_{|\Re\{y_k\}|\to 0} & \eta_j(\dot{v}) = 2 \end{array}\right\} \text{given } \dot{v} = -\operatorname{sgn}\big\{\Re\{y_k\}\big\}. \tag{3.17}
$$

3. Conclusions Regarding the Intrinsic Affinity

Eq. (3.17) reflects the following characteristics of the intrinsic affinity associated with the pair of cells constituting a specific column of the route-table and their relationship with the MF output:

1. If the intrinsic affinity associated with one of the two cells constituting a column, is higher than $T_i = 2$, then the other one must be smaller than $T_i = 2$.

2. The farther the intrinsic affinity value η is from $T_i = 2$ in the range of $[2 \leqslant \eta < \infty)$, the closer its dual pair is to 1 and vice-versa.

3. The higher the absolute value of the MF output related to the kth user, the higher the intrinsic affinity associated with the cell representing the MF solution symbol-value $\operatorname{sgn}\big\{\Re\{y_k\}\big\}$, and the closer the intrinsic affinity associated with the other cell to 1; By contrast, the smaller the absolute value of the MF output of user k, the closer both intrinsic affinity values are to $T_i = 2$.

The above-mentioned trends may be confirmed in the intrinsic affinity table recorded for our $K = 5$-user example in Fig. 3.13 (a). As seen in Table 3.1, the absolute value of the MF output of the first

user is -3.291, which is higher than that of the other four users' MF outputs. As a result, the intrinsic affinity η_{-1} associated with the cell of the 1st row and the 1st column is also substantially higher than those of the other four cells representing the other four users' MF solution. The corresponding η values evaluated from Eq. (3.14) become '25226' and '2.07', '2.06', '2.08' as well as '2.02', respectively.

3.4.3 Log-Likelihood Function of the K-bit vectors

The LLF value of an arbitrary K-bit vector $\dot{\mathbf{v}}$ being transmitted under the simplest DS-CDMA UL model supporting K users as defined by Fig. 3.4 and Eq. (3.1), may be expressed as:

$$\mathfrak{L}(\dot{\mathbf{v}}) \triangleq 2\Re\{\dot{\mathbf{v}}^H \mathbf{y}\} - \dot{\mathbf{v}}^H \mathbf{R} \dot{\mathbf{v}}, \tag{3.18}$$

where we have $\mathbf{R} = \mathbf{H}^H \mathbf{C}^T \mathbf{C} \mathbf{H}$. Eq. (3.18) also quantifies the merit of each legitimate K-bit vector, similarly to the objective function of the ML algorithm used for finding the ML solution. The difference between the ACO-based MUD algorithm and the ML algorithm of Section 2.4.4 is that the latter evaluates the K-bit vector LLF given in Eq. (3.18) for $\dot{\mathbf{v}}$ 2^K times, namely one for each of the legitimate K-bit vector in the full set $\mathbb{V}^{(K)}$, in order to capture the ML solution. By contrast, given that $\mathbf{x}_m^{(n)}$ denotes the mth K-bit vector in the search-pool $\mathbf{X}^{(n)}$ having ζ vectors during the nth search iteration, Eq. (3.18) is evaluated for $m = 1, 2, \ldots, \zeta$ and $n = 1, 2, \ldots, \Xi$, i.e. $(\zeta \cdot \Xi)$ times, where we typically have $\zeta \ll 2^K$. Since typically there are identical K-bit vectors in the search-space, we denote the set containing all the unique vector-values during the nth iteration by $\mathbb{X}^{(n)}$ and the size of the corresponding set as $\sharp\mathbb{X}^{(n)} \leqslant \zeta$. Since $\mathbb{X}$ denotes the set containing all the unique K-bit vectors captured throughout the optimization process carried out within a specific symbol-duration, we arrive at $\sharp\mathbb{X} \leqslant \zeta\Xi$. In practice we are likely to have $\sharp\mathbb{X} \ll \zeta \cdot \Xi$. More quantitatively, observe in Fig. 3.8 for our $K = 5$-user example, that we have $\sharp\mathbb{X} = 13$ and $\zeta \cdot \Xi = 10 \times 10 = 100$.

When considering a more practical example, given $K = 32$ as well as $\zeta = 10$ and $\Xi = 10$, the objective function is evaluated at the most $\zeta \cdot \Xi = 100$ times, which is much less than the potentially excessive complexity of evaluating the objective function 2^{32} times, as required by the ML MUD algorithm.

3.4.4 Pheromone Update

Let us now continue by considering the pheromone update block of Fig. 3.9. As observed in the foraging behaviour of the ants in nature, every ant in the ACO-aided MUD will leave a certain amount of pheromone along the route it follows. The more ants pursue a particular route, the more pheromone will be assigned to the route. Analogously to the ants in nature, which use the distance as their 'route-quality' criterion, the quality of the route in our algorithm is quantified in terms of its LLF.

3.4.4.1 Pheromone Definition

Except for the 1st iteration, the pheromone associated with each cell of the route-table is constituted by three components. The first component is inherited from the pheromone associated with each cell of the route-table during the previous iteration after taking into account also the associated pheromone

evaporation rate. The second component is given by the pheromone generated by the ζ artificial ants along the routes followed by them. The same amount of pheromone is added to each of the K cells constituting the route. The amount of pheromone deposited is equivalent to the LLF of the K-bit vector represented by the route, plus an iteration-specific offset $t^{(n)}$. More specifically, the offset $t^{(n)}$ of the nth iteration is a non-negative scalar added to the pheromone generated by each of the ζ artificial ants to ensure that all the pheromone values are non-negative. Accordingly, we may set:

$$t^{(n)} = \begin{cases} 0 & \text{if } \min\limits_{1 \leqslant m \leqslant \zeta} \left\{ \mathfrak{L}\left(\mathbf{x}_m^{(n)}\right) \right\} \geqslant 0 \\ -\min\limits_{1 \leqslant m \leqslant \zeta} \left\{ \mathfrak{L}\left(\mathbf{x}_m^{(n)}\right) \right\} & \text{if } \min\limits_{1 \leqslant m \leqslant \zeta} \left\{ \mathfrak{L}\left(\mathbf{x}_m^{(n)}\right) \right\} < 0. \end{cases} \tag{3.19}$$

The third component is an extra 'elite contribution' added to the cells constituting the 'elite' route, which had the highest LLF during all previous search iterations, which was marked by the grey stripe in Fig. 3.10. The amount of the extra 'elite' pheromone is equivalent to the sum of the vector LLF values related to the 'elite' route plus the offset $t^{(n)}$ multiplied by a positive weighting factor. Below, we will elaborate on the above-mentioned three pheromone components.

1. Pheromone evaporation

In order to avoid that the pheromone level associated with a cell changes dramatically, the pheromone of each cell of the route-table accumulated throughout the previous iterations is remembered. However, over-emphasizing the effect of the accumulated pheromone should also be avoided. Hence only a fraction of the previously accumulated pheromone will be retained, mimicking the precess of pheromone evaporation [129, 133–135]. The fraction of pheromone evaporated is controlled by the evaporation rate ρ, which is an important parameter of the ACO-based MUD algorithm, that may be fixed, regardless of the channel conditions. We opted for using $\rho = 0.5$. Hence, during the nth ACO-based search iteration, given the accumulated pheromone $\boldsymbol{\tau}^{(n)}$, the pheromone associated with the $2K$ cells constituting the route-table is set to $\rho \cdot \boldsymbol{\tau}^{(n)}$ for the next iteration.

2. Pheromone associated with each route

Based on the above discussions, the amount of pheromone assigned to each cell constituting a specific route is set to the LLF of the K-bit vector. More explicitly, the amount of pheromone assigned to a particular route pursued by the mth ant during the nth iteration is formulated as

$$\boldsymbol{\tau}_m^{(n)} = \left[\mathfrak{L}(\mathbf{x}_m^{(n)}) + t^{(n)} \right] \cdot \underline{\mathbf{x}}_m^{(n)}, \tag{3.20}$$

where $\mathbf{x}_m^{(n)}$ represents the specific K-symbol vector corresponding to the route produced by the mth ant during the nth iteration and $\mathfrak{L}(\mathbf{x}_m^{(n)})$ denotes the vector-LLF related to the K-symbol vector-value. Furthermore, $\underline{\mathbf{x}}_m^{(n)}$ is the $(2 \times K)$-element matrix hosting binary values and representing the route pursued by the mth ant having the vector-value $\mathbf{x}_m^{(n)}$ in the route-table, where element '1' implies that the corresponding cell is part of the route, while '0' means that the corresponding cell is not part of the route.. For instance, if we consider our $K = 5$-bit vector produced by the mth ant given by $\mathbf{x}_m^{(n)} = [-1, +1, +1, -1, +1]^T = \mathbf{v}_{19}^{(5)}$ as shown in Fig. 3.10(b) Part (II), then the route representing the $K = 5$-bit vector will be

$$\mathbf{x}_m^{(n)} = [-1, +1, +1, -1, +1]^T \;\Rightarrow\; \underline{\mathbf{x}}_m^{(n)} = \begin{bmatrix} 1 & 0 & 0 & 1 & 0 \\ 0 & 1 & 1 & 0 & 1 \end{bmatrix}. \tag{3.21}$$

3. Extra pheromone for the elite route

Furthermore, an extra amount of pheromone quantified by $\sigma \cdot \mathfrak{L}(\mathbf{x}_*^{(n)})$ is assigned to the route corresponding to the most likely K-symbol vector $\tilde{\mathbf{x}}_*^{(n)}$ found so far, where σ represents the weighting factor of the pheromone assigned to a meritorious K-symbol vector. Hence, the 'extra' pheromone associated with the elite route may be quantified as

$$\boldsymbol{\tau}_*^{(n)} = \sigma \cdot \left[\mathfrak{L}(\mathbf{x}_*^{(n)}) + t^{(n)}\right] \cdot \underline{\mathbf{x}}_*^{(n)}, \tag{3.22}$$

where $\mathbf{x}_*^{(n)}$ represents the 'elite' vector-value having the highest LLF and hence deemed to be the most likely transmitted vector among all the K-symbol vectors generated throughout the previous n ACO-based search iterations. Still referring to Eq. 3.22, $\underline{\mathbf{x}}_*^{(n)}$ is the $(2 \times K)$-element matrix having a logical '1' in the positions representing the route corresponding to the K-symbol vector $\mathbf{x}_*^{(n)}$. In our $K = 5$-user example of Fig. 3.10 the elite route was highlighted with the grey stripe having a width σ times thicker than the line representing a single route, where we have $\sigma = 8$, as listed in Table 3.4.

Finally, the $(2 \times K)$-element pheromone matrix generated for the $(n+1)$st iteration is formulated as [129]

$$\boldsymbol{\tau}^{(n+1)} = \rho \boldsymbol{\tau}^{(n)} + \sum_{m=1}^{\zeta} \boldsymbol{\tau}_m^{(n)} + \boldsymbol{\tau}_*^{(n)}, \tag{3.23}$$

where the ordinary pheromone $\boldsymbol{\tau}_m^{(n)}$ associated with the mth route $m = 1, 2, \ldots, \zeta$ and the extra pheromone $\boldsymbol{\tau}_*^{(n)}$ associated with the elite route are quantified in Eq. (3.20) and Eq. (3.22), respectively.

3.4.4.2 Pheromone properties

1. The role of the elite vector's extra pheromone

As seen in Eq. (3.23), the pheromone update is constituted by three components, where the weights of the three components are adjustable. The weight of the 'elite' vector is typically set to be higher, such as $\sigma = 8$ in order to emphasize the significance of the elite-vector-value. The value of the $(2 \times K)$-element pheromone matrix $\boldsymbol{\tau}^{(n+1)}$ quantifying the total amount of pheromone associated with each cell during the $(n+1)$st iteration is also substantially dependent on the incremental pheromone matrix $\boldsymbol{\tau}_*^{(n)}$, which in turn is strongly dependent on the elite vector-value $\mathbf{x}_*^{(n)}$ of Eq. 3.22 encountered during the nth iteration and on the $\sigma \cdot \mathfrak{L}(\mathbf{x}_*^{(n)}$ factor.

This property can be observed throughout the search process of our $K = 5$-user example. All the K-symbol vectors in the search-pool generated during the 1st iteration are represented by the corresponding lines in Fig. 3.10 (a) Part (II). Nine different K-symbol vectors were generated during the 1st iteration and $\mathbf{v}_{20}^{(5)}$ is seen to be the 'most popular' vector, since it was selected by two of the $\zeta = 10$ ants, while all the other eight vectors were selected by a single ant. Moreover, as observed in Table 3.2 $\mathbf{v}_{17}^{(5)}$ is the elite vector having the highest LLF of 2.973, among the nine different vectors $\mathbf{v}_{17}^{(5)}$, $\mathbf{v}_{19}^{(5)}$, $\mathbf{v}_{22}^{(5)}$, $\mathbf{v}_{24}^{(5)}$, $\mathbf{v}_{20}^{(5)}$, $\mathbf{v}_{31}^{(5)}$, $\mathbf{v}_{25}^{(5)}$, $\mathbf{v}_{27}^{(5)}$, $\mathbf{v}_{30}^{(5)}$ found in the search-pool during the 1st iteration. Observe in the 3rd row and 9th column of Table 3.2 that the amount of the pheromone added to the five cells of the route representing $\mathbf{v}_{17}^{(5)}$, which is 2.97, is less than that added to the five cells of the route representing $\mathbf{v}_{20}^{(5)}$, which is $2 \times \mathfrak{L}(\mathbf{v}_{20}^{(5)}) = 2 \cdot 2.60 = 5.20$, as observed in line 8 and column 9 of Table 3.2. Moreover,

the extra pheromone quantified by $8 \times \mathfrak{L}(\mathbf{v}_{17}^{(5)}) = 23.784$ is substantially more than that added to the five-cells representing any of the non-elite vectors of Table 3.2. Therefore, since a high pheromone level is dedicated to the five cells of the route representing the elite vector, the incremental pheromone added to the five cells of the route representing the elite vector-value in the next iteration will significantly exceed the incremental pheromone deposited in the other five cells. As the pheromone level associated with each cell during the 1st iteration was set to an identical value of '0.01', the pheromone associated with each cell during the 2nd iteration essentially becomes equivalent to the incremental pheromone added to each cell.

The K-symbol vector, which is represented by the route associated with the K highest-pheromone cells in each of the K columns of the route-table termed as the highest-pheromone vector. The highest-pheromone vector of each iteration is marked by a grey stripe in Fig. 3.10(a)∼(i) Part (I). As exemplified by Fig. 3.10 (b) Part (I), the highest-pheromone vector encountered during the 2nd iteration is $\mathbf{v}_{17}^{(5)} = [-1, +1, +1, +1, +1]$, which was the elite K-symbol vector during the 1st iteration.

2. Convergence of the highest-pheromone-route to the elite route

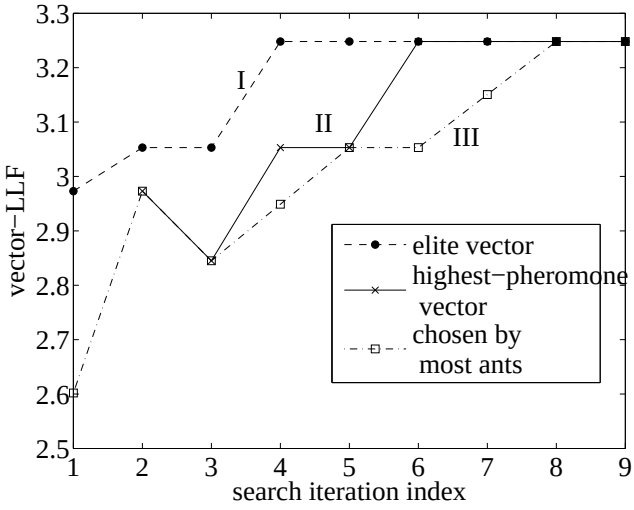

Figure 3.14: Curve I: LLF of the elite K-bit vector. Curve II: LLF of the highest-pheromone vector of the specific iteration considered; Curve III, LLF of the vector in the search-pool, which was chosen by the largest fraction of ants during each ACO-based search iteration of the given five-user example.

However, since the pheromone level of the current iteration has to take into account the pheromone level retained from the previous iteration, the highest-pheromone route of a specific iteration may not be the same as the elite vector in the search-pool generated during the previous iteration. This pheromone level may be observed in Fig. 3.14, where the piecewise linear Curve I represents the elite vector having the highest vector-LLF throughout all the previous iterations according to its definition. By contrast, Curve II represents the highest-pheromone vector of each specific iteration, which only reaches the vector-LLF of the elite-vector at iteration six, while Curve III represents the vector chosen by the largest fraction of ants during a certain iteration. As seen from Fig. 3.14, curve II does not overlap with curve I during every iteration. Curve II follows the trend of curve I two iterations later. This phenomenon can be alternatively observed in Fig. 3.10(a)∼(i) Part (I) and Fig. 3.10(a)∼(i) Part (II). The grey cells representing the K-bit vector having the highest pheromone level throughout

the 1st to the 9th iteration in Part (I) of Fig. 3.10(a)∼(i), are alternatively characterized by curve II in Fig. 3.14. On the other hand, the route highlighted with grey colors in Fig. 3.10(a)∼(i)(II) represents the elite route corresponding to the vector having the highest LLF during each of the nine iterations, which is equivalently characterized by the piecewise-linear curve I in Fig. 3.14. As observed from Fig. 3.10(a)∼(i), the grey cells in Part (I) are not always equivalent to the route highlighted with grey colors in Part (II), as reinforced by the difference seen between Curve I and Curve II in Fig. 3.14.

To elaborate a little bit further, there appears to be a two-iteration delay between Curves II and I. In other words, the K-bit vector having the highest pheromone during a certain iteration becomes the same as the elite K-bit vector was two iterations ago, as shown by Curve II. This latency is caused by the un-evaporated pheromone that remained in the constituent cells of the vectors, which are different from the elite vector. Hence, as a mixture of the highly weighted pheromone deposited in the constituent cells of the elite vector and the residual pheromone passed on from the previous iteration, the K-bit vector having the highest pheromone level during a certain iteration might not be the elite vector during the same iteration. Therefore, one or two further iterations may be needed for sufficient pheromone to evaporate, so that the elite vector may indeed have the highest amount of pheromone.

3.4.5 Symbol Probability

3.4.5.1 Definition of Symbol Probability

The probability associated with a certain cell of the route-table quantifies the likelihood of the corresponding symbol-value being transmitted, which is re-estimated during each ACO-based search iteration due to the update of the pheromone level associated with each cell constituting the route-table. The two probabilities associated with the two cells constituting a certain column of the route-table should always sum to unity, regardless of the probability associated with each cell. The bits associated with the pair of cells constituting the kth column for $k = 1, 2, \ldots, K$ jointly quantify the ACO-based MUD's estimate of the bits transmitted by the kth user. Naturally the sum of the two probabilities of the pair of legitimate bits transmitted by the kth user should be one, for $k = 1, 2, \ldots, K$. Therefore, given the merit of each cell quantified during the nth ACO-based search iteration as $\mathfrak{m}_{ik}^{(n)}$, for $i = 1, 2$ and $k = 1, 2, \ldots, K$, the probability $P_{+k}^{(n)}$ (or $P_{+k}^{(n)}$) of the bit $+1$ (or -1) being transmitted by the kth user is defined as the ratio of

$$P_{ik}^{(n)} = \frac{\mathfrak{m}_{ik}^{(n)}}{\mathfrak{m}_{1k}^{(n)} + \mathfrak{m}_{2k}^{(n)}}. \tag{3.24}$$

Furthermore, the merit $\mathfrak{m}_{ik}^{(n)}$ of each cell constituting the route-table is jointly determined by the intrinsic affinity η_{ik} and the pheromone $\tau_{ik}^{(n)}$ associated with it. The relative importance of the two components η_{ik} and $\tau_{ik}^{(n)}$ may be adjusted with the aid of the exponents α and β that are non-negative scalars, yielding η_{ik}^{β} and $(\tau_{ik}^{(n)})^{\alpha}$. Then the merit of the (i, k)th cell during the nth iteration is quantified by the product

$$\mathfrak{m}_{ik}^{(n)} = (\tau_{ik}^{(n)})^{\alpha} \eta_{ik}^{\beta}. \tag{3.25}$$

Upon substituting the merit $\mathfrak{m}_{ik}^{(n)}$ from Eq. (3.25) into Eq. (3.24), the bit probability associated with the (i,k)th cell during the nth ACO-based search iteration may be quantified as

$$P_{ik}^{(n)} = \frac{\left(\tau_{ik}^{(n)}\right)^{\alpha} \cdot \eta_{ik}^{\beta}}{\left(\tau_{1k}^{(n)}\right)^{\alpha} \cdot \eta_{1k}^{\beta} + \left(\tau_{2k}^{(n)}\right)^{\alpha} \cdot \eta_{2k}^{\beta}} \tag{3.26}$$

for the row index $i = 1, 2$, column index $k = 1, 2, \ldots, K$ and iteration index $n = 1, 2, \ldots, \Xi$.

3.4.5.2 Properties of the Symbol Probability

The probabilities seen on top of the bars in Part (II) of Fig. 3.10(a)∼(i) quantify the likelihood of the legitimate symbols $\{+1, -1\}$ being transmitted by the $K = 5$ users. As illustrated in Part (II) of Fig. 3.10(a)∼(i) during each of the nine iterations, the sum of the two probabilities associated with the complementary cells constituting the same column is always unity. During each iteration, based on the $2 \times 5 = 10$ bit probabilities seen in Part (II), the probabilities of any of the thirty-two legitimate $K = 5$-symbol vector may be readily calculated as the product of the $K = 5$-bit probabilities seen on top of the five cells. Naturally, the sum of the thirty-two vector probabilities is also unity. Additionally, the probabilities associated with the two legitimate bit values of the $k = 1$st user is 1 and 0, as shown in Fig. 3.10(a) Part (I). Then the probabilities of all the sixteen $K = 5$-bit vectors having a 1st bit of $v_1 = +1$ are zero, since the product of $0 \cdot P_{i2} \cdot P_{i3} \cdot P_{i4} \cdot P_{i5}$ is zero, regardless of the values of P_{ik}, $i = 1, 2$ and $k = 2, \ldots, 5$, as also observed from Table 3.2. By contrast, the joint total probability of all the other sixteen vectors having $v_1 = -1$ is one. As a result, Part (III) of each of Fig. 3.10(a)∼(i) only portrays the legitimate received signals corresponding to the sixteen $K = 5$-bit vectors having probabilities larger than zero. The sixteen vectors of Part (III) in Fig. 3.10(a)∼(i) constitute the first-half of the ranked list of vectors in Table 3.8 having LLFs larger than zero.

1. Inconsistency between the pheromone-level and the bit probability

The bit probability associated with each cell is jointly determined by the pheromone-level and the intrinsic affinity associated with that cell. As seen from the ten bit-probabilities written on top of the bars during the 1st iteration illustrated in Fig. 3.10(a) Part (I), when the pheromone associated with each cell is as low as $\tau_{ik}^{(1)} = 0.01$, the probability P_{ik} associated with the (i,k)th cell is proportional to the ratio of the weighted intrinsic affinity η_{ik}^{β} and the sum of the two weighted intrinsic affinities $\eta_{\pm k}^{\beta}$ associated with the pair of cells constituting the kth column, as illustrated in Fig. 3.13(b).

The weighting factor of the intrinsic affinity and of the pheromone level of our example was set to $\beta = 6$ and $\alpha = 0.9$. As a result, the dynamic range of η_{ik}^{β} and $(\tau_{ik}^{(n)})^{\alpha}$ is about $0 \sim 70$, as illustrated in Fig. 3.13(b) and in Fig. (3.10)(a)∼(i) Part (II). Thus, the influence of the intrinsic affinity and of the pheromone level may be deemed comparable.

As a result, although the pheromone-level associated with the route-table is biased towards the elite vector, as discussed in the last few paragraphs of Section 3.4.4.2, the bit-probabilities which directly determine the K-bit vectors in the search-pool during each iteration are not always consistent with the pheromone-level. As exemplified by Fig. 3.10(d) Part(I), although the pheromone-level associated with the two cells constituting the 3rd column of the route-table are approximately $\tau_{-3}^{(4)} = 53$ and $\tau_{-3}^{(4)} = 38$, the bit-probabilities associated with the same cells are $p_{-3}^{(4)} = 0.49$ and $p_{-3}^{(4)} = 0.51$. This is a consequence of the substantial influence of the intrinsic affinities, as illustrated in Fig. 3.13,

where the two cells have the weighted intrinsic affinities of $\eta_{-3}^6 = 1.94^6 = 51.97$ and $\eta_{-3}^6 = 2.06^6 = 76.20$, respectively. This inconsistency between the 'highest-pheromone' K-bit vector and the 'highest-probability' K-bit vector may also be observed during the 6th and the 7th iteration of our five-user example characterized in Fig. 3.10(f) and (g). As illustrated in Fig. 3.10(f) Part (I) during the 6th iteration, the pheromone-level associated with the $(-1, 4)$ cell is lower than that of the cell $(+1, 4)$, whilst the bit-probability of $P^{(n)}(v_k = -1) = 0.56$ is higher than the 0.44 probability of the other cell. Additionally, as illustrated in Fig. 3.10(g) Part (I), the pheromone-level associated with the $(-1, 4)$ cell is lower than that of the cell $(+1, 4)$, albeit the bit probability of $P^{(n)}(v_k = -1) = 0.50$ is nearly equivalent to that of the other cell.

The influence of the intrinsic affinities - which is linked to the MF outputs' real part - on calculating the bit-probability delays the convergence of the vectors in the search-pools to the elite vector, as will be detailed in Section 3.4.6.2 after highlighting the algorithm's operation as well as the properties of search-pool.

3.4.6 Creating the search-pool

3.4.6.1 Methodology

The surfaces plotted in Part (III) during each of the nine iterations in Fig. 3.10(a)∼(i) characterize the probabilities of all the sixteen vectors having a first bit of -1, as listed in Fig. 3.8 during each of the nine iterations. The probabilities of all the legitimate K-bit vectors being transmitted may be calculated as the product of the K individual bit-probabilities. However, we would like to avoid calculating all the 2^K vector probabilities, since we aim for reducing the exponentially increasing complexity imposed by the ML algorithm.

The search-pool is defined as a $(\zeta \times K)$-element matrix, where ζ is the number of K-bit vectors generated during each search-iteration, as illustrated in Fig. 3.15. To be consistent with the size of the $(K \times 1)$-bit transmit signal column vector $\mathbf{v}$, each vector is also treated as a column in the matrix.

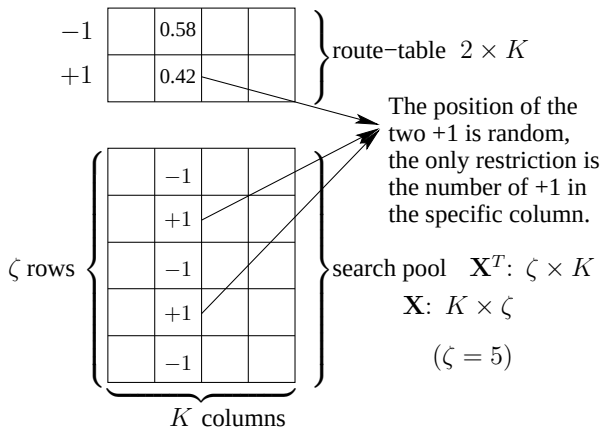

Figure 3.15: Example of the kth column constituting the search-pool according to the two symbol-probabilities associated with the two cells constituting the kth column of the route-table, for $k = 2$ and $\zeta = 5$.

The ζ vectors in the search-pool are generated on a bit-by-bit basis. In other words, the generation

of the ζ bits for the kth symbols of all the ζ vectors in the search-pool we only consider the two probabilities associated with the two cells constituting the kth column of the route-table. Additionally, the generation of the kth column of the search-pool $\mathbf{X}^T$ is not affected either by the two probabilities in any of the other $(K-1)$ columns or by the bits constituting the other $(K-1)$ columns of the $(\zeta \times K)$-element search-pool matrix $\mathbf{X}^T$.

The probability associated with a cell of the search table should match the ratio of the number of ants choosing the cell divided by the total number of ants ζ. More quantitatively, given the two probabilities $P_{\pm k}$ and the total number of ants ζ, $\lfloor \zeta \cdot P_{-k} \rceil$ number of ants will choose -1 for the kth symbol, where the notation of $\lfloor x \rceil$ represents the integer nearest to the decimal number x. This is exemplified in Fig. 3.15 in conjunction with $\zeta = 5$, $P_{-2} = 0.58$, $P_{+2} = 0.42$. Hence $\lfloor 5 \cdot 0.42 \rceil = \lfloor 2.1 \rceil = 2$ number of '+1' bits will appear in the 2nd column of the search-pool $\mathbf{X}^T$.

Given the $(2 \times K)$-bit probabilities associated with each cell constituting the route-table, as shown in Fig. 3.10(a)∼(i) Part (I), the ζ vectors constituting the search-pool shown in Fig. 3.10(a)∼(i) Part (II) are represented by ζ number of routes. The shape of each unique route is described by a vector and the width of the route seen in Fig. 3.10(a)∼(i) Part (II) quantifies the number of vectors having the same vector elements. Hence the number of routes passing through a certain cell $(\pm k)$, associated with $k = 1, \ldots, 5$ in Fig. 3.10(a)∼(i) Part (II) should be equal to $\lfloor \zeta \cdot P_{\pm k} \rceil$, which is the integer nearest to ζ multiplied by the probability associated with the specific cell, as indicated by the decimal numbers seen on top of the bars in Fig. 3.10(a)∼(i) Part (I). For example, we have $P_{-3} = 0.68$ and $P_{+3} = 0.32$ in Fig. 3.10(h) Part (I), given $\zeta = 10$ in our $K = 5$-user example. Hence the number of 'artificial ants' passing through the $(-1, 3)$ cell of Fig. 3.10(h) Part (II) is the integer nearest to (10×0.68), yielding 7. The width of the two bold lines seen in Fig. 3.10(h) Part (II) are 4 and 3 units, respectively, corresponding to the 4 observations of $\mathbf{v}_{21}^{(5)}$ and 3 observations of $\mathbf{v}_{23}^{(5)}$ in the search-pool that are illustrated by crosses seen on top of the legitimate received signals in Fig. 3.10(h) Part (III). The number of routes including the $(+1, 3)$ cell is the integer nearest to (10×0.32), yielding 3.

3.4.6.2 Properties of the search-pool

1. Inconsistency between the 'prediction' and actual K-bit vector probability

A unique set encompassing the 2^K vector probabilities associated with the 2^K legitimate K-symbol vectors may be obtained from $\mathbf{P}^{(n)}$ encompassing all the $2 \cdot K$ symbol probabilities associated with each cell of the $(2 \times K)$-element route-table during the nth iteration. Before the search-pool is generated for a specific iteration, these vector probabilities may be obtained beforehand. Hence these theoretically calculated probabilities may be referred to as 'predicted' vector probabilities. More specifically, given $\dot{\mathbf{v}}^{(K)} = [\dot{v}_1, \dot{v}_2, \cdots, \dot{v}_K]$, the predicted vector probability associated with the trial vector may be readily expressed as

$$P_{\mathrm{p}}^{(n)}(\dot{\mathbf{v}}^{(K)}) = \prod_{k=1}^{K} P^{(n)}(\dot{v}_k), \tag{3.27}$$

where the bit-probability $P^{(n)}(\dot{v}_k)$ may be picked from the matrix $\mathbf{P}^{(n)}$.

Another K-bit vector-probability associated with each K-bit vector during each iteration may be termed as the actual vector-probability, which can only be determined after all the ζ vectors

constituting the search-pool were generated. Then the actual vector probability $P_{\text{a}}^{(n)}(\dot{\mathbf{v}}^{(K)})$ of a trial vector $\dot{\mathbf{v}}^{(K)}$ during the nth iteration is defined as the ratio of the number of vectors in the search-pool taking value $\dot{\mathbf{v}}^{(K)}$ and of the total number of vectors ζ in the search-pool.

The 'predicted' vector probability $P_{\text{p}}^{(n)}(\dot{\mathbf{v}}^{(K)})$ of a legitimate trial vector $\dot{\mathbf{v}}^{(K)}$ may deviate from the actual vector probability $P_{\text{a}}^{(n)}(\dot{\mathbf{v}}^{(K)})$ for two reasons, as detailed below.

1. A large number of possible search-pool vectors may be generated according to a given bit-probability matrix based on the random positions of the ζ bits in each column of the search-pool.

To elaborate a little further, the number of logical -1 or $+1$ values appearing in a certain column of the search-pool may be simply determined on the basis of their probability. The specific row indexes within the column do not have to be stipulated. As a result, given $P_{\pm k}^{(n)}$ and the number of ants ζ, the number of ζ-bit-columns containing $\zeta_{-k}^{(n)}$ number of '-1' values and having the remaining $\zeta_{+k}^{(n)}$ number of symbols as '$+1$' may be expressed as

$$\mathbf{C}_{\zeta}^{\zeta_{-k}^{(n)}} = \binom{\zeta}{\zeta_{-k}^{(n)}} = \frac{\zeta!}{\zeta_{-k}^{(n)}!(\zeta - \zeta_{-k}^{(n)})!}, \tag{3.28}$$

where we have $\zeta_{-k}^{(n)} = \zeta \cdot P_{-k}^{(n)}$. Then the number of possible K-column search-pool vectors is given by $\mathbf{P}^{(n)}$, which is the product of the number of entries given by Eq.(3.28), yielding $\prod_{k=1}^{K} \mathbf{C}_{\zeta}^{\zeta_{-k}^{(n)}}$. Therefore, the search-pool generated during the nth iteration is only a specific manifestation of all the $\prod_{k=1}^{K} \mathbf{C}_{\zeta}^{\zeta_{-k}^{(n)}}$ possible candidates.

An example of two different manifestations of the search-pool generated according to the same probability matrix is shown in Fig. 3.16, where we have $K = 2$ and $\zeta = 4$. The (2×2) route-table and the associated bit-probability of each cell is seen at the left of Fig. 3.16(a). Furthermore, the vector-probabilities of all the four vectors calculated from the four bit-probabilities by applying Eq. (3.27) are seen at the right of Fig. 3.16(a). The two different (4×2)-element search-pools seen in Fig. 3.16(b) (I) and Fig. 3.16(b) (II) are both generated according to the bit-probabilities shown in Fig. 3.16(a). However, the actual probabilities of the four vectors in the search-pool shown in Fig. 3.16(b) (I) are significantly different from the predicted probabilities calculated from the route-table shown at the left-hand side of Fig. 3.16(a). On the other hand, the actual probabilities of the four vectors in the search-pool of Fig. 3.16(b) (II) are identical to the predicted values shown in Fig. 3.16(a).

2. The 'predicted' probability of a trial vector may also deviate from the actual vector probability, because the size of the search-pool may be insufficiently large for the sample to match the predicted probabilities.

The deviation of the search-pool content from its prediction may be observed in Fig. 3.8 and in Fig. 3.10(a) ∼(i) Part (III) in the $K = 5$-user example as well. Both the bars plotted in Fig. 3.8 as well as the surfaces plotted in Fig. 3.10(a)∼(i)(III) quantify the 'predicted' probabilities associated with the sixteen vectors whose predicted probabilities of occurrence in the search-pool are non-zero. The simulation results provided for our $K = 5$-user example in Fig. 3.8 and in Fig. 3.10(a) ∼(i) Part (III) were selected so that the actual probability of each vector in the search-pool during each iteration approaches its predicted probability as closely as possible. This is highlighted in Fig. 3.17, illustrating the match between the 'predicted' and the actual probabilities associated with the ML solution in the search-pool of the specific simulation scenario previously portrayed in Fig. 3.10. Since the number of

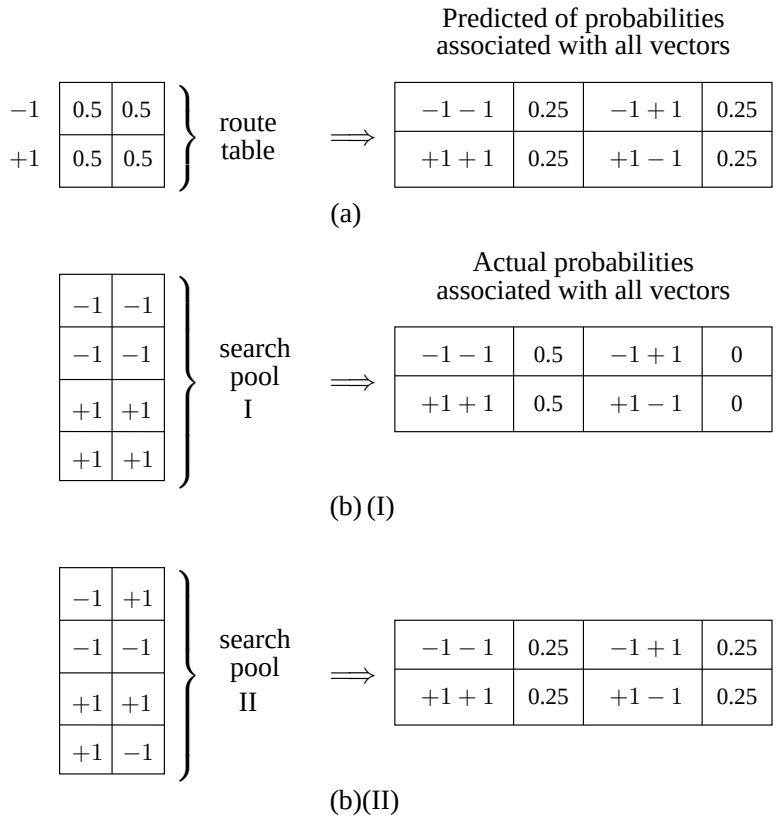

Figure 3.16: Example of two search-pool manifestations according to the same bit-probabilities associated with the route-table (a). As a result, the proportions of the four legitimate vectors constituting the two different search-pools seen in (b) I and (b) II are different.

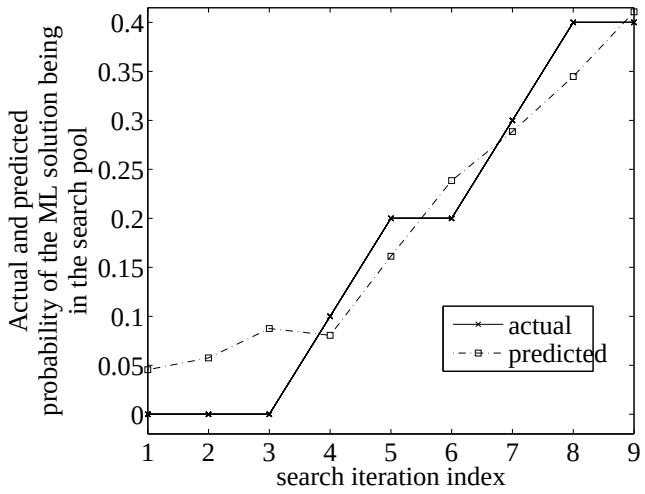

Figure 3.17: The 'predicted' and the actual probability of the ML solution being in the search-pool, which is calculated by consecutively multiplying the relevant symbol-probabilities retrieved from the matrix $\mathbf{P}^{(n)}$ as well as the actual probabilities of the ML solution being part of the $\zeta = 10$ vectors constituting the search-pool during each ACO-based search iteration for the system parameters given in Table 3.1.

trials is not sufficiently high, given that only $\zeta = 10$ vectors are in the search-pool, the actual relative frequency of a certain vector in the search-pool does not always accurately match its predicted value. For example, when the 'predicted' vector probabilities of $\mathbf{v}_{23}^{(5)}$, $\mathbf{v}_{18}^{(5)}$ and $\mathbf{v}_{28}^{(5)}$ are all higher than that

associated with $\mathbf{v}_{17}^{(5)}$, and the predicted number of ants associated with these vectors determined by $\lfloor \zeta \cdot P_{\mathrm{p}}^{(1)}(\mathbf{v}_{23}^{(5)}) \rceil$, $\lfloor \zeta \cdot P_{\mathrm{p}}^{(1)}(\mathbf{v}_{18}^{(5)}) \rceil$ and $\lfloor \zeta \cdot P_{\mathrm{p}}^{(1)}(\mathbf{v}_{28}^{(5)}) \rceil$ is one, then none of $\mathbf{v}_{23}^{(5)}$, $\mathbf{v}_{18}^{(5)}$ and $\mathbf{v}_{28}^{(5)}$ is selected for inclusion in the search-pool of the 1st iteration, given that the size of the search-pool is equivalent to the number of ants ζ.

2. search-pool diversity for avoiding early convergence

Having a sufficiently diverse population for the sake of avoiding premature convergence of the vectors in the search-pool during the nth iteration is determined by the bit-probability matrix $\mathbf{P}^{(n)}$, since the ζ vectors constituting the search-pool are generated with the aid of $\mathbf{P}^{(n)}$.

More specifically, if the difference between the predicted and actual probabilities is small, then there will be more 'diverse',i.e. dissimilar K-bit vectors among the ζ vectors in the search-pool.

As shown during the 1st iteration of our five-user example in Fig. 3.10(a) Part (I), the bit-probabilities seen on top of the cells ranging from the 2nd to the 5th column are all relatively close to 0.5, which results in a relatively high degree of vector-diversity i.e. dissimilarity in the search-pool. As illustrated by both Fig. 3.8 as well as Fig. 3.10(a) Part (II) and Fig. 3.10(a) Part (III), nine different vectors emerge among the $\zeta = 10$ vectors of the search-pool during the 1st iteration. By contrast, observe in the search-pool during the 2nd iteration that a certain tendency to converge to $\mathbf{v}_{17}^{(5)}$ is visible, since now three vectors in the search-pool assume the value of $\mathbf{v}_{17}^{(5)}$ in Fig. 3.10(b) Part (III). As a result, the number of different K-bit vectors found in the search-pool during the 2nd iteration is reduced from nine to seven. Furthermore, since the four different bit-probabilities of the two cells constituting the other four columns are gradually increased, the number of different K-bit vectors appearing in the search-pool is further reduced from seven to six during the 3rd, 4th, 5th iteration and finally to five during the 7th, 8th and 9th iteration, as readily observed from Fig. 3.10(b)∼(i) Part (II) and Fig. 3.10(b)∼(i) Part (III). The above-mentioned observation is further augmented by Fig. 3.18.

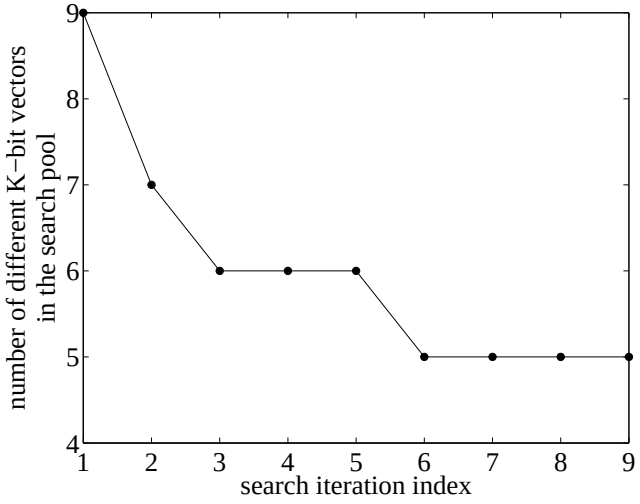

Figure 3.18: Number of different K-bit vectors among the $\zeta = 10$ vectors in the search-pool during each ACO-based search iteration for the system parameters of Table 3.1.

When the difference of the symbol-probabilities associated with the two cells constituting the same column is increased, more and more ants will choose the same route representing the most likely K-bit

vector. Thus a gradual convergence is observed.

Throughout the search process illustrated in Fig. 3.10, the search-pool has been converging towards the MF solution of $\mathbf{v}_{20}^{(5)}$ during the 1st iteration, towards $\mathbf{v}_{17}^{(5)}$ during the 2nd iteration, $\mathbf{v}_{19}^{(5)}$ during the 3rd iteration, $\mathbf{v}_{19}^{(5)}$ and $\mathbf{v}_{23}^{(5)}$ during the 4th iteration, $\mathbf{v}_{23}^{(5)}$ during the 5th iteration, the 6th iteration, and finally returning to the ML solution $\mathbf{v}_{21}^{(5)}$ during the 7th, the 8th and the 9th iteration. The change in the center of convergence versus the search-pool iteration index is the stepwise linear Curve III in Fig. 3.14.

3. Convergence of the search-pool to the elite K-bit vector

As discussed in Section 3.4.4.2, the convergence or appearance to the elite K-bit vector is slower than the initial emergence of the elite vector. However, the convergence of the search-pool to the elite K-bit vector is even slower than that of the pheromone-level. This is simply owing to the joint consideration of the pheromone and the intrinsic affinity, when the bit-probabilities are evaluated, which in turn are used to generate the ζ vectors constituting the search-pool.

When comparing the stepwise linear Curves II and III in Fig. 3.14, the above-mentioned slower convergence of the search-pool to the ML solution compared to that of the pheromone does not become conspicuous before the 6th iteration, as seen in Fig. 3.10(b)(c)(e) Part (I).

As observed in Fig. 3.10(d) Part (I), the highest-'pheromone' vector is $\mathbf{v}_{23}^{(5)} = [-1, +1, -1, -1, +1]$, but since the difference between the pheromone-level associated with the two cells of the 3rd column is not so significant, the pheromone-related convergence process from $\mathbf{v}_{17}^{(5)} = [-1, +1, +1, +1, +1]$ to $\mathbf{v}_{23}^{(5)}$ was completed during the 4th iteration. Therefore, the bit-probabilities associated with the pair of cells in the 3rd column is predominantly determined by the intrinsic affinities of $\eta_{-3}^{6} = 53.97$ and $\eta_{+3}^{6} = 76.2$, as shown in Fig. 3.13(b), which exhibit a more substantial difference than the pheromone densities. There is a similar reason behind the inconsistency observed between the pheromone-level and the bit-probability associated with the pair of cells constituting the 4th column during the 6th and 7th iteration, as shown in Fig. 3.10(f) Part (I) and Fig. 3.10(g) Part (I), respectively. Therefore, when the pheromone-level of a certain K-bit vector is not particularly high, the convergence of the search-pool population to the highest-pheromone vector will be further slowed down by taking into account the intrinsic affinity, which determines the bit-probabilities.

Hence, the speed of the pheromone-based convergence to the elite K-bit vector can be adjusted by appropriately tuning the parameters ρ and σ of Eq. (3.23) and Eq. (3.22), which control the effect of the pheromone and the weight of the elite vector's incremental pheromone, respectively. Apart from ρ and σ in Eq. (3.23) and Eq. (3.22), the speed of the search-pool population's convergence may also be adjusted by tuning the parameters α and β, which quantify the weight of the pheromone and the intrinsic affinity, respectively. More specifically, increasing the value of ρ, β or decreasing the value of σ, α, results in reducing the speed of convergence of the search-pool's population to the elite vector. By contrast, decreasing the value or ρ, β or increasing the value of σ, α results in increasing the convergence speed of the search-pool's population to the elite K-bit vector.

3.5 Summary of the ACO-based MUD Algorithm

3.5.1 Global view of the ACO-based MUD algorithm

Based on the search process exemplified in Fig. 3.10 and on the combined effects of all the parameters, the following conclusions may be drawn regarding the ACO-based MUD algorithm.

1. Observe in Table 3.1 in conjunction with Fig. 3.13(a) that the closer the real part of the MF output $\Re\{y_k\}$ to 0, the lower the influence of the corresponding MF solution of $\text{sgn}(\Re\{y_k\})$ becomes. As a result, the two intrinsic affinities of $\eta_{\pm k}$ are close to two and the two symbol probabilities of $P^{(1)}(v_k = \pm 1)$ are close to 0.5 during the 1st iteration. Therefore the ζ vectors in the search-pool become more dissimilar or diverse during the 1st iteration. Hence we have an increased chance for the vectors different from the MF solution to emerge in the search-pool during the 1st iteration.

2. The K-bit vectors, whose LLFs are scattered around the MF-solution's LLF value will be favoured for inclusion in the search-pool during the 1st iteration, as observed from Fig. 3.5.

3. The specific K-bit vector having the highest LLF will be chosen as the elite vector during a search iteration, and the pheromone-level will be increased along the elite-route representing the elite K-bit vector during both the current and the next iteration. Then the LLFs of all the K-bit vectors appearing in the search-pool during the next iteration will be clustered around the LLFs of the elite K-bit vector.

4. Recall from Fig. 3.14 that owing to the influence of the existent pheromone-level and due to the contribution of the intrinsic affinity, the convergence of the search-pool's population to the elite K-bit vector is typically delayed by a few iterations to the fist emergence of the elite K-bit vector.

5. The delayed convergence of the search-pool population to the elite K-bit vector allows the emergence of new vectors, whose LLFs are centered around the LLF of the elite vector, which may in fact have superior LLF.

6. The above steps 4 and 5 are repeated, until the globally optimal K-bit vector was found or the affordable complexity was exhausted.

7. Finally, all the ants will converge to the globally optimal route corresponding to the ML solution.

3.5.2 Effect of the ACO-MUD parameters

- Throughout the entire search process carried by the ACO-based MUD algorithm, as exemplified in Fig. 3.5(a), the search-pool's population gradually evolves from a group of diverse or dissimilar K-bit vectors centered around the MF solution to the K-bit ML solution.
- The search-pool's vectors are centered around the elite K-bit vector having the highest LLF among all the vectors captured by the search-pool so far.
- The *direction* of the search-pool's evolution is controlled by the pheromone, where the pheromone is proportional to sum or average of the LLFs of all the vectors captured during the most recent iteration. The direction of evolution is particularly influenced by the amount of incremental pheromone, leading to the elite K-bit vector.

- The *speed* of search-pool's population evolution is jointly controlled by α, β, σ and ρ, which are the weight of the pheromone, the weight of the intrinsic affinity, the weight of the elite vector and the pheromone evaporation rate, respectively.
- Since the search-pool evolution process considered endeavors to host a population centered around the elite vector, once the *globally optimal* K-bit vector is captured, no new elite vector will be found during the remaining iterations, as illustrated by the subplots ranging from 'iter 4' to 'iter 8' in both Fig. 3.5(a) and (b). Hence, the globally optimal K-bit vector will be deemed to be the elite K-bit vector throughout the remaining search iterations.
- As a result, the pheromone-level of the globally optimum ML solution will be repeatedly increased allowing the entire search-pool to gradually *converge* to the globally optimal solution again, as inferred from the subplots ranging from 'iter 4' to 'iter 8' in Fig. 3.5(b).

Below, we will continue our discussions regarding the effects of each parameter listed in Table 3.4 in more detail.

1. A high β in Eq. (3.26) will speed up the search-pool population's evolution driven by the pheromone-level;
2. A high σ in Eq. (3.22) will expedite the convergence of the search-pool's evolution towards the elite K-bit vector;
3. Increasing α of Eq. (3.26) will result in a consistently high influence of the initial search-pool population, which is determined by the MF output's real part, hence reducing the speed of its convergence, as driven by the pheromone-level.
4. A high ρ in Eq. (3.23) will further slow down the convergence of the search-pool population's evolution to the elite vector by reducing the convergence rate of the pheromone to the elite K-bit vector through emphasizing the influence of the existent pheromone-level.
5. However, the appropriate choice of β and ρ in Eqs. (3.26) and (3.23) will prevent the search-pool's population from pre-maturely converging to a sub-optimal elite K-bit vector before the globally optimum ML solution is captured.
6. A high ζ value results in a large search-pool, which may result in an increased complexity.
7. However, too small a ζ value may reduce the chance of the search-pool to capture a new elite K-bit vector having a superior LLF in comparison to the current elite vector-LLF; or it way further slow down the search-pool's convergence rate.
8. Finally, the number of iterations Ξ should also be appropriately selected, so that the globally optimal ML solution may be captured, before the affordable number of Ξ search iterations was exhausted and without imposing an unnecessarily high complexity.

The above conclusions and performance trends have also been summarized in Table 3.6.

Parameter implication		Pheromone Convergence		search-pool Convergence		Complexity		Par. value
		Rapid	Slow	Rapid	Slow	High	Low	
Evaporation rate	ρ	$\downarrow$	$\uparrow$	$\downarrow$	$\uparrow$	$\uparrow$	$\downarrow$	0.5
Weight for the elite ant	σ	$\uparrow$	$\downarrow$	$\uparrow$	$\downarrow$	$\downarrow$	$\uparrow$	8
Weight of pheromone	α			$\uparrow$	$\downarrow$	$\downarrow$	$\uparrow$	0.9
Weight of intrinsic affinity	β			$\downarrow$	$\uparrow$	$\uparrow$	$\downarrow$	6
Number of ants	ζ			$\uparrow$	$\downarrow$	$\uparrow$	$\downarrow$	10
Number of iterations	Ξ					$\uparrow$	$\downarrow$	10

Table 3.6: Effect of each parameters of the ACO-based MUD algorithm on the behaviour of the optimization process, where 'High' and 'Low' indicates the effect of a particular parameter in a specific row on the system's complexity.

3.5.3 ACO versus ML algorithm

We will predict the attainable BER performance as well as the complexity imposed by the ACO-based MUD algorithm compared to that of the ML MUD algorithm in the context of our $K = 5$-user example.

1. Near-ML BER performance

1. Provided that all the parameters have been set appropriately, namely as discussed in Section 3.5.2, the ML solution will be finally captured by the search process of the ant-colony-based MUD optimization algorithm, which emerges from the MF solution, as summarized in Section 3.5.1.

2. Therefore, the BER of the system employing the ACO-based MUD algorithm should not be inferior to that employing the ML MUD algorithm.

This is verified by our five-user example as illustrated in Fig. 3.5, Fig. 3.8 and Fig. 3.10 and will be further demonstrated in Chapters 4 and 5, when the ACO-based MUD algorithm is applied in a Multi-Functional Antenna Array (MFAA)-assisted MC DS-CDMA system and in an STBC-aided cooperative DS-CDMA system.

2. Reduced Complexity

1. The complexity imposed by the ACO-based MUD algorithm is predominantly due to the calculation of the LLFs of all the K-bit vectors captured in the search-pool throughout the search process.

Hence the complexity varies from symbol-duration to symbol duration. More specifically, on one hand the complexity depends on the parameters of the algorithm, such as the search-pool size ζ, the maximum number of affordable search iterations Ξ, etc as indicated in Table 3.6. On the other hand, the complexity is also related to the CIR of each symbol transmitted by the users supported by the system as well as on the AWGN level encountered during a specific symbol duration.

An extreme scenario to consider is, when the CIR and the AWGN during a certain symbol duration leads to high MF output real parts for all the users. Then the high intrinsic affinities associated with the all cells resembling the MF solution will result in symbol probabilities for all these cells, which hence results in having identical K-bit vectors in the search-pool during the 1st iteration, which is the MF solution. In this scenario the LLF only has to be evaluated once.

This does not prevent the system from achieving a near-ML BER, as detailed below. The associated high MF output real part also implies having a high influence for the MF solution, which indeed has a sufficiently high probability to be the ML solution.

2. The complexity of the exhaustive search imposed by the ML MUD is constant, regardless whether the MF solution is or is not the globally optimal solution.

Similarly, regardless of the channel conditions, the vector-LLFs have to be evaluated 2^K times for every symbol duration, when searching for the globally optimal solution. Naturally, when the complexity imposed may become un-affordable.

3. By contrast, the search carried out by the ACO-based MUD algorithm is focussed on the vectors having high vector-LLFs, instead of the exhaustive search carried out by the ML-based MUD algorithm, as illustrated in Fig. 3.5.

Secondly, as discussed above, the complexity of the ACO-based MUD is also determined by the Hamming or Euclidean distance between the MF and the ML solution. When the MF solution is also the globally optimum solution with a high probability, the complexity imposed by the ACO-based MUD algorithm may be further reduced.

4. Therefore, the complexity imposed by the ACO-based MUD algorithm is expected to be substantially lower than that of the ML algorithm, especially when the number of users supported by the system is high.

This was exemplified by our detailed $K = 5$-user example. Although the MF solution was far from the ML solution, the ACO-based search process required the LLF values of only 13 K-bit vectors in order to capture the globally optimum ML solution, as observed in Fig. 3.5, Fig. 3.8 or Fig. 3.10. By contrast, the LLFs of all the thirty-two legitimate vectors have to be calculated for the ML MUD in order to find the ML solution.

These facts will be further demonstrated in Chapter 4 and Chapter 5, when the ACO-based MUD algorithm will be applied in a MFAA assisted MC DS-CDMA system and in a STBC aided cooperative DS-CDMA system, respectively.

3.5.4 ACO versus Genetic Algorithm Aided MUD

Below we will provide a brief comparison between the ACO-baesd MUD and the GA-based MUD, both of which are population-based optimization algorithms developed from the biological instincts of ants and from the generic principles of evolution. They both endeavor to find the globally optimal solution at a significantly lower complexity than the ML algorithm.

The flow-chart of the GA-based MUD algorithm is illustrated Fig. 3.19. In a K-user system, the ACO-based MUD algorithm differs from the GA-based MUD algorithm in two important aspects.

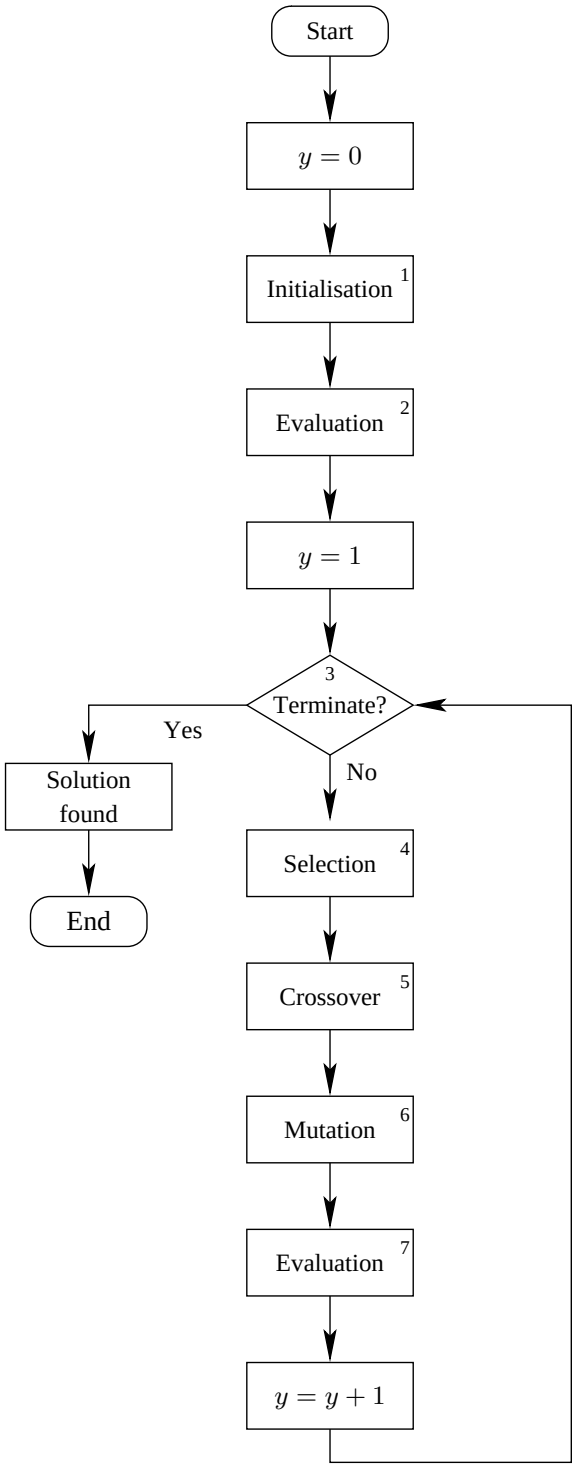

Figure 3.19: Flow chart of the GA-based MUD algorithm.

1. Most manipulations in the GA-based MUD algorithm operate on the entire K-symbol vector as a whole. By contrast, most of the operations in the ACO-based MUD algorithm are carried out on a bit-by-bit basis.

2. The bit-based processes in the GA-aided MUD algorithm are typically guided random processes, while the bit-by-bit operations of the ACO-based MUD algorithm are driven by the bit-probabilities.

Below we will elaborate on the above two points in more detail.

3.5.4.1 Bit-by-bit versus vector-based operation

1. ACO-based MUD algorithm

In terms of the ACO-based MUD algorithm, the $(2 \times K)$-element *route-table* converts the 2^K legitimate vectors to $2K$ legitimate bits, which allows most of the functions of the optimization algorithm to be realized on a bit-by-bit basis.

For instance, the driving force of the convergence, namely the increased amount of pheromone as well as the factor preventing premature convergence, namely the intrinsic affinity and the retention of a fraction of the existing pheromone, constitute properties associated with each of the $2K$ legitimate bits.

Naturally, the bit-by-bit based functions do not prevent the ACO-based MUD algorithm from employing the information obtained on a K-bit vector basis. For example, the objective function allows us to take into account the effect of co-channel users, as indicated by Step 7 of Fig. 3.9. However, this information is ultimately exploited to update the properties of each bit of a K-bit vector, as represented by the 'pheromone update' process of 'Step 3' in Fig. 3.9.

In conclusion, as specified in Section 3.3, the initial search-pool of the ACO-based MUD algorithm is generated with the aid of the MF outputs. The ACO MUD exploits the fitness of the entire K-bit vector to update its constituent bit probabilities, since each of the $2K$ bits of the route-table is shared by 2^{K-1} K-bit vectors.

2. GA-based MUD algorithm

By contrast, since there is no 'route-table' in the GA-based MUD algorithm, the beneficial bit-by-bit operations of the ACO-based MUD cannot be exploited.

Indeed, diverse algorithms may be employed by the GA-aided MUD's initialization block of Step 1 in Fig. 3.19 so that the initial K-bit vectors are not generated randomly. For example, the MF can be used as the basis of toggling all the K bits in the interest of finding improved 'individuals' for the initial pool.

The individual steps of the GA-aided MUD were detailed in [93].

3. Advantages of bit-by-bit ACO operations

The advantages of the bit-by-bit operations are briefly summarized below:

1. The exploitation of the bit-probabilities will avoid unintelligent random manipulations, hence avoiding the generation of low-probability K-bit vectors, which allows us to reduce the complexity imposed.

2. The ACO MUD was an intricate control over each of the legitimate bits of the K-bit vector, as will be detailed in Chapter 6.

A further aspect worth of mentioning is the two-way conversion between bit-based processing and vector-based processing achieved by the ACO-based MUD algorithm. On one hand, the 'pheromone update' process portrayed in Step 3 of Fig. 3.9 converts the K-bit vectors to bit-based quantities. On the other hand, the 'search-pool generation' process represented by Step 5 in Fig. 3.9 converts the bit-based manipulations to vector-based operations to be carried out in Step 6 and Step 7 of Fig. 3.9.

3.5.4.2 Random versus Probabilistic Search

There is no direct provision in the GA-based MUD algorithm for evaluating the bit-probabilities. In other words, the probability of each of the $2K$ bits is inaccessible in the GA-based MUD algorithm. To circumvent this problem, the concept of the so-called population-based soft GA MUD of [94] was conceived. Nonetheless, bit-based operations, such as the cross-over and mutation of the K-bit vectors may be employed by the GA-based MUD algorithm in order to support the 'evolution' of the GA's K-bit individuals as detailed in Table. 3.7. By contrast, the 'evolution' of the search-pool's evolution carried out in the ACO-based MUD algorithm is directed by the bit-probability quantifying the normalized merit of the relevant symbol.

Compared to the ACO-based MUD, the optimization process implemented by the GA-based MUD is not guided by the bit-probabilities, it is rather more randomly oriented. Hence the GA-based MUD may require a larger population size for finding the globally optimum ML solution.

For example, in the GA-based MUD the bits of the candidate vector are randomly mutated. By contrast, the probability of each bit in the ACO-aided MUD is jointly determined by the MF output's real part as well as by the LLFs of all the vectors in the search-pool encompassing that specific symbol-value. In other words, if the probability of a certain symbol being '+1' (or '−1') is close to one, no operations will be wasted on considering any K-bit vectors having '−1' (or '+1') in that particular bit-position.

As exemplified by our $K = 5$-user example, when the probability of the MF solution's 1st symbol being identical to the ML solution's 1st symbol is high, as reflected by the high intrinsic affinity associated with the $(1, 1)$ cell illustrated in Fig. 3.13(a), the probability of the ζ ants choosing '−1' for the 1st symbol during the first iteration is close to 1.0, as observed from Fig. 3.10(a) Part (I). Hence, no K-bit vectors having the 1st symbol of '+1' will be included in the search-pool during the first iteration, resulting in no pheromone being added to the $(2, 1)$ cell. Hence no vectors having the 1st symbol being '+1' is included in the search-pool during the second, or in fact during all the remaining iterations. The influence of the first bit may be verified with the aid of Table 3.2, where the LLFs of all the sixteen K-bit vectors having the first symbol as '+1' are negative and hence they are inferior to the other sixteen vectors.

Hence, the rationale of generating K-bit vectors according to the probabilities quantified by the MF outputs' real parts and the vectors LLFs that have been included in the previous search-pool prevents the system from calculating the LLFs of vectors having a low probability of becoming the globally optimal ML solution.

Based on the above discussions, the main differences and similarities between the GA-based MUD and the ACO-based MUD are listed in Table 3.7.

FUNCTION	GA	ACO
Initialization	**initialization**	**generating search-pool**
	vector-basis ⟨ *a priori* probability ⟩	symbol-by-symbol basis ⟨ MF outputs ⟩
	Step 1	step 1 → 2 → 3 → 4 → 5 (Step 3: trivial pheromone)
Evolution	**selection**	**incremental pheromone**
	vector-basis ⟨ *fitness* value ⟩	symbol-by-symbol basis ⟨ *fitness* value ⟩
	Step 4	Step 3
	cross over	**calculating probability**
	symbol-basis ⟨ random ⟩	symbol-by-symbol basis ⟨ *fitness* value+MF ⟩
	Step 5	Step 4
	mutation	**generating search-pool**
	symbol-basis ⟨ random ⟩	symbol-by-symbol basis ⟨ symbol-value probability ⟩
	Step 6	Step 5
Evaluation *fitness* value	**evaluation**	**calculating LLF**
	vector-value	vector-value
	step 7	step 7
Use of *fitness* value	**selection**	**pheromone update**
	vector-basis ⟨ *fitness* value ⟩	symbol-by-symbol basis ⟨ *fitness* value ⟩
	Step 4	Step 3
Avoiding pre-mature convergency	**mutation**	**intrinsic affinity**
	symbol-basis ⟨ random ⟩	symbol-by-symbol basis ⟨ MF outputs ⟩
	Step 6	Step 3
		existing pheromone
		symbol-by-symbol basis ⟨ *fitness* value ⟩
		Step 3

Table 3.7: Comparison between processes of ACO-based and GA-based MUD algorithm in realizing the key functions constituting the MUD optimization process. The content inside '⟨ ⟩' are the property or variable determining the above manipulation. The index of step in the GA column refers to the numbered blocks in GA's flow-chart in Fig. 3.19, while that in the ACO collumn refers to the numbered blocks in flow-chart of ACO algortihm in Fig. 3.9. And the '*fitness* value' is the real scalar obtained by substituting the variable representing the candidate solution with the vector-value under consideration in the objective function.

3.6 Summary

The ACO-based MUD algorithm has been detailed in this chapter. The $(2 \times K)$-element *route-table* represents the K-bit MUD problem as a *graph-based search* problem. The evaluation of the 2^K legitimate vectors has been transformed to that of the $2K$ legitimate bits with the aid of the *route-table*. This is achieved by exploiting the *incremental pheromone* which assists the evaluation of the *search-pool* from the MF solution to the ML solution. At the same time, the *intrinsic affinity* as well as the relatively slow evaporation of the *existing pheromone* level prevent the optimization procedure from *premature convergence* to locally optimal solutions.

The total size of the search space is quantified by the product of the number of ants ζ and the number of iterations Ξ, rather than by 2^K. As opposed to the GA-based MUD algorithm, most of the functions of the ACO-based search process are manipulated on a *bit-by-bit* basis, which reduces the *complexity* imposed and allows the *LLRs* associated with each bit/symbol to be exploited.

Chapter 4

ACO-Aided Detection for Multi-Functional Antenna Arrays

Orthogonal Frequency Division Multiplexing (OFDM) [164–167] employs U orthogonal subcarriers to transmit U parallel data streams in order to achieve a high transmission rate. As a benefit of the reduced data-rate of each subchannel facilitated enabled by the serial-to-parallel conversion of the high-rate serial data-stream, accurate synchronization of the OFDM system may be more readily achieved. Moreover, by inserting a guard interval between each OFDM symbol, the channel-induced Inter-Symbol Interference (ISI) and Inter-Channel Interference (ICI) may be mitigated. The principle of Code-Division Multiple-Access (CDMA) and OFDM signalling may be amalgamated, which leads to the concept of Multi Carrier CDMA (MC-CDMA) which attracted substantial research interest in the field of wireless communications [9, 10, 167–174].

In contrast to the Single-Input Single-Output (SISO) system employed in Chapter 3, in this chapter we consider a Single-Input Multiple-Output (SIMO) UL system, which employs antenna arrays at the BS's receiver. Smart antennas have attracted intensive investigations owing to its capability of enhancing the attainable system performance with the aid of their multiplexing gain, beamforming gain and or diversity gain [18, 19, 21, 23, 24, 27, 28, 30, 31, 33, 175–180]. To elaborate a little further, beamforming techniques rely on $\lambda/2$-spaced elements and are capable of creating angularly selective beams.

By contrast, the family of spatial diversity schemes includes Space-Time Block Codes (STBC) [181], Space-Time Spreading (STS) [182], Space-Time Trellis Codes (STTCs) [183], Linear Dispersion Codes (LDC) [184] and their differentially encoded, non-coherently detected counterparts [185]. In contrast to beamforming schemes, spatial diversity schemes require the independent fading of each channel, so that the maximum attainable diversity gain may indeed be achieved.

The stylized Multi-Functional Antenna Array (MFAA) concept of Fig. 4.1 combines the above-mentioned beamforming and spatial diversity techniques. This is achieved by arranging for the antennas to have multiple $\lambda/2$-spaced elements for creating beamformings and these beamformer arrays may then be replicated at distances of $5 - 10\lambda$ in order to achieve a spatial diversity gain provided by independently fading channels.

To elaborate a little further, beamforming constitutes an 'angularly selective' filtering technique [32,

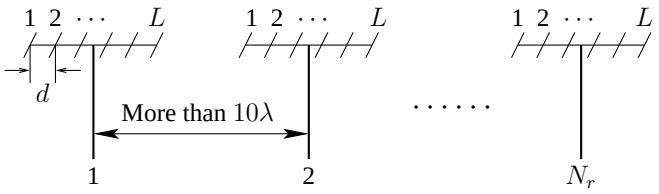

Figure 4.1: Multi-Functional Antenna-Array (MFAA) employing N_r receive antenna arrays, each having L $\lambda/2$-spaced elements.

33], where the direction of the transmitter's DownLink (DL) beam may be automatically adjusted to the direction of the desired user by appropriately updating the array weights. The same techniques are applicable to receiver beamforming at the BS in the UL.

Unlike in [186–188], where orthogonal Walsh-Hadamad (WH) codes were employed as the Time-Domain (TD) spreading sequences for downlink transmission, in this chapter, non-orthogonal codes are employed, which typically result in Multi-User Interference (MUI). The mitigation of the MUI requires the employment of Multi-User Detection (MUD) [93,189]. The optimal Maximum Likelihood (ML) MUD carries out an exhaustive search for all the legitimate combinations of the transmitted symbols of all the users. Naturally, this technique has a complexity that increases exponentially with the number of users, as well as with the number of bits per symbol, which motivates the development of reduced-complexity near-optimal ACO-based MUDs for the MFAA assisted MC DS-CDMA UL.

The novelty of this chapter is that the ACO-based MUD is then further developed for employment in the MFAA assisted MC DS-CDMA UL, which supports both receiver diversity and receiver beamforming. Again, we will demonstrate that similarly to the single-carrier CDMA system of Chapter 3 and regardless of the number of subcarriers or of the specific MFAA configuration, the MD DS-CDMA system employing the proposed ACO-based MUD is capable of supporting $K = 32$ users with the aid of 31-chip Gold codes used as the TD spreading sequence. This is achieved without any significant performance degradation compared to the corresponding single-user benchmark system. As a further benefit, similarly to the single-carrier CDMA system of Chapter 3, the number of FLOPS imposed by the proposed ACO-based MUD is a factor of 10^8 lower than that of the ML MUD. We also demonstrate that at a given increase of the complexity, the MFAA will allow the ACO-based MUD to achieve a higher SNR gain than the corresponding Single-Input Single-Output (SISO) MC DS-CDMA system [131].

The rest of this chapter is organized as follows. Different types of MC DS-CDMA transmission schemes will be briefly introduced in Section 4.1. Additionally, the MFAA assisted receiver as well as the objective function considered are also highlighted in Section 4.1. In Section 4.2, the ACO-based MUD algorithm of Chapter 3 is developed further for application in the MFAA assisted MC DS-CDMA system considered. Then, both the achievable BER performance and the complexity imposed will be analyzed in Section 4.3. Finally, we will conclude our discourse in Section 4.4.

4.1 System Description

The system model employed in this chapter is derived from the Single-Input Single-Output (SISO) DS-CDMA UL depicted in Fig. 2.4, where a single receiver antenna is installed at the BS. By contrast, in the system structure proposed in this chapter, an antenna array comprising N_r beamformers each having L antenna elements is installed at the BS to receive the superimposed signals of the K UL users, as seen in Fig. 4.1. Apart from the MFAA used, the 'CDMA spreading' block of Fig. 4.1 is also different. More explicitly, a single-carrier DS CDMA scheme was used in the 'CDMA spreading' block of Fig. 2.4, while a MC DS-CDMA spreading scheme was incorporated in the 'CDMA spreading' block of Fig. 4.2.

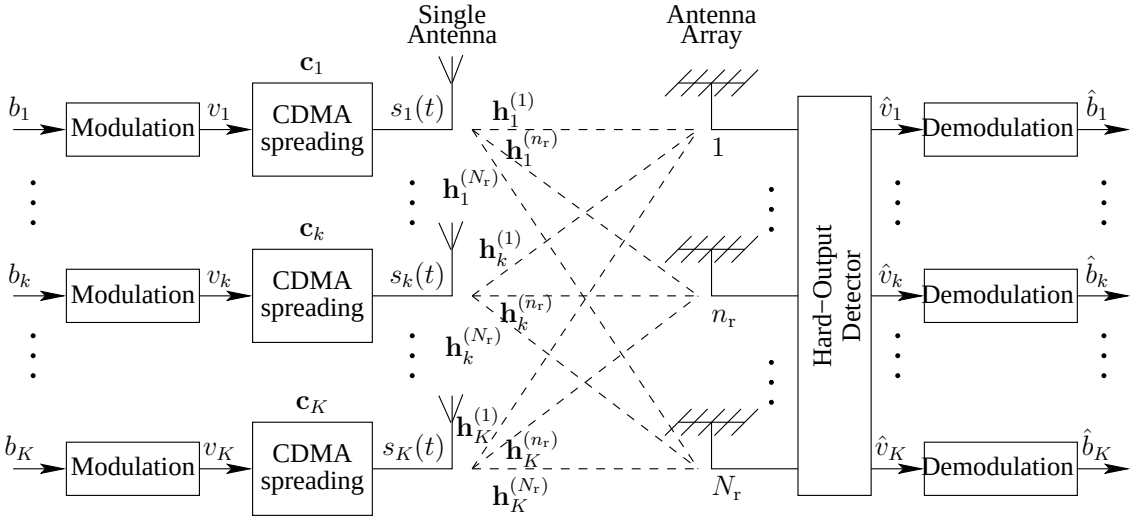

Figure 4.2: Block diagram of the multiuser MFAA-aided MC DS-CDMA UL considered in Chapter 4, which evolved from the Single-Input Single-Output (SISO) MU UL system's transceiver block diagram depicted Fig. 2.4. The mere difference between this architecture and that of Fig. 2.4 is that MFAAs are employed . The specific structure of the transmitter's 'CDMA spreading' block and that of the receiver's 'Hard-Output Detector' will be detailed in Fig. 4.4 and Fig. 4.7, respectively.

The family of multi-carrier systems emerged from the classic concept of OFDM [17], which found its way into diverse wireless systems. Just to mention a few, Wireless Local Area Networks (WLAN) specified by the IEEE 802.11 standards [190], the Digital Studio Broadcast (DAB) [191] and Digital Video Broadcast (DVB) [192] systems, as well as the WiMAX [14] and the Third-Generation Partnership Project's Long-Term Evolution (3GPP-LTE) [15] advocate OFDM. However, the performance of OFDM may readily be improved with the aid of spreading techniques. More specifically, Direct Sequence (DS) spreading known from classic single-carrier DS-CDMA is capable of mitigating the effects of Time-Domain (TD) fading, as detailed in [93], which occurs in time-selective fading scenarios. By contrast, in frequency-selective fading scenarios Frequency-Domain (FD) spreading may be invoked [17], which spreads each subcarrier's signal across all the subcarriers. Multiple users are then supported by superimposing the FD spreading codes on top of each other instead of overlaying them in the TD, as in MC DS-CDMA. Thirdly, the multi-carrier signal may also be spread in the Spatial Domain (SD) to multiple transmit antennas, as in Space-Time Spreading (STS) schemes [93]. The most flexible schemes emerge, however, when TD-, FD- and SD- spreading are employed jointly in form of 3D spreading, which is capable of mitigating the effects of fading in all three domains. A

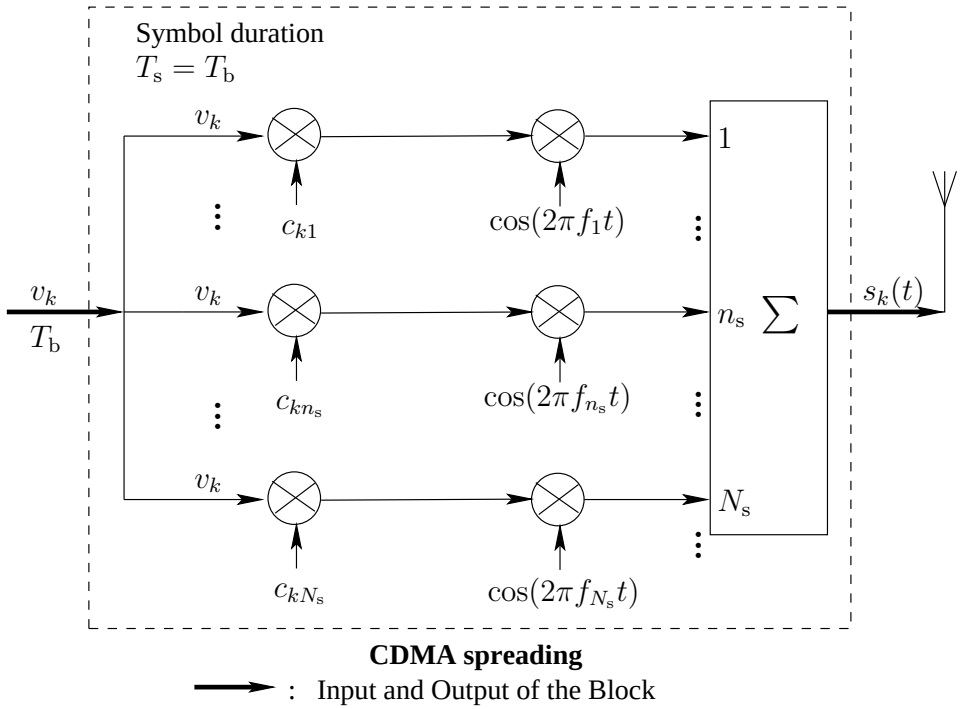

Figure 4.3: CDMA spreading schematic for the kth user's transmitter, when FD-spreading across N_s subcarriers are activated in the the MC DS-CDMA system considered.

further benefit of 3D spreading is that a potentially reduced complexity is achieved, which becomes plausible with the aid of the following simple example. When aiming for supporting say $K = 512$ users employing TD- or FD- spreading and a ML MUD would require the evaluation of 2^{512} potential 512-bit MU vectors, which is clearly unrealistic. By contrast, we may invoke a TD Spreading Factor (SF) $\text{TD}_{\text{SF}} = 8$, a $\text{FD}_{\text{SF}} = 8$ and $\text{TD}_{\text{SF}} = 8$, which requires the evaluation of $2^8 + 2^8 + 2^8 = 3 \cdot 256$ decision vectors. Alternatively, when considering a matched filter, instead of requiring 512 multiplications for the correlation receiver, only $3 \cdot 8 = 24$ multiplications are imposed.

The schematic of multicarrier CDMA using F-domain spreading [5,193–195] is depicted in Fig. 4.3, where each data symbol is copied to N_s subcarriers using a N_s-chip spreading code. Then the n_sth parallel substream seen in Fig. 4.3 modulates the subcarrier frequency f_{n_s}, for $n_s = 1, 2, \ldots, N_s$.

The CDMA spreading scheme of Fig. 4.3 can also be employed by each individual transmitter of a multi-user system [196]. Hence, each user is assigned a unique user-specific N_s-chip FD spreading code. The signal transmitted by different users may then be separated at the receiver by exploiting the knowledge of the users' unique spreading code. When using synchronous downlink transmissions and orthogonal WH codes, a near-single-user performance may be achieved over AWGN channels. However, the orthogonality of WH codes for transmission over dispersive channels is destroyed. Fortunately the MUI and ISI may be mitigated with the aid of MUDs, such as the ACO-aided MUD of Chapter 3.

The maximum FD diversity gain may be achieved, if each individual subcarrier experiences independent fading. Naturally, this may only be achieved, if the subcarriers' frequency separation exceeds the coherence bandwidth of the channel [193], which potentially requires a high system bandwidth.

In contrast to the above-mentioned FD-spread MC CDMA systems, in the TD-spread family the

original data stream is first serial-to-parallel converted to U parallel substreams, as seen in Fig. 4.4, which results in a new extended symbol duration, having a length of U times the orgininal input data symbol length. Then each substream is spread using a specific DS spreading code in the TD, so that each symbol is mapped to and transmitted over N_s chip intervals constituting the U-fold extended symbol duration. Then each chip modulates a unique subcarrier specified by the index of the data stream. Hence we may argue that in TD-spread MC CDMA each subcarrier's signal is similar to that of a conventional single-carrier DS-CDMA scheme [9].

In our Multi-Functional Antenna-Array (MFAA) assisted MC DS-CDMA system of Fig. 4.2 each physical link between the K UL users and a single element of the receiver's MFAA is a SISO TD-spread MC DS-CDMA UL system.

4.1.1 Transmitter Model

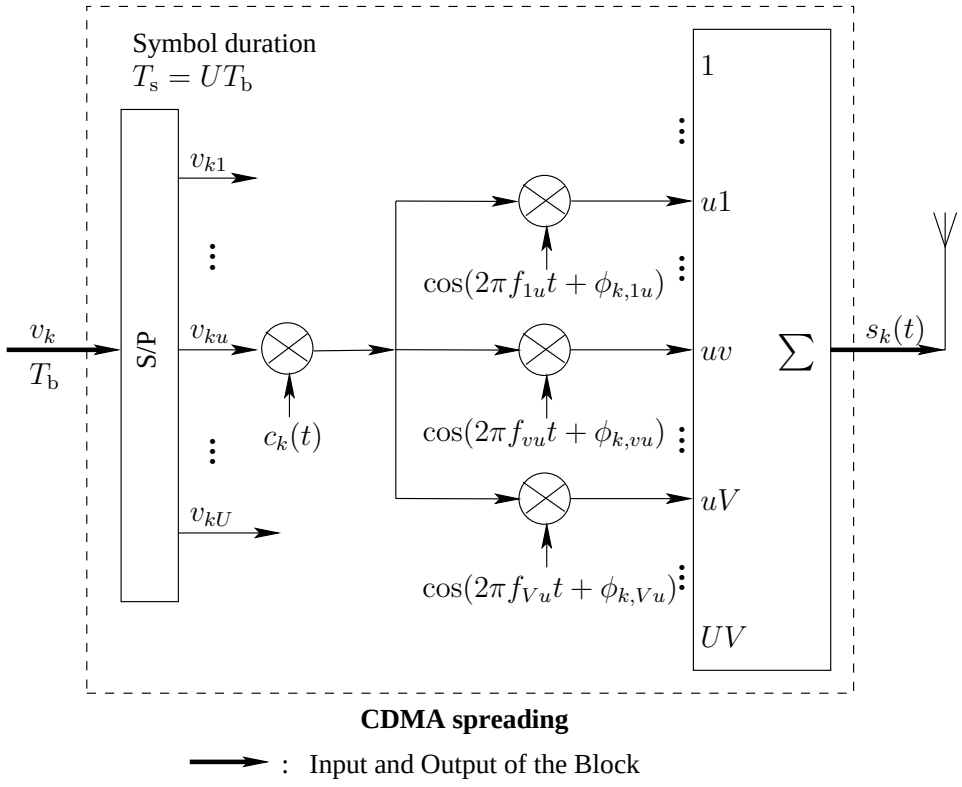

Figure 4.4: The kth user's 'CDMA spreading' block seen in Fig. 4.2, when a total of $U \cdot V$ subcarriers are employed in the MC DS-CDMA-II scheme considered.

In this subsection, the generalized MC DS-CDMA system of Fig. 4.4 [11, 12] is reviewed. At the transmitter side of each UL user, the binary data stream b_k having a bit duration of T_b is BPSK modulated and then DS-spread as shown in Fig. 4.2. The 'CDMA spreading' block of Fig. 4.2 carries out the spreading of the signal both in the TD and FD. To expound further, the TD spreading is achieved by multiplying the original signal with a N_s-chip quasi-orthogonal code $\mathbf{c}_k$, which is specifically assigned to the kth user. The FD spreading is achieved by mapping each branch of the power-normalized signal to V subcarriers having a frequency separation of $f_c = 1/T_c$, where T_c is the chip duration. In its simplest form the latter mapping to V subcarriers may represent copying, i.e. replicating each signal

V times. Alternatively, this can be carried out with the aid of a FD-spreading operation, which allows us to avoid the V-fold effective throughput reduction of the V-fold subcarrier repetition.

The class of orthogonal multicarrier DS-CDMA systems - which was referred to as the family of multicarrier DS-CDMA-II systems by the authors of [93] have been studied in great depth in [9, 197–199]. The orthogonal multicarrier DS-CDMA transmitter of Fig. 4.4 spreads the serial-to-parallel converted data streams using a spreading code $\mathbf{c}_k$ in the TD so that the resultant spectrum of each subcarrier remains orthogonal in the FD, while maintaining the minimum frequency separation [9,198].

The spectrum of the multicarrier DS-CDMA-II signal is shown in Fig. 4.5, where the sinc-function-shaped FD sprectral lobes appear as a consequence of using a rectangular TD window at the modulator. Again, in the multicarrier DS-CDMA-II system the subcarrier frequencies are chosen to be orthogonal to each other with the minimum frequency separation of $f_c = 1/T_c$.

More specifically, a total of UV subcarriers are arranged according to the following matrix:

$$f_{vu} = \begin{bmatrix} f_{11} & f_{12} & \cdots & f_{1U} \\ f_{21} & f_{22} & \cdots & f_{2U} \\ \vdots & \vdots & \ddots & \vdots \\ f_{V1} & f_{V2} & \cdots & f_{VU} \end{bmatrix}. \tag{4.1}$$

By defining the basis frequency f_0 as indicated in Fig. 4.5, we may introduce the single subcarrier subscript of

$$i = (u-1)U + v. \tag{4.2}$$

Then the (v,u)th frequency element of the matrix represented by Eq. (4.1) can be specified as:

$$f_i \equiv f_{vu} = f_0 + i/T_c = f_0 + (u-1)U/T_c + v/T_c. \tag{4.3}$$

In Eq. (4.1) the subcarriers $\{f_{1u},\ f_{2u},\ \cdots,\ f_{Vu}\}$ within the uth column are the V subcarriers carrying the same baseband BPSK signal $v_{ku}(t)$, i.e. the uth branch of the kth user, as observed in Fig. 4.4. As seen in Fig. 4.5, the FD separation of $\Delta = f_{(v+1)u} - f_{vu}$ between two adjacent subcarriers used for transmitting the same signal v_{ku} is equivalent to $\Delta f = Uf_c = U/T_c$. Hence, the specific arrangement of the frequencies related to the UV subcarriers ensures that the subcarrier frequencies used for transmitting the same signal are as far as possible from each other in the FD to ensure their independent fading, in order to achieve the maximum frequency diversity gain.

Then, the TD DS spread signal of the uth sub-stream, $u = 1, 2, \ldots, U$, will be mapped to a group of V parallel subcarrier frequencies $\{f_{1u}, f_{2u}, \ldots, f_{Vu}\}$. More specifically, the uth branch of the kth user's signal v_{ku} transmitted over the vth subcarrier may be expressed as

$$s_{k,vu}(t) = \sqrt{\frac{2P_b}{V}} v_{ku}(t) c_k(t) \cos(2\pi f_{vu} t + \phi_{k,vu}), \tag{4.4}$$

where P_b was originally defined as the power of each bit, more specifically, the power of each BPSK modulated symbol v_{ku}, $k = 1, 2, \ldots, K$ and $u = 1, 2, \ldots, U$. $1/V$ represents the power-scaling factor, which evenly spreads the power of the signal over each of the V subcarriers. Furthermore, $\phi_{k,vu}$ represents the phase angles introduced by the carrier modulation process. Finally, the signal transmitted

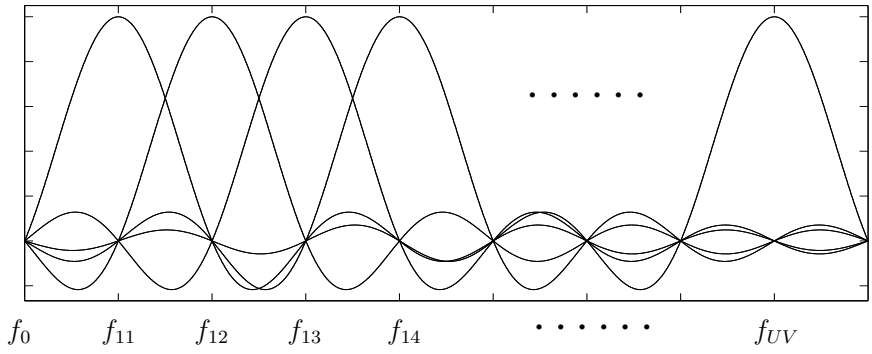

Figure 4.5: The $U \cdot V$ orthogonal subcarriers modulated by each of the K MC DS-CDMA users.

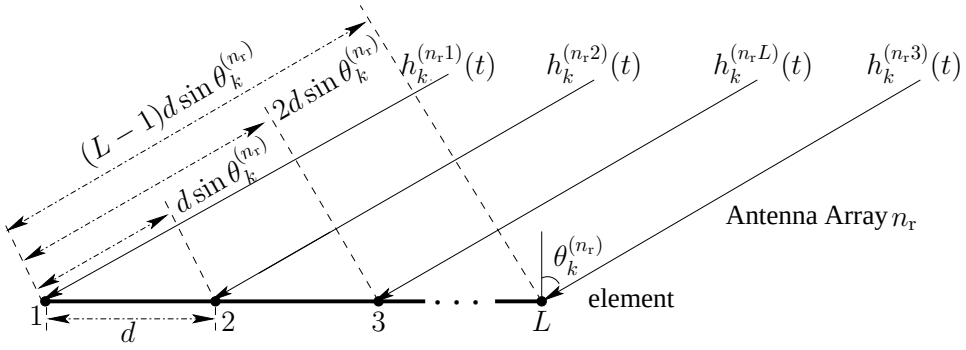

Figure 4.6: Illustration of BeamForming (BF) technique when the signals transmitted from the kth user are received by the n_{r}th antenna array encompassing L elements.

by the kth user's single antenna is the superposition of the UV signals mapped to the UV subcarriers. Therefore, the transmitted signal of user k may be expressed as

$$s_k(t) = \sum_{u=1}^{U} \sum_{v=1}^{V} \sqrt{\frac{2P_{\mathrm{b}}}{V}} v_{ku}(t) c_k(t) \cos(2\pi f_{vu} t + \phi_{k,vu}). \tag{4.5}$$

4.1.2 Channel Model

We assume that at the Base-Station (BS) there are N_r receiver antenna arrays, as shown in Fig. 4.5 and Fig. 4.6, which are located sufficiently far apart so that the corresponding received MC DS-CDMA signals experience independent fading, when they reach the different antenna arrays. Each of the N_r antenna arrays consists of L elements separated by a distance of d, which is usually half a wavelength. As observed from Fig. 4.6, the L CIR taps experienced by the signal transmitted from the same user to the L elements of each of the N_{r} antenna arrays are correlated with each other. Therefore, we will first outline the channel model for the waves arriving from each user to the first of the L array elements of a given antenna array. Then the remaining $(L-1)$ CIR taps related to the other $(L-1)$ array elements, ranging from the 2nd to the Lth, will be derived according to their relationship with the CIR corresponding to the 1st element.

We commence our discourse by introducing the frequency-selective channel model considered, where the transmitted signal is received over Q independent slowly-varying flat fading channels. More

specifically, the complex low-pass equivalent representation of the CIR experienced by subcarrier vu of user k may be expressed as:

$$h_{k,vu}^{(n_r 1)}(t) = \sum_{q=1}^{Q} \alpha_{k,vu,q}^{(n_r 1)} \delta(t - \tau_{kq}) \exp\left\{ j\psi_{k,vu,q}^{(n_r 1)} \right\}, \tag{4.6}$$

where q is the index of the CIR taps, $\delta(\cdot)$ is the Dirac function, $\alpha_{k,vu,q}^{(n_r 1)}$, $\psi_{k,vu,q}^{(n_r 1)}$ and τ_{kq} are the random CIR tap amplitudes, phase and delays, respectively.

If the symbol rate is high, resulting in frequency selective fading, then serial-to-parallel conversion of the original data stream to a number of reduced-rate substreams may be needed, in order to increase the chip duration and hence to avoid frequency selective fading. The system model of Fig. 4.4 includes a S/P converter, which converts the original symbol stream v_k of user k to U substreams, each of which is transmitted over a U-times longer symbol duration of $T_s = UT_b$.

Based on the system model proposed in this chapter, we assume the absence of ISI, hence we have $Q = 1$ in Eq. (4.6). Hence, flat-fading is encountered by each subcarrier signal. Therefore, the above-mentioned frequency selective channel model of Eq. (4.6) describing the CIR between the kth user and the 1st array element of the n_rth antenna array on subcarrier vu may be simplified to a flat-fading channel model, yielding

$$h_{k,vu}^{(n_r 1)}(t) = \alpha_{k,vu}^{(n_r 1)} \delta(t - \tau_k) \exp\left\{ j\psi_{k,vu}^{(n_r 1)} \right\}. \tag{4.7}$$

According to Fig. 4.6, the phase difference between the lth element and the 1st element associated with a given antenna array is

$$\Delta\psi_k^{(n_r l)} = \psi_k^{(n_r l)} - \psi_k^{(n_r 1)} = 2\pi(l-1)\frac{d}{\lambda}\sin\theta_k^{(n_r)}, \quad l = 1, \ldots, L, \tag{4.8}$$

where $\theta_k^{(n_r)}$ is the average Direction-Of-Arrival (DOA) from the kth user to the n_rth antenna array. In this study, the distribution of the users' DOAs at the base station is determined using the Geometrically Based Single Bounce Circular Model (GBSBCM) [200], where the average DOA is the DOA of the line-of-sight (LOS) path. Slow DOA evolution was assumed for each user and hence the users' DOAs may judiciously be assumed to remain fixed during each received data-burst.

For simplicity, we assume that there is no angular spread. Then the Spatio-Temporal Channel Impulse Response (ST-CIR) $h_{uv,k}^{(n_r l)}$ encountered by the signal transmitted from the kth user over the uvth subcarrier to the lth array element of the n_rth antenna can be expressed as

$$\begin{aligned} h_{k,vu}^{(n_r l)}(t) &= h_{k,vu}^{(n_r 1)}(t) \exp\left\{ j2\pi\frac{d}{\lambda}(l-1)\sin\theta_k^{(n_r)} \right\} \\ &= \alpha_{k,vu}^{(n_r 1)} \delta(t - \tau_k) \exp\left\{ j\left[\psi_{k,vu}^{(n_r 1)} + (l-1)2\pi\frac{d}{\lambda}\sin\theta_k^{(n_r)} \right] \right\}, \end{aligned} \tag{4.9}$$

for $n_r = 1, \ldots, N_r$; $l = 1, \ldots, L$; $u = 1, 2, \ldots, U$; $v = 1, 2, \ldots, V$; and $k = 1, 2, \ldots, K$. Since both the Rayleigh distributed envelope $\alpha_{k,vu}^{(n_r 1)}$ of the CIR as well as the phase $\psi_{k,vu}^{(n_r 1)}$ of the CIR spanning from the kth user to the 1st array element of the n_rth antenna array may be deemed constant for the array elements belonging to the same antenna array, upon substituting $\alpha_{k,vu}^{(n_r 1)}$ and $\psi_{k,vu}^{(n_r 1)}$ for $\alpha_{k,vu}^{(n_r)}$ and $\psi_{k,vu}^{(n_r)}$, as well as $\tau_k = 0$ into Eq. (4.9), we arrive at

$$h_{k,vu}^{(n_r l)} = \alpha_{k,vu}^{(n_r)} \exp\left\{ j\left[\psi_{k,vu}^{(n_r)} + (l-1)2\pi\frac{d}{\lambda}\sin\theta_k^{(n_r)} \right] \right\}. \tag{4.10}$$

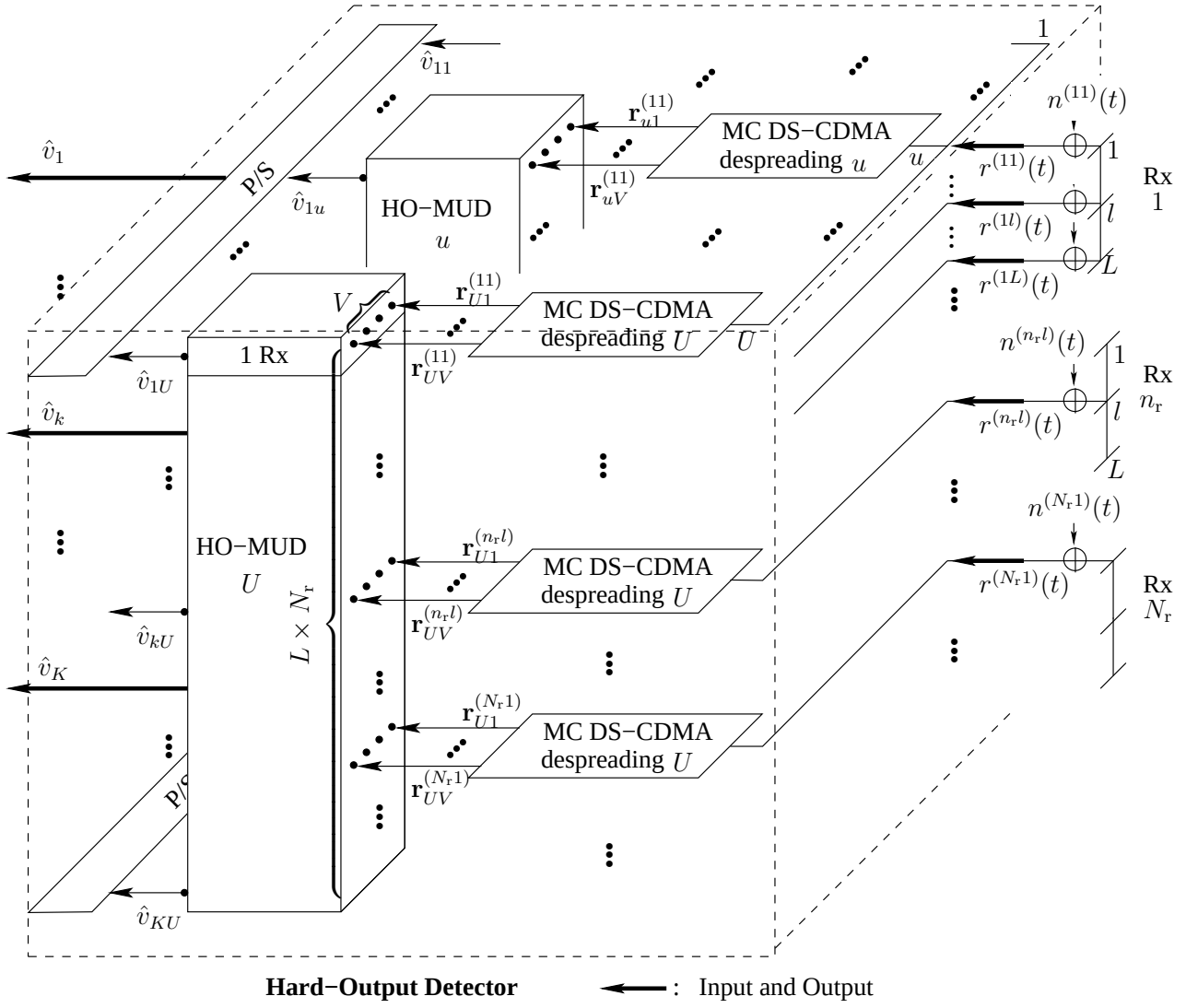

Figure 4.7: Detailed structure of the 'Hard-Output Detector' of the system depicted in Fig. 4.2, where N_{r} antenna arrays each comprising L elements were installed at the BS in order to provide both a diversity gain as well as beamforming gain.

4.1.3 Receiver Model

We assume that K synchronous MC DS-CDMA users are supported by the system. Then the signal received at the lth array element of the n_{r}th antenna array at the BS may be expressed as:

$$\begin{aligned} r^{(n_{\mathrm{r}}l)}(t) &= \sum_{k=1}^{K}\sum_{v=1}^{V}\sum_{u=1}^{U} s_{k,vu}(t)h_{k,vu}^{(n_{\mathrm{r}}l)}(t) + n(t) \\ &= \sum_{k=1}^{K}\sum_{v=1}^{V}\sum_{u=1}^{U} \sqrt{\frac{2P_{\mathrm{b}}}{V}}\alpha_{k,vu}^{(n_{\mathrm{r}}l)} v_{ku} c_k(t) \cos\Big(2\pi f_{vu} + \varphi_{k,vu}^{(n_{\mathrm{r}}l)}\Big) + n^{(n_{\mathrm{r}}l)}(t), \end{aligned} \tag{4.11}$$

where we have

$$\varphi_{k,vu}^{(n_{\mathrm{r}}l)} = \phi_{k,vu}^{(n_{\mathrm{r}}l)} + \psi_{k,vu}^{(n_{\mathrm{r}})} + (l-1)2\pi\frac{d}{\lambda}\sin\theta_k^{(n_{\mathrm{r}})} - 2\pi f_{vu}\tau_k \tag{4.12}$$

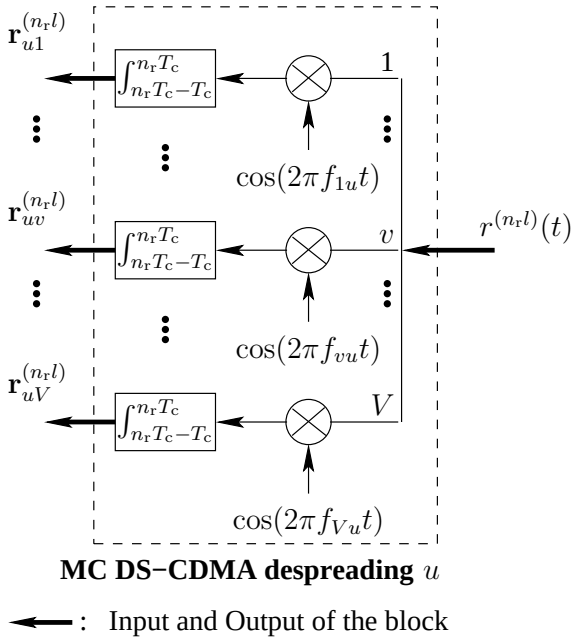

Figure 4.8: Detailed schematic of the 'MC DS-CDMA despreading u' block in Fig. 4.7 processing the signal received from the lth element of antenna n_r.

and the random phase of $\psi_{k,vu}^{(n_r)} + (l-1)2\pi\frac{d}{\lambda}\sin\theta_k^{(n_r)}$ imposed on the subcarrier frequency f_{vu}, was introduced by the channel spanning from the kth user to the lth array element of the n_rth antenna array. As suggested by Eq. 4.8, the phase $\psi_{k,vu}^{(n_r l)}$ introduced by the CIR correponding to the vuth subcarrier frequency spanning from the kth user to the lth array element of the n_rth antenna array is constituted by the sum of that introduced by the CIR of the kth user impinging on the 1st element of the n_rth array plus the phase difference between the 1st and the lth array element. Finally, $n(t)$ is the AWGN having a zero mean and a double-sided power spectral density of $N_0/2$.

According to Fig. 4.7, regardless of the antenna array index n_r and of the array element index l, the received signal $r^{(n_r l)}(t)$ will be first input to the U MC DS-CDMA blocks corresponding to the U groups of subcarrier frequencies $\{f_{1u}, f_{2u}, \ldots, f_{Vu}\}$, $u = 1, 2, \ldots, U$, as seen in the matrix of Eq. (4.1). The detailed structure of the uth MC DS-CDMA despreading block is depicted in Fig. 4.8.

The despreading scheme of Fig. 4.8 is quite similar to the receiver arrangement shown in Fig. 4(c) of [196] and to Fig. 3 of [201]. However, the main difference between Fig. 4.8 and the latter two figures lies in whether or not the TD-despreading is carried out simultaneously with the FD-despreading. More explicitly, in Fig. 3 of [201], the TD spreading sequence c_t is multiplied with the signal before the signal is integrated from 0 to T_s,. Hence, the output of each integrator block shown in Fig. 3 of [201] is identical to the MF output in both the TD and FD.

By contrast, the TD despreading was not incorporated into the MC DS-CDMA despreading scheme shown in Fig. 4.8, because we aimed for expressing the signal received by the lth array element of the n_rth antenna array on a subcarrier-by-subcarrier basis to ensure that the corresponding mathematical formulation shown in Eq. (2.25) remained valid, which was derived for a DS-CDMA system using TD fomulation spreading.

As shown in Fig. 4.8, the input signal $r^{(n_r l)}(t)$ of the uth MC DS-CDMA spreading block is firstly

multiplied with a group of cosine waveforms associated with the group of subcarrier frequencies $\{f_{1u}, f_{2u}, \ldots, f_{Vu}\}$. Then the resultant signals of the V branches are passed through the integrators having a time-constant of the chip-duration, where we have $n_{\rm s} = 1, 2, \ldots, N_{\rm s}$ in Fig. 4.8. Below, we assume that the reference subcarrier is $v = 1$ and $u = 1$. Then the output $r_{k,vu}^{(n_{\rm r}l)}(t)$ of the integrator operating during the $n_{\rm s}$th chip interval related to the vuth subcarrier frequency and processing the signal of the $(n_{\rm r}, l)$th antenna element may be expressed as:

$$\begin{aligned} r_{11,n_{\rm s}}^{(n_{\rm r}l)}(t) &= \int_{n_{\rm s}T_{\rm c}-T_{\rm c}}^{n_{\rm s}T_{\rm c}} r^{(n_{\rm r}l)}(t)\cos\Big(2\pi f_{11}t + \varphi_{k,11}^{(n_{\rm r}l)}\Big)dt \\ &= \int_{n_{\rm s}T_{\rm c}-T_{\rm c}}^{n_{\rm s}T_{\rm c}} \sum_{k=1}^{K}\sum_{v=1}^{V}\sum_{u=1}^{U}\sqrt{\frac{2P_{\rm b}}{V}}\alpha_{k,vu}^{(n_{\rm r}l)}v_{ku}c_k(t)\cos\Big(2\pi f_{vu}t + \varphi_{k,vu}^{(n_{\rm r}l)}\Big)\cos\Big(2\pi f_{11}t + \varphi_{k,11}^{(n_{\rm r}l)}\Big) + \\ &\quad \int_{n_{\rm s}T_{\rm c}-T_{\rm c}}^{n_{\rm s}T_{\rm c}} n^{(n_{\rm r}l)}(t)\cos\Big(2\pi f_{11}t + \varphi_{k,11}^{(n_{\rm r}l)}\Big)dt. \end{aligned} \tag{4.13}$$

As demonstrated in Fig. 4.5, the frequency of each subcarrier employed by the MC DS-CDMA class II transmit scheme is orthogonal to each other, yielding:

$$\int_{n_{\rm s}T_{\rm c}-T_{\rm c}}^{n_{\rm s}T_{\rm c}} \cos\Big(2\pi f_i t + \varphi_{k,i}^{(n_{\rm r}l)}\Big)\cos\Big(2\pi f_j t + \varphi_{k,j}^{(n_{\rm r}l)}\Big)dt = 0, \text{ for } i \neq j, \tag{4.14}$$

where f_i or f_j associated with $i, j \in [1, UV]$ provide an alternative representation of f_{vu} with $u \in [1, U]$ and $v \in [1, V]$, where the relationship between these two representations was defined in Eqs. (4.2) and 4.3. Additionally, when we have $i = j$, i.e. when we consider the same subcarrier frequency f_i, we have

$$\int_{n_{\rm s}T_{\rm c}-T_{\rm c}}^{n_{\rm s}T_{\rm c}} \cos\Big(2\pi f_i t + \varphi_{k,i}^{(n_{\rm r}l)}\Big)\cos\Big(2\pi f_i t + \varphi_{k,i}^{(n_{\rm r}l)}\Big)dt = \frac{1}{2}. \tag{4.15}$$

Therefore, Eq. (4.13) may be simplified to

$$r_{11,n_{\rm s}}^{(n_{\rm r}l)}(t) = \sqrt{\frac{P_{\rm b}}{V}}\sum_{k=1}^{K}\alpha_{k,vu}^{(n_{\rm r}l)}\psi_{k,vu}^{(n_{\rm r}l)}v_{k1}c_{kn_{\rm s}} + \int_{n_{\rm s}T_{\rm c}-T_{\rm c}}^{n_{\rm s}T_{\rm c}} n^{(n_{\rm r}l)}(t)\cos\Big(2\pi f_{11}t + \varphi_{k,11}^{(n_{\rm r}l)}\Big)dt, \tag{4.16}$$

where we have $h_{k,vu}^{(n_{\rm r}l)} = \alpha_{k,vu}^{(n_{\rm r}l)}\psi_{k,vu}^{(n_{\rm r}l)}$. The second term of Eq. (4.16), namely $\int_{n_{\rm s}T_{\rm c}-T_{\rm c}}^{n_{\rm s}T_{\rm c}} n^{(n_{\rm r}l)}(t)\cos\Big(2\pi f_{11}t + \varphi_{k,11}^{(n_{\rm r}l)}\Big)dt$ may be considered as the Fourier transform of the TD AWGN variable $n^{(n_{\rm r}l)}(t)$, a zero mean and a variance of $\sigma_{\mathfrak{n}}^2 = N_0/2{\cdot}T_{\rm c}$. When $T_{\rm c}$ is normalized to one, the variance of $\int_{n_{\rm s}T_{\rm c}-T_{\rm c}}^{n_{\rm s}T_{\rm c}} n^{(n_{\rm r}l)}(t)\cos\Big(2\pi f_{11}t + \varphi_{k,11}^{(n_{\rm r}l)}\Big)dt$ becomes $\sigma_{\mathfrak{n}}^2 = N_0/2$.

Hence, Eq. 4.16 can be alternatively represented with the aid of discrete numbers as:

$$r_{11,n_{\rm s}}^{(n_{\rm r}l)} = \sqrt{\frac{P_{\rm b}}{V}}\sum_{k=1}^{K}c_{kn_{\rm s}}h_{k,11}^{(n_{\rm r}l)}v_{k1} + n_{11,n_{\rm s}}^{(n_{\rm r}l)}, \tag{4.17}$$

where $n_{11,n_{\rm s}}^{(n_{\rm r}l)} = \int_{n_{\rm s}T_{\rm c}-T_{\rm c}}^{n_{\rm s}T_{\rm c}} n^{(n_{\rm r}l)}(t)\cos\Big(2\pi f_{11}t + \varphi_{k,11}^{(n_{\rm r}l)}\Big)dt$ is a Gaussian distributed complex random variable having a mean of zero and a variance of $\sigma_{\mathfrak{n}}^2 = N_0/2$. If we normalize the power of the signal to $P_{\rm b} = 1$ and introduce the notation of $\xi = \sqrt{1/V}$, Eq. (4.17) may be simplified as:

$$r_{11,n_{\rm s}}^{(n_{\rm r}l)} = \xi\sum_{k=1}^{K}c_{kn_{\rm s}}h_{k,11}^{(n_{\rm r}l)}v_{k1} + n_{11,n_{\rm s}}^{(n_{\rm r}l)}. \tag{4.18}$$

4.1.4 Objective Function

Recall from Eq. (4.18) that $r_{11,n_s}^{(n_r l)}$ describes the signal received during the n_sth chip interval on the $(u,v) = (1,1)$th subcarrier. Then we may explicitly describe all the N_s signals received from the $n_s = 1$st to the $n_s = N_s$th chip interval on subcarrier $(u,v) = (1,1)$ as follows:

$$\begin{array}{rcccccccccc} r_{11,1}^{(n_r l)} & = & c_{11}\ h_{1,11}^{(n_r l)} v_{11} & + & c_{21}\ h_{2,11}^{(n_r l)} v_{21} & + & \cdots & + & c_{K1}\ h_{K,11}^{(n_r l)} v_{K1} & + & n_{11,1}^{(n_r l)} \\ r_{11,2}^{(n_r l)} & = & c_{12}\ h_{1,11}^{(n_r l)} v_{1} & + & c_{22}\ h_{2,11}^{(n_r l)} v_{21} & + & \cdots & + & c_{K2}\ h_{K,11}^{(n_r l)} v_{K2} & + & n_{11,2}^{(n_r l)} \\ \vdots & & \vdots & & \vdots & & & & \vdots & & \vdots \\ r_{11,N_s}^{(n_r l)} & = & c_{1N_s} h_{1,11}^{(n_r l)} v_{11} & + & c_{2N_s} h_{2,11}^{(n_r l)} v_{21} & + & \cdots & + & c_{KN_s} h_{K,11}^{(n_r l)} v_{K1} & + & n_{11,N_s}^{(n_r l)} \end{array} . \tag{4.19}$$

The set of equations in Eq. (4.19) is similar to the signals received in the SISO MU system of Chapter 2 during the N_s chip itervals, which was quantified in Eq. (2.25). Alternatively, we may express Eq. (4.19) in a matrix-form as:

$$\mathbf{r}_{11}^{(n_r l)} = \xi \mathbf{C} \mathbf{H}_{11}^{(n_r l)} \mathbf{v}_1 + \mathbf{n}_{11}^{(n_r l)}, \tag{4.20}$$

which can be expanded as:

$$\begin{bmatrix} r_{11,1}^{(n_r l)} \\ r_{11,2}^{(n_r l)} \\ \vdots \\ r_{11,N_s}^{(n_r l)} \end{bmatrix} = \xi \begin{bmatrix} c_{11} & c_{21} & \cdots & c_{K1} \\ c_{12} & c_{22} & \cdots & c_{K2} \\ \vdots & \vdots & \cdots & \vdots \\ c_{1N_s} & c_{2N_s} & \cdots & c_{KN_s} \end{bmatrix} \begin{bmatrix} h_{11,1}^{(n_r l)} & 0 & \cdots & 0 \\ 0 & h_{11,2}^{(n_r l)} & \cdots & 0 \\ \vdots & \vdots & \ddots & \vdots \\ 0 & 0 & \cdots & h_{11,K}^{(n_r l)} \end{bmatrix} \begin{bmatrix} v_{11} \\ v_{21} \\ \vdots \\ v_{K1} \end{bmatrix} + \begin{bmatrix} n_{11,1}^{(n_r l)} \\ n_{11,2}^{(n_r l)} \\ \vdots \\ n_{11,N_s}^{(n_r l)} \end{bmatrix} . \tag{4.21}$$

More generally, when we refer to an arbitrary subcarrier index of (u,v) instead of $(1,1)$, we will have

$$\mathbf{r}_{vu}^{(n_r l)} = \xi \mathbf{C} \mathbf{H}_{vu}^{(n_r l)} \mathbf{v}_u + \mathbf{n}_{vu}^{(n_r l)}, \tag{4.22}$$

which can be expanded as:

$$\begin{bmatrix} r_{vu,1}^{(n_r l)} \\ r_{vu,2}^{(n_r l)} \\ \vdots \\ r_{vu,N_s}^{(n_r l)} \end{bmatrix} = \xi \begin{bmatrix} c_{11} & c_{21} & \cdots & c_{K1} \\ c_{12} & c_{22} & \cdots & c_{K2} \\ \vdots & \vdots & \cdots & \vdots \\ c_{1N_s} & c_{2N_s} & \cdots & c_{KN_s} \end{bmatrix} \begin{bmatrix} h_{vu,1}^{(n_r l)} & 0 & \cdots & 0 \\ 0 & h_{vu,2}^{(n_r l)} & \cdots & 0 \\ \vdots & \vdots & \ddots & \vdots \\ 0 & 0 & \cdots & h_{vu,K}^{(n_r l)} \end{bmatrix} \begin{bmatrix} v_{1u} \\ v_{2u} \\ \vdots \\ v_{Ku} \end{bmatrix} + \begin{bmatrix} n_{vu,1}^{(n_r l)} \\ n_{vu,2}^{(n_r l)} \\ \vdots \\ n_{vu,N_s}^{(n_r l)} \end{bmatrix} , \tag{4.23}$$

where we have

$$\mathbf{C} = [\mathbf{c}_1, \mathbf{c}_2, \ldots, \mathbf{c}_K] \tag{4.24}$$

$$\mathbf{H}_{vu}^{(n_r l)} = \mathrm{diag}\left\{ \left[h_{vu,1}^{(n_r l)}, h_{vu,2}^{(n_r l)}, \ldots, h_{vu,K}^{(n_r l)} \right] \right\} \tag{4.25}$$

$$\mathbf{v}_u = [v_{1u}, v_{2u}, \ldots, v_{Ku}]^T \tag{4.26}$$

$$\mathbf{n}_{vu}^{(n_r l)} = \left[n_{vu,1}^{(n_r l)}, n_{vu,2}^{(n_r l)}, \ldots, n_{vu,N_s}^{(n_r l)} \right]^T . \tag{4.27}$$

Eqs. (4.22) and (4.23) are similar to the matrix equations describing the received signal with the aid of $\mathbf{C}$, $\mathbf{H}$, $\mathbf{v}$ and $\mathbf{n}$ in Eqs. (2.27) and (2.28).

If the subscript v sweeps across the range spanning from 1 to V, with an increment of 1, the number of equations characterizing the N_s-chip intervals received on subcarrier $v = 1$ in Eq. (4.19) will increase from N_s to VN_s, describing all the N_s-chip signals over all the V subcarriers. Similarly, the matrix formulation of Eq. (4.20) may also be extended to $v = 2, 3, \ldots, V$, yielding:

$$\mathbf{r}_1^{(n_r l)} = \xi \bar{\mathbf{C}}^{(n_r l)} \mathbf{H}_1^{(n_r l)} \bar{\mathbf{v}}_1^{(n_r l)} + \mathbf{n}_1^{(n_r l)}, \tag{4.28}$$

where we have the $(VN_s \times 1)$-element received signal vector formulated as

$$\mathbf{r}_1^{(n_r l)} = \begin{bmatrix} \mathbf{r}_{11}^{(n_r l)} \\ \mathbf{r}_{21}^{(n_r l)} \\ \vdots \\ \mathbf{r}_{V1}^{(n_r l)} \end{bmatrix}, \tag{4.29}$$

the $(VN_s \times VK)$-element TD-spreading code matrix expressed as

$$\bar{\mathbf{C}}^{(n_r l)} = \begin{bmatrix} \mathbf{C} & \mathbf{0} & \cdots & \mathbf{0} \\ \mathbf{0} & \mathbf{C} & \cdots & \mathbf{0} \\ \vdots & \vdots & \ddots & \vdots \\ \mathbf{0} & \mathbf{0} & \cdots & \mathbf{C} \end{bmatrix}. \tag{4.30}$$

Furthermore, the $(VK \times VK)$-element CIR matrix $\mathbf{H}_1^{(n_r l)}$ is given by

$$\mathbf{H}_1^{(n_r l)} = \begin{bmatrix} \mathbf{H}_{11}^{(n_r l)} & \mathbf{0} & \cdots & \mathbf{0} \\ \mathbf{0} & \mathbf{H}_{21}^{(n_r l)} & \cdots & \mathbf{0} \\ \vdots & \vdots & \ddots & \vdots \\ \mathbf{0} & \mathbf{0} & \cdots & \mathbf{H}_{V1}^{(n_r l)} \end{bmatrix}, \tag{4.31}$$

the $(VK \times 1)$-element matrix $\bar{\mathbf{v}}_1^{(n_r l)}$ is expressed as

$$\bar{\mathbf{v}}_1^{(n_r l)} = \begin{bmatrix} \mathbf{v}_1 \\ \mathbf{v}_1 \\ \vdots \\ \mathbf{v}_1 \end{bmatrix}, \tag{4.32}$$

and finally the $(VN_s \times 1)$-element AWGN vector is formulated as:

$$\mathbf{n}_1^{(n_r l)} = \begin{bmatrix} \mathbf{n}_{11}^{(n_r l)} \\ \mathbf{n}_{21}^{(n_r l)} \\ \vdots \\ \mathbf{n}_{V1}^{(n_r l)} \end{bmatrix}. \tag{4.33}$$

We can further generalize Eq. (4.28) so that it can represent the N_s-chip receiver outputs v_{1u}, v_{2u}, …, v_{Ku} of the K users on subcarriers $\{f_{1u}, f_{2u}, \cdots, f_{Vu}\}$, yielding

$$\mathbf{r}_u^{(n_r l)} = \xi \bar{\mathbf{C}}_u^{(n_r l)} \mathbf{H}_u^{(n_r l)} \bar{\mathbf{v}}_u^{(n_r l)} + \mathbf{n}_u^{(n_r l)}, \tag{4.34}$$

where we have

$$\mathbf{r}_u^{(n_r l)} = \begin{bmatrix} \mathbf{r}_{1u}^{(n_r l)} \\ \mathbf{r}_{2u}^{(n_r l)} \\ \vdots \\ \mathbf{r}_{Vu}^{(n_r l)} \end{bmatrix}. \tag{4.35}$$

Then the $(VK \times VK)$-element CIR matrix $\mathbf{H}_u^{(n_r l)}$ is given by

$$\mathbf{H}_u^{(n_r l)} = \begin{bmatrix} \mathbf{H}_{1u}^{(n_r l)} & \mathbf{0} & \cdots & \mathbf{0} \\ \mathbf{0} & \mathbf{H}_{2u}^{(n_r l)} & \cdots & \mathbf{0} \\ \vdots & \vdots & \ddots & \vdots \\ \mathbf{0} & \mathbf{0} & \cdots & \mathbf{H}_{Vu}^{(n_r l)} \end{bmatrix}, \tag{4.36}$$

the $(VK \times 1)$-element matrix $\bar{\mathbf{v}}_u^{(n_r l)}$ is expressed as:

$$\bar{\mathbf{v}}_u^{(n_r l)} = \begin{bmatrix} \mathbf{v}_u \\ \mathbf{v}_u \\ \vdots \\ \mathbf{v}_u \end{bmatrix}, \tag{4.37}$$

and finally the $(VN_s \times 1)$-element AWGN vector is formulated as:

$$\mathbf{n}_u^{(n_r l)} = \begin{bmatrix} \mathbf{n}_{1u}^{(n_r l)} \\ \mathbf{n}_{2u}^{(n_r l)} \\ \vdots \\ \mathbf{n}_{Vu}^{(n_r l)} \end{bmatrix}. \tag{4.38}$$

Then, the $N_r LV$ number of FD-despread baseband signal inputs of the ACO-MUD u seen in Fig. 4.7, which provides the HO detection results for $\mathbf{v}_u = [v_{1u}, v_{2u}, \ldots, v_{Ku}]^T$, can be represented by:

$$\mathbf{r}_u = \xi \bar{\mathbf{C}} \mathbf{H}_u \bar{\mathbf{v}}_u + \mathbf{n}_u, \tag{4.39}$$

where the $(N_r LVN_s \times 1)$-element despread received signal vector is expressed as

$$\mathbf{r}_u = \begin{bmatrix} \mathbf{r}_u^{(11)} \\ \mathbf{r}_u^{(12)} \\ \vdots \\ \mathbf{r}_u^{(N_r L)} \end{bmatrix}. \tag{4.40}$$

Still referring to Eq. (4.39) the $(N_r LVN_s \times N_r LVK)$-element TD spreading code matrix is given by:

$$\bar{\mathbf{C}} = \begin{bmatrix} \mathbf{C}^{(n_r l)} & \mathbf{0} & \cdots & \mathbf{0} \\ \mathbf{0} & \mathbf{C}^{(n_r l)} & \cdots & \mathbf{0} \\ \vdots & \vdots & \ddots & \vdots \\ \mathbf{0} & \mathbf{0} & \cdots & \mathbf{C}^{(n_r l)} \end{bmatrix}, \tag{4.41}$$

the $(N_{\mathrm{r}}LVK \times N_{\mathrm{r}}LVK)$-element CIR matrix $\mathbf{H}_u$ is described by:

$$\mathbf{H}_u = \begin{bmatrix} \mathbf{H}_u^{(11)} & \mathbf{0} & \cdots & \mathbf{0} \\ \mathbf{0} & \mathbf{H}_u^{(12)} & \cdots & \mathbf{0} \\ \vdots & \vdots & \ddots & \vdots \\ \mathbf{0} & \mathbf{0} & \cdots & \mathbf{H}_u^{(N_{\mathrm{r}}L)} \end{bmatrix}, \tag{4.42}$$

the $(N_{\mathrm{r}}LVK \times 1)$-element matrix $\bar{\mathbf{v}}_u$ is formulated as:

$$\bar{\mathbf{v}}_u = \begin{bmatrix} \mathbf{v}_u^{(11)} \\ \mathbf{v}_u^{(12)} \\ \vdots \\ \mathbf{v}_u^{(N_{\mathrm{r}}L)} \end{bmatrix}, \tag{4.43}$$

and finally, the $(N_{\mathrm{r}}LVN_{\mathrm{s}} \times 1)$-element AWGN vector is expressed in the form of:

$$\mathbf{n}_u = \begin{bmatrix} \mathbf{n}_u^{(11)} \\ \mathbf{n}_u^{(12)} \\ \vdots \\ \mathbf{n}_u^{(N_{\mathrm{r}}L)} \end{bmatrix}. \tag{4.44}$$

Hence, $N_{\mathrm{r}}LVN_{\mathrm{s}}$ number of baseband received signals are required by the ACO-based MUD in order to detect the K-symbol vector $\hat{\mathbf{v}}_u$.

Briefly returning to Eq. (4.39), $\mathbf{n}_u$ is a $(VN_{\mathrm{r}}LN_{\mathrm{s}})$-element complex-valued Gaussian variable having a mean of $\mathbf{M}_{\mathfrak{n}} = \mathbf{0}^{(VN_{\mathrm{r}}LN_{\mathrm{s}})}$ and a variance of $\mathbf{\Sigma}_{\mathfrak{n}} = \sigma_{\mathfrak{n}}^2\mathbf{I}^{(VN_{\mathrm{r}}LN_{\mathrm{s}})}$. Therefore, given a certain K-symbol vector $\dot{\mathbf{v}}$, $\mathbf{r}_u$ is a $(VN_{\mathrm{r}}LN_{\mathrm{s}})$-element complex Gaussian variable having a mean of $\mathbf{M}_{\boldsymbol{r}} = \xi\bar{\mathbf{C}}\mathbf{H}_u\bar{\dot{\mathbf{v}}}$ and a variance of $\mathbf{\Sigma}_{\mathfrak{r}} = \sigma_{\mathfrak{n}}^2\mathbf{I}^{(VN_{\mathrm{r}}LN_{\mathrm{s}})}$, where the $(VN_{\mathrm{r}}LK)$-element vector $\bar{\dot{\mathbf{v}}}$ is given as:

$$\bar{\dot{\mathbf{v}}}^{(VN_{\mathrm{r}}LK)} = \begin{bmatrix} \dot{\mathbf{v}}^{(K)} \\ \dot{\mathbf{v}}^{(K)} \\ \vdots \\ \dot{\mathbf{v}}^{(K)} \end{bmatrix}. \tag{4.45}$$

The corresponding $D = VN_{\mathrm{r}}LK$-dimensional complex Gaussian PDF given in Eq. (2.67) is repeated here for convenience:

$$p(\mathbf{r}) = \frac{1}{\pi^D} \frac{\exp\left[-\frac{1}{2}(\mathbf{r} - \mathbf{M}_{\mathfrak{r}})^H 2\mathbf{\Sigma}_{\mathfrak{r}}^{-1}(\mathbf{r} - \mathbf{M}_{\mathfrak{r}})\right]}{\det(\mathbf{\Sigma}_{\mathfrak{r}})}, \tag{4.46}$$

in conjunction with

$$\begin{aligned} \mathbf{M}_{\mathfrak{r}} &= \xi\bar{\mathbf{C}}\mathbf{H}_u\bar{\dot{\mathbf{v}}}, \\ \mathbf{\Sigma}_{\mathfrak{r}} &= \sigma_{\mathfrak{n}}^2\mathbf{I}^{(VN_{\mathrm{r}}LN_{\mathrm{s}})}, \\ D &= VN_{\mathrm{r}}LN_{\mathrm{s}}. \end{aligned} \tag{4.47}$$

Upon substituting the relevant parameters with their specific definitions given in Eq. (4.47), we arrive at the conditional PDF of the received signal, given that $\dot{\mathbf{v}}^{(K)}$ was transmitted:

$$\begin{aligned} p(\mathbf{r}_u|\dot{\mathbf{v}}) &= \frac{1}{\pi^{VN_{\mathrm{r}}LN_{\mathrm{s}}}\det(\sigma_{\mathfrak{n}}^2\mathbf{I})}\exp\left(-\frac{1}{2}(\mathbf{r}_u-\xi\bar{\mathbf{C}}\mathbf{H}_u\bar{\dot{\mathbf{v}}})^H 2(\sigma_{\mathfrak{n}}^2\mathbf{I})^{-1}(\mathbf{r}_u-\xi\bar{\mathbf{C}}\mathbf{H}_u\bar{\dot{\mathbf{v}}})\right) \\ &= \frac{1}{\pi^{VN_{\mathrm{r}}LN_{\mathrm{s}}}(\sigma_{\mathfrak{n}}^2)^{VN_{\mathrm{r}}LN_{\mathrm{s}}}\det(\mathbf{I})}\exp\left(-\frac{1}{\cancel{2}}(\mathbf{r}_u-\xi\bar{\mathbf{C}}\mathbf{H}_u\bar{\dot{\mathbf{v}}})^H\frac{\cancel{2}}{\sigma_{\mathfrak{n}}^2}\mathbf{I}^{-1}(\mathbf{r}_u-\xi\bar{\mathbf{C}}\mathbf{H}_u\bar{\dot{\mathbf{v}}})\right) \\ &= \frac{1}{(\pi\sigma_{\mathfrak{n}}^2)^{VN_{\mathrm{r}}LN_{\mathrm{s}}}\cdot 1}\exp\left(-\frac{1}{\sigma_{\mathfrak{n}}^2}(\mathbf{r}_u-\xi\bar{\mathbf{C}}\mathbf{H}_u\bar{\dot{\mathbf{v}}})^H\mathbf{I}(\mathbf{r}_u-\xi\bar{\mathbf{C}}\mathbf{H}_u\bar{\dot{\mathbf{v}}})\right) \\ &= \frac{1}{(\pi\sigma_{\mathfrak{n}}^2)^{VN_{\mathrm{r}}LN_{\mathrm{s}}}}\exp\left(-\frac{1}{\sigma_{\mathfrak{n}}^2}(\mathbf{r}_u-\xi\bar{\mathbf{C}}\mathbf{H}_u\bar{\dot{\mathbf{v}}})^H(\mathbf{r}_u-\xi\bar{\mathbf{C}}\mathbf{H}_u\bar{\dot{\mathbf{v}}})\right) \\ &= \frac{1}{(\pi\sigma_{\mathfrak{n}}^2)^{VN_{\mathrm{r}}LN_{\mathrm{s}}}}\exp\left(-\frac{1}{\sigma_{\mathfrak{n}}^2}\|\mathbf{r}_u-\xi\bar{\mathbf{C}}\mathbf{H}_u\bar{\dot{\mathbf{v}}}\|^2\right), \end{aligned} \tag{4.48}$$

which is valid in the system context described by Eq. (2.25).

In Eq. (4.48) the Euclidean distance component is the dominant part, which changes with the value of $\dot{\mathbf{v}}$. Additionally, according to Eq. (4.39), Eq. (4.48) may be alternatively presented as the sum of the Euclidean distances between the received signals $\mathbf{r}_{vu}^{n_{\mathrm{r}}l}$ and the transmitted signal $\dot{\mathbf{v}}$ appropriately processed by $\xi\bar{\mathbf{C}}\mathbf{H}_{vu}^{(n_{\mathrm{r}}l)}$ and associated with each array element on each subcarrier frequency over all the $N_{\mathrm{r}}L$ array elements and V subcarrier frequencies. By defining the received signal vector $\mathbf{r}_{vu}^{(n_{\mathrm{r}}l)}$, we have

$$\|\mathbf{r}_u-\xi\bar{\mathbf{C}}\mathbf{H}_u\bar{\dot{\mathbf{v}}}\|^2=\sum_{n_{\mathrm{r}}=1}^{N_{\mathrm{r}}}\sum_{l=1}^{L}\sum_{v=1}^{V}\|\mathbf{r}_{vu}^{(n_{\mathrm{r}}l)}-\xi\bar{\mathbf{C}}\mathbf{H}_{vu}^{(n_{\mathrm{r}}l)}\dot{\mathbf{v}}\|^2. \tag{4.49}$$

By defining the Euclidean distance associated with the CIR matrix $\mathbf{H}_{vu}^{(n_{\mathrm{r}}l)}$ and the received signal vector $\mathbf{r}_{vu}^{(n_{\mathrm{r}}l)}$ as $\mathfrak{D}_{vu}^{(n_{\mathrm{r}}l)}(\dot{\mathbf{v}})$, each of the superimposed Euclidean distance components included in Eq. (4.49) can be expanded according to Eq. (2.78), yielding

$$\mathfrak{D}_{vu}^{(n_{\mathrm{r}}l)}(\dot{\mathbf{v}})=\mathbf{r}_{vu}^{(n_{\mathrm{r}}l)H}\mathbf{r}_{vu}^{(n_{\mathrm{r}}l)}-\left[2\xi\Re\{\dot{\mathbf{v}}^H\mathbf{y}_{vu}^{(n_{\mathrm{r}}l)}\}-\xi^2\dot{\mathbf{v}}^H\mathbf{R}_{vu}^{(n_{\mathrm{r}}l)}\dot{\mathbf{v}}\right], \tag{4.50}$$

where the correlation matrix $\mathbf{R}_{vu}^{(n_{\mathrm{r}}l)}$ of the spreading code matrix $\mathbf{C}$ rotated by the channel-matrix $\mathbf{H}_{vu}^{(n_{\mathrm{r}}l)}$ is given by:

$$\mathbf{R}_{vu}^{(n_{\mathrm{r}}l)}=\mathbf{H}_{vu}^{(n_{\mathrm{r}}l)H}\mathbf{C}^T\mathbf{C}\mathbf{H}_{vu}^{(n_{\mathrm{r}}l)}, \tag{4.51}$$

and the MF output $\mathbf{y}_{vu}^{(n_{\mathrm{r}}l)}$ of the superimposed baseband signal of all the K users associated with each subcarrier vu is given by

$$\mathbf{y}_{vu}^{(n_{\mathrm{r}}l)}=\mathbf{H}_{vu}^{(n_{\mathrm{r}}l)H}\mathbf{C}^T\mathbf{r}_{vu}^{(n_{\mathrm{r}}l)}. \tag{4.52}$$

It may be observed from Eq. (4.50) that the value $(\mathbf{r}_{vu}^{(n_{\mathrm{r}}l)H}\mathbf{r}_{vu}^{(n_{\mathrm{r}}l)})$ does not change with the trial vector-value $\dot{\mathbf{v}}$, regardless of the array element index n_{r}, l or of the subcarrier frequency v.

Hence, the maximization of the conditional probability given in Eq. (4.48) - which quantifies the probability of receiving $\mathbf{r}_u$ as given by Eq. (4.39) for the MFAA assisted MC DS-CDMA UL considered, provided that $\dot{\mathbf{v}}$ was transmitted over the full set $\mathbb{V}^{(K)}$ - is equivalent to the minimization of the sum of Euclidean distances given in Eq. (4.50) over all the V subcarrier frequencies related to the uth branch,

and over all the $N_{\mathrm{r}}L$ array elements. Furthermore, this may be shown to be equivalent to maximizing the sum of the LLFs that were originally defined by Eq. (2.80), which is repeated here for convenience

$$\mathfrak{L}_{vu}^{(n_{\mathrm{r}}l)}(\dot{\mathbf{v}}) = 2\xi\Re\{\dot{\mathbf{v}}^H\mathbf{y}_{vu}^{(n_{\mathrm{r}}l)}\} - \xi^2\dot{\mathbf{v}}^H\mathbf{R}_{vu}^{(n_{\mathrm{r}}l)}\dot{\mathbf{v}}, \tag{4.53}$$

over all the V subcarriers and $N_{\mathrm{r}}L$ antenna array elements, yielding:

$$\begin{aligned}\mathfrak{L}_u(\dot{\mathbf{v}}) &= \sum_{n_{\mathrm{r}}=1}^{N_{\mathrm{r}}}\sum_{l=1}^{L}\sum_{v=1}^{V}\mathfrak{L}_{vu}^{(n_{\mathrm{r}}l)}(\dot{\mathbf{v}}) \\ &= \sum_{n_{\mathrm{r}}=1}^{N_{\mathrm{r}}}\sum_{l=1}^{L}\sum_{v=1}^{V}\Big(2\xi\Re\{\dot{\mathbf{v}}^H\mathbf{y}_{vu}^{(n_{\mathrm{r}}l)}\} - \xi^2\dot{\mathbf{v}}^H\mathbf{R}_{vu}^{(n_{\mathrm{r}}l)}\dot{\mathbf{v}}\Big).\end{aligned} \tag{4.54}$$

Hence, the detector's output vector given by the ML MUD algorithm using the objective function of Eq. (4.54) may be quantified as:

$$\begin{aligned}\hat{\mathbf{v}} &= \arg\max_{\dot{\mathbf{v}}\in\mathbb{V}^{(K)}}\sum_{n_{\mathrm{r}}=1}^{N_{\mathrm{r}}}\sum_{l=1}^{L}\sum_{v=1}^{V}\mathfrak{L}_{vu}^{(n_{\mathrm{r}}l)}(\dot{\mathbf{v}}) \\ &= \arg\max_{\dot{\mathbf{v}}\in\mathbb{V}^{(K)}}\sum_{n_{\mathrm{r}}=1}^{N_{\mathrm{r}}}\sum_{l=1}^{L}\sum_{v=1}^{V}\Big(2\xi\Re\{\dot{\mathbf{v}}^H\mathbf{y}_{vu}^{(n_{\mathrm{r}}l)}\} - \xi^2\dot{\mathbf{v}}^H\mathbf{R}_{vu}^{(n_{\mathrm{r}}l)}\dot{\mathbf{v}}\Big).\end{aligned} \tag{4.55}$$

4.2 ACO Based MUD Algorithm

As seen in Fig. 4.7, each of the U substream's input to the ACO-based MUD generates a $(K \times 1)$-element vector, say $\hat{\mathbf{v}}_u$, for the K-user transmit signal vector of the uth substream bit, say $\mathbf{v}_u$. As detailed in Section 4.1.3, the signals transmitted on the different subcarriers are orthogonal to each other. Hence, no Inter-Carrier-Interference (ICI) will be imposed by the subcarriers on each other after FD-despreading. As the U parallel signals transmitted by the same user are differentiated by their subcarrier frequencies, the U number of ACO-based MUDs seen in Fig. 4.7 may operate in parallel without interfering with each other.

The flow-chart as well as the variables used by the ACO-based MUD algorithm have been detailed in Sections 3.3 and 3.4.

Since the signals belonging to the U branches are considered separately, the main task of each ACO-based MUD seen in Fig. 4.7 remains the mitigation of the MUI introduced by the non-orthogonal TD spreading codes, which is similar to the main task of the ACO-based MUD in the context of the SISO DS-CDMA system detailed in Chapter 3. Hence, the *route table* employed by the ACO-based MUD algorithm in the context of the MFAA assisted MC DS-CDMA system remains a $(2 \times K)$-element matrix, as illustrated in Table 4.1.

As observed in Table 4.1, each of the K columns has two rows corresponding to the two legitimate symbol-value and the globally optimal solution provided by the uth ACO-based MUD seen in Fig. 4.7 is the K-symbol vector $\hat{\mathbf{v}}_u$, which can be represented by a unique route passing through a single cell in each column.

	1	$\cdots$	k	$\cdots$	K
1	$v_{1u} = -1$	$\cdots$	$v_{ku} = -1$	$\cdots$	$v_{Ku} = -1$
2	$v_{1u} = +1$	$\cdots$	$v_{ku} = +1$	$\cdots$	$v_{Ku} = +1$

Table 4.1: The $(2 \times K)$-element route-table employed by the uth ACO-based MUD shown in Fig. 4.7 for the MFAA assisted MC DS-CDMA UL supporting K users with the aid of UV subcarriers, where U signals are transmitted in parallel by each user during each symbol interval.

4.2.1 Log-Likelihood Function of the K-User Vector

Recall from Chapter 3 that the ACO based MUD algorithm is a meta-heuristic learning algorithm that evolves its search pool from the initial setting towards finding the globally optimal solution. As observed from Table 3.5, apart from the internal communication between each component of the ACO based MUD algorithm, it also has to communicate with its environment, both in order to initialize its search pool as well as to calculate the fitness value of all the K-symbol vectors constituting the search pool, so that convergence may be achieved by generating gradually increased fitness values during future iterations. More concretely, the variables characterizing the algorithm and the environment in terms of the CIR and received signals, for example, are related to each other with the aid of the symbol LLFs and vector LLFs, as observed in Table 3.5.

Each K-bit vector captured by the searching pool is characterized by a certain fitness value, also known as the vector-LLF, as observed from Table 3.5, which is calculated by substituting the symbol $\dot{\mathbf{v}}$ in the objective function for the K-bit vector considered.

As for the ML algorithm, the vector-LLF may be quantified by Eq. (4.53), which characterizes the likelihood of a certain vector $\mathbf{v}_u$ being transmitted during a specific symbol interval of the MFAA-assisted MC DS-CDMA system having $N_{\mathrm{r}}L$ antenna array elements and V subcarriers. However, the symbol-LLF given in Eq. (4.54) has to be appropriately scaled, before it can be incorporated in the ACO-based search process quantifying the merit of incorporating a specific K-symbol vector in the search pool.

As observed in Eq. (4.54), the original signal v_{ku}, $u = 1, 2, \ldots, U$ and $k = 1, 2, \ldots, K$, is transmitted at a normalized power of $1/V$ on each of the V subcarriers, since the transmitted symbol has to obey the power constraint stipulated by $\sum_{v=1}^{V} \xi_{vu} = 1$. However, as a benefit of invoking a sophisticated MFAA at the BS's receivers, the power of the signal is increased at the price of increasing the receiver's complexity, as we will detail in Section 4.3. In other words, in contrast to the transmitter, no power-constraint is imposed at the receiver. Therefore, the K-bit vector-LLF is actually increased by a factor of $N_{\mathrm{r}}L$. We note that this factor will affect all the 2^K LLFs associated with the K-bit vectors in an identical manner and hence may be neglected during their comparison. More quantitatively, recall from Eq. (3.18) that the fitness value that will be used for updating the *pheromone* associated with each cell in the route-table is given by:

$$\begin{aligned} \mathfrak{L}_u^{\mathrm{ACO}}(\dot{\mathbf{v}}) &= \frac{1}{N_{\mathrm{r}}L} \mathfrak{L}_u(\dot{\mathbf{v}}) \\ &= \frac{1}{N_{\mathrm{r}}L} \sum_{n_{\mathrm{r}}=1}^{N_{\mathrm{r}}} \sum_{l=1}^{L} \sum_{v=1}^{V} \mathfrak{L}_{vu}^{(n_{\mathrm{r}}l)}(\dot{\mathbf{v}}) \end{aligned}$$

$$= \frac{1}{N_{\mathrm{r}}L} \sum_{n_{\mathrm{r}}=1}^{N_{\mathrm{r}}} \sum_{l=1}^{L} \sum_{v=1}^{V} \Big(2\xi \Re\{ \dot{\mathbf{v}}^H \mathbf{y}_{vu}^{(n_{\mathrm{r}}l)} \} - \xi^2 \dot{\mathbf{v}}^H \mathbf{R}_{vu}^{(n_{\mathrm{r}}l)} \dot{\mathbf{v}} \Big) \tag{4.56}$$

where the objective function $\mathfrak{L}_u(\dot{\mathbf{v}})$ was quantified in Eq. (4.54).

4.2.2 Log-Likelihood Function of the Symbols

Similarly to Section 3.4.1, the symbol-LLF is defined as $\mathfrak{l}_{u,ij} \equiv \mathfrak{l}_{u,-j} \equiv \mathfrak{l}(v_{ju} = -1)$ for $i = 1$; and $\mathfrak{l}_{u,ij} \equiv \mathfrak{l}_{u,+j} \equiv \mathfrak{l}(v_{ju} = +1)$ for $i = 2$, which is extracted from the K-bit vector-LLF of Eq. (4.54). More quantitatively, given Eq. (4.54), the symbol-LLF $\mathfrak{l}_{u,\pm j}$ associated with the $(1, j)$th and $(2, j)$th cell in the route-table of Table 4.1 of the uth ACO-based MUD of Fig. 4.7 may be quantified as:

$$\begin{aligned} \mathfrak{l}_{u,\pm j} &= \sum_{n_{\mathrm{r}}=1}^{N_{\mathrm{r}}} \sum_{l=1}^{L} \sum_{v=1}^{V} \Big(2\xi \Re\big\{ \pm 1 \cdot y_{vu,j}^{(n_{\mathrm{r}}l)} \big\} - \xi^2 \pm 1 \cdot \mathbf{R}_{vu,jj}^{(n_{\mathrm{r}}l)} \cdot \pm 1 \Big) \\ &= \sum_{n_{\mathrm{r}}=1}^{N_{\mathrm{r}}} \sum_{l=1}^{L} \sum_{v=1}^{V} \Big(\pm 2\xi \Re\big\{ y_{vu,j}^{(n_{\mathrm{r}}l)} \big\} - \xi^2 R_{vu,jj}^{(n_{\mathrm{r}}l)} \Big), \end{aligned} \tag{4.57}$$

where $y_{vu,j}^{(n_{\mathrm{r}}l)}$ is the jth element of the vector $\mathbf{y}_{vu}^{(n_{\mathrm{r}}l)}$ in Eq. (4.52) representing the MF output and $R_{vu,jj}^{(n_{\mathrm{r}}l)}$ is the jth diagonal element of $\mathbf{R}_{vu}^{(n_{\mathrm{r}}l)}$ in Eq. (4.51). The K diagonal elements of $\mathbf{R}_{vu}^{(n_{\mathrm{r}}l)}$ represent the auto-correlation coefficients of each of the K users' spreading-code matrix $\mathbf{C}$. More particularly, the jth diagonal element of $\mathbf{R}_{vu}^{(n_{\mathrm{r}}l)}$ can be calculated by:

$$R_{vu,jj}^{(n_{\mathrm{r}}l)} = h_{j,vu}^{(n_{\mathrm{r}}l)H} \mathbf{c}_j^T \mathbf{c}_j h_{j,vu}^{(n_{\mathrm{r}}l)} = \left| h_{j,vu}^{(n_{\mathrm{r}}l)} \right|^2, \tag{4.58}$$

regardless of $v = 1, 2, \ldots, V$, $n_{\mathrm{r}} = 1, 2, \ldots, N_{\mathrm{r}}$, $l = 1, 2, \ldots, L$ and $u = 1, 2, \ldots, U$. Furthermore, the MF output $y_{vu,j}^{(n_{\mathrm{r}}l)}$ of the jth user observed for a specific subcarrier in conjunction with a specific antenna array element may be formulated as:

$$y_{vu,j}^{(n_{\mathrm{r}}l)} = h_{j,vu}^{(n_{\mathrm{r}}l)H} \mathbf{c}_j^T \mathbf{r}_{vu}^{(n_{\mathrm{r}}l)}, \tag{4.59}$$

which is the HO coherent detection result generated in Fig. 4.9 without mitigating the MUI imposed by the other $(K - 1)$ users. Upon substituting $y_{vu,j}^{(n_{\mathrm{r}}l)}$ and $R_{vu,jj}^{(n_{\mathrm{r}}l)}$ from Eq. (4.58) and (4.59), into the symbol-LLF associated with ± 1 when v_{ju} is considered at the vuth subcarrier in conjunction with the (n_{r}, l)th antenna array element may alternatively be quantified as:

$$\mathfrak{l}_{vu,\pm j}^{(n_{\mathrm{r}}l)} = \pm 2\xi \Re\big\{ y_{vu,j}^{(n_{\mathrm{r}}l)} \big\} - \xi^2 \left| h_{j,vu}^{(n_{\mathrm{r}}l)} \right|^2. \tag{4.60}$$

Therefore, the superimposed scalar quantifying the symbol-LLFs related to the symbol transmitted by the jth user on the uth branch may be alternatively quantified as:

$$\mathfrak{l}_{u,\pm j} = \sum_{n_{\mathrm{r}}=1}^{N_{\mathrm{r}}} \sum_{l=1}^{L} \sum_{v=1}^{V} \Big(\pm 2\xi \Re\big\{ y_{vu,j}^{(n_{\mathrm{r}}l)} \big\} - \xi^2 \left| h_{j,vu}^{(n_{\mathrm{r}}l)} \right|^2 \Big). \tag{4.61}$$

The CIR tap $h_{j,vu}^{(n_{\mathrm{r}}l)}$ of Eq. (4.60) in the symbol-LLF expression associated with a single MFAA element on a single subcarrier obeys the average power constraint of

$$E\left[\left| h_{j,vu}^{(n_{\mathrm{r}}l)} \right|^2 \right] = 1. \tag{4.62}$$

Hence, the mean of the superimposed symbol-LLFs averaged over all the V subcarriers is equivalent to the mean of the symbol-LLF obtained for the single-carrier DS-CDMA system in Eq. (3.9), yielding:

$$E\left[\sum_{v=1}^{V} \mathfrak{l}_{vu,\pm j}^{(n_r l)}\right] = E\left[\mathfrak{l}_{\pm j}\right] = 1, \tag{4.63}$$

where $\mathfrak{l}_{\pm j}$ was formulated in Eq. (3.9) as:

$$\mathfrak{l}_{\pm j} = \pm 2\Re\{y_j\} - |h_j|^2. \tag{4.64}$$

As for the single-carrier DS-CDMA system of Chapter 3, the symbol-LLF of Eq. (4.61) will be mapped to the intermediate variable $d_{\pm j}$ with the aid of Eq. (3.11), which is repeated here for convenience as:

$$d_{u,\pm j} = 1 + \exp(-\mathfrak{l}_{u,\pm j}). \tag{4.65}$$

Then the intrinsic affinity $\eta_{\pm j}$ may be formulated as:

$$\begin{aligned} \eta_{u,\pm j} &= 1 + \frac{d_{u,\mp j}}{d_{u,\pm j}}, \\ &= 1 + \frac{1 + \exp(-\mathfrak{l}_{u,\mp j})}{1 + \exp(-\mathfrak{l}_{u,\pm j})}, u = 1, \ldots, U, j = 1, \ldots, K, \end{aligned} \tag{4.66}$$

where the index $u = 1, \ldots, U$ was introduced. Recall from Eq. (4.63), that the mean value of symbol-LLF is 1. However, by summing the symbol-LLFs of $\sum_{v=1}^{V} \mathfrak{l}_{vu,\pm j}^{(n_r l)}$, each associated with a single MFAA element over all the $N_r L$ elements, as demonstrated in Eq. (4.61), the mean given in Eq. (4.63) will be multiplied by a factor of $N_r L$. Therefore, the resultant value has to be normalized by a factor of $1/(N_r L)$, so that it fits the context of Eq. (4.66), yielding:

$$\mathfrak{l}_{u,\pm j}^{\mathrm{ACO}} = \frac{1}{N_r L} \sum_{n_r=1}^{N_r} \sum_{l=1}^{L} \sum_{v=1}^{V} \left(\pm 2\xi \Re\left\{ y_{vu,j}^{(n_r l)} \right\} - \xi^2 \left| h_{j,vu}^{(n_r l)} \right|^2 \right). \tag{4.67}$$

Below we will consider an example for $N_r = 3$ and $L = 4$, assuming that we have $\Re\left\{ y_{vu,j}^{(n_r l)} \right\} = 0.5/\sqrt{V}$ and $\left| h_{j,vu}^{(n_r l)} \right|^2 = 1$ for $v = 1, 2, \ldots, V$. Then, according to Eq. (4.60) we arrive at $\sum_{v=1}^{V} \mathfrak{l}_{vu,+j}^{(n_r l)} = 0$ and $\sum_{v=1}^{V} \mathfrak{l}_{vu,-j}^{(n_r l)} = -2$.

Let us first consider a SISO MC DS-CDMA system, where only a single antenna is installed at both the BS and the MSs.. Then, we have $\mathfrak{l}_{u,+j} = \sum_{v=1}^{V} \mathfrak{l}_{vu,+j} = 0$ and $\mathfrak{l}_{u,-j} = \sum_{v=1}^{V} \mathfrak{l}_{vu,-j} = -2$. According to Eq. (4.66), we have

$$\begin{aligned} \eta_{u,+j} &= 1 + \frac{1 + \exp(-\mathfrak{l}_{u,-j})}{1 + \exp(-\mathfrak{l}_{u,+j})} \\ &= 1 + \frac{1 + \exp(2)}{1 + \exp(0)} \doteq 5.19 \end{aligned} \tag{4.68}$$

and

$$\begin{aligned} \eta_{u,-j} &= 1 + \frac{1 + \exp(-\mathfrak{l}_{u,+j})}{1 + \exp(-\mathfrak{l}_{u,-j})} \\ &= 1 + \frac{1 + \exp(0)}{1 + \exp(2)} \doteq 1.24. \end{aligned} \tag{4.69}$$

These intrinsic affinity values are similar to the values obtained in the context of the DS-CDMA system in Section 3.4.2, provided that the CIR and the noise encountered on each subcarrier is the same as that encountered in the single-carrier DS-CDMA system, since the signal transmitted by each subcarrier is normalized by a factor of $\sqrt{1/V}$.

However, for MFAAs associated with $N_r = 3$ each having $L = 4$ array elements at the BS, the un-normalized symbol-LLF associated with the same symbol becomes

$$\begin{aligned} \mathfrak{l}_{u,+j} &= \sum_{n_r=1}^{3} \sum_{l=1}^{4} \sum_{v=1}^{V} \mathfrak{l}_{vu,+j}^{(n_r l)} \\ &= 3 \times 4 \times 0 = 0 \end{aligned} \tag{4.70}$$

and

$$\begin{aligned} \mathfrak{l}_{u,-j} &= \sum_{n_r=1}^{3} \sum_{l=1}^{4} \sum_{v=1}^{V} \mathfrak{l}_{vu,-j}^{(n_r l)} \\ &= 3 \times 4 \times (-2) = -24. \end{aligned} \tag{4.71}$$

According to Eq. (4.66), we have

$$\begin{aligned} \eta_{u,+j} &= 1 + \frac{1 + \exp(-\mathfrak{l}_{u,-j})}{1 + \exp(-\mathfrak{l}_{u,+j})} \\ &= 1 + \frac{1 + \exp(24)}{1 + \exp(0)} \doteq 1 + 1.32 \times 10^{10} \doteq 1.32 \times 10^{10} \end{aligned} \tag{4.72}$$

and

$$\begin{aligned} \eta_{u,-j} &= 1 + \frac{1 + \exp(-\mathfrak{l}_{u,+j})}{1 + \exp(-\mathfrak{l}_{u,-j})} \\ &= 1 + \frac{1 + \exp(0)}{1 + \exp(24)} \doteq 1 + 7.55 \times 10^{-11} \doteq 1. \end{aligned} \tag{4.73}$$

As demonstrated in Sections 3.4.2.2 and 3.5.4, if the difference between the two intrinsic affinities associated with the two legitimate values of the same symbol is substantial, the search pool will pre-maturely converge to the MF solution during the first ACO-based search iteration, rather than exploring a diverse range of solutions.

Hence, to avoid the above-mentioned premature convergence, the symbol-LLF will be normalized by a factor of $1/(N_r L)$, as shown in Eq. (4.67). Upon employing Eq. (4.67), the appropriate symbol-LLF that will be used by the ACO-based MUD algorithm in the MFAA assisted MC DS-CDMA UL associated with $N_r = 3$ and $L = 4$ becomes

$$\begin{aligned} \mathfrak{l}_{u,+j} &= \frac{1}{3 \times 4} \sum_{n_r=1}^{3} \sum_{l=1}^{4} \sum_{v=1}^{V} \mathfrak{l}_{vu,+j}^{(n_r l)} \\ &= \frac{1}{3 \times 4} 3 \times 4 \times 0 = 0 \end{aligned} \tag{4.74}$$

and

$$\begin{aligned} \mathfrak{l}_{u,-j} &= \frac{1}{3 \times 4} \sum_{n_r=1}^{3} \sum_{l=1}^{4} \sum_{v=1}^{V} \mathfrak{l}_{vu,-j}^{(n_r l)} \\ &= \frac{1}{3 \times 4} 3 \times 4 \times (-2) = -2. \end{aligned} \tag{4.75}$$

Then, upon substituting the $\mathfrak{l}_{u,\pm j}$ values calculated in Eqs. (4.74) and (4.75) into Eq. (4.67), we arrive at the same symbol-LLFs as those obtained in Section 3.4.1 for the SC-DS-CDMA system.

Having determined the symbol-LLFs and the vector-LLFs, let us now characterize the achievable system performance.

4.3 Performance Analysis

In this section, we continue by quantifying the attainable frequency- and spatial diversity gain as well as the beamforming gain provided by the system.

4.3.1 SINR Enhancement

Based on Eq. (3.2) the TD MF output of the Uth branch may be written as:

$$\begin{aligned}\mathbf{y}_u &= \xi \sum_{n_\mathrm{r}=1}^{N_\mathrm{r}} \sum_{l=1}^{L} \sum_{v=1}^{V} \mathbf{R}_{vu}^{(n_\mathrm{r}l)} \mathbf{v}_u + \sum_{n_\mathrm{r}=1}^{N_\mathrm{r}} \sum_{l=1}^{L} \sum_{v=1}^{V} \mathbf{H}_{vu}^{(n_\mathrm{r}l)} \mathbf{C}^T \mathbf{n}_{vu}^{(n_\mathrm{r}l)} \\ &= \xi \sum_{n_\mathrm{r}=1}^{N_\mathrm{r}} \sum_{l=1}^{L} \sum_{v=1}^{V} \mathbf{R}_{vu}^{(n_\mathrm{r}l)} \mathbf{v}_u + \sum_{n_\mathrm{r}=1}^{N_\mathrm{r}} \sum_{l=1}^{L} \sum_{v=1}^{V} \tilde{\mathbf{n}}_{vu}^{(n_\mathrm{r}l)}. \end{aligned} \tag{4.76}$$

The correlation matrix of the received signal asscociated with a single subcarrier and a single antenna array element may be formulated as:

$$\mathbf{R}_{vu}^{(n_\mathrm{r}l)} = \begin{bmatrix} \left|h_{1,vu}^{(n_\mathrm{r}l)}\right|^2 & \rho_{12} h_{1,vu}^{(n_\mathrm{r}l)*} h_{2,vu}^{(n_\mathrm{r}l)} & \cdots & \rho_{1K} h_{1,vu}^{(n_\mathrm{r}l)*} h_{K,vu}^{(n_\mathrm{r}l)} \\ \rho_{12} h_{2,vu}^{(n_\mathrm{r}l)*} h_{1,vu}^{(n_\mathrm{r}l)} & \left|h_{2,vu}^{(n_\mathrm{r}l)}\right|^2 & \cdots & \rho_{1K} h_{2,vu}^{(n_\mathrm{r}l)*} h_{K,vu}^{(n_\mathrm{r}l)} \\ \vdots & \vdots & \ddots & \vdots \\ \rho_{1K} h_{K,vu}^{(n_\mathrm{r}l)*} h_{1,vu}^{(n_\mathrm{r}l)} & \rho_{2K} h_{K,vu}^{(n_\mathrm{r}l)*} h_{2,vu}^{(n_\mathrm{r}l)} & \cdots & \left|h_{K,vu}^{(n_\mathrm{r}l)}\right|^2 \end{bmatrix}, \tag{4.77}$$

where ρ_{ij} represents the cross-correlation coefficient between the codes $\mathbf{c}_i$ and $\mathbf{c}_j$. Then, apart from the AWGN components, the desired signal plus the interfering signal may be expressed as:

$$\bar{\mathbf{y}}_{vu}^{(n_\mathrm{r}l)} = \begin{bmatrix} \left|h_{1,vu}^{(n_\mathrm{r}l)}\right|^2 v_{1u} + \rho_{12} h_{1,vu}^{(n_\mathrm{r}l)*} h_{2,vu}^{(n_\mathrm{r}l)} v_{2u} + \cdots + & \rho_{1K} h_{1,vu}^{(n_\mathrm{r}l)*} h_{K,vu}^{(n_\mathrm{r}l)} v_{Ku} \\ \left|h_{2,vu}^{(n_\mathrm{r}l)}\right|^2 v_{2u} + \rho_{12} h_{2,vu}^{(n_\mathrm{r}l)*} h_{1,vu}^{(n_\mathrm{r}l)} v_{1u} + \cdots + & \rho_{1K} h_{2,vu}^{(n_\mathrm{r}l)*} h_{K,vu}^{(n_\mathrm{r}l)} v_{Ku} \\ \vdots \quad + \quad \vdots \quad + \ddots + & \vdots \\ \left|h_{K,vu}^{(n_\mathrm{r}l)}\right|^2 v_{Ku} + \rho_{1K} h_{K,vu}^{(n_\mathrm{r}l)*} h_{1,vu}^{(n_\mathrm{r}l)} v_{1u} + \cdots + & \rho_{(K-1)K} h_{K,vu}^{(n_\mathrm{r}l)*} h_{K-1,vu}^{(n_\mathrm{r}l)} v_{(K-1)u} \end{bmatrix}. \tag{4.78}$$

Based on Eq. (4.76), the resultant correlation matrix incorporated in the final form of the MF output provided for $\hat{\mathbf{v}}_u$ becomes

$$\mathbf{R}_{vu}^{(n_\mathrm{r}l)} = \begin{bmatrix} \sum_{n_\mathrm{r}=1}^{N_\mathrm{r}}\sum_{l=1}^{L}\sum_{v=1}^{V}\left|h_{1,vu}^{(n_\mathrm{r}l)}\right|^2 & \rho_{12}\sum_{n_\mathrm{r}=1}^{N_\mathrm{r}}\sum_{l=1}^{L}\sum_{v=1}^{V}h_{1,vu}^{(n_\mathrm{r}l)*}h_{2,vu}^{(n_\mathrm{r}l)} \\ \rho_{12}\sum_{n_\mathrm{r}=1}^{N_\mathrm{r}}\sum_{l=1}^{L}\sum_{v=1}^{V}h_{2,vu}^{(n_\mathrm{r}l)*}h_{1,vu}^{(n_\mathrm{r}l)} & \sum_{n_\mathrm{r}=1}^{N_\mathrm{r}}\sum_{l=1}^{L}\sum_{v=1}^{V}\left|h_{2,vu}^{(n_\mathrm{r}l)}\right|^2 \\ \vdots & \vdots \\ \rho_{1K}\sum_{n_\mathrm{r}=1}^{N_\mathrm{r}}\sum_{l=1}^{L}\sum_{v=1}^{V}h_{K,vu}^{(n_\mathrm{r}l)*}h_{1,vu}^{(n_\mathrm{r}l)} & \rho_{2K}\sum_{n_\mathrm{r}=1}^{N_\mathrm{r}}\sum_{l=1}^{L}\sum_{v=1}^{V}h_{K,vu}^{(n_\mathrm{r}l)*}h_{2,vu}^{(n_\mathrm{r}l)} \end{bmatrix}$$
$$\begin{bmatrix} \cdots & \rho_{1K}\sum_{n_\mathrm{r}=1}^{N_\mathrm{r}}\sum_{l=1}^{L}\sum_{v=1}^{V}h_{1,vu}^{(n_\mathrm{r}l)*}h_{K,vu}^{(n_\mathrm{r}l)} \\ \cdots & \rho_{1K}\sum_{n_\mathrm{r}=1}^{N_\mathrm{r}}\sum_{l=1}^{L}\sum_{v=1}^{V}h_{2,vu}^{(n_\mathrm{r}l)*}h_{K,vu}^{(n_\mathrm{r}l)} \\ \ddots & \vdots \\ \cdots & \sum_{n_\mathrm{r}=1}^{N_\mathrm{r}}\sum_{l=1}^{L}\sum_{v=1}^{V}\left|h_{K,vu}^{(n_\mathrm{r}l)}\right|^2 \end{bmatrix}. \tag{4.79}$$

Then the MF output y_{ku} for the uth symbol transmitted by the kth user can be formulated as:

$$\begin{aligned} y_{ku} =& \xi\sum_{n_\mathrm{r}=1}^{N_\mathrm{r}}\sum_{l=1}^{L}\sum_{v=1}^{V}\left|h_{k,vu}^{(n_\mathrm{r}l)}\right|^2 v_{ku} + \xi\sum_{j=1,j\neq k}^{K}\rho_{jk}\sum_{n_\mathrm{r}=1}^{N_\mathrm{r}}\sum_{l=1}^{L}\sum_{v=1}^{V}h_{k,vu}^{(n_\mathrm{r}l)*}h_{j,vu}^{(n_\mathrm{r}l)}v_{ju} \\ &+ \sum_{n_\mathrm{r}=1}^{N_\mathrm{r}}\sum_{l=1}^{L}\sum_{v=1}^{V}\tilde{n}_{vu}^{(n_\mathrm{r}l)}. \end{aligned} \tag{4.80}$$

Given that the mean $E[h_{k,vu}^{(n_\mathrm{r}l)}]$ of the random variable constituted by the CIR tap and the mean $E[\tilde{n}_{k,vu}^{(n_\mathrm{r}l)}]$ of the noise component are both zero, regardless of the indices n_r, l, k, v or u, the power of the desired signal in Eq. (4.80) may be represented as

$$\begin{aligned} &\mathrm{Var}\left(\xi\sum_{n_\mathrm{r}=1}^{N_\mathrm{r}}\sum_{l=1}^{L}\sum_{v=1}^{V}\left|h_{k,vu}^{(n_\mathrm{r}l)}\right|^2 v_{ku}\right) \\ =&E\left[\left(\xi\sum_{n_\mathrm{r}=1}^{N_\mathrm{r}}\sum_{l=1}^{L}\sum_{v=1}^{V}\left|h_{k,vu}^{(n_\mathrm{r}l)}\right|^2 v_{ku} - E\left[\xi\sum_{n_\mathrm{r}=1}^{N_\mathrm{r}}\sum_{l=1}^{L}\sum_{v=1}^{V}\left|h_{k,vu}^{(n_\mathrm{r}l)}\right|^2\right]\right)^2\right] \\ =&E\left[\left(\xi\sum_{n_\mathrm{r}=1}^{N_\mathrm{r}}\sum_{l=1}^{L}\sum_{v=1}^{V}\left|h_{k,vu}^{(n_\mathrm{r}l)}\right|^2 v_{ku}\right)^2\right]. \end{aligned} \tag{4.81}$$

Since the CIR taps and the transmitted signal are independent of each other, Eq.(4.81) may be further streamlined as

$$\xi^2 E\left[\left(\sum_{n_\mathrm{r}=1}^{N_\mathrm{r}}\sum_{l=1}^{L}\sum_{v=1}^{V}\left|h_{k,vu}^{(n_\mathrm{r}l)}\right|^2 v_{ku}\right)^2\right] = \xi^2 N_\mathrm{r}^2 L^2 V^2. \tag{4.82}$$

When we have $n_\mathrm{r} \neq \dot{n}_\mathrm{r}$ or $v \neq \dot{v}$, the CIR taps related to the different MFAA element or to different subcarriers are mutually indepedent, hence $\left|h_{k,vu}^{(n_\mathrm{r}l)}\right|^2$ and $\left|h_{k,\dot{v}u}^{(\dot{n}_\mathrm{r}\dot{l})}\right|^2$ are uncorrelated random variables,

yielding:

$$\begin{aligned} & E\left[\left|h_{k,vu}^{(n_{\mathrm{r}}l)}\right|^2\left|h_{k,\dot{v}u}^{(\dot{n}_{\mathrm{r}}\dot{l})}\right|^2 v_{ku}^2\right] \\ =& E\left[\left|h_{k,vu}^{(n_{\mathrm{r}}l)}\right|^2\right] E\left[\left|h_{k,\dot{v}u}^{(\dot{n}_{\mathrm{r}}\dot{l})}\right|^2\right] E\left[v_{ku}^2\right] \\ =& 1\times 1\times 1 = 1. \end{aligned} \tag{4.83}$$

By contrast, when we have $n_{\mathrm{r}} = \dot{n}_{\mathrm{r}}$ and $v = \dot{v}$, regardless whether $l = \dot{l}$ or $l \neq \dot{l}$, the corresponding two CIRs of the same MFAA n_{r} and of the same subcarrier vu are perfectly correlated, regardless of the index of the array element l. More specifically, as it may be inferred from Eq. (4.10), given that $h_{k,vu}^{(n_{\mathrm{r}})}$ represents the CIR spanning from the kth user to the 1st element of the n_{r}th MFAA on the vuth subcarrier, the CIR spanning from the same user to the same MFAA on the same subcarrier to the lth array element may be expressed as:

$$\begin{aligned} h_{k,vu}^{(n_{\mathrm{r}}l)} &= \alpha_{k,vu}^{(n_{\mathrm{r}})} \exp\left\{j\left[\psi_{k,vu}^{(n_{\mathrm{r}})} + (l-1)2\pi\frac{d}{\lambda}\sin\theta_k^{(n_{\mathrm{r}})}\right]\right\} \\ &= h_{k,vu}^{(n_{\mathrm{r}})}\exp(j\delta_l), \end{aligned} \tag{4.84}$$

where we have

$$h_{k,vu}^{(n_{\mathrm{r}})} = \alpha_{k,vu}^{(n_{\mathrm{r}})}\exp\left\{j\psi_{k,vu}^{(n_{\mathrm{r}})}\right\} \tag{4.85}$$

and

$$\delta_l = (l-1)2\pi\frac{d}{\lambda}\sin\theta_k^{(n_{\mathrm{r}})}. \tag{4.86}$$

Therefore, in the process of evaluating the power of the desired signal given by the first term of $\xi\sum_{n_{\mathrm{r}}=1}^{N_{\mathrm{r}}}\sum_{l=1}^{L}\sum_{v=1}^{V}\left|h_{k,vu}^{(n_{\mathrm{r}}l)}\right|^2 v_{ku}$ in Eq. (4.80), we have

$$\begin{aligned} & E\left[\left|h_{k,vu}^{(n_{\mathrm{r}}l)}\right|^2\left|h_{k,vu}^{(n_{\mathrm{r}}\dot{l})}\right|^2\right] \\ =& E\left[\left|h_{k,vu}^{(n_{\mathrm{r}})}\exp(j\delta_l)\right|^2\left|h_{k,vu}^{(n_{\mathrm{r}})}\exp(j\delta_{\dot{l}})\right|^2\right] \\ =& E\left[\left|h_{k,vu}^{(n_{\mathrm{r}})}\right|^2\left|h_{k,vu}^{(n_{\mathrm{r}})}\right|^2\right] = 1. \end{aligned} \tag{4.87}$$

Similarly, when the power of the interfering signal in Eq. (4.80) is evaluated, for $n_{\mathrm{r}} = \dot{n}_{\mathrm{r}}$ and $v = \dot{v}$ we have

$$\begin{aligned} & E\left[h_{j,vu}^{(n_{\mathrm{r}}\dot{l})*}h_{k,vu}^{(n_{\mathrm{r}}\dot{l})}h_{k,vu}^{(n_{\mathrm{r}}l)*}h_{j,vu}^{(n_{\mathrm{r}}l)}v_{ju}^2\right] \\ =& E\left[h_{j,vu}^{(n_{\mathrm{r}}\dot{l})*}h_{k,vu}^{(n_{\mathrm{r}})}h_{k,vu}^{(n_{\mathrm{r}})*}\exp\left[j(\delta_l-\delta_{\dot{l}})\right]h_{j,vu}^{(n_{\mathrm{r}}l)}\right]E\left[v_{ju}^2\right] \\ =& E\left[h_{j,vu}^{(n_{\mathrm{r}}\dot{l})*}\left|h_{k,vu}^{(n_{\mathrm{r}})}\right|^2\exp\left[j(\delta_l-\delta_{\dot{l}})\right]h_{j,vu}^{(n_{\mathrm{r}}l)}\right] \\ =& E\left[\left|h_{k,vu}^{(n_{\mathrm{r}})}\right|^2 h_{j,vu}^{(n_{\mathrm{r}}\dot{l})*}h_{j,vu}^{(n_{\mathrm{r}}l)}\exp\left[j(\delta_l-\delta_{\dot{l}})\right]\right] \\ =& E\left[\left|h_{k,vu}^{(n_{\mathrm{r}})}\right|^2\left|h_{j,vu}^{(n_{\mathrm{r}})}\right|^2\exp\left[j2(\delta_l-\delta_{\dot{l}})\right]\right] \\ =& E\left[\left|h_{k,vu}^{(n_{\mathrm{r}})}\right|^2\right]E\left[\left|h_{j,vu}^{(n_{\mathrm{r}})}\right|^2\right]E\left[\exp\left[j2(\delta_l-\delta_{\dot{l}})\right]\right] \\ =& 1\times 1\times 1 = 1. \end{aligned} \tag{4.88}$$

Otherwise, when we have either $n_{\mathrm{r}} \neq \dot{n}_{\mathrm{r}}$ or $v \neq \dot{v}$, the two CIR taps associated either with different MFAA elements, or with different subcarriers, or alternatively with different users are mutually independent, yielding

$$E\left[h_{k,\dot{v}u}^{(\dot{n}_{\mathrm{r}}\dot{l})*} h_{k,\dot{v}u}^{(n_{\mathrm{r}}\dot{l})}\right] = E\left[h_{k,\dot{v}u}^{(\dot{n}_{\mathrm{r}}\dot{l})*}\right] E\left[h_{k,vu}^{(n_{\mathrm{r}}l)}\right]. \tag{4.89}$$

As a result, when we have either $n_{\mathrm{r}} \neq \dot{n}_{\mathrm{r}}$ or $v \neq \dot{v}$ and when the power of the interfering component imposed by the jth user, $j = 1, 2, \ldots, K$ and $j \neq k$ is calculated, the following relationship holds:

$$\begin{aligned} & E\left[h_{j,\dot{v}u}^{(\dot{n}_{\mathrm{r}}\dot{l})*} h_{k,\dot{v}u}^{(\dot{n}_{\mathrm{r}}\dot{l})} h_{k,vu}^{(n_{\mathrm{r}}l)*} h_{j,vu}^{(n_{\mathrm{r}}l)} v_{ju}^2\right] \\ =& E\left[h_{j,\dot{v}u}^{(\dot{n}_{\mathrm{r}}\dot{l})*}\right] E\left[h_{k,\dot{v}u}^{(\dot{n}_{\mathrm{r}}\dot{l})}\right] E\left[h_{k,vu}^{(n_{\mathrm{r}}l)*}\right] E\left[h_{j,vu}^{(n_{\mathrm{r}}l)}\right] E\left[v_{ju}^2\right] \\ =& 0 \times 0 \times 0 \times 0 \times 1 = 0. \end{aligned} \tag{4.90}$$

Then, the variance of the interfering component $\xi \sum_{j=1,j\neq k}^{K} \rho_{jk}$, namely $\sum_{n_{\mathrm{r}}=1}^{N_{\mathrm{r}}} \sum_{l=1}^{L} \sum_{v=1}^{V} h_{k,vu}^{(n_{\mathrm{r}}l)*} h_{j,vu}^{(n_{\mathrm{r}}l)} v_{ju}$ of Eq. (4.80) may be written as:

$$\begin{aligned} & \xi^2 E\left[\left(\sum_{j=1,j\neq k}^{K} \rho_{jk} \sum_{n_{\mathrm{r}}=1}^{N_{\mathrm{r}}} \sum_{l=1}^{L} \sum_{v=1}^{V} h_{k,vu}^{(n_{\mathrm{r}}l)*} h_{j,vu}^{(n_{\mathrm{r}}l)} v_{ju}\right)^2\right] \\ =& \xi^2 \sum_{j=1,j\neq k}^{K} \rho_{jk}^2 \sum_{\dot{l}=1}^{L} \sum_{l=1}^{L} \sum_{n_{\mathrm{r}}=1}^{N_{\mathrm{r}}} \sum_{v=1}^{V} h_{j,vu}^{(n_{\mathrm{r}}\dot{l})*} h_{k,vu}^{(n_{\mathrm{r}}\dot{l})} h_{k,vu}^{(n_{\mathrm{r}}l)*} h_{j,vu}^{(n_{\mathrm{r}}l)} \\ +& \xi^2 \sum_{j=1,j\neq k}^{K} \rho_{jk}^2 \sum_{\dot{l}=1}^{L} \sum_{l=1}^{L} \sum_{n_{\mathrm{r}}=1}^{N_{\mathrm{r}}} \sum_{v=1}^{V} \sum_{\dot{n}_{\mathrm{r}}=1,\dot{n}_{\mathrm{r}}\neq n_{\mathrm{r}}}^{N_{\mathrm{r}}} \sum_{\dot{v}=1,\dot{v}\neq v}^{V} h_{j,\dot{v}u}^{(\dot{n}_{\mathrm{r}}\dot{l})*} h_{k,\dot{v}u}^{(\dot{n}_{\mathrm{r}}\dot{l})} h_{k,vu}^{(n_{\mathrm{r}}l)*} h_{j,vu}^{(n_{\mathrm{r}}l)} \\ =& \xi^2 \sum_{j=1,j\neq k}^{K} \rho_{jk}^2 L^2 \times N_{\mathrm{r}} \times V \times 1 \\ +& \xi^2 \sum_{j=1,j\neq k}^{K} \rho_{jk}^2 L^2 \times N_{\mathrm{r}} \times (N_{\mathrm{r}} - 1) \times V \times (V - 1) \times 0 \\ =& \xi^2 \sum_{j=1,j\neq k}^{K} \rho_{jk}^2 L^2 \times N_{\mathrm{r}} \times V. \end{aligned} \tag{4.91}$$

Finally, since the noise processes encountered at different array elements or at different subcarriers are mutually independent, the variance of the AWGN component in Eq. (4.80) can be expressed as:

$$E\left[\left(\sum_{n_{\mathrm{r}}=1}^{N_{\mathrm{r}}} \sum_{l=1}^{L} \sum_{v=1}^{V} \tilde{n}_{vu}^{(n_{\mathrm{r}}l)}\right)^2\right] = \sum_{n_{\mathrm{r}}=1}^{N_{\mathrm{r}}} \sum_{l=1}^{L} \sum_{v=1}^{V} E\left[\left(\tilde{n}_{vu}^{(n_{\mathrm{r}}l)}\right)^2\right] = N_{\mathrm{r}} L V. \tag{4.92}$$

From the above analysis we can draw the following conclusions related to the MF output in the MFAA assisted MC DS-CDMA UL:

1. The spatial- and frequency-diversity gain achieved by the independently fading of CIRs of the different antenna arrays and of the orthogonal frequencies carrying the same signal will both increase the power of the desired signal, hence mitigating the effects of the interference.

2. On the other hand, the beamforming gain achieved by the $\lambda/2$-spaced elements of each array will enhance both the power of the desired signal as well as that of the interference, while leaving the power of the noise unaffected.

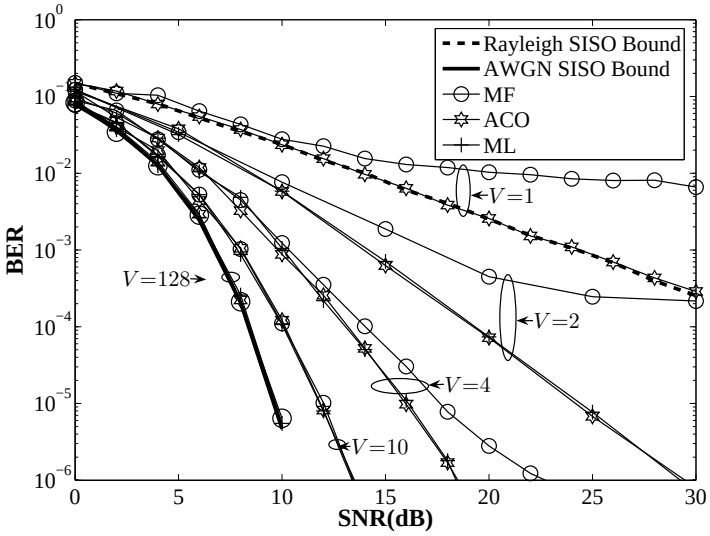

Figure 4.9: BER versus SNR performance of the ACO based MUD in the SISO MC DS-CDMA UL, over uncorrelated Rayleigh channels when $N_s = 31$-chip Gold sequences are employed and $K = 32$ users are supported. All system parameters were summarized in Table 4.2 and the system's schematic was portrayed in Fig. 4.2. The effective throughput is one Bbp/Hz.

3. Hence, both the beamforming gain as well as the frequency- and the spatial-diversity gain will enhance the attainable SNR. However, only the frequency-and spatial-diversty gains will increase the SINR, while the beamforming array gain will only mitigate the MUI, if it arrives from an angle, which is sufficiently different from that of the desired signal.

4.3.2 Simulation Results

Fig. 4.9 shows the BER versus SNR performance of the MRC-based correlation detector, of the ML MUD and of the ACO-based MUD. Again, the number of subcarriers was varied across a wide range, spanning the interval of $V = 1, \ldots, 128$. Both the uplink MC DS-CDMA system employing the MRC-based correlation detector and the ACO-based MUD are capable of supporting $K = 32$ users, while imposing a low to moderate complexity. By contrast, the MC DS-CDMA system employing the ML MUD has an excessive complexity for $K = 32$ users, which is on the order of $O(2^{32})$. Fig. 4.10 shows the complexity imposed versus the number of users supported at SNR = 10dB for the MRC-based correlation detector, for the ML MUD and for the ACO-based MUD along with a different number of subcarriers, varying from $V = 1, \ldots, 128$.

As seen in Fig. 4.9, the ACO-based MUD is capable of approaching the BER performance of the ML MUD, regardless of the number of subcarriers. On the other hand, as shown in Fig. 4.10, regardless of the number of subcarriers, the complexity of the ACO-based MUD - which was evaluated in terms of the number of FLoating Operation Per Second (FLOPS) - is similarly low to that of the MRC-MF and it is only a fraction of that of the ML MUD, especially when the number of users supported is high. For example, for $K = 32$, the complexity of the ACO-based MUD is deemed to be a factor of 10^8 lower than that of the MLD.

Throughout our simulations we assumed that the TD spreading sequences were the $N_s = 31$-

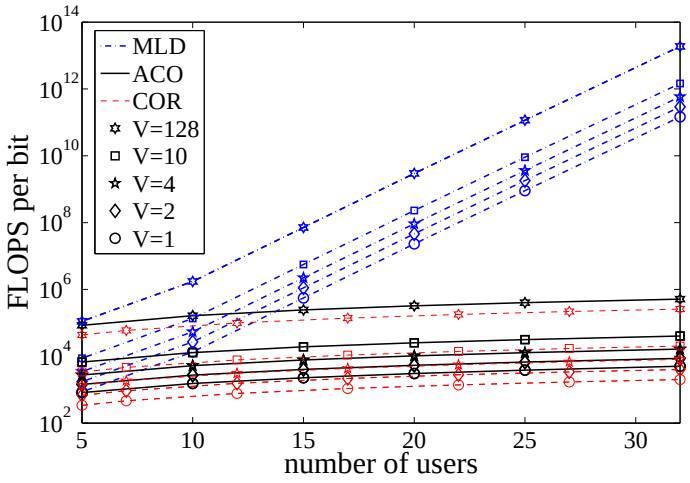

Figure 4.10: Complexity (FLOPS/bit) per user per bit evaluated in terms of the number of FLoating Point Operations (FLOPS) versus the number of users supported in the uplink of the MC DS-CDMA system considered using $V = 1, 2, 4, 10, 128$ subcarriers and $N_c = 31$-chip Gold codes for TD-spreading. All system parameters were summarized in Table 4.2. The system's schematic was portrayed in Fig. 4.2.

chip Gold codes and the parameters of the ACO MUD are listed in Table 4.3, while those of the MC-DS-CDMA system in Table 4.2.

System	Modem	BPSK
	Multiple access mothod	DS-CDMA
	Spreading code	Gold code
	Spreading factor	$N_s = 31$
	No. of transmit antennas	1
	No. of receive antenna arrays	$N_r = 1, 2, 3, 4$
	No. of elements per receive antenna array	$L = 1, 2, 3, 4$
	No. of subcarriers	$V = 1, 2, 4, 8, \ldots, 128$
	No. of users	$K = 32$
	Channnel	Uncorrelated Rayleigh fading

Table 4.2: Parameters for the MFAA assisted DS-CDMA UL.

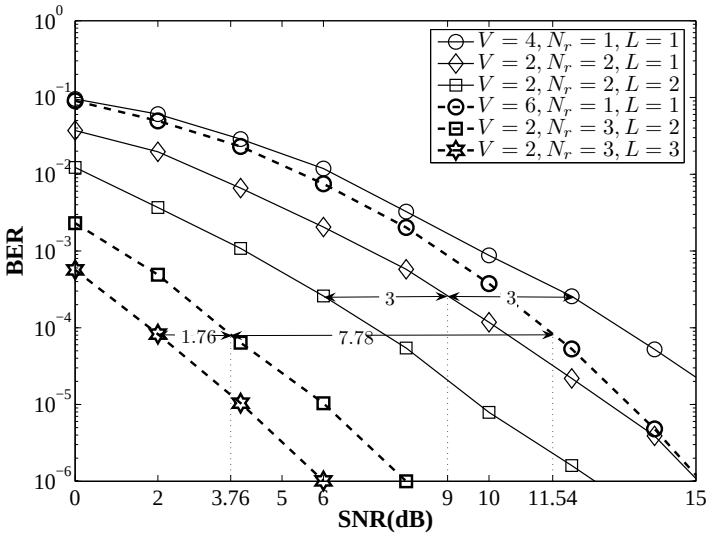

Figure 4.11: BER versus SNR performance of the ACO based MUD in the MFAA-assisted MC DS-CDMA UL for transmitting over uncorrelated Rayleigh channels, when $N_s = 31$-chip Gold sequences are employed and $K = 32$ users are supported. All system parameters were summarized in Table 4.2 and the system's schematic was portrayed in Fig. 4.2. The effective throughput was one Bbp/Hz.

Implication	Value
Initial pheromone	$\tau = 0.01$
Evaporation rate	$\rho = 0.5$
Number of ants	$\zeta = 10$
Number of iterations	$\Xi = 10$
Weight of pheromone	$\alpha = 0.9$
Weight of intrinsic affinity	$\beta = 6$
Weight for the elite ant	$\sigma = 8$

Table 4.3: Parameters of the ACO-based MUD algorithm applied. All system parameters were summarized in Table 4.2 and the system's schematic was portrayed in Fig. 4.2.

The BER performance of the ACO-based MUD, of the MRC based MF and of the ML MUD of the SISO MC DS-CDMA system are presented in Fig. 4.9, while the BER performance of the ACO-based MUD employed in the MFAA-assisted MC DS-CDMA system can be observed in Fig. 4.11. Additionally, the diversity gain $\Delta\Upsilon_D$, beamforming gain $\Delta\Upsilon_A$ as well as the SNR gain $\Delta\Upsilon_S$ versus the number of receive antennas employed in the MFAA-assisted MC DS-CDMA UL may be studied in Fig. 4.12.

Firstly, as seen in Fig. 4.9, Fig. 4.11 and Fig. 4.13, the ACO-based MUD is capable of approaching the BER performance of the ML MUD at a similarly low complexity as that of the MRC-MF, regardless of the value of V, L or N_r. For instance, when the number of users is $K = 32$, the complexity of the ACO-based MUD may be deemed to be a factor of 10^8 lower than that of the ML MUD.

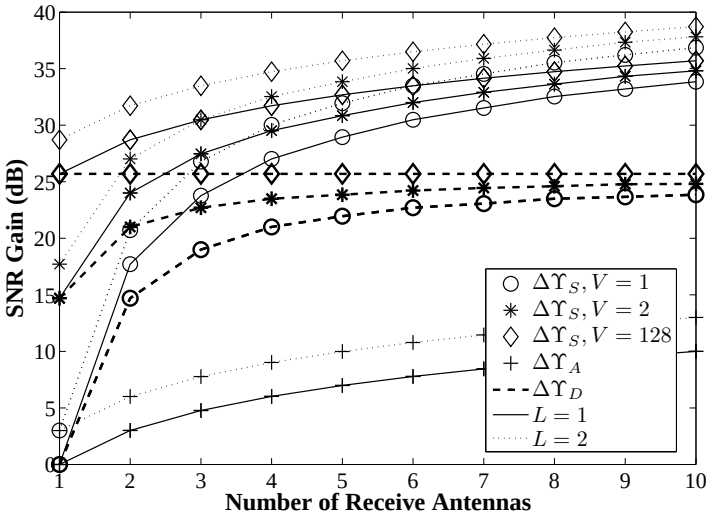

Figure 4.12: The diversity gain $\Delta\Upsilon_{\rm D}$, the BF gain $\Delta\Upsilon_{\rm A}$ and the SNR gain $\Delta\Upsilon_{\rm S}$ versus the number of receiver antennas in conjunction with different number of subcarriers V and with $L = 1$ or 2 elements per antenna array at a BER of 10^{-4}. Uncorrelated Rayleigh channels are considered, $N_{\rm s} = 31$-chip Gold sequences are employed and $K = 32$ users are supported. All system parameters were summarized in Table 4.2 and the system's schematic was portrayed in Fig. 4.2. The effective throughput was one Bbp/Hz.

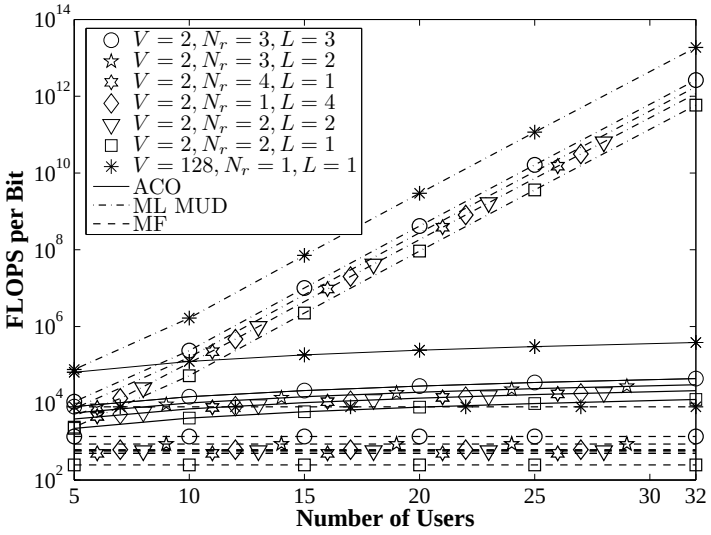

Figure 4.13: Complexity versus the number of users for the ML MUD, the ACO based MUD and the MF aided MFAA assisted MC DS-CDMA UL at SNR = 10dB, when $N_{\rm s} = 31$-chip Gold sequences are employed. All system parameters were summarized in Table 4.2 and the system's schematic was portrayed in Fig. 4.2. The effective throughput was one Bbp/Hz.

Secondly, the SNR gain of the MFAA-assisted MC DS-CDMA UL experienced at a certain BER value is the sum of the diversity gain and the beamforming gain. More explicitly, the diversity gain $\Upsilon_{\rm D}$ is monotonically increasing with the diversity order of $\gamma_{\rm d} = V \times N_{\rm r}$, while the beamforming gain $\Upsilon_{\rm A}$ is directly quantified as $10\lg(\gamma_{\rm a}) = 10\lg(N_{\rm r} \times L)$. The BF gain $\Delta\Upsilon_{\rm A}$ experienced at the BER of 10^{-4} attained by the different MFAA-assisted MC DS-CDMA systems having the same diversity gain as the single-user SISO DS-CDMA benchmark system has been recorded in Fig. 4.11.

Thirdly, as seen in Fig. 4.13, the complexity of the ACO based MUD associated with a low number of subcarriers, such as $V = 2$, but using the $L = 2$ and $N_r = 2$ MFAA-assisted MC DS-CDMA configuration is not as high as that in the SISO MC DS-CDMA system using $N_r = 1$, $L = 1$ in conjunction with a large number of subcarriers, such as $V = 128$. However, Figs. 4.11 and 4.12 show that the BER of the ACO based MUD in the former system improved more substantially than that in the latter system, which may be explained as follows.

First of all, the BER performance of the ACO based MUD is determined by the SNR gain, which is constituted by the sum of the diversity gain and the beamforming gain. On one hand, in the SISO MC DS-CDMA system associated with $N_r = 1$ and $L = 1$, the increased number of subcarriers V only provides a diversity gain, but no BF gain. However, as shown in Fig. 4.12, no significant incremental diversity gain is observed upon increasing the diversity order beyond $\gamma_d = 5$, which would be equivalent to $V = 5$ in a SISO MC DS-CDMA system, since the achievable diversity gain saturates, when the diversity order is increased, leading to a near-Gaussian performance. By contrast, in the MFAA-assisted MC DS-CDMA system, apart from the diversity gain contributed by increasing either V or N_r, an additional BF gain is achieved upon increasing either N_r or L. Furthermore, in contrast to the diversity gain, the attainable BF gain does not have a strict physical upper bound, as observed in Fig. 4.12. Naturally, however, increasing V, N_r and L will commensurately increase the complexity imposed.

Therefore, at a given complexity, the BER performance of the ACO based MUD can be improved more substantially in the context of the MFAA-assisted MC DS-CDMA system than in its SISO counterpart, since the SNR gain achieved by employing an $(L \times N_r)$-element MFAA in a V-subcarrier system is significantly higher than that attained by increasing the number of subcarriers V by a factor of $(N_r \times L)$ in the context of the SISO MC DS-CDMA benchmark system.

4.4 Summary

In this chapter we demonstrated that MC DS-CDMA schemes relying on MFAA are capable of achieving BF gains, frequency-diversity as well as spatial-diversity at the same time. A sophisticated ACO-based MUD was designed for the MFAA assisted MC DS-CDMA UL, which is capable of approaching the optimum ML performance at a significantly reduced complexity, regardless of the number of subcarriers, of the number of elements per antenna array or of the number of antenna arrays. Our simulation results also demonstrate that increasing the number of receive antenna arrays and the number of elements per antenna array in the MFAA aided MC DS-CDMA system will allow the ACO based MUD to achieve a higher BER performance improvement than that attained upon increasing the number of subcarriers in the SISO MC DS-CDMA benchmark system.

Finally, the attainable SNR gain as well as the complexity imposed by the ACO based MUD algorithm in different SISO or MFAA assisted MC DS-CDMA systems are summarized in Table 4.4.

System		SNR gain (dB)	Complexity (FLOPS)
SISO SC DS-CDMA	$V = 1$, $N_r = 1$, $L = 1$	0	3.75×10^3
MFAA assisted MC DS-CDMA	$V = 4$, $N_r = 1$, $L = 1$	20.4	1.5×10^4
	$V = 6$, $N_r = 1$, $L = 1$	22.46	2.25×10^4
	$V = 2$, $N_r = 2$, $L = 1$	23.4	1.5×10^4
	$V = 2$, $N_r = 2$, $L = 2$	26.4	3×10^4
	$V = 2$, $N_r = 3$, $L = 2$	30.24	4.5×10^4
	$V = 2$, $N_r = 3$, $L = 3$	32	6.75×10^4
SISO MC DS-CDMA	$V = 2$, $N_r = 1$, $L = 1$	14.5	7.5×10^3
	$V = 4$, $N_r = 1$, $L = 1$	20.8	1.5×10^4
	$V = 10$, $N_r = 1$, $L = 1$	24.0	5.25×10^4
	$V = 128$, $N_r = 1$, $L = 1$	26.0	4.8×10^5

Table 4.4: SNR gain and complexity of different DS-CDMA systems with various parameters, when $K = 32$ users are supported with Gold codes having a length of $N_s = 31$ chips in combination with the ACO-based MUD and a BER of 1×10^{-4} is achieved. The parameters of the ACO-based MUD algorithm applied in all systems were summarized in Table 4.2 and the system's schematic was portrayed in Fig. 4.2.

Chapter 5

ACO Aided MUD for STBC-CDMA

5.1 Introduction

Space-Time Block Codes (STBC) [181, 202] may be employed in wireless communication system to transmit multiple replicas of a certain symbol over a number of antennas so that the reliability of the signal-transmission can be improved with the aid of diversity gain. The fact that the wireless channel is typically Rayleigh faded, may result in several received replicas which experience different attenuations and phase rotations. This may be exploited to improve the probability of correctly decoding the received signals. As a further benefit, STBC is capable of combining all the copies of the received signal in an optimal way.

In this chapter, two transmit antennas are used by each Mobile Station (MS) to construct an STBC for uplink (UL) transmissions. At the carrier frequency of 2GHz, the wavelength is 15cm and hence the afforded antenna-separation at the shirt-pocket-sized MS is insufficient to ensure independent fading of the two antennas' signals.

However, assuming an antenna-separation of say 30 cm, i.e. two wavelengths at 2 GHz in a laptop transmitter might provide sufficiently decorrelation for approaching our idealized assumption of having independent fading. Alternatively, two single-antenna-aided mobiles may form a distributed $\mathcal{G}_2$ space-time code, which would have a near-perfect relay-link between them, provided that the cooperating mobiles are sufficiently close to each other. Naturally, this requires the creation of two time - or frequency - slots for the classic broadcast-phase and cooperation-phase of the mobiles, as detailed in [203], hence potentially halving the total system's throughput in exchange for the $\mathcal{G}_2$-STBC based 2nd-order diversity.

However, the BER performance of the ACO based MUD algorithm of [130, 131] exhibits an error-floor. Against this background, in this treatise, a novel ACO based MUD algorithm is proposed for mitigating the error floor.

The outline of this chapter is as follows. The system's architecture is detailed in Section 5.2, while Section 5.3 briefly reviews the ACO-aided MUD algorithm of Chapter 5 applied in the STBC-assisted DS-CDMA system. This is followed by the introduction of an improved ACO-aided MUD algorithm invoked for the proposed system. Both ACO-based ST/MUDs algorithms are then employed in the context of an $R = 7$-user system and the simulation results are interpreted in Section 5.4.

Our simulation results detailed in Section 5.5 demonstrate the success of the proposed algorithm in improving the ACO based MUD of [130, 131], despite operating at a low complexity. Our conclusions are provided in Section 5.6.

5.2 System Description

As seen in Fig. 5.1 in each user's transmitter, the bit stream is firstly space-time block coded according to the $\mathcal{G}_2$ principle [181]. The signals v_{k1} and v_{k2} are input to the two $\mathcal{G}_2$ branches within the first symbol duration, while during the second symbol interval, $-v_{k2}^*$ and v_{k1}^* are transmitted. The symbols of both branches are spread using the same CDMA spreading code $\mathbf{c}_k$ having a length of N_s chips, which is assigned by the BS to the kth user. Then the signals are transmitted from the two antennas via the independently faded non-dispersive Rayleigh channels h_{k1} and h_{k2} respectively, for all the $k = 1, 2, \ldots, K$ users. The real and imaginary parts of the complex-valued Gaussian distributed fading envelope have a mean of zero and a variance of 1/2.

Finally, during each of the N_s chip intervals of the two symbol durations, the composite multiuser signal is given by the sum of all the symbols transmitted from the $2K$ antennas of the K users via the $2K$ channels plus the Additive White Gaussian Noise (AWGN). The AWGN encountered during the first and the second symbol duration can be encapsulated in the $(N_\mathrm{s} \times 1)$-element vectors $\mathbf{n}_1$ and $\mathbf{n}_2$, respectively. Each element n_{in_s}, for $i = 1, 2$ and $n_s = 1, 2, \ldots, N_\mathrm{s}$ is an instantaneous value of a complex-valued Gaussian random variable with a zero-mean and a variance of $2\sigma_\mathbf{n}^2$. Hereby, the $(N_\mathrm{s} \times 1)$-element signal vectors $\mathbf{r}_1$ and $\mathbf{r}_2$ containing the signals received during the N_s chip intervals in the first and the second symbol duration are quantified by

$$\mathbf{r}_1 = \xi \sum_{k=1}^{K} \mathbf{c}_k \left[h_{k,11} v_{k1} + h_{k,21} v_{k2} \right] + \mathbf{n}_1, \tag{5.1}$$

$$\mathbf{r}_2 = \xi \sum_{k=1}^{K} \mathbf{c}_k \left[h_{k,21} v_{k1}^* - h_{k,11} v_{k2}^* \right] + \mathbf{n}_2, \tag{5.2}$$

where $\xi = 1/\sqrt{2N_\mathrm{s}}$ is the energy of the signal transmitted from each antenna within every chip-duration.

The transmitted signal vector $\mathbf{v}_k = [v_{k1}, v_{k2}]^T$ contains the original symbols v_{k1} and v_{k2} of the kth user. In order to generate the received signal vector, firstly the $(N_\mathrm{s} \times 1)$-element signal vector $\mathbf{r}_2$ received during the second symbol duration is Hermitian transposed, yielding $\mathbf{r} = [\mathbf{r}_1^T, \mathbf{r}_2^H]^T$. Then the estimated complex-valued Channel Impulse Response (CIR) taps associated with the two antennas are used to construct the channel-matrix of

$$\mathbf{H}_k = \begin{bmatrix} h_{k1} & h_{k2} \\ h_{k2}^* & -h_{k1}^* \end{bmatrix}. \tag{5.3}$$

Thirdly, the $(N_\mathrm{s} \times 1)$-element AWGN vector $\mathbf{n}_2$ encountered during the second symbol duration is also Hermitian transposed to form $\mathbf{n} = [\mathbf{n}_1^T, \mathbf{n}_2^H]^T$.

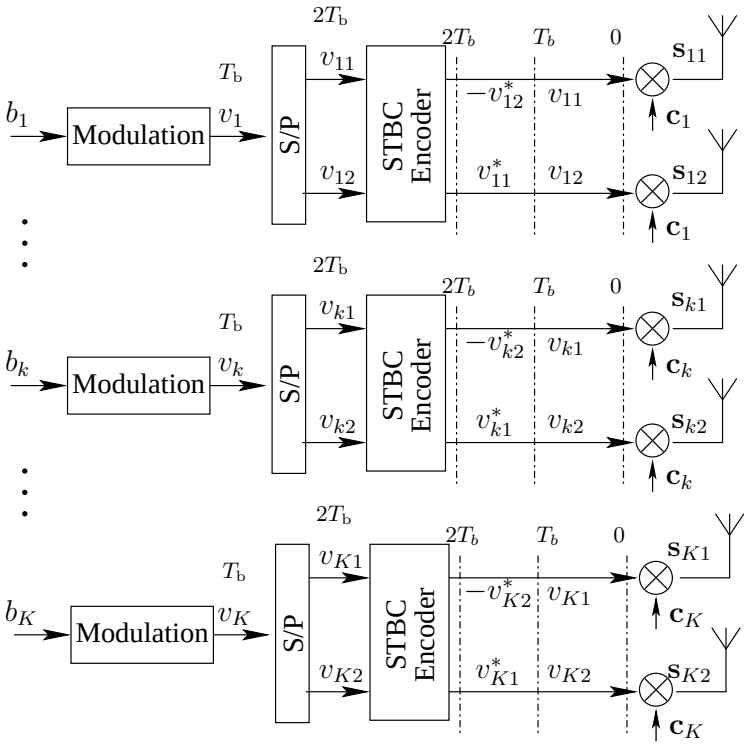

(a) Transmitter of the geographically scattered K number of MSs.

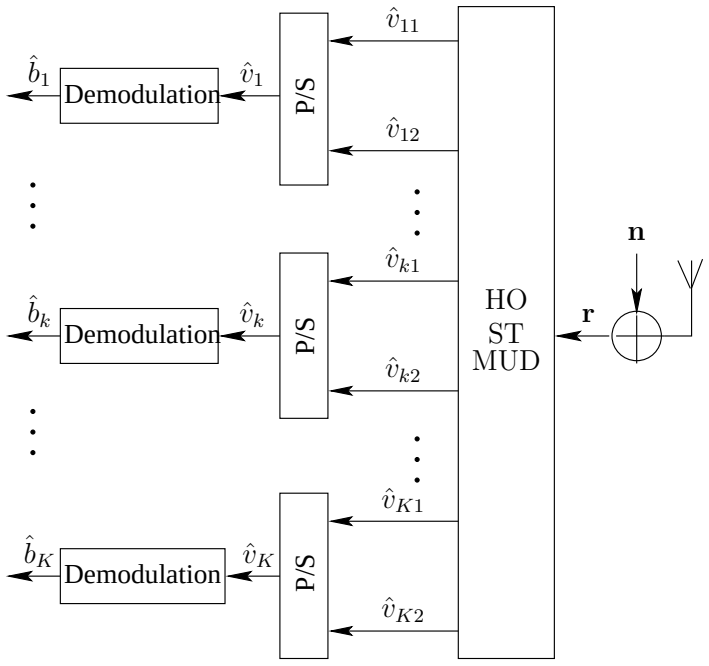

(b) Receiver at the BS.

Figure 5.1: Transceiver schematic of the STBC-assisted two-transmit antenna aided DS-CDMA UL supporting K users. The corresponding single-antenna system was shown in Fig. 3.4

Therefore, the $(2N_s \times 1)$-element received signal vector $\mathbf{r}$ can be expressed as:

$$\mathbf{r} = \xi \sum_{k=1}^{K} \mathbf{C}_k \mathbf{H}_k \mathbf{v}_k + \mathbf{n} = \xi \mathbf{C}\mathbf{H}\mathbf{v} + \mathbf{n}, \tag{5.4}$$

where we have

$$\mathbf{C} = \big[\mathbf{C}_1, \mathbf{C}_2, \ldots, \mathbf{C}_K\big] \tag{5.5}$$

$$\mathbf{H} = \mathrm{diag}\big\{\mathbf{H}_1, \mathbf{H}_2, \ldots, \mathbf{H}_K\big\} \tag{5.6}$$

$$\mathbf{v} = \big[\mathbf{v}_1^T, \mathbf{v}_2^T, \ldots, \mathbf{v}_K^T\big]^T, \tag{5.7}$$

and

$$\mathbf{C}_k = \begin{bmatrix} \mathbf{c}_k & \mathbf{0}^{(N_\mathrm{s})} \\ \mathbf{0}^{(N_\mathrm{s})} & \mathbf{c}_k \end{bmatrix}, \tag{5.8}$$

where $\mathbf{0}^{(N_\mathrm{s})}$ represents the $(N_\mathrm{s} \times 1)$-element null vector having all the N_s entries as zero.

5.3 Ant-Colony Optimization Aided Space-Time MUD

5.3.1 Traditional ACO Aided ST-MUD

The MUD's goal is to identify the $2K$-element ML data-vector of the K twin-antenna-aided users at the BS with a high probability, despite searching through only a small fraction of the 2^{2K}-element search-space.

5.3.1.1 Route Table

i	$v_i^{(1)}$	$j=1$	$j=2$	$j=3$	$j=4$	$\cdots$	$j=2K-1$	$j=2K$
1	$+1$	$v_{11}=v_1^{(1)}$	$v_{12}=v_1^{(1)}$	$v_{21}=v_1^{(1)}$	$v_{22}=v_1^{(1)}$	$\ldots$	$v_{K1}=v_1^{(1)}$	$v_{K2}=v_1^{(1)}$
2	-1	$v_{11}=v_2^{(1)}$	$v_{12}=v_2^{(1)}$	$v_{21}=v_2^{(1)}$	$v_{22}=v_2^{(1)}$	$\ldots$	$v_{K1}=v_2^{(1)}$	$v_{K2}=v_2^{(1)}$

Table 5.1: The $(2 \times 2K)$-element route-table of the multi-user STBC decoder employing the ACO principle of [130, 131], when the system supports K users and each MS is equipped with two transmit antennas. The corresponding $(2 \times K)$-element single-antenna based route-table was portrayed in Fig. 3.6.

The interpretations of the number of rows and columns associated with the $(2 \times 2K)$-element route-table are the same, as in the MC DS-CDMA system of [130]. More explicitly, the rows in Tab. 5.1 represent the legitimate BPSK modulated symbols $+1$ and -1, while the columns of the route-table are the $2K$-element twin-antenna symbols of the K users. In terms of ACO parlance, the two rows of the table provide the two options for an artificial ant to consider during its passage through the set of legitimate $2K$-element data vectors. In Tab. 5.1, the legitimate symbols $+1$ and -1 are represented by $v_1^{(1)}$ and $v_2^{(1)}$, respectively.

The symbol $\mathbf{v}_i^{(m)}$ is introduced in order to represent the ith legitimate BPSK symbol combination in the full set containing all the $\mathcal{M} = 2^m$ m-bit symbol combinations. The index i is defined as the decimal interpretation of the binary symbol vector plus one. The binary symbol vector is obtained by assigning $+1$ to 0 and -1 to 1. The symbol-value in the jth column and ith row of the route-table is denoted by $v_i^{(1)}$, for $j = 1, \ldots, 2K$ and $i = 1, 2$.

5.3.1.2 Cellular Likelihood

The cellular likelihood $\mathfrak{l}(b_{ji})$ represents the likelihood that the BPSK symbol b_{ji} was transmitted as the jth element of the $2K$-element vector, which corresponds to the jth row and the ith column of the $(2 \times 2K)$-element route-table adopted by the traditional hard-output ACO algorithm, which may be formulated as [129]:

$$\mathfrak{l}_{ij} = 2\Re\{\xi v_i^{(1)} y_j\} - \xi^2 v_i^{(1)} R_{jj} v_i^{(1)}, \quad j = 1, 2, \ldots, 2K; \quad i = 1, 2; \tag{5.9}$$

where y_j is the jth element of the $(2K \times 1)$-element matched filter output vector $\mathbf{y}$ given by

$$\begin{aligned} \mathbf{y} &= \mathbf{H}^H \mathbf{C}^T \mathbf{r} = \xi \mathbf{H}^H \mathbf{C}^T \mathbf{C}\mathbf{H}\mathbf{v} + \mathbf{H}^H \mathbf{C}^T \mathbf{n} \\ &= \xi \mathbf{R}\mathbf{v} + \tilde{\mathbf{n}}. \end{aligned} \tag{5.10}$$

Furthermore, $\mathbf{R}$ in Eq.(5.9) is the $(2K \times 2K)$-element correlation matrix of the composite spreading and channel matrix $\mathbf{CH}$, where we have

$$\begin{aligned} \mathbf{R} &= \mathbf{H}^H \mathbf{C}^T \mathbf{C}\mathbf{H} \\ &= \begin{bmatrix} \mathbf{\Sigma}_1 & \rho_{12}\,\mathbf{\Lambda}_{12} & \cdots & \rho_{1K}\mathbf{\Lambda}_{1K} \\ \rho_{12}\,\mathbf{\Lambda}_{21} & \mathbf{\Sigma}_2 & \cdots & \rho_{2K}\mathbf{\Lambda}_{2K} \\ \vdots & \vdots & \ddots & \vdots \\ \rho_{1K}\mathbf{\Lambda}_{K1} & \rho_{2K}\mathbf{\Lambda}_{K2} & \cdots & \mathbf{\Sigma}_K \end{bmatrix}, \end{aligned} \tag{5.11}$$

and $\mathbf{\Sigma}_k = \left(\sum_{i=1}^{2} |h_{ki}|^2\right)\mathbf{I}_2$, while $\mathbf{\Lambda}_{kj} = \mathbf{H}_k^H \mathbf{H}_j$ for $k = 1, \ldots, K, j = 1, \ldots, K$ and $j \neq k$. Finally, $\mathbf{I}_2$ represents a (2×2)-element identity matrix while the correlation coefficient ρ_{kj} between $\mathbf{c}_k$ and $\mathbf{c}_j$ is given by $\rho_{kj} = \mathbf{c}_k^T \mathbf{c}_j / N_\mathrm{s} = \sum_{n_s=1}^{N_\mathrm{s}} c_{kn_s} c_{jn_s} / N_\mathrm{s}$, for $k = 1, \ldots, K, j = 1, \ldots, K$ and $j \neq k$.

Therefore, R_{jj} in Eq.(5.9) is the jth diagonal element of $\mathbf{R}$, whose value is $\sum_{i=1}^{2} |h_{ki}|^2$.

5.3.1.3 Vector Likelihood

The likelihood of a particular $(2K \times 1)$-element K-user twin-antenna vector $\mathbf{v}_i^{(2K)}$ in the full set $\mathbb{S}^{(2K)}$ containing all the 2^{2K} vectors is given by

$$\mathfrak{L}(\mathbf{v}_i^{(2K)}) = 2\Re\{\xi \mathbf{v}_i^{(2K)T} \mathbf{y}\} - \xi^2 \mathbf{v}_i^{(2K)T} \mathbf{R} \mathbf{v}_i^{(2K)}, \quad i = 1, 2, \ldots, 2^{2K} \tag{5.12}$$

where $\mathbf{v}_i^{(2K)}$ is the route followed by one of the ζ ants in the route-table, which is formed by concatenating the $2K$ passages chosen by that particular ant, yielding:

$$\mathbf{v}_i^{(2K)} = [v_{\imath_1}^{(1)} \;\; v_{\imath_2}^{(1)} \;\; \cdots \;\; v_{\imath_{2K}}^{(1)}]^T \quad \forall\, j = 1, \ldots, 2K : \imath_j \in \{1, 2\}. \tag{5.13}$$

5.3.1.4 Traditional Algorithm of Determining N

Let us now briefly review the algorithm of determining the number of ants choosing each symbol included in the traditional ACO-MUD detailed in Chapter 3. In the ACO-aided benchmarker ST-MUD algorithm characterized by Alg. 1 of this section, both the probability matrix $\mathbf{P}$ and the integer matrix $\mathbf{N}$ have the same size as the $(2 \times 2K)$-element route-table. Each element of the matrix $\mathbf{N}$ represents the number of ants choosing the corresponding entry in the route-table. For each of the $2K$ columns in the route-table, the sum of the numbers of ants choosing the two entries should be equivalent to the total number ζ of artificial ants adopted by the algorithm, yielding $N_{j1} + N_{j2} = \zeta$, for $j = 1, \ldots, 2K$.

Firstly, N_{ji_1} ants choose the specific route-table entry associated with the higher probability, where N_{ji_1} is calculated as the rounded value of the product of $(\zeta \times P'_{ji_1})$. Similarly, N_{ji_2} represents the number of ants, which choose the other route-table entry, namely that associated with the lower probability, where we have $N_{ji_2} = \zeta - N_{ji_1}$.

The interpretations of the 'sort' function and '$\imath$' function of Alg. 1 are provided in the Appendix. The ACO algorithm portrayed above is then embedded into the STBC MUD and the achievable

Algorithm 1: Traditional Algorithm of Determining $\mathbf{N}$

input : $(2 \times 2K)$-element double precision matrix $\mathbf{P}$

output: $(2 \times 2K)$-element integer matrix $\mathbf{N}$

for $j = 1, 2, \ldots, 2K$ **do**

$\mathbf{P}'_j = \text{sort}(\mathbf{P}_j)$

$\mathbf{i} = \imath(\mathbf{P}'_j, \mathbf{P}_j)$

$N_{ji_1} = \lfloor \zeta \times P'_{ji_1} \rceil$

$N_{ji_2} = \zeta - N_{ji_1}$

performance of the system considered is characterized in Fig. 5.4. As observed in Fig. 5.4, the BER versus SNR curve of the system employing the ACO-aided hard-decision STBC MUD exhibits an error-floor. Hence, in the next section we will propose a novel ACO-aided MUD algorithm, which will enable the fully-loaded system supporting as many users as the number of chips in the spreading sequence to approach the BER performance achieved by the single-user system.

5.3.2 Improved ACO aided ST-MUD

In this section, a novel ACO-based hard-output ST-MUD algorithm is proposed in order to provide an improved BER performance at the cost of a moderate complexity increase. To elaborate a little further, the proposed algorithm is different from the traditional ACO based MUD algorithm, as it has been stated in Subsection 5.3.1 in three different aspects, which are the size of the route-table, the formula derived for calculating the cellular likelihood of each cell and the algorithm used for calculating the integer matrix $\mathbf{N}$ of Alg. 1. For the sake of completeness, we briefly describe the above three aspects as well as the evaluation of the vector likelihood adopted by the proposed ACO based MUD algorithm.

5.3.2.1 Route Table

i	$\mathbf{v}_i^{(2)T}$	$j=1$	$j=2$	$\cdots$	$j=K$
		$\mathbf{v}_1=[v_{11}\ v_{12}]^T$	$\mathbf{v}_2=[v_{21}\ v_{22}]^T$	$\cdots$	$\mathbf{v}_K=[v_{K1}\ v_{K2}]^T$
1 $[+1\ +1]$		$\mathbf{v}_1=\mathbf{v}_1^{(2)}$	$\mathbf{v}_2=\mathbf{v}_1^{(2)}$	$\cdots$	$\mathbf{v}_K=\mathbf{v}_1^{(2)}$
2 $[+1\ -1]$		$\mathbf{v}_1=\mathbf{v}_2^{(2)}$	$\mathbf{v}_2=\mathbf{v}_2^{(2)}$	$\cdots$	$\mathbf{v}_K=\mathbf{v}_2^{(2)}$
3 $[-1\ +1]$		$\mathbf{v}_1=\mathbf{v}_3^{(2)}$	$\mathbf{v}_2=\mathbf{v}_3^{(2)}$	$\cdots$	$\mathbf{v}_K=\mathbf{v}_3^{(2)}$
4 $[-1\ -1]$		$\mathbf{v}_1=\mathbf{v}_4^{(2)}$	$\mathbf{v}_2=\mathbf{v}_4^{(2)}$	$\cdots$	$\mathbf{v}_K=\mathbf{v}_4^{(2)}$

Table 5.2: $(4\times K)$-element route-table of the MU STBC decoder employing the improved ACO algorithm, when the system supports K users and each MS is equipped with two transmit antennas. An example of the corresponding $(2\times K)$-element single-antenna based route-table was portrayed in Table 5.1.

The route-table in the proposed ACO based ST-MUD algorithm has $(4\times K)$-element, where we have $m=2$. More explicitly, the four entries of each column correspond to the $(\mathcal{M}=2^m=4)$ legitimate $(m=2)$-symbol combinations, as indicated in Tab. 5.2, which should be contrasted to Table 5.1 and Fig. 3.6 of the conventional single-antenna-aided MUDs.

5.3.2.2 Cellular Likelihood

As shown in Subsection. 5.3.1, for $m=2$ the submatrix $\mathbf{R}_{jj}^{(2)}$, $j=1,\ldots,K$ is a diagonal matrix. Therefore, the cellular likelihood $\tilde{\mathfrak{l}}_{ji}$ of the (i,j)th cell can be expressed as

$$\begin{aligned}\mathfrak{l}_{ji}^{(4\times K)} &= 2\Re\{\xi\mathbf{v}_i^{(2)T}\mathbf{y}_j^{(2)}\}-\xi^2\mathbf{v}_i^{(2)T}\mathbf{R}_{jj}^{(2)}\mathbf{v}_i^{(2)}\\ &= \mathfrak{l}_{\varphi_j\imath_1}^{(2\times 2K)}+\mathfrak{l}_{\psi_j\imath_2}^{(2\times 2K)}, \qquad \imath_1,\imath_2\in\{1,2\}\\ &\qquad \forall\ j=1,2,\ldots,K \text{ and } i=1,2,3,4;\end{aligned} \tag{5.14}$$

subject to $\varphi_j=(2j-1)$, $\psi_j=2j$ and $\mathbf{v}_i^{(2)}=[v_{\imath_1}^{(1)}\ \ v_{\imath_2}^{(1)}]^T$.

5.3.2.3 Vector Likelihood

The formula quantifying the vector likelihood adopted by the improved ACO based ST-MUD algorithm remains the same as in Eq. (5.12), which is adopted by the traditional ACO based ST-MUD algorithm. The only difference lies in the formation of the $(2K\times 1)$-element candidate vector $\mathbf{v}_i^{(2K)}$ that concatenates all the K number of 2-by-1 passages pursued by the same ant, yielding

$$\begin{aligned}\mathbf{v}_i^{(2K)} &= [\mathbf{v}_{\imath_1}^{(2)}\ \ \mathbf{v}_{\imath_2}^{(2)}\ \ \cdots\ \ \mathbf{v}_{\imath_K}^{(2)}]^T\\ &\qquad \forall\ j=1,\ldots,K:\imath_j\in\{1,2,3,4\}.\end{aligned} \tag{5.15}$$

5.3.2.4 Improved Algorithm of Determining N

Both the probability matrix $\mathbf{P}$ and the integer matrix $\mathbf{N}$ have the same size as the $(4\times K)$-element route-table. However, the technique of determining $\mathbf{N}$ shown in Alg. 1 of this section as part of

the traditional ACO-MUD algorithm of Chapter 3 may become unable to provide an integer-valued matrix $\mathbf{N}$ having reasonable entries for the improved ACO based ST-MUD algorithm. For example, let us assume that the probabilities of choosing the four entries associated with the jth column, $j = 1, 2, \ldots, K$ are given by the probability vector $\mathbf{P}_j = [0.36, 0.27, 0.15, 0.22]$, and $\zeta = 10$ artificial ants are used by the ACO aided ST-MUD algorithm. Then, we have $\widetilde{\mathbf{N}}_j = \zeta \mathbf{P}_j = [3.6, 2.7, 1.5, 2.2]$. According to the traditional way of determining $\mathbf{N}$ in Alg. 1 as part of the traditional ACO-MUD introduced in Chapter 3 the number of ants $\mathbf{N}_j$ choosing the four entries in the jth column of the route-table are determined as the rounded integers of $\widetilde{\mathbf{N}}_j$, yielding $\mathbf{N}_j = [4, 3, 2, 2]$, where the sum of the four integer elements equals to $11 > \zeta = 10$. In order to determine the 2^m integers in a more beneficial manner, an improved algorithm of deriving $\mathbf{N}$ from $\mathbf{P}$ is proposed for the scenarios associated with $m > 1$, as detailed in the flow-chart of Alg. 2.

In order to illustrate the advantages of the new algorithm, the same probability vector $\mathbf{P}_j = [0.36, 0.27, 0.15, 0.22]$ will be used as the input vector in the following example. Firstly, the value of each element in $\mathbf{N}_j$ is directly given by the integer part of each element in the vector $\widetilde{\mathbf{N}}_j$, yielding $\mathbf{N}_j = [3, 2, 1, 2]$. Then, if the sum of all the four integer elements in the vector $\mathbf{N}_j$ is less than ζ, the jth loop of Alg. 1 has to be continued, since some of the ants have not as yet carried out their decisions. More qualitatively, $\sum_{i=1}^{4} N_{ji}$ ants have already made their decisions, but the remaining $(\zeta - \sum_{i=1}^{4} N_{ji})$ ants have to make their impending choices among the four cells in the current column. The decision is made according to the value of the decimal part of the four elements of $\widetilde{\mathbf{N}}_j$, which is represented by the (4×1)-element vector $\dot{\mathbf{N}}_j$. In the example, we have $\dot{\mathbf{N}}_j = [0.6, 0.7, 0.5, 0.2]$

In order to carry out this decision, the four elements in $\dot{\mathbf{N}}_j$ will be ranked in ascending order according to their values. Secondly, the cell associated with the value having the highest rank will be selected as the decision of an ant randomly chosen from the remaining $(\zeta - \sum_{i=1}^{4} N_{ji})$ ants, yielding the vector with the updated values $\mathbf{N}_j = [3, 3, 1, 2]$. Then the cells will be selected from the queue constructed according to the rank of their associated value in $\dot{\mathbf{N}}_j$. In the given example, the output vector will then be further updated as $\mathbf{N}_j = [4, 3, 1, 2]$. The selection process will not be curtailed, until all the ζ ants have made their unique decisions. As the sum of all the elements in $\mathbf{N}_j$ in the given example is equivalent to $\sum_{i=1}^{4} N_{ji} = \zeta = 10$, the process can be curtailed and the final output is the vector $\mathbf{N}_j = [4, 3, 1, 2]$.

All in all, compared to the traditional ACO based MUD of Alg. 1, the improved MUD of Alg. 2 has not increased the number of cells contained by the route-table nor has it increased the complexity of calculating the cellular likelihood. Additionally, the same formula was adopted by both algorithms to calculate the vector likelihood.

Despite these identical properties, the improved ACO based MUD algorithm increases the number of candidate vectors appearing in the search pool by reducing the difference between the probabilities associated with each cell within a column, while still making them equally informative. Therefore a better BER performance is expected at the price of a moderately increased complexity imposed by calculating the vector likelihood associated with the increased number of vectors. The simulation results quantifying the achievable BER performance as a function of the complexity imposed will be detailed in Section 5.5.

Algorithm 2: Improved Algorithm of Determining $\mathbf{N}$

input : $(4 \times K)$-element double precision matrix $\mathbf{P}$
output: $(4 \times K)$-element integer matrix $\mathbf{N}$

for $j = 1, 2, \ldots, K$ **do**
  $\widetilde{\mathbf{N}}_j = \mathbf{P}_j \times \zeta$
  $\mathbf{N}_j = \lfloor \widetilde{\mathbf{N}}_j \rfloor$
  if $\left(\zeta - \sum_{i=1}^{4} N_{ji}\right) \geqslant 1$ **then**
    $\dot{\mathbf{N}}_j = \widetilde{\mathbf{N}}_j - \mathbf{N}_j$
    $\dot{\mathbf{N}}'_j = \mathrm{sort}\left(\dot{\mathbf{N}}_j\right)$
    $\mathbf{i} = \imath\left(\dot{\mathbf{N}}'_j, \dot{\mathbf{N}}_j\right)$
    $l = 0$
    while $\left(\zeta - \sum_{i=1}^{4} N_{ji}\right) \geqslant 1$ **do**
      $l = l + 1$
      $N_{ji_l} = N_{ji_l} + 1$

5.4 Comparison of the Traditional and Improved ACO-Aided ST-MUD

In this section, we will comparatively study the *traditional* ACO-MUD detailed in Chapter 3 and the *improved* ACO-based HO ST/MUD techniques of Alg. 1 and Alg. 2 in multiuser-interference-infested and AWGN contaminated STBC scenario. We stipulate the following preliminary assumptions:

1. We have $K = 7$ users transmitted in the STBC assisted DS-CDMA UL, with each user relying on two transmit antennas and two symbols are transmitted after $\mathcal{G}_2$ space-time coding within two symbol durations.

2. The channel state matrix $\mathbf{H}$ and the received signal vector $\mathbf{r}$ are omitted here to save space.

3. All the $2K = 14$ symbols transmitted by the $K = 7$ users within the block duration considered are $\mathbf{v} = [+1\ +1\ -1\ -1\ +1\ -1\ +1\ +1\ +1\ +1\ -1\ -1\ +1\ -1]$.

4. $\zeta = 20$ ants are employed by both algorithms to obtain the ST/MUD's HO results.

5. The symbol-value probability matrix, the search pool and the pheromone density associated with each cell during the first three search iterations are given in Tables 5.7−5.14. This is because the simulation results obtained during the first three iterations are sufficiently accurate to indicate the difference between the *improved* and the *traditional* ACO based ST/MUDs of Alg. 1 and Alg. 2. Hence they assist us in interpreting all the main characteristics of both algorithms.

6. Additionally, the scalars representing the symbol-values constituting the transmit signal vector $\mathbf{v}$ are highlighted by using bold characters in Tables 5.7−5.14 to directly quantify the symbol LLF l_{ij}, the intermediate variable d_{ij}, the intrinsic affinity η_{ij}, the symbol-value probability $P_{ij}^{(n)}$ and the pheromone density $\tau_{ij}^{(n)}$, regardless of whether it is associated with the *traditional* ACO-MUD of Chapter 3 or the *improved* ACO-based ST-MUD of Alg. 1 and Alg. 2 respectively.

7. By contrast, the vector highlighted by using bold characters in Tables 5.7−5.14 encompassing the search pool during every iteration is the 'elite' vector-value of search pool during that particular search iteration.

8. Additionally, the transmitted signal vector is also listed at the bottom of all the six search pools as seen in Tables 5.7−5.14.

9. The framed box distinguished with the aid of dotted lines and associated with a specific column in Tables 5.5, 5.7, 5.9, 5.10, 5.12 and 5.13 represents the 'erroneous' indication of the properties. More precisely, the row associated with the highest intrinsic affinity or the highest symbol-probability or the highest pheromone level in a particular column distinguished by dotted frame is not the row corresponding to the symbol that is actually transmitted.

10. By contrast, the framed box drawn in solid-line associated with a certain column in Tables 5.5, 5.7, 5.9, 5.10, 5.12 and 5.13 indicates that the previous 'erroneous' properties have been 'corrected' so that the row associated with the highest intrinsic affinity, symbol-value probability or pheromone is the row corresponding to the symbol that is actually transmitted.

Below we will compare the *traditional* ACO-MUD of Chapter 3 and the *advanced* ACO-based ST/MUD with special emphasis on the symbol LLF $\mathfrak{l}_{ij}$ of Eq. (5.9) and Eq. (5.14), the intermediate variable d_{ij} of Eq. (3.11) and the intrinsic affinity η_{ij} of Eq. (3.12), which keep the same value throughout the Ξ search iterations carried out within one STBC-block duration.

5.4.1 Algorithmic Components

5.4.1.1 Symbol LLF

Any LLF associated with a certain two-symbol vector in Table 5.3(a) employed by the improved ACO-based ST/MUD algorithm is the sum of the LLFs associated with the two symbols constituting the two-symbol STBC vector. More quantitatively, the relationship between the symbol LLFs of the traditional and of the improved ACO-based ST/MUD algorithms can be represented by:

$$\mathfrak{l}_{k}^{(4\times K)}\left(\mathbf{v}_{i}^{(2)}\right)=\mathfrak{l}_{2k-1}^{(2\times 2K)}\left(v_{i1}^{(2)}\right)+\mathfrak{l}_{2k}^{(2\times 2K)}\left(v_{i2}^{(2)}\right), \tag{5.16}$$

or equivalently

$$\mathfrak{l}_{k}^{(4\times K)}\left(\mathbf{v}_{i}^{(2)}\right)=\mathfrak{l}_{k,1}^{(2\times 2K)}\left(v_{i1}^{(2)}\right)+\mathfrak{l}_{k,2}^{(2\times 2K)}\left(v_{i2}^{(2)}\right), \tag{5.17}$$

where $\mathfrak{l}_{2k-1}^{(2\times 2K)}\left(v_{i1}^{(2)}\right)$ indicates the LLF associated with the 1st symbol in $\mathbf{v}_{i}^{(2)}$, which is identical to the alternative representation $\mathfrak{l}_{k,1}^{(2\times 2K)}\left[v_{i1}^{(2)}\right]$. Similarly, $\mathfrak{l}_{2k}^{(2\times 2K)}\left[v_{i2}^{(2)}\right]$ and $\mathfrak{l}_{k,2}^{(2\times 2K)}\left[v_{i2}^{(2)}\right]$ also indicate the same entry in Tab. 5.3(b).

It is worth mentioning that this relationship would not be valid for arbitrary m-symbol vectors, when we have $m > 2$. For example, when we have $m = 4$, the simple relationship shown in Eq. (5.17) becomes invalid, yielding:

$$\mathfrak{l}_{k_1k_2}^{(4\times K)}\left(\mathbf{v}_{i_1}^{(2)},\mathbf{v}_{i_2}^{(2)}\right)\neq\mathfrak{l}_{k_1}^{(4\times K)}\left(\mathbf{v}_{i_1}^{(2)}\right)+\mathfrak{l}_{k_2}^{(4\times K)}\left(\mathbf{v}_{i_2}^{(2)}\right). \tag{5.18}$$

(a) Symbol LLF $\mathfrak{l}_{ij}$ of *improved* ACO $(4 \times K)$.

$\mathbf{v}^{(2)}$ \ k	1	2	3	4	5	6	7
$[+1\ +1]$	**-0.40**	-14.44	-5.29	**-0.35**	**-0.53**	-1.80	0.37
$[+1\ -1]$	-0.82	-6.76	**2.30**	-0.57	-0.40	-0.03	**0.92**
$[-1\ +1]$	-1.45	-4.23	-10.54	0.23	-0.26	-1.84	-2.90
$[-1\ -1]$	-1.87	**3.45**	-2.95	0.00	-0.12	**-0.08**	-2.35

(b) Symbol LLF $\mathfrak{l}_{ij}$ of *traditional* ACO $(2 \times 2K)$.

$v^{(1)}$ \ k	1		2		3		4	
	1	2	1	2	1	2	1	2
$+1$	**-0.04**	**-0.35**	-7.85	-6.59	**0.56**	-5.85	**-0.37**	**0.03**
-1	-1.09	-0.78	**2.35**	**1.09**	-4.69	**1.73**	0.20	-0.20

$v^{(1)}$ \ k	5		6		7	
	1	2	1	2	1	2
$+1$	**-0.30**	**-0.23**	-0.45	-1.35	**1.14**	-0.77
-1	-0.02	-0.10	**-0.49**	**0.41**	-2.13	**-0.22**

Table 5.3: Symbol LLF associated with each cell constituting the $(4 \times K)$-element and $(2 \times 2K)$-element route-tables of the improved and of the traditional ACO based HO ST/MUD algorithms, when both of them are applied to detect the 14 symbols of the twin-antenna-based $K = 7$-user example.

Since two replicas of the original symbols are transmitted by each user with the aid of a single user-specific spreading code, for $m = 2$ no MUI will be imposed, when the LLF of the two-symbol STBC vector of the user is calculated. More explicitly, the (2×2)-element $\mathbf{R}_{jj}^{(2)}$ denoted by

$$\begin{aligned}\mathbf{R}_{jj}^{(2)} &= \begin{bmatrix} R_{(o+1)(o+1)} & R_{(o+1)(o+2)} \\ R_{(o+2)(o+1)} & R_{(o+2)(o+2)} \end{bmatrix} \\ &= \begin{bmatrix} \sum_{i=1}^{2} |h_{ji}|^2 & 0 \\ 0 & \sum_{i=1}^{2} |h_{ji}|^2 \end{bmatrix} \\ & \qquad o = 2(j-1), \quad j = 1, \ldots, K, \end{aligned} \tag{5.19}$$

is a diagonal matrix, as mentioned previously in the context of Eq. (5.11). However, when we have $m > 2$, the jth $(m \times m)$-element diagonal matrix $\mathbf{R}_{jj}^{(m)}$ on the diagonal of the correlation matrix $\mathbf{R}$

(a) Intermedia variable d_{ij} of *improved* ACO $(4 \times K)$.

$\mathbf{v}^{(2)}$ \ k	1	2	3	4	5	6	7
$[+1\ +1]$	**0.40**	0.00	0.01	**0.41**	**0.37**	0.14	0.59
$[+1\ -1]$	0.30	0.00	**0.91**	0.36	0.40	0.49	**0.71**
$[-1\ +1]$	0.19	0.01	0.00	0.56	0.44	0.14	0.05
$[-1\ -1]$	0.13	**0.97**	0.05	0.50	0.47	**0.48**	0.09
sum	1.03	0.98	0.96	1.83	1.67	1.25	1.45

(b) Intermedia variable d_{ij} of *traditional* ACO $(2 \times 2K)$.

$v^{(1)}$ \ k	1		2		3		4	
	1	2	1	2	1	2	1	2
$+1$	**0.49**	**0.41**	0.00	0.00	**0.64**	0.00	**0.41**	**0.51**
-1	0.25	0.31	**0.91**	**0.75**	0.01	**0.85**	0.55	0.45
sum	0.74	0.73	0.91	0.75	0.65	0.85	0.96	0.96

$v^{(1)}$ \ k	5		6		7	
	1	2	1	2	1	2
$+1$	**0.42**	**0.44**	0.39	0.21	**0.76**	0.32
-1	0.49	0.48	**0.38**	**0.60**	0.11	**0.44**
sum	0.92	0.92	0.77	0.81	0.86	0.76

Table 5.4: Intermediate variable d_{ij} translating the symbol LLF ι_{ij} to the intrinsic affinity η_{ij} associated with each cell constituting the $(4 \times K)$-element and $(2 \times 2K)$-element route-tables of the improved and of the traditional ACO based HO ST/MUD algorithms, when both of them are applied to detect the 14 symbols of the $K = 7$-user STBC example.

given by Eq. (5.11) is no longer a diagonal matrix. More quantitatively, we have

$$\mathbf{R}_{jj}^{(m)} = \begin{bmatrix} R_{(o+1)(o+1)} & R_{(o+1)(o+2)} & \cdots & R_{(o+1)(o+m)} \\ R_{(o+2)(o+1)} & R_{(o+2)(o+2)} & \cdots & R_{(o+2)(o+m)} \\ \vdots & \vdots & \ddots & \vdots \\ R_{(o+m)(o+1)} & R_{(o+m)(o+2)} & \cdots & R_{(o+m)(o+m)} \end{bmatrix}$$
$$o = m(j-1), \quad j = 1, \ldots, 2K/m, \qquad (5.20)$$

which includes N_{i} non-zero interference terms $R_{(o+p)(o+q)} \neq 0$ when we have $|p-q| > 1$, which are introduced owing to the non-zero correlation between each pair of non-orthogonal spreading codes.

Additionally we have

$$N_{\mathrm{i}} = \begin{cases} m^2 - 2m, & \text{if } m \text{ is even,} \\ m^2 - 2m - 1, & \text{if } m \text{ is odd.} \end{cases} \tag{5.21}$$

In order to ensure the 'intrinsic affinity' of all the cells in the route-table are positive values, hereby introduced an intermediate variable to transform the symbol-LLFs, some of which may be negative, to positive 'intrinsic affinity' values. The intermediate variable d_{ij} of the (i,j)th cell of the route-table is defined as

$$d_{ij} = \frac{1}{1 + \exp(-\iota_{ij})}. \tag{5.22}$$

More details regarding the properties of the intermediate variable will be provided in Section 3.4.2.1. The intermediate variables associated with all the cells constituting both the $(4 \times K)$-element route-table of the advanced ACO algorithm as well as the $(2 \times 2K)$-element route-table of the traditional ACO algorithm are exemplified in Tables 5.4(a) and 5.4(b), respectively, which were extracted from our simulations.

With the intermediate variables given in Table 5.4, the intrinsic affinity η_{ij} associated with $x = 1,2,3,4,\ j = 1,\ldots,K$ for the advanced ACO algorithm and with $x = 1,2\ j = 1,\ldots,2K$ for the traditional ACO algorithm can be expressed as

$$\eta_{xj} = \frac{\sum_{i=1}^{I} d_{ij}}{\sum_{i=1}^{I} d_{ij} - d_{xj}}, \tag{5.23}$$

where we have

$$\begin{cases} I = 4, & x = 1,\ldots,4 \quad j = 1,2,\ldots,K, & \text{when the } \textit{advanced} \text{ ACO is applied;} \\ I = 2, & x = 1,2 \qquad\ \ j = 1,2,\ldots,2K, & \text{when the } \textit{traditional} \text{ ACO is applied.} \end{cases} \tag{5.24}$$

5.4.1.2 Intrinsic Affinity

Based on the definition of Eq. (3.12) in Chapter 3, Tables 5.5(a) and 5.5(b) show all the intrinsic affinities associated with all the cells constituting both the $(4 \times K)$-element route-table of the advanced ACO algorithm as well as of the $(2 \times 2K)$-element route-table of the traditional ACO algorithm, respectively. As detailed previously in Section 3.4.2.2, provided that the intrinsic affinity η_{ij} exceeds a certain threshold, the symbol-value or two-symbol STBC vector represented by the (i,j)th cell becomes identical to the MF solution.

More explicitly, as detailed in Section 3.4.2.2, the intrinsic affinity threshold associated with the $(2 \times K)$-element route-table is 2, which may be interpreted with the aid of Tab. 5.5(b), where the intrinsic affinity associated with the MF solution of each column is seen to be larger than 2, while the other intrinsic affinity value of the same column is lower than 2.

(a) Intrinsic affinity η_{ij} of the *improved* ACO $(4 \times K)$.

$\mathbf{v}^{(2)}$ \ k	1	2	3	4	5	6	7
$[+1\ +1]$	**1.64**	1.00	1.01	**1.29**	**1.28**	1.13	1.69
$[+1\ -1]$	1.42	1.00	**17.62**	1.24	1.31	1.65	**1.98**
$[-1\ +1]$	1.23	1.01	1.00	1.44	1.35	1.12	1.04
$[-1\ -1]$	1.15	**63.74**	1.05	1.38	1.39	**1.62**	1.06

(b) Intrinsic affinity η_{ij} of the *traditional* ACO $(2 \times 2K)$.

$v^{(1)}$ \ k	1		2		3		4	
	1	2	1	2	1	2	1	2
$+1$	**2.95**	**2.31**	1.00	1.00	**70.73**	1.00	**1.74**	**2.13**
-1	1.51	1.76	**2346.26**	**545.94**	1.01	**298.16**	2.35	1.89

$v^{(1)}$ \ k	5		6		7	
	1	2	1	2	1	2
$+1$	**1.86**	**1.93**	2.03	1.34	**8.14**	1.71
-1	2.16	2.08	**1.97**	**3.93**	1.14	**2.40**

Table 5.5: Intrinsic affinity η_{ij} associated with each cell constituting the $(4 \times K)$-element and $(2 \times 2K)$-element route-tables of the improved and of the traditional ACO based HO ST/MUD algorithms, when both of them are applied to detect the 14 symbols of the $K = 7$ user STBC example.

Below we will derive the intrinsic affinity threshold associated with Eq. (5.23),when we have $I = 4$ in Eq. (5.24), yielding:

$$\eta_{xj} = \frac{\sum_{i=1}^{4} d_{ij}}{\sum_{i=1}^{4} d_{ij} - d_{xj}} = 1 + \frac{d_{xj}}{\sum_{i,i\neq\imath}^{4} d_{ij}}, \qquad x = 1, 2, 3, 4. \tag{5.25}$$

Recall that we have $d_{ij} \in (0, 1)$, and the decision threshold is given by $\Re\{y_j\}$=0 or $\Re\{\mathbf{y}_j\}$=$[0\ \ 0]^T$, we have

$$\imath_{ij}^{(4\times K)} = 2\Re\left\{\xi \mathbf{v}_i^{(2)T} \mathbf{y}_j^{(2)}\right\} - \xi^2 \mathbf{v}_i^{(2)T} \mathbf{R}_{jj}^{(2)} \mathbf{v}_i^{(2)} \quad \forall\ j = 1, 2, \ldots, K \text{ and } i = 1, 2, 3, 4; \tag{5.26}$$

where the second term, namely $\xi^2 \mathbf{v}_i^{(2)T} \mathbf{R}_{jj}^{(2)} \mathbf{v}_i^{(2)} = \xi^2 \sum_{\imath=1}^{2} |h_{j\imath}|^2$ is a constant for all values of i. Hence, if the MF's output vector for the jth user satisfies $\Re\{\mathbf{y}_j^{(2)}\}$=$[0\ \ 0]^T$, then we have $\imath_{ij}^{(4\times K)} = \xi^2 \sum_{\imath=1}^{2} |h_{j\imath}|^2$,

which is a constant regardless of the row index i. In this scenario, we have $d_{1j} = d_{2j} = d_{3j} = d_{4j}$. As a result, we can express the threshold value $\bar{\eta}_{ij}$ of η_{ij}, which is given when we have $\Re\{\mathbf{y}_j^{(2)}\}=[0 \;\; 0]^T$ in Eq. (5.25), yielding

$$\begin{aligned}\bar{\eta}_{xj} &= \frac{\sum_{i=1}^{4} d_{ij}}{\sum_{i=1}^{4} d_{ij} - d_{xj}} \\ &= 1 + \frac{d_{xj}}{\sum_{i,i\neq\imath}^{4} d_{ij}} \\ &= 1 + \frac{1}{3}. \end{aligned} \tag{5.27}$$

To summarize, the value domain of η_{ij} can be expressed as:

$$\begin{array}{ll} \eta_{ij} \in (1+\frac{1}{3}, +\infty) & \text{if } \mathbf{v}_i^{(2)} = [\hat{v}_{j1}^{\mathrm{MF}} \quad \hat{v}_{j2}^{\mathrm{MF}}] \\ \eta_{ij} \in (1, 1+\frac{1}{3}) & \text{if } \mathbf{v}_i^{(2)} = [-\hat{v}_{j1}^{\mathrm{MF}} \quad -\hat{v}_{j2}^{\mathrm{MF}}] \end{array} . \tag{5.28}$$

This can be further interpreted with the aid of Table 5.5(a), where the intrinsic affinity η_{ij} associated with the cell representing $\hat{\mathbf{v}}_j^{\mathrm{MF}}$, namely the MF solution corresponding to the jth user, is higher than $(1 + 1/3)$. By contrast, the intrinsic affinity η_{ij} associated with the cell representing $-\hat{\mathbf{v}}_j^{\mathrm{MF}}$ is lower than $(1+1/3)$. The validity of this rule is demonstrated in every column of Table 5.5(a) corresponding to the indices of all the $K = 7$ users. Moreover, the MF solution $\hat{\mathbf{v}}_j^{\mathrm{MF}}$, related to each user and the opposite solution $-\hat{\mathbf{v}}_j^{\mathrm{MF}}$ for $j = 1, 2, \ldots, 7$ and the corresponding intrinsic affinities were extracted from Table 5.5(a) and are summarized in Table 5.6.

j	$[\hat{v}_{j1}^{\mathrm{MF}}$	$\hat{v}_{j2}^{\mathrm{MF}}]$	$\eta_j(\mathbf{v}_j^{\mathrm{MF}})$	$[-\hat{v}_{j1}^{\mathrm{MF}}$	$-\hat{v}_{j2}^{\mathrm{MF}}]$	$\eta_j(-\mathbf{v}_j^{\mathrm{MF}})$
1	$[+1$	$+1]$	1.64	$[-1$	$-1]$	1.15
2	$[-1$	$-1]$	63.74	$[+1$	$+1]$	1.00
3	$[+1$	$-1]$	17.62	$[-1$	$+1]$	1.00
4	$[-1$	$+1]$	17.62	$[+1$	$-1]$	1.24
5	$[-1$	$-1]$	1.39	$[+1$	$+1]$	1.28
6	$[+1$	$-1]$	1.65	$[-1$	$+1]$	1.12
7	$[+1$	$-1]$	1.98	$[-1$	$+1]$	1.04

Table 5.6: Fourteen intrinsic affinities associated with the (2×7) cells extracted from Table 5.5(a). The two intrinsic affinities seen in each row are vector elements given by the MF solution, and the opposite vector elements, related to the jth user, for $j = 1, 2, \ldots, 7$.

Similarly to our discussions in Section 3.4.2.2, here $(1 + 1/3)$ is the intrinsic affinity threshold, and $+1$, $+\infty$ represent two the extremes of the value domain for η_{ij}. The closer the intrinsic affinity associated with the MF solution $\eta_j(\mathbf{v}_j^{\mathrm{MF}})$ to $+\infty$, the closer the MF solution to -1.

Since the threshold used for separating the decision intervals between the MF solution and its opposite was reduced from 2 to $(1 + 1/3)$, when our improved algorithm was applied instead of the

traditional algorithm of Chapter 3, the values of the intrinsic affinities associated with the improved ACO ST/MUD algorithm in Table 5.5(a) are typically lower and converge more rapidly upon invoking iterative detection when compared to those employed by the traditional ACO ST/MUD algorithm shown in Table 5.5(b). In other words, the difference between the two values within the same column of Table 5.5(b) tends to be higher than the pairwise difference between any two from the four values within a certain column of Table 5.5(a).

This observation also applies when the symbol probabilities associated with each cell of the (4×7)-element route-table employed by the improved ACO algorithm and of the (2×14)-element route-table employed by the traditional ACO algorithm are compared in Table 5.7(a) and Table 5.7(b).

5.4.1.3 Symbol Probabilities

Based on the intrinsic affinity of Tables 5.5(a) and 5.5(b), the symbol probability tables may be calculated with the aid of Eq. (3.24) in Section 3.4.5.1 as follows:

$$P_{ij}^{(n)} = \frac{\left(\tau_{ij}^{(n)}\right)^{\alpha} \cdot \eta_{ij}^{\beta}}{\left(\tau_{1j}^{(n)}\right)^{\alpha} \cdot \eta_{1j}^{\beta} + \left(\tau_{2j}^{(n)}\right)^{\alpha} \cdot \eta_{2j}^{\beta}}, \tag{5.29}$$

where we have $n = 1, 2, \ldots, N$ and

$$\begin{cases} i = 1, \ldots, 4 \quad j = 1, 2, \ldots, K, & \text{when the } \textit{advanced} \text{ ACO is applied;} \\ i = 1, 2 \qquad\quad j = 1, 2, \ldots, 2K, & \text{when the } \textit{traditional} \text{ ACO is applied.} \end{cases} \tag{5.30}$$

For the first iteration associated with $n = 1$, the initial pheromone values $\tau_{ij}^{(1)} = 0.01$ and the intrinsic affinity of η_{ij} seen in Table 5.5(a) are employed. Then the symbol probabilities associated with the (4×7)-element route-table and (2×14)-element route-table employed by the improved and the traditional ACO-based MUD algorithm can be seen in Table 5.7. More detailed interpretations related to the symbol probabilities calculated for the traditional ACO-based MUD algorithm can be found in Section 3.4.5.

Tables 5.7(a) and 5.7(b) record the calculated symbol probabilities associated with each legitimate twin-symbol STBC vector and the resultant single symbol, when the improved ACO ST/MUD and the traditional ACO ST/MUD are applied, respectively.

The four numbers seen in the jth column of Table 5.7(a) represent the scenario, where the twin-symbol STBC vector having the highest probability among the four symbol probabilities constituting a column is not identical to the ML solution, which was highlighted by the bold characters. For example, the 4th, 5th and the 6th column of the ML solution is the 1st, 1st and the 4th row respectively, as highlighted by bold characters in Table 5.7(a). However, the row indeces having the highest symbol probabilities in the 4th, 5th and the 6th column of Table 5.7(a) are three, four and two respectively. Similarly, the corresponding boxes associated with $k = 4, 5$ and 6 in Table 5.7(b) also suggests that the cell having the highest probability is not the bold number associated with the specific symbol which forms part of the ML solution.

This leads to a more diverse search pool content for the improved ACO-based MUD algorithm. Hence, when the symbol-probability provides the wrong 'guidance' concerning a specific symbol-value

(a) Symbol probability $P_{ij}^{(1)}$ of the *improved* ACO $(4 \times K)$.

$\mathbf{v}^{(2)}$ \ k	1	2	3	4	5	6	7
$[+1\ +1]$	**0.58**	0.00	0.00	**0.19**	**0.19**	0.05	0.27
$[+1\ -1]$	0.25	0.00	**1.00**	0.16	0.23	0.47	**0.70**
$[-1\ +1]$	0.10	0.00	0.00	0.37	0.27	0.05	0.01
$[-1\ -1]$	0.07	**1.00**	0.00	0.28	0.31	**0.43**	0.02

(b) Symbol probability $P_{ij}^{(1)}$ of the *traditional* ACO $(2 \times 2K)$.

$v^{(1)}$ \ k	1		2		3		4	
	1	2	1	2	1	2	1	2
$+1$	**0.98**	**0.84**	0.00	0.00	**1.00**	0.00	**0.14**	**0.67**
-1	0.02	0.16	**1.00**	**1.00**	0.00	**1.00**	0.86	0.33

$v^{(1)}$ \ k	5		6		7	
	1	2	1	2	1	2
$+1$	**0.29**	**0.39**	0.54	0.00	**1.00**	0.12
-1	0.71	0.61	**0.46**	**1.00**	0.00	**0.88**

Table 5.7: Symbol probability $P_{ij}^{(1)}$ associated with each cell constituting the $(4 \times K)$-element and $(2 \times 2K)$-element route-tables of the improved and of the traditional ACO based HO ST/MUD algorithms during the *first* ACO-based search iteration, when both of them are applied to detect the 14 STBC symbols of the $K = 7$-user example.

or a twin-symbol combination, since this is not actually part of the ML solution, then the probability of the wrong bit-combination becoming incorporated in the ML solution will be higher during the first iteration of the improved ACO-based ST/MUD algorithm, as compared to the same probability estimated by the traditional ACO-based ST/MUD algorithm.

As seen from the $(4 \times K)$-element route-table in Tab. 5.7(a), the probability for the twin-symbol combinations $\mathbf{v}_4^{\mathrm{ML}} = [+1\ +1]$ and $\mathbf{v}_5^{\mathrm{ML}} = [+1\ +1]$ in the 4th and the 5th columns to be incorporated in the ML-solution is $P_{14}^{(1)} = 0.19$ and $P_{15}^{(1)} = 0.19$. Correspondingly, the probabilities of the four symbols constituting $\mathbf{v}_4^{\mathrm{ML}} = [+1\ +1]$ and $\mathbf{v}_5^{\mathrm{ML}} = [+1\ +1]$, which is represented by the cells $(1, 7)$, $(1, 8)$ and $(1, 9)$ and $(1, 10)$ in the $(2 \times 2K)$-element route-table of Table 5.7(b) is 0.14, 0.67, 0.29 and 0.39 respectively, leading to a joint probability of $0.14 \times 0.67 = 0.0938$ and $0.29 \times 0.39 = 0.1131$ for the two twin-symbol combinations to be incorporated in the ML-solution. Observe that both of these are lower than the probabilities of 0.19 and 0.19, as calculated by the improved ACO-based ST/MUD algorithm.

In other words, the ML solution will have a lower probability to be included in the search pool of the traditional ACO-based MUD algorithm of Table 5.7(b) than that in the improved ACO-based

MUD algorithm of Table 5.7(a).

5.4.1.4 Search Pool

The search pool of the improved ACO-based MUD algorithm is shown in Table 5.8(a), which is constructed on a twin-symbol by twin-symbol basis according to the rules outlined in Section 5.3.2.4. By contrast, that obtained by the traditional ACO-based MUD algorithm is shown in Table 5.8(b), which was created according to the rules highlighted in Section 5.3.1.4, as detailed in Section 3.4.6.1.

(a) *Improved* ACO ($4 \times K$).

Row index	LLF
[0 3 1 3 1 3 1]	8.08
[1 3 1 3 3 3 0]	4.77
[0 3 1 2 3 1 1]	6.56
[0 3 1 0 2 1 0]	5.22
[0 3 1 2 3 3 1]	7.77
[1 3 1 1 2 1 1]	4.88
[0 3 1 3 0 1 1]	6.90
[0 3 1 2 1 1 1]	6.85
[0 3 1 2 1 3 0]	6.68
[1 3 1 0 1 1 1]	5.29
[1 3 1 1 0 1 1]	5.26
[0 3 1 2 0 0 1]	5.37
[0 3 1 2 3 3 1]	7.77
[3 3 1 3 2 3 0]	2.75
[0 3 1 1 0 3 0]	7.08
[2 3 1 3 2 1 1]	4.82
[1 3 1 3 3 2 1]	4.60
[0 3 1 0 1 3 1]	**8.59**
[2 3 1 2 2 1 0]	3.82
[0 3 1 0 3 3 1]	7.93
[0 3 1 0 0 3 1]	9.24

(b) *Traditional* ACO ($2 \times 2K$).

Row index	LLF
[0 0 1 1 0 1 1 0 1 1 0 1 0 1]	6.56
[0 0 1 1 0 1 1 0 1 0 1 1 0 1]	8.35
[0 0 1 1 0 1 1 1 1 1 0 1 0 1]	6.24
[0 1 1 1 0 1 1 0 0 1 1 1 0 0]	5.23
[0 0 1 1 0 1 1 0 1 1 0 1 0 1]	6.56
[0 0 1 1 0 1 1 1 1 0 0 1 0 1]	6.53
[0 1 1 1 0 1 1 1 1 1 0 1 0 0]	4.18
[0 0 1 1 0 1 1 0 1 1 1 1 0 1]	7.77
[0 0 1 1 0 1 1 1 1 1 1 1 0 1]	7.46
[0 0 1 1 0 1 1 0 0 0 1 1 0 1]	**8.90**
[0 0 1 1 0 1 1 0 0 0 1 1 0 1]	**8.90**
[0 0 1 1 0 1 1 1 0 1 0 1 0 1]	6.62
[0 0 1 1 0 1 1 0 1 0 0 1 0 1]	6.95
[0 0 1 1 0 1 0 0 1 0 0 1 0 1]	6.96
[0 0 1 1 0 1 1 0 1 1 1 1 0 1]	7.77
[0 0 1 1 0 1 1 0 1 0 0 1 0 1]	6.95
[0 1 1 1 0 1 0 1 1 0 0 1 0 1]	4.88
[0 0 1 1 0 1 0 0 1 1 0 1 0 1]	6.49
[0 0 1 1 0 1 1 0 0 1 1 1 0 1]	8.32
[0 0 1 1 0 1 1 1 0 1 1 1 0 1]	8.08
[0 0 1 1 0 1 0 0 0 0 1 1 0 1]	9.24

Table 5.8: Search pools obtained by the improved and the traditional ACO based HO ST/MUD algorithms during the *first* ACO-based search iteration , when both of them are applied to detect the 14 symbols of the $K = 7$-user example.

The rows highlighted in bold characters in Tables 5.8 (a) and (b) indicate the 'elite' K-bit vector within the corresponding search pool having the highest LLF value. Additionally, the search pool

obtained by both algorithms during the second and third ACO-based search iteration is illustrated in Tables 5.11 and 5.14, respectively.

(a) Pheromone density $\tau_{ij}^{(2)}$ of *improved* ACO $(4 \times K)$.

$\mathbf{v}^{(2)}$ \ k	1	2	3	4	5	6	7
$[+1\ +1]$	**153.52**	0.01	0.01	**95.74**	**24.62**	5.37	30.34
$[+1\ -1]$	24.81	0.01	**189.72**	17.23	104.20	49.62	**159.38**
$[-1\ +1]$	8.65	0.01	0.01	44.83	21.50	4.60	0.01
$[-1\ -1]$	2.75	**189.72**	0.01	31.93	39.41	**130.14**	0.01

(b) Pheromone density $\tau_{ij}^{(2)}$ of *traditional* ACO $(2 \times 2K)$.

$v^{(1)}$ \ k	1		2		3		4	
	1	2	1	2	1	2	1	2
$+1$	**210.86**	**196.57**	0.01	0.01	**210.86**	0.01	**18.33**	**166.87**
-1	0.01	14.30	**210.86**	**210.86**	0.01	**210.86**	192.53	44.00

$v^{(1)}$ \ k	5		6		7	
	1	2	1	2	1	2
$+1$	**117.22**	**129.60**	68.93	0.01	**210.86**	9.42
-1	93.65	81.27	**41.94**	**210.86**	0.01	**201.45**

Table 5.9: Pheromone density $\tau_{ij}^{(2)}$ associated with each cell constituting the $(4 \times K)$-element and $(2 \times 2K)$-element route-tables of the improved and of the traditional ACO based HO ST/MUD algorithms during the *first* ACO-based search iteration, when both of them are applied to detect the 14 symbols of the $K = 7$-user example considered.

5.4.1.5 Pheromone Density

The pheromone density update rule applied in both the traditional and in the improved ACO-based MUD algorithm was the same, as discussed in Section 3.4.4.1. In order to provide further insights, the pheromone density values associated with each cell constituting the (4×7)-element and (2×14)-element route-table employed by the improved and the traditional ACO-based ST/MUD algorithm during the first and second ACO-based search iteration are listed in Tables 5.9 and 5.12, respectively.

(a) Symbol-value probability $P_{ij}^{(2)}$ of *improved* ACO $(4 \times K)$.

$\mathbf{v}^{(2)}$ \ k	1	2	3	4	5	6	7
$[+1\ +1]$	**0.91**	0.00	0.00	**0.37**	**0.11**	0.00	0.08
$[+1\ -1]$	0.07	0.00	**1.00**	0.06	0.48	0.31	**0.92**
$[-1\ +1]$	0.01	0.00	0.00	0.36	0.14	0.00	0.00
$[-1\ -1]$	0.00	**1.00**	0.00	0.20	0.28	**0.68**	0.00

(b) Symbol-value probability $P_{ij}^{(2)}$ of *traditional* ACO $(2 \times 2K)$.

$v^{(1)}$ \ k	1		2		3		4	
	1	2	1	2	1	2	1	2
$+1$	**1.00**	**0.98**	0.00	0.00	**1.00**	0.00	**0.02**	**0.87**
-1	0.00	0.02	**1.00**	**1.00**	0.00	**1.00**	0.98	0.13

$v^{(1)}$ \ k	5		6		7	
	1	2	1	2	1	2
$+1$	**0.33**	**0.50**	0.38	0.00	**1.00**	0.01
-1	0.67	0.50	**0.62**	**1.00**	0.00	**0.99**

Table 5.10: Symbol probability $P_{ij}^{(2)}$ associated with each cell constituting the $(4 \times K)$-element and $(2 \times 2K)$-element route-tables of both the improved and of the traditional ACO based HO ST/MUD algorithms during the *second* ACO-based search iteration, when both of them are applied to detect the 14 symbols of the $K = 7$-user example considered.

5.4.2 Global Discussions

In this subsection we will analyze the improved ACO ST/MUD algorithm's capability of successfully capturing the ML solution, at a fraction of the full-search complexity in comparison to that of the traditional one. The properties discussed in this subsection are updated during each ACO-based search iteration.

5.4.2.1 Correct Detection Probability Improvement

As an alternative interpretation, we may consider the search process carried out by the ACO-based MUD algorithm reminiscent of the action of an FEC decoder, where the intrinsic affinity generated by the MF output may be viewed as the soft-input and the ML solution as the hard-output. Hence, the aim of the search process becomes that of correcting the 'erroneous' symbols, which are constituted by the different symbols of the MF solution and the ML solution, as indicated by the dashed-line box in the intrinsic affinity matrix of Table 5.5.

(a) *Improved* ACO ($4 \times K$).									(b) *Traditional* ACO $2 \times 2K$.																				
Row index								LLF	Row index																				LLF
[0	3	1	3	2	3	1]		7.92	[0	0	1	1	0	1	1	0	1	0	0	1	0	1]					6.95
[0	3	1	3	3	3	1]		7.46	[0	0	1	1	0	1	1	1	0	1	0	1	0	1]					6.62
[0	3	1	2	3	3	1]		7.77	[0	0	1	1	0	1	1	0	1	0	1	1	0	1]					8.35
[0	3	1	0	2	1	1]		6.96	[0	0	1	1	0	1	1	0	1	0	0	1	0	1]					6.95
[0	**3**	**1**	**0**	**1**	**3**	**1]**		**8.59**	[0	0	1	1	0	1	1	0	1	0	0	1	0	1]					6.95
[0	3	1	0	3	3	1]		7.93	[0	0	1	1	0	1	1	0	0	1	1	1	0	1]					8.32
[0	3	1	1	1	3	0]		6.77	[0	0	1	1	0	1	1	0	1	1	1	1	0	1]					7.77
[0	3	1	0	1	3	0]		6.84	[0	0	1	1	0	1	1	0	1	0	0	1	0	1]					6.95
[1	3	1	2	3	1	1]		5.22	[0	0	1	1	0	1	1	0	1	1	1	1	0	1]					7.77
[0	**3**	**1**	**0**	**1**	**3**	**1]**		**8.59**	[0	0	1	1	0	1	1	0	1	1	0	1	0	1]					6.56
[0	**3**	**1**	**0**	**1**	**3**	**1]**		**8.59**	**[0**	**0**	**1**	**1**	**0**	**1**	**1**	**0**	**0**	**0**	**1**	**1**	**0**	**1]**					**8.90**
[0	3	1	3	1	3	1]		8.08	[0	0	1	1	0	1	1	0	1	1	0	1	0	1]					6.56
[0	3	1	2	3	3	1]		7.77	[0	0	1	1	0	1	1	0	0	1	1	1	0	1]					8.32
[0	3	1	0	0	1	1]		7.37	[0	0	1	1	0	1	1	0	1	1	1	1	0	1]					7.77
[1	3	1	2	0	3	1]		6.79	[0	0	1	1	0	1	1	1	1	0	1	1	0	1]					7.92
[0	3	1	2	1	1	1]		6.85	[0	0	1	1	0	1	1	0	1	0	1	1	0	1]					8.35
[0	3	1	3	1	3	1]		8.08	**[0**	**0**	**1**	**1**	**0**	**1**	**1**	**0**	**0**	**0**	**1**	**1**	**0**	**1]**					**8.90**
[0	3	1	0	1	1	1]		6.89	[0	0	1	1	0	1	1	1	0	1	0	1	0	1]					6.62
[0	3	1	2	3	1	1]		6.56	[0	0	1	1	0	1	1	0	1	1	1	1	0	1]					7.77
[0	3	1	2	2	3	1]		8.35	**[0**	**0**	**1**	**1**	**0**	**1**	**1**	**0**	**0**	**0**	**1**	**1**	**0**	**1]**					**8.90**
[0	3	1	0	0	3	1]		9.24	[0	0	1	1	0	1	0	0	0	0	1	1	0	1]					9.24

Table 5.11: Search pools obtained by the improved and by the traditional ACO based HO ST/MUD algorithms during the *second* ACO-based search iteration, when both of them are applied to detect the 14 symbols of the given $k = 7$ user example.

Tables 5.7(a), 5.10(a) and 5.13(a) summarized the symbol-probabilities during the first three search iterations. The 4th, 5th and 6th twin-symbol combinations of Table 5.7(a) are erroneous and the *improved* ACO-based ST/MUD is capable of 'correcting' two of them, when the first search iteration is completed, as shown in Table 5.10. As compared to the symbol probabilities estimated by the *traditional* ACO-based ST/MUD algorithm, which were portrayed in Tables 5.7(b), 5.10(b) and 5.13(b), two 'erroneous' bits remain uncorrected after the first and second iterations are finished.

More specifically, observe from Table 5.13(a) that the 'erroneous' bit represented by the $\hat{\mathbf{v}}_5 = [+1 \quad -1]$ values of the 4th column as determined by $P_{2,5}^{(3)} = 0.52$ is different from the ML solution of $\hat{\mathbf{v}}_5^{\mathrm{ML}} = [+1 \quad +1]$, but only in the second position. Hence, we only have a single erroneous bit in the HO vector, when the vector containing pure logical ones is generated according to the bit-probabilities. By

(a) Pheromone density $\tau_{ij}^{(3)}$ of *improved* ACO $(4 \times K)$.

$\mathbf{v}^{(2)}$ \ k	1	2	3	4	5	6	7
$[+1\ +1]$	**282.84**	0.00	0.00	**178.34**	**26.47**	2.69	28.79
$[+1\ -1]$	24.42	0.00	**312.95**	15.39	190.09	64.67	**284.17**
$[-1\ +1]$	4.32	0.00	0.00	71.73	33.98	2.30	0.00
$[-1\ -1]$	1.38	**312.95**	0.00	47.50	62.41	**243.30**	0.00

(b) Pheromone density $\tau_{ij}^{(3)}$ of *traditional* ACO $(2 \times 2K)$.

$v^{(1)}$ \ k	1		2		3		4	
	1	2	1	2	1	2	1	2
$+1$	**329.79**	**322.64**	0.00	0.00	**329.79**	0.00	**9.17**	**286.64**
-1	0.00	7.15	**329.79**	**329.79**	0.00	**329.79**	320.63	43.16

$v^{(1)}$ \ k	5		6		7	
	1	2	1	2	1	2
$+1$	**186.34**	**215.09**	88.62	0.00	**329.79**	4.71
-1	143.45	114.70	**241.17**	**329.79**	0.00	**325.09**

Table 5.12: Pheromone density $\tau_{ij}^{(3)}$ associated with each cell constituting the $(4 \times K)$-element and $(2 \times 2K)$-element route-tables of the improved and the traditional ACO based HO ST/MUD algorithms during the *second* ACO-based search iteration , when both of them are applied to detect the 14 symbols of the $K = 7$-user example.

contrast, the number of erroneous bits found at the output of the *traditional* ACO-based ST/MUD algorithm is only the true value, when a single vector is allowed to be generated according to the specific symbol-value probabilities, as observed from Table 5.13(b).

This argument exemplified the superiority of the *improved* ACO-based ST/MUD of Alg. 2 over the *traditional* Alg. 1.

5.4.2.2 Symbol Probability Convergence versus Pheromone Convergency

As discussed with reference to Fig. 3.14 in Section 3.4.6.2, the bit-probability's convergence to the 'elite' K-bit vector is typically delayed with respect to the pheromone's convergence due to the delayed effect of the intrinsic affinity.

As demonstrated in Table 5.12(b), the pheromone-level associated with the 1st symbol transmitted by the 5th user suggests that a $+1$ was transmitted, when the second search iteration was completed. However, the bit-probability of $P_{+9}^{(3)} = 0.34 < P_{-9}^{(3)} = 0.66$ shown in column 5-1 of Table 5.13(b) suggests that a -1 is likely to have been transmitted by v_{51} instead of $+1$, as suggested by the pheromone level of $\tau_{+9}^{(3)} = 186.34 > \tau_{-9}^{(3)} = 143.45$, as illustrated by Table 5.12(b).

(a) Symbol-value probability $P_{ij}^{(3)}$ of *improved* ACO ($4 \times K$).

$\mathbf{v}^{(2)}$ \ k	1	2	3	4	5	6	7
$[+1\ +1]$	**0.95**	0.00	0.00	**0.42**	**0.08**	0.00	0.05
$[+1\ -1]$	0.04	0.00	**1.00**	0.04	0.52	0.25	**0.95**
$[-1\ +1]$	0.00	0.00	0.00	0.35	0.13	0.00	0.00
$[-1\ -1]$	0.00	**1.00**	0.00	0.19	0.27	**0.75**	0.00

(b) Symbol-value probability $P_{ij}^{(3)}$ of *traditional* ACO ($2 \times 2K$).

$v^{(1)}$ \ k	1		2		3		4	
	1	2	1	2	1	2	1	2
$+1$	**1.00**	**0.99**	0.00	0.00	**1.00**	0.00	**0.01**	**0.92**
-1	0.00	0.01	**1.00**	**1.00**	0.00	**1.00**	0.99	0.08

$v^{(1)}$ \ k	5		6		7	
	1	2	1	2	1	2
$+1$	**0.34**	**0.53**	0.33	0.00	**1.00**	0.00
-1	0.66	0.47	**0.67**	**1.00**	0.00	**1.00**

Table 5.13: Symbol-value probability $P_{ij}^{(3)}$ associated with each cell constituting the $(4 \times K)$-element and $(2 \times 2K)$-element route-tables of the improved and the traditional ACO based HO ST/MUD algorithms during the *third* ACO-based search iteration , when both of them are applied to detect the 14 symbols of the $K = 7$-user example.

However, this delayed relationship between a bit-probability and the corresponding pheromone-level is not so pronounced in the *improved* ACO-based ST/MUD algorithm. This is demonstrated by the simulation results recorded after the first search iteration was completed. The highest values of $P_{14}^{(2)} = 0.37$ and $P_{46}^{(2)} = 0.68$ within the 4th and 6th columns of Table 5.10(a) were generated by the same twin-symbol combination of $\hat{\mathbf{v}}_4 = [+1\ \ +1]$ and $\hat{\mathbf{v}}_6 = [-1\ \ -1]$, which have the highest amount of pheromone given by $\tau_{14}^{(2)} = 95.74$ and $\tau_{46}^{(2)} = 130.14$, as observed in Table 5.9(a).

5.4.2.3 Diversity of the Decision Candidates in the Search Pool

A large variety of K-bit vectors appear in the initial search pool of Table 5.8(a), obtained by the *improved* ACO-based ST/MUD algorithm during the first iteration, which was as high as 19 obtained by the $\zeta = 20$ ants. A large diversity of the vectors potentially results in slow convergence, but allows us to avoid settling on a locally optimal solution. Hence, it allows the consecutive search iterations to locate the globally optimal solution.

By contrast, as shown in Table 5.8(b), the average LLFs of the K-bit vectors captured in the

(a) *Improved* ACO ($4 \times K$).		(b) *Traditional* ACO $2 \times 2K$.	
Row Index	LLF	Row Index	LLF
[0 3 1 0 2 3 1]	8.59	[0 0 1 1 0 1 1 0 1 1 1 1 0 1]	7.77
[0 3 1 0 1 1 1]	6.89	[0 0 1 1 0 1 1 0 1 0 0 1 0 1]	6.95
[0 3 1 2 2 3 1]	8.35	[0 0 1 1 0 1 1 0 1 1 1 1 0 1]	7.77
[0 3 1 3 1 3 1]	8.08	[0 0 1 1 0 1 1 0 0 0 0 1 0 1]	7.25
[0 3 1 2 1 3 1]	8.32	[0 0 1 1 0 1 1 0 1 0 1 1 0 1]	8.35
[1 3 1 3 1 3 1]	6.40	[0 0 1 1 0 1 1 0 1 0 0 1 0 1]	6.95
[0 3 1 2 1 1 1]	6.85	[0 0 1 1 0 1 1 0 0 1 1 1 0 1]	8.32
[0 3 1 2 1 3 1]	8.32	[0 0 1 1 0 1 1 0 0 1 1 1 0 1]	8.32
[0 3 1 2 3 3 1]	7.77	**[0 0 1 1 0 1 1 0 0 0 1 1 0 1]**	**8.90**
[0 3 1 3 0 3 1]	8.55	[0 0 1 1 0 1 1 0 1 0 1 1 0 1]	8.35
[0 3 1 2 3 3 1]	7.77	[0 0 1 1 0 1 1 0 1 1 1 1 0 1]	7.77
[0 3 1 0 1 3 1]	8.59	[0 0 1 1 0 1 1 0 1 0 0 1 0 1]	6.95
[0 3 1 3 3 1 0]	5.02	[0 0 1 1 0 1 1 0 1 1 1 1 0 1]	7.77
[0 3 1 0 1 1 1]	6.89	[0 0 1 1 0 1 1 0 1 1 0 1 0 1]	6.56
[0 3 1 0 3 3 1]	7.93	[0 0 1 1 0 1 1 0 1 0 0 1 0 1]	6.95
[0 3 1 0 1 1 1]	6.89	[0 0 1 1 0 1 1 1 0 0 1 1 0 1]	8.55
[0 3 1 2 2 3 1]	8.35	[0 0 1 1 0 1 1 0 1 0 1 1 0 1]	8.35
[0 3 1 0 3 3 1]	7.93	[0 0 1 1 0 1 1 1 0 0 0 1 0 1]	6.90
[0 3 1 0 0 3 1]	**9.24**	[0 0 1 1 0 1 1 0 1 1 1 1 0 1]	7.77
[0 3 1 2 2 3 1]	8.35	[0 0 1 1 0 1 1 0 0 1 1 1 0 1]	8.32
[0 3 1 0 0 3 1]	9.24	[0 0 1 1 0 1 0 0 0 0 1 1 0 1]	9.24

Table 5.14: Search pools obtained by the improved and the by traditional ACO based HO ST/MUD algorithms during the *third* ACO-based search iteration , when both of them are applied to detect the 14 symbols of the $K = 7$-user example.

initial search pool of the *traditional* ACO-based ST/MUD algorithm tend to be significantly higher, but less diverse during the first iteration, as compared to that of the *improved* ACO-based ST/MUD algorithm. As a result, the lack of population diversity - which may be attributed to the less evenly distributed intrinsic affinity for the *traditional* ACO-based ST/MUD algorithm - limits the ability of the search pool to capture the globally optimal solution during the forthcoming iterations.

5.4.2.4 Error Correction Process

As mentioned in Section 5.4.2.1, the conversion of he MF solution to the ML solution of the search pool may be regarded as an 'error correction' procedure of gradually correcting the bits, which are

	$K = 7$-bit vector represented by row indices	Probability of vector-value		
		Iter 1	Iter 2	Iter 3
ML	[0 0 1 1 0 1 0 0 0 0 1 1 0 1]	0.0035	0.0017	0.0011
	[0 0 1 1 0 1 1 0 0 0 1 1 0 1]	0.0217	0.0846	0.1089
	[0 0 1 1 0 1 1 0 1 0 1 1 0 1]	0.0532	0.1718	0.2113
	[0 0 1 1 0 1 1 0 0 1 1 1 0 1]	0.0340	0.0846	0.0965
MF	[0 0 1 1 0 1 1 0 1 1 0 1 0 1]	0.0976	0.1053	0.0923

Table 5.15: Probabilities of some of the high-LLF K-bit vector being captured for the search pool of the *traditional* ACO-based ST/MUD algorithm during the first three search iterations in the $K = 7$ user example considered.

	Vector-value represented by row indices	Probability of vector-value		
		Iter 1	Iter 2	Iter 3
ML	[0 3 1 0 0 3 1]	0.0063	0.0235	0.0227
	[0 3 1 0 1 3 1]	0.0076	0.1026	0.1478
	[0 3 1 2 2 3 1]	0.0174	0.0291	0.0308
	[0 3 1 0 2 3 1]	0.0090	0.0299	0.0370
	[0 3 1 2 1 3 1]	0.0149	0.0998	0.1232
	[0 3 1 3 1 3 1]	0.0112	0.0582	0.0669
MF	[0 3 1 2 3 1 1]	0.0219	0.0252	0.0213

Table 5.16: Probabilities of some of the high-LLF $K = 7$-bit vectors captured for the search pool of the *improved* ACO-based ST/MUD algorithm during the first three search iterations in the $K = 7$ user example considered in Section 5.4.

regarded as 'errors', because they are different for the MF solution and the ML solution, regardless whether the *traditional* or the *improved* ACO-based ST/MUD algorithm is utilised.

The 'correction' procedure is usually carried out in the following way. Let us assume that there are N_e number of different symbols between the MF solution and the ML solution. The ACO search process always 'corrects' the pheromone-level, then the symbol-probabilities associated with the $(N_e - 1)$ symbols, then 'correct' the same attributes associated with the last of the N_e 'erroneous' symbols.

The above-mentioned 'error correction' process may become successful as long as the bit-probability of the last bit is sufficiently high to motivate at least one ant to choose it, although it was decreased during the process while the ACO algorithm corrected the other $(N_e - 1)$ symbols.

This can be verified by our $K = 7$-user example. During the third iteration, when all the $(N_e - 1) = (3 - 1)$ 'erroneous' twin-symbol combinations of our $N_e = 3$ scenario associated with the $k = 4$th and $k = 6$th users have been corrected, as shown in the bit-LLF list of Table 5.13(a), the last 'erroneous' twin-symbol combination is that of the $k = 5$th user. At that moment, the probability associated with

$\hat{\mathbf{v}}_5^{\mathrm{ML}} = [+1 \quad +1]$ is 0.08, which has a chance of being selected by $\zeta \times P_{15}^{(3)} = 20 \times 0.08 \approx 2$ ants. As a result, the probabilities of $P_{14}^{(3)} = 0.42$ and $P_{46}^{(6)} = 0.75$ associated with the other two combinations of $\hat{\mathbf{v}}_4^{\mathrm{ML}} = [+1 \quad +1]$ and $\hat{\mathbf{v}}_6^{\mathrm{ML}} = [-1 \quad -1]$, that are part of the ML-solution, but not of the MF-solution have already found their way into the search pool. Hence the complete ML solution finally appears in the search pool during the 3rd iteration, as shown in Table 5.13(a).

By contrast, as shown in Table 5.13(b) for the *traditional* ACO-based ST/MUD algorithm, we have $N_{\mathrm{e}} = 4$, bits that are part of the ML solution, but not of the MF solution, which correspond to the 1st symbol transmitted by user $k = 4$, the 1st and the 2nd symbols transmitted by user $k = 5$, and the 1st symbol transmitted by user $k = 6$. Hence, we have to ensure that the relevant probabilities increase to a sufficiently high value, so that the lowest possible number of vectors contain $\hat{v}_{51}^{\mathrm{ML}} = +1$, $\hat{v}_{52}^{\mathrm{ML}} = +1$,$\hat{v}_{61}^{\mathrm{ML}} = -1$ instead of the $\hat{v}_{51}^{\mathrm{MF}} = -1$, $\hat{v}_{52}^{\mathrm{MF}} = -1$,$\hat{v}_{61}^{\mathrm{MF}} = +1$. Observe in Table 5.13(b) that the probability associated with $\hat{v}_{41}^{\mathrm{ML}} = +1$ of the ML-solution has already become as low as $P_{14}^{(3)} = 0.01$. This phenomenon is also shown from an alternatively perspective by Table 5.15, where the probability of the ML solution appearing in the search pool during the third iteration has already been reduced to a value as low as 0.0011, which suggests that the ML solution only has a marginal chance of being incorporated.

In other words, when the speed of convergence to the other $(N_{\mathrm{e}}-1)$ symbols (or symbol-combinations) which are part of the ML but not of the MF solution is slower than the pheromone-evaporation rate associated with most recent symbols (or symbol-combinations) that were part of the ML solution, then the ML solution may not find its way back into the search-pool again.

As shown in Table 5.16, the probability associated with the sub-optimal vector-values of [0 3 1 0 1 3 1] and [0 3 1 2 1 3 1] increases throughout the first three iterations and finally the algorithm 'corrects' the last erroneous symbol with a probability of 0.1478 and 0.1232.

5.5 Simulation Results

Two system scenarios are considered in this section, both of which are STBC-assisted two transmit antenna aided DS-CDMA systems. In one of the scenarios we employ m-sequence based DS-spreading using a spreading factor of $N_{\mathrm{s}} = 7$, while in the other scenario we use Gold code based spreading associated with $N_{\mathrm{s}} = 31$. For the sake of convenience, the fully-loaded DS-CDMA system supporting $K = 7$ users and employing a set of m sequences having a length of $N_{\mathrm{s}} = 7$ is referred to as the $m7K7$ system and that supporting $K = 32$ users with the aid of a set of Gold codes having a length of $N_{\mathrm{s}} = 31$ is referred to as the G31K32 system.

5.5.1 Performance of the m-Sequence-based System

Apart from using a different number of artificial ants ζ, all the other parameters characterizing the ACO algorithms are identical in the traditional and in the proposed ST-MUD algorithms, which are listed in Table. 5.18.

The complexity imposed is quantified in terms of the number of FLoating point Operations Per Second (FLOPS) within a STBC block duration, divided by the number of users K. Since both the

System	Modem	BPSK
	Multiple access method	DS-CDMA
	Spreading code	m-sequence
	Spreading factor	$N_s = 7$
	No. of transmit antennas	1
	No. of receive antenna arrays	$N_r = 1$
	No. of users	$K = 3, 5, 7$
	Channel	Uncorrelated Rayleigh fading

Table 5.17: Parameters for the STBC-CDMA system employing the ACO based ST-MUD algorithm.

ACO parameters	
Initial pheromone	$\tau = 0.01$
Evaporation rate	$\rho = 0.5$
Maximum number of iterations	$\Xi = 10$
Weight of pheromone	$\alpha = 1$
Weight of intrinsic affinity	$\beta = 6$
Weight of the elite ant	$\sigma = 8$

Table 5.18: Basic simulation parameters used in Section 5.5.

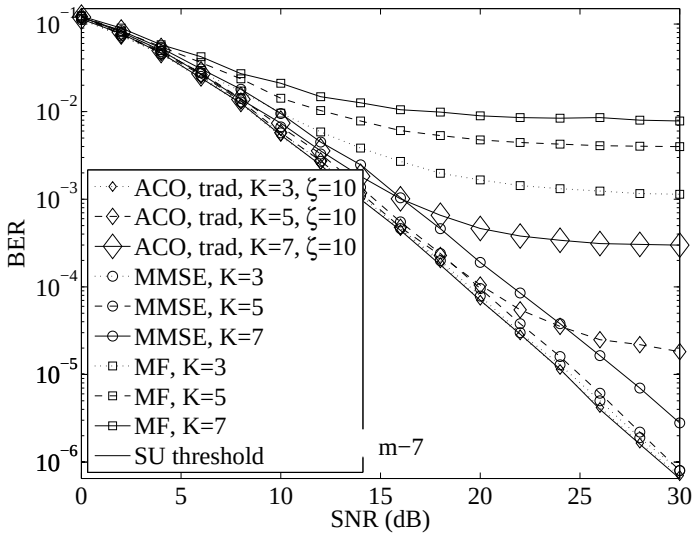

Figure 5.2: Comparison of the BER performances achieved by the STBC assisted two transmit antenna aided DS-CDMA UL employing the conventional ACO, MMSE and MF based HO detection schemes, where $K = 3$, $K = 5$ and $K = 7$ users are supported by the m-sequence having seven chips. The system's schematic is shown in Fig. 5.1 and all parameters are summarized in Table 5.17.

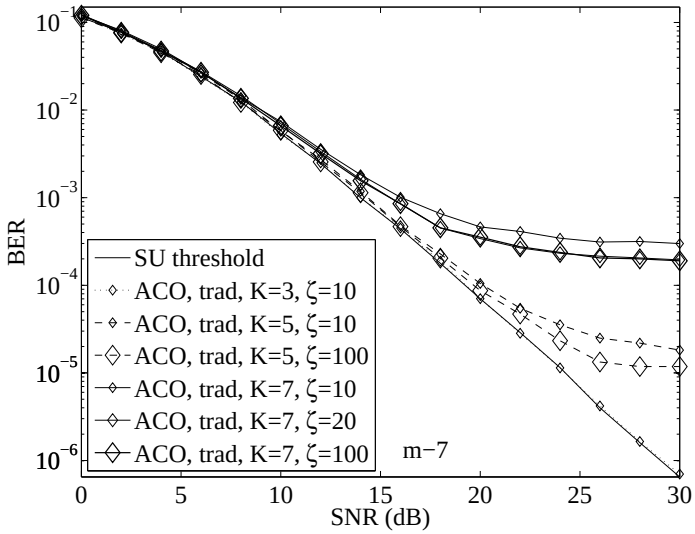

Figure 5.3: Comparison of the BER performances achieved by the STBC assisted two transmit antenna aided DS-CDMA UL employing different detection schemes, where $K = 7$ users are supported by the m-sequence having a length of 7. The system's schematic is shown in Fig. 5.1 and all parameters are summarized in Table 5.17.

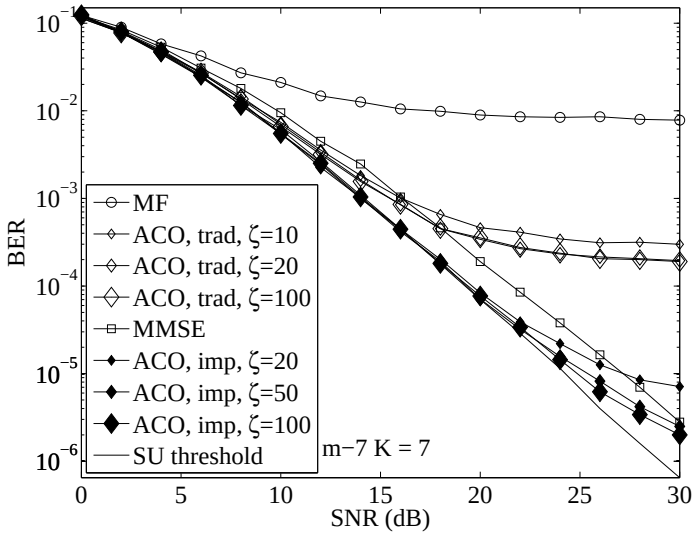

Figure 5.4: Comparison of the BER performances achieved by the STBC assisted two transmit antenna aided DS-CDMA UL employing different detection schemes, where $K = 7$ users are supported by the m-sequence having a length of 7 chips. The system's schematic is shown in Fig. 5.1 and all parameters are summarized in Table 5.17.

channel quality and the AWGN vector encountered vary from block to block, the number of times we have to evaluate the $2K$-element vector-LLF, which predetermines the total complexity imposed by the ACO algorithm is different in the consecutive block durations. Hence, in order to characterize the time-variant complexity of the ACO-aided ST-MUD algorithm more accurately, the PDF of the complexity was plotted in Fig. 5.5 and Fig. 5.8 at different SNRs ranging from 0dB to 30dB. As seen from Fig. 5.5 (a) to Fig. 5.5 (d) and in Fig. 5.8 (a) to Fig. 5.8 (d), when the SNR increases from 0dB to 30dB, gradually decreasing complexities are imposed by both the traditional and the improved ACO ST-MUD algorithms in both the $m7K7$ system and the G31K32 system.

The MF, the MMSE and the traditional ACO-based ST/MUD algorithms applied in the STBC assisted twin-transmit antenna aided DS-CDMA UL are characterized in Fig. 5.2 for transmission over uncorrelated flat fading Rayleigh channels. The m-sequence based spreading codes have a length of $N_s = 7$ chips. The traditional ACO algorithm employs $\zeta = 10$ ants. All three HO MUD algorithms exhibit error floors to different degree, when the number of users supported by the $N_s = 7$-chip m-sequences increases from $K = 3$ to $K = 5$ and finally to $K = 7$. As expected, the MF-based single-user detector has the worst BER performance, as seen in Fig. 5.2. When $K = 3$ and $K = 5$ users are supported by the system, its performance is close to the Single-User (SU) benchmark. However, when the number of users increases from $K = 5$ to $K = 7$, an error floor occurs, as shown by the solid line marked by the circle in Fig. 5.2.

Finally, when $K = 3$ users are supported by the system, the *traditional* ACO-based ST/MUD algorithm allows the $K = 3$-user system to approach the performance of the SU benchmark. However, when $K = 5$ and $K = 7$ users are supported, the *traditional* ACO-based ST/MUD algorithm having $\zeta = 10$ ants fails to eliminate the error floor. As shown by the dashed line marked by diamonds and by the solid line seen in Fig. 5.2, when $K = 5$ and $K = 7$ users are supported by the STBC DS-CDMA UL with the aid of m-sequences having $N_s = 7$ chips, the performance of the system using the *traditional* ACO-based ST/MUD algorithm employing $\zeta = 10$ ants becomes worse than that of the MMSE algorithm.

Naturally, enhancing the BER performance becomes possible by increasing the number of ants from ζ 10 to 20 or even 100. However, as seen in Fig. 5.3, despite increasing by the number of ants from $\zeta = 10$ to $\zeta = 100$, when $K = 5$ users are supported, the achievable BER improvement remains fairly insignificant. Similarly, despite an increase in the number of ants from ζ 20 to 100, when $K = 7$ users are supported, the BER performance of the $K = 7$-user system does not substantially improve.

The failure of the *traditional* ACO-based ST/MUD algorithm to improve the MU system's BER performance by increasing the number of ants ζ is also demonstrated in Fig. 5.4, where the BER performance achieved by the $m7K7$ system employing the MMSE ST-MUD algorithm is seen to be better than that of the *traditional* ACO ST-MUD algorithm employing $\zeta = 100$ ants, which is achieved as a benefit of the MMSE MUD's higher complexity, as revealed by Fig. 5.5 (e).

This fact demonstrated the need for the *improved* ACO-based ST/MUD. Again the difference between the *traditional* and *improved* ACO-based MUD was detailed in Section 5.3.2.

As shown in Fig. 5.4, the *improved* ACO-based ST/MUD algorithm shows a significant BER performance improvement, substantially reducing the error floor of the traditional ACO-aided MUD algorithm. More specifically, the *improved* ACO-based ST/MUD algorithm employing $\zeta = 100$ ants enables the fully-loaded $m7K7$ system to approach the performance of the SU benchmark. Despite its superior performance, the complexity imposed by the *improved* ACO-based ST/MUD algorithm having $\zeta = 100$ ants is only slightly higher than that of the traditional ACO-aided ST-MUD and it is lower than that of the MMSE ST-MUD algorithm, as shown in Fig. 5.5 (e). The complexity of the proposed ACO algorithm is typically about 1000 times lower than that of the ML algorithm. The detailed complexity estimates quantified in terms of FLOPS for each individual step carried out by the MF, MMSE, ML, as well as by the traditional and the improved ACO-based MUD algorithms recorded in the context of the $m7K7$ system are listed in Table 5.19.

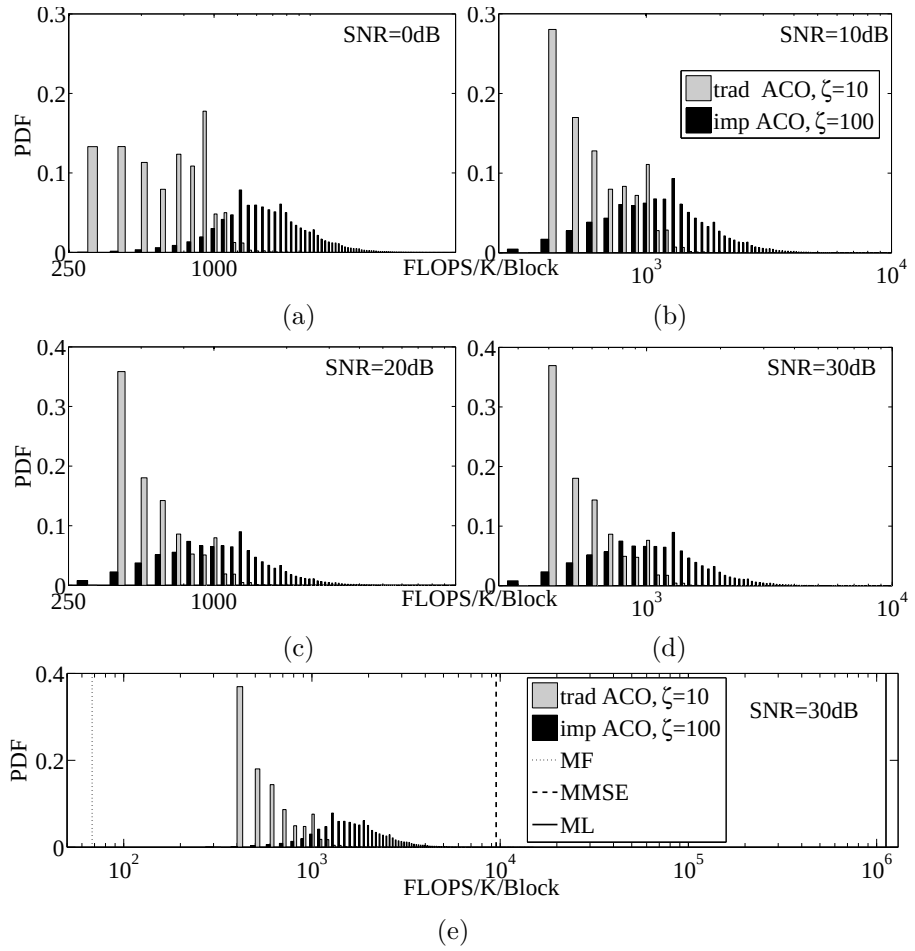

Figure 5.5: PDF of the complexity associated with different detection schemes in the STBC assisted two transmit antenna aided DS-CDMA UL adopting m-sequences having$N_s = 7$ and supporting $K = 7$ users.

5.5.2 Performance of the Gold Code-based System

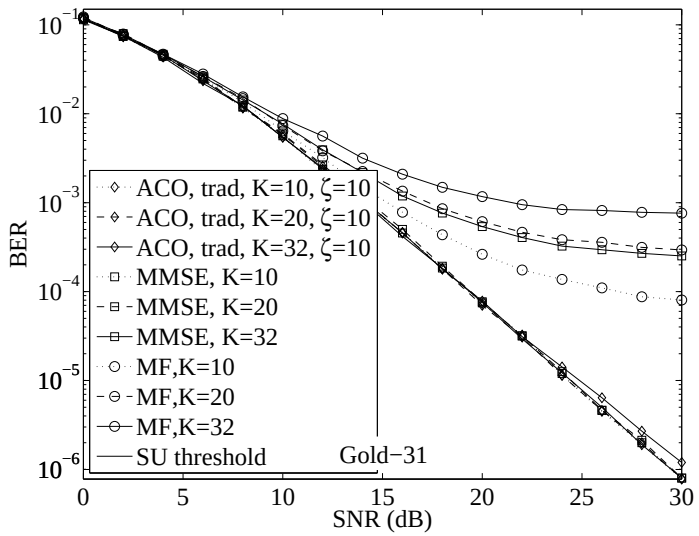

Figure 5.6: Comparison of the BER performances achieved by the STBC assisted two transmit antenna aided DS-CDMA UL employing different detection schemes, where $K = 32$ users are supported by Gold codes having a length of $N_s = 31$ chips. The system's schematic is shown in Fig. 5.1 and all parameters are summarized in Table 5.20.

operation	MF	MMSE	ML	ACO1①	ACO2②
$\mathbf{y}$③	68	68	68	68	56
	×1	×1	×1	×1	×1
	68	**68**	**68**	**68**	**56**
$\mathbf{R}$③	–	24.0	24.0	24.0	–
		×1	×1	×1	
		24.0	**24.0**	**24.0**	
Matrix Inversion③ $(2K \times 2K)$④	–	9348	–	–	–
		×1			
		9348			
Objective Function Evaluation③	–	–	68.4	68.4	34.3
			×16384	×2.9⑤	×19.9⑤
			1.1e^6	**195.1**⑤	**680.9**⑤
others⑥	–	84	–	277.1⑤	747.9⑤
total⑥	**259.9**	**9524**	**1.1e^6**	**564.2**⑤	**1463.0**⑤

① The traditional ACO-based ST/MUD algorithm having a $(2 \times 2K)$-element route-table and $\zeta = 10$ ants

② The improved ACO-based ST/MUD algorithm having a $(4 \times K)$-element route-table and $\zeta = 100$ ants

③ The first of the three rows describing a specific process in all algorithms quantifies the number of FLOPS per user per STBC-block per unit time the process is operated; the second row represents the number of times the particular process is carried out during the corresponding algorithm; the third row represents the total number of FLOPS impose per user during an STBC-block.

④ The dimension of the complex-valued square matrix is $2K$, however it has to be transformed to a real-value square matrix having a size of $(2 \cdot 2K) \times (2 \cdot 2K)$. The interested readers is referred to Appendix 1.

⑤ It is the mean.

⑥ This row quantifies the total number of FLOPS per user during a single STBC-block.

Table 5.19: FLOPS consumed by each of the principle steps taken by all the algorithms in the STBC-m7K7 system. All the data in this table has been approximated in such a way that only the first digit after the decimal point is remained to save the space.

Observe in Fig. 5.6 that similarly to the MU DS-CDMA UL employing m-sequences, when the number of users increases from $K = 10$ to 20 and to 30, the MF based system shows a persistent error floor. However, in contrast to the MU DS-CDMA UL employing m-sequences, observe in Fig. 5.6 that when the number of users increases from $K = 10$ to 20 and to 30, the MMSE-detection aided system only exhibits an error floor when $K = 32$ users are supported. Furthermore, as evidenced by

System	Modem	BPSK
	Multiple access mothod	DS-CDMA
	Spreading code	Gold code
	Spreading factor	$N_s = 31$
	No. of transmit antennas	1
	No. of receive antenna arrays	$N_r = 1$
	No. of users	$K = 10, 20, 32$
	Channel	Uncorrelated Rayleigh fading

Table 5.20: Parameters for the STBC-CDMA system employing the ACO based ST-MUD algorithm.

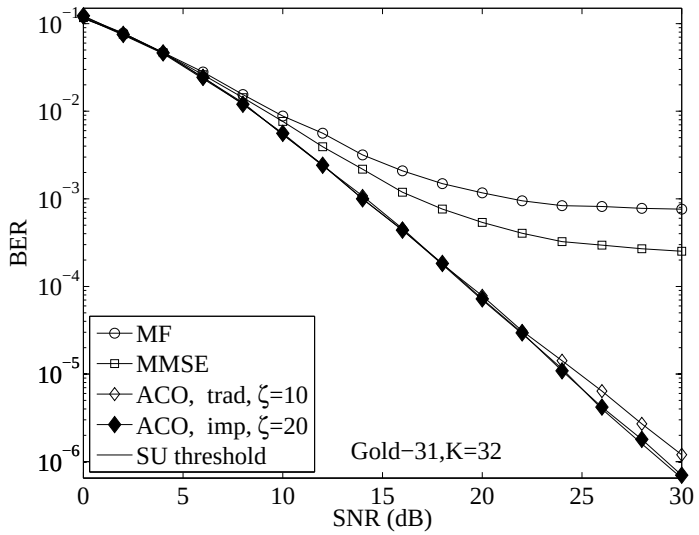

Figure 5.7: Comparison of the BER performances achieved by the STBC assisted two transmit antenna aided DS-CDMA UL employing different detection schemes, where $K = 32$ users are supported by Gold codes having a length of $N_s = 31$ chips. The system's schematic is shown in Fig. 5.1 and all parameters are summarized in Table 5.20.

Fig. 5.6, when the number of users increases from $K = 10$ to $K = 20$, the *traditional* ACO-based ST/MUD algorithm having $\zeta = 10$ ants enables the $K = 10$ and $K = 20$ user system to approach the performance of the SU benchmark. A slight degradation is observed for the *traditional* ACO-based ST/MUD algorithm, when the system is required to support $K = 32$ users.

Fig. 5.7 provides further insights by characterizing the difference between the BER performances achieved by the traditional and the proposed ACO ST-MUD algorithm, which is seen to be substantially lower for the G31K32 system compared to the $m7K7$ system. However, the BER performance achieved by the system employing the proposed ACO algorithm is still better than that of the traditional ACO ST-MUD.

Returning for a moment to the associated complexity characterized in Fig. 5.8 (e), the number of FLOPS to be carried out by the ACO ST-MUD algorithms is significantly lower than that of the MMSE ST-MUD, despite their improved BER performance. Furthermore, in the $K = 32$ user-

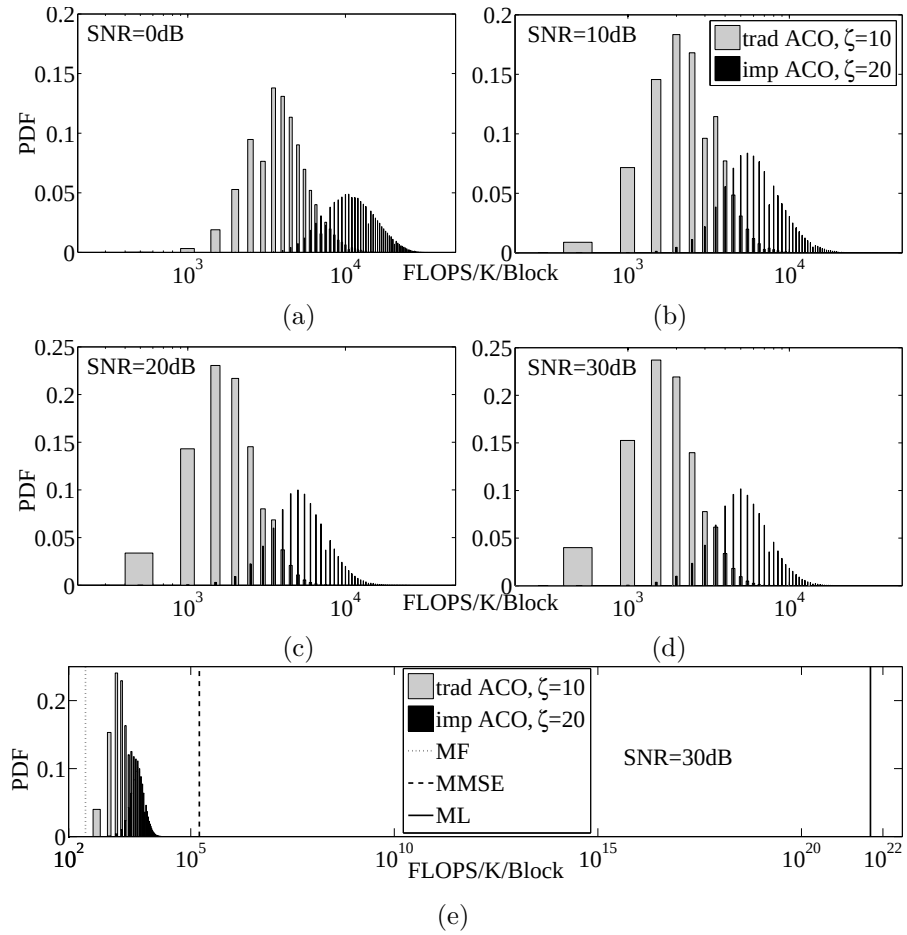

Figure 5.8: PDF of the complexity associated with different detection schemes in the STBC assisted two transmit antenna aided DS-CDMA UL adopting Gold codes having a length of $N_s = 31$ to support $K = 32$ users of different SNR.

scenarios both ACO algorithms impose a factor 10^{18} lower complexity than the ML algorithm, while allowing the G31K32 system to perform similarly to the single-user system. The detailed complexity estimates quantified in terms of the number of FLOPS for each individual processing step carried out by the MF, MMSE, ML as well as the traditional and the improved ACO-based MUD algorithm aided G31K32 systems are listed in Table 5.21.

5.6 Conclusion

In this chapter, we first applied the *traditional* ACO-based ST/MUD algorithm of Chapter 3 in the STBC aided, twin-transmit-antenna assisted DS-CDMA UL.. Then in Section 5.3.2, we proposed an *improved* ACO based ST-MUD algorithm applied in the STBC-assisted two transmit antenna aided DS-CDMA system. The advantages of the improved algorithm over the traditional algorithm were demonstrated for a $K = 7$ user example. The BER performance provided by the improved ACO algorithm was characterized by simulation in the context of MU systems employing different spreading codes. Finally, the PDF of the complexity imposed by a range of detection algorithms, including both the improved and the traditional ACO algorithms was portrayed in order to demonstrate the advantages of the improved ACO aided ST-MUD algorithm.

Operation	MF	MMSE	ML	ACO1①	ACO2②
$\mathbf{y}$③	259.9	259.9	259.9	259.9	247.9
	×1	×1	×1	×1	×1
	259.9	**259.9**	**259.9**	**259.9**	**247.9**
$\mathbf{R}$③	–	24.0	24.0	24.0	–
		×1	×1	×1	
		24.0	**24.0**	**24.0**	
Matrix Inversion③ $(2\cdot2K\times2\cdot2K)$④	–	162148	–	–	–
		×1			
		162148			
Objective Function Evaluation③	–	–	268.1	268.1	121.6
			×$1.8e^{19}$	×8.7⑤	×40.2⑤
			$4.9e^{21}$	**2332.4**⑤	**4886.8**⑤
Others⑥	–	384	–	196.4⑤	2341.9⑤
Total⑥	**259.9**	**162820**	**$4.9e^{21}$**	**2812.7**⑤	**7263.0**⑤

① The traditional ACO-based ST/MUD algorithm having a $(2 \times 2K)$-element route-table and $\zeta = 10$ ants

② The improved ACO-based ST/MUD algorithm having a $(4 \times K)$-element route-table and $\zeta = 100$ ants

③ The first of the three rows describing a specific process in all algorithms quantifies the number of FLOPS per user per STBC-block per unit time the process is operated; the second row represents the number of times the particular process is carried out during the corresponding algorithm; the third row represents the total number of FLOPS impose per user during an STBC-block.

④ The dimension of the complex-valued square matrix is $2K$, however it has to be transformed to a real-value square matrix having a size of $(2 \cdot 2K) \times (2 \cdot 2K)$. The interested readers is referred to Appendix 1.

⑤ It is the mean.

⑥ This row quantifies the total number of FLOPS per user during a single STBC-block.

Table 5.21: FLOPS consumed by each of the principle steps taken by all the algorithms in the STBC-G31K32 system.All the data in this table has been approximated in such a way that only the first digit after the decimal point is remained to save the space.

Chapter 6

ACO-based Soft-Output MUD in the DS-CDMA UL

6.1 Introduction

In this chapter, the channel coded MU system of Chapter 3 is employed. The idea of employing channel coding or Forward Error Correction (FEC) coding in wireless communication systems was proposed by Shannon [204], who predicted that arbitrarily reliable communications are realizeble, provided that sufficient redundant information bits were attached to the information source bits. Both block codes and Convolutional Codes (CCs) can be categorized as systematic and non-systematic codes, depending on whether the output codewords of the encoder retain the entire original information bits as parts of the encoded codeword [205].

As suggested in [205], instead of making a binary decision for each demodulated symbol, it is beneficial for the detector to forward the probability of a binary one and binary zero for a certain bit, to the FEC codeword, which we refer to as the detector Soft-Output (SO). Naturally, the detector's SO provides the channel decoder with substantially more information than the Hard Output (HO) binary decisions. Hence a significantly lower Bit Error Ratio (BER) can be achieved at a given E_b/N_0, as demonstrated for example in [205].

Therefore, in order to supply the channel decoder of each user with soft information so that a reduced BER may be achieved by the MU system, a SO MUD may be invoked to mitigate the MUI and provide the FEC decoder of each user with soft information. However, most of the ACO-based MUD schemes found in the open literature at the time of writing are only capable of providing hard-decision outputs for the channel decoder.

Against this background, *ACO-based SO MUD schemes* are proposed in this chapter. More specifically, two schemes, namely the *MAximum-Approximation (MAA)* and the *MUlti-input Approximation (MUA)* aided SO-ACO algorithms are introduced in detail in this chapter.

We will demonstrate that the DS-CDMA UL system exploiting the soft outputs of the novel MUA SO-ACO based MUDs is capable of outperforming its counterpart based on hard-decision outputs. Our simulation results will also demonstrate that increasing the number of inputs provided for the MUA algorithm has significantly improved the achievable BER performance compared to that of the

MAA SO-ACO algorithm, approaching the single-user performance, at a fraction of the Bayesian detector's complexity.

The rest of this chapter is organized as follows. The above-mentioned soft information, namely the LLR of each bit transmitted by all the users in the DS-CDMA UL will be derived in Section 6.2 along with the Bayesian algorithm of obtaining the LLRs. In Sections 6.3 and 6.4, the MAA and MUA assisted ACO-based SO MUD algorithms will be introduced, including the relevant theoretical background. Following by the discussion of the complexity estimation of both algorithms in Section 6.5, the corresponding performance results will be provided in Section 6.6. Finally, we will conclude our discourse in Section 6.7

6.2 Theoretical Background

The soft information quantifying our confidence in a binary decision concerning a certain detected and demodulated bit is quantified by the corresponding Log-Likelihood Ratio (LLR). As discussed in Section 2.6, the LLR regarding a bit transmitted and received in a single user system within a particular symbol duration, is derived from the logarithm of the ratio of the *a posteriori* probabilities of a binary one and zero, based on the received signal.

In this section, we will derive the LLR of a general MIMO Multi-User (MU) UL scenario, and then apply it to our K-user Single-Input Single-Output (SISO) DS-CDMA sytem in Section 6.2.1. In Section 6.2.2, we will provide more details on the system model characterizing two different SO ACO-based MUD algorithms. Finally, in Sections 6.3 and 6.4, we will stipulate some preliminary assumptions that are essential in order to interpret the algorithms.

6.2.1 LLRs in a Multi-User DS-CDMA System

The derivation of the LLRs encountered in a multi-user UL scenario is provided in this subsection with the aid of the system model shown in Fig. 6.1. In contrast to the single-user system model given

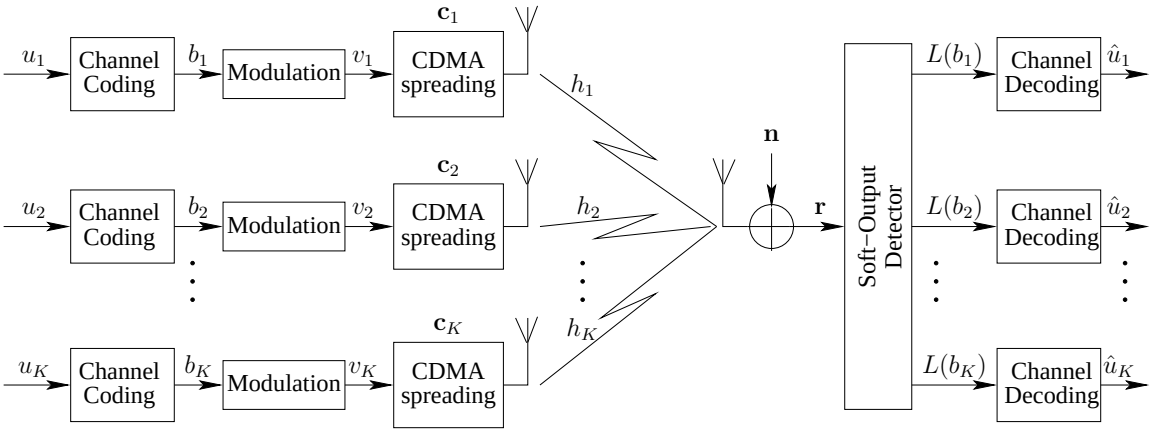

Figure 6.1: Block diagram of a channel coded multi-user system employing time-domain DS-CDMA techniques and soft-output detectors, which estimate the LLRs of the transmitted bits of each user. This is the most basic block diagram. A more sophisticated block diagram will be developed in Chapter 5.

by $r = hv + n$, when K users are supported by the N_s-chip CDMA spreading codes, the system model

of Fig. 6.1 may be characterized with the aid of N_s equations as:

$$\begin{array}{rcccccccccccc} r_1 & = & c_{11} & h_1 v_1 & + & c_{21} & h_2 v_2 & + & \cdots & + & c_{K1} & h_K v_K & + & n_1 \\ r_2 & = & c_{12} & h_1 v_1 & + & c_{22} & h_2 v_2 & + & \cdots & + & c_{K2} & h_K v_K & + & n_2 \\ \vdots & & & \vdots & & & \vdots & & & & & \vdots & & \vdots \\ r_{N_s} & = & c_{1N_s} & h_1 v_1 & + & c_{2N_s} & h_2 v_2 & + & \cdots & + & c_{KN_s} & h_K v_K & + & n_{N_s} \end{array}, \tag{6.1}$$

where r denotes the chip-index. The subscript of c ranges from 1 to K and indicates the user-index, while the second subscript of c ranges from 1 to N_s and specifies the chip-index. Hence c_{kn_s} specifies the n_sth chip of the kth user's N_s-chip CDMA spreading sequence.

Alternatively, Eq. (6.1) may be expressed in matrix-form as:

$$\mathbf{r} = \mathbf{CHv} + \mathbf{n}$$

$$\begin{bmatrix} r_1 \\ r_2 \\ \vdots \\ r_{N_s} \end{bmatrix} = \begin{bmatrix} c_{11} & c_{21} & \cdots & c_{K1} \\ c_{12} & c_{22} & \cdots & c_{K2} \\ \vdots & \vdots & \cdots & \vdots \\ c_{1N_s} & c_{2N_s} & \cdots & c_{KN_s} \end{bmatrix} \begin{bmatrix} h_1 & 0 & \cdots & 0 \\ 0 & h_2 & \cdots & 0 \\ \vdots & \vdots & \ddots & \vdots \\ 0 & 0 & \cdots & h_K \end{bmatrix} \begin{bmatrix} v_1 \\ v_2 \\ \vdots \\ v_K \end{bmatrix} + \begin{bmatrix} n_1 \\ n_2 \\ \vdots \\ n_{N_s} \end{bmatrix}. \tag{6.2}$$

As always, it is more informative to quantify the reliability of each decision to be passed to the next-stage channel decoder in order to carry out iterative channel decoding. The LLR of the received signal r expressed in terms of selecting $+1$ or -1 for v has been used to quantify the reliability and the final form of $L(r)$ in Eq. (2.111).

For the sake of convenience, we consider user 1 as the reference user of our K-user system, whose LLR will be derived below. The derivation of the LLRs of user $k = 1$ may be readily extended to an arbitary user k, for $k = 2, \ldots, K$. Provided that both $v_1 = +1$ and $v_1 = -1$ are transmitted with a probability of 0.5, when r_{n_s} is received, the LLR of r_{n_s} is given by definition as

$$l_1 = L_1(r_{n_s}) = \ln \frac{p(r_{n_s}|v = +1)}{p(r_{n_s}|v = -1)}, \quad n_s = 1, \ldots, N_s. \tag{6.3}$$

In the single-user system described by $r = hv + n$, the *a priori* condional PDF $p(r|v = \pm 1)$ may be accurately modelled by the PDF of the complex-valued Gaussian distributed random variables, as seen in Eq. (2.91) and Eq. (2.92). However, as observed from the system model defined for a multiuser system in Eq. (6.1), $p(r_{n_s}|v = +1)$ cannot be described by a known PDF for the chip-interval $n_s = 1, \ldots, N_s$, unless the transmitted signals $v_2, \cdots, v_K$ are known. In other words, unless all the elements of $\mathbf{v} = [v_1\ v_2\ \cdots\ v_K]^T$ are known, $p(r_{n_s}|\mathbf{v})$ cannot be described by the complex-valued Gaussian PDFs of Eq. (2.91) and Eq. (2.92).

However, as suggested by Eq. (6.3), when $v_1 = +1$ is transmitted, there are 2^{K-1} bit-combinations for the remaining $(K-1)$ users. Hence, in order to get an accurate estimate of $p(r|v = +1)$, we have to take all the 2^{K-1} possible values into consideration. More quantitatively, we have

$$p(r_{n_s}|v_1 = +1) = \sum_{i=1}^{2^{K-1}} p(r_{n_s}|\mathbf{v}_{1+,i}^{(K)}), \quad n_s = 1, \ldots, N_s, \tag{6.4}$$

where $\mathbf{v}_{1+,i}^{(K)}$ denotes the ith vector from the set of all the 2^{K-1} vectors $i = 1, 2, \ldots, 2^{K-1}$, where the first element is always $v_1 = +1$. Similarly, when $v_1 = -1$ is transmitted, we have

$$p(r_{n_s}|v_1 = -1) = \sum_{i=1}^{2^{K-1}} p(r_{n_s}|\mathbf{v}_{1-,i}^{(K)}), \quad n_s = 1, \ldots, N_s. \tag{6.5}$$

Given the probabilities $p(r_{n_s}|v_1 = +1)$ and $p(r_{n_s}|v_1 = +1)$ quantified in Eq. (6.4) and Eq. (6.5), the initial representation of the LLRs defined in Eq. (6.3) may be formulated as:

$$\begin{aligned} l_1 = L_1(r_{n_s}) &= \ln \frac{p(r_{n_s}|v = +1)}{p(r_{n_s}|v = -1)} \\ &= \ln \frac{\sum_{i=1}^{2^{K-1}} p(r_{n_s}|\mathbf{v}_{1+,i}^{(K)})}{\sum_{i=1}^{2^{K-1}} p(r_{n_s}|\mathbf{v}_{1-,i}^{(K)})}, \quad n_s = 1, \ldots, N_s. \end{aligned} \tag{6.6}$$

where the probabilities $p(r_{n_s}|\mathbf{v}^{(K)1\pm,i})$ for $i = 1, 2, \ldots, 2^{K-1}$ are all given by the PDF of the complex-valued Gaussian distributed random variable.

Table. 6.1 provides an example illustrating the value of the vectors $\mathbf{v}_{3\pm,i}^{(5)}$ for $i = 1, 2, \ldots, 32$, when $K = 5$ users are supported by the CDMA system and the reference user's index is $k = 3$.

Let us denote the vector comprising the K users' random binary elements as $\dot{\mathbf{v}}^{(K)}$. When each bit of the K-user signal vector $\dot{\mathbf{v}}^{(K)}$ is represented by an N_s-chip spreading code and hence may be viewed as being repeatedly transmitted for N_s chip durations, with c_{kn_s} having different values for $n_s = 1, \ldots, N_s$, N_sth-order diversity may be achieved, provided that all chips fade independently. Hence, by jointly evaluating the probability $p(r_{n_s}|\dot{\mathbf{v}}^{(K)})$ over the N_s equations quantifying the signal r_{n_s} received over the $n_s = 1, \ldots, N_s$ chip durations, more accurate LLRs can be generated for quantifying the reliability of the final decision between $v = +1$ and $v = -1$. More explicitly, in this case the LLRs are calculated based on the probability $p(\mathbf{r}|\dot{\mathbf{v}}^{(K)})$, rather than on $p(r_{n_s}|\dot{\mathbf{v}}^{(K)})$, regardless of the values taken by $n_s \in [1, N_s]$. Therefore, the LLRs quantified in Eq.(6.6) may be more accurately formulated as

$$l_1 = L_1(\mathbf{r}) = \ln \frac{\sum_{i=1}^{2^{K-1}} p(\mathbf{r}|\mathbf{v}_{1+,i}^{(K)})}{\sum_{i=1}^{2^{K-1}} p(\mathbf{r}|\mathbf{v}_{1-,i}^{(K)})}. \tag{6.7}$$

Hence, if the probabilites $p(\mathbf{r}|\mathbf{v}_{1\pm,i}^{(K)})$ for $i = 1, 2, \ldots, 2K-1$ employed in Eq. (6.7) may be quantified, the final form of the LLR l_1 of user $k = 1$ expressed as a function $L_1(\mathbf{r})$ of the received signal $\mathbf{r}$ during a certain symbol interval may be found, because all the vectors $\mathbf{v}_{k\pm,i}^{(K)}$ for $i = 1, 2, \ldots, 2K-1$ can be simplified to a trial vector $\dot{\mathbf{v}}^{(K)}$ constituted by an arbitrary combination of K binary elements, regardless of the value of k and i, as well as regardless whether $+1$ or -1 was transmitted. Below we will focus our attention on the derivation of $p(\mathbf{r}|\dot{\mathbf{v}}^{(K)})$ for the system model defined by Eq. (6.1).

To generalize the derivation of the probability $p(\mathbf{r}|\dot{\mathbf{v}}^{(K)})$ to a more generic system model constituted by a group of D equations (rather then N_s equations as illustrated in Eq. (6.1)), when D different

$v_3 = +1$							$v_3 = -1$				
		$\mathbb{V}_{3+}^{(5)}$							$\mathbb{V}_{3-}^{(5)}$		
0	0	0	0	0	$\mathbf{v}_{3+,1}^{(5)}$	$\mathbf{v}_{3-,1}^{(5)}$	0	0	1	0	0
0	0	0	0	1	$\mathbf{v}_{3+,2}^{(5)}$	$\mathbf{v}_{3-,2}^{(5)}$	0	0	1	0	1
0	0	0	1	0	$\mathbf{v}_{3+,3}^{(5)}$	$\mathbf{v}_{3-,3}^{(5)}$	0	0	1	1	0
0	0	0	1	1	$\mathbf{v}_{3+,4}^{(5)}$	$\mathbf{v}_{3-,4}^{(5)}$	0	0	1	1	1
0	1	0	0	0	$\mathbf{v}_{3+,5}^{(5)}$	$\mathbf{v}_{3-,5}^{(5)}$	0	1	1	0	0
0	1	0	0	1	$\mathbf{v}_{3+,6}^{(5)}$	$\mathbf{v}_{3-,6}^{(5)}$	0	1	1	0	1
0	1	0	1	0	$\mathbf{v}_{3+,7}^{(5)}$	$\mathbf{v}_{3-,7}^{(5)}$	0	1	1	1	0
0	1	0	1	1	$\mathbf{v}_{3+,8}^{(5)}$	$\mathbf{v}_{3-,8}^{(5)}$	0	1	1	1	1
1	0	0	0	0	$\mathbf{v}_{3+,9}^{(5)}$	$\mathbf{v}_{3-,9}^{(5)}$	1	0	1	0	0
1	0	0	0	1	$\mathbf{v}_{3+,10}^{(5)}$	$\mathbf{v}_{3-,10}^{(5)}$	1	0	1	0	1
1	0	0	1	0	$\mathbf{v}_{3+,11}^{(5)}$	$\mathbf{v}_{3-,11}^{(5)}$	1	0	1	1	0
1	0	0	1	1	$\mathbf{v}_{3+,12}^{(5)}$	$\mathbf{v}_{3-,12}^{(5)}$	1	0	1	1	1
1	1	0	0	0	$\mathbf{v}_{3+,13}^{(5)}$	$\mathbf{v}_{3-,13}^{(5)}$	1	1	1	0	0
1	1	0	0	1	$\mathbf{v}_{3+,14}^{(5)}$	$\mathbf{v}_{3-,14}^{(5)}$	0	1	1	0	1
1	1	0	1	0	$\mathbf{v}_{3+,15}^{(5)}$	$\mathbf{v}_{3-,15}^{(5)}$	1	1	1	1	0
1	1	0	1	1	$\mathbf{v}_{3+,16}^{(5)}$	$\mathbf{v}_{3-,16}^{(5)}$	1	1	1	1	1

Table 6.1: An example when $K = 5$ users are supported and each user transmits a BPSK symbol within a symbol interval. The full set $\mathbb{V}^{(5)}$ containing all the 32 legitimate transmitted vectors is divided into two subsets, namely $\mathbb{V}_{3+}^{(5)}$, $\mathbb{V}_{3-}^{(5)}$ according to the polarity of the symbol transmitted by the 3rd user.

signals are received that constitute a D-element vector $\mathbf{r}$, we will use D instead of N_s in the following derivation. The final form for the LLR l_1 of user $k = 1$ in the current system model of Eq. (6.1) may be readily obtained by assigning $D = N_\mathrm{s}$ in the final formula.

As seen in Eq. (6.2), the D-element noise vector $\mathbf{n}$ is a D-dimensional complex-valued Gaussian distributed random variable with the vector of component averages given by a D-element vector $\mathbf{M}_{\mathbf{n}}$ and the variance given by a $(D \times D)$-element matrix $\mathbf{\Sigma}_{\mathbf{n}}$, which are defined as

$$\begin{aligned} \mathbf{M}_{\mathbf{n}} &= \mathbf{0}^{(D)}; \\ \mathbf{\Sigma}_{\mathbf{n}} &= E\left[(\mathbf{n} - \mathbf{M}_{\mathbf{n}})(\mathbf{n} - \mathbf{M}_{\mathbf{n}})^H\right] \\ &= E(\mathbf{n}\mathbf{n}^H) = \sigma_{\mathbf{n}}^2 \mathbf{I}^{(D)}, \end{aligned} \tag{6.8}$$

where $\mathbf{0}^{(D)}$ and $\mathbf{I}^{(D)}$ are the $(D \times 1)$-element zero vector and the $(D \times D)$-element identity matrix, respectively.

As seen in Eq. (6.2), we have

$$\mathbf{r} = \mathbf{C}\mathbf{H}\mathbf{v} + \mathbf{n}, \tag{6.9}$$

where ($\mathbf{CHv}$) is a ($D \times 1$)-element complex-valued vector having known elements, given the value of $\mathbf{C}$, $\mathbf{H}$ and $\mathbf{v}$. The family of D-element complex-valued Gaussian distributions is closed under linear transformations [160] implying that a linear transformation of a Gaussian distributed variable is also Gaussian distributed. Hence, provided that n is normally distributed with a mean of $\mathbf{M}_{\mathfrak{n}}$ and variance of $\mathbf{\Sigma}_{\mathfrak{n}}$, its linearly transformed version of $\mathbf{r} = \mathbf{n} + \mathbf{CHv}$ is also normally distributed, which is formulated as:

$$\mathbf{n} + \mathbf{CHv} \sim \mathcal{N}_D^{\mathrm{c}}(\mathbf{M}_{\mathfrak{n}} + \mathbf{CHv}, \mathbf{\Sigma}_{\mathfrak{n}}). \tag{6.10}$$

Hence, we have

$$\mathbf{r}^{(D)} \sim \mathcal{N}_D^{\mathrm{c}}(\mathbf{M}_{\mathfrak{n}} + \mathbf{CHv}, \mathbf{\Sigma}_{\mathfrak{n}}). \tag{6.11}$$

The PDF of a D-element complex-valued Gaussian distributed random variable $\mathfrak{x} \sim \mathcal{N}_D^{\mathrm{c}}(\mathbf{M}_{\mathfrak{x}}, \mathbf{\Sigma}_{\mathfrak{x}})$ is given by

$$p(\mathbf{x}) = \frac{1}{\pi^D} \frac{\exp\left(-\frac{1}{2}(\mathbf{x} - \mathbf{M}_{\mathfrak{x}})^H 2\mathbf{\Sigma}_{\mathfrak{x}}^{-1}(\mathbf{x} - \mathbf{M}_{\mathfrak{x}})\right)}{\det(\mathbf{\Sigma}_{\mathfrak{x}})}, \tag{6.12}$$

and upon substituting the vector of averages and the matrix of variance values by the values in Eq. (6.11), the conditional PDF of the D-element complex-valued Gaussian distributed random variable $\mathbf{r}$ under the condition that $\dot{\mathbf{v}}^{(K)}$ was transmitted can be further expressed as:

$$\begin{aligned}
p(\mathbf{r}|\dot{\mathbf{v}}^{(K)}) &= \frac{1}{\pi^D \det(\sigma_{\mathfrak{n}}^2\mathbf{I})} \exp\left(-\frac{1}{2}(\mathbf{r} - \mathbf{CH}\dot{\mathbf{v}}^{(K)})^H 2(\sigma_{\mathfrak{n}}^2\mathbf{I})^{-1}(\mathbf{r} - \mathbf{CH}\dot{\mathbf{v}}^{(K)})\right) \\
&= \frac{1}{\pi^D(\sigma_{\mathfrak{n}}^2)^D \det(\mathbf{I})} \exp\left(-\frac{1}{\cancel{2}}(\mathbf{r} - \mathbf{CH}\dot{\mathbf{v}}^{(K)})^H \frac{\cancel{2}}{\sigma_{\mathfrak{n}}^2}\mathbf{I}^{-1}(\mathbf{r} - \mathbf{CH}\dot{\mathbf{v}}^{(K)})\right) \\
&= \frac{1}{(\pi\sigma_{\mathfrak{n}}^2)^D \cdot 1} \exp\left(-\frac{1}{\sigma_{\mathfrak{n}}^2}(\mathbf{r} - \mathbf{CH}\dot{\mathbf{v}}^{(K)})^H\mathbf{I}(\mathbf{r} - \mathbf{CH}\dot{\mathbf{v}}^{(K)})\right) \\
&= \frac{1}{(\pi\sigma_{\mathfrak{n}}^2)^D} \exp\left(-\frac{1}{\sigma_{\mathfrak{n}}^2}(\mathbf{r} - \mathbf{CH}\dot{\mathbf{v}}^{(K)})^H(\mathbf{r} - \mathbf{CH}\dot{\mathbf{v}}^{(K)})\right) \\
&= \frac{1}{(\pi\sigma_{\mathfrak{n}}^2)^D} \exp\left(-\frac{1}{\sigma_{\mathfrak{n}}^2}\|\mathbf{r} - \mathbf{CH}\dot{\mathbf{v}}^{(K)}\|^2\right).
\end{aligned} \tag{6.13}$$

The above equation quantifies the conditional probability of receiving $\mathbf{r}$, when $\dot{\mathbf{v}}^{(K)}$ was transmitted, which can be readily extended to $p(\mathbf{r}|\mathbf{v}_{1\pm,i}^{(K)})$, with $i = 1, 2, \ldots, 2^{K-1}$. Hence, the LLR l_1 of user $k = 1$, which is based on the D-element received signal vector $\mathbf{r}$, can be extended from Eq.(6.7) as follows

$$\begin{aligned}
l_1 = L_1(\mathbf{r}) &= \ln \frac{\sum_{i=1}^{2^{K-1}} p(\mathbf{r}|\mathbf{v}_{1+,i}^{(K)})}{\sum_{i=1}^{2^{K-1}} p(\mathbf{r}|\mathbf{v}_{1-,i}^{(K)})} \\
&= \ln \frac{\sum_{i=1}^{2^{K-1}} \frac{1}{(\pi\sigma_{\mathfrak{n}}^2)^D} \exp\left(-\frac{1}{\sigma_{\mathfrak{n}}^2}\|\mathbf{r} - \mathbf{CHv}_{1+,i}^{(K)}\|^2\right)}{\sum_{i=1}^{2^{K-1}} \frac{1}{(\pi\sigma_{\mathfrak{n}}^2)^D} \exp\left(-\frac{1}{\sigma_{\mathfrak{n}}^2}\|\mathbf{r} - \mathbf{CHv}_{1-,i}^{(K)}\|^2\right)}
\end{aligned}$$

$$= \ln \frac{\sum_{i=1}^{2^{K-1}} \exp\left(-\frac{1}{\sigma_{\mathfrak{n}}^2}\|\mathbf{r} - \mathbf{CHv}_{1+,i}^{(K)}\|^2\right)}{\sum_{i=1}^{2^{K-1}} \exp\left(-\frac{1}{\sigma_{\mathfrak{n}}^2}\|\mathbf{r} - \mathbf{CHv}_{1-,i}^{(K)}\|^2\right)}. \tag{6.14}$$

Naturally, this definition may be readily extended to an arbitary user index k, yielding the LLR of the symbol transmitted by user k as

$$l_k = L_k(\mathbf{r}) = \ln \frac{\sum_{i=1}^{2^{K-1}} \exp\left(-\frac{1}{\sigma_{\mathfrak{n}}^2}\|\mathbf{r} - \mathbf{CHv}_{k+,i}^{(K)}\|^2\right)}{\sum_{i=1}^{2^{K-1}} \exp\left(-\frac{1}{\sigma_{\mathfrak{n}}^2}\|\mathbf{r} - \mathbf{CHv}_{k-,i}^{(K)}\|^2\right)}. \tag{6.15}$$

Eq. (6.15) defines the LLR of the symbol transmitted by user k, when $M = 1$ bit is transmitted over $D = N_{\mathrm{s}}$ chip intervals. The matrices $\mathbf{r}$, $\mathbf{C}$, $\mathbf{H}$ and $\mathbf{v}$ will have their respective definitions, depending on the specific system scenario considered. This formulation can be further expanded, when an $\mathcal{M}$-ary modulation scheme is employed to transmit N_{t} symbols per user over $D = aN_{\mathrm{s}}$ chip intervals, for $a = 1, 2, \ldots, \infty$.

We will first discuss the expansion of Eq. (6.15), when an $\mathcal{M}$-ary modulation scheme is employed for transmitting N_{t} symbols over $D = N_{\mathrm{s}}$ chip intervals. Under this assumption, $(M \times N_{\mathrm{t}} \times K)$ bits are transmitted and there are $2^{MN_{\mathrm{t}}K}$ legitimate vectors that may have been transmitted during the D chip durations considered. Therefore, the definition of the LLR of the mth bit mapped to the $\imath$th symbol transmitted by the kth user can be extended from Eq. (6.15) as

$$l_{k\imath m} = L_{k\imath m}(\mathbf{r}) = \ln \frac{\sum_{i=1}^{2^{MN_{\mathrm{t}}K-1}} \exp\left(-\frac{1}{\sigma_{\mathfrak{n}}^2}\|\mathbf{r} - \mathbf{CHv}_{k\imath m+,i}^{(N_{\mathrm{t}}K)}\|^2\right)}{\sum_{i=1}^{2^{MN_{\mathrm{t}}K-1}} \exp\left(-\frac{1}{\sigma_{\mathfrak{n}}^2}\|\mathbf{r} - \mathbf{CHv}_{k\imath m-,i}^{(N_{\mathrm{t}}K)}\|^2\right)}. \tag{6.16}$$

As seen from Eq. (6.16), the final form of the LLRs is independent of the value D, although naturally, the dimension or the size of the $(D \times 1)$-element vector $\mathbf{r}$, of the $(D \times N_{\mathrm{t}}K)$-element matrix $\mathbf{C}$, of the $(N_{\mathrm{t}}K \times N_{\mathrm{t}}K)$-element matrix $\mathbf{H}$ and of the $(N_{\mathrm{t}}K \times 1)$-element $\mathcal{M}$-ary modulated vector $\mathbf{v}$ will be commensurately expanded, as D is increased from N_{s} to aN_{s}.

Let us consider the DS-CDMA uplink associated with $M = 1$, $N_{\mathrm{t}} = 1$ and $D = N_{\mathrm{s}}$. In Chapter 5 a BPSK modulated $\boldsymbol{\mathcal{G}}_2$ space-time coded system is investigated, where we have $M = 1$, $N_{\mathrm{t}} = 2$ and $D = 2N_{\mathrm{s}}$.

It may be intuitively observed from Tab. 6.1 that for $K = 5$, $N_{\mathrm{t}} = 1$ and $M = 1$, there are always $2^{MN_{\mathrm{t}}K-1}$ vectors, where the mth bit of the $\imath$th symbol transmitted by the kth user after demodulation becomes '0'. Naturally, there is another set of $2^{MN_{\mathrm{t}}K-1}$ vectors, where the mth bit of the $\imath$th symbol transmitted by the kth user becomes demodulated as '1'. Therefore, the accurate LLR of a single bit requires the calculation of an exponential function of the noise-power-normalized Euclidean distance according to

$$\mathfrak{E}(\dot{\mathbf{v}}^{(N_{\mathrm{t}}K)}) \triangleq \exp\left[-\frac{1}{\sigma_{\mathfrak{n}}^2}\|\mathbf{r} - \mathbf{CH}\dot{\mathbf{v}}^{(N_{\mathrm{t}}K)}\|^2\right], \tag{6.17}$$

which is evaluated 2^{MN_tK-1} times for $\dot{\mathbf{v}}^{(N_tK)} = \mathbf{v}^{(K)}_{k\imath m+,i}$ when we have $i = 1, 2, \ldots, 2^{MN_tK-1}$ in the numerator and another 2^{MN_tK-1} times for $\dot{\mathbf{v}}^{(N_tK)} = \mathbf{v}^{(K)}_{k\imath m-,i}$ in the denominator. In other words, to precisely evaluate the LLRs associated with a single bit, the exponential of the noise-power-normalized Euclidean distance of all the 2^{MN_tK} legitimate vectors that may have been transmitted during the D chip intervals considered must be evaluated.

This complexity may become excessive, since it inreases exponentially with MN_tK, namely with the total number of coded bits transmitted during each detection period constituted by the $a \cdot N_s$ chip durations.

In this chapter we aim for designing reduced-complexity near-ML ant-colony optimization (ACO) based soft-output (SO) multi-user detection (MUD) algorithms, which evaluate Eq. (6.17) only a limited number of times and yet capture the ML-solution with a high probability. The ACO based SO-MUD algorithm will enable the detector to locate the dominant vectors, which contribute to the sum in both the numerator and denominator of Eq. (6.16) most substantially. Hence, upon omitting the less important vectors but retaining the most important ones, the LLR calculated by the ACO based SO-MUD algorithm approaches the accurate value. Despite its near-ML performance, the complexity imposed by the ACO based SO-MUD algorithm may be a factor of $10^{10}\sim10^{20}$ lower than that of the optimal exhaustive search based algorithm.

Again, the Euclidean norm expression seen in both the numerator and denominator of Eq. (6.15) associated with a certain K-symbol vector $\dot{\mathbf{v}}$ is the Euclidean distance between the noise-contaminated and interference-infested actual received signal vector $\mathbf{r}$ and the legitimate noiseless, but channel-rotated, spread received signal vector $\mathbf{CH}\dot{\mathbf{v}}$, provided that $\dot{\mathbf{v}}$ was transmitted, as defined by Eq. (2.76) and repeated here for convenience:

$$\mathfrak{D}(\dot{\mathbf{v}}) \triangleq \|\mathbf{r} - \mathbf{CH}\dot{\mathbf{v}}\|^2. \tag{6.18}$$

6.2.2 Overview of the Soft-Output ACO MUD

Fig. 6.2 shows a more comprehensive channel coded DS-CDMA UL system model derived from Fig. 6.1, where each of the K MS transmitters and the BS receiver employ a single transmit and receive antenna. The difference between Fig. 6.2 and Fig. 6.1 is the inclusion of the bit interleaver Π of Fig. 6.2. In communication systems, the interleaver is employed to enhance the attainable performance of the Forward Error Correcting (FEC) codes by dispersing the burst errors, hence resulting in independent errors. If the number of erroneous bits within a code word exceeds the error-correcting capability of the FEC code, the entire codeword tends to contain more errors than in the absence of FEC. Interleaving of the original data stream will address this problem by shuffling the bits of the input bit stream, hence when the interleaved bit are contaminated by the channel, the erroneous bits are typically more evenly distributed than without interleaving. This aids the FEC decoder.

As observed from Fig. 6.2, the entire system can be divided into two parts, the inner codec and outer codec. The inner codec is shown within the dashed frame of Fig. 6.2. The inner codec of Fig. 6.2 operates on a symbol-by-symbol basis, in conjunction with a different random CIR matrix $\mathbf{H}$ and AWGN vector $\mathbf{n}$ during each symbol. Our $K = 5$-user example, which was detailed in Section 3.2.2 is also revisited in this chapter. Explicitly, a specific symbol duration along with its CIR matrix, transmit symbols and received signal are considered in Table 3.1 in the context of the inner codec. By

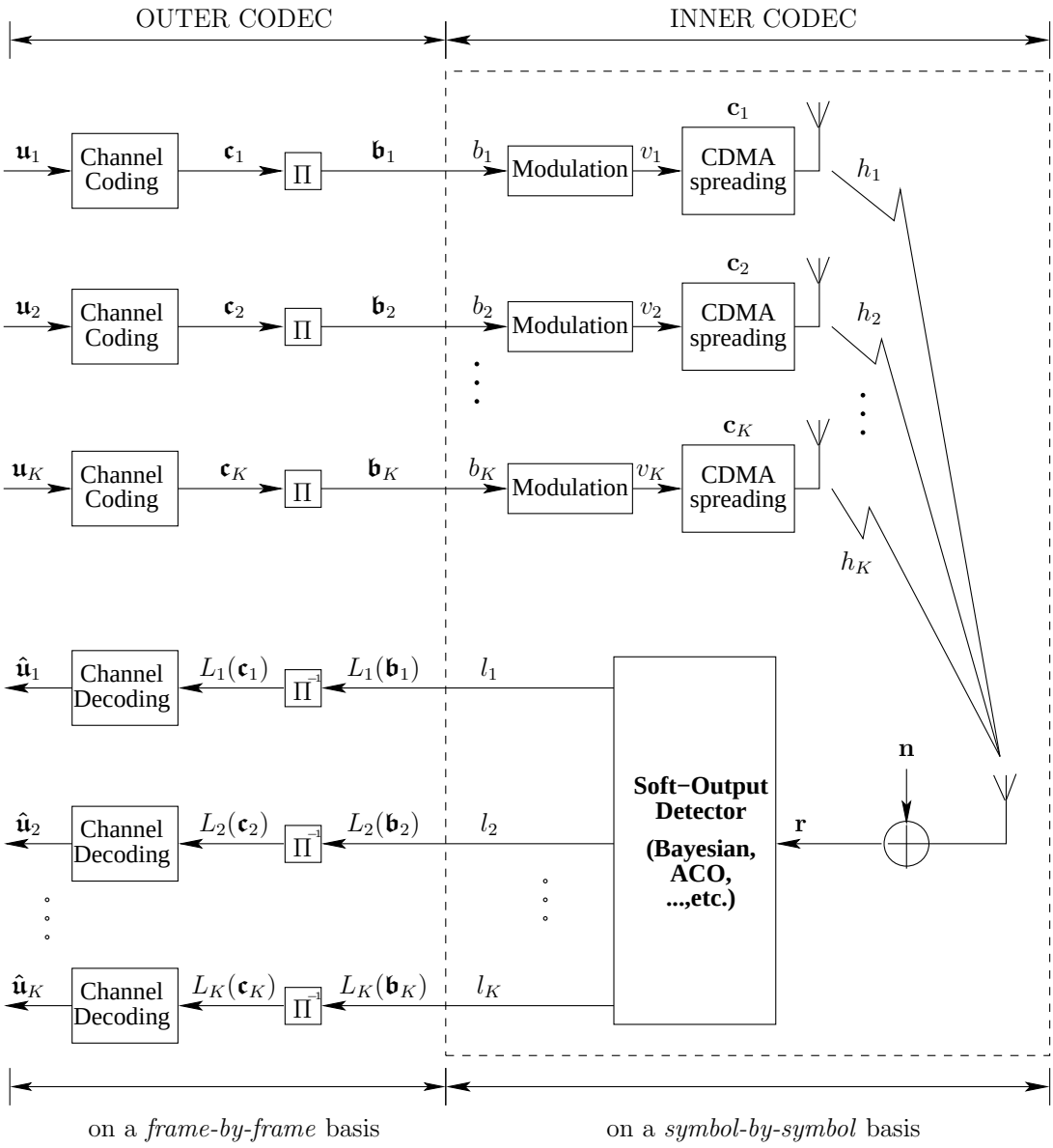

Figure 6.2: Expansion of the system model of Fig. 6.1, when an interleaver and deinterleaver is employed in the transmitter and receiver of each user at both the MS and BS side. The components within the dashed frame are related to the design of the MAA and MUA ACO-based SO MUD algorithms.

contrast, the outer codec of Fig. 6.2 operates on a frame-by-frame basis. Each frame is constituted of N_{u} uncoded bits, or N_{c} coded bits or N_{c} real-valued LLRs.

More specifically, the kth user's N_{u}-bit data sequence $\mathbf{u}_k = \{u_k[i]\}$; for $i = 1, \ldots, N_{\mathrm{u}}$ is firstly channel encoded using a Convolutional Code (CC) at a rate of $R_{\mathrm{c}} = N_{\mathrm{u}}/N_{\mathrm{c}}$, yielding the coded sequence $\mathbf{c}_k = \{c_k[i]\}$ for $i = 1, \ldots, N_{\mathrm{c}}\}$. After the random bit interleaver Π of Fig. 6.2 we arrive at the interleaved bit stream $\mathbf{b}_k$, which is Binary-Phase-Shift-Keying (BPSK) modulated, yielding the BPSK modulated symbol stream $\mathbf{v}_k$. Then each symbol v_k of the symbol stream $\mathbf{v}_k$ is spread by employing a user-specific N_{s}-chip DS spreading sequence waveform $\mathbf{c}_k$. Then, the N_{s}-element vector $\mathbf{c}_k v_k$ is transmitted from a single transmit antenna. The chip-signal $c_{n_{\mathrm{s}}} v_k$ propagates from the kth MS's UL transmit antenna to the BS's receive antenna over a single-path flat Rayleigh fading channel h_k, which is assumed to be constant over an N_{s}-chip symbol duration. During the n_{s}th chip interval, where we have $n_{\mathrm{s}} = 1, \ldots, N_{\mathrm{s}}$, the received signal $r_{n_{\mathrm{s}}}$ is constituted by the superposition of the signals

transmitted from the K MSs, which is also contaminated by the Additive White Gaussian Noise (AWGN). Thus, during a symbol interval, the $N_{\rm s}$ received chip-signals $r_{n_{\rm s}}$, $n_{\rm s} = 1, 2, \ldots, N_{\rm s}$ can still be accurately described by the $N_{\rm s}$ equations constituting Eq. (6.1). The base-band equivalent $N_{\rm s}$-chip received signal vector is still accurately represented by Eq. (6.2), which is repeated here as

$$\mathbf{r} = \mathbf{CHv} + \mathbf{n}. \tag{6.19}$$

In this system scenario, the accurate LLR l_k of user k is given by Eq. (6.15), which is the equation used by the Bayeisan detector to evaluate the LLR of a certain symbol transmitted by user k, formulated as:

$$l_k^{\rm BAY} = \ln \frac{\sum\limits_{\mathbf{v}_{k+,i} \in \mathbb{V}_{k+}^{(K)}} \exp\left\{ \frac{-1}{\sigma_{\rm n}^2} \|\mathbf{r} - \mathbf{CHv}_{k+,i}\|^2 \right\}}{\sum\limits_{\mathbf{v}_{k-,i} \in \mathbb{V}_{k-}^{(K)}} \exp\left\{ \frac{-1}{\sigma_{\rm n}^2} \|\mathbf{r} - \mathbf{CHv}_{k-,i}\|^2 \right\}}, \quad i = 1, \ldots, 2^{K-1}. \tag{6.20}$$

Since the ACO-based SO MUD algorithm aims for approximating the LLR l_k given by Eq. (6.15) at a significantly reduced complexity, only a limited number of K-bit vectors should be considered during the calculation of l_k in the numerator and denominator, yielding:

$$l_k^{\rm ACO} = \ln \frac{\sum\limits_{\tilde{\mathbf{x}}_{k+,i} \in \tilde{\mathbb{X}}_{k+}} \exp\left\{ \frac{-1}{\sigma_{\rm n}^2} \|\mathbf{r} - \mathbf{CH}\tilde{\mathbf{x}}_{k+,i}\|^2 \right\}}{\sum\limits_{\tilde{\mathbf{x}}_{k-,i} \in \tilde{\mathbb{X}}_{k-}} \exp\left\{ \frac{-1}{\sigma_{\rm n}^2} \|\mathbf{r} - \mathbf{CH}\tilde{\mathbf{x}}_{k-,i}\|^2 \right\}}, \quad i = 1, \ldots, \tilde{x}_k, \quad \tilde{x}_k \ll 2^{K-1}, \tag{6.21}$$

where $\tilde{\mathbb{X}}_{k\pm}$ represents the final search-pool of the ACO-based SO MUD algorithm, which hosts all the K-bit vectors used to calculate the LLR l_k. More specifically, the numerator of Eq. (6.21) is the sum of the exponential functions of the Euclidean distances of Eq. (6.17) associated with all the K-bit vectors $\tilde{\mathbf{x}}_{k+,i}$ included in the set $\tilde{\mathbb{X}}_{k+}$. Similarly, the denominator of Eq. (6.21) is the sum of the exponential functions of the Euclidean distances of Eq. (6.17) associated with all the K-bit vectors $\tilde{\mathbf{x}}_{k-,i}$ constituting the set $\tilde{\mathbb{X}}_{k-}$. The number of elements in the search-pools $\tilde{\mathbb{X}}_{k+}$ and $\tilde{\mathbb{X}}_{k-}$ is denoted by $\tilde{x}_k$.

We may refer to the search-pool obtained by the HO ACO-MUD relying on the flow-chart depicted in Fig. 3.9, as $\mathbb{X}^{(K)}$. $\mathbb{X}^{(K)}$, which may host all the unique K-symbol vectors generated by the search process, corresponding to all the unique K-bit vectors captured by the search-pool $\mathbf{X}^{(n)}$ of the nth ACO based search iteration for $n = 1, 2, \ldots, \Xi$. The maximum number of search iterations is Ξ. During each iteration, each of the ζ artificial ants will generate a K-bit trial-vector. The final search-pool $\mathbb{X}^{(K)}$ generated by the Ξ-iteration search process contains x different K-bit vectors, where we have $x \leqslant x_{\max} = \Xi \times \zeta$. This implies that the final search-pool $\mathbb{X}^{(K)}$ hosts only a small fraction of the entire set of $\mathbb{V}^{(K)}$ containing all the 2^K legitimate K-bit combinations, which results in a significantly reduced complexity compared to the exhaustive search process carried out by the ML detectors. For more details on the ACO-based HO MUD, the interested readers are referred to [129–131] or Chapter 3.

In order to generate the two final search-pools $\tilde{\mathbb{X}}_{k\pm}$, we may immediately partition the original search-pool $\mathbb{X}$ into the two subsets of $\mathbb{X}_{k+}$ and $\mathbb{X}_{k-}$ based on the polarity of the kth symbol of the K-bit vectors in $\mathbb{X}$. We denote the number of combinations in the subset $\mathbb{X}_{k\pm}$ as $x_{k\pm}$. However, we may find that we have $x_{k+} \neq x_{k-}$ most of the time and that sometimes we may even have x_{k+} or $x_{k-} = 0$, which results in either the numerator or the denominator of Eq. (6.21) becoming zero. This results in the corresponding LLR becoming $\pm\infty$, which in turn results in a potential error propagation during the channel decoding procedure.

To avoid this situation, we will have to modify the search process in order to ensure that the sets $\mathbb{X}_{k\pm}$ are not empty. Depending on the number of K-bit vectors that are finally incorporated into the final search-pool $\mathbb{X}_{k\pm}$, we propose two different ACO-based SO MUD algorithms, namely the MAximum Approximation (MAA) algortihm and the Multi-Input Approximation (MUA) algorithm, which are detailed in Sections 6.3 and 6.4, respectively.

6.3 Maximum Approximation SO ACO-MUD

The aim of the MAA SO ACO-based MUD algorithm employed in a K-user Single-Input Single Output (SISO) system is to search for the two most dominant K-symbol vectors having the kth symbol of '+1' and '−1' respectively, in order to calculate the LLR l_k of the symbol transmitted by the kth user.

6.3.1 Theoretical Background

The LLR l_k of the symbol transmitted by the kth user in the K-user DS-CDMA UL obtained by the Bayesian detector is repeated here from Eq. (6.20) as:

$$l_k^{\mathrm{BAY}} = \ln \frac{\sum\limits_{\mathbf{v}_{k+,i} \in \mathbb{V}_{k+}^{(K)}} \exp\left\{\frac{-1}{\sigma_{\mathrm{n}}^2}\|\mathbf{r} - \mathbf{CHv}_{k+,i}\|^2\right\}}{\sum\limits_{\mathbf{v}_{k-,i} \in \mathbb{V}_{k-}^{(K)}} \exp\left\{\frac{-1}{\sigma_{\mathrm{n}}^2}\|\mathbf{r} - \mathbf{CHv}_{k-,i}\|^2\right\}}, \quad i = 1, \ldots, 2^{K-1}. \tag{6.22}$$

Again, recall from Eq. (6.21) that the LLR l_k^{ACO} of the kth user obtained by the ACO based SO MUD algorithm may be formulated as:

$$l_k^{\mathrm{ACO}} = \ln \frac{\sum\limits_{\tilde{\mathbf{x}}_{k+,i} \in \tilde{\mathbb{X}}_{k+}} \exp\left\{\frac{-1}{\sigma_{\mathrm{n}}^2}\|\mathbf{r} - \mathbf{CH}\tilde{\mathbf{x}}_{k+,i}\|^2\right\}}{\sum\limits_{\tilde{\mathbf{x}}_{k-,i} \in \tilde{\mathbb{X}}_{k-}} \exp\left\{\frac{-1}{\sigma_{\mathrm{n}}^2}\|\mathbf{r} - \mathbf{CH}\tilde{\mathbf{x}}_{k-,i}\|^2\right\}}, \quad i = 1, \ldots, \tilde{x}_k, \;\; \tilde{x}_k \ll 2^{K-1}, \tag{6.23}$$

as long as the exponential Euclidean distances of $\tilde{\mathbf{x}}_{k\pm,i}$ are the $\tilde{x}_k$ most dominant terms in the numerator and denominator of Eq. (6.22).

To avoid having an exponentially increasing computational complexity, the sums in the numerator and denominator of Eq. (6.23) are replaced by their most dominant term, i.e. by the highest term, as

suggested in [17], yielding:

$$l_k^{\text{MAA}} = \ln \frac{\exp\left\{\frac{-1}{\sigma_n^2}\|\mathbf{r} - \mathbf{CH}\hat{\mathbf{x}}_{k+}\|^2\right\}}{\exp\left\{\frac{-1}{\sigma_n^2}\|\mathbf{r} - \mathbf{CH}\hat{\mathbf{x}}_{k-}\|^2\right\}}, \\ = -\frac{1}{\sigma_{\mathfrak{n}}^2}\left(\|\mathbf{r} - \mathbf{CH}\hat{\mathbf{x}}_{k+}\|^2 - \|\mathbf{r} - \mathbf{CH}\hat{\mathbf{x}}_{k-}\|^2\right), \tag{6.24}$$

where $\hat{\mathbf{x}}_{k\pm}$ represents the vector having the highest likelihood value in the set $\mathbb{X}_{k\pm}$. For simplicity, the above equation may also be expressed as:

$$l_k^{\text{MAA}} = -\frac{1}{\sigma_{\mathfrak{n}}^2}\left[\mathfrak{D}\left(\hat{\mathbf{x}}_{k+}\right) - \mathfrak{D}\left(\hat{\mathbf{x}}_{k-}\right)\right], \tag{6.25}$$

where $\mathfrak{D}\left(\hat{\mathbf{x}}_{k\pm}\right) = \|\mathbf{r} - \mathbf{CH}\hat{\mathbf{x}}_{k\pm}\|^2$ represents the Euclidean distance between the actual received signal vector $\mathbf{r}$ within a certain symbol duration and the legitimate noiseless, channel-rotated received signal vector corresponding to a specific transmitted signal vector $\hat{\mathbf{x}}_{k\pm}$.

6.3.2 Flow Chart of the MAA Algorithm

The flow-chart of the MAA algorithm is depicted in Fig. 6.3. We will examplify each step of the algorithm shown in Fig. 6.3 with the aid of the $K = 5$-user example in conjunction with the parameters given in Table 3.1. Additionally, the LLFs of all the $2^5 = 32$ legitimate $K = 5$-bit vectors generated by the five users are listed in Table 6.2, where the vectors are ordered according to their LLF values.

1. Step 1 - Calculate the intrinsic affinity $\boldsymbol{\eta}$

This step incorporates Step 1 of 'Calculate Symbol LLF' and Step 2 of 'Calculate Intrinsic Affinity' of the HO ACO-based MUD algorithm shown in Fig. 3.9. It calculates the $(2 \times K)$-element intrinsic affinity matrix $\boldsymbol{\eta}$, namely the intrinsic affinity associated with each cell in the route table. The formula of calculating the intrinsic affinity $\boldsymbol{\eta}$ from the real parts of the MF output $\Re\{\mathbf{y}\}$ as well as the CIR matrix $\mathbf{H}$ are given in Eqs. (3.9), (3.11), (3.12), (3.13) and (3.14).

2. Step 2 - HO ACO search process

This step is equivalent to iteratively executing 'Step 3' to 'Step 7' of the flow-chart in Fig. 3.9. Explicitly, the 'ACO search process' block of Fig. 6.3 encompasses all the functional blocks of the HO ACO-based MUD algorithm required to find the ML solution, as introduced in Section 3.3.

As usual, the above-mentioned HO ACO-based search process will populate the search-pool $\mathbb{X}^{(K)}$ containing all the K-symbol vectors generated during the entire search process carried out by Step 2 of the flow-chart in Fig. 6.3. All the K-bit vectors included in the search-pool $\mathbb{X}^{(5)}$ are listed in Table 6.3, which are further detailed in Tables 6.4∼6.7.

3. Step 3 - Binary decision whether to activate an extra ACO search

Based on all the K-bit vectors in the resultant search-pool $\mathbb{X}$ of the HO ACO search process carried out in Step 2, the evaluation of the LLRs associated with each of the K users will commence. The K LLRs are then forwarded to the channel decoding stage associated with the K symbols transmitted within the same symbol duration and evaluated during K loops. Specifically, l_k associated with the symbol transmitted by the kth user will be evaluated during the kth loop.

rank	i	$\mathbf{v}_i^{(5)}$					num of errors	LLF	note
1	21	-1	$+1$	-1	$+1$	$+1$	0	3.248	$\hat{\mathbf{v}}^{\mathrm{ML}}$
2	23	-1	$+1$	-1	-1	$+1$	1	3.053	
3	17	-1	$+1$	$+1$	$+1$	$+1$	1	2.973	
4	19	-1	$+1$	$+1$	-1	$+1$	2	2.845	
5	22	-1	$+1$	-1	$+1$	-1	1	2.826	
6	24	-1	$+1$	-1	-1	-1	2	2.713	
7	18	-1	$+1$	$+1$	$+1$	-1	2	2.649	
8	20	-1	$+1$	$+1$	-1	-1	3	2.602	$\hat{\mathbf{v}}^{\mathrm{MF}}$
9	29	-1	-1	-1	$+1$	$+1$	1	2.491	
10	31	-1	-1	-1	-1	$+1$	2	2.390	
11	25	-1	-1	$+1$	$+1$	$+1$	2	2.324	
12	27	-1	-1	$+1$	-1	$+1$	3	2.290	
13	30	-1	-1	-1	$+1$	-1	2	2.201	
14	32	-1	-1	-1	-1	-1	3	2.182	
15	28	-1	-1	$+1$	-1	-1	4	2.178	
16	26	-1	-1	$+1$	$+1$	-1	3	2.131	
17	12	$+1$	-1	$+1$	-1	-1	5	-9.744	
18	10	$+1$	-1	$+1$	$+1$	-1	4	-10.224	
19	16	$+1$	-1	-1	-1	-1	4	-10.241	
20	11	$+1$	-1	$+1$	-1	$+1$	4	-10.247	
21	4	$+1$	$+1$	$+1$	-1	-1	4	-10.260	
22	3	$+1$	$+1$	$+1$	-1	$+1$	4	-10.631	
23	9	$+1$	-1	$+1$	$+1$	$+1$	3	-10.646	
24	2	$+1$	$+1$	$+1$	$+1$	-1	3	-10.646	
25	15	$+1$	-1	-1	-1	$+1$	3	-10.647	
26	8	$+1$	$+1$	-1	-1	-1	3	-10.649	
27	14	$+1$	-1	-1	$+1$	-1	3	-10.655	
28	7	$+1$	$+1$	-1	-1	$+1$	2	-10.923	
29	1	$+1$	$+1$	$+1$	$+1$	$+1$	2	-10.935	
30	6	$+1$	$+1$	-1	$+1$	-1	2	-10.969	
31	13	$+1$	-1	-1	$+1$	$+1$	2	-10.979	
32	5	$+1$	$+1$	-1	$+1$	$+1$	1	-11.161	

Table 6.2: All the 32 legitimate vectors in the full set $\mathbb{V}^{(5)}$ ranked by the LLF value under the system parameters given in Table 3.1.

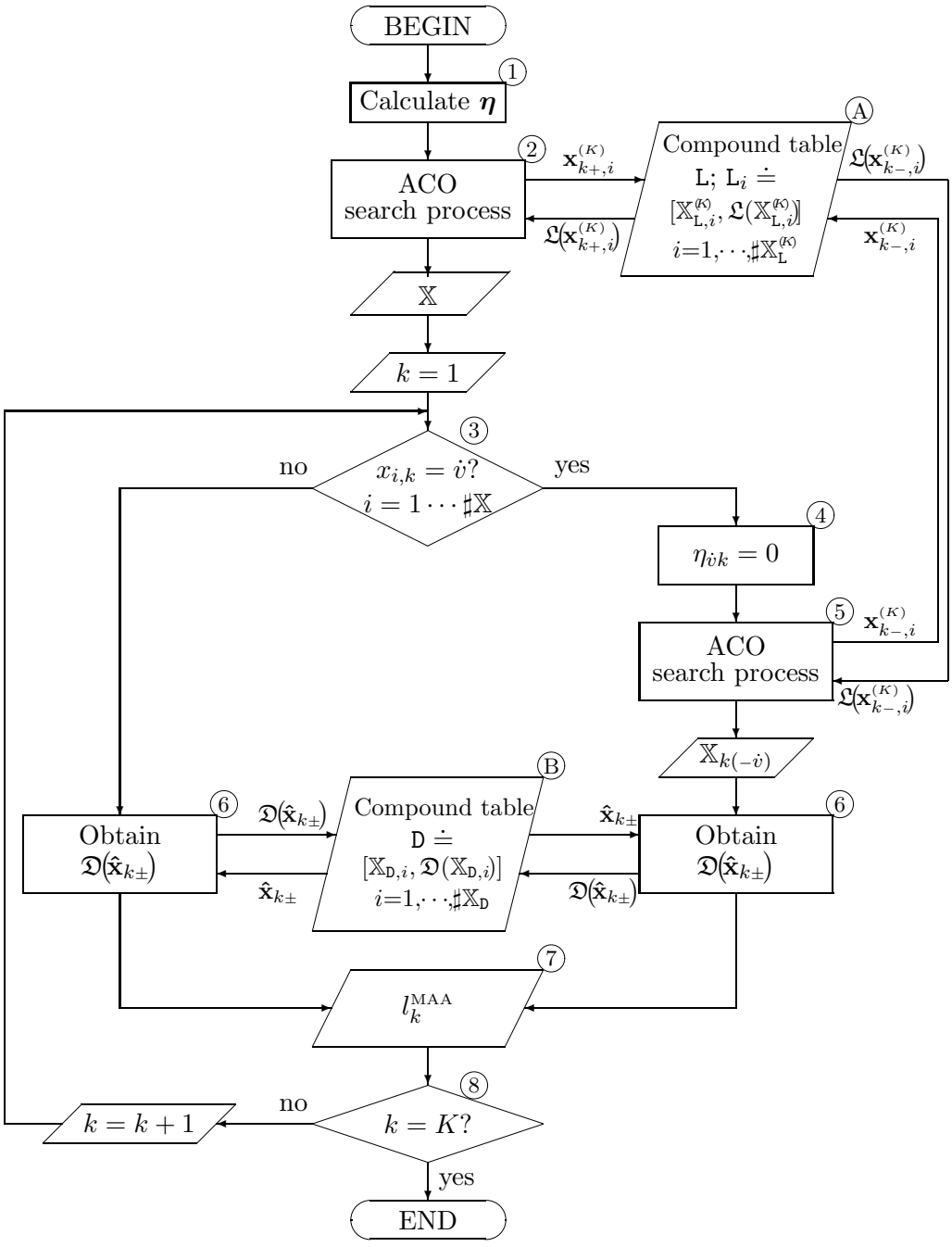

Figure 6.3: Flow-chart of the SO ACO-based MAA MUD algorithm.

As observed from Step 3 of the flow-chart in Fig. 6.3, there are two options for carrying out the evaluation process in order to obtain l_k, depending on the specific condition tested in Step 3 of Fig. 6.3. More specifically, if the kth symbol of all the K-bit vectors constituting the search-pool $\mathbb{X}$ are identical, another HO ACO search process has to be activated in order to generate an updated search-pool, which contains at least one K-bit vector having a different bit in the kth symbol position.

4. Step 4 - Setting the relevant intrinsic affinity to zero

In order to ensure that the search-pool does contain at least one K-bit vector having a specific bit in the kth element, which is different from the kth element of all the other $(K-1)$ vectors, we set

$\mathbb{V}^{(5)}$	$\mathbb{X}_{1+}^{(5)}$	$\mathbb{V}_{1+}^{(5)}$ $\bar{\mathbb{X}}_{1+}^{(5)}$ $\tilde{\mathbb{X}}_{1+}^{(5)}$	$\mathbb{V}^{(5)}$	$\mathbb{X}_{1-}^{(5)}$	$\mathbb{V}_{1-}^{(5)}$ $\bar{\mathbb{X}}_{1-}^{(5)}$ $\tilde{\mathbb{X}}_{1-}^{(5)}$
$\mathbf{v}_{21}^{(5)}$	-1 $+1-1+1+1$	$\mathbf{v}_{1+,13}^{(5)}$ $\bar{\mathbf{x}}_{1+,1}$ $\tilde{\mathbf{x}}_{1+,1}$			
$\mathbf{v}_{23}^{(5)}$	-1 $+1-1-1+1$	$\mathbf{v}_{1+,15}^{(5)}$ $\bar{\mathbf{x}}_{1+,2}$ $\tilde{\mathbf{x}}_{1+,2}$			
$\mathbf{v}_{17}^{(5)}$	-1 $+1+1+1+1$	$\mathbf{v}_{1+,9}^{(5)}$ $\bar{\mathbf{x}}_{1+,3}$ $\tilde{\mathbf{x}}_{1+,3}$			
$\mathbf{v}_{19}^{(5)}$	-1 $+1+1-1+1$	$\mathbf{v}_{1+,11}^{(5)}$ $\bar{\mathbf{x}}_{1+,4}$ $\tilde{\mathbf{x}}_{1+,4}$			
$\mathbf{v}_{22}^{(5)}$	-1 $+1-1+1-1$	$\mathbf{v}_{1+,14}^{(5)}$ $\bar{\mathbf{x}}_{1+,5}$ $\tilde{\mathbf{x}}_{1+,5}$			
$\mathbf{v}_{24}^{(5)}$	-1 $+1-1-1-1$	$\mathbf{v}_{1+,16}^{(5)}$ $\bar{\mathbf{x}}_{1+,6}$			
$\mathbf{v}_{18}^{(5)}$	-1 $+1+1+1-1$	$\mathbf{v}_{1+,10}^{(5)}$ $\bar{\mathbf{x}}_{1+,7}$			
$\mathbf{v}_{20}^{(5)}$	-1 $+1+1-1-1$	$\mathbf{v}_{1+,12}^{(5)}$ $\bar{\mathbf{x}}_{1+,8}$			
$\mathbf{v}_{31}^{(5)}$	-1 $-1-1-1+1$	$\mathbf{v}_{1-,15}^{(5)}$ $\bar{\mathbf{x}}_{1-,1}$ $\tilde{\mathbf{x}}_{1-,1}$			
$\mathbf{v}_{25}^{(5)}$	-1 $-1+1+1+1$	$\mathbf{v}_{1-,9}^{(5)}$ $\bar{\mathbf{x}}_{1-,2}$ $\tilde{\mathbf{x}}_{1-,2}$			
$\mathbf{v}_{27}^{(5)}$	-1 $-1+1-1+1$	$\mathbf{v}_{1-,11}^{(5)}$ $\bar{\mathbf{x}}_{1-,3}$ $\tilde{\mathbf{x}}_{1-,3}$			
$\mathbf{v}_{30}^{(5)}$	-1 $-1-1+1-1$	$\mathbf{v}_{1-,14}^{(5)}$ $\bar{\mathbf{x}}_{1-,4}$ $\tilde{\mathbf{x}}_{1-,4}$			
$\mathbf{v}_{32}^{(5)}$	-1 $-1-1-1-1$	$\mathbf{v}_{1-,16}^{(5)}$ $\bar{\mathbf{x}}_{1-,5}$ $\tilde{\mathbf{x}}_{1-,5}$			

Table 6.3: Results of Steps 4, 5 and 6 in Fig. 6.4, when the MUA algorithm is applied for generating the LLR l_1, while using the system parameters of Table 3.1. The search-pool obtained by the HO ACO-based MUD is illustrated in Fig. 3.5 and the LLFs of all the 32 legitimate K-bit vectors are given in Table 6.2.

$\eta_{\dot{v}k} = 0$ in Fig. 6.3.

5. Step 5 - Extra ACO-based search process

This step is essentially identical to Step 2 of Fig. 6.3 and it is also identical to the entire flow-chart of Fig. 3.9, except for a small difference between the HO ACO-based search process carried out in Step 5 of Fig. 3.9 and that in Step 2 of Fig. 6.3. More explicitly, the difference is that the intrinsic affinity used to guide the ACO search process both in Step 2 of Fig. 6.3 and in the entire flow-chart of Fig. 3.9 is characterized by Eqs. (3.9) to (3.14), which is in turn governed by the real parts of the MF outputs $\Re\{\mathbf{y}\}$ and by the CIR matrix $\mathbf{H}$. By contrast, the intrinsic affinity $\boldsymbol{\eta}$ to be used by Step 5 of Fig. 6.3 is updated from the original intrinsic affinity matrix $\boldsymbol{\eta}$, in conjunction with nulling $\eta_{\dot{v}k}$ in Step 4 of Fig. 6.3.

The immediate result of the intrinsic nulling operation of Step 4 in Fig. 6.3 is that the kth symbol of all the K-bit vectors constituting the search-pool provided by the extra ACO-based MUD search process now becomes $-\dot{v}$. Therefore the search-pool generated after the extra ACO search process is denoted as $\mathbb{X}_{k(-\dot{v})}$.

6. Step 6 - Obtaining the pair of dominant K-bit vectors and their Euclidean distances

Once both of the subsets $\mathbb{X}_{k+}^{(K)}$ and $\mathbb{X}_{k-}^{(K)}$ contain at least one K-bit vector, the two dominant K-bit vectors $\hat{\mathbf{x}}_{k\pm}$ having the highest LLF in each set can be identified. Then the corresponding Euclidean distances of $\hat{\mathbf{x}}_{k\pm}$ can be obtained by substituting $\dot{\mathbf{v}}$ in Eq. (6.18) for the K-bit vector $\hat{\mathbf{x}}_{k\pm}$.

As shown in Table 6.3, there is no K-bit vector having its $k = 1$st symbol set to $+1$ in the original

search-pool of $\mathbb{X}^{(5)}$, which was generated by the initial HO ACO-based MUD denoted by Step 2 of Fig. 6.3. Hence, the condition of Step 3 in Fig. 6.3 is fulfilled. As a result, the operations in Steps 4∼6 will be carried out, with $\eta_{-1} = 0$ set in Step 4. Given the extra K-bit vectors captured by the search-pool $\mathbb{X}^{(5)}_{1+}$, the most dominant K-bit vectors in $\mathbb{X}^{(5)}_{1+}$ and $\mathbb{X}^{(5)}_{1-}$ can be identified and hence the LLR l_1 of the bit v_1 transmitted by the $k = 1$st user may be obtained.

By contrast, during the evaluation of l_k, $k = 2, 3, 4, 5$, the search-pool $\mathbb{X}^{(5)}$ contains K-bit vectors having their kth symbol set to both $+1$ and -1. Hence the condition tested in Step 3 of Fig. 6.3 will not be fulfilled.

Hence the algorithm will proceed from Step 3 to Step 7 through Step 6 along on the left branch of Fig. 6.3, where the two dominant K-bit vectors $\hat{\mathbf{x}}_{k-}$ in each set $\mathbb{X}^{(K)}_{k+}$ and $\mathbb{X}^{(K)}_{k-}$ may now be directly identified.

As indicated in Tables 6.4∼6.7, the two most dominant K-bit vectors $\hat{\mathbf{x}}_{k\pm}$ in each subset are $\bar{\mathbf{x}}_{k\pm,1}$ or $\tilde{\mathbf{x}}_{k\pm,1}$. More explicitly, as observed from Tables 6.4∼6.7, we have $\hat{\mathbf{x}}_{2+} = \mathbf{v}^{(5)}_{21}$, $\hat{\mathbf{x}}_{2-} = \mathbf{v}^{(5)}_{31}$; $\hat{\mathbf{x}}_{3+} = \mathbf{v}^{(5)}_{17}$, $\hat{\mathbf{x}}_{3-} = \mathbf{v}^{(5)}_{21}$; $\hat{\mathbf{x}}_{4+} = \mathbf{v}^{(5)}_{21}$, $\hat{\mathbf{x}}_{4-} = \mathbf{v}^{(5)}_{23}$; $\hat{\mathbf{x}}_{5+} = \mathbf{v}^{(5)}_{21}$ and $\hat{\mathbf{x}}_{5-} = \mathbf{v}^{(5)}_{22}$.

$\mathbb{V}^{(5)}$	$\mathbb{X}^{(5)}_{2+}$	$\mathbb{V}^{(5)}_{2+}$ $\bar{\mathbb{X}}^{(5)}_{2+}$ $\tilde{\mathbb{X}}^{(5)}_{2+}$	$\mathbb{V}^{(5)}$	$\mathbb{X}^{(5)}_{2-}$	$\mathbb{V}^{(5)}_{2-}$ $\bar{\mathbb{X}}^{(5)}_{2-}$ $\tilde{\mathbb{X}}^{(5)}_{2-}$
$\mathbf{v}^{(5)}_{21}$	-1 $+1$ $-1+1+1$	$\mathbf{v}^{(5)}_{2+,13}$ $\bar{\mathbf{x}}_{2+,1}$ $\tilde{\mathbf{x}}_{2+,1}$	$\mathbf{v}^{(5)}_{31}$	-1 -1 $-1-1+1$	$\mathbf{v}^{(5)}_{2-,15}$ $\bar{\mathbf{x}}_{2-,1}$ $\tilde{\mathbf{x}}_{2-,1}$
$\mathbf{v}^{(5)}_{23}$	-1 $+1$ $-1-1+1$	$\mathbf{v}^{(5)}_{2+,15}$ $\bar{\mathbf{x}}_{2+,2}$ $\tilde{\mathbf{x}}_{2+,2}$	$\mathbf{v}^{(5)}_{25}$	-1 -1 $+1+1+1$	$\mathbf{v}^{(5)}_{2-,9}$ $\bar{\mathbf{x}}_{2-,2}$ $\tilde{\mathbf{x}}_{2-,2}$
$\mathbf{v}^{(5)}_{17}$	-1 $+1$ $+1+1+1$	$\mathbf{v}^{(5)}_{2+,9}$ $\bar{\mathbf{x}}_{2+,3}$ $\tilde{\mathbf{x}}_{2+,3}$	$\mathbf{v}^{(5)}_{27}$	-1 -1 $+1-1+1$	$\mathbf{v}^{(5)}_{2-,11}$ $\bar{\mathbf{x}}_{2-,3}$ $\tilde{\mathbf{x}}_{2-,3}$
$\mathbf{v}^{(5)}_{19}$	-1 $+1$ $+1-1+1$	$\mathbf{v}^{(5)}_{2+,11}$ $\bar{\mathbf{x}}_{2+,4}$ $\tilde{\mathbf{x}}_{2+,4}$	$\mathbf{v}^{(5)}_{30}$	-1 -1 $-1+1-1$	$\mathbf{v}^{(5)}_{2-,14}$ $\bar{\mathbf{x}}_{2-,4}$ $\tilde{\mathbf{x}}_{2-,4}$
$\mathbf{v}^{(5)}_{22}$	-1 $+1$ $-1+1-1$	$\mathbf{v}^{(5)}_{2+,14}$ $\bar{\mathbf{x}}_{2+,5}$ $\tilde{\mathbf{x}}_{2+,5}$	$\mathbf{v}^{(5)}_{32}$	-1 -1 $-1-1-1$	$\mathbf{v}^{(5)}_{2-,16}$ $\bar{\mathbf{x}}_{2-,5}$ $\tilde{\mathbf{x}}_{2-,5}$
$\mathbf{v}^{(5)}_{24}$	-1 $+1$ $-1-1-1$	$\mathbf{v}^{(5)}_{2+,16}$ $\bar{\mathbf{x}}_{2+,6}$			
$\mathbf{v}^{(5)}_{18}$	-1 $+1$ $+1+1-1$	$\mathbf{v}^{(5)}_{2+,10}$ $\bar{\mathbf{x}}_{2+,7}$			
$\mathbf{v}^{(5)}_{20}$	-1 $+1$ $+1-1-1$	$\mathbf{v}^{(5)}_{2+,12}$ $\bar{\mathbf{x}}_{2+,8}$			

Table 6.4: Results of Steps 4, 5 and 6 in Fig. 6.4, when the MUA algortihhm is used for generating the LLR l_2 while using the system parameters of Table 3.1. The search-pool obtained by the HO ACO-based MUD is illustrated in Fig. 3.5 and the LLFs of all the 32 legitimate K-bit vectors are displayed in Table 6.2. Additionally, the number of K-bit vectors included in the final search-pool $\mathbb{X}_{2\pm}$ for calculating l_2 in the given five-user example is $\tilde{x}_2 = 5$. All the $5 \times 2 = 10$ K-bit vectors included in the final search-pool $\mathbb{X}_{2\pm}$ are listed in the left and right column above the horizontal line between the rows $\mathbf{v}^{(5)}_{22}$ and $\mathbf{v}^{(5)}_{24}$.

7. Step 7 - Calulate the LLR l_k of the symbol transmitted by the kth user

Eq. (6.25) provides the LLR l_k formulated by the MAA algorithm, where only two terms are required in order to obtain l_k. More specifically, we have to identify the two most dominant K-bit vectors $\hat{\mathbf{x}}_{k\pm}$ in the subsets $\mathbb{X}_{2\pm}$, where $\hat{\mathbf{x}}_{k\pm}$ are the particular K-bit vectors satisfying the following two conditions:

- their kth symbol is ± 1;
- they have the highest LLF among all the K-bit vectors having the kth bit value of ± 1 in $\mathbb{X}$.

$\mathbb{V}^{(5)}$	$\mathbb{X}^{(5)}_{3+}$			$\mathbb{V}^{(5)}_{3+}$ $\bar{\mathbb{X}}^{(5)}_{3+}$ $\tilde{\mathbb{X}}^{(5)}_{3+}$	$\mathbb{V}^{(5)}$	$\mathbb{X}^{(5)}_{3-}$			$\mathbb{V}^{(5)}_{3-}$ $\bar{\mathbb{X}}^{(5)}_{3-}$ $\tilde{\mathbb{X}}^{(5)}_{3-}$
$\mathbf{v}^{(5)}_{17}$	$-1+1$	$+1$	$+1+1$	$\mathbf{v}^{(5)}_{3+,9}$ $\bar{\mathbf{x}}_{3+,1}$ $\tilde{\mathbf{x}}_{3+,1}$	$\mathbf{v}^{(5)}_{21}$	$-1+1$	-1	$+1+1$	$\mathbf{v}^{(5)}_{3-,9}$ $\bar{\mathbf{x}}_{3+,1}$ $\tilde{\mathbf{x}}_{3+,1}$
$\mathbf{v}^{(5)}_{19}$	$-1+1$	$+1$	$-1+1$	$\mathbf{v}^{(5)}_{3+,11}$ $\bar{\mathbf{x}}_{3+,2}$ $\tilde{\mathbf{x}}_{3+,2}$	$\mathbf{v}^{(5)}_{23}$	$-1+1$	-1	$-1+1$	$\mathbf{v}^{(5)}_{3-,11}$ $\bar{\mathbf{x}}_{3+,2}$ $\tilde{\mathbf{x}}_{3+,2}$
$\mathbf{v}^{(5)}_{18}$	$-1+1$	$+1$	$+1-1$	$\mathbf{v}^{(5)}_{3+,10}$ $\bar{\mathbf{x}}_{3+,3}$ $\tilde{\mathbf{x}}_{3+,3}$	$\mathbf{v}^{(5)}_{22}$	$-1+1$	-1	$+1-1$	$\mathbf{v}^{(5)}_{3-,10}$ $\bar{\mathbf{x}}_{3-,3}$ $\tilde{\mathbf{x}}_{3-,3}$
$\mathbf{v}^{(5)}_{20}$	$-1+1$	$+1$	$-1-1$	$\mathbf{v}^{(5)}_{3+,12}$ $\bar{\mathbf{x}}_{3+,4}$ $\bar{\mathbf{x}}_{3+,4}$	$\mathbf{v}^{(5)}_{24}$	$-1+1$	-1	$-1-1$	$\mathbf{v}^{(5)}_{3-,12}$ $\bar{\mathbf{x}}_{3-,4}$ $\bar{\mathbf{x}}_{3-,4}$
$\mathbf{v}^{(5)}_{25}$	$-1-1$	$+1$	$+1+1$	$\mathbf{v}^{(5)}_{3+,13}$ $\bar{\mathbf{x}}_{3+,5}$ $\tilde{\mathbf{x}}_{3+,5}$	$\mathbf{v}^{(5)}_{31}$	$-1-1$	-1	$-1+1$	$\mathbf{v}^{(5)}_{3-,15}$ $\bar{\mathbf{x}}_{3-,5}$ $\tilde{\mathbf{x}}_{3-,5}$
$\mathbf{v}^{(5)}_{27}$	$-1-1$	$+1$	$-1+1$	$\mathbf{v}^{(5)}_{3+,15}$ $\bar{\mathbf{x}}_{3+,6}$	$\mathbf{v}^{(5)}_{30}$	$-1-1$	-1	$+1-1$	$\mathbf{v}^{(5)}_{3-,14}$ $\bar{\mathbf{x}}_{3-,6}$
					$\mathbf{v}^{(5)}_{32}$	$-1-1$	-1	$-1-1$	$\mathbf{v}^{(5)}_{3-,16}$ $\bar{\mathbf{x}}_{3-,7}$

Table 6.5: Results of Steps 4, 5 and 6 in Fig. 6.4, when the MUA algortihhm is used for generating the LLR l_3 while using the system parameters of Table 3.1. The search-pool obtained by the HO ACO-based MUD is illustrated in Fig. 3.5 and the LLFs of all the 32 legitimate K-bit vectors are displayed in Table 6.2. Additionally, the number of K-bit vectors included in the final search-pool $\mathbb{X}_{3\pm}$ for calculating l_3 in the given five-user example is $\tilde{x}_3 = 5$. All the $5 \times 2 = 10$ K-bit vectors included in the final search-pool $\mathbb{X}_{3\pm}$ are listed in the left and right column above the horizontal line between the rows $\mathbf{v}^{(5)}_{25}$ and $\mathbf{v}^{(5)}_{27}$.

$\mathbb{V}^{(5)}$	$\mathbb{X}^{(5)}_{4+}$			$\mathbb{V}^{(5)}_{4+}$ $\bar{\mathbb{X}}^{(5)}_{4+}$ $\tilde{\mathbb{X}}^{(5)}_{4+}$	$\mathbb{V}^{(5)}$	$\mathbb{X}^{(5)}_{4-}$			$\mathbb{V}^{(5)}_{4-}$ $\bar{\mathbb{X}}^{(5)}_{4-}$ $\tilde{\mathbb{X}}^{(5)}_{4-}$
$\mathbf{v}^{(5)}_{21}$	$-1+1-1$	$+1$	$+1$	$\mathbf{v}^{(5)}_{4+,11}$ $\bar{\mathbf{x}}_{4+,1}$ $\tilde{\mathbf{x}}_{4+,1}$	$\mathbf{v}^{(5)}_{23}$	$-1+1-1$	-1	$+1$	$\mathbf{v}^{(5)}_{4-,11}$ $\bar{\mathbf{x}}_{4-,1}$ $\tilde{\mathbf{x}}_{4-,1}$
$\mathbf{v}^{(5)}_{17}$	$-1+1+1$	$+1$	$+1$	$\mathbf{v}^{(5)}_{4+,9}$ $\bar{\mathbf{x}}_{4+,2}$ $\tilde{\mathbf{x}}_{4+,2}$	$\mathbf{v}^{(5)}_{19}$	$-1+1+1$	-1	$+1$	$\mathbf{v}^{(5)}_{4-,9}$ $\bar{\mathbf{x}}_{4-,2}$ $\tilde{\mathbf{x}}_{4-,2}$
$\mathbf{v}^{(5)}_{22}$	$-1+1-1$	$+1$	-1	$\mathbf{v}^{(5)}_{4+,12}$ $\bar{\mathbf{x}}_{4+,3}$ $\tilde{\mathbf{x}}_{4+,3}$	$\mathbf{v}^{(5)}_{24}$	$-1+1-1$	-1	-1	$\mathbf{v}^{(5)}_{4-,12}$ $\bar{\mathbf{x}}_{4-,3}$ $\bar{\mathbf{x}}_{4-,3}$
$\mathbf{v}^{(5)}_{18}$	$-1+1+1$	$+1$	-1	$\mathbf{v}^{(5)}_{4+,10}$ $\bar{\mathbf{x}}_{4+,4}$ $\tilde{\mathbf{x}}_{4+,4}$	$\mathbf{v}^{(5)}_{20}$	$-1+1+1$	-1	-1	$\mathbf{v}^{(5)}_{4-,10}$ $\bar{\mathbf{x}}_{4-,4}$ $\bar{\mathbf{x}}_{4-,4}$
$\mathbf{v}^{(5)}_{25}$	$-1-1+1$	$+1$	$+1$	$\mathbf{v}^{(5)}_{4+,13}$ $\bar{\mathbf{x}}_{4+,5}$	$\mathbf{v}^{(5)}_{31}$	$-1-1-1$	-1	$+1$	$\mathbf{v}^{(5)}_{4-,15}$ $\bar{\mathbf{x}}_{4-,5}$
$\mathbf{v}^{(5)}_{30}$	$-1-1-1$	$+1$	-1	$\mathbf{v}^{(5)}_{4+,16}$ $\bar{\mathbf{x}}_{4-,6}$	$\mathbf{v}^{(5)}_{27}$	$-1-1+1$	-1	$+1$	$\mathbf{v}^{(5)}_{4-,13}$ $\bar{\mathbf{x}}_{4+,6}$
					$\mathbf{v}^{(5)}_{32}$	$-1-1-1$	-1	-1	$\mathbf{v}^{(5)}_{4-,16}$ $\bar{\mathbf{x}}_{4-,7}$

Table 6.6: Results of Steps 4, 5 and 6 in Fig. 6.4, when the MUA algortihhm is used for generating the LLR l_4 while using the system parameters of Table 3.1. The search-pool obtained by the HO ACO-based MUD is illustrated in Fig. 3.5 and the LLFs of all the 32 legitimate K-bit vectors are displayed in Table 6.2. Additionally, the number of K-bit vectors included in the final search-pool $\mathbb{X}_{4\pm}$ for calculating l_4 in the given five-user example is $\tilde{x}_4 = 4$. All the $4 \times 2 = 8$ K-bit vectors included in the final search-pool $\mathbb{X}_{4\pm}$ are listed in the left and right column above the horizontal line between the rows $\mathbf{v}^{(5)}_{18}$ and $\mathbf{v}^{(5)}_{25}$.

Again, as detailed in Section 6.3.1, the LLR l_k associated with the bit transmitted by the kth user can be quantified as:

$$l_k^{\text{MAA}} = -\frac{1}{\sigma_{\mathbf{n}}^2}\left[\mathfrak{D}\left(\hat{\mathbf{x}}_{k+}\right) - \mathfrak{D}\left(\hat{\mathbf{x}}_{k-}\right)\right], \tag{6.26}$$

where the Euclidean distances $\mathfrak{D}\left(\hat{\mathbf{x}}_{k\pm}\right)$ are calculated within Stpe 6 of Fig. 6.3.

8. Termination condition

Finally, the procedure of determining the LLRs for all the K symbols transmitted within a specific

$\mathbb{V}^{(5)}$	$\mathbb{X}^{(5)}_{5+}$		$\mathbb{V}^{(5)}_{5+}$ $\bar{\mathbb{X}}^{(5)}_{5+}$ $\tilde{\mathbb{X}}^{(5)}_{5+}$	$\mathbb{V}^{(5)}$	$\mathbb{X}^{(5)}_{5-}$		$\mathbb{V}^{(5)}_{5-}$ $\bar{\mathbb{X}}^{(5)}_{5-}$ $\tilde{\mathbb{X}}^{(5)}_{5-}$
$\mathbf{v}^{(5)}_{21}$	$-1+1-1+1$	$+1$	$\mathbf{v}^{(5)}_{5+,11}$ $\bar{\mathbf{x}}_{5+,1}$ $\tilde{\mathbf{x}}_{5+,1}$	$\mathbf{v}^{(5)}_{22}$	$-1+1-1+1$	-1	$\mathbf{v}^{(5)}_{5-,11}$ $\bar{\mathbf{x}}_{5-,1}$ $\tilde{\mathbf{x}}_{5-,1}$
$\mathbf{v}^{(5)}_{23}$	$-1+1-1-1$	$+1$	$\mathbf{v}^{(5)}_{5+,12}$ $\bar{\mathbf{x}}_{5+,2}$ $\tilde{\mathbf{x}}_{5+,2}$	$\mathbf{v}^{(5)}_{24}$	$-1+1-1-1$	-1	$\mathbf{v}^{(5)}_{5-,12}$ $\bar{\mathbf{x}}_{5-,2}$ $\bar{\mathbf{x}}_{5-,2}$
$\mathbf{v}^{(5)}_{17}$	$-1+1+1+1$	$+1$	$\mathbf{v}^{(5)}_{5+,9}$ $\bar{\mathbf{x}}_{5+,3}$ $\tilde{\mathbf{x}}_{5+,3}$	$\mathbf{v}^{(5)}_{18}$	$-1+1+1+1$	-1	$\mathbf{v}^{(5)}_{5-,9}$ $\bar{\mathbf{x}}_{5-,3}$ $\tilde{\mathbf{x}}_{5-,3}$
$\mathbf{v}^{(5)}_{19}$	$-1+1+1-1$	$+1$	$\mathbf{v}^{(5)}_{5+,10}$ $\bar{\mathbf{x}}_{5+,4}$ $\tilde{\mathbf{x}}_{5+,4}$	$\mathbf{v}^{(5)}_{20}$	$-1+1+1-1$	-1	$\mathbf{v}^{(5)}_{5-,10}$ $\bar{\mathbf{x}}_{5-,4}$ $\bar{\mathbf{x}}_{5-,4}$
$\mathbf{v}^{(5)}_{31}$	$-1-1-1-1$	$+1$	$\mathbf{v}^{(5)}_{5+,16}$ $\bar{\mathbf{x}}_{5+,5}$ $\tilde{\mathbf{x}}_{5+,5}$	$\mathbf{v}^{(5)}_{30}$	$-1-1-1+1$	-1	$\mathbf{v}^{(5)}_{5-,15}$ $\bar{\mathbf{x}}_{5-,5}$ $\bar{\mathbf{x}}_{5-,5}$
$\mathbf{v}^{(5)}_{25}$	$-1-1+1+1$	$+1$	$\mathbf{v}^{(5)}_{5+,13}$ $\bar{\mathbf{x}}_{5+,6}$ $\tilde{\mathbf{x}}_{5+,6}$	$\mathbf{v}^{(5)}_{32}$	$-1-1-1-1$	-1	$\mathbf{v}^{(5)}_{5-,16}$ $\bar{\mathbf{x}}_{5-,6}$ $\bar{\mathbf{x}}_{5-,6}$
$\mathbf{v}^{(5)}_{27}$	$-1-1+1-1$	$+1$	$\mathbf{v}^{(5)}_{5+,14}$ $\bar{\mathbf{x}}_{5+,7}$				

Table 6.7: Results of Steps 4, 5 and 6 in Fig. 6.4, when the MUA algortihhm is used for generating the LLR l_5 while using the system parameters of Table 3.1. The search-pool obtained by the HO ACO-based MUD is illustrated in Fig. 3.5 and the LLFs of all the 32 legitimate K-bit vectors are displayed in Table 6.2. Additionally, the number of K-bit vectors included in the final search-pool $\mathbb{X}_{5\pm}$ for calculating l_5 in the given five-user example is $\tilde{x}_5 = 6$. All the $6 \times 2 = 12$ K-bit vectors included in the final search-pool $\mathbb{X}_{5\pm}$ are listed in the left and right column above the horizontal line between the rows $\mathbf{v}^{(5)}_{25}$ and $\mathbf{v}^{(5)}_{27}$.

bit-duration will be terminated if reach $k = K$. When k is less than K, the value of k will be increased by 1 to activate the next loop of evaluating l_{k+1}, which recommences from Step 3 of Fig. 6.3.

6.4 Multi-Input Approximation SO ACO-MUD

The MUA algorithm employed by the ACO-based SO MUD aims for populating both final search-pools $\tilde{\mathbb{X}}_{k\pm}$ with the maximum possible number of different K-bit vectors. When the LLR l_k of the kth symbol is evaluated, two parallel search processes are invoked for each of the K users, in order to ensure that the maximum possible number of different K-bit vectors is generated to ascertain that we do have vectors, where the kth symbol is both $+1$ and -1. Thus, we create both final search-pools $\tilde{\mathbb{X}}_{k+}$ and $\tilde{\mathbb{X}}_{k-}$ from the output of the corresponding two search processes.

6.4.1 Theoretical Background

In contrast to the LLR l_k provided by the Bayesian detector, which was derived in Section 6.2.1 and repeated here for convenience:

$$l_k^{\mathrm{BAY}} = \ln \frac{\sum\limits_{\mathbf{v}_{k+,i} \in \mathbb{V}^{(K)}_{k+}} \exp\left\{ \frac{-1}{\sigma_{\mathbf{n}}^2} \|\mathbf{r} - \mathbf{C}\mathbf{H}\mathbf{v}_{k+,i}\|^2 \right\}}{\sum\limits_{\mathbf{v}_{k-,i} \in \mathbb{V}^{(K)}_{k-}} \exp\left\{ \frac{-1}{\sigma_{\mathbf{n}}^2} \|\mathbf{r} - \mathbf{C}\mathbf{H}\mathbf{v}_{k-,i}\|^2 \right\}}, \quad i = 1, \ldots, 2^{K-1}. \tag{6.27}$$

the ACO-based SO MUD algorithm aims for reducing the complexity, while tending to the accurate value of l_k using the following approximation:

$$l_k^{\mathrm{MUA}} = \ln \frac{\sum_{\tilde{\mathbf{x}}_{k+,i} \in \tilde{\mathbb{X}}_{k+}} \exp\left\{ \frac{-1}{\sigma_{\mathfrak{n}}^2} \|\mathbf{r} - \mathbf{C}\mathbf{H}\tilde{\mathbf{x}}_{k+,i}\|^2 \right\}}{\sum_{\tilde{\mathbf{x}}_{k-,i} \in \tilde{\mathbb{X}}_{k-}} \exp\left\{ \frac{-1}{\sigma_{\mathfrak{n}}^2} \|\mathbf{r} - \mathbf{C}\mathbf{H}\tilde{\mathbf{x}}_{k-,i}\|^2 \right\}}, \quad i = 1, \ldots, \tilde{x}_k, \quad \tilde{x}_k \ll 2^{K-1}. \tag{6.28}$$

We may assume that the K-bit vectors constituting the final search-pool $\tilde{\mathbb{X}}_{k+}$ are ordered according to their LLF values of Eq. (2.80), which are required to satisfy the following two conditions:

- The number of K-bit vectors in both search-pools is the same, namely $\tilde{x}_k$;
- The polarity of the LLFs associated with each pair of K-bit vectors in both final search-pools $\tilde{\mathbb{X}}_{k+}$ should remain unchanged for all the $\tilde{x}_k$ pairs of vectors constituting $\tilde{\mathbb{X}}_{k+}$.

Since we want $\tilde{\mathbb{X}}_{k\pm}$ to contain the most dominant $\tilde{x}_k$ number of vectors of the original search-pool $\mathbb{X}_{k\pm}$, we firstly sort all the elements of $\mathbb{X}_{k\pm}$ in descending order according to their LLFs given in Eq. (2.80), yielding their sorted counterparts $\bar{\mathbb{X}}_{k\pm}$. We then denote the ith element in the subset $\bar{\mathbb{X}}_{k\pm}$ as $\bar{\mathbf{x}}_{k\pm,i}$. Thus, the most dominant vector of both sets is $\bar{\mathbf{x}}_{k\pm,1}$. Furthermore, we set the polarity Γ_k of the kth detected bit to the sign of the difference between the LLFs of $\bar{\mathbf{x}}_{k\pm,1}$ and $\bar{\mathbf{x}}_{k\pm,1}$, i.e. we have $\Gamma_k = \mathrm{sgn}\{\mathfrak{L}[\bar{\mathbf{x}}_{k\pm,1}] - \mathfrak{L}[\bar{\mathbf{x}}_{k\pm,1}]\}$. We may introduce an error, when we include the K-bit vector-pair $\bar{\mathbf{x}}_{k\pm,i}$ in the calculation of l_k, if in contrast to the above definition of Γ_k we have $\mathfrak{L}[\bar{\mathbf{x}}_{k\pm,1}] - \mathfrak{L}[\bar{\mathbf{x}}_{k\pm,1}] = -\Gamma_k$. To address this problem, we only incorporate the vector-pair $\bar{\mathbf{x}}_{k\pm,i}$ into the pools $\tilde{\mathbb{X}}_{k+}$ and $\tilde{\mathbb{X}}_{k-}$, if and only if we have $\{\mathfrak{L}[\bar{\mathbf{x}}_{k\pm,i}] - \mathfrak{L}[\bar{\mathbf{x}}_{k\pm,i}]\} \cdot \{\mathfrak{L}[\bar{\mathbf{x}}_{k\pm,1}] - \mathfrak{L}[\bar{\mathbf{x}}_{k\pm,1}]\} > 0$, in other words when both of these multiplicative terms have an identical polarity.

6.4.2 Flow-Chart of the MUA Algorithm

The objective of the MUA algorithm is to create the search-pool $\tilde{\mathbb{X}}_{k+}$ and $\tilde{\mathbb{X}}_{k-}$ having $\tilde{x}_k$ number of decision candidates obeying Eq. (6.28). An attractive algorithm to realize this goal is summarized in Fig. 6.4.

The essential difference between the flow-chart of the MUA algorithm of Fig. 6.4 and the MAA algorithm of Fig. 6.3 lies in the absence of the decision encapsulated in Step 3 of Fig. 6.3, which determines whether an extra search iteration should be carried out. In other words, two HO ACO search processes will be carried out for calculating the LLRs l_k for all $k = 1, 2, \ldots, K$ without imposing any further conditions.

Below we will interpret each step shown in the flow-chart of Fig. 6.4.

1. Step 1 - Calculate the intrinsic affinity $\boldsymbol{\eta}$

This step is identical to Step 1 depicted in Fig. 6.3, where the $(2 \times K)$-element intrinsic affinity matrix $\boldsymbol{\eta}$, namely the intrinsic affinity associated with each cell in the route table is calculated. Since no modifications are necessary, the formula of calculating the intrinsic affinity $\boldsymbol{\eta}$ from the real parts

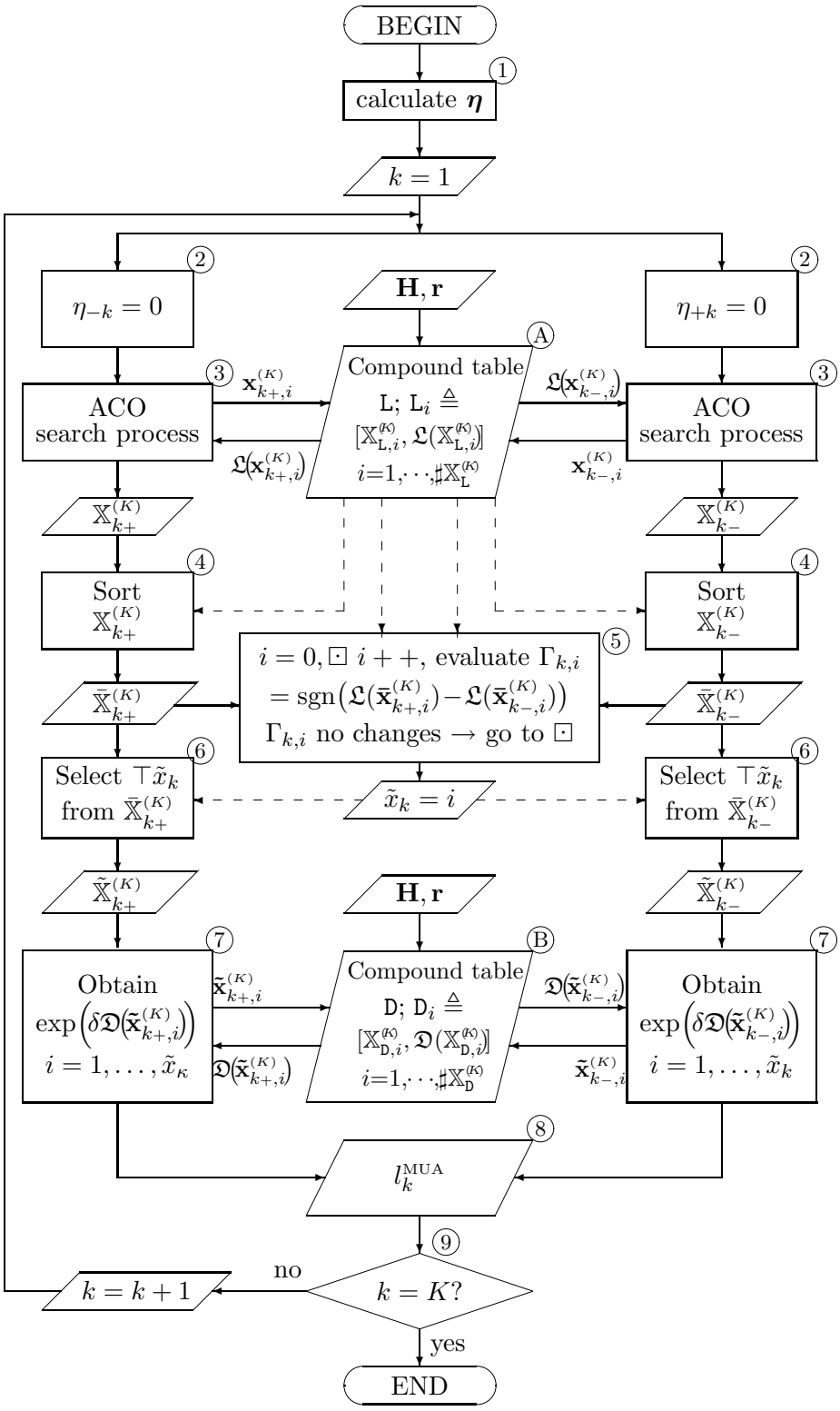

Figure 6.4: Flow-chart of the SO ACO-based MUA algorithm.

of the MF output $\Re\{\mathbf{y}\}$ as well as the CIR matrix $\mathbf{H}$ are given in Eqs. (3.9), (3.11), (3.12), (3.13) and (3.14).

2. Step 2 - Setting the relevant intrinsic affinity to zero

In order to ensure that the search-pool does contain at least one K-bit vector having a specific bit in the kth element, which is different from the kth element of all the other $(K-1)$ vectors, we set $\eta_{\dot{v}k} = 0$ in Fig. 6.4.

3. Step 3 - HO ACO search process

This step is equivalent to Step 2 and Step 5 in Fig. 6.3. In other words, the 'ACO search process' is identical to a complete HO ACO-based search process required in order to find the ML solution, as introduced in Section 3.3.

Since the intrinsic affinity associated with the cell in the 1st row of the kth column of the route table as shown in Table 3.6 has been set to zero, all the K-bit vectors constituting the search-pool generated by the HO ACO search process in Step 3 of the left wing in Fig. 6.4 will have the kth symbol equivalent to '+1'. Hence the search-pool includes all the K-bit vectors captured during the entire search process of Step 3 in the left wing can be denoted as $\mathbb{X}_{k+}^{(K)}$.

On the other hand, since the intrinsic affinity associated with the $(2,k)$th cell is zero, all the K-bit vectors in the search-pool generated by the HO ACO search process in Step 3 of the right wing in Fig. 6.4 will have the kth symbol equivalent to '-1'. Therefore the search-pool encompassing all the K-bit vectors captured during the entire search process of Step 3 of the right wing may be denoted as $\mathbb{X}_{k-}^{(K)}$.

4. Step 4 - Sort the original search-pool

Then the K-bit vectors constituting either one of the two search-pools $\mathbb{X}_{k\pm}^{(K)}$ will be sorted in a descending order according to their fitness value quantified in terms of the OF, obtained by substituting the vector $\dot{\mathbf{v}}$ of the LLF in Eq. (6.29) with the vector $\mathbf{x}_{k\pm,i}$, with $i = 1, 2, \ldots, \sharp\mathbb{X}_{k\pm}^{(K)}$, where $\sharp\mathbb{X}_{k\pm}^{(K)}$ denotes the cardinality of the sets $\mathbb{X}_{k\pm}^{(K)}$, i.e. the number of K-bit vectors constituting the sets $\mathbb{X}_{k\pm}^{(K)}$.

Again, the LLF values associated with a certain K-bit vector $\dot{\mathbf{v}}$ may be expressed in terms of the given MF output $\mathbf{y}$ and correlation matrix $\mathbf{R}$ as:

$$\mathfrak{L}(\dot{\mathbf{v}}) \triangleq 2\Re\{\dot{\mathbf{v}}^H\mathbf{y}\} - \dot{\mathbf{v}}^H\mathbf{R}\dot{\mathbf{v}}. \tag{6.29}$$

This formula is identical to Eq. (2.80). As a result, the sorted sets maybe denoted as $\bar{\mathbb{X}}_{k\pm}^{(K)}$, where the vector having the highest LLF value in each set is denoted as $\bar{\mathbf{x}}_{k+,1}$ and $\bar{\mathbf{x}}_{k+,1}$, respectively.

5. Step 5,6 - Select the final search-pool

We may define $\Gamma_k = \text{sgn}[\mathfrak{L}(\bar{\mathbf{x}}_{k+,1}) - \mathfrak{L}(\bar{\mathbf{x}}_{k-,1})]$ as the binary flag indicating the result of the comparison between the LLF associated with the most dominant K-bit vector in each of the two sets $\mathbb{X}_{k+}^{(K)}$ and $\mathbb{X}_{k-}^{(K)}$. We may introduce an error, when we include the vector-pair $\mathbf{x}_{k\pm,i}$ in the calculation of l_k^{MUA}, if $\mathfrak{L}(\mathbf{x}_{k+,i}) - \mathfrak{L}(\mathbf{x}_{k-,i}) = -\Gamma_k$. To address this problem, we only incorporate the vector-pair $\mathbf{x}_{k\pm,i}$ into the pair of calculation pools $\tilde{\mathbf{X}}_{k\pm}^{(K)}$ respectively, if and only if we have $\mathfrak{L}(\mathbf{x}_{k+,i}) - \mathfrak{L}(\mathbf{x}_{k-,i}) = -\Gamma_k$. In Step 6, the notation $\top\tilde{x}_\kappa$ represents the highest ranked $\tilde{x}_\kappa$ number of elements in the ordered set $\tilde{\mathbf{x}}_\kappa^{\pm}$.

In order to generate the final search-pool according to the above rule, the following simple algorithm may be formulated:

1. Compare the LLF values of the two most dominant vectors $\mathbf{x}_{k\pm,1}$ in $\mathbb{X}_{k+}^{(K)}$ and $\mathbb{X}_{k-}^{(K)}$, respectively and evaluate $\Gamma_k = \text{sgn}[\mathfrak{L}(\mathbf{x}_{k+,1}) - \mathfrak{L}(\mathbf{x}_{k-,1})]$;

2. Set $i = 2$;

3. **if** $(\text{sgn}[\mathfrak{L}(\mathbf{x}_{k+,i}) - \mathfrak{L}(\mathbf{x}_{k-,i})] = \Gamma_k \ \wedge \ i \leqslant \min\{x_{k+}, x_{k-}\})$, then

   - Incorporate $\mathbf{x}_{k\pm,i}$ into $\mathbb{X}_{k\pm}^{(K)}$, respectively;
   - $i = i + 1$ and goto Item 3.

   else Exit.

Below we will exemplify Steps 4, 5, 6, and 7 in the context of our five-user example in Table 6.4 $\sim$ Table 6.7.

Assume that the search-pools $\mathbb{X}_{k\pm}^{(K)}$ generated by the 'ACO search process' in the left and right wing of Fig. 6.4 are given by the K-bit vectors listed in the left and right columns of Table 6.4 $\sim$ Table 6.7, when $k = 2$, 3, 4 and 5.

Observe from Table 6.4 that we have $\mathfrak{L}(\mathbf{v}_{21}^{(5)}) > \mathfrak{L}(\mathbf{v}_{31}^{(5)})$, corresponding to $\mathbf{v}_2^{\text{ML}} = +1$. In other words, the LLF associated with the K-bit vector in the left column of Table 6.4 is higher than that in the right column of the same row. This comparison result is valid for all the ten K-bit vectors contained by the top five rows of the two columns. Hence we have $\tilde{x}_2 = 5$. Therefore all the five K-bit vectors of $\mathbf{v}_{21}^{(5)}$, $\mathbf{v}_{23}^{(5)}$, $\mathbf{v}_{17}^{(5)}$, $\mathbf{v}_{19}^{(5)}$, $\mathbf{v}_{22}^{(5)}$ will be included in the numerator of Eq. (6.28), while $\mathbf{v}_{31}^{(5)}$, $\mathbf{v}_{25}^{(5)}$, $\mathbf{v}_{27}^{(5)}$, $\mathbf{v}_{30}^{(5)}$, $\mathbf{v}_{32}^{(5)}$ will be included in the denominator of Eq. (6.28).

Let us now consider Table 6.5, where we have $\mathfrak{L}(\mathbf{v}_{17}^{(5)}) < \mathfrak{L}(\mathbf{v}_{21}^{(5)})$, corresponding to $\mathbf{v}_3^{\text{ML}} = -1$. Hence, the LLF of the K-bit vector in the left column of Table 6.5 is smaller than that in the right column of the same row. This relationship is maintained between the two K-bit vectors throughout the first to the fifth row of Table 6.5. However, this relationship becomes invalid again in the sixth row of Table 6.5, where we have $\mathfrak{L}(\mathbf{v}_{27}^{(5)}) > \mathfrak{L}(\mathbf{v}_{30}^{(5)})$. Hence, to avoid a potential error, the vectors $\mathbf{v}_{27}^{(5)}$ and $\mathbf{v}_{30}^{(5)}$ will not be incorporated into $\mathbb{X}_{3+}^{(5)}$ and $\mathbb{X}_{3-}^{(5)}$, respectively. Then we have $\tilde{x}_3 = 5$. As a result, the final search-pool $\mathbb{X}_{3+}^{(5)}$ will merely contain $\mathbf{v}_{17}^{(5)}$, $\mathbf{v}_{19}^{(5)}$, $\mathbf{v}_{18}^{(5)}$, $\mathbf{v}_{20}^{(5)}$, $\mathbf{v}_{25}^{(5)}$; while $\mathbb{X}_{3-}^{(5)}$ will only contain $\mathbf{v}_{21}^{(5)}$, $\mathbf{v}_{23}^{(5)}$, $\mathbf{v}_{22}^{(5)}$, $\mathbf{v}_{24}^{(5)}$, $\mathbf{v}_{31}^{(5)}$.

Let us now observe Table 6.6, where we have $\mathfrak{L}(\mathbf{v}_{21}^{(5)}) > \mathfrak{L}(\mathbf{v}_{23}^{(5)})$, corresponding to $\mathbf{v}_4^{\text{ML}} = +1$. The required relationship has not been maintained beyond the fourth row, since we have $\mathfrak{L}(\mathbf{v}_{25}^{(5)}) < \mathfrak{L}(\mathbf{v}_{31}^{(5)})$, leading to $\tilde{x}_4 = 4$. Therefore, the final search-pool $\mathbb{X}_{4+}^{(5)}$ contains the four K-bit vectors of $\mathbf{v}_{21}^{(5)}$, $\mathbf{v}_{17}^{(5)}$, $\mathbf{v}_{22}^{(5)}$, $\mathbf{v}_{18}^{(5)}$ only. Correspondingly, $\mathbb{X}_{4-}^{(5)}$ contains the four K-bit vectors: $\mathbf{v}_{23}^{(5)}$, $\mathbf{v}_{19}^{(5)}$, $\mathbf{v}_{24}^{(5)}$, $\mathbf{v}_{20}^{(5)}$.

Finally, as observed from Table 6.7, the relationship of $\mathfrak{L}(\mathbf{v}_{21}^{(5)}) > \mathfrak{L}(\mathbf{v}_{22}^{(5)})$, which corresponds to $\mathbf{v}_4^{\text{ML}} = +1$ has been satisfied throughout the first row to the sixth row of Table 6.7. Hence the final search-pool $\mathbb{X}_{5+}^{(5)}$ contains the six K-bit vectors: $\mathbf{v}_{21}^{(5)}$, $\mathbf{v}_{23}^{(5)}$, $\mathbf{v}_{17}^{(5)}$, $\mathbf{v}_{19}^{(5)}$, $\mathbf{v}_{31}^{(5)}$, $\mathbf{v}_{25}^{(5)}$; while $\mathbb{X}_{5-}^{(5)}$ contains the K-bit vectors: $\mathbf{v}_{22}^{(5)}$, $\mathbf{v}_{24}^{(5)}$, $\mathbf{v}_{18}^{(5)}$, $\mathbf{v}_{20}^{(5)}$, $\mathbf{v}_{30}^{(5)}$, $\mathbf{v}_{32}^{(5)}$.

7. Step 7 - Determine the exponential Euclidean distances

Given all the K-bit vectors in the final search-pool $\mathbb{X}_{k\pm}^{(K)}$, we are now ready to calculate the LLR l_k for the symbol transmitted by the kth user according to Eq. (6.28) in the context of the MUA algorithm.

As suggested by Eq. (6.28), each K-bit input vector has to be incorporated in the numerator or denominator of Eq. (6.28). This is achieved by substituting $\dot{\mathbf{v}}$ of Eq. (6.17) for $\tilde{\mathbf{x}}_{k\pm,i}$ in Eq. (6.28) with

$i = 1, 2, \ldots, \tilde{x}_k$, and the related noise-power-normalized Euclidian distance formula is repeated here for convenience as

$$\mathfrak{E}(\dot{\mathbf{v}}) \triangleq \exp\left[-\frac{1}{\sigma_{\mathfrak{n}}^2}\|\mathbf{r} - \mathbf{C}\mathbf{H}\dot{\mathbf{v}}\|^2\right]. \tag{6.30}$$

The parameter δ indicated in Step 7 of Fig. 6.4 obeys $\delta = -[\sigma_{\mathfrak{n}}^2]^{-1}$.

8. Step 8 - calculate the LLR of the kth symbol

Given the $\tilde{x}_k$ number of K-bit vectors in the final search-pool $\mathbb{X}_{k\pm}^{(K)}$, the ultimate form of the LLR l_k associated with the kth user may now be readily obtained in the form of

$$l_k^{\text{MUA}} = \ln \frac{\displaystyle\sum_{\tilde{\mathbf{x}}_{k+,i} \in \tilde{\mathbb{X}}_{k+}} \exp\left\{\frac{-1}{\sigma_n^2}\|\mathbf{r} - \mathbf{C}\mathbf{H}\tilde{\mathbf{x}}_{k+,i}\|^2\right\}}{\displaystyle\sum_{\tilde{\mathbf{x}}_{k-,i} \in \tilde{\mathbb{X}}_{k-}} \exp\left\{\frac{-1}{\sigma_n^2}\|\mathbf{r} - \mathbf{C}\mathbf{H}\tilde{\mathbf{x}}_{k-,i}\|^2\right\}}, \quad i = 1, \ldots, \tilde{x}_k, \quad \tilde{x}_k \ll 2^{K-1}. \tag{6.31}$$

9. Step - 9 Termination decision

Finally, once the LLRs associated with all the K symbols transmitted by the K users have been obtained, the MUA SO ACO-based MUD algorithm will be terminated for the specific symbol duration considered.

6.5 Complexity Issues

As the search procedure of the MUA algorithm progresses during a certain symbol interval, a large number of vectors will repeatedly appear in the search-pools $\mathbb{X}_{k\pm}$ during the search processes employed for evaluating the LLRs of different users k, $k = 1, \ldots, K$. For example, the same K-bit trial vector may appear in the search-pool $\mathbb{X}_{k_1\pm}$, $\mathbb{X}_{k_2\pm}$, $\mathbb{X}_{k_3\pm}$, when we have $k_1 \neq k_2 \neq k_3$. As observed from Tables 6.3∼6.7 of our $K = 5$-user example, the ML solution $\mathbf{v}_{21}^{(5)}$ appears in $\mathbb{X}_{1-}^{(5)}$, $\mathbb{X}_{2+}^{(5)}$,$\mathbb{X}_{3-}^{(5)}$,$\mathbb{X}_{4+}^{(5)}$,$\mathbb{X}_{5+}^{(5)}$, respectively.

Thus, we may create a list containing all the different vectors appearing during the current symbol interval along with their likelihood values, as shown in Table 6.8. The same mechanism can be used to

i	Vector value $\mathbf{x}_{\mathtt{L},i}^{(K)}$	LLF $\mathfrak{L}\left[\mathbf{x}_{\mathtt{L},i}^{(K)}\right]$
1	$[+1 \;\; -1 \;\; +1 \;\; +1 \;\; \cdots \;\; -1]$	3.45
2	$\cdots$	$\cdots$

Table 6.8: Compound table L in Figs. 6.3 and 6.4.

obtain the Euclidean distance associated with a specific K-bit vector, as shown in Table 6.9, which is used during the calculation of l_k in Eq. (6.28). In conclusion, the complexity of the MUA algorithm is significantly reduced, as we will quantify in the context of Fig. 6.6. The likelihood value of a specific K-bit vector may be directly obtained from the table without further calculations, provided that it has already been calculated for this symbol interval.

i	Vector value $\mathbf{x}_{\mathtt{D},i}^{(K)}$	Euclidean distance $\mathfrak{D}\left[\mathbf{x}_{\mathtt{D},i}^{(K)}\right]$
1	$[+1 \ -1 \ +1 \ +1 \ \cdots \ -1]$	2.28
2	$\cdots$	$\cdots$

Table 6.9: Compound table D in Figs. 6.3 and 6.4.

Tables 6.8 and 6.9 represent the actions of Steps A and B depicted both in Figs. 6.3 and 6.4. The tables L and D shown in the flow-charts of Fig. 6.3 and 6.4 are defined in a way that each row in them contains two elements: the K-bit vector $\mathbf{x}_{\mathtt{L},i}^{(K)} \in \mathbb{X}_{\mathtt{L}}^{(K)}$ and the LLF $\mathfrak{L}(\mathbf{x}_{\mathtt{L},i}^{(K)})$ of it or the K-bit vector $\mathbf{x}_{\mathtt{D},i}^{(K)} \in \mathbb{X}_{\mathtt{D}}^{(K)}$ and the Euclidean distance $\mathfrak{D}(\mathbf{x}_{\mathtt{D},i}^{(K)})$ of it. Each K-bit vector is different from all the other K-bit vectors in the same table. Furthermore, $\sharp\mathbb{X}_{\mathtt{L}}$ or $\sharp\mathbb{X}_{\mathtt{D}}$ represents the cardinality of the set $\mathbb{X}_{\mathtt{L}}$ or $\mathbb{X}_{\mathtt{D}}$, which contains all the different K-bit candidate-vectors whose LLFs or Euclidean distances have been calculated during the current bit-interval.

It is worth mentioning that the MAA SO ACO based MUD algorithm of Section 6.3 may be regarded as a special case of the MUA algorithm. More explicitly, the final form of the kth user's LLRs in the MAA algorithm is described by Eq. (6.28). However, the specific values of the parameters $\tilde{x}_k$ and $\tilde{\mathbb{X}}_{k\pm}$ in Eq. (6.28) are given for the MAA algorithm by $\tilde{x}_k = 1$ and $\tilde{\mathbb{X}}_{k\pm} = \{\tilde{\mathbf{x}}_{k\pm,1}\}$, where we have

$$\begin{aligned} \tilde{\mathbf{x}}_{k+,1} &= \arg \max_{\tilde{\mathbf{x}}_{k+,i} \in \tilde{\mathbb{X}}_{k+}} \{\mathfrak{L}(\tilde{\mathbf{x}}_{k+,i})\} \\ \tilde{\mathbf{x}}_{k-,1} &= \arg \max_{\tilde{\mathbf{x}}_{k-,i} \in \tilde{\mathbb{X}}_{k-}} \{\mathfrak{L}(\tilde{\mathbf{x}}_{k-,i})\}. \end{aligned} \tag{6.32}$$

6.6 Simulation Results

The proposed SO ACO-based MUD was combined with a half-rate Recursive Systematic Convolutional (RSC) code having a constraint length of 3 and employing the BCJR algorithm [206]. The octally represented generator and feedback polynominals of the RSC code were 7 and 5. The parameters used for the SO-ACO MUDs are summarized in Table 6.10. Additionally, 31-chip Gold codes are employed to spread the BPSK baseband modulated symbols, before they are transmitted from the antenna of each MS. All the codes constituting the spreading code set were listed in Table 2.5. Fig. 6.5 shows that the DS-CDMA UL supporting $K = 32$ users with the aid of $N_s = 31$-chip Gold codes is capable of approaching the corresponding single-user system's BER, regardless, whether the soft-output or hard-output ACO-based MUD is used. However, the soft-output ACO-assisted DS-CDMA scheme shows a significant SNR improvement compared to its hard-output ACO-assisted counterpart. We may also observe in Fig. 6.5 that the BER performance of both SO-ACO assisted DS-CDMA ULs supporting $K = 32$ users approach that of their Bayesian counterparts, when supporting $K = 5$ users. The Bayesian decision assisted DS-CDMA UL supports only $K = 5$ users because the complexity of the system supporting a higher number of users becomes excessive.

Fig. 6.6 shows that the complexity of the ACO-based MUD is only a fraction of that of the ML or Bayesian detector, again, regardless whether hard- or soft-output aided detection is used. More quantatively, when the number of users reaches $K = 32$, the complexity of both the hard-output and

CC parameters	Modem	BPSK
	Code rate	1/2
	Constraint length	3
	Octal generator polynominal	(031, 027)
SISO-ACO parameters	Initial pheromone	$\tau = 0.01$
	Evaporation rate	$\rho = 0.5$
	Number of ants	$\zeta = 10$
	Number of iterations	$\Xi = 10$
	Weight of pheromone	$\alpha = 1$
	Weight of intrinsic affinity	$\beta = 6$
	Weight for the elite ant	$\sigma = 8$
Interleaver parameters	Type	random
	Memory	10^4 bits

Table 6.10: Basic simulation parameters used in Section 6.6.

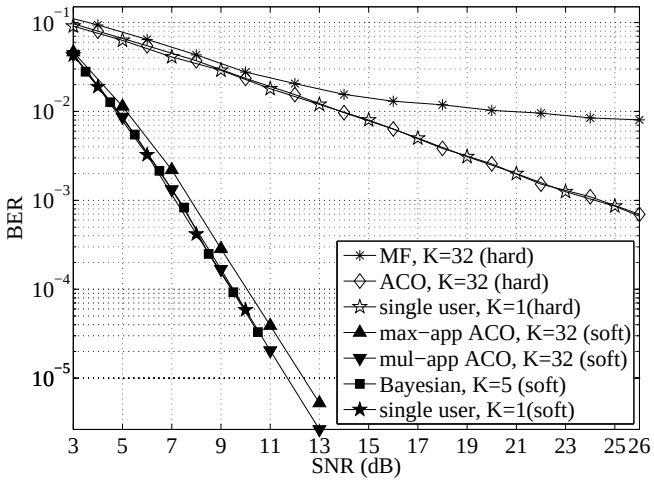

Figure 6.5: BER versus SNR performance of the uplink DS-CDMA system for transmission over uncorrelated flat Rayleigh fading channels using $N_c = 31$-chip Gold codes.

of the soft-output ACO is nearly a factor of 10^8 lower than that of the optimum Bayesian detector.

We observe a performance gap in Fig. 6.5 between the curve representing the MAA SO ACO-based MUD and the Bayesian MUD. This is because the MAA SO ACO-based MUD employs only the most dominant component in both the numerator and the denominator of Eq. (6.21) for calculating the LLRs, thus the LLR value is not as accurate as that obtained by the Bayesian MUD or by the MUA assisted SO ACO-based MUD. However, the BER performance of the MUA SO ACO-based MUD assisted DS-CDMA UL matches that of the Bayesian MUD and it exhibits a substantial improvement compared to the MAA SO ACO-based MUD, while the complexity of the former is only slightly increased compared to that of the latter, as shown in Fig. 6.6.

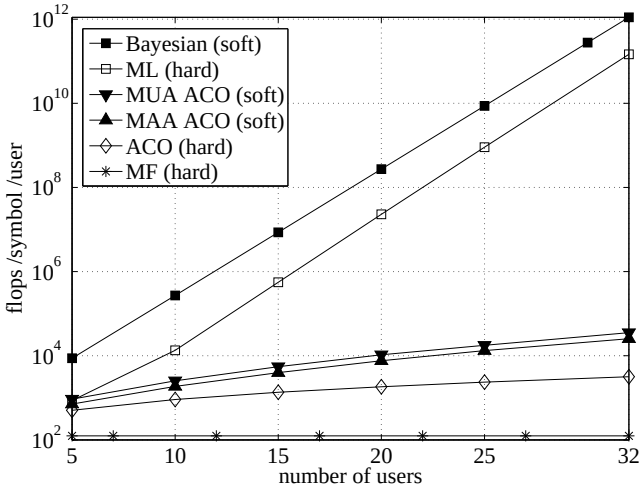

Figure 6.6: Complexity per transmitted bit per user versus the number of users of the DS-CDMA system employing $N_c = 31$-chip Gold codes.

6.7 Chapter Summary

In this chapter, we have derived the *LLR*s in the context of the DS-CDMA UL using the *Bayesian* MUD of Eq. (6.20). In order to approximate the accurate LLRs provided by the Bayesian algorithm at an affordable complexity, two ACO-based SO MUD algorithm were proposed, namely the *MAA* algorithm of Section 6.3 and the *MUA* algorithm of Section 6.4.

Observe in Fig. 6.5 that the proposed MUA SO ACO-based MUD is capable of approaching the single-user performance, when combined with a 1/2-rate convolutional code, as seen for the DS-CDMA UL supporting $K = 32$ users by employing 31-chip Gold sequences. The complexity of the MUA SO ACO-based MUD is nearly a factor of 10^8 lower than that of the Bayesian MUD, as evidenced by Fig. 6.6. The BER performance of the DS-CDMA UL documented in Fig. 6.5 and employing the MUA assisted SO ACO-based MUD shows an improvement over the MAA assisted SO ACO-based MUD, while the complexity of the former is only slightly higher than that of the latter, as evidenced by Fig. 6.6.

Chapter 7

Three - Stage Concatenated Turbo MUD

7.1 Introduction

In Fig. 6.1 of Chapter 6, we have introduced a soft-input channel decoding scheme for each user in order to enhance the BER performance achieved by the MU DS-CDMA system. The introduction of the soft-input channel decoding scheme required the Soft-Output (SO) ACO-based MUD algorithm, which was detailed in Chapter 6.

Furthermore, in Chapter 5, we proposed a STBC assisted DS-CDMA MU system, where each user employed two antennas for transmitting two symbols in two symbol-durations in order to achieve a second-order diversity gain. The employment of STBCs for each user further improved the attainable performance, which was achieved by detecting $2K$ instead of K symbols during each activation of the ACO-based MUD algorithm. In this chapter familiarity with Chapters 5 and 6 is assumed.

The assumption of having independent fading for the two transmit antennas of shirt-pocket-sized communicators is unrealistic. However, assuming an antenna-separation of say 30 cm, i.e. two wavelengths at 2 GHz in a laptop PC's transmitter might provide sufficient decorrelation for approaching our idealized assumption of having independent fading. Alternatively, two single-antenna-aided mobiles may form a distributed $\mathcal{G}_2$ space-time code, which would have a near-perfect relay-link between them, provided that they are sufficiently close to each other. Naturally, this requires the creation of two time- or frequency-slots for the classic broadcast-phase and cooperation-phase of the mobiles, as detailed in [203], hence potentially halving the total system's throughput in exchange for the $\mathcal{G}_2$-STBC based 2nd-order diversity.

Based on the solutions in Chapters 5 and 6, in this chapter, we will propose a novel ACO-based SO ST/MUD algorithm, which jointly carries out the STBC decoding for each user and simultaneously mitigates the multiuser-interference, while achieving a second-order diversity gain. The proposed algorithm will enable each of the K active users to approach the single-user performance at a significantly reduced complexity, which is a factor 10^{17} lower for the specific application scenario considered, than that of the ML MUD for $K = 32$ users.

On the other hand, in order to achieve a near-capacity performance, channel coding is used and

iterative decoding is employed by exchanging extrinsic information between the receiver modules [205].

The insightful concept of turbo coding was proposed by Berrou *et. al* [36] in 1993, where the authors reported an outstanding coding gain, approaching the Shannonian predictions. In his treatise, two 1/2-rate Recursive Systematic Convolutional (RSC) encoders are used at the transmitter side of each user supported by the system. The information sequence is encoded twice, with an interleaver is inserted between the two encoders so that the input of the two encoders are statistically independent of each other.

At the receiver side, the first RSC decoder provides a soft output giving an estimate of the original data sequence solely based on the demodulator's soft output. This estimate will then be used to provide *extrinsic* information for the other constituent decoder. The extrinsic information provided for a given bit is based not on the demodulator's output for that particular bit, but on the soft-information of the surrounding bits and on the constraints imposed by the specific code used. The extrinsic information produced by the first RSC decoder is then used by the second RSC decoder as the *a priori* information, which is then combined with the demodulator's soft-output in order to enable the second RSC to produce its soft extrinsic information.

During the second iteration, the extrinsic information produced by the second RSC is then fed back to the first RSC as the *a priori* information and using this extra soft information the first RSC decoder is expected to correct more bit errors. This cycle continues and during each iteration, both RSC decoders provide soft extrinsic information for each other.

When multiple users are supported by the system, the function of a SO MUD is to extract soft information associated with each individual symbol transmitted by each individual user from the superimposed multi-user received signal, so that the interference imposed by all the other users may be mitigated. The ACO-based SO ST/MUD is invoked to produce near-optimal soft information in order to approach the performance of the optimum SO/MUD, namely that of the Bayesian MUD algorithm at a significantly reduced complexity.

Observe in the system's schematic seen in Fig. 7.1 that we employ a RSC code as the outer code and a Unity-Rate Code (URC) as the inner code for each user. Both of these channel decoders benefit from the soft information provided by the ACO-based SO ST/MUD of each individual user.

In [43] iterative decoding was invoked for exchanging extrinsic information between a soft-output symbol detector and an outer channel decoder in order to combat the effects of Inter-Symbol Interference (ISI). In [207] iterative decoding was carried out by exchanging information between an outer convolutional decoder and an inner Trellis Coded Modulation (TCM) decoder. The authors of [45, 46] presented a unified theory of Bit-Interleaved Coded Modulation (BICM). On the other hand, the employment of the iterative detection principle in [47] was considered for iterative soft demapping in the context of BICM, where a soft demapper was used between the multilevel demodulator and the channel decoder. Additionally, in [52] an iteratively detected scheme was proposed for the Rayleigh fading MIMO channel, where an orthogonal STBC scheme was considered as the inner code combined with an additional block code as the outer channel code. It was demonstrated in [208] that a recursive inner code is needed in order to avoid the formation of a Bit Error Ratio (BER) floor, when employing iterative decoding. In [55], unity-rate inner codes were employed for designing low complexity turbo codes suitable for bandwidth and power limited systems having stringent BER requirements.

The EXtrinsic Information Transfer (EXIT) charts [209] have been used for analyzing the extrinsic information exchange between iterative decoder components, when different amounts of *a priori* information ranging from $[0, 1]$ was provided for the decoder. The amount of either the extrinsic output or the *a priori* input soft information of a transmission frame may be quantified in terms of the Mutual Information (MI) between the soft-information and its hard-decision based version within a specific frame. At a given input *a priori* MI, the extrinsic MI is quantified as the average MI over all the transmitted frames.

For a three-stage concatenated system employing both an inner codec and an outer codec to carry out iterative turbo detection, EXIT charts have been used to predict the achievable BER performance as a function of both the iteration index and of E_b/N_0.

However, the accuracy of the EXIT-chart always depends on the interleaver length. For short interleavers, EXIT-band charts have been proposed [210], where the width of the EXIT band is defined as the standard deviation of the MI values averaged over all the transmitted frames and again, it depends on the interleaver length. **In this treatise, we will use EXIT-band chart to predict the E_b/N_0 convergence threshold of the system of Fig. 7.1 using the SO-ACO based ST-MUD assisted by a URC used as the inner codec and a 1/2-rate RSC outer codec.** Our results will demonstrate that EXIT-band-charts are capable of characterizing the iterative behavior of the system considered.

The rest of the chapter is organized as follows. In Section 7.2, the system's and our system model are characterized. The SO/ACO based ST/MUD algorithm is described in detail in Section 7.3. The BER performance of the proposed system, the EXIT-band-charts and our complexity estimates are characterized in Section 7.4. Finally, our conclusions are provided in Section 7.5.

7.2 System Description

The DS-CDMA uplink studied in this contribution is shown in Fig. 7.1. More specifically, the block diagram of the mobile transmitter of the kth user and the Base-Station's (BS) receiver are depicted in Fig. 7.1(a) and Fig. 7.1(b), respectively. Below, we will use calligraphic characters to represent the vector containing all the bits/symbols transmitted or received by user k during a certain transmitted frame, such as in $\mathbf{c}_k^{\mathrm{I}}$. Furthermore, we will use bold characters to represent the vector or matrix containing all the elements associated with a specific user or with all the K users, within a symbol block duration, a symbol duration or a chip interval.

As shown in Fig. 7.1(a), the N_u-bit source stream $\mathbf{u}_k$ of the kth user, $k = 1, 2, \ldots, K$ is first encoded by a 1/2-rate RSC code, yielding the N_c-bit RSC coded bit stream $\mathbf{c}_k^{\mathrm{I}}$. Then it is interleaved by a random bit interleaver Π_{I} providing the output bit stream $\mathbf{u}_k^{\mathrm{II}}$. The bit stream $\mathbf{u}_k^{\mathrm{II}}$ is then further encoded by a URC scheme generating the coded bit stream $\mathbf{c}_k^{\mathrm{II}}$. After passing through another random bit interleaver Π_{II}, the interleaved URC coded bit stream $\mathbf{b}_k$ is then modulated using a BPSK scheme, yielding the modulated symbol stream $\mathbf{v}_k$. Finally, after Serial-to-Parallel (S/P) conversion, the parallel $N_c/2$-length symbol streams $\mathbf{v}_{k1}$ and $\mathbf{v}_{k2}$ of Fig. 7.1(a) are rearranged by the $\mathcal{G}_2$ Alamouti space-time coding scheme [181], yielding the N_c-length symbol stream. Then each of the two parallel symbol streams is direct-sequence spread using the user-specific quasi-orthogonal spreading sequence

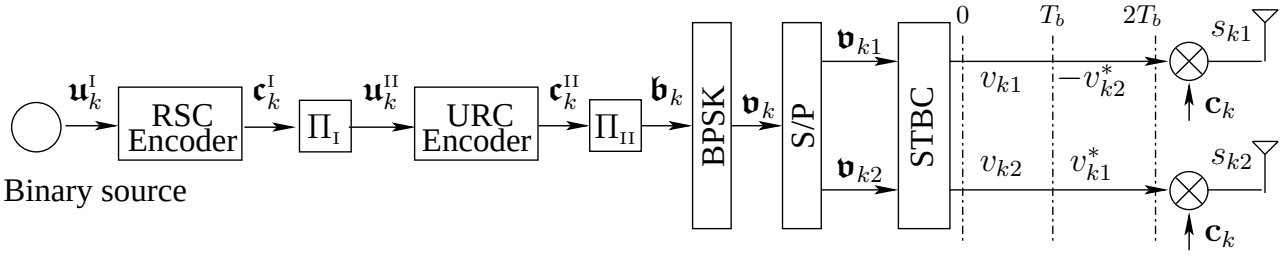

(a) Transmitter of user k.

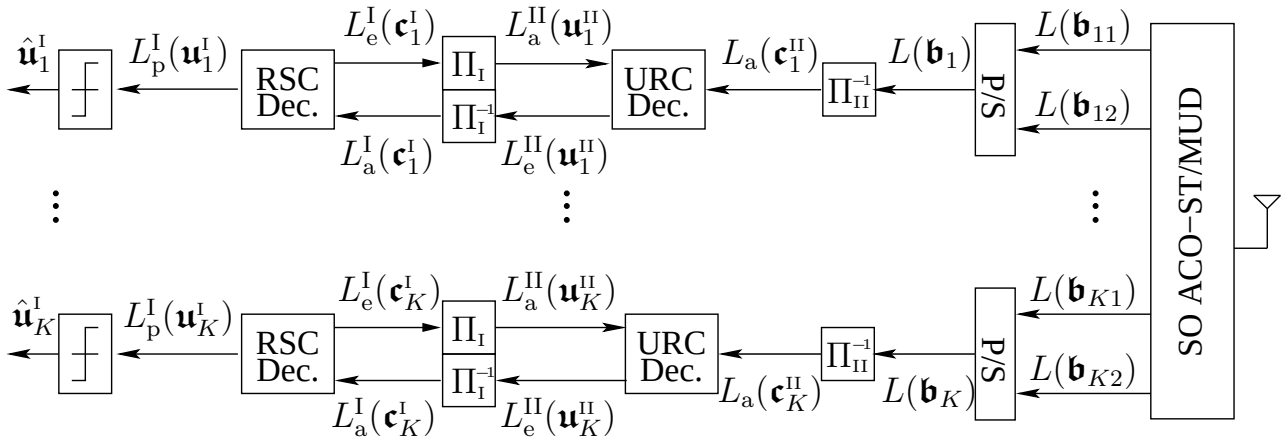

(b) Receiver at the BS.

Figure 7.1: Schematic of a DS-CDMA uplink employing RSC, URC, STBC, space-time multiuser detection as well as iterative decoding.

$\mathbf{c}_k$ of N_s chips. The $(N_\mathrm{s} \times N_\mathrm{c})$-chip signal streams of each user are then transmitted to the BS from two transmit antennas.

Let assume for simplicity that the signals are transmitted to the BS over non-dispersive, slowly fading channels, which exhibit a constant envelope over a STBC block duration. Then, it can be shown that the received complex-valued observations obtained from the $2N_\mathrm{s}$ chip durations of a STBC period can be written as

$$\mathbf{r} = \xi \mathbf{C}\mathbf{H}\mathbf{v} + \mathbf{n}, \tag{7.1}$$

where $\xi{=}1/\sqrt{2N_\mathrm{s}}$ is a normalization factor, $\mathbf{C}{=}[\mathbf{C}_1, \mathbf{C}_2, \cdots, \mathbf{C}_K]$ obeys $\mathbf{C}_k = \mathbf{c}_k \otimes \mathbf{I}_2$, where $\mathbf{c}_k$ is the kth user's spreading sequence, $\mathbf{I}_2$ is a (2×2)-element identity matrix and $\otimes$ denotes the *Kronecker product* operation. Furthermore, we have $\mathbf{H} = \mathrm{diag}\{\mathbf{H}_1, \mathbf{H}_2, \cdots, \mathbf{H}_K\}$ in (7.1), where

$$\mathbf{H}_k = \begin{bmatrix} h_{k1} & h_{k2} \\ h_{k2}^* & -h_{k1}^* \end{bmatrix} \tag{7.2}$$

accounts for the space-time fading channels, $\mathbf{v} = \left[\mathbf{v}_1^T, \mathbf{v}_2^T, \ldots, \mathbf{v}_K^T\right]^T$ associated with $\mathbf{v}_k = [v_{k1}, v_{k2}]^T$ contains the $2K$ coded bits to be transmitted and, finally, $\mathbf{n} = \left[\mathbf{n}_1^T, \mathbf{n}_2^H\right]^T$ associated with $\mathbf{n}_\jmath = [n_{\jmath 1}, n_{\jmath 2}, \cdots, n_{\jmath N_\mathrm{s}}]^T$, $\jmath = 1, 2$, denotes the complex-valued Gaussian noise samples, which have a zero mean and a common variance of $\frac{1}{2}\sigma_\mathfrak{n}^2 = N_0/(2E_\mathrm{b}(\mathfrak{b})) = N_0/(E_\mathrm{b}(\mathbf{u}^\mathrm{I}))$ in both the real and imaginary component of $\mathfrak{n}$, where E_b is the energy per URC coded bit.

The extrinsic soft information, which is quantified in terms of the Logarithmic Likelihood Ratios (LLR) is iteratively exchanged between the URC and the RSC decoder of Fig. 7.1. In Fig. 7.1(b), $L(\cdot)$ denotes the LLRs of the bits concerned, where the superscript 'I' or 'II' indicate the first and the second decoder, namely the RSC and URC decoders. Additionally, the subscripts 'a', 'p' and 'e' represent the *a priori*, *a posteriori* and extrinsic information, respectively.

As shown in Fig. 7.1(b), the observation vector $\mathbf{r}$ received during a STBC block duration is first input to the SO-ACO/ST-MUD, which generates the $(2K \times 1)$-element soft output vector $\mathbf{L}$ containing the LLRs of all the $2K$ bits transmitted during a STBC block duration. After receiving $N_c/2$ $2K$-element vectors output from the SO-ACO/ST-MUD during the $N_c/2$ STBC block duration, the $2K$ LLR streams $L(\mathfrak{b}_{11})$, ..., $L(\mathfrak{b}_{K2})$ stream comprising the $(N_c \times K)$ number of LLRs associated with all the $(N_c \times K)$ bits transmitted by all the K users during a transmission frame interval are input into the K P/S converters and are converted back to K number of LLR streams $L(\mathfrak{b}_1)$, ..., $L(\mathfrak{b}_K)$. As shown in Fig. 7.1(b), for the kth user, for $k = 1, \ldots, K$, the extrinsic LLR stream $L(\mathfrak{b}_k)$ generated by the SO ACO-based ST-MUD is first deinterleaved by the second random soft-bit deinterleaver Π_{II}^{-1}, yielding $L_{\text{a}}^{\text{II}}(\mathfrak{c}_k^{\text{II}})$. Then the URC decoder processes the $L_{\text{a}}^{\text{II}}(\mathfrak{c}_k^{\text{II}})$ comprising the LLR values of the URC-encoded bit stream $\mathfrak{c}_k^{\text{II}}$ in combination with the LLR stream $L_{\text{a}}^{\text{II}}(\mathfrak{u}_k^{\text{II}})$ containing the *a priori* LLR values of the URC uncoded bit stream $\mathfrak{u}_k^{\text{II}}$ to generate the extrinsic LLR values of the URC uncoded bit stream $\mathfrak{u}_k^{\text{II}}$, yielding the LLR stream $L_{\text{e}}^{\text{II}}(\mathfrak{u}_k^{\text{II}})$. Then, the extrinsic LLR stream $L_{\text{e}}^{\text{II}}(\mathfrak{u}_k^{\text{II}})$ is deinterleaved by the first random soft-bit deinterleaver Π_{I}^{-1} of Fig. 7.1(b), yielding the deinterleaved LLR stream $L_{\text{a}}^{\text{I}}(\mathfrak{c}_k^{\text{I}})$, which constitutes at the same time the *a priori* LLR stream of the RSC coded bits $\mathfrak{c}_k^{\text{I}}$.

Next, the *a priori* LLR values of the RSC coded bit stream $\mathfrak{c}_k^{\text{I}}$ represented by $L_{\text{a}}^{\text{I}}(\mathfrak{c}_k^{\text{I}})$ are input to the RSC decoder in order to generate the extrinsic LLR values for the RSC coded bit stream $\mathfrak{c}_k^{\text{I}}$ of Fig. 7.1(b), yielding $L_{\text{e}}^{\text{I}}(\mathfrak{c}_k^{\text{I}})$. After appropriately reordering the LLR values by the first soft-bit interleaver Π_{I}, the interleaved LLR stream $L_{\text{a}}^{\text{II}}(\mathfrak{u}_k^{\text{II}})$ is then fed back to the URC decoder in conjunction with the input of the *a priori* LLR values of all the URC coded bits $L_{\text{a}}(\mathfrak{c}_k^{\text{II}})$ of Fig. 7.1(b) to generate the extrinsic LLR values $L_{\text{e}}^{\text{II}}(\mathfrak{u}_k^{\text{II}})$ for all the bits $\mathfrak{u}_k^{\text{II}}$ during the second iteration. Again, after passing through the second random soft-bit deinterleaver Π_{I}^{-1}, the deinterleaved LLR stream $L_{\text{a}}^{\text{I}}(\mathfrak{c}_k^{\text{I}})$ is input to the RSC decoder as the *a priori* information of the coded bits $\mathfrak{c}_k^{\text{I}}$ during the second iteration.

As for the RSC decoder during the last iteration, instead of the extrinsic LLR values of the coded bits $L_{\text{e}}^{\text{I}}(\mathfrak{c}_k^{\text{I}})$, only the stream $L_{\text{p}}^{\text{I}}(\mathfrak{u}_k^{\text{I}})$ of Fig. 7.1(b) containing the *a posteriori* LLR values of all the original uncoded binary source $\mathfrak{u}_k^{\text{I}}$ are required. More explicitly, the *a posteriori* LLR values $L_{\text{p}}^{\text{I}}(\mathfrak{u}_k^{\text{I}})$ are then fed into the hard-output decision device of Fig. 7.1(b) in order to determine the final detection output for the binary source bit stream $\mathfrak{u}_k^{\text{I}}$ of the kth user.

7.3 Soft-Output of ACO-Aided Space-Time Multiuser Detection

7.3.1 Derivation of the LLRs

The derivation of the LLRs associated with a certain bit belonging to a certain user in a MU DS-CDMA system having a single transmit antenna at each MS and a single receive antenna at the BS has been extensively discussed in Section 6.2.1. The difference between the K-user Single-Input Single-Output (SISO) DS-CDMA system considered in Chapter 6 and its twin-transmit-antenna aided counterpart

of this chapter lies in the length of the sequence to be detected upon each activation of the MUD. As widely recognized [181, 202], when two transmit antennas are employed by each MS, two symbols will be transmitted within two independent symbol intervals, which constitutes a STBC block duration. The CIR matrix $\mathbf{H}$, the received signal vector $\mathbf{r}$ as well as the AWGN vector $\mathbf{n}$ encountered during a specific STBC block will be used to obtain the Hard-Output (HO) detection result $\hat{\mathbf{v}}$ encompassing all the $2K$ symbols transmitted within the STBC block duration, or the Soft-Output (SO) detection result $\mathbf{L} = L(\hat{\mathbf{v}})$ encompassing all the $2K$ LLRs associated with the $2K$ transmit symbols.

Therefore, the size of all the matrices $\mathbf{C}$, $\mathbf{H}$, $\mathbf{r}$ and $\mathbf{n}$ is commensurately extended. For example, the length of the AWGN vector $\mathbf{n}$ is increased from N_s to $2N_\mathrm{s}$, when the twin-transmit-antenna aided DS CDMA UL is considered instead of the SISO DS CDMA UL detected in Section 6.2.1.

The LLR value $L(\mathfrak{b}_{k\imath})$ of Fig. 7.1(b) associated with the $\imath$th symbol for $\imath = 1$ or 2 and transmitted by the kth user for $k = 1, \ldots, K$ within a certain STBC block duration is denoted as $l_{k\imath}$ for simplicity, which is defined by [211]

$$l_{k\imath} = \ln \frac{P(v_{k\imath} = +1|\mathbf{r}, \mathbf{H})}{P(v_{k\imath} = -1|\mathbf{r}, \mathbf{H})}, \imath = 1, 2 \qquad k = 1, 2, \ldots, K. \tag{7.3}$$

Upon applying the Bayesian rule of probability [160] and assuming that the *a priori* probabilities of both 0 and 1 are 0.5, Eq. (7.3) can be further elaborated on as

$$l_{k\imath}^{\mathrm{BAY}} = \ln \frac{\sum_{\mathbf{v}_{\kappa+,i}^{(M)} \in \mathbb{V}_{\kappa+,i}^{(M)}} p(\mathbf{r}|\mathbf{v}_{\kappa+,i}^{(M)}, \mathbf{H})}{\sum_{\mathbf{v}_{\kappa+,i}^{(M)} \in \mathbb{V}_{\kappa+,i}^{(M)}} p(\mathbf{r}|\mathbf{v}_{\kappa+,i}^{(M)}, \mathbf{H})}, \quad i = 1, \ldots, \frac{\mathcal{M}}{2}, \qquad \text{subject to } \kappa = 2(k-1) + \imath, \tag{7.4}$$

where $M = 2K$ denotes the number of elements in each vector and $\mathcal{M} = 2^M = 2^{2K}$ is the cardinality of the full set containing all the legitimate $2K$-bit vectors of the M-symbol BPSK modulated binary source combinations. Furthermore, $\mathbf{v}_{\kappa+,i}^{(M)}$ in Eq. (7.4) defines the set containing the $(\mathcal{M}/2)$ vectors having the κth symbol given by $+1$. The index κ in Eq. (7.4) is an integer ranging from 1 to $2K$ and v_κ in the $2K$-element vector $\mathbf{v}$ represents the same element as v_{ki} iff we have $\kappa = 2(k-1) + i$.

In Eq. (7.1) the $2N_\mathrm{s}$-element AWGN vector $\mathbf{n}$ having elements $n_{\jmath n_\mathrm{s}}$ for $\jmath = 1, 2$ and $n_s = 1, 2, \ldots, N_\mathrm{s}$ is an instantaneous sample of the complex-valued Gaussian random variable $\mathfrak{n}$ having a mean of $\mu_\mathfrak{n} = 0$ and a variance of $\sigma_\mathfrak{n}^2 = N_0/E_\mathrm{b}(\mathfrak{b})$. In other words, we have $n_{\jmath n_\mathrm{s}} \sim \mathcal{N}^\mathrm{c}(\mu_\mathfrak{n}, \sigma_\mathfrak{n}^2)$. According to [160], the PDF of the d-dimensional complex Gaussian variable $\mathbf{n} \sim \mathcal{N}_d^\mathrm{c}(\mathbf{M}_\mathfrak{n}, \mathbf{\Sigma}_\mathfrak{n})$ is given by

$$p(\mathbf{n}) = \frac{1}{\pi^D} \frac{\exp\left[-\frac{1}{2}(\mathbf{n} - \mathbf{M}_\mathfrak{n})^H 2\mathbf{\Sigma}_\mathfrak{n}^{-1}(\mathbf{n} - \mathbf{M}_\mathfrak{n})\right]}{\det(\mathbf{\Sigma}_\mathfrak{n})}. \tag{7.5}$$

In Eq.(7.5), the number of elements in the random vector is $2N_\mathrm{s}$, while the vectors $\mathbf{M}_\mathfrak{n}$ and $\mathbf{\Sigma}_\mathfrak{n}$ contain the mean vector and the variance vector hosting the mean and variance of each random variable element of $\mathbf{n}$, which can be defined as

$$\begin{aligned} \mathbf{M}_\mathfrak{n} &= \mathbf{0}^{(2N_\mathrm{s})}; \quad D = 2N_\mathrm{s} \\ \mathbf{\Sigma}_\mathfrak{n} &= E\left((\mathbf{n} - \mathbf{M}_\mathfrak{n})(\mathbf{n} - \mathbf{M}_\mathfrak{n})^H\right) \\ &= E(\mathbf{n}\mathbf{n}^H) = \sigma_\mathfrak{n}^2 \mathbf{I}^{(2N_\mathrm{s})}, \end{aligned} \tag{7.6}$$

where $\mathbf{0}^{(2N_\mathrm{s})}$ and $\mathbf{I}^{(2N_\mathrm{s})}$ are the $(2N_\mathrm{s}\times 1)$-element zero-vector and the $(2N_\mathrm{s}\times 2N_\mathrm{s})$-element unity-matrix, respectively.

The spreading-code matrix $\mathbf{C}$ of Eq. (7.4) is known to the BS and during a specific STBC block interval, the CIR matrix $\mathbf{H}$ may be determined using channel estimation techniques. Hence, given the vector $\mathbf{v}$ in Eq. (7.4) a particular value $\mathbf{v}\in\mathbb{V}^{(2K)}$ for $i=1,2,\ldots,2^{2K}$, $\mathbf{r}$ in Eq. (7.1) equals to a random sample $\mathbf{n}$ plus a constant $\xi\mathbf{CHv}$. Hence, upon introducing another random vector variable $\mathfrak{r}$ for describing the conditional scenario of $(\mathbf{r}|\mathbf{C},\mathbf{H},\mathbf{v})$ or $(\mathbf{r}|\mathbf{H},\mathbf{v})$ for short, according to the properties of the complex-valued Gaussian random vector, the PDF of $\mathfrak{r}$ will have the same shape as that of $\mathfrak{n}$, with a mean of $\mathbf{M}_\mathfrak{r}=\mathbf{M}_\mathfrak{n}+\xi\mathbf{CHv}$ and a variance of $\mathbf{\Sigma}_\mathfrak{r}=\mathbf{\Sigma}_\mathfrak{n}$. Based on the above arguments related to Eq. (7.6), the conditional PDF can be formulated as

$$\begin{aligned} p(\mathbf{r}|\mathbf{H},\mathbf{v}) &= \frac{1}{\pi^D}\frac{\exp\left(-\frac{1}{2}(\mathbf{r}-\mathbf{M}_\mathfrak{r})^H 2\mathbf{\Sigma}_\mathfrak{r}^{-1}(\mathbf{r}-\mathbf{M}_\mathfrak{r})\right)}{\det(\mathbf{\Sigma}_\mathfrak{r})} \\ &= \frac{1}{(\pi\sigma_\mathfrak{n}^2)^{2N_s}}\exp\left(-\frac{1}{\sigma_\mathfrak{n}^2}\|\mathbf{r}-\xi\mathbf{CHv}\|^2\right). \end{aligned} \tag{7.7}$$

By assigning $M=2K$ in Eq. (7.4), as well as $\mathbf{v}=\mathbf{v}_{\kappa\pm,i}^{(2K)}$ and substituting them into Eq. (7.4) in conjunction with the conditional PDF of Eq. (7.7), the final form of the LLR calculated by the Bayesian detector is given by

$$\begin{aligned} l_\kappa^{\mathrm{BAY}} &= \ln\frac{\displaystyle\sum_{\mathbf{v}_{\kappa+,i}^{(2K)}\in\mathbb{V}_{\kappa+}^{(2K)}}\frac{1}{(\pi\sigma_N^2)^{2N_s}}\exp\left(-\frac{1}{\sigma_N^2}\|\mathbf{r}-\xi\mathbf{CHv}_{\kappa+,i}^{(2K)}\|^2\right)}{\displaystyle\sum_{\mathbf{v}_{\kappa-,i}^{(2K)}\in\mathbb{V}_{\kappa-}^{(2K)}}\frac{1}{(\pi\sigma_N^2)^{2N_s}}\exp\left(-\frac{1}{\sigma_N^2}\|\mathbf{r}-\xi\mathbf{CHv}_{\kappa-,i}^{(2K)}\|^2\right)} \\ &= \ln\frac{\displaystyle\sum_{\mathbf{v}_{\kappa+,i}^{(2K)}\in\mathbb{V}_{\kappa+}^{(2K)}}\exp\left(-\frac{1}{\sigma_\mathfrak{n}^2}\|\mathbf{r}-\xi\mathbf{CHv}_{\kappa+,i}^{(2K)}\|^2\right)}{\displaystyle\sum_{\mathbf{v}_{\kappa-,i}^{(2K)}\in\mathbb{V}_{\kappa-}^{(2K)}}\exp\left(-\frac{1}{\sigma_\mathfrak{n}^2}\|\mathbf{r}-\xi\mathbf{CHv}_{\kappa-,i}^{(2K)}\|^2\right)}, \\ & i=1,\ldots,2^{2K-1} \end{aligned} \tag{7.8}$$

for $\kappa=1,2,\ldots,K,\ldots,2K$. Observe in (7.8) that provided the optimum MUD is employed, computing $l_{k\imath}$ of the $\imath$th bit transmitted by the kth user requires the exhaustive evaluation of all the $\mathcal{M}=2^{2K}$ legitimate vectors. Hence, the associated complexity is on the order of $\mathcal{O}(2^{2K})$. By contrast, when using the ACO/ST-MUD, the LLRs $l_{k\imath}$ only have to be evaluated for a low number of legitimate vectors [212]. Hence, its complexity may be significantly lower than that of the optimum MUD. More quantitatively, recall from Eq. (6.21) that the LLRs are calculated as

$$\begin{aligned} l_\kappa^{\mathrm{ACO}} &= \ln\frac{\displaystyle\sum_{\tilde{\mathbf{x}}_{\kappa+,i}^{(2K)}\in\tilde{\mathbb{X}}_{\kappa+}^{(2K)}}\exp\left(-\frac{1}{\sigma_\mathfrak{n}^2}\|\mathbf{r}-\xi\mathbf{CH}\tilde{\mathbf{x}}_{\kappa+,i}^{(2K)}\|^2\right)}{\displaystyle\sum_{\tilde{\mathbf{x}}_{\kappa-,i}^{(2K)}\in\tilde{\mathbb{X}}_{\kappa-}^{(2K)}}\exp\left(-\frac{1}{\sigma_\mathfrak{n}^2}\|\mathbf{r}-\xi\mathbf{CH}\tilde{\mathbf{x}}_{\kappa-,i}^{(2K)}\|^2\right)}, \\ & i=1,\ldots,\tilde{x}_\kappa,\quad \tilde{x}_\kappa\ll 2^{2K-1}, \end{aligned} \tag{7.9}$$

by the ACO algorithm for $\kappa = 1, 2, \ldots, 2K$. In (7.9), $\tilde{\mathbf{x}}_{\kappa+,i}^{(2K)}$ and $\tilde{\mathbf{x}}_{\kappa-,i}^{(2K)}$ are $2K$-bit vectors having elements of $+1$ and -1, for $i = 1, \ldots, \tilde{x}_\kappa$, respectively, while $\tilde{\mathbb{X}}_{\kappa+}^{(2K)}$ and $\tilde{\mathbb{X}}_{\kappa-}^{(2K)}$ are the two sets hosting the two types of vectors that are used for computing the soft outputs and $\tilde{x}_\kappa = \sharp\tilde{\mathbb{X}}_{\kappa\pm}^{(2K)}$ is the number of vectors, i.e. the size of the corresponding two sets.

In the next sections, we will formulate the algorithm of maximizing the value of $\tilde{x}_\kappa$ and describe the generation of the search-pool $\tilde{\mathbb{X}}_{\kappa\pm}^{(2K)}$, while imposing a significantly lower complexity than that of the Bayesian detector.

7.3.2 Soft-Output ACO-based ST-MUD Algorithm

The soft-output ACO-based ST-MUD algorithm employs the HO ACO-based ST-MUD algorithm of Chapter 5 in order to generate the candidate pools $\tilde{\mathbb{X}}_{\kappa\pm}^{(2K)}$ of the proposed STBC-assisted twin-transmit antenna aided DS-CDMA system. The algorithmic steps are summarized in Table 7.1 and may be contrasted to the HO MUD of Chapter 5. Then, based on the two candidate pools $\tilde{\mathbb{X}}_{\kappa\pm}^{(2K)}$ that comprise all the vectors that will be used to calculate the value of l_κ^{ACO}, the LLR of the κth symbol will be calculated according to Eq. (7.9). Below, we will summarize the SO ACO-based ST-MUD algorithm using the flow-chart of Fig. 7.2.

Step 1	When the left-wing branch of the κth ACO-based search iteration is carried out, two of the entries constituting the kth column of the $(4 \times K)$-element route-table $\boldsymbol{\eta}$ will be set to zero, subject to $k = \lceil \kappa/2 \rceil$. The indeces of the two entries can be found in Eq. (7.10).
Step 2	When the left-wing of the κth ACO-based search iteration is carried out, two among the entries constituting the kth column of the $(4 \times K)$-element route-table $\boldsymbol{\eta}$ will be set to zero, subject to $k = \lceil \kappa/2 \rceil$. The indeces of the two entries can be found in Eq. (7.11).
Step 3&6	The compound table `L` or `D` are defined so that each row contains two compound elements: the $2K$-bit vector $\mathbf{x}_{\mathrm{L},i}^{(2K)} \in \mathbb{X}_{\mathrm{L}}^{(2K)}$ and the LLF function $\mathfrak{L}(\mathbf{x}_{\mathrm{L},i}^{(2K)})$ of it or the $2K$-bit vector $\mathbf{x}_{\mathrm{D},i}^{(2K)} \in \mathbb{X}_{\mathrm{D}}^{(2K)}$ and the Euclidean distance $\mathfrak{D}(\mathbf{x}_{\mathrm{D},i}^{(2K)})$ of it. Each $2K$-bit vector is different from all the other $2K$-bit vectors in the same table. Furthermore, $\sharp\mathbb{X}_{\mathrm{L}}$ or $\sharp\mathbb{X}_{\mathrm{D}}$ is the cardinality of set $\mathbb{X}_{\mathrm{L}}$ or $\mathbb{X}_{\mathrm{D}}$, which contains all the different $2K$-bit binary candidate-vectors whose LLFs or Euclidean distances have been calculated during the current STBC-block duration.
Step 4	$\top\tilde{x}_\kappa$ means the highest-ranked $\tilde{x}_\kappa$ number of elements in the ordered set $\tilde{\mathbf{x}}_\kappa^{\pm}$.
Step 5	$\delta = -[\sigma_{\mathbf{n}}^2]^{-1}$.
Step 7	$\tilde{x}_\kappa = \sharp\tilde{\mathbb{X}}_{\kappa+}^{(2K)} = \sharp\tilde{\mathbb{X}}_{\kappa-}^{(2K)}$ is the cardinality of the two sets $\tilde{\mathbb{X}}_{\kappa\pm}^{(2K)}$ having the same number of members.

Table 7.1: Detailed interpretation of each step in the SO ACO-based ST-MUD algorithms's flow chart of Fig. 7.2. The HO MUD's equivalent steps were summarized in Section 3.3.

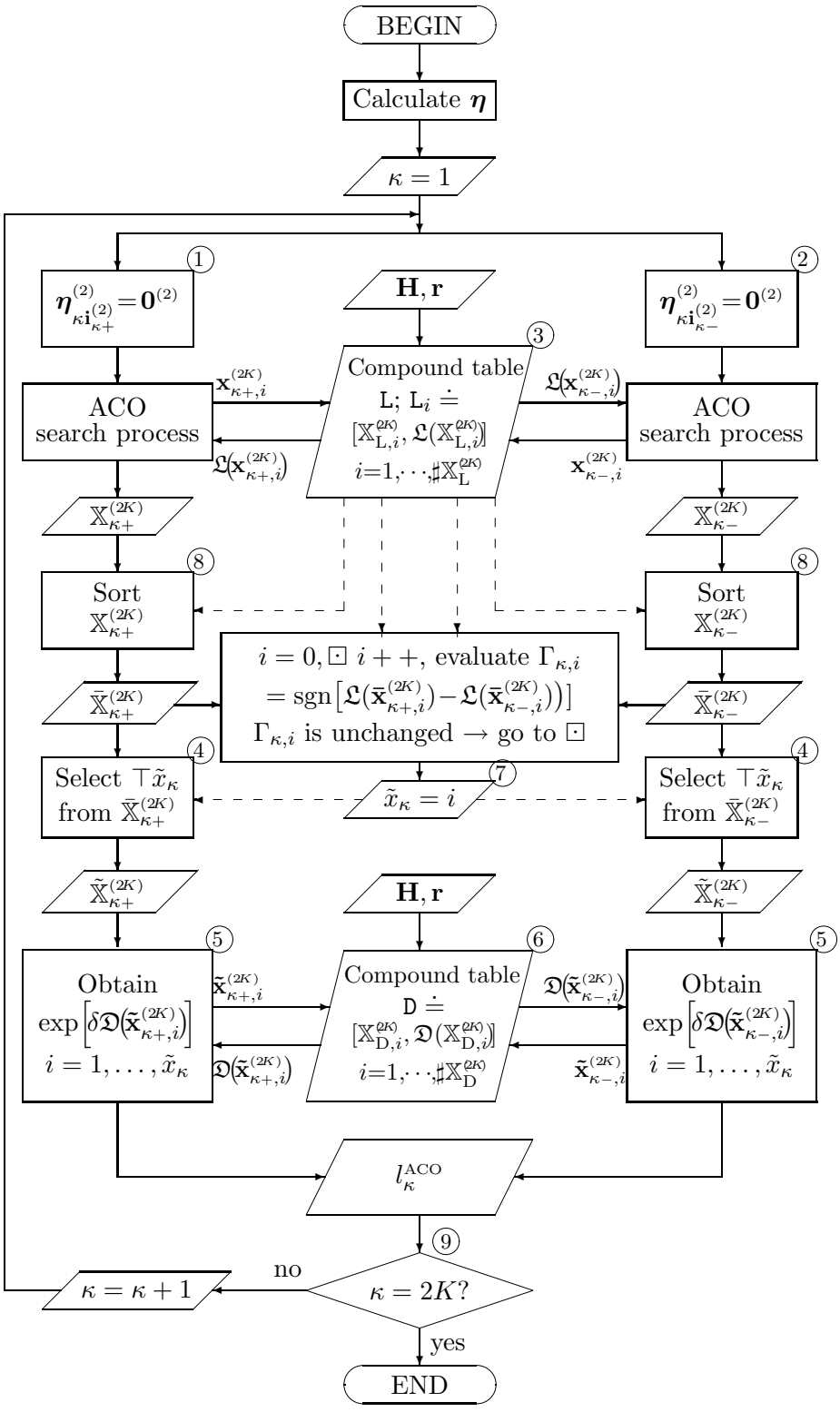

Figure 7.2: Flow-chart of the SO ACO-based ST-MUD algorithm. The corresponding HO flow-chart was detailed in Fig. 3.9.

The size of the route-table is determined by the two symbol-intervals of the STBC assisted system considered in this chapter, as seen in Table 7.2 for the equivalent HO system. Since two symbols are transmitted during each STBC signalling block, the number of rows has increased from two in Fig. 3.6

to four. Explicitly, the number of cells constituting each column of the route-table is determined by 2^M, where M represents the number of symbols transmitted by each individual user employing a specific spreading code.

Therefore, regardless of the number of antennas or antenna arrays employed by the receiver, in a single-transmit antenna aided system the route table employed by the ACO-based MUD algorithm has $(2 \times K)$ elements.

By contrast, when the two-transmit-antenna-aided $\mathcal{G}_2$ STBC is employed, where two symbols are transmitted per STBC signalling block, the size of the route table becomes $(4 \times K)$, despite using a single receive antenna in this chapter. The advantage of the *improved* ACO-based ST/MUD employing the $(4 \times K)$-element route-table of Table 7.2 over the *traditional* one employing the $(2 \times 2K)$-element route-table of Table 5.1 was demonstrated in Fig. 5.4 of Chapter 5.

i	$\mathbf{v}_i^{(2)T}$	$j=1$	$j=2$	$\cdots$	$j=K$
		$\mathbf{v}_1=[v_{11}\ v_{12}]^T$	$\mathbf{v}_2=[v_{21}\ v_{22}]^T$	$\cdots$	$\mathbf{v}_K=[v_{K1}\ v_{K2}]^T$
1	$[+1\ +1]$	$\mathbf{v}_1=\mathbf{v}_1^{(2)}$	$\mathbf{v}_2=\mathbf{v}_1^{(2)}$	$\cdots$	$\mathbf{v}_K=\mathbf{v}_1^{(2)}$
2	$[+1\ -1]$	$\mathbf{v}_1=\mathbf{v}_2^{(2)}$	$\mathbf{v}_2=\mathbf{v}_2^{(2)}$	$\cdots$	$\mathbf{v}_K=\mathbf{v}_2^{(2)}$
3	$[-1\ +1]$	$\mathbf{v}_1=\mathbf{v}_3^{(2)}$	$\mathbf{v}_2=\mathbf{v}_3^{(2)}$	$\cdots$	$\mathbf{v}_K=\mathbf{v}_3^{(2)}$
4	$[-1\ -1]$	$\mathbf{v}_1=\mathbf{v}_4^{(2)}$	$\mathbf{v}_2=\mathbf{v}_4^{(2)}$	$\cdots$	$\mathbf{v}_K=\mathbf{v}_4^{(2)}$

Table 7.2: $(4 \times K)$-element route-table of the MU STBC decoder employing the improved ACO algorithm, when the system supports K users and each MS is equipped with two transmit antennas.

As observed from Fig. 7.2, the major difference between the ACO-based SO MUD algorithm applied in the twin-transmit-antenna assisted STBC aided DS-CDMA UL and that applied in the SISO DS-CDMA UL is related to Steps 1 and 2, compared to Step 2 in Fig. 6.4. More explicitly, the $(4 \times K)$-element route-table replaces the original $(2 \times K)$-element route-table employed by the traditional ACO-based ST/MUD algorithm of Fig. 3.9 applied in the single-transmit antenna assisted DS-CDMA UL.

Furthermore, the number of elements in each vector of the search-pool $\mathbb{X}_{\kappa\pm}^{(2K)}$, as well as in the sorted search-pool $\bar{\mathbb{X}}_{\kappa\pm}^{(2K)}$ and in the final search-pool $\tilde{\mathbb{X}}_{\kappa\pm}^{(2K)}$ becomes $2K$ as well. Finally, the number of loops invoked to estimate all the LLRs associated with all the symbols transmitted within a STBC-block duration also becomes $2K$, as observed from Step 9 of Fig. 7.2.

The LLR values l_κ^{ACO} of the κth symbol, $\kappa = 1, 2 \ldots K \ldots 2K$, are evaluated in $2K$ consecutive loops of Fig. 7.2. However, the $(4 \times K)$-element intrinsic affinity matrix $\boldsymbol{\eta}$, whose value will be repeatedly used during the $2K$ loops of Fig. 7.2, will have to be evaluated before the first loop. In order to calculate the value of l_κ^{ACO}, the algorithm is carried out in two parallel branches associated with the κth symbol being $+1$ and -1, respectively. More specifically, both branches are carried out based on an updated $(4 \times K)$-element intrinsic affinity matrix $\boldsymbol{\eta}_{\kappa+}$ or $\boldsymbol{\eta}_{\kappa-}$, whose value has been obtained before the hard-output ACO search process was activated. As detailed in Steps 1-7 of Fig. 7.2, in order to ensure that the artificial ants generate K-bit vectors with the κth symbol being ± 1, the elements in $\boldsymbol{\eta}$ associated with the κth symbol being ∓ 1 have to be set to zero. Instead of setting only one entry in the $(2 \times K)$-element intrinsic affinity matrix $\boldsymbol{\eta}$ to zero, which is the case when the

system supports K users and employs only a single transmit antenna per user, now two entries of the $(4 \times K)$-element intrinsic affinity matrix $\boldsymbol{\eta}$ will be set to zero, because our K-user system employs two transmit antennas for each user with the aid of the $\mathcal{G}_2$ STBC code. More explicitly, the row-index vector $\mathbf{i}_{\kappa+}^{(2)}$ indicated in Step 1 within the left wing of Fig. 7.2 in order to activate the ACO-search that ultimately results in the numerator of Eq. (7.9) $\tilde{\mathbb{X}}_{\kappa+}^{(2K)}$ is stipulated by:

$$\mathbf{i}_{\kappa+}^{(2)} = \begin{cases} [3,4]^T & \text{if } 1 \equiv \kappa \pmod 2 \\ [2,4]^T & \text{if } 0 \equiv \kappa \pmod 2 \end{cases}. \tag{7.10}$$

By contrast, in order to obtain the set $\tilde{\mathbb{X}}_{\kappa-}^{(2K)}$ for calculating the denominator of Eq. (7.9), the row-index vector $\mathbf{i}_{\kappa-}^{(2)}$ used for resetting the intrisic affinity in Step 2 within the right wing of Fig. 7.2 is given as

$$\mathbf{i}_{\kappa-}^{(2)} = \begin{cases} [1,2]^T & \text{if } 1 \equiv \kappa \pmod 2 \\ [1,3]^T & \text{if } 0 \equiv \kappa \pmod 2 \end{cases}. \tag{7.11}$$

After this update, the search process will be activated based on the value of $\boldsymbol{\eta}_{\kappa\pm}$. The remaining details of calculating the probabilities associated with the entries of the route-table, the selection of the artificial ants, the pheromone update algorithms and the termination condition will not be repeated here, since they were detailed in Section 5.3.2 and in [130].

After the 'ACO search process' of Fig. 7.2 terminates, the search-pools $\mathbb{X}_{\kappa\pm}^{(2K)}$ generated by the two parallel search processes will continue in the 'Sort' and 'Select' blocks in order to generate the pools $\tilde{\mathbb{X}}_{\kappa\pm}^{(2K)}$, as detailed in Section 6.4.2 and in [212]. Given the two pools $\mathbb{X}_{\kappa\pm}^{(2K)}$, the Euclidean distance of each vector belonging to the sets $\mathbb{X}_{\kappa\pm}^{(2K)}$ may be obtained and then the resultant LLR value l_{κ}^{ACO} can be evaluated based on Eq. (7.9).

The two compound tables `L` and `D` seen in Fig. 7.2 store the LLF values and the Euclidean distances of the $2K$-bit vectors that have been generated by the artificial ants in the current STBC block duration. Recall that these tables were exemplified in Tables 6.8 and 6.9 for a HO scenario. More explicitly, the compound element in the first column of every row of the compound table `L` (or `D`) is a certain $2K$-bit vector, while the element of the second column records its LLF (or Euclidean distance) associated with that specific $2K$-bit vector. The $2K$-bit vector stored in each row of both tables is unique. These two compound tables are set up to reduce the computational complexity imposed. More specifically, a certain $2K$-bit vector may be captured by the search-pool more than once throughout the entire ACO-based search procedure, which is activated once per STBC block duration. However, the LLF or the Euclidean distance associated with any $2K$-bit vector does not have to be calculated more than once. By recording all the unique $2K$-bit vectors captured during a STBC block in `L` and `D`, the repeated calculation of the LLFs or Euclidean distances of the same $2K$-bit vector may be avoided. Additionally, all the contents in the two compound tables have to be cleared when the soft-output ACO-based STBC-MUD algorithm is concluded for a specific STBC block duration.

7.4 Performance Results

In this section, we consider the K-user DS-CDMA UL employing two transmit antennas and a single receive antenna in order to demonstrate the performance improvements achievd by the SO-ACO

based ST-MUD algorithm associated with the system proposed in Fig. 7.1. Again, the system of Fig. 7.1 employs a URC encoder, RSC encoder, STBC encoder and DS-CDMA spreading at each MS's transmitter in conjunction with the SO-ACO based ST-MUD and the per-user URC as well as RSC decoder at the BS's receiver. All simulation parameters are listed in Table 7.3.

System	Modem	BPSK
	Multiple access mothod	DS-CDMA
	Spreading code	Gold code
	Spreading factor	$N_s = 31$
	No. of transmit antennas	2
	No. of receive antennas	1
	No. of users	K=1, 10, 20, 32
	Channnel	Uncorrelated Rayleigh fading
RSC	Code rate	1/2
	Constraint length	3
	Feedback generator	5
	Feedforward generator	7
URC	Constraint length	2
	Feedback generator	3
	Feedforward generator	2
SO-ACO/ ST-MUD	Initial pheromone	$\tau = 0.01$
	Evaporation rate	$\rho = 0.5$
	Number of ants	$\zeta = 10$
	Number of iterations	$\Xi = 10$
	Weight of pheromone	$\alpha = 1$
	Weight of intrinsic affinity	$\beta = 6$
	Weight for the elite ant	$\sigma = 8$
Interleaver	Type	random
	size	N_c=2×10^1,10^2, 10^3,10^4 bits

Table 7.3: Parameters for the RSC-coded and URC precoded STBC-CDMA system employing the SO-ACO based ST-MUD algorithm.

7.4.1 Exit-band Charts

Fig. 7.3 depicts the EXIT chart [209] of the 1/2-rate RSC outer code as well as of the URC precoded STBC assisted DS-CDMA spread K-user system employing the SO-ACO based ST-MUD aided URC inner code associated with the parameters outlined in Table 7.3 for different E_b/N_0 values. As detailed

E_b/N_0 (dB)	Total No. of iterations	No. of successfully decoded frames out of 100
1.7	100	0
1.8	100	4
1.9	100	9
2.0	100	56
2.1	100	86
2.2	50	99
2.3	50	100
2.5	10	100

Table 7.4: The number of successfully decoded frames out of 100 frames after a sufficiently high number of iterative extrinsic information exchanges between the URC and the RSC decoders at different E_b/N_0 values for the system of Fig. 7.1 using the parameters of Table 7.3 in conjunction with $N_u = 10,000$ bits, when the system supports $K = 1$ user.

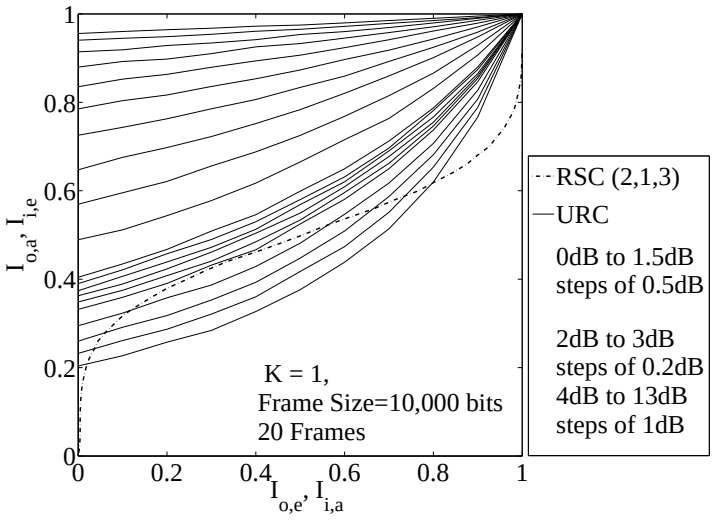

Figure 7.3: EXIT chart of the outer and inner decoders of the system. The EXIT chart of the inner decoder was recorded for E_b/N_0 values ranging from 0dB to 13dB. Each input frame of the outer codec has a length of $N_u = 10,000$ bits and that of the inner codec has a length of $N_c = 20,000$ bits.

in [203], the URC codec is used for ensuring that the EXIT chart of the inner code reaches the $(1, 1)$ point of perfect convergence, which corresponds to vanishingly low BER. In order to ensure that the exchange of extrinsic information between the inner decoder and the outer decoder allows convergence to the $(1, 1)$ point at a specific E_b/N_0 value, the EXIT curve of the inner and outer decoder should not intersect before approaching the $I_{o,e} = 1.0$ vertical line. Provided that this condition is satisfied, an open tunnel should appear in the EXIT chart. Moreover, the number of turbo detection iterations required by the system to approach the $(1, 1)$ point is expected to be increasingly higher, as the open tunnel is getting narrower. As observed from Fig. 7.3, an open EXIT tunnel emerges at $E_b/N_0 = 2$dB.

However, as seen from the BER versus E_b/N_0 curves displayed in Fig. 7.13, the BER does not

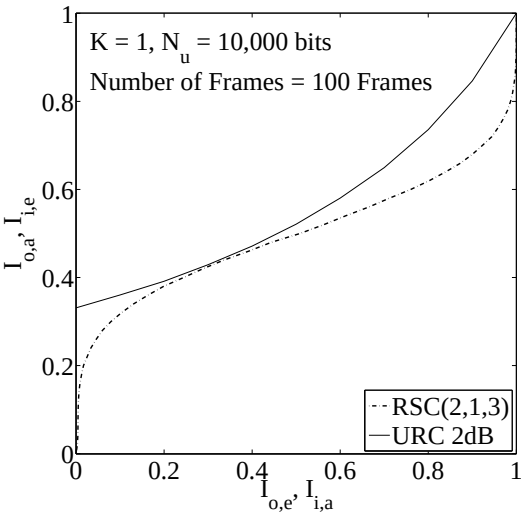

Figure 7.4: EXIT chart of the outer and inner decoders of the system investigated at $E_b/N_0 = 2$ dB. Each input frame of the outer codec has a length of $N_u = 10,000$ bits and that of the inner codec has a length of $N_c = 20,000$ bits.

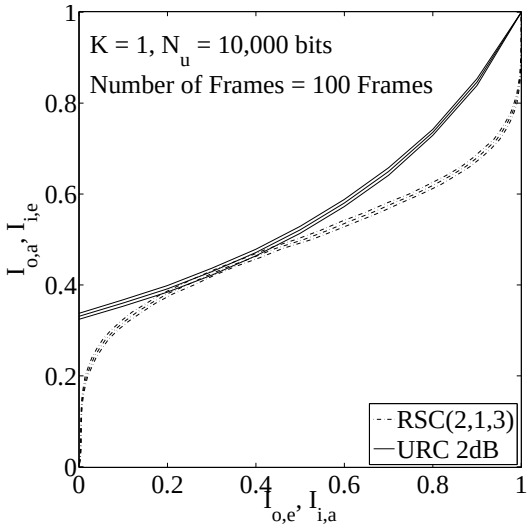

Figure 7.5: EXIT chart of the outer and inner decoders of the system investigated at $E_b/N_0 = 2$ dB. Each input frame of the outer codec has a length of $N_u = 10,000$ bits and that of the inner codec has a length of $N_c = 20,000$ bits.

become infinitesimally low at $E_b/N_0 = 2.0$ dB, it is 10^{-1} after 10 iterations of exchanging the extrinsic information between the RSC and the URC decoders.

This mismatch between the BER versus E_b/N_0 curves of Fig. 7.13, Fig. 7.14 and the EXIT-chart seen in Fig. 7.3 is a consequence of the limited interleaver length of $N_c = 20,000$ bits. More specifically, the output extrinsic MI value used to plot the EXIT-curves of the URC as well as of the RSC in Fig. 7.3 is actually the mean MI averaged over 20 frames. Since the interleaver length is limited, both the per-frame-BER and the MI varies between different frames. Therefore, as demonstrated in Table 7.4 for specific E_b/N_0 values, some of the decoded frames become error-free after a given number of iterations, while others cannot be successfully decoded.

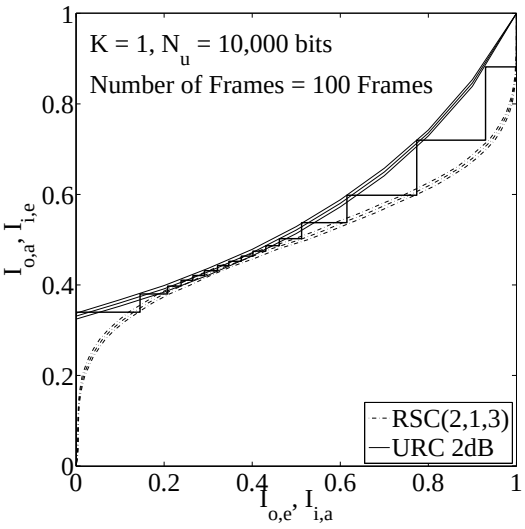

Figure 7.6: Decoding trajectory of the iteratively detected RSC-coded and URC-precoded STBC-CDMA system employing the SO-ACO based ST/MUD associated for a particular transmitted frame at $E_b/N_0 = 2$ dB, when reaching the $(1, 1)$ point of the EXIT chart.

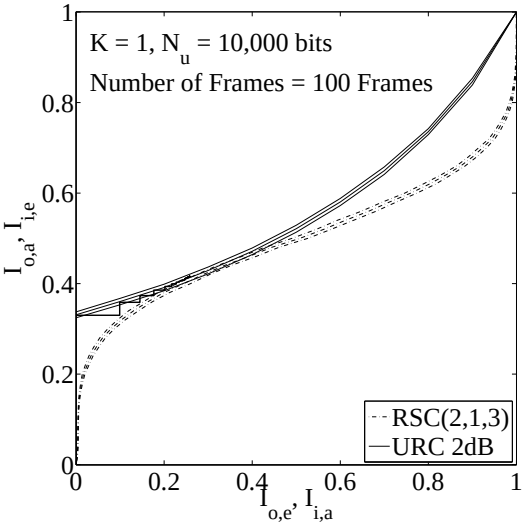

Figure 7.7: Decoding trajectory of the iteratively detected RSC-coded and URC-precoded STBC-CDMA system employing the SO-ACO based ST/MUD associated for a particular transmitted frame at $E_b/N_0 = 2$ dB, when failing to reach the $(1, 1)$ point of the EXIT chart.

In order to predict the E_b/N_0 required by a particular system to reach an infinitesimally low BER after the affordable number of iterations, while assuming a limited interleaver length, EXIT-band-chart [210] are introduced.

Before introducing the EXIT-band-chart philosophy, let us briefly review the methodology of plotting an EXIT curve. Any EXIT-chart curve is constituted by consecutively connecting N_{MI} points, whose x-coordinate values quantify the input MI value ranging from '0.00' to '1.00'. As exemplified by any of the solid curves in Fig. 7.3 or Fig. 7.4, we have $N_{\text{MI}} = 11$, corresponding to the input MI values for the 11 points characterizing each curve ranging from 0.00 to 1.00, incremented by 0.1. When considering N_{f} frames transmitted in order to obtain a specific point of an EXIT-chart curve, even

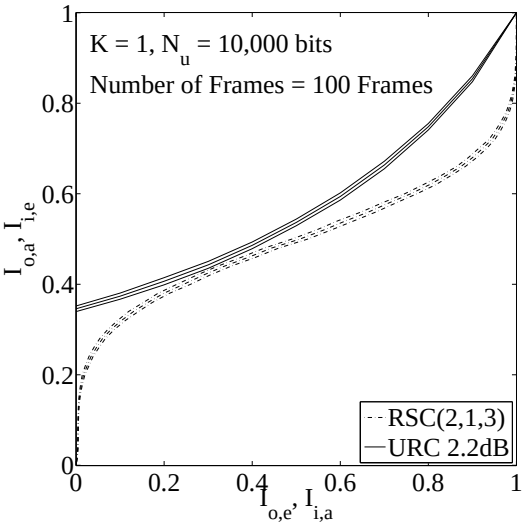

Figure 7.8: EXIT chart of the inner and outer decoders of the system investigated at $E_b/N_0 = 2.2$ dB. Each input frame of the outer codec has a length of $N_u = 10,000$ bits and that of the inner codec has a length of $N_c = 20,000$ bits.

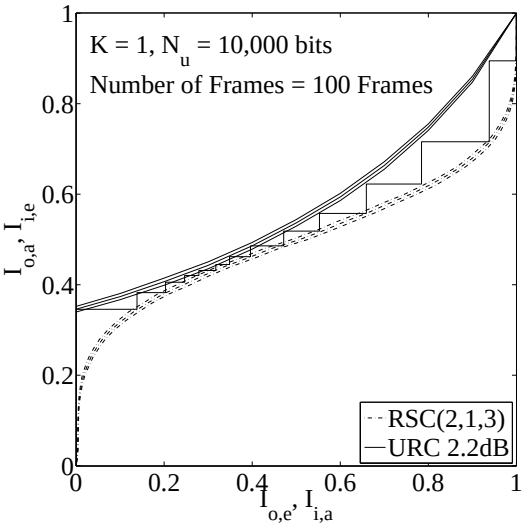

Figure 7.9: Decoding trajectory of the iteratively detected RSC-coded and URC-precoded STBC-CDMA system employing the SO-ACO based ST/MUD associated for a particular transmitted frame at $E_b/N_0 = 2.2$ dB, when reaching the $(1, 1)$ point of the EXIT chart.

when the input MI values of all the N_f transmitted frames are identical, the output MI values of the N_f frames are expected to be different. The y-coordinate of any point characterizing a single EXIT-curve is the mean value generated by averaging over the N_f different output MI values associated with the N_f transmitted frames. More specifically, given the x-coordinate of the ith point characterizing an EXIT-curve as the input MI value of

$$x_i^{\text{EXIT}} = M_i^{\text{in}} = (i-1) \times \frac{1}{N_{\text{MI}}}, \tag{7.12}$$

the corresponding y-coordinate of the ith point may be expressed as

$$y_i^{\text{EXIT}} = \mu_i = \frac{1}{N_f} \sum_{n_f=1}^{N_f} M_{i,n_f}^{\text{out}}, \tag{7.13}$$

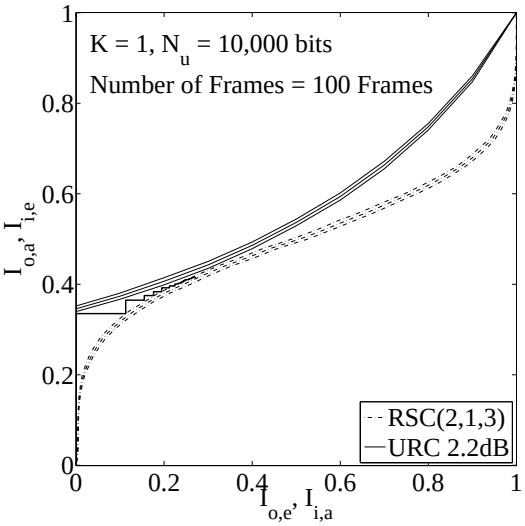

Figure 7.10: Decoding trajectory of the iteratively detected RSC-coded and URC-precoded STBC-CDMA system employing the SO-ACO based ST/MUD associated for a particular transmitted frame at $E_b/N_0 = 2.2$ dB, when failing to reach the $(1, 1)$ point of the EXIT chart.

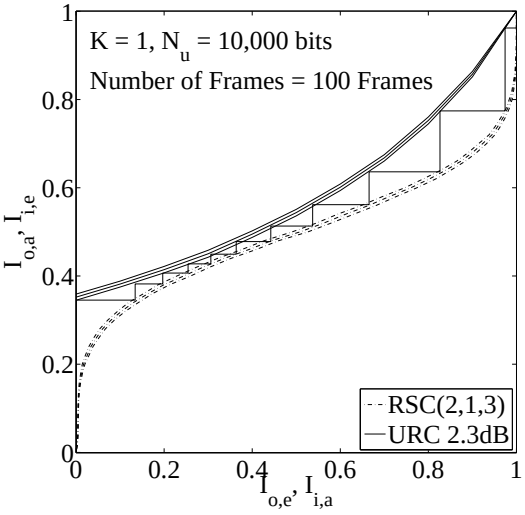

Figure 7.11: Decoding trajectory of the iteratively detected RSC-coded and URC-precoded STBC-CDMA system employing the SO-ACO based ST/MUD associated for a particular transmitted frame at $E_b/N_0 = 2.3$ dB, when reaching the $(1, 1)$ point of the EXIT chart.

where M_{i,n_f} represents the output MI associated with the n_fth frame at the input MI quantified by Eq. (7.12).

However, when the frame size N_c quantifying the number of bits constituting each of the N_f frames is insufficiently long, the deviation among the N_f output MI values associated with the N_f frames becomes high and hence using the mean μ_i of the N_f values is inaccurate in characterizing the distribution of the N_f output MI values.

Against this background, the EXIT-band chart philosophy was proposed [210] in order to consider not only the mean value of the N_f output MI values, but also their standard deviation. As a result, the EXIT-band chart curves more comprehensively characterize the N_f output MI values associated with the N_f transmitted frames at any given input MI value. Hence a more accurate performance

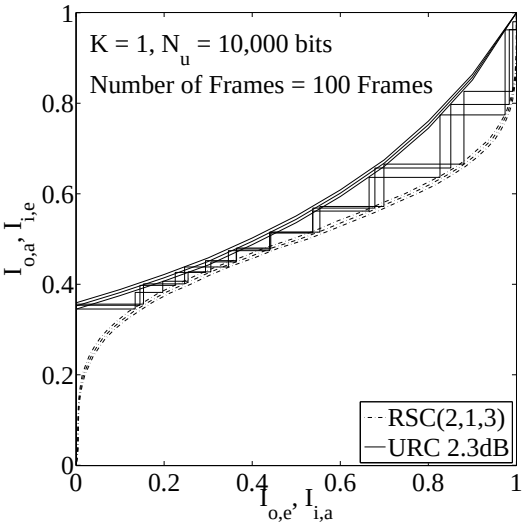

Figure 7.12: Three different decoding trajectories of the iteratively detected RSC-coded and URC-precoded STBC-CDMA system employing the SO-ACO based ST/MUD for three different frames at $E_b/N_0 = 2.3$dB.

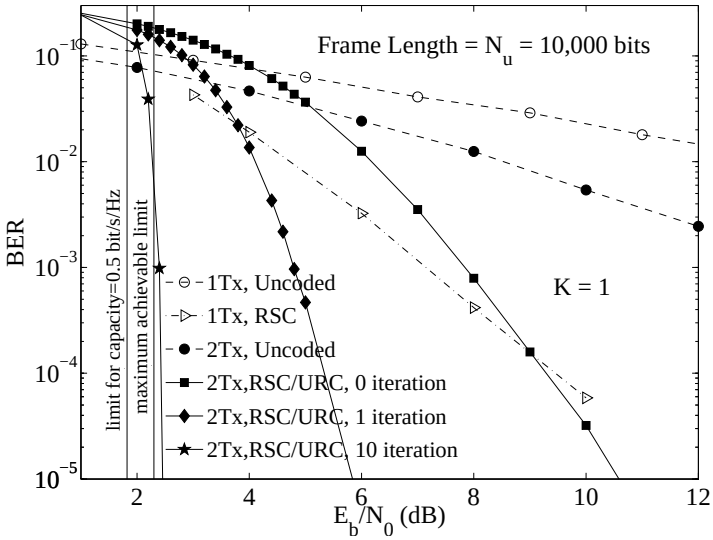

Figure 7.13: Performance comparison of the URC-precoded and non-precoded RSC-coded twin-antenna-aided or single-antenna aided DS-CDMA system, when a single user is supported and the SO-ACO based ST/MUD algorithm is employed using the system parameters outlined in Table 7.3. The interleaver length was $N_c = 20,000$ bits, where the 1/2 rate RSC code was employed to encode every input frame having a length of $N_u = 10,000$ bits.

prediction may be expected. More concretely, the EXIT-band-chart curves associated with a decoder at a specific E_b/N_0 value is constituted by three curves, namely the mean MI outputs as well as the mean MI outputs plus the standard deviations and the mean MI outputs minus the standard deviations, respectively. More quantitatively, for any index value $i = 1, 2, \ldots, N_{MI}$, the standard deviation σ_i of the N_f output MI values at the input MI value quantified by Eq. 7.12 may be formulated as

$$\sigma_i = \sqrt{\sum_{f=1}^{N_f} \frac{(x_f - \mu_i)^2}{N_f}}, \quad i = 1, 2, \ldots, N_{MI}. \tag{7.14}$$

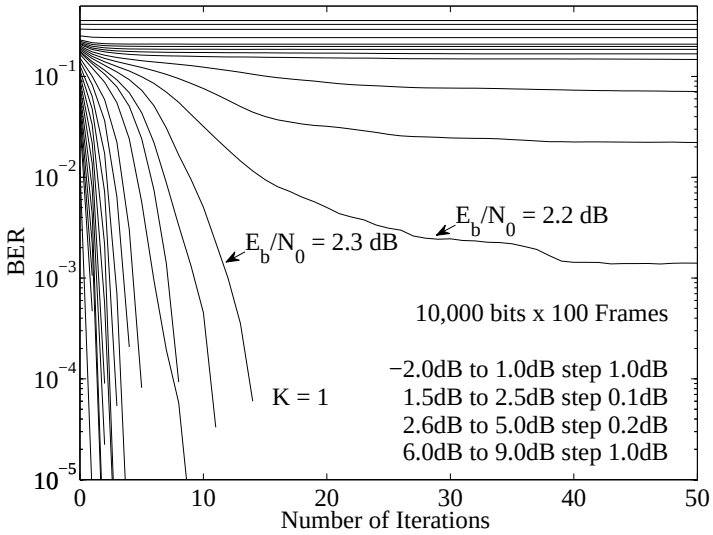

Figure 7.14: Performance comparison of the single-user URC-precoded RSC-coded twin-antenna-aided STBC-CDMA system employing the SO/ACO based ST-MUD algorithm at different E_b/N_0 values plotted versus the number of iterations exchanging extrinsic information between the URC and the RSC decoders, when the length of the information source frame was $N_u = 10,000$ bits and the interleaver length was $N_c = 20,000$ bits.

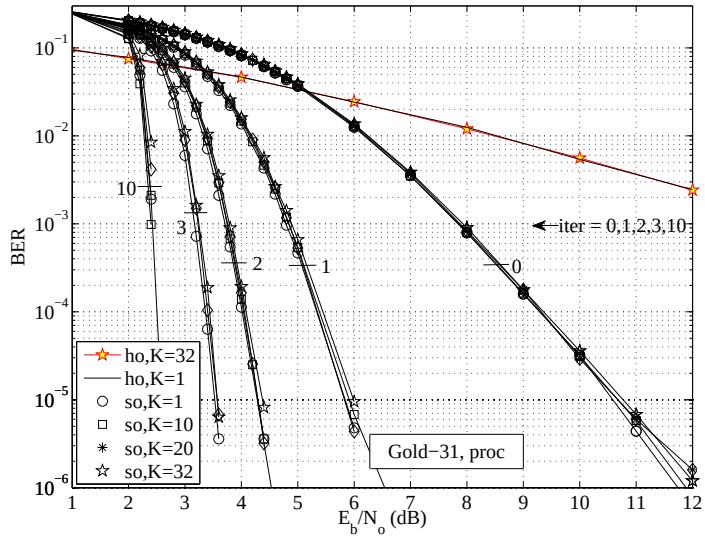

Figure 7.15: Performance comparison of the URC-precoded and non-precoded RSC-coded twin-antenna-aided or single-antenna aided DS-CDMA system, when $K = 1$, 10, 20 and 32 users are supported and the SO-ACO based ST/MUD algorithm is employed using the system parameters outlined in Table 7.3. The interleaver length was $N_c = 20,000$ bits, where the 1/2 rate RSC code was employed to encode every input frame having a length of $N_u = 10,000$ bits.

Then, at a given input MI quantified by

$$x_i^{\text{EXIT-band}} = M_i^{\text{in}} = (i-1) \times \frac{1}{N_{\text{MI}}}, \tag{7.15}$$

we record the y-coordinate value $y_{i,1}^{\text{EXIT-band}}$ representing the average output MI quantified by

$$y_{i,1}^{\text{EXIT-band}} = \mu_i = \frac{1}{N_f} \sum_{n_f=1}^{N_f} M_{i,n_f}^{\text{out}}, \tag{7.16}$$

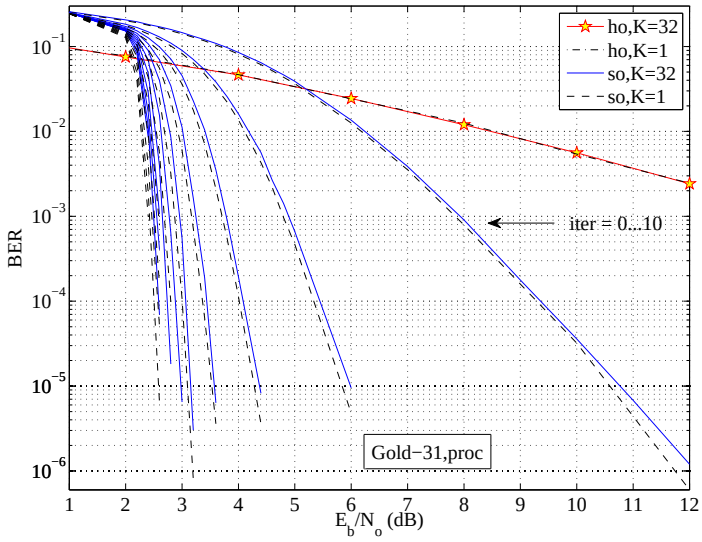

Figure 7.16: Performance comparison of the URC-precoded and non-precoded RSC-coded twin-antenna-aided or single-antenna aided DS-CDMA system, when $K = 1$ and 32 users are supported and the SO-ACO based ST/MUD algorithm is employed using the system parameters outlined in Table 7.3. The interleaver length was $N_c = 20,000$ bits, where the 1/2 rate RSC code was employed to encode every input frame having a length of $N_u = 10,000$ bits.

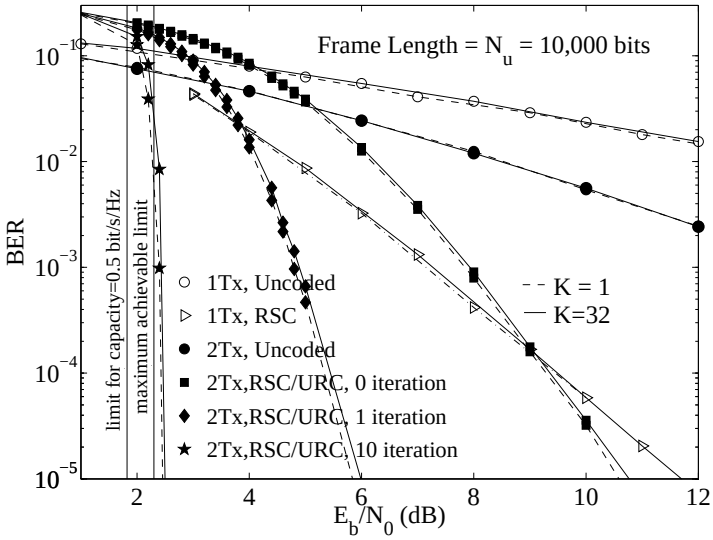

Figure 7.17: Performance comparison of the URC-precoded and non-precoded RSC-coded twin-antenna-aided or single-antenna aided DS-CDMA system for $K = 1$ and $K = 32$ users supported by the system employing the SO-ACO based ST/MUD algorithm and using the system parameters outlined in Table 7.3. The interleaver length was $N_c = 20,000$ bits, and the 1/2 rate RSC code was employed to encode every input frame having a length of $N_u = 10,000$ bits.

as well as the y-coordinates $y_{i,2}^{\text{EXIT-band}}$ $y_{i,3}^{\text{EXIT-band}}$ given by the above-mentioned mean value plus and minus the standard deviation σ_i, respectively. More quantitatively, we have

$$\begin{aligned} y_{i,2}^{\text{EXIT-band}} &= \mu_i + \sigma_i; \\ y_{i,3}^{\text{EXIT-band}} &= \mu_i - \sigma_i. \end{aligned} \tag{7.17}$$

Then the curves constituting the three-curve EXIT-band chart characterizing the output MI values of a codec at different input MI values ranging from 0.00 to 1.00 are plotted by connecting the N_{MI}

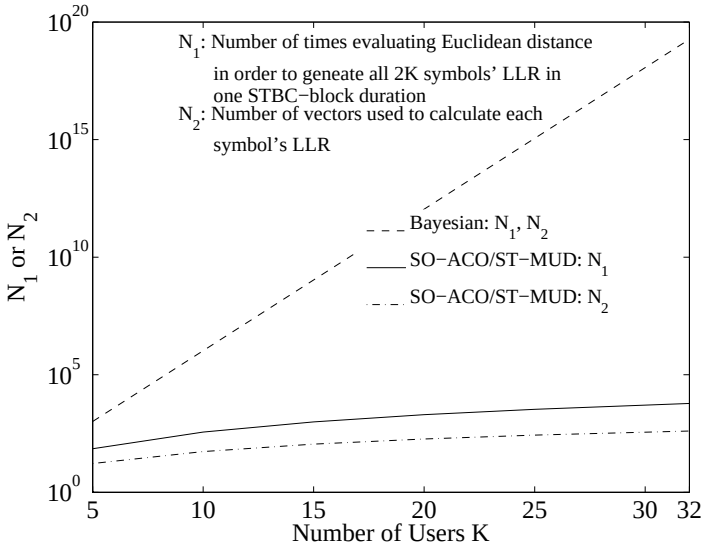

Figure 7.18: Complexity comparison of the SO-ACO based ST-MUD algorithm and of the Bayesian algorithm plotted versus the number of users supported by the twin-antenna-aided system.

points $y_{i,j}^{\text{EXIT-band}}$ at the integer index values i ranging from 1 to N_{MI}, for $j = 1$, 2 and 3, respectively.

In contrast to the EXIT-chart of Figs. 7.3 and 7.4, the EXIT-band-charts shown in Fig. 7.5 to Fig. 7.11 more accurately predict the BER trends of Fig. 7.13 and Fig. 7.14. Observe that a narrow but open tunnel can be seen between the URC's and of the RSC's EXIT curve in Fig. 7.4 at $E_{\text{b}}/N_0 = 2.0$ dB. Moreover, our informal investigations characterized in the fourth row of Table 7.4 suggest that 56 out of 100 frames allow the decoder to arrive at the $I_{\text{e,o}} = 1$ line. The Monte-Carlo simulation based decoding trajectory of one of the 56 successfully decoded frames is displayed in Fig. 7.6, while that of an unsuccessfully decoded frame is plotted in Fig. 7.7.

Secondly, as seen in Fig. 7.8, the URC EXIT-band-chart curve recorded at $E_{\text{b}}/N_0 = 2.2$ dB only 'just' intersects the RSC's EXIT-band-chart curve. We might define a marginally open tunnel as the one that allows 99% of the decoded frames to pass through the tunnel, as characterized in the sixth row of Table 7.4. The Monte-Carlo simulation based decoding trajectories of a frame passing through and that of a frame failing to get through the middle of the tunnel are plotted in Fig. 7.9 and Fig. 7.10, respectively.

By contrast, the tunnel becomes widely open in Fig. 7.11, when E_{b}/N_0 is increased from 2.2 dB to 2.3 dB. As a result, when the system parameters of Table 7.3 are used in conjunction with $N_{\text{u}} = 10,000$ bits and $K = 1$ user, all frames transmitted at $E_{\text{b}}/N_0 = 2.3$ dB can be error-freely detected at the receiver after iteratively exchanging extrinsic information between the URC decoder and the RSC decoder a certain number of times. The above-mentioned phenomenon is in agreement with the trends shown in Fig. 7.14, where error floors have been observed, when the E_{b}/N_0 value was below 2.2 dB.

7.4.2 BER performance

As seen from Fig. 7.14, when the E_{b}/N_0 value is lower than 2.3 dB, regardless of how many iterations are carried out to exchange extrinsic information between the URC and RSC decoder, a BER-floor

emerges. As observed from Fig. 7.14, the BER is reduced upon increasing the E_b/N_0 values and beyond 2.3 dB the error floor disappears. Naturally, this E_b/N_0 value is above the capacity limit, and the actually encountered E_b/N_0 distance from capacity depends on the specific parameters of the RSC and URC coding schemes.

The BER versus E_b/N_0 curves of the STBC assisted twin-transmit-antenna aided DS-CDMA system supporting $K = 1$ and $K = 32$ users are plotted in Fig. 7.16, where the extrinsic information is exchanged 1∼10 times between the URC and RCS decoder of each user at the BS. As seen from Fig. 7.16, when the number of iterations increases, the BER performance of the system is dramatically improved. However, the incremental E_b/N_0 gain is gradually decreased, when the number of turbo iterations increases from $I = 1$ to 10.

It may also be observed from Figs. 7.15 and 7.16 that no BER degradation is observed upon increasing the number of users from $K = 1$ to 32.

We found that the E_b/N_0 threshold required for the proposed system using the parameters of Table 7.4 in conjunction with $N_u = 10,000$ bits and $K = 1$ user to operate near the capacity of 0.5 bit/s/Hz is 2.3 dB, which is represented by the vertical line indicating the 'maximum achievable rate limit' in Fig. 7.13. As observed from Fig. 7.13, for 10 iterations, the BER versus E_b/N_0 curves diverge from the maximum achievable rate limit by as little as 0.1 dB.

7.4.3 Complexity Calculation

As observed from Fig. 7.17, when $K = 32$ users are supported by the system employing the parameters of Table 7.3, the BER performance of the $K = 32$-user system approaches that of the single-user system with a degradation of less than 0.01 dB. However, the complexity of the SO-ACO based ST-MUD algorithm that detects the $2 \times 32 = 64$ symbols transmitted by the $K = 32$ users within each STBC-block duration is significantly lower than that of the optimal Bayesian algorithm. More quantitatively, the number of Euclidean distance evaluations imposed by the SO-ACO based ST-MUD algorithm within a STBC-block duration for $K = 32$ users is as low as about 10^3, which is a fraction of 10^{-17} compared to the 10^{20} evaluations required by the Bayesian algorithm.

7.5 Conclusions

In this chapter, we have proposed a URC precoded, 1/2-rate RSC and STBC coded three-stage concatenated multiuser DS-CDMA system, where each user is equipped with a twin-transmit-antenna, which enables each user to achieve an effective throughput of 0.5 bit/s/Hz within about 0.5 dB of the single-user E_b/N_0 limit. EXIT-band-charts have been used to accurately predict the minimum tolerable E_b/N_0 level required by the system to approach capacity at a given interleaver length. The EXIT-band-charts of Fig. 7.11 guaranteed a better BER predicition, compared to the traditional EXIT-charts. More specifically, when using 10 iterations between the URC and RSC soft-decoders, the system becomes capable of achieving an infinitesimally low BER at E_b/N_0 values that are only about 0.05 dB higher than what was predicted by the EXIT-band-charts. The achievable BER performance as well as the prediction accuracy of the EXIT-band-chart have been investigated, when the frame length was varied from $N_u = 10$ bits, 100 bits, 1,000bits and finally to 10,000 bits.

The following observations can be made from the results obtained from the simulations. Firstly, a second-order diversity gain has been achieved by the twin-transmit-antenna system. Additionally, by employing the proposed SO-ACO based ST/MUD at the receiver in conjunction with Gold-codes having a length of 31 chips, up to $K = 32$ users may be supported at a trivially increased E_b/N_0 requirement, while achieving the same BER performance as the single user system employing the same number of iterations. The system's complexity was about 10^{17} lower than that of the Bayesian detector for the specific scenario considered.

Chapter 8

Conclusions and Future Work

In this concluding chapter, a summary of the thesis and the main findings of our investigations will be presented. This will be followed by a range of ideas on future research.

8.1 Summary and Conclusions

8.1.1 System Characteristics

In this subsection, we will compare the different systems investigated, namely the MC DS-CDMA of Chapter 4, the MFAA assisted MC DS-CDMA of Chapter 4, the STBC aided DS-CDMA of Chapter 5 and the STBC assisted three-stage concatenated RSC as well as URC coded turbo iteratively decoded DS-CDMA UL of Chapter 7.

The main characteristics of the four systems are outlined in Table 8.1, including their bandwidth requirements, spreading code, the number of transmit/receive antennas, delay, the normalized throughput, as well as the transmitter and receiver schematic. Some of these characteristics are further detailed in the forthcoming sections.

For example, if the system is not strictly band-limited, then the achievable transmission rate may be increased by employing parallel subcarriers. Provided that each subcarrier's signal is spread over all subcarriers and that the subcarriers fade independently, a substantial frequency diversity gain may be achieved, which may significantly reduce the system's BER and/or increase the number of users supported by the system.

Additionally, if we employ several transmit and/or receive antennas, or MFAAs, a higher-order diversity gain and beamforming gain will be attained.

8.1.1.1 Frequency Resources

More quantitatively, when the MC DS-CDMA system class II [93] of Chapter 4 is considered, V subcarriers are used, each of which has a bandwidth of f_c. Therefore, a diversity order of V is achieved at the price of a V-fold transmission bandwidth expansion, provided that the subcarriers are sufficiently far apart to experience independent fading. It is worth emphasizing however that given a

		MC	MFAA	STBC	STBC+turbo
RESOURCES	Normalized Bandwidth	V	UV	1	1
		Vth-order diversity gain	U: Subcarrier symbol duration $T_b \rightarrow UT_b$ V: Vth-order transmit diversity gain Subcarrier-power is $1/V$		
	Spreading Code	31	31	31	31
		$K = 32$ users	$K = 32$ users	$K = 32$ users	$K = 32$ users
	Number of Antennas	1 Tx 1 Rx	1 Tx N_r number of L-element Rx	2 Tx 1 Rx	2 Tx 1 Rx
			N_r: N_rth-order receive diversity gain L: Lth-order array gain	2nd order diversity gain	2nd order diversity gain
Delay		0	UT_b	$2T_b$	$N_cT_b + 2N_iN_cT_d$ ①
BER		Fig. 4.9	Fig. 4.11	Figs. 5.4, 5.7	Fig. 7.16
Transmitter Scheme		Figs. 4.2, 4.4	Figs. 4.2, 4.4	Fig. 5.1(a)	Fig. 7.1(a)
Receiver Scheme		Figs. 4.7, 4.8 N_r=U=L=1	Figs. 4.7, 4.8	Fig. 5.1(b)	Fig. 7.1(b)

① T_d: Time required by URC or RSC for obtaining soft-output per trellis state.

① N_i: Number of turbo decoding iterations.

Table 8.1: Characteristics of the multiuser schemes investigated.

fixed total power, the transmit diversity gain achieved upon sharing the power across V subcarriers is expected to be lower than the receive-diversity gain of V receiver antennas, for example.

Observe in the second cell of the first row of Table 8.1 that a UV-fold bandwidth expansion was required by the MFAA system of Chapter 4. More explicitly, in the system schematic of Fig. 4.2, UV subcarriers having a bandwidth of UVf_c were invoked for transmitting U symbols per user. Each symbol was spread to V subcarriers, but this does not lead to a V-fold reduced throughput, if V

spreading codes are stacked up in parallel in the FD.

When we have $V = 1$ for example, the duration of the U subcarrier symbols is expanded by a factor of U. Given that the symbol duration in a single-carrier system is T_b, the multi-carrier system's symbol duration becomes $U \times T_b$. We may argue that we transmit U original serial symbols by mapping each one of them to U orthogonal subcarriers, which extends their time duration by a factor of U, as seen in the first row of Table 8.1.

Again, when we activate V subcarriers to transmit a single symbol, a Vth order diversity gain can be expected in exchange for a V-fold increased bandwidth. Naturally, the power assigned to each of the V subcarriers is limited to a fraction of $1/V$ of the total power, as seen in the second column of the first row in Table 8.1.

8.1.1.2 Spreading Codes

The specific choice of the spreading codes plays a crucial role in characterizing the overall system performance, as detailed in [17, 93]. When for example orthogonal Walsh-Hadamard (WH) codes are used, the maximum number of users that may be supported is $K = N_s$, where N_s is the spreading factor. By contrast, when employing non-orthogonal codes, such as those used in this thesis, more than N_s users may be supported at the costs of encountering more substantial MUI even for transmission over non-dispersive channels. Hence non-orthogonal codes typically require powerful MUDs, such as those designed in this thesis.

By assigning a unique user-specific spreading code having a length of $N_s = 31$ chips, a maximum of $K = 32$ users were supported by the system. Provided that the received signal is detected by the appropriate MUD algorithms, the BER performance of the 'MC', 'MFAA', 'STBC', 'STBC+turbo' systems of Chapters 4, Chapter 5, and 7 supporting 32 users was capable of approaching the single-user system's BER performance.

8.1.1.3 The Number of Antennas

MIMO techniques were detailed in [203], for example. When the distances between the adjacent antennas or antenna arrays is sufficiently high to facilitate the independent fading of their signals, then a commensurate diversity gain is achieved. Hence, when we have N_r receive antenna arrays, as proposed in the MFAA system of Chapter 4, a N_rth-order receive diversity gain can be achieved.

By contrast, the L $\lambda/2$-spaced beamforming elements are unable to provide a receive diversity gain, since the distance between any two adjacent elements is insufficient to induce independent fading. Indeed, having a spacing of $\lambda/2$ results in signals having a phase rotation of π, since λ corresponds to 2π. However, the receiver array elements collect the signals arriving from the same direction and the power of the received signal is expected to be increased upon increasing L. Hence a Lth order array gain is achieved by the L elements of an antenna array, as observed from the lower part of the third row in Table 8.1.

8.1.1.4 Transeiver Schematic and Performance

All the above-mentioned four systems were investigated, when supporting $K = 32$ users. The key challenge was that of designing ACO-based MUD algorithms capable of approaching the single user performance at an affordable complexity. The indices of the figures portraying the schematics as well as the associated salient performance characteristics are also summarized in Table 8.1.

8.1.2 MUD Algorithm Design

8.1.2.1 Generic MUD Algorithm

Table 8.2 outlines all the matrices as well as the key inputs, the *a priori* known, as well as the calculated intermediate variables and the final outputs, in terms of the MUD algorithm.

As observed in Table 8.2, the definition of these variables is determined by the different system parameters in the context of their different system scenarios. These variables are defined for a single detection-window duration, which may contain a single symbol interval for detecting one symbol per user as in the MC system of Chapter 4, or may contain U symbol intervals for detecting U symbols per user in the MFAA system of Chapter 4, or alternatively, two symbol intervals for detecting two symbols per user, as in the STBC or STBC+turbo system of Chapter 7.

The notations used in Table 8.2 are defined as follows. Firstly, the notation exemplified by $(K \times K) \times \{V\}$, indicates that the variable listed in the first column of the row considered is a $(K \times K)$-element matrix in the context of the system characterized in the current column. Furthermore, V *different* versions of that matrix having different entries for each version are invoked during a specific detection window of the MUD algorithm. Hence the variable V in braces indicates that V *different* matrices are invoked. By contrast, the notations obeying the form $(K \times K) \times [V]$ indicate that the V copies of the $(K \times K)$-element matrix considered in the current system is repeated V times with identical entries. Additionally, the numbers in the round brackets indicate the size of the matrix involved in the equation immediately below.

As seen from the first row of Table 8.2, the received signal vector $\mathbf{r}$ of all the four K-user systems has as many elements as the number of chips constituting a detection window, which is N_s, when no STBC is employed and $2N_\mathrm{s}$, when the $\mathcal{G}_2$ STBC scheme is used.

Still referring to Table 8.2, except for $\mathbf{r}$ and $\mathbf{C}$, the size of all the other matrices namely of $\mathbf{H}$, $\mathbf{y}$, $\mathbf{R}$, $\hat{\mathbf{v}}$ and $\hat{\mathbf{L}}$ used in the four systems is determined by the number of symbols detected in a single detection window duration, namely K for the non-STBC-aided systems and $2K$ for the STBC systems. Naturally, the CIR matrix $\mathbf{H}$ encompasses all the CIR taps associated with each of the K users, while the MF output vector $\mathbf{y}$ hosts all the $K/2K$ MF outputs; the correlation matrix $\mathbf{R}$ hosts the correlation coefficients between the composite spreading-code vectors of each user. Furthermore, the HO detection outputs $\hat{\mathbf{v}}$ or the SO detection outputs $\hat{\mathbf{L}}$ quantify the single-symbol or double-symbol detection results associated with each detection-window.

Finally, the matrix $\mathbf{C}$ in the second row of Table 8.2 is a rectangular matrix, which has different number of rows and columns in all the four systems investigated. More specifically, the number of rows is equivalent to the number of received signals in the time domain, which is N_s for the non-STBC-

		MC	MFAA	STBC	STBC+turbo
Input	$\mathbf{r}$	$(N_s \times 1) \times \{V\}$	$(N_s \times 1) \times \{VN_rLU\}$	$(2N_s \times 1) \times \{1\}$	$(2N_s \times 1) \times \{1\}$
		Eq. (4.22) without subscripts n_r,u,l	Eq. (4.22)	Eq. (5.4)	Eq. (5.4)
Known	$\mathbf{C}$	$(N_s \times K) \times [V]$	$(N_s \times K) \times [VN_rLU]$	$(2N_s \times 2K) \times [1]$	$(2N_s \times 2K) \times [1]$
		Eq. (2.30)	Eq. (4.24)	Eqs. (5.5) (5.8)	Eqs. (5.5) (5.8)
	$\mathbf{H}$	$(K \times K) \times \{V\}$	$(K \times K) \times \{VN_rLU\}$	$(2K \times 2K) \times \{1\}$	$(2K \times 2K) \times \{1\}$
		Eq. (4.25) without subscripts n_r,u,l	Eq. (4.25)	Eqs. (5.6) (5.3)	Eqs. (5.6) (5.3)
	ξ	$\frac{1}{\sqrt{V}}$	$\frac{1}{\sqrt{V}}$	$\frac{1}{\sqrt{2}}$	$\frac{1}{\sqrt{2}}$
Intermediate calculated	$\mathbf{y}$	$(K \times 1) \times \{V\}$	$(K \times 1) \times \{VN_rLU\}$	$(2K \times 1) \times \{1\}$	$(2K \times 1) \times \{1\}$
		Eq. (4.52) without subscripts n_r,u,l	Eq. (4.52)	Eq. (5.10)	Eq. (5.10)
	$\mathbf{R}$	$(K \times K) \times \{V\}$	$(K \times K) \times \{VN_rLU\}$	$(2K \times 2K) \times \{1\}$	$(2K \times 2K) \times \{1\}$
		Eq. (4.51) without subscripts n_r,u,l	Eq. (4.51)	Eq. (5.11)	Eq. (5.11)
Output	$\hat{\mathbf{v}}$	$(K \times 1) \times [1]$	$(K \times 1) \times \{U\}$	$(2K \times 1) \times [1]$	$(2K \times 1) \times [1]$
	$\hat{\mathbf{L}}$	N/A	N/A	N/A	$(2K \times 1) \times [1]$

① $\mathbf{A}$ with $(a \times b) \times \{x\}$: There are x different versions of the $(a \times b)$-element matrix $\mathbf{A}$ invoked during a detection interval of the MUD algorithm, whose entries are independent of each other and are different for all the x versions.

② $\mathbf{A}$ with $(a \times b) \times [x]$: There are x identical versions of the $(a \times b)$-element matrix $\mathbf{A}$ invoked during a detection interval of the MUD algorithm. All the x counterparts of $\mathbf{A}$ have the same entries.

Table 8.2: *Input*, *output*, the *known* and *intermediate calculated* variables of the ML or ACO-based SO/HO-MUD algorithm in the channel models considered under various multiuser system schemes investigated in this thesis.

assisted systems and $2N_s$ for the STBC-assisted systems. The number of columns in $\mathbf{C}$, is equivalent to the number of symbols transmitted in all the system scenarios, namely K for the non-STBC-assisted systems or $2K$ for the STBC-aided systems.

Hence the matrix $\mathbf{C}$ is the intermediate variable mapping the faded signal from each of the $K/2K$ symbols to the $N_s/2N_s$ chip-signals received during the $N_s/2N_s$ chip-intervals.

It is worth emphasizing that although UK symbols are transmitted during the U symbol intervals, the number of symbols to be detected by the MUD algorithm in the MFAA system still remains K instead of UK. As a benefit of the orthogonality of the UV subcarriers, the received signal components

only have to be combined, when the components belong to the same symbol. Hence the entire set of VUN_rL demodulated signal versions may be divided into U groups, where all the VN_rL signals constituting a group contains the K symbols transmitted by the K users over a specific subcarrier having the same index u. In other words, instead of detecting the UK symbols with the aid of a single MUD, we may invoke U MUDs, each independently detecting K symbols.

8.1.2.2 ACO-based MUD Algorithms

The main elements characterizing the ACO-based HO/SO MUD algorithms are outlined for the four main system scenarios considered in Chapters 3, 4 and 5 of this treatise in Table 8.3. Among all the properties listed in the first column of Table 8.3, the first two, namely the *symbol-LLF* and the *vector-LLF* may be interpreted as the 'interfaces' between the *system* models and the *algorithms*. More explicitly, both the 'symbol-LLF' and the 'vector-LLF' are generated from the inputs constituted by the *calculated* variables of the system defined in Table 8.2. In turn, the symbol-LLF and vector-LLF also constitute the input of the ACO-based HO/SO algorithms.

Except for the 'symbol-LLF' and 'vector-LLF' values, most of the other values listed in the first column of Table 8.3 have inputs from and generate outputs for the internal blocks of the ACO-based HO/SO MUD algorithms. Therefore, the key to designing the ACO-based HO/SO MUD algorithms for different scenarios is that of quantifying the 'symbol-LLF' and 'vector-LLF' in the context of different transceiver schematics.

As observed from the first (and the second) row of Table 8.3, the symbol-LLF (and vector-LLF) combines the symbol-probabilities of all the received signal replicas originating from a specific symbol, which results in a diversity gain.

Additionally, a beneficial diversity gain is achieved at the cost of increasing the receiver's complexity by combining all received signal replicas. Moreover, the size of the route table and all other matrices of the ACO-based MUD algorithm remains $(2 \times K)$ for BPSK modulated systems.

By contrast, when the diversity-order is increased at the transmitter side, resulting in two transmitted replicas of the same symbol, the number of rows in the route-table employed by the ACO-based MUD algorithm will be doubled in order to incorporate all legitimate combinations of the jointly detected signals. The associated diversity gain is reflected in terms of the improved symbol-LLFs of the ACO-based MUD algorithm.

Hence, when M symbols are transmitted by the same user in an non-orthogonal regime, the route-table and all the other associated matrices have a size of $(2^M \times K)$ elements for BPSK modulation. By contrast, when U symbols are transmitted by the same user on orthogonal subcarriers, the U symbols can be detected in isolation by U ACO-based MUDs, since they do not interfere with each other. When considering ACO-based HO MUD algorithms, the primary differences in calculating the 'symbol-LLF' and 'vector-LLF' of the different transceiver schemes were detailed in Sections 3.4.1 and 3.4.3. Additionally, the technique of calculating the *intrinsic affinity* and creating the *search-pool* according to the *symbol-probability* matrix is also different for the four transceivers of Table 8.3, because the route table has four rows instead of two, when a $\mathcal{G}_2$ STBC is employed, as observed in the last two columns of the fourth and the seventh row of Table 8.3.

	MC	MFAA	STBC	STBC+turbo
Output	$(K \times 1)$ binary	$(K \times 1) \times \{U\}$ binary	$(2K \times 1)$ binary	$(2K \times 1)$ soft
Symbol-LLF	$\iota_{ij} \leftarrow i, \xi,$ $\{y_{v,j}\}, \{R_{v,jj}\},$ for all $v = 1, \ldots, V$	$\iota_{u,ij} \leftarrow i, \xi,$ $\{y_{vu,j}^{(n_r l)}\}, \{R_{vu,jj}^{(n_r l)}\},$ for all $v = 1, \ldots, V,$ $n_r = 1, \ldots, N_r$ $l = 1, \ldots, L$	$\iota_{ij} \leftarrow i, \xi,$ $\{\mathbf{y}_j^{(2)}\}, \{\mathbf{R}_{jj}^{(2)}\}$	$\iota_{ij} \leftarrow i, \xi,$ $\{\mathbf{y}_j^{(2)}\}, \{\mathbf{R}_{jj}^{(2)}\}$
	Eq. (4.67) with $N_r = L = 1$	Eq. (4.67)	Eq. (5.14)	Eq. (5.14)
Vector-LLF	$\mathfrak{L}(\mathbf{x}_m^{(n)}) \leftarrow \mathbf{x}_m^{(n)}, \xi,$ $\{\mathbf{y}_v\}, \{\mathbf{R}_v\},$ for all $v = 1, \ldots, V$	$\mathfrak{L}_u(\mathbf{x}_m^{(n)}) \leftarrow \mathbf{x}_m^{(n)}, \xi,$ $\{\mathbf{y}_{vu,j}^{(n_r l)}\}, \{\mathbf{R}_{vu,jj}^{(n_r l)}\},$ for all $v = 1, \ldots, V,$ $n_r = 1, \ldots, N_r$ $l = 1, \ldots, L$	$\mathfrak{L}(\mathbf{x}_m^{(n)}) \leftarrow \mathbf{x}_m^{(n)}, \xi,$ $\mathbf{y}, \mathbf{R}$	$\mathfrak{L}(\mathbf{x}_m^{(n)}) \leftarrow \mathbf{x}_m^{(n)}, \xi,$ $\mathbf{y}, \mathbf{R}$
	Eq. (4.56) with $N_r = L = 1$	Eq. (4.56)	Eq. (5.12)	Eq. (5.12)
Intrinsic affinity	$\boldsymbol{\eta}$ $(2 \times K) \times \{1\}$ $\eta_{ij} \leftarrow \iota_{qj}$ $q = 1, 2$	$\boldsymbol{\eta}$ $(2 \times K) \times \{U\}$ $\eta_{u,ij} \leftarrow \iota_{u,qj}$ $q = 1, 2$	$\boldsymbol{\eta}$ $(4 \times K)$ $\eta_{ij} \leftarrow \iota_{qj}$ $q = 1, 2, 3, 4$	$\boldsymbol{\eta}$ $(4 \times K) \times \{2 \cdot 2K\}$ $\eta_{\kappa\pm,ij} \leftarrow \kappa, \pm\iota_{qj}$ $q = 1, 2, 3, 4,$
	Eqs. (3.11) (3.12)	Eqs. (3.11) (3.12)	Eqs. (5.22) (5.25)	Eqs. (5.22) (5.25) Eqs. (7.10) (7.11)
Pheromone density	$\boldsymbol{\tau}^{(n)}$ $(2 \times K) \times \{1\}$ $\boldsymbol{\tau}^{(n+1)} \leftarrow$ $\boldsymbol{\tau}^{(n)}, \boldsymbol{\tau}_*^{(n)}, \boldsymbol{\tau}_m^{(n)}$	$\boldsymbol{\tau}^{(n)}$ $(2 \times K) \times \{U\}$ $\boldsymbol{\tau}^{(n+1)} \leftarrow$ $\boldsymbol{\tau}^{(n)}, \boldsymbol{\tau}_*^{(n)}, \boldsymbol{\tau}_m^{(n)}$	$\boldsymbol{\tau}^{(n)}$ $(4 \times K) \times \{1\}$ $\boldsymbol{\tau}^{(n+1)} \leftarrow$ $\boldsymbol{\tau}^{(n)}, \boldsymbol{\tau}_*^{(n)}, \boldsymbol{\tau}_m^{(n)}$	$\boldsymbol{\tau}^{(n)}$ $(4 \times K) \times \{2 \cdot 2K\}$ $\boldsymbol{\tau}^{(n+1)} \leftarrow$ $\boldsymbol{\tau}^{(n)}, \boldsymbol{\tau}_*^{(n)}, \boldsymbol{\tau}_m^{(n)}$
	Eqs. (3.20)∼(3.23)	Eqs. (3.20)∼(3.23)	Eqs. (3.20)∼(3.23)	Eqs. (3.20)∼(3.23)
Symbol-probability	$\mathbf{P}^{(n)}$ $(2 \times K) \times \{1\}$ $\mathbf{P}^{(n)} \leftarrow \boldsymbol{\eta}, \boldsymbol{\tau}^{(n)}$	$\mathbf{P}^{(n)}$ $(2 \times K) \times \{U\}$ $\mathbf{P}^{(n)} \leftarrow \boldsymbol{\eta}, \boldsymbol{\tau}^{(n)}$	$\mathbf{P}^{(n)}$ $(2 \times K) \times \{1\}$ $\mathbf{P}^{(n)} \leftarrow \boldsymbol{\eta}, \boldsymbol{\tau}^{(n)}$	$\mathbf{P}^{(n)}$ $(2 \times K) \times \{2 \cdot 2K\}$ $\mathbf{P}^{(n)} \leftarrow \boldsymbol{\eta}, \boldsymbol{\tau}^{(n)}$
	Eq. (3.26)	Eq. (3.26)	Eq. (3.26)	Eq. (3.26)
Search-pool	$\mathbf{x}^{(n)}$ $(\zeta \times K) \times \{1\}$ $\mathbf{x}^{(n)} \leftarrow \mathbf{P}^{(n)}$	$\mathbf{x}^{(n)}$ $(\zeta \times K) \times \{U\}$ $\mathbf{x}^{(n)} \leftarrow \mathbf{P}^{(n)}$	$\mathbf{x}^{(n)}$ $(\zeta \times K) \times \{1\}$ $\mathbf{x}^{(n)} \leftarrow \mathbf{P}^{(n)}$	$\mathbf{x}^{(n)}$ $(\zeta \times K) \times \{2 \cdot 2K\}$ $\mathbf{x}^{(n)} \leftarrow \mathbf{P}^{(n)}$
	Alg. 1 in Sec 5.3.1.4	Alg. 1 in Sec 5.3.1.4	Alg. 2 in Sec 5.3.1.4	Alg. 2 in Sec 5.3.1.4

Table 8.3: Components of ACO-based HO or SO MUD algorithms in various multiuser system schemes investigated in this thesis.

On the other hand, when the MUA assisted ACO-based SO MUD algorithm of Section 6.4 is considered in the last column of Table 8.3, the ACO-based HO MUD algorithm is activated $2 \cdot 2K$ times to evaluate the LLRs associated with the $2K$ symbols, which requires the update of the intrinsic affinity matrix every time, before the ACO-based HO MUD algorithm is activated, as indicated in the last column of the fourth row of Table 8.3.

8.1.3 Performance Comparisons

		MC	MFAA	STBC	STBC+turbo
BER	Performance	Fig. 4.9	Fig. 4.11	Figs. 5.4, 5.7	Fig. 7.16
	Influential parameters	V	VN_rL		N_i
	$K = 32$	Single-user performance	Single-user performance	Single-user performance	Single-user performance
Complexity	results	Fig. 4.10	Fig. 4.13	Figs. 5.5, 5.8	Fig. 7.18
	Per bit complexity	$\propto V$	$\propto VN_rL$		$\propto N_i$ $\mathsf{C}_{\text{ACO}} \gg \mathsf{C}_{\text{URC}} + \mathsf{C}_{\text{RSC}}$
	$K > 1$	linearly $\propto K$	linearly $\propto K$	linearly $\propto K$	linearly $\propto K$

Table 8.4: Achievable BER performance and the complexity of the ACO-based HO or SO MUDs investigated for $K = 32$ users.

The achievable BER performance and the complexity imposed by the ACO-based HO or SO MUD in the context of the four main systems investigated in Chapters 4, 5, 6 and 7 of this treatise are summarized in Table 8.4.

8.1.3.1 BER performance

As observed in Table 8.4, the attainable BER performance of the single-user benchmarker as well as of a $K = 32$-user system is portrayed in the light of the per-bit complexity for the four systems considered.

Firstly, the BER achieved by a single-user MC system is determined by the number of subcarriers V, and the higher the number of subcarriers, the more substantial the diversity gain, which results in an improved BER performance. Secondly, the BER performance of a single-user aided MFAA MC DS-CDMA system is jointly determined by the product of the number of subcarriers V, the number of receive antenna arrays N_r and the number of array elements L per antenna. An SNR gain may be achieved, when any of these system parameters is increased in order to improve the attainable BER performance. However, all the system parameters are fixed in the STBC assisted system. Finally, the

BER performance of the iteratively decoded STBC assisted DS-CDMA system is determined by the number of iterations N_{i}.

8.1.3.2 Complexity Comparisons

The complexity imposed by the four systems is summarized in Table 8.4 and it is further discussed below.

Firstly, when a single user is supported by the MC DS-CDMA system, the MF-based detection complexity per user is linearly proportional to the number of subcarriers V. Similarly, upon increasing the number of resolvable CIR taps by one the system has to generate one extra MF output for a single user. Similarly, in the MFAA assisted MC DS-CDMA system of Chapter 4, the complexity per user may also deemed to be linearly proportional to the product of $VN_{\mathrm{r}}L$, since it is dominated by the calculation of the $VN_{\mathrm{r}}L$ MF outputs. Finally, when the iterative detection aided STBC single-user system is considered, the complexity per bit is linearly dependent on the number of turbo decoding iterations and it is dominated by that of the ACO algorithm.

Let us now consider the scenario, when the number of users increases from $K = 1$ to 32. The size of the matrices used by the ACO-based HO/SO MUD algorithm, namely that of the CIR matrix $\mathbf{H}$ and of the correlation matrix $\mathbf{R}$ is linearly proportional to K, as seen in Table 8.2. Since both the number of rows and columns of $\mathbf{R}$ is proportional to K, the total complexity becomes proportional to K^2. However, the per-symbol complexity is only linearly increased with K, since the total complexity is divided by the number of symbols K or $2K$. The total number of OF evaluations is predominantly determined by the number of K-bit vectors in the search-pool, which is given by the product of the number of ants and the number of search iterations, namely by $\zeta \cdot \Xi$. Clearly, these two parameters are not dependent on the number of users supported by the system.

Therefore, based on Table 8.4, we may draw the following conclusions. Regardless of the system parameters, the four ACO-based HO/SO MUD aided K-user systems of Table 8.4, $K = 1, \ldots, 32$, are capable of approaching the single-user performance at the cost of a per-symbol complexity, which is linearly proportional to the number of users K, rather than increasing exponentially, as for the ML MUD.

8.1.4 Performance versus Complexity Comparisons

In this section, the three main systems, namely the MC DS-CDMA system of Chapter 4, the MFAA assisted MC DS-CDMA UL of Chapter 4 and the RSC as well as URC-aided iteratively detected STBC DS-CDMA UL of Chapter 7 are studied in Fig. 8.1 to Fig. 8.4. All these figures quantify the E_{b}/N_0 required by the different systems as a function of the per-bit complexity imposed, when aiming for achieving a BER of 1×10^{-4}. The per-bit complexity was quantified in terms of the number of FLoating-point-Operations Per Second (FLOPS) imposed by the receiver.

Hence, when the MC DS-CDMA UL of Chapter 4, and the MFAA assisted MC DS-CDMA UL of Chapter 4 are investigated without employing channel codes, their per-bit complexity is identical. By contrast, when the turbo detected STBC assisted DS-CDMA UL of Chapter 7 is considered, the per-bit complexity of the receiver has two components, namely the bit-LLR calculation of all the coded

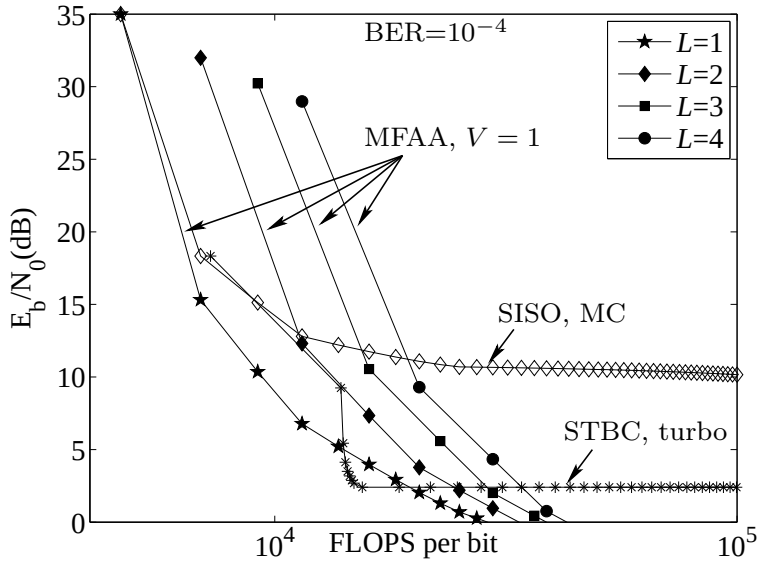

Figure 8.1: The required E_b/N_0 versus the per-bit complexity quantified in terms of the FLOPS imposed by the ACO-based SO or HO MU algorithms in the context of the $K = 32$-user MC, MFAA and turbo detected STBC at the target BER of 1×10^{-4}. $V = 1$ subcarriers are employed by the $K = 32$-user MFAA systems.

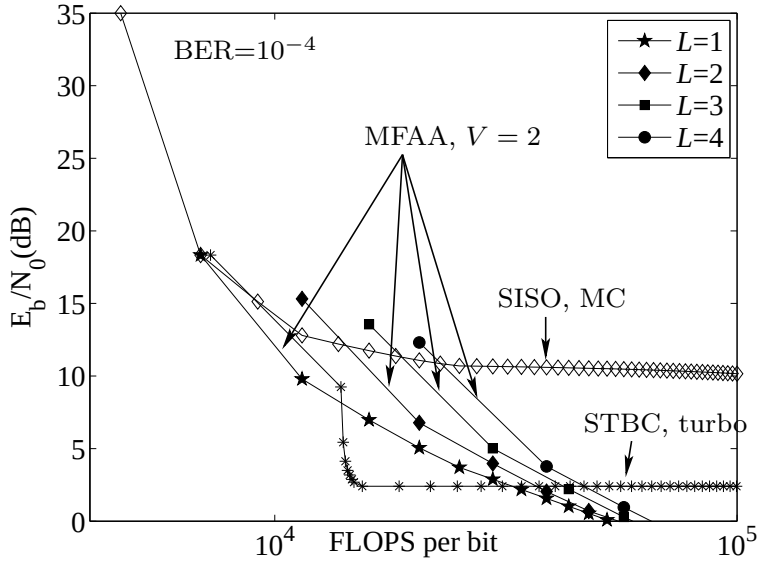

Figure 8.2: The required E_b/N_0 versus the per-bit complexity quantified in terms of the FLOPS imposed by the ACO-based SO or HO MU algorithms in the context of the $K = 32$-user MC, MFAA and turbo detected STBC at the target BER of 1×10^{-4}. $V = 2$ subcarriers are employed by the $K = 32$-user MFAA systems.

bits and that of the URC and RSC aided turbo detection process.

More specifically, the complexity imposed by the ACO-based HO MUD algorithms is dominated by the calculation of the OF, while that of the SO MUD algoriths is predetermined by the evaluation of the OF for the K-bit vectors, captured by the search-pool as well as by the calculation of the Euclidean distances of the K-bit vectors included in the final search-pool.

On the other hand, the complexity imposed by the URC and RSC decoders is dependent on

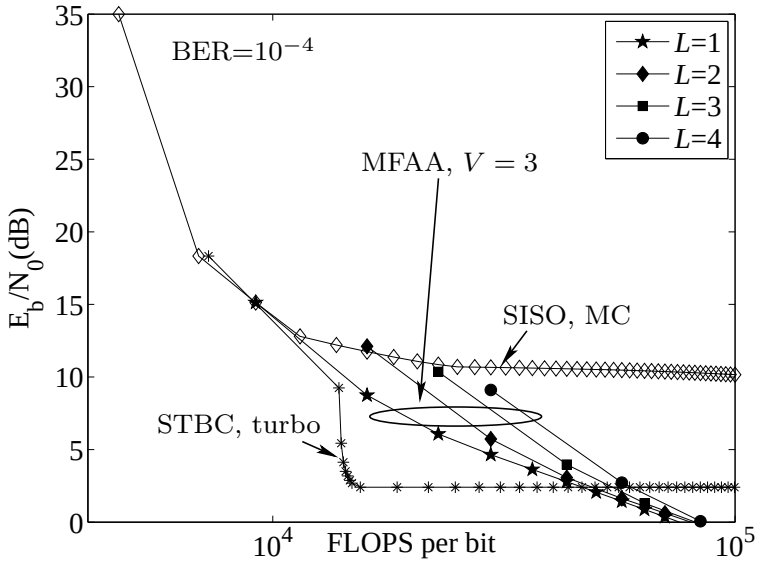

Figure 8.3: The required E_b/N_0 versus the per-bit complexity quantified in terms of the FLOPS imposed by the ACO-based SO or HO MU algorithms in the context of the $K = 32$-user MC, MFAA and turbo detected STBC at the target BER of 1×10^{-4}. $V = 3$ subcarriers are employed by the $K = 32$-user MFAA systems.

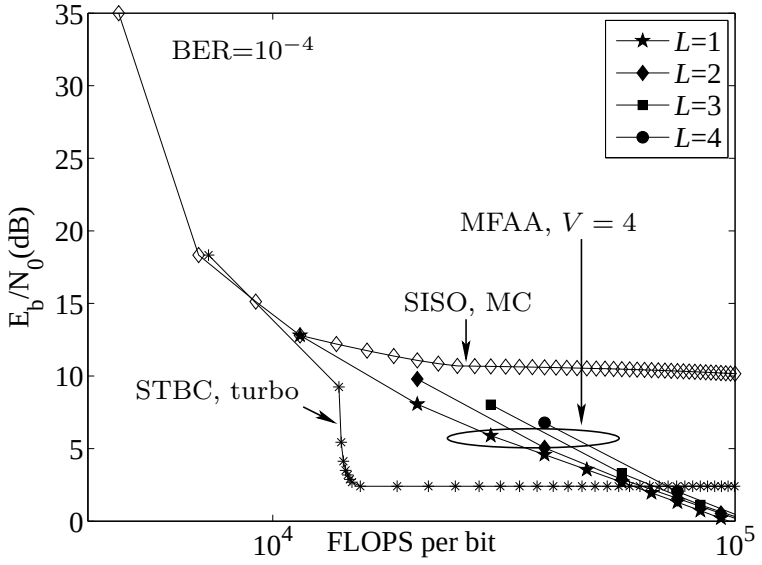

Figure 8.4: The required E_b/N_0 versus the per-bit complexity quantified in terms of the FLOPS imposed by the ACO-based SO or HO MU algorithms in the context of the $K = 32$-user MC, MFAA and turbo detected STBC at the target BER of 1×10^{-4}. $V = 4$ subcarriers are employed by the $K = 32$-user MFAA systems.

the number of trellis states, which is determined by the *constraint length* and the specific *generator polynominals* of the URC and RSC decoders, which were given in Table 7.3. The per-trellis-state complexity imposed by the RSC as well as URC decoders and expressed in terms of the number of FLOPS may be shown to yield the values given in Tables 8.5 and 8.6, respectively. Compared to the per-bit complexity imposed by the ACO-based HO/SO MUD algorithm, the complexity of the RSC and URC may be deemed modest, when a single iteration is carried out between these two components, before exchanging extrinsic information with the ACO-MUD.

Output of the RSC decoder	during the n_ith iteration	FLOPS per bit per iteration
a posteriori LLRs of the information source bits	N_i	99
extrinsic LLRs of the coded bits	$1, \ldots, (N_\mathrm{i} - 1)$	110

Table 8.5: The complexity expressed in terms of the number of FLOPS per coded bit for the RSC decoder per turbo iteration.

Input of the URC decoder	during the n_ith iteration	FLOPS per bit per iteration
without *a priori* LLRs of the coded bits	1	41
with *a priori* LLRs of the coded bits	$2, \ldots, N_\mathrm{i}$	46

Table 8.6: The complexity expressed in terms of the number of FLOPS per coded bit for the URC decoder per turbo iteration.

8.2 Suggestions for Future Research

We would like to conclude by suggesting the following topics of interest for future investigations:

1. In Chapter 4, three different MC DS-CDMA schemes have been introduced and the MC DS-CDMA Type II scheme [93] has been investigated in detail. However, we may also invoke frequency-domain spreading instead of subcarrier repetition, which was classified as a Type I scheme in [93]. By vertically stacking V spreading codes in the FD, the user capacity is increased by a factor of V. However, this system requires a more powerful MUD algorithm, which motivates further research.

2. In Chapters 5 and 7, we have employed an STBC assisted transceiver, while assuming that the maximum attainable transmit diversity can be achieved, since the transmit antennas experience independent fading. In reality, there may be a non-negligible correlation between the signals, hence the associated performance erodes. This performance erosion may be eliminated with the aid of distributed space-time codes, as detailed for example in [203].

3. In Chapter 7, we have designed an ACO-based SO ST/MUD in order to exploit the *extrinsic* LLRs provided by all the coded bits constituting a frame transmitted by each user. Unfortunately, however, the ACO-based SO ST/MUD is unable to exploit the *a priori* LLRs of the coded bits. Hence, it is an ambitious design objective to conceive a soft-in soft-output ACO-based MUD, which can make use of the *a priori* LLRs provided by the URC decoder for all the coded bits, since then iterative detection may be carried out by exchanging extrinsic information among three components, namely the ACO MUD, the URC and the RSC decoder. As a result, the 'maximum achievable rate' defined in Chapter 7 is expected to be closer to the ultimate capacity limit.

4. The ACO-aided MUD techniques proposed in this treatise may also be invoked for creating powerful Multi-User Transmission (MUT) schemes.

5. The proposed ACO algorithms may also be employed for finding optimum routes in both ad hoc and cooperative wireless networks.

List of Symbols

General notation

- The superscript * is used to indicate complex conjugation. Therefore, a^* represents the complex conjugate of the variable a.
- The superscript ^{T} is used to indicate matrix transpose operation. Therefore, $\mathbf{a}^T$ represents the transpose of the matrix $\mathbf{a}$.
- The superscript ^{H} is used to indicate complex conjugate transpose operation. Therefore, $\mathbf{a}^H$ represents the complex conjugate transpose of the matrix $\mathbf{a}$.
- The notation $*$ denotes the convolutional process. Therefore, $a * b$ represents the convolution between variables a and b.
- The notation $\hat{x}$ represents the estimate of x.
- The notation $X(f)$ is the Fourier Transform of $x(t)$.

Special symbols

$\mathbf{A}$: The system matrix in a CDMA system or a ST system.

b_i: The coefficient taps of the backward filters of the Decision Feedback Equalizer.

$\boldsymbol{b}$: A symbol vector, or combination, representing one of the possible transmited symbol sequence.

d_{free}: The minimum free Euclidean distance.

c^W: Walsh spreading code

c^R: Random spreading code.

D: The diversity quantity.

D_I: The diversity quantity of I component.

D_Q: The diversity quantity of Q component.

$\bar{D}$: The signal set dimensionality.

c_k: The coded symbol of the encoder at instance k.

$\mathbf{c}_j^i$: The M-ary multilevel RBF network's centres at node-j and level-i.

C_i: The coefficient taps of the forward filters of the Decision Feedback Equalizer.

E_b: Bit energy.

E_s: Symbol energy.

$E[k]$: The expected value of k.

f_n: The adaptive modem mode switching thresholds at mode n.

f_{RBF}^i: The conditional PDF of the M-ary multilevel RBF equaliser, at level-i.

$G(D)$: The generator polynomials matrix for Convolutional codes.

$H^i(D)$: The coefficients of the generator polynomials for bit i in TCM codes.

h_i: The channel's impulse response.

I_n: The random TTCM symbol-interleaver size in terms of the number of bits for adaptive modem mode n.

K: The number of users.

$\bar{K}$: The Rician fading parameter.

L: The number of resolvable paths in wideband channels.

$\bar{L}$: The memory length of CIR, i.e. $L-1$.

L: The "length" of the shortest error event path or the Hamming distance of a code.

$L(j,m)$: The branch label for transition from state j when the imput symbol is m.

m: The decision feedback equaliser's feedforward order.

m_I: The branch metrics for I component.

m_Q: The branch metrics for Q component.

$\bar{\mathsf{m}}$: The number of information bits in a modulated symbol.

$\tilde{\mathsf{m}}$: The number of encoded information bits in a modulated symbol.

m: The number of bits in a modulated symbol.

M: The number of levels of a multi-level modulation scheme, PSK or QAM.

M: The number of possible values of a source symbol.

M_o: The number of modulation modes in an adaptive modulation scheme.

$\mathcal{M}$: The number of RBF centres or the number of independant basis functions of the RBF equaliser.

n: The decision feedback equaliser's feedback order.

$n_{s,i}$: The number of channel states or the number of hidden nodes, at level-i of M-ary multilevel RBF equaliser.

$n_{s,f}$: The number of scalar centres or channel states, of the reduced complexity RBF equaliser.

N: The number of symbols produced in each transmission interval, or the number of symbols per JD block.

$n(t)$: AWGN added to the transmitted signal.

N_0: Single-sided power spectral density of white noise.

P: The population size of GA.

P_b: Bit error probability.

P_m: The probability of mutation in GA.

Q: The number of chips in each spreading sequence, spreading factor.

$\bar{\mathsf{Q}}$: The first spreading ratio of the DS-RR scheme.

$\tilde{\mathsf{Q}}$: The second spreading ratio of the DS-RR scheme.

R: Coding rate.

r'_I: The I component of the decoupled channel output, in the I/Q-TEQ scheme.

r'_Q: The Q component of the decoupled channel output, in the I/Q-TEQ scheme.

S: The number of coding states, which is equals to 2^ν.

S_n: The trellis state at time instant n.

T: The mating pool size of GA.

u_k: The input symbol to the encoder at instance k.

V_m: The mth modulation mode of the adaptive modulation scheme, which has a total of M_o different modulation modes.

w_j^i: The M-ary multilevel RBF equaliser's weight at node-j and level-i.

x_k: The transmitted symbol at instance k.

y_k: The received symbol at instance k.

Y: The number of generations of GA.

α: The forward variable of a MAP decoder.

β: The backward variable of a MAP decoder.

$\chi(i, b)$: The subset that contains all the phasors for which the position i of the phasor has the binary value b, $b \in \{0, 1\}$.

γ: The branch transition metric of a MAP decoder.

γ_{dfe}: The SNR at the output of the DFE.

$\Gamma_o(k)$: The SINR of the user-k at the output of the JD-MMSE-DFE.

ν: The code memory.

$\Omega(\boldsymbol{b})$: The correlation metric of symbol vector $\boldsymbol{b}$.

σ_S^2: The complex signal's variance.

σ_N^2: The complex noise's variance.

π: Interleaver.

π^{-1}: Deinterleaver.

τ: The decision feedback equaliser's decision delay.

φ_i: The nonlinear activation function of multilevel RBF equaliser at level-i.

Glossary

16QAM	16-level Quadrature Amplitude Modulation
3G	Third generation
4QAM	4-level Quadrature Amplitude Modulation
64QAM	64-level Quadrature Amplitude Modulation
8PSK	8-level Phase Shift Keying
APP	A Posteriori Probability
ATM	Asynchronous Transfer Mode
AWGN	Additive White Gaussian Noise
BbB	Burst-by-Burst
BER	Bit error ratio, the number of the bits received incorrectly
BICM	Bit Interleaved Coded Modulation
BICM-ID	Bit-Interleaved Coded Modulation with Iterative decoding
BPS	Bits per modulated symbol
BPSK	Binary Phase Shift Keying
BS	A common abbreviation for Base Station
CCI	Co-Channel Interference
CDMA	Code Division Multiple Access
CIR	Channel Impulse Response
CM	Coded Modulation
CM-GA-MUD	Coded Modulation assisted Genetic Algorithm based Multiuser Detection
CM-JD-CDMA	Coded Modulation-assisted Joint Detection-based CDMA
CT-TEQ	Conventional Trellis-based Turbo Equalisation
D/A	Digital to Analogue

DAB	Digital Audio Broadcasting
DC	Decoding Complexity
DFE	Decision Feedback Equalizer
DFT	Digital Fourier Transform
DoS-RR	Double-Spreading aided Rake Receiver
DS	Direct Sequence
DTTB	Digital Terrestrial Television Broadcast
DVB	Digital Video Broadcasting
ECL	The Effective Code Length or the "length" of the shortest error event path.
EFF	Error Free Feedback
E_b/N_0	Ratio of bit energy to noise power spectral density.
FDM	Frequency Division Multiplexing
FEC	Forward Error Correction
FED	Free Euclidean distance
FER	Frame error rate
FFT	Fast Fourier Transform
G	Coding Gain
GA	Genetic Algorithm
HT	Hilly Terrain, channel impulse response of a hilly terrain environment.
I	The In-phase component of a complex quantity.
I/Q-TEQ	In-phase/Quadrature-phase Turbo Equalisation
IC	Interference Cancellation
IL	interleaver block length
IQ-CM	IQ-interleaved Coded Modulation
ISI	Intersymbol Interference
JD	Joint Detection
JD-MMSE-DFE	Joint Detection scheme employing MMSE-DFE
LMS	Least Mean Square, a stochastic gradient algorithm used in adapting the equalizer's coefficients in a non-stationary environment

log-domain	logarithmic-domain
LP	Logarithmic-domain Probability
MAI	Multiple Access Interference
MAP	Maximum A Posteriori
MC-CDMA	Multi-Carrier Code Division Multiple Access
MIMO	Multi-Input Multi-Output
ML	Maximum Likelihood
MMSE	Minimum Mean Square Error
MMSE-BLE	Minimum Mean Square Error based Block Linear Equaliser
MMSE-DFE	Minimum Mean Square Error based Decision Feedback Equaliser
MPSK	M-ary Phase Shift Keying
MRC	Mixed Radix Conversion
MSE	Mean Square Error, a criterion used to optimised the coefficients of the equalizer such that the ISI and the noise contained in the received signal is jointly minimised.
MUD	Multi-User Detection
OFDM	Orthogonal Frequency Division Multiplexing
OMPX	Orthogonal Multiplexing
PDF	Probability Density Function
PN	Pseudo-Noise
PSD	Power Spectral Density
PSK	Phase Shift Keying
Q	The Quadrature-phase component of a complex quantity.
QAM	Quadrature Amplitude Modulation
QPSK	Quadrature Phase Shift Keying
RBF	Radial Basis Function
RBF-DFE	RBF assisted Decision Feedback Equaliser
RBF-TEQ	Radial Basis Function based Turbo Equalisation
RCPC	Rate-Compatible Puncture Convolutional

RSC	Recursive Systematic Convolutional
SbS	Symbol-by-Symbol
SER	Symbol Error Ratio
SISO	Soft-Input-Soft-Output
SNR	Signal to Noise Ratio, noise energy compared to the signal energy
SOVA	Soft-Output Viterbi Algorithm
SP	Set Partitioning
STBC	Space-Time Block Coding
STBC-DoS-RR	Space-Time Block Coding-assisted Double-Spread Rake Receiver
STBC-IQ	Space-Time Block Coding based IQ-interleaved
STC	Space-Time Coding
STS	Space-Time Spreading
STTC	Space-Time Trellis Coding
TC	Turbo Coding
TCM	Trellis Coded Modulation
TDD	Time Division Duplex
TDMA	Time Division Multiple Access
TEQ	Turbo Equalisation
TTCM	Turbo Trellis Coded Modulation
TU	Typical Urban, channel impulse response of an urban environment.
TuCM	Turbo Coded Modulation
UMTS	Universal Mobile Telecommunication System
UTRA	UMTS Terrestrial Radio Access
VA	Viterbi Algorithm
WMF	Whitening Matched Filter
ZFE	Zero Forcing Equalizer.

Bibliography

[1] J. K. M. M. S. P. J. T. H. Ekstrom, A Furuskar and M. Wahlqvist, "Technical solutions for the 3g long-term evolution," *IEEE Communication Magazine*, vol. 44, pp. 38–45, March 2006.

[2] T. S. G. R. A. Network, "Physical layer aspects for evolved universal terrestrial radio access (utra) (release 7)." technique report of 3rd Generation Partnership Project (3GPP), 2006.

[3] J.-P. L. N. Yee and G. P. Fettweis, "Multicarrier cdma in indoor wireless radio networks," in *Proceedings of PIMRC93*, (Yokohama, Japan), pp. 109–113, October 1993.

[4] K. Fazel and L. Papke, "On the performance of convolutionally-coded CDMA/OFDM for mobile communication system," in *PIMRC'93*, pp. 468–472, 1993.

[5] A. Chouly, A. Brajal, and S. Jourdan, "Orthogonal multicarrier techniques applied to direct sequence spread spectrum CDMA systems," in *Proceedings of the IEEE Global Telecommunications Conference 1993*, (Houston, TX, USA), pp. 1723–1728, 29 November – 2 December 1993.

[6] L. Vandendorpe, "Multitone direct sequence CDMA system in an indoor wireless environment," in *Proceedings of IEEE SCVT 1993*, (Delft, The Netherlands), pp. 4.1:1–8, October 1993.

[7] V. M. Dasilva and E. S. Sousa, "Multicarrier orthogonal cdma signals for quasi- synchronous communication systems," *IEEE Journal on Selected Areas in Communications*, vol. 12, pp. 842–852, June 1994.

[8] L. Vandendorpe, "Multitone spread spectrum multiple access communications system in a multipath rician fading channel," *IEEE Transaction on Vehicular Technology*, vol. 44, no. 2, pp. 327–337, 1995.

[9] E. Sourour and M. Nakagawa, "Performance of rothogonal multicarrier cdma in a multipath fading channel," *IEEE Transactions on Communications*, vol. 44, pp. 356–367, March 1996.

[10] R. Prasad and S. Hara, "Overview of multi-carrier CDMA," in *Proceedings of the IEEE International Symposium on Spread Spectrum Techniques and Applications (ISSSTA)*, (Mainz, Germany), pp. 107–114, 22–25 September 1996.

[11] L.-L. Yang and L. Hanzo, "Performance of generalized multicarrier DS-CDMA over Nakagami-m fading channels," *IEEE Transactions on Communications*, vol. 50, pp. 956–966, June 2002.

[12] L.-L. Yang and L. Hanzo, "Performance of generalized multicarrier DS-CDMA over using various chip waveforms," *IEEE Transactions on Communications*, vol. 51, pp. 748–752, May 2003.

[13] L. Hanzo and L-L. Yang, E. L. Kuan and K. Yen, *Single- and Multi-Carrier CDMA*. New York, USA: John Wiley, IEEE Press, 2003.

[14] Z. T. K.H. Teo and J. Zhang, "The mobile broadband wimax standard," *IEEE Signal Processing Magazine*, vol. 24, pp. 144–148, September 2007.

[15] J. S. E. Dahlman, S. Parkvall and P. Beming, *3G Evolution, Second Edition: HSPA and LTE for Mobile Broadband, 2 edition*. Oxford, UK: Academic Press, 2008.

[16] A. Kaye and D. George, "Transmission of multiplexed pam signals over multiple channel and diversity systems.," *IEEE Transaction on Communication Technology*, pp. 520–525, October 1970.

[17] L. Hanzo, M. Munster, B. J. Choi, and T. Keller, *OFDM and MC-CDMA for Broadband Multi-User Communications, WLANs and Broadcasting*. John Wiley and IEEE Press, 2003.

[18] D. J. E. S. C. Swales, M. A. Beach and J. P. McGeehan, "The performance enhancement of multibeam adaptive base-station antennas for cellular land mobile radio systems," *IEEE Transactions on Vehicular Technology*, vol. 39, pp. 56–67, February 1990.

[19] M. V. S. Anderson, M. Millnert and B. Wahlberg, "An adaptive array for mobile communication systems," *IEEE Transactions on Vehicular Technology*, vol. 40, pp. 230–236, February 1991.

[20] G. J. Foschini, Jr., "Layered Space-time architecture for wireless communication in a fading environment when using multi-element antennas," *Bell Labs Tech. J.*, pp. 41–59, 1996.

[21] A. Paulraj and C. Papadias, "Space-time processing for wireless communications," *IEEE Signal Processing Magazine*, vol. 14, pp. 49–83, November 1997.

[22] L. Godara, "Applications of antenna arrays to mobile communications, part I: Performance improvement, feasibility, and system considerations," *Proceedings of the IEEE*, vol. 85, pp. 1029–1060, July 1997.

[23] L. Godara, "Applications of antenna arrays to mobile communications, part II: Beam-forming and direction-of-arrival considerations," *Proceedings of the IEEE*, vol. 85, pp. 1193–1245, August 1997.

[24] S. Affes and P. Mermelstein, "A new receiver structure for asynchronous cdma:star - the spatio-temporal array-receiver," *IEEE Journal on Selected Areas in Communications*, vol. 16, pp. 1411–1422, October 1998.

[25] J. S. L. T. F. Wong, T. M. Lok and M. D. Zoltowski, "A linear receiver for direct-sequence spread-spectrum multiple-access systems with antenna arrays and blind adaptation," *IEEE Transactions on Information Theory*, vol. 44, pp. 659–676, March 1998.

[26] G. D. G. P. W. Wolniansky, G. J. Foschini and R. A. Valenzuela, "V-blast: an architecture for realizing very high data rates over the rich-scattering wireless chan nel," in *Proceeding IEEE ISSSE-98.*, (Pisa, Italy), pp. 295–300, September 1998.

[27] Y. Li and N. Sollenberger, "Adaptive antenna arrays for ofdm systems with cochannel interference," *IEEE Transactions on Communications*, vol. 47, pp. 217–229, February 1999.

[28] M. D. Anna and A. H. Aghvami, "Performance of optimum and suboptimum combining at the antenna array of a w-cdma system," *IEEE Journal on Selected Areas in Communications*, vol. 17, pp. 1030–1039, December 1999.

[29] A. M. S. E. N. Onggosanusi and B. D. V. Veen, "Canonical space-time processing for wireless communications," *IEEE Transactions on Communications*, vol. 48, pp. 1669–1680, October 2000.

[30] N. Herscovici and C. Christodoulou, "Potentials of smart antennas in cdma systems and uplink improvements," *IEEE Antennas and Propagation Magazine*, vol. 43, pp. 172–177, October 2001.

[31] C. R. N. S. A. Zekavat and S. Shattil, "Oscillating-beam smart antenna arrays and multicarrier systems: Achieving transmit diversity, frequency diversity, and directionality," *IEEE Transactions on Vehicular Technology*, vol. 51, pp. 1030–1039, September 2002.

[32] H. Trees, *Optimum array processing Part IV of Detection, Estimation and Modulation Theory*. New York, USA: John Wiley and Sons, Inc., 2002.

[33] J. Blogh and L. Hanzo, *Third-generation systems and intelligent wireless networking: smart antennas and adaptive modulation*. Chichester, UK: John Wiley and Sons, Ltd, 2002.

[34] L. Hanzo and C. H. Wong and M. S. Yee, *Adaptive Wireless Transceivers: Turbo-Coded, Turbo-Equalized and Space-Time Coded TDMA, CDMA and OFDM Systems*. New York, USA: John Wiley, IEEE Press, 2002.

[35] G. Forney, *Concatenated codes*. Cambridge, Massachusetts, USA: MIT Press, 1966.

[36] C. Berrou and A. Glavieux and P. Thitimajshima, "Near Shannon Limit Error-Correcting Coding and Decoding: Turbo Codes," in *Proceedings of the International Conference on Communications*, (Geneva, Switzerland), pp. 1064–1070, May 1993.

[37] D. Divsalar and F. Pollara, "Multiple turb o codes for deep-space communications," tech. rep., Pasadena, CA, May 1995.

[38] S. Benedetto and G. Montorsi, "Iterative decoding of serially conatenated convolutional codes," *Electronics Letters*, pp. 1186–1187, 1996.

[39] S. Benedetto, D. Divsalar, G. Montorsi, and F. Pollara, "Analysis, design, and iterative decoding of double serially concatenated codes with interleavers," *IEEE Journal on Selected Areas in Communications*, vol. 16, pp. 231–244, Feb. 1998.

[40] D. Raphaeli and Y. Zarai, "Combined turb o equalization and turb o decoding," in *Proceedings of IEEE Global Telecommunications Conference (GLOBECOM)*, vol. 2, (Phoenix, AZ), pp. 639–643, November 1997.

[41] D. Raphaeli and Y. Zarai, "Combined turbo equalization and turbo decoding," *IEEE Communications Letters*, vol. 2, pp. 107–109, April 1998.

[42] R. Ramamurthy and W. Ryan, "Convolutional double accumulate codes (or double turbo dpsk)," *IEEE Communications Letters*, vol. 5, pp. 157–159, April 2001.

[43] C. Douillard, A. Picart, M. Jézéquel, P. Didier, C. Berrou, and A. Glavieux, "Iterative correction of intersymbol interference: Turbo-equalization," *European Transactions on Communications*, vol. 6, pp. 507–511, September-October 1995.

[44] S. Benedetto, D. Divsalar, G. Motorsi, and F. Pollara, "A soft-input soft-output app module for iterative decoding of concatenated codes," *IEEE Communication Letters*, pp. 22–24, 1997.

[45] G. T. G. Caire and E. Biglieri, "Bit-interleaved coded modulation," in *Proceedings of IEEE International Symposium on Information Theory (ISIT)*, p. 96, June-July 1997.

[46] G. Caire and G. Taricco and E. Biglieri, "Bit-Interleaved Coded Modulation," *IEEE Transactions on Information Theory*, vol. 44, pp. 927–946, May 1998.

[47] J. S. e. S. ten Brink and R.-H. Yan, "Iterative demapping and decoding for multi-level modulation," in *IEEE Global Telecommunications Conference (GLOBCOM)*, vol. 1, (Sydney,NSW), pp. 579–584, June-July 1998.

[48] X. Li and J.A. Ritcey, "Bit-interleaved coded modulation with iterative decoding," *IEEE Communications Letters*, vol. 1, November 1997.

[49] X. Li and J.A. Ritcey, "Bit-interleaved coded modulation with iterative decoding using soft feedback," *IEE Electronics Letters*, vol. 34, pp. 942–943, May 1998.

[50] X. Li and J.A. Ritcey, "Trellis-Coded Modulation with Bit Interleaving and Iterative Decoding," *IEEE Journal on Selected Areas in Communications*, vol. 17, April 1999.

[51] X. Wang and H. Poor, "Iterative (turbo) soft interference cancellation and decoding for coded CDMA," *IEEE Transactions on Communications*, vol. 47, pp. 1046–1061, July 1999.

[52] D. W. e. A. Sezgin and V. Kuehn, "Analysis of mapping strategies for turbo-coded space-time block codes," in *Proceedings of IEEE Information Theory Workshop*, vol. 1, (Paris, France), pp. 103–106, March-April 2003.

[53] S. Benedetto, D. Divsalar, G. Montorsi, and F. Pollara, "Serial concatenation of interleaved codes: Performance analysis, design and iterative decoding," *IEEE Transactions on Information Theory*, vol. 44, pp. 909–926, May 1998.

[54] S. D. D. Divsalar and F. Pollara, "Low complexity turb o-like codes," in *2nd International Symposium on Turbo Codes and Related Topics*, vol. 1, (Brest, France), pp. 73–80, September 2000.

[55] S. D. D. Divsalar and F. Pollara, "Serial concatenated trellis coded modulation with rate-1 inner code," in *IEEE Global Telecommunications Conference (GLOBE-COM)*, vol. 2, (San Francisco, CA), p. 777782, 2000.

[56] K. Narayanan, "Effect of precoding on the convergence of turb o equalization for partial resp onse channels," *IEEE Journal on Selected Areas in Communications*, vol. 19, pp. 686–698, April 2001.

[57] I. Lee, "The effect of a precoder on serially concatenated coding systems with an isi channel," *IEEE Transactions on Communications*, vol. 49, pp. 1168–1175, July 2001.

[58] D. D. L. Lifang and S. Dolinar, "Iterative demodulation, demapping, and decoding of coded non-square qam," *IEEE Transactions on Communications*, vol. 53, pp. 16–19, Januarary 2005.

[59] G. Foschini Jr. and M. Gans, "On limits of wireless communication in a fading environment when using multiple antennas," *Wireless Personal Communications*, vol. 6, pp. 311–335, March 1998.

[60] E. Viterbo and J. Boutros, "A universal lattice code decoder for fading channels," *IEEE Transactions on Information Theory*, vol. 45, pp. 1639–1642, July 1999.

[61] P. Aggarwal and X. D. Wang, "Multilevel sequential monte carlo algorithms for MIMO demodulation," *IEEE Transactions on Wireless Communications*, vol. 6, pp. 750–758, Feb. 2007.

[62] H. V. Poor, *An Introduction to Signal Detection and Estimation.* New York, USA: Springer, 2nd ed., 1994.

[63] D. North, "Analysis of the factors which determine singal/noise discrimination in radar.," *Technical Report PTR-6-C.*, June 1943. Reprinted in *Proceedings of IEEE*, vol. 51, July, 1963.

[64] S. Verdu, "Optimum sequence detection of asynchronous multiple-access communications," *International Symposium on Information Theory*, p. 80, September 1983.

[65] S. Verdu, "Minimum probability of error for asynchronous multiple access communication systems," *Proceeding of 1983 IEEE Military Communications Conference*, pp. 213–219, November 1983.

[66] S. Verdu, *Optimum multiuser signal detection*. University of Illinois at Urbana-Champaign: PhD thesis, August 1984.

[67] B. M. S. Chen, A. K. Samingan and L. Hanzo, "Adaptive minimum-ber linear multiuser detection for ds-cdma signals in multipath channels," *IEEE Transactions on signal processing*, vol. 49, pp. 1240–1247, June 2001.

[68] K. R. P. J. Luo and P. K. Willett, "A sub-optimal soft decision PDA method for binary quadratic programming," *Proceeding of 2001 IEEE International Conference on Systems, Man and Cybernetics*, vol. 5, no. 5, pp. 3140–3145, 2001.

[69] R. Lupas and S. Verdu, "Linear multiuser detectors for synchronous Code-Division Multiple-Access channels," *IEEE Transactions on Information Theory*, vol. 35, pp. 123–136, Jan 1989.

[70] D. Shnidman, "A generalized Nyquist criterion and an optimum linear receiver for a pulse modulation system.," *Bell System Technical Journal*, pp. 2163–2177, November 1967.

[71] S. Verdu, "Near-far resistant receivers for ds/ssma communications.," *U.S. Army Research Proposal, Contract DAAL03-87-K-0062*, 1986.

[72] R. S. Z. Xie and C. Rushforth, "A family of suboptimum detectors for coherent multiuser communications.," *IEEE Journal on Selected Areas in Communications*, pp. 683–690, May 1990.

[73] U. Madhow and M. L. Honig, "Mmse interference suppression for direct-sequence spread spectrum cdma.," *IEEE Transactions on Communciations*, pp. 3178–3188, December 1994.

[74] F. T. M. Rupf and J. L. Massey, "User-spreading demodulation for code-division multiple-access systems.," *IEEE Journal on Selected Areas in Communications*, vol. 12, pp. 3178–3188, December 1994.

[75] T. K. Kashihara, "Adaptive cancellation of mutual interference in spread spectrum multiple access.," *Proceeding of 1980 IEEE International Communications Conference*, vol. 44, no. 4, pp. 1–5, 1980.

[76] M. K. Varanasi and B. Aazhang, "Near-optimal detection in synchronous Code-Division Multiple-Access systems," *IEEE Transactions on Communications*, vol. 39, pp. 725–736, May 1991.

[77] M. K. Varanasi, "Decision feedback multiuser detection: a systematic approach," *IEEE Transactions on Information Theory*, vol. 45, pp. 219–240, Janurary 1999.

[78] M. K. Varanasi, "Group detection for synchronous Gaussian Code-Division Multiple-Access channels," *IEEE Transactions on Information Theory*, vol. 41, pp. 1083–1096, July 1995.

[79] P. W. J. Luo, K. Pattipati and G. Levchuk, "Optimal grouping algorithm for a group decision feedback detector in synchronous Code Division Multi-Access communications," *IEEE Transactions on Communications*, vol. 51, pp. 341–346, March 2003.

[80] S. Verdú, *Multiuser Detection*. Cambridge, UK: Cambridge University Press, 1998.

[81] M. Tanner, *Tools for Statistics Inference*. New York: Springer, 1991.

[82] X. Wang and R. Chen, "Adaptive bayesian multiuser detection for synchronous CDMA with Gaussian and impulsive noise," *IEEE Transactions on Signal Processing*, vol. 47, pp. 2013–2028, July 2000.

[83] R. Chen and T.-H. Li, "Blind restoration of linearly degraded discrete signals by Gibbs sampler," *IEEE Transactions on Signal Processing*, vol. 43, pp. 2410–2413, 1995.

[84] E.-L. K. L. Hanzo, L.-L. Yang and K. Yen, *OFDM and MC-CDMA for Broadband Multi-User Communications, WLANs and Broadcasting*. Chichester, UK: John Wiley and Sons, Ltd, 2003.

[85] J. Boutrous and E. Viterbo, "Signal space diversity: A power and bandwidth efficient diversity technique for the rayleigh fading channel," *IEEE Transactions on Information Theory*, vol. 44, pp. 1453–1467, July 1998.

[86] K. M. W. Z.-Q. L. W. K. Ma, T. N. Davidson and P.-K. Ching, "Quasi-maximum-likelihood multiuser detection using semi-definite relaxation with application to synchronous CDMA," *IEEE Transactions on Signal Processing*, vol. 50, pp. 912–922, April 2002.

[87] P. W. J. Luo, K. Pattipati and G. Levchuk, "A class of coordinate descent methods for multiuser detection," *ICASSP2000*, vol. 48, pp. 1374–1383, August 2000.

[88] G. K. Glover, F. M. Amini and B. Alidaee, *A New Evolutionary Metaheuristic for the Unconstrained Binary Quadratic Programming*. School of Business, University of Colorado, Boulder: A case study of the Scatter Search, September 1999.

[89] D. P. Bertsekas, *Nonlinear Programming*. Belmont, MA: Athena Scientific Press, 1999.

[90] J. N. T. D. P. Bertsekas and C. Wu, "Rollout algorithms for combinatorial optimization," *Journal of Heuristics*, vol. 5, pp. 89–108, 1999.

[91] R. M. Golden, *Mathematical Methods for Neural Network Analysis and Design*. Cambridge, MA: The MIT Press, 1996.

[92] C. Ergun and K. Hacioglu, "Multiuser detection using a genetic algorithm in CDMA communication systems," *IEEE Transactions on Communications*, June 2000.

[93] E.-L. K. L. Hanzo, L.-L. Yang and K. Yen, *Single- and Multi-Carrier DS-CDMA Multi-User Detection, Space-Time Spreading, Synchronisation and Standards*. Chichester, UK: John Wiley and Sons, Ltd, 2003.

[94] S.-X. N. M. Jiang and L. Hanzo, "Hybrid iterative multiuser detection for channel coded space division multiple access OFDM systems," *IEEE Transactions on Vehicular Technology*, vol. 55, pp. 115–127, Janurary 2006.

[95] T. C. Fogarty, "Using the genetic algorithm to adapt intelligent systems," *Proceedings of the IEE Colloquium on Symbols Versus Neurons*, vol. 12, pp. 1–4, Janurary 1990.

[96] D. Fogel, "What is evolutionary computation?," *IEEE Spectrum*, vol. 37, pp. 28–32, February 2000.

[97] J. Kennedy and R. Eberhart, "Particle swarm optimization," *Proceedings of the IEEE International Conference on Neural Networks*, vol. 4, pp. 1942–1948, 1995.

[98] M. Dorigo and L. Gambardella, "Ant colony system: a cooperative learning approach to the travelling salesman problem," *IEEE Transactions on Evolutionary Computation*, vol. 1, pp. 53–66, April 1997.

[99] M. Dorigo and G. D. Caro, "Ant colony optimization: a new meta-heuristic," *Proceedings of the Congress on Evolutionary Computation*, vol. 2, pp. 1470–1477, 1999.

[100] M. M. M. Dorigo, L. Gambardella and T. Stutzle, "Guest editorial: special section on any colony optimization," *IEEE Transactions on Evolutionary Computation*, vol. 6, pp. 317–319, August 2002.

[101] S. Thoen, L. Deneire, L. V. der Perre, M. Engels, and H. D. Man, "Constrained least squares detector for OFDM/SDMA-based wireless networks," *IEEE Transactions on Wireless Communications*, vol. 2, pp. 129–140, Jan. 2003.

[102] G. J. Foschini, "Layered space-time architecture for wireless communication in fading environments when using multiple antennas," *Bell Labs Technical Journal*, vol. 2, pp. 41–59, 1996.

[103] X. D. Wang and H. V. Poor, "Iterative (turbo) soft interference cancellation and decoding for coded CDMA," *IEEE Transactions on Communications*, vol. 47, pp. 1046–1061, July 1999.

[104] U. Fincke and M. Pohst, "Improved methods for calculating vectors of short length in a lattice, including a complexity analysis," *Mathematics of Computation*, vol. Vol. 44, pp. 463–471, April 1985.

[105] M. O. Damen, K. Abed-Meraim, and J. C. Belfiore, "Generalised sphere decoder for asymmetrical space-time communication architecture," *Electronics Letters*, vol. 36, pp. 166–167, Jan. 2000.

[106] D. Gesbert, "Robust linear MIMO receivers: a minimum error-rate approach," *IEEE Transactions on Signal Processing*, vol. 51, pp. 2863–2871, Nov. 2003.

[107] B. M. Hochwald and S. ten Brink, "Achieving near-capacity on a multiple-antenna channel," *IEEE Transactions on Communications*, vol. 51, pp. 389–399, Mar. 2003.

[108] H. Vikalo, B. Hassibi, and T. Kailath, "Iterative decoding for MIMO channels via modified sphere decoding," *IEEE Transactions on Wireless Communications*, vol. 3, pp. 2299–2311, Nov. 2004.

[109] R. Gallager, "Low-density parity-check codes," *IRE Transactions on Information Theory*, vol. 8, pp. 21–28, Jan. 1962.

[110] S. Chen, N. N. Ahmad, and L. Hanzo, "Adaptive minimum bit-error rate beamforming," *IEEE Transactions on Wireless Communications*, vol. 4, pp. 341–348, Mar. 2005.

[111] Z. Yang, C. Liu, and J. He, "A new approach for fast generalized sphere decoding in MIMO systems," *IEEE Signal Processing Letters*, vol. 12, pp. 41–44, Jan. 2005.

[112] H. Zhu, B. Farhang-Boroujeny, and R. R. Chen, "On performance of sphere decoding and markov chain monte carlo detection methods," *IEEE Signal Processing Letters*, vol. 12, pp. 669–672, Oct. 2005.

[113] H. Lee, B. Lee, and I. Lee, "Iterative detection and decoding with an improved v-BLAST for MIMO-OFDM systems," *IEEE Journal on Selected Areas in Communications*, vol. 24, pp. 504–513, Mar. 2006.

[114] Z. Guo and P. Nilsson, "Algorithm and implementation of the K-best sphere decoding for MIMO detection," *IEEE Journal on Selected Areas in Communications*, vol. 24, pp. 491–503, Mar. 2006.

[115] R. Wang and G. B. Giannakis, "Approaching MIMO channel capacity with soft detection based on hard sphere decoding," *IEEE Transactions on Communications*, vol. 54, pp. 587–590, Apr. 2006.

[116] R. S. Mozos and M. J. F. G. Garcia, "Efficient complex sphere decoding for MC-CDMA systems," *IEEE Transactions on Wireless Communications*, vol. 5, pp. 2992–2996, Nov. 2006.

[117] B. Farhang-Boroujeny, H. Zhu, and Z. Shi, "Markov chain monte carlo algorithms for CDMA and MIMO communication systems," *IEEE Transactions on Signal Processing*, vol. 54, pp. 1896–1909, May 2006.

[118] M. D. A. Colorni and V. Maniezzo, "Distributed optimization by ant colonies," *Proceedings of the European Conference on Artificial Life*.

[119] T. St

[120] V. M. M. Dorigo and A. Colorni, "Ant system: optimization by a colony of cooperating agents," *IEEE Transactions on Systems, Man and Cybernetics, Part-B*, vol. 26, pp. 29–41, February 1996.

[121] M. Dorigo and L.-M. Gambardella, "Ant colony system: a cooperative learning approach to the traveling salesman problem," *IEEE Transactions on Evolutionary Computation*, vol. 1, pp. 53–66, April 1997.

[122] C. F. E.-G. Talbi, O. Roux and D. Robillard, "Parallel ant colonies for the quadratic assignment problem," *Future Generation Computer Systems*, vol. 17, pp. 441–449, Januruary 2001.

[123] V. M. M. T. A. Colorn, M. Dorigo, "Ant system for job-shop scheduling," *JORBEL-Belgian Journal of Operations Research, Statistics and Computer Science*, vol. 34, pp. 39–53, 1994.

[124] G.-D. Caro and M. Dorigo, "Mobile agents for adaptive routing," *Proceedings of IEEE Hawaii International Conference on System Sciences*, vol. 7, pp. 74–83, 1998.

[125] K.-M. Sim and W.-H. Sun, "Ant colony optimization for routing and load-balancing: survey and new directions," *IEEE Transactions on Systems, Man and Cybernetics, Part A*, vol. 33, pp. 560–572, September 2003.

[126] X.-M. G. P. Wang and G.-L. Liu, "Multi-qos routing for leo satellite networks," *Proceedings of IEEE International Conference on Advanced Communication Technology*, vol. 1, pp. 728–731, 2007.

[127] G.-D. C. M. Dorigo and L.-M. Gambardella, "Ant algorithms for distributed discrete optimition," *Proceedings of the International Conference on Artificial Life*, vol. 5, pp. 137–172, 1999.

[128] T. St

[129] J.-J. Lai and J.-K. Lain, "Antenna-diversity-assisted ant-colony-based multiuser detection for ds-cdma systems," *Proceedings of the IEEE International Workshop on Cellular Neural Networks and Their Applications*, vol. 3, pp. 106–109, 2005.

[130] L.-L. Y. C. Xu and L. Hanzo, "Ant-colony-based multiuser detection for mc ds-cdma systems," *Proceedings of the IEEE Vehicular Technology conference, Fall*.

[131] L.-L. Y. C. Xu, B. Hu and L. Hanzo, "Ant-colony-based multiuser detection for multi-functional antenna array assisted mc ds-cdma systems," *IEEE Transactions on Vehicular Technology*, vol. 57, pp. 658–663, January 2008.

[132] P. P. M. Birattari and M. Dorigo, "On the invariance of any colony optimization," *IEEE Transactions on Evolutionary Computation*, vol. 11, pp. 732–742, December 2007.

[133] A. B. B. N. S. L. Hijazi and S. Das, "Ant-colony based optimal MC-CDMA multiuser detector," *Proceedings of the IEEE International Conference on Wireless and Mobile Computing, Networking and Communications*, vol. 1, pp. 128–132, 2005.

[134] S. L. Hijazi and B. Natarajan, "Novel low-complexity DS-CDMA multiuser detector based on ant colony optimization," *Proceedings of IEEE Vehicular Technology Conference*, vol. 3, pp. 1939–1943, 2004.

[135] B. N. S. L. Hijazi and S. Das, "An ant-colony algorithm for multi-user detection in wireless communication systems," *Proceedings of Genetic and Evolutionary Computation Conference*.

[136] S. L. Hijazi and B. Natarajan, "Near-optimal multiuser detection in asynchronous mc-cdma via the ant colony approach," *Proceedings of the IEEE International Symposium on Wireless Pervasive Computing*, vol. 1, pp. 274–279, 2007.

[137] P.-P. Grass, "La reconstruction du nid et les coordinations inter-individuelles chez belicositermes natalensis et cubitermes sp," in *La thorie de la Stigmergie : Essai dinterprtation du comportement des termites constructeurs*, vol. 6, (Insectes Sociaux), pp. 41–80, 1959.

[138] J. P. J.L. Denebourg and J. Verhaeghe, "Probabilistic behaviour in ants : a strategy of errors?," *Journal of Theoretical Biology*, vol. 5, no. 105, pp. 234–241, 1983.

[139] F. Moyson and B. Manderick, "The collective behaviour of ants: an example of self-organization in massive parallelism," in *Proceedings of AAAI Spring Symposium on Parallel Models of Intelligence*, (Stanford, California), 1988.

[140] J.-L. D. e. J.-M. P. S. Goss, S. Aron, "The self-organized exploratory pattern of the argentine ant," *Naturwissenschaften*, vol. 76, no. 1, pp. 579–581, 1989.

[141] M. P. F. W. M. Ebling, M. Di Loreto and D. Jefferson, "An ant foraging model implemented on the time warp operating system," in *Proceedings of the SCS Multiconference on Distributed Simulation*, 1998.

[142] V. M. Dorigo M. and A. Colorni, "Positive feedback as a search strategy," rapport technique numro 91-016,, Dip. Elettronica, Politecnico di Milano, Italy, 1991.

[143] V. M. M. Dorigo and A. Colorni, "Ant system: optimization by a colony of cooperating agents," *IEEE Transactions on Systems, Man, and Cybernetics–Part B*, vol. 26, no. 1, pp. 29–41, 1996.

[144] T. Sttzle and H. Hoos, "Max-min ant system," *Future Generation Computer Systems*, vol. 16, no. 1, pp. 889–914, 2000.

[145] M. Dorigo and L. Gambardella, "Ant colony system : A cooperative learning approach to the traveling salesman problem," *IEEE Transactions on Evolutionary Computation*, vol. 1, no. 1, pp. 53–66, 1997.

[146] J. B. R. Schoonderwoerd, O. Holland and L. Rothkrantz, "Ant-based load balancing in telecommunication networks," *Adaptive Behaviour*, vol. 5, no. 2, pp. 169–207, 1997.

[147] T. Sttzle, "Parallelization strategies for ant colony optimization)," in *Proceedings of PPSN-V, Fifth International Conference on Parallel Problem Solving from Nature*, vol. 1498, (Zurich, Switzerland), pp. 722–731, 1998.

[148] M. D. e. G. T. . Bonabeau, *Swarm intelligence*. UK: Oxford University Press, 1999.

[149] G. D. C. M. Dorigo and T. Sttzle, "Special issue on,"

[150] M. M. D. Merkle and H. Schmeck, "Ant colony optimization for resource-constrained project scheduling," in *Proceedings of the Genetic and Evolutionary Computation Conference (GECCO 2000)*, pp. 893–900, 2000.

[151] W. Gutjahr, "A graph-based ant system and its convergence," *Future Generation Computer Systems*, vol. 16, no. 2, pp. 873–888, 2000.

[152] D. M. S. Iredi and M. Middendorf, "Bi-criterion optimization with multi colony ant algorithms, evolutionary multi-criterion optimization," in *First International Conference (EMO01)*, (Zurich, Switzerland), pp. 359–372, 2001.

[153] G. J. A. de Campos, L. M. and J. M. Puerta, "Learning bayesian networks by ant colony optimisation: Searching in two different spaces," *Mathware and Soft Computing*, vol. 9, no. 2, pp. 2–3, 2002.

[154] L. G. L. Bianchi and M.Dorigo, "An ant colony optimization approach to the probabilistic traveling salesman problem, ppsn-vii," in *Seventh International Conference on Parallel Problem Solving from Nature, Lecture Notes in Computer Science*, (Berlin, Allemagne), pp. 40–52, 2002.

[155] N. M. M. Zlochin, M. Birattari and M. Dorigo, "Model-based search for combinatorial optimization: A critical survey," *Annals of Operations Research*, vol. 131, pp. 373–395, 2004.

[156] R. A. H. A. Shmygelska and H. H. Hoos, "An ant colony algorithm for the 2d hp protein folding problem," in *Proceedings of the 3rd International Workshop on Ant Algorithms/ANTS 2002, Lecture Notes in Computer Science*, pp. 40–52, 2002.

[157] L.-L. Y. C. Xu, R. G. Maunder and L. Hanzo, "Near-optimum soft-output ant-colony-optimization based multiuser detection for the DS-CDMA," *IEEE International Conference on Communications*.

[158] L.-L. Y. C. Xu, R. G. Maunder and L. Hanzo, "Near-optimum multiuser detectors using soft-output ant-colony-optimization for the DS-CDMA uplink," *IEEE Signal Processing Letters*, vol. 16, pp. 137 –140, January 2009.

[159] B. Y. L. Hanzo, T.H. Liew, *Turbo Coding, Turbo Equalisation and Space-Time Coding*. Chichester, UK: John Wiley and Sons, Ltd, 2002.

[160] S. Kay, *Fundamentals of Statistical Signal Processing, Estimation Theory*. New Jersey, USA: Prentice Hall, 1993.

[161] Wikipedia, "Normal distribution — wikipedia, the free encyclopedia," 2010. [Online; accessed 6-January-2010].

[162] Wikipedia, "Np-hard — wikipedia, the free encyclopedia," 2009. [Online; accessed 7-January-2010].

[163] S. N. L. Hanzo, J.S. Blogh, *3G, HSPA and FDD versus TDD Networking, Second Edition*. Chichester, UK: John Wiley and Sons, Ltd, 2008.

[164] L. Hanzo, W. Webb, and T. Keller, *Single- and Multi-carrier Quadrature Amplitude Modulation*. New York, USA: IEEE Press-John Wiley, April 2000.

[165] S. B. Weinstein and P. M. Ebert, "Data transmission by frequency division multiplexing using the discrete fourier transform," *IEEE Transactions on Communication Technology*, vol. COM–19, pp. 628–634, October 1971.

[166] J. Bingham, "Multicarrier modulation for data transmission: an idea whose time has come," *IEEE Communications Magazine*, pp. 5–14, May 1990.

[167] I. Kalet, "The multitone channel," *IEEE Transactions on Communications*, vol. 37, pp. 119–124, February 1989.

[168] D.-W. Lee and L. Milstein, "Analysis of a multicarrier ds-cdma code-acquisition system," *IEEE Transactions on Communications*, vol. 47, pp. 1233–1244, August 1999.

[169] L.-L. Yang and L. Hanzo, "Blind soft-detection assisted frequency-hopping multciarrier ds-cdma systems," in *Proceedings of IEEE GLOBECOM'99*, (Rio de Janeiro, Brazil), pp. 842–846.

[170] S. Slimane, "Mc-cdma with quadrature spreading for wireless communication systems," *European Transactions on Telecommunications*, vol. 9, pp. 371–378, July-August 1998.

[171] L. L. Yang and L. Hanzo, "Blind joint soft-detection assisted slow frequency-hopping multicarrier DS-CDMA," *IEEE Transactions on Communication*, vol. 48, no. 9, pp. 1520–1529, 2000.

[172] X. Gui and T. Ng, "Performance of asynchronous orthogonal multicarrier CDMA system in frequency selective fading channel," *IEEE Transactions on Communications*, vol. 47, pp. 1084–1091, July 1999.

[173] L.-L. Yang and L. Hanzo, "Slow frequency-hopping multicarrier ds-cdma," in *International Symposium on Wireless Personal Multimedia Communciation (WPMC'99)*, (Amsterdam, The Netherlands), pp. 224–229.

[174] R. Li and G. Stette, "Time-limited orthogonal multicarrier modulation schemes," *IEEE Transactions on Communications*, vol. 43, pp. 1269–1272, February/March/April 1995.

[175] L. N. K. Bose, C. R. Rao and C. Godara, *Handbook of statistics 10, signal process- ing and its applications: constrained beamforming and adaptive algorithms.* Amsterdam, The Netherlands: Amsterdam, 1993.

[176] D. H. Johnson and D. E. Dudgeon, *Array signal processing: concepts and techniques.* Englewood Cliffs: Englewood Cliffs: NJ:prentice-Hall, 1993.

[177] R. A. Monzingo and T. W. Miller, *Introduction to adaptive arrays.* New York, USA: Wiley, 1980.

[178] V. J. Garg and L. Huntington, "Application of adaptive array antenna to a tdma cellular/pcs system," *IEEE Communications Magazine*, vol. 35, pp. 148–152, October 1997.

[179] J. Schodorf and D. Williams, "Array processing techniques for multiuser detection," *IEEE Transactions on Communications*, vol. 45, pp. 1375–1378, November 1997.

[180] S. A. Zekavat and C. R. Nassar, "Smart antenna arrays with oscillating beam patterns: characterization of transmit diversity in semi-elliptic coverage," *IEEE Transactions on Communications*, vol. 50, pp. 1549–1556, October 2002.

[181] S. M. Alamouti, "A Simple Transmit Diversity Technique for Wireless Communications," *IEEE Journal on Selected Areas in Communications*, vol. 16, pp. 1451–1458, October 1998.

[182] B. Hochwald, T. L. Marzetta, and C. B. Papadias, "A transmitter diversity scheme for wideband CDMA systems based on space-time spreading," *IEEE Journal on Selected Areas in Communications*, vol. 19, pp. 48–60, Jan. 2001.

[183] V. Tarokh, N. Seshadri, and A. R. Calderbank, "Space-Time Codes for High Data Rate Wireless Communication: Performance Criterion and Code Construction," *IEEE Transactions on Information Theory*, vol. 44, pp. 744–765, March 1998.

[184] D. Brennan, "Linear diversity combining techniques," *Proc. IRE*, vol. 47, pp. 1075–1102, 1959.

[185] C. Y. Wei, L. Wang, and L. Hanzo, "Iterative irregular sphere detection in high-rate downlink SDMA systems," *IEEE Transactions on Vehicular Technology*, vol. 58, pp. 3855–3861, Sept. 2009.

[186] L.-L. Y. B. Hu and L. Hanzo, "Performance of the smart antenna aided multicarrier DS-CDMA uplink," *IEEE 60th Vehicular Technology Conference*.

[187] L.-L. Y. B. Hu and L.Hanzo, "Performance of the smart antenna aided generalized multicarrier ds-cdma downlink using both time-domain spreading and steered space-time spreading," *IEEE 62nd Vehicular Technology Conference*, vol. 1, pp. 458–462, September 2005.

[188] L.-L. Y. C. Xu, B. Hu and L. Hanzo, "Multi-functional antenna array assisted MC DS-CDMA using downlink preprocessing based on singular value decomposition," *Proceedings of the IEEE Vehicular Technology conference, Spring*.

[189] S. Verdú, "Minimum probability of error for asynchronous Gaussian multiple-access channel," *IEEE Transactions on Communications*, vol. 32, pp. 85–96, January 1986.

[190] L. K. P. S. B.P. Crow, I. Widjaja, "Ieee 802.11 wireless local area networks," *IEEE Communication Magazine*, vol. 35, pp. 116–126, September 1997.

[191] ETSI, *Digital Audio Broadcasting (DAB)*, 2nd ed., May 1997. ETS 300 401.

[192] ETSI, *Digital Video Broadcasting (DVB); Framing structure, channel coding and modulation for digital terrestrial television*, August 1997. EN 300 744 V1.1.2.

[193] N. Yee, J.-P. Linnartz, and G. Fettweis, "Multicarrier CDMA in indoor wireless radio networks," *IEICE Transactions on Communications*, vol. E77-B, pp. 900–904, July 1994.

[194] B. M. Popovic, "Spreading sequences for multicarrier CDMA systems," *IEEE Transactions on Comminications*, vol. 47, no. 6, pp. 918–926, 1999.

[195] N. Yee, J.-P. Linnartz, and G. Fettweis, "Multicarrier CDMA in indoor wireless radio networks," in *PIMRC'93*, pp. 109–113, 1993.

[196] S. Hara and R. Prasad, "Overview of multicarrier CDMA," *IEEE Communications Magazine*, pp. 126–133, December 1997.

[197] V. M. DaSilva and E. S. Sousa, "Multicarrier orthogonal CDMA codes for quasi-synchronous communication systems," *IEEE Journal on Selected Areas in Communications*, vol. 14, pp. 502–511, April 1996.

[198] J.-P. L. N. Yee and G. P. Fettweis, "Performance of orthogonal CDMA codes for quasi-synchronous communication systems," in *Proceedings of IEEE ICUPC 1993*, (Ottawa, Canada), pp. 995–999, October 1993.

[199] Y. Sanada and M. Nakagawa, "A multiuser interference cancellation technique utilizing convolutional codes and multicarrier modulation for wireless indoor communications," *IEEE Journal on Selected Areas in Communications*, vol. 14, pp. 1500–1509, October 1996.

[200] K. W. S. T. S. R. R. B. Ertel, P. Cardieri and J. H. Reed, "Overview of spatial channel models for antenna array communication systems," *IEEE Personal Communications Magaziney*, vol. 5, pp. 10–22, February 1998.

[201] L.-L. Y. B. Hu and L. Hanzo, "Near-optimum soft-output ant-colony-optimization based multiuser detection for the DS-CDMA," *IEEE Vehicular Technology Conference Fall*.

[202] V. Tarokh, H. Jafarkhani, and A. R. Calderbank, "Space-time block coding for wireless communications: Performance results," *IEEE Journal on Selected Areas in Communications*, vol. 17, pp. 451–460, March 1999.

[203] M. E.-H. L. Hanzo, O. Alamri and N. Wu, *Near-Capacity Multi-Functional MIMO Systems*. USA: John Wiley and Sons, Ltd, 2009.

[204] C. E. Shannon, "A mathematical theory of communication," *Bell System Technical Journal*, vol. 27, pp. 379–423, 1948.

[205] L. Hanzo, T.H. Liew and B.L. Yeap, *Turbo Coding, Turbo Equalisation and Space Time Coding for Transmission over Wireless channels*. New York, USA: John Willy IEEE Press, 2002.

[206] L.R. Bahl and J. Cocke and F. Jelinek and J. Raviv, "Optimal Decoding of Linear Codes for Minimising Symbol Error Rate," *IEEE Transactions on Information Theory*, vol. 20, pp. 284–287, March 1974.

[207] S. Benedetto, D. Divsalar, G. Montorsi and F. Pollara, "A Soft-Input Soft-Output APP Module for Iterative Decoding of concatenated codes," *IEEE Communications Letter*, vol. 1, pp. 22–24, January 1997.

[208] G. M. S. Benedetto, D. Divsalar and F. Pollara, "Serial concatenation of interleaved codes: performance analysis, design, and iterative decoding," *IEEE Transactions on Information Theory*, vol. 44, pp. 909–926, May 1998.

[209] S. ten Brink, "Convergence of iterative decoding," *Electronics Letters*, vol. 35, pp. 806–808, May 1999.

[210] J. W. Lee and R. E. Blahut, "Generalized EXIT chart and BER analysis of finite-length turbo codes," in *Proceedings of the IEEE Global Telecommunications Conference*, vol. 4, (San Fransisco, CA, USA), pp. 2067–2072, December 2003.

[211] J. Hagenauer, "The exit chart - introduction to extrinsic information transfer in iterative processing," in *Proceeding of the European Signal Processing Conference*, vol. 2, (Vienna, Austria), pp. 1541–1548, September 2004.

[212] L.-L. Y. C. Xu, R. G.Maunder and L. Hanzo, "Near-Optimum Multiuser Detectors Using Soft-Output Ant-Colony-Optimization for the DS-CDMA Uplink," *IEEE Signal Processing Letters*, vol. 57, pp. 137–140, February 2009.